Modelling of gas transport in coal - a hybrid coupled dual porosity and discrete fracture approach

Min Chen

Geoenvironmental Research Centre
Cardiff School of Engineering
Cardiff University

Thesis submitted in candidature for the degree of Doctor of Philosophy at Cardiff University

December 2019

Declaration

This work has not been submitted in substance for any other degree or award at this or any other university or place of learning, nor is being submitted concurrently in candidature for any degree or other award.

Signed…… *Date* ……

Statement 1

This thesis is being submitted in partial fulfilment of the requirements for the degree of PhD.

Signed…… *Date* ……

Statement 2

This thesis is the result of my own independent work/investigation, except where otherwise stated. Other sources are acknowledged by explicit references. The views expressed are my own.

Signed…… *Date* ……

Statement 3

I hereby give consent for my thesis, if accepted, to be available for photocopying and for interlibrary loan, and for the title and summary to be made available to outside organisations.

Signed…… *Date* ……

Acknowledgement

First of all, I would like to express my deep and sincere gratitude to my supervisor, Professor Hywel Thomas, for his continuous encouragement, technical and academical guidance throughout the various stage of my PhD. I am really grateful for the opportunity provided for me to study at Cardiff University.

I would also express my deep thanks to my co-supervisor, Dr Lee Hosking for his continuous encouragement, technical support and academical guidance with patience during the period of this research, which enabled my research work to move forward smoothly. This thesis could not be completed within three years without his contribution, technical comments and inspiration. I am deeply impressed with his profound scientific visions and rigorous academic attitudes.

The work undertaken would not have be possible without the invaluable financial support of this research through PhD fellowship from China Scholarship Council (CSC) during the period of my PhD study. Hence, this sponsorship is gratefully acknowledged.

My thanks also go to all the past and present members of the Geoenvironmental Research Centre (GRC) at Cardiff University for their support and friendship. Aleksandra, Alejandro, Irfan, Shakil, Renato, Jack, James, Jamie, Hishiv, Manhui Wang, Manju, Richard, Sivachidambaram, Sanjana, Zhihong Zhang, Ni An, Wu Gao, Maram, Deborah, Dawnn, Fiachra, Xiao Yin, Linyong Cui among many others. It has been good fun to work with such a variety of characters. I am very thankful for the happy time we have spent together.

Last but not least, I must owe my greatest thank to my dearest parents and sisters for their continuous support, inspiration and everlasting love. Without their constant love and strong support, none of my achievement would have been possible.

Publications

Journal papers:

1. **Chen, M.**, Hosking, L.J., Sandford, R.J. and Thomas, H.R., 2019. Dual porosity modelling of the coupled mechanical response of coal to gas flow and adsorption. International Journal of Coal Geology, 205, pp.115-125.
2. **Chen, M.**, Hosking, L.J., Sandford, R.J. and Thomas, H.R., Numerical analysis of improvements to CO_2 injectivity in coal seams through stimulated fracture connection to the injection well. Rock mechanics and rock engineering (under review).
3. **Chen, M.**, Hosking, L.J., Sandford, R.J. and Thomas, H.R., A coupled compressible flow and geomechanics model for dynamic fracture aperture during carbon sequestration in coal. International Journal for Numerical and Analytical Methods in Geomechanics (under review).
4. Hosking, L.J., **Chen, M.**, Sandford, R.J. and Thomas, H.R., Analysis of coupled dual porosity thermo-hydro-chemo-mechanical behaviour during CO_2 injection in coal. Geomechanics for Energy and the Environment (under review).

Conference papers

1. **Chen, M**., Hosking, L.J. and Thomas, H.R., 2018, October. Non-isothermal Gas Flow During Carbon Sequestration in Coalbeds. In The 8th International Congress on Environmental Geotechnics.
2. Thomas, H.R., Hosking, L.J., Sandford, R.J., Zagorščak, R., **Chen, M**. and An, N., 2018, October. Deep Ground and Energy: Carbon Sequestration and Coal Gasification. In The 8th International Congress on Environmental Geotechnics.

Manuscript to be submitted

1. **Chen, M**., Hosking, L.J. and Thomas, H.R. Modelling adsorption-diffusion process of gas transport in coal matrix.

Summary

This thesis describes an investigation of coupled thermal–hydraulic-chemical–mechanical (THCM) behaviour of rock with a complex fracture system, which has been achieved through the advancement and application of a theoretical and numerical modelling platform of THCM processes.

A hybrid coupled dual continuum and discrete fracture model has been developed based on the thermoporoelastic theory, which considers multiphase fluid flow, heat transfer, geochemical processes, and deformation in discretely fractured rock such as coal. The uniformly distributed natural fracture network, composed of micro-fractures, and the rock matrix itself have been modelled using a dual porosity approach. Large-scale fractures have been represented explicitly as discrete fractures. The coupling between the different media has been achieved via a mass and heat exchange processes.

Appropriate relationships were incorporated in the model to accurately describe the major thermodynamic properties of compressible fluids and the chemo-mechanical deformation of coal during carbon dioxide (CO_2) sequestration and coalbed methane (CBM) recovery. Furthermore, a new porosity-permeability model was derived in this work describing feedback of the physical and chemical mechanisms of deformation on coal structure and fluid flow, which provides an improved physical interpretation for changes of the pore space.

The developed model has been implemented in an existing coupled thermal, hydraulic, chemical, and mechanical framework. A numerical solution was presented using the Galerkin finite element method for the spatial discretisation and the finite difference method for temporal discretisation. The discrete fractures were idealised as lower-dimensional geometric objects with the discrete fracture elements located on the edges of continuum elements sharing the same nodes. The coupling between the two flow systems was achieved by using the principle of superposition.

Verification of the approach proposed has been addressed via a series of benchmark tests. The results obtained provided an evaluation of the numerical implementation of the theoretical framework for non-isothermal unsaturated flow in deformable fractured rock, which established a good level of confidence in the accuracy of the implementation of the theoretical and numerical formulations. Validation of the model using experimental data on coal-gas interactions and field data of CBM production has been included to examine the capacities of the proposed model to interpret processes in the material behaviour and various physical mechanisms involved. These tests have indicated that the model is capable of simulating the key physical and chemical processes occurring during CBM recovery and CO_2 storage into coal seams.

A set of simulations have been performed to study the coupled THCM behaviour of low permeability coal reservoirs during CBM recovery and CO_2 injection, and the effect of hydraulic fracturing stimulation on the CBM production and CO_2 injectivity has been considered. A substantive insight into the coupled behaviour has been gained. Overall, analysis of the evolutions of the primary field variables indicated that the fluid pressure, temperature, and pore structure in coal seams were influenced by CBM recovery and CO_2 injection. CO_2 injection induced swelling can cause loss of permeability and eventual rebound of coal permeability during CO_2 sequestration with enhanced CBM recovery. Comparison of cumulative gas production and injection shown that CO_2 injection together with hydraulic fracturing treatment was an effective solution to increase the CBM production and improve the injectivity of CO_2 in low permeability coal seams.

In this work, the new capabilities of the model have been demonstrated with regards to the investigation of the coupled processes of a coal-gas system. In particular, the model can be further utilised in the study of a broad new range of applications involving non-isothermal, multiphase, multicomponent gas/chemical transport and deformation in unconventional gas reservoirs.

Nomenclature

Note: the subscript parameter α is used to denote the pore regions and becomes f in the fracture continuum, m in the matrix continuum and F in the discrete hydraulic fractures. β is used to denote the phase and becomes s for solid phase, g for gas phase and l for water phase.

$a_{\mathrm{m}\alpha}$	Coefficient accounting for the intermolecular interactions in the mixture
$a^{i}_{\mathrm{m}\alpha}$	Pure component factors for intermolecular interactions
$\boldsymbol{A}$	Defined in equation (4.59)
A_{fm}	Interfacial fracture-matrix specific area
A_T	Coefficient related to thermal deformation
A^{i}_{s}	Coefficient related to adsorption-induced swelling by component *i*
$\boldsymbol{B}$	Strain-displacement matrix
$\tilde{\mathrm{b}}_1$	Biot's effective stress coefficient
$\tilde{\mathrm{b}}_2$	Biot's effective stress coefficient
b^{i}_{L}	Affinity equilibrium constant of gas component *i*
$b^{i}_{L\infty}$	Affinity at infinite temperature
$b_{\mathrm{m}\alpha}$	Effective volume of the molecules contained in one mole of bulk gas
$b^{i}_{\mathrm{m}\alpha}$	Pure component factors for effective volume
$\mu^{0}_{\mathrm{g}\alpha}$	Gas mixture viscosity at low pressure
$\mathbf{C}$	Defined in equation (4.59)
$C_{\mathrm{c}_\alpha \mathrm{l}_\alpha}$	Defined in equations (3.43), (3.44) and (3.45)
$C_{\mathrm{c}_\alpha \mathrm{T}_\alpha}$	Defined in equations (3.43), (3.44) and (3.45)
$C_{\mathrm{c}_\alpha \mathbf{u}_\mathrm{s}}$	Defined in equations (3.43) and (3.44)
$\mathbf{C}_{\mathrm{c_m c_m}}$	Defined in equation (4.26)
$\mathbf{C}_{\mathrm{c_m l_m}}$	Defined in equation (4.26)
$\mathbf{C}_{\mathrm{c_m T_m}}$	Defined in equation (4.26)
$\mathbf{C}_{\mathrm{c_m} \mathbf{u}_\mathrm{s}}$	Defined in equation (4.26)
$\mathbf{C}^{\mathrm{fF}}_{\mathrm{c_f c_m}}$	Defined in equation (4.27)
$\mathbf{C}^{\mathrm{fF}}_{\mathrm{c_f c_f}}$	Defined in equation (4.27)
$\mathbf{C}^{\mathrm{fF}}_{\mathrm{c_f l_f}}$	Defined in equation (4.27)

$\mathbf{C}^{\mathrm{fF}}_{\mathrm{c_f T_m}}$ Defined in equation (4.27)

$\mathbf{C}^{\mathrm{fF}}_{\mathrm{c_f T_f}}$ Defined in equation (4.27)

$\mathbf{C}^{\mathrm{fF}}_{\mathrm{c_f}\mathbf{u}_\mathrm{s}}$ Defined in equation (4.27)

$c^{t}_{\mathrm{g}\alpha}$ Total gas concentration

c^{i}_{gA} Arithmetic means of gas concentrations of gas component *i*

c_{l} Water compressibility

$C_{\mathrm{l}_\alpha \mathrm{c}_\alpha}$ Defined in equations (3.64), (3.65) and (3.66)

$C_{\mathrm{l}_\alpha \mathrm{l}_\alpha}$ Defined in equations (3.64), (3.65) and (3.66)

$C_{\mathrm{l}_\alpha \mathrm{T}_\alpha}$ Defined in equations (3.64), (3.65) and (3.66)

$C_{\mathrm{l}_\alpha \mathbf{u}_\mathrm{s}}$ Defined in equations (3.64) and (3.65)

$\mathbf{C}_{\mathrm{l_m c_m}}$ Defined in equation (4.37)

$\mathbf{C}_{\mathrm{l_m c_f}}$ Defined in equation (4.37)

$\mathbf{C}_{\mathrm{l_m l_m}}$ Defined in equation (4.37)

$\mathbf{C}_{\mathrm{l_m T_m}}$ Defined in equation (4.37)

$\mathbf{C}_{\mathrm{l_m T_f}}$ Defined in equation (4.37)

$\mathbf{C}_{\mathrm{l_m}\mathbf{u}_\mathrm{s}}$ Defined in equation (4.37)

$\mathbf{C}^{\mathrm{fF}}_{\mathrm{l_f c_m}}$ Defined in equation (4.38)

$\mathbf{C}^{\mathrm{fF}}_{\mathrm{l_f c_f}}$ Defined in equation (4.38)

$\mathbf{C}^{\mathrm{fF}}_{\mathrm{l_f l_f}}$ Defined in equation (4.38)

$\mathbf{C}^{\mathrm{fF}}_{\mathrm{l_f T_m}}$ Defined in equation (4.38)

$\mathbf{C}^{\mathrm{fF}}_{\mathrm{l_f T_f}}$ Defined in equation (4.38)

$\mathbf{C}^{\mathrm{fF}}_{\mathrm{l_f}\mathbf{u}_\mathrm{s}}$ Defined in equation (4.38)

c_{m} Elastic drained compressibility of the porous matrix

$C^{0}_{p\mathrm{g}\alpha}$ Specific heat capacity for ideal gases

$C_{p\beta}$ Specified heat capacity of phase β

$\mathbf{C}_{\mathrm{T_m c_m}}$ Defined in equation (4.48)

$\mathbf{C}_{\mathrm{T_m T_m}}$ Defined in equation (4.48)

$\mathbf{C}^{\mathrm{fF}}_{\mathrm{T_f c_f}}$ Defined in equation (4.49)

$\mathbf{C}^{\mathrm{fF}}_{\mathrm{T_f T_f}}$ Defined in equation (4.49)

$C_{\mathrm{T}_\alpha \mathrm{T}_\alpha}$	Defined in equations (3.118), (3.119) and (3.120)
$C_{\mathrm{T}_\alpha \mathrm{c}_\alpha}$	Defined in equations (3.118), (3.119) and (3.120)
$C_{\mathbf{u}_\mathrm{s} \mathrm{c}_\alpha}$	Defined in equations (3.138)
$C_{\mathbf{u}_\mathrm{s} \mathrm{l}_\alpha}$	Defined in equations (3.138)
$C_{\mathbf{u}_\mathrm{s} \mathrm{T}_\alpha}$	Defined in equations (3.138)
$C_{\mathbf{u}_\mathrm{s} \mathbf{u}_\mathrm{s}}$	Defined in equations (3.138)
$\mathbf{C}_{\mathbf{u}_\mathrm{s} \mathrm{c}_\mathrm{m}}$	Defined in equation (4.58)
$\mathbf{C}_{\mathbf{u}_\mathrm{s} \mathrm{c}_\mathrm{f}}$	Defined in equation (4.58)
$\mathbf{C}_{\mathbf{u}_\mathrm{s} \mathrm{l}_\mathrm{m}}$	Defined in equation (4.58)
$\mathbf{C}_{\mathbf{u}_\mathrm{s} \mathrm{l}_\mathrm{f}}$	Defined in equation (4.58)
$\mathbf{C}_{\mathbf{u}_\mathrm{s} \mathrm{T}_\mathrm{m}}$	Defined in equation (4.58)
$\mathbf{C}_{\mathbf{u}_\mathrm{s} \mathbf{u}_\mathrm{s}}$	Defined in equation (4.58)
c_s	Elastic compressibility of the solid constituent
c_s^i	Concentration of adsorbed gas component *i*
c_α^i	Gas concentration of component *i*
$DC_{p\mathrm{g}\alpha}$	Departure function of specific heat capacity
$\boldsymbol{D}_\mathrm{e}$	Elasticity matrix
D_g^i	Diffusion coefficient of gas component *i*
E	Bulk Young's modulus
E_{in}^i	Interaction energy between the adsorbate and the adsorbent
E_m	Young's modulus of porous matrix
$\mathbf{f}_{\mathrm{g,m}}^j$	Defined in equation (4.26)
$\mathbf{f}_{\mathrm{g,fF}}^j$	Defined in equation (4.27)
$\mathbf{f}_{\mathrm{l,m}}$	Defined in equation (4.37)
$\mathbf{f}_{\mathrm{l,fF}}$	Defined in equation (4.38)
$\mathbf{f}_{\mathrm{T,fF}}$	Defined in equation (4.49)
$\mathbf{f}_{\mathrm{T,m}}$	Defined in equation (4.48)
$\mathbf{f}_{\mathbf{u}_\mathrm{s}}$	Defined in equation (4.58)
H_g	Specific enthalpy
h_T	Heat transfer coefficient between the fracture and matrix continua

$\mathbf{J}_{\mathrm{g}\alpha}^{i}$	Total flux of gas component *i*
$\mathbf{J}_{\beta adv}$	Advective components of heat flux
$\mathbf{J}_{\beta con}$	Conductive components of heat flux
K_b	Bulk modulus of fractured porous media
$K_{\mathrm{c}_\alpha \mathrm{c}_\alpha}$	Defined in equations (3.44) and (3.45)
$K_{\mathrm{c}_\alpha \mathrm{T}_\alpha}$	Defined in equations (3.44) and (3.45)
$\mathbf{K}_{\mathrm{c_f c_f}}^{\mathrm{fF}}$	Defined in equation (4.27)
$\mathbf{K}_{\mathrm{c_f T_f}}^{\mathrm{fF}}$	Defined in equation (4.27)
$K_{\mathrm{l}_\alpha \mathrm{l}_\alpha}$	Defined in equations (3.64), (3.65) and (3.66)
$\mathbf{K}_{\mathrm{l_m l_m}}$	Defined in equations (3.37)
$\mathbf{K}_{\mathrm{l_f l_f}}^{\mathrm{fF}}$	Defined in equations (3.38)
K_{n0}	Initial normal fracture stiffness
K_t	Shear stiffness of fractures
$K_{\mathrm{T}_\alpha \mathrm{T}_\alpha}$	Defined in equations (3.118), (3.119) and (3.120)
$K_{\mathrm{T}_\alpha \mathrm{T}_\alpha}^{\mathrm{v}}$	Defined in equations (3.118), (3.119) and (3.120)
$\mathrm{K}_{\mathrm{T}_\alpha \mathrm{c}_\alpha}^{\mathrm{v}}$	Defined in equations (3.118), (3.119) and (3.120)
$\mathbf{K}_{\mathrm{T_m c_m}}^{\mathrm{v}}$	Defined in equation (4.48)
$\mathbf{K}_{\mathrm{T_m T_m}}$	Defined in equation (4.48)
$\mathbf{K}_{\mathrm{T_m T_m}}^{\mathrm{v}}$	Defined in equation (4.48)
$\mathbf{K}_{\mathrm{T_f c_f}}^{\mathrm{v}}$	Defined in equation (4.49)
$\mathbf{K}_{\mathrm{T_f T_f}}^{\mathrm{fF}}$	Defined in equation (4.49)
$\mathbf{K}_{\mathrm{T_f T_f}}^{\mathrm{v}}$	Defined in equation (4.49)
$K_{\mathrm{r}\beta\alpha}$	Relative permeability
K_α	Absolute permeability
$k_{\beta\alpha}$	Hydraulic conductivity
l_b	Typical thickness of a matrix block
N	Power exponent of relative permeability of gas phase in fracture.
n_{node}	Number of element node
$N_{s\alpha}$	Shape function
n_α	Porosity of different domain

n_g	Number of gas component
n_β	Volume fraction of phase β
$\mathbf{m}$	Unit vector
M_g^i	Molar mass of gas component i
$p_{0,\alpha}$	Characteristic pressure
P_L^i	Langmuir pressure constant
$Q_{c_\alpha}^i$	Defined in equations (3.52), (3.53) and (3.54)
Q_{l_α}	Defined in equations (3.73), (3.74) and (3.75)
Q_{T_α}	Defined in equations (3.125), (3.126) and (3.127)
q_β	Heat source
R	Universal gas constant
$R_{g\alpha}^i$	sink-source term for geochemical reactions
$R_{g\alpha\to ad}^i$	Amount gas adsorbed
r	Exponent for diffusion coefficient
$\mathbf{R}_m$	Rotation matrix
$S_{g\alpha}$	Degrees of gas saturation in fracture continuum
S_{le}	Effective water saturation
S_{lmax}	Maximum water saturation
S_{lr}	Residual water saturation
$S_{l\alpha}$	Degree of water saturation
s_α	Capillary pressure
T_α	Temperature
T_0	Reference temperature
T_β	Temperature of phase β
t	Time
$\boldsymbol{TL}_{abs}$	Matrices of absolute tolerances
$\boldsymbol{TL}_{rel}$	Matrices of relative tolerances
U_β	Specific internal energy of phase β
u_a	Pre-pressure related with surface stress change
u_F	Fluid pressure in large scale fractures
$u_{g\alpha 0}$	Reference gas pressure

$\mathbf{u}_{\mathrm{s}}$	Displacement vector
$u_{s,d}$	Shear displacement
$u_{\beta\alpha}$	Fluid pressure
u_{α}	Effective average pore pressure
V	Bulk volume
V^{i}	Adsorbed concentration of gas component *i*
V_{L}^{i}	Langmuir volume constant of gas component *i*
V_{L0}^{i}	Theoretical maximum adsorption capacity for gas component *i*
$V_{\mathrm{m}\alpha}^{r}$	Real gas molar volume
V_{α}	Pore volume of each continuum
$\mathbf{v}_{\beta\alpha}$	Flow velocity
$\bar{V}_{b}$	Molar volume of the bulk fluid
v	Possion's ratio
w	Hydraulic fracture aperture
w_{nmax}	Maximum closure of the fracture aperture
w_{s}	Shear dilation
w_{s-ap}	Normal displacement the peak shear stress
W_{β}	Mechanical heat flux of phase β
$x_{\mathrm{g}\alpha}^{i}$	Molar fraction of gas component *i*
X_{α}^{i}	Mass fraction of gas component *i*
Z_{α}	Gas compressibility factor
$\boldsymbol{\sigma}$	Total stress tensor
$\boldsymbol{\sigma}^{e}$	Effective stress tensor
σ_{gD}	First order mass exchange coefficient for diffusion of component *i*
σ_{n}	Normal stress acting on the fracture
σ^{s}	Surface stress due to gas adsorption
$\sigma_{\mathrm{s-peak}}$	Peak shear stress
σ_{n}'	Effective normal stress acting on the fracture
$\bar{\sigma}$	Mean stress
$\sigma_{\beta v}$	First order mass exchange coefficient for advective flow
ε_{v}	Volumetric strain

$\boldsymbol{\varepsilon}$	Total strain vector
$\boldsymbol{\varepsilon}^e$	Elastic strain vector
ε^s	Thermal expansion-contraction strain
ε_{sl}	Local swelling strain
λ_β	Thermal conductivity of phase β
$\lambda_{e\alpha}$	Effective thermal conductivity
$\theta_{g\alpha}$	volumetric gas content
$\theta_{l\alpha}$	Volumetric water content
Γ	Number of moles of fluid molecules adsorbed on the fluid-solid interface
Γ^{max}	Langmuir adsorption constant
$\Gamma_{l\alpha}$	Mass exchange of water between the different pore domains
$\Gamma_{\beta\alpha}^i$	Mass exchange between different pore regions
$\tau_{g\alpha}$	Gas tortuosity factor
τ_c	Shear strength
τ	Shear stress
τ^i	Sorption time
ρ_β	Density of phase β
$\mu_{g\alpha}^0$	Gas mixture viscosity at low pressure
$\mu_{g\alpha}^D$	Gas mixture viscosity adjustment for dense gases
μ_{JT}	Joule–Thomson coefficient
μ_β	Fluid viscosity
α_{lT}	Thermal expansion coefficient of water
α_T	Thermal expansion coefficient
φ	Dilation angle
φ_o	Orientation of the fracture
γ	A constant based on the water retention characteristics
ψ	A constant based on the water retention characteristics
Λ	Ratio of local swelling to global swelling
Φ^i	Reduction coefficient related with temperature increase
Φ_a	Internal friction angle
ω_α	Primary variables

$\widehat{\omega}_{\alpha}$	Approximate value of the primary variable
$\omega_{g\alpha}^{ij}$	Binary gas interaction parameter between the molecules of components *i* and *j*
ϖ_i	surface fractional coverage of gas component *i*
ξ	Constant material parameter
Ω_l	An empirical coefficient
δV	Elemental volume
ζ	Residual force
∇	Gradient operator
∇_l	Lower dimensional gradient operator

Contents

1 Introduction 1-1
1.1 Introduction 1-1
1.2 CO_2 sequestration in coal seams 1-4
1.3 Pilot trials of CO_2 sequestration with ECBM recovery 1-6
1.4 Study objectives 1-9
1.5 Research background 1-10
1.6 Scope and limitations 1-13
1.7 Overview of the thesis 1-14
1.8 References 1-16
2 Literature review 2-1
2.1 Introduction 2-1
2.2 Structural characterisation of coal 2-2
2.3 Gas adsorption and induced coal swelling 2-5
2.3.1 Gas adsorption in coal 2-5
2.3.2 Sorption-induced swelling/shrinkage of coal 2-11
2.3.3 Relationship between strains and adsorbed gas volume 2-16
2.4 Gas transport behaviour in coalbeds 2-17
2.4.1 Diffusion in coal matrix 2-17
2.4.2 Flow in fracture system 2-22
2.5 Modelling of CO_2 storage and enhanced coalbed methane recovery 2-29
2.5.1 Conceptual models for representation of fractured porous media 2-30
2.5.2 Coupled simulation of CO_2 sequestration and CBM recovery 2-34
2.6 Conclusions 2-37
2.7 References 2-39
3 Theoretical Formulation 3-1
3.1 Introduction 3-1
3.2 Theoretical formulation – general aspects 3-2
3.3 Multicomponent gas transport 3-5
3.3.1 Gas transport in the matrix continuum 3-7
3.3.2 Gas transport in fracture continuum 3-9
3.3.3 Gas transport in discrete hydraulic fractures 3-11
3.3.4 Mass exchange 3-12

3.3.5 Governing equations for multicomponent gas transport 3-13
3.4 Water transfer 3-16
3.4.1 Mechanisms of water transfer 3-17
3.4.2 Mass exchange term for water 3-18
3.4.3 Governing equations for water transfer 3-19
3.5 Heat transfer 3-20
3.5.1 Heat transfer in the matrix continuum 3-23
3.5.2 Heat transfer in the fracture continuum 3-24
3.5.3 Heat transfer in discrete hydraulic fractures 3-25
3.5.4 Heat exchange 3-27
3.5.5 Governing equations for heat transport 3-28
3.6 Deformation 3-28
3.6.1 Effective stress 3-29
3.6.2 Elastic constitutive relationships 3-30
3.6.3 Thermal and adsorption-desorption-induced swelling-shrinkage 3-31
3.6.4 Governing equation for deformation 3-33
3.7 Porosity and permeability of the fracture and matrix continuum 3-33
3.8 Mechanical behaviour in discrete fractures 3-40
3.9 Conclusions 3-44
3.10 References 3-46
4 Numerical Formulation 4-1
4.1 Introduction 4-1
4.2 Spatial discretisation 4-1
4.2.1 Spatial discretisation of governing equations for gas transport 4-2
4.2.2 Spatial discretisation of governing equations for water transfer 4-12
4.2.3 Spatial discretisation of governing equations for heat transfer 4-16
4.2.4 Spatial discretisation of governing equations for deformation 4-20
4.3 Temporal discretisation 4-24
4.4 Coupling between transport and exchange/reaction terms 4-27
4.5 Conclusions 4-28
4.6 References 4-31
5 Model Verification 5-1
5.1Introduction 5-1
5.2 Variably saturated flow in a dual permeability system (Test I) 5-3

5.2.1 Simulation conditions 5-3
5.2.2 Results and discussion 5-4
5.3 Gas flow with and without adsorption (Test II) 5-18
5.3.1 Simulation conditions 5-18
5.3.2 Results and discussion 5-19
5.4 Transient flow of heat (Test III) 5-6
5.4.1 Heat conduction and convection (Test III-a) 5-6
5.4.2 Joule-Thomson cooling effect (Test III-b) 5-9
5.5 Elastic deformation behaviour (Test IV) 5-11
5.5.1 Simulation conditions 5-12
5.5.2 Results and discussion 5-13
5.6 Flow in a porous medium with discrete fractures (Test V) 5-14
5.6.1 Simulation conditions 5-15
5.6.2 Results and discussion 5-16
5.7 Coupled thermo-hydro-mechanical behaviour (Test VI) 5-16
5.7.1 1-D consolidation (Test VI-a) 5-18
5.7.2 The effect of pressure on fracture aperture (Test VI-b) 5-24
5.7.3 Thermo-hydro-elastic response of rock under thermal loading (Test VI-c) 5-28
5.8 Specific conclusions 5-34
5.9 General conclusions 5-36
5.10 References 5-38
6 Model Validation and Application 6-1
6.1 Introduction 6-1
6.2 Effects of temperature on adsorption characteristics 6-2
6.2.1 Experimental results of gas adsorption 6-2
6.2.2 Material parameters and matching results 6-4
6.3 Mechanical response of coal to adsorptive gases 6-6
6.3.1 Experimental results of coal deformation and permeability 6-6
6.3.2 Matching of experimental data 6-10
6.3.3 The coupling between adsorption and swelling 6-17
6.3.4 Dynamics of coal porosity and permeability 6-18
6.4 Prediction of CBM recovery performance including multi-phase flow 6-25
6.4.1 Model domain and material parameters 6-29
6.4.2 History matching of field production data and discussion 6-37

6.4.3 Parameteric sensitivity analysis 6-38
6.5 Specific conclusions 6-43
6.6 General conclusions 6-45
6.7 References 6-46
7 Coupled THCM behaviour during CO_2 sequestration with enhanced CBM recovery 7-1
7.1 Introduction 7-1
7.1.1 Simulation conditions and material parameters 7-2
7.2 Simulation results and discussion 7-7
7.2.1 Coupled THCM behaviour during CBM production 7-7
7.2.2 Coupled THCM behaviour during CO_2 injection and ECBM recovery 7-13
7.3 Conclusions 7-24
7.4 References 7-26
8 Conclusions and suggestions for future research 8-1
8.1 Introduction 8-1
8.2 Theoretical and numerical model development 8-2
8.3 Model verification 8-5
8.4 Model validation and application 8-7
8.5 Coupled THCM behaviour during CH_4 production and CO_2 injection 8-9
8.6 Overall conclusions 8-10
8.7 Suggestions for future research 8-13
Appendix A A-1

1

Introduction

1.1 Introduction

Global warming, a major aspect of climate change, has received increasing attention in recent decades (MacDowell *et al.* 2010; Davis *et al.* 2019; Hoteit *et al.* 2019). This environmental issue is primarily attributed to increases in emission of greenhouse gases in the Earth's atmosphere resulting from anthropogenic activities, such as carbon dioxide (CO_2), methane (CH_4), and nitrous oxide (NO) (UNEP, 2019). These gases increase the entrapment of heat from the sun, preventing heat from leaving the earth's atmosphere and making the Earth warmer, which is also known as the greenhouse effect. Human-induced warming reached approximately 1°C (likely between 0.8°C and 1.2°C) above pre-industrial levels in 2017, increasing at 0.2°C (likely between 0.1°C and 0.3°C) per decade (IPCC, 2018). If the current warming rate continues, a temperature threshold (global warming of 1.5°C) will be exceeded between 2030 to 2052, associated with serious climate-related risks such as rising sea levels, regional changes in precipitation, and more frequent extreme weather events (IPCC, 2018), with serious implications for human society and the natural environment.

The relative contributions of greenhouse gases to the greenhouse effect are: 63.6% from CO_2, 19.2% from CH_4, 5.7% from NO and chlorofluorocarbons (CFCs), and 11.5% from other sources (Mavor *et al.* 2002). In recent years, the relative contributions of CO_2 to the greenhouse effect is increasing (Ritchie and Roser, 2017). The reduction of CO_2 emissions into the atmosphere has the potential to decrease the intensity of the greenhouse effect. To limit global warming to 1.5°C, the IPCC (2018) reports that anthropogenic global net CO_2 emissions must fall by about 45% by 2030 from 2010 levels and reach ‘net zero’ by 2050. However, CO_2 generated by human activities cannot, in reality, be brought to zero instantaneously because most CO_2 originates from the combustion of fossil fuels, including

electricity generation, transportation, and domestic heating (IPCC, 2018). It is apparent that fossil fuels will remain an important component of the world's energy supply in the coming decades because of techno-economic inertia, such as availability, competitive cost, easy transportation and storage, and large reserves (Bachu and Shaw 2003; Briefing 2013; IEA, 2018).

Concerns due to anthropogenically forced climate change, mainly owing to emissions of CO_2, have resulted in a number of initiatives to reduce CO_2 emissions, including improving the efficiency of energy utilisation and conversion, reducing the carbon intensity of fuels (such as from coal to unconventional gas), developing power generation using nuclear and renewable energy sources (e.g. wind, solar, geothermal, tidal and hydroelectric energy), and CO_2 capture and storage (CCS), or more broadly utilisation and storage (CCUS), in geological formations, i.e. geological sequestration. Among these means, CCS has been broadly recognised as having the potential to play a key role in meeting climate change targets, delivering low carbon heat and power, decarbonising industry and, more recently, its ability to facilitate the net removal of CO_2 from the atmosphere (Gu 2009; Bui *et al.* 2018). In comparison with the pure CCS technology, CCUS technology is becoming more popular in recent years, because CCUS pays more attention to the valorisation of the captured CO_2. It is however recognised that options for the potential economic use of CO_2 do not cover the true extent of CO_2 capture and removal that is required. Furthermore, many CO_2 utilisation options ultimately return CO_2 to the atmosphere, reducing their effectiveness.

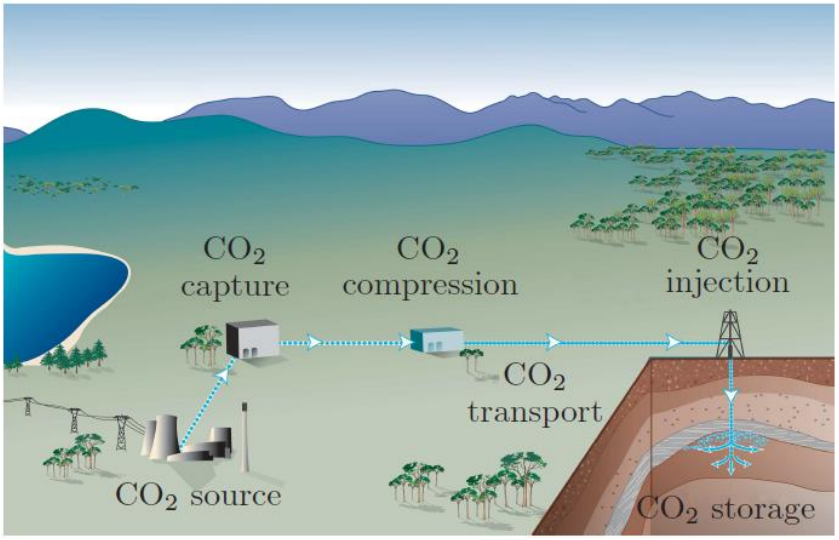

Figure 1.1 Major stages of geo-sequestration of CO_2 (Komarova 2012).

In general, the geological sequestration process of CO_2 is a physical process involving three major stages, as illustrated in Figure 1.1: (i) capture of CO_2, whereby CO_2 is separated from flue gas and compressed at the point sources, such as large industry and power plants, (ii) transportation, whereby the CO_2 is transported to the storage sites by pipeline, ship, rail, or road, (iii) geological storage, whereby the CO_2 is injected into the selected geological formation deep underground (Global CCS Institute, 2012). The focus of the present work is laid on the modelling of specific processes taking place at the end of the sequestration process, that is, injection and storage.

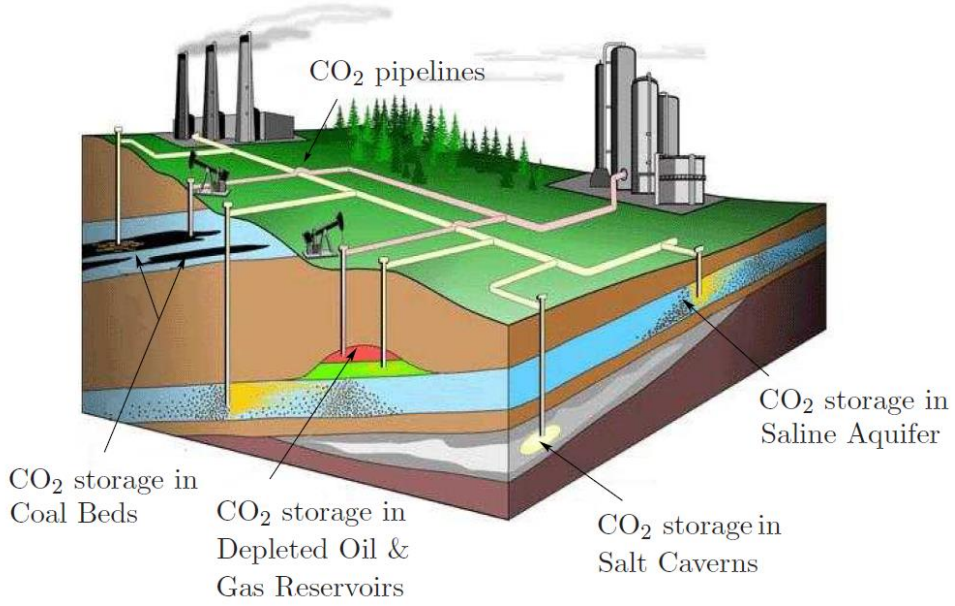

Figure 1.2 Schematic of the suggested geological sinks for CO_2 storage (Komarova 2012).

There are different types of geological sequestration sinks that can be used for CO_2 storage, these are, mainly, depleted oil and gas reservoirs, deep saline reservoirs, and deep unmineable coal seams, as shown in Figure 1.2. Formations such as salt caverns, salt formations, depleted CO_2 domes, and carbonaceous shales are also potential host formations (White *et al.* 2003). However, the retention mechanisms of CO_2 in different geological media are not the same. For example, dominant storage mechanisms may be solubility trapping in reservoir oil and formation water or adsorption trapping in deep coal beds (Bachu and Shaw 2003). Depleted oil and gas reservoirs and deep unmineable coal seams are attractive geological formations for CO_2 sequestration due to their potential to achieve added value through the enhanced recovery of oil or natural gas concurrently with CO_2 sequestration, which can be used to offset costs (Stevens *et al.* 2001; Liu *et al.* 2017a).

1.2 CO_2 sequestration in coal seams

The concept of coal seam sequestration was first proposed by Alberta Energy in 1991 (White *et al.* 2005) and has received considerable attention in subsequent decades. The advantages of CO_2 sequestration in deep unmineable coal seams include the huge remaining coal resources around the world. Conventional coal mining is in decline in many countries, a trend that is expected to continue around the world, giving new opportunities to use remaining coal resources in situ. In addition, it is a prerequisite that coalbed methane utilisation should not lead to additional CO_2 emissions, which in most cases requires further CCUS. Coal seams have an excellent potential to handle these excess CO_2 emissions, since it is well established that the CO_2 adsorption capacity of coal compared to CH_4. The competitive displacement and recovery of coalbed methane (CBM) using CO_2 is called enhanced coalbed methane (CO_2-ECBM) recovery, which can extend the life of mature CBM fields and help offset the cost of CO_2 storage (Mavor *et al.* 2002; White *et al.* 2005; Pini 2009).

From the point of energy security, coalbed sequestration of CO_2 has positive implications for energy supply. Currently, the production of conventional hydrocarbon resources may not meet the increasing global energy demand. Secure energy supply is critical to prosperity in the industrialised world and a prerequisite for sustainable development in developing countries with economies in transition. Natural gas, including unconventional gas, has been considered as the cleanest burning fossil fuel, which includes shale gas and CBM. The International Energy Agency (IEA) (2018) predicts that natural gas is the fastest growing fossil fuel, overtaking coal by 2030 to become the second-largest source of energy after oil. Therefore, the exploitation of CBM plays an important role in global energy supply to both developed and developing countries.

The commercial extraction of CBM is now well-established in a number of countries around the world, including the USA, Australia, China, India, and Canada (Moore 2012). CBM can be extracted from coalbeds in two ways. The first stage is conventional primary recovery of CBM, which is performed by pumping out water or hydraulic fracturing to depressurise the reservoir, facilitating the production of around 20-60% of the CBM originally present in the reservoir (White *et al.* 2005). The secondary (enhanced) recovery is through the injection of CO_2, N_2, or their mixtures to increase CBM recovery (Mukherjee and Misra 2018). Increase of CBM production by injection of CO_2 or N_2 is achieved through lowering the partial

pressure of CH_4 present in the open spaces of the reservoir so that enhances desorption of methane gas from the wall of small pore spaces. The CH_4 molecules are displaced into the coal natural fracture system and to the production well (Mavor *et al.* 2002; Busch and Gensterblum 2011; Lin *et al.* 2018).

Coalbeds are generally considered as dual porosity system consisting of porous matrix containing multiscale pore structure and a cleat network compared with conventional reservoirs. A series of complex physical and chemical responses during CO_2 sequestration and CBM recovery, for example, gas desorption/adsorption, coal swelling deformation, complex diffusion regimes in the coal matrix, two phase flow in coal cleats, temperature fluctuation can occur (Chattaraj *et al.* 2016; Masoudian 2016; Fan *et al.* 2019b). As a consequence, the technical development of CO_2 sequestration and the associated ECBM recovery requires a detailed understanding of the physical and chemical processes involved, including their coupled interactions.

Despite recent advances in the experimental research on the coupled behaviour important for CO_2-ECBM recovery, laboratory conditions are often different from field conditions. On the other hand, it is expensive and challenging to achieve sufficient monitoring resolution to properly interpret the coupled behaviour at depth in-situ. Theoretical and numerical models complemented by laboratory and field investigations can provide an invaluable platform for the assessment and prediction of the coupled processes involved under a range of different conditions. It is well established that numerical models can be applied to demonstrate technical understanding through theoretical developments and validation with experimental measurements (Hosking 2014; Keles *et al.* 2019), which is necessary for designing and evaluating CO_2 sequestration and ECBM recovery projects.

This work is motivated by the field observation and aims to build on previous numerical modelling works to give a greater insight into the coupled non-isothermal fluid flow and chemo-mechanical deformation phenomenon. CO_2 storage with ECBM recovery is a complex physical and chemical process coupling solid deformation, gas adsorption/desorption, gas transport, water flow, and thermal transfer. Therefore, a major component of this research is the development of a coupled non-isothermal, multiphase-multicomponent flow and geomechanics model to predict the short-term and long-term behaviour of a coal-gas-water system for CO_2 sequestration and CO_2-ECBM recovery. Whilst a large part of the developed theoretical and computational platform is intended to

be relevant to the application mentioned above, the specific emphasis of this work is put on advancing the understanding of the fracture flow coupled with chemo-mechanical deformation under non-isothermal conditions.

The current field status of CO_2 sequestration and CO_2-CBM recovery is reviewed in the next section, this is followed in section 1.4 by the principle objectives. An overview of the research background is presented in section 1.5. In section 1.6, the scope and limitation of this work are provided, with an overview of the thesis given in section 1.7.

1.3 Pilot trials of CO_2 sequestration with ECBM recovery

In the past two decades, a number of CO_2-ECBM recovery projects ranging from small to large scale have been completed or are currently underway or planned. Table 1.1 presented a summary of field tests of CO_2-ECBM recovery which have been performed. It can be seen that half of these field trials were carried out in United States, followed by China with four field projects at various scales. The technique was first used in 1995 in the San Juan Basin in New Mexico (USA), where pure CO_2 was injected in the Allison Unit (Reeves *et al.* 2003; Reeves 2005). After a 6-year primary production period via 16 producing wells, 336,000 t CO_2 was injected. In addition, there are another four projects with an injection amount exceeding 1,000 t, including one over 10,000 t in the San Juan Basin. For the other three projects over 1,000 t, multiple injection wells were used. The Alison Unit in the San Juan Basin remains the largest demonstration of CO_2-ECBM recovery to date.

The first ECBM recovery field trial in China was a collaborative single-well project between China and Canada conducted in the Qinshui Basin. A total of 192 t CO_2 was injected into the anthracite formation at a depth of 472 m using 13 injection cycles (Wong *et al.* 2007). Although the injectivity of CO_2 decreased initially due to coal swelling, the gas production rate increases significantly from an average of 490 m^3/d before CO_2 injection to 1,186 m^3/d after CO_2 injection (Pan *et al.* 2018). Subsequently, a multi-well ECBM recovery project was completed using three injection wells and eight offset CBM recovery wells. A total of 4,491 t CO_2 was injected during the whole project.

Table 1.1 Summary of field trials of CO_2-enchanced coalbed methane recovery (adapted from Pan *et al.* 2018).

Country	Project name	Injection dates	Well type	Total injection (t)
USA	Allison Unit, San Juan Basin	Apr 1995-Aug 2001	4 injection wells, 16 production wells, and 1 pressure observation well	336,000
	Pump Canyon, San Juan Basin	July 2008–Aug 2009	1 injection well, 3 production well	16,699
	Tanquary Farms test site, Illinois Basin	Summer 2008	1 injection well, 3 monitoring wells	92.3
	Virginia Central Appalachian Basin Coal Test	Jan 2009–Feb 2009	1 injection, 7 adjacent production wells	~900
	Lignite Field Validation Test, Williston Basin	Mar 2009	1 injection well, 4 monitoring well	90
	Black Warrior Basin Coal Test	Jun-Aug 2010	1 injection well, hydraulic fractured. 3 monitoring wells	252
	Marshall County project, Northern Appalachian Basin	Sep 2009-Dec 2013	2 horizontal injection wells, adjacent production wells	4,968
	Buchanan County, Central Appalachian Basin	July–Aug 2015	3 injection wells	1,470
China	Qinshui Basin ECBM, 2004	Apr–Jun 2004	Single vertical well huff and puff	192
	Qinshui Basin ECBM 2010	Apr–May 2010	Single vertical well huff and puff	233.6
	APP ECBM, Ordos Basin	Sep 2011–Mar 2012	1 multilateral horizontal injection well; 1 monitoring well	460
	Qinshui Basin multiple wells	2013–2015	3 injectionm 8 production or Monitoring wells	4,491
Canada	FBV 4A Micro-Pilot Test, Western Canada Sedimentary Basin	1998	1 injection well	201
	CSEMP, Western Canadian Sedimentary Basin	Jun 2006	1 injection well, 3 monitoring wells	unknown
Japan	Yubari field test, Ishikari Coal Basin	Late 2004-Sep 2007	1 injection well, 1 production well	~800
Poland	RECOPOL, upper Silesian coal basin	Aug 2004-May 2005	1 injection well, 1 production well	760

A CO_2-ECBM recovery project was performed near the town of Yubari on the island of Hokkaido in northern Japan in the period between May 2004 and October 2007. The target coal seam was a 5-6 m thick Yubari coal seam located at a depth of 900 m. Single well and multi-well CO_2 injection tests were performed. There were a variety of tests conducted in the injection well, including an initial water injection fall-off test and a series of CO_2 injection and fall-off tests. It was estimated that low injectivity of CO_2 was caused by the reduction in permeability induced by coal swelling. It was also indicated that the coal matrix swelling might create a high stress zone near to the injection well (Fujioka *et al.* 2010).

A pilot site for CO_2 storage in coal seams was set up and used in the Upper Silesian Coal Basin in Poland, the main aim of this project was to investigate the technical and economic feasibility of this type of CO_2 storage under European conditions (van Bergen *et al.* 2006; van Bergen *et al.* 2009). About 760 t CO_2 were injected into the reservoir from August 2004 to June 2005. Compared to baseline production, the production of CBM increased significantly because of the injection activities (van Bergen et al. 2009). Nonetheless, recovery of methane was low, which can be attributed to low flow rates into and out of the coal. A reduction in permeability was observed due to swelling of the coal, which in turn affected the CO_2 injectivity. The permeability was enhanced to an effective level after a hydraulic fracture treatment to allow continuous injection, although a high injection pressure was required (van Bergen *et al.* 2009).

For most cases of ECBM recovery in lower permeability coals, permeability and injectivity loss were observed, although an injectivity increase was also reported in some projects for at least a period of time during injection, such as in the Fenn Big Valley (FBV 4A) trial performed by the Alberta Research Council (Mavor *et al.* 2004). It is believed that the increase in injectivity was due to water saturation reduction overcoming any reduction in injectivity caused by swelling.

In summary, the field projects described have had some positive implications for CO_2 storage and the simultaneous increase in CBM recovery. Injectivity issues associated with coal swelling nonetheless remain one of main technical constraints, and more attempts are required to address this issue. Reservoir simulation is an important tool to improve our current understanding of the response of coal seams to CO_2 injection. Considering the difficulty of monitoring the coupled phenomena occurring in the field setting, especially when a great large amount of CO_2 is injected, the continued development of theoretical and

numerical modelling capabilities for improved reservoir simulation remains a widely used method to evaluate the CO_2 sequestration and ECBM recovery performance in most projects.

1.4 Study objectives

This study focuses on the development of a coupled THCM model using a new theoretical framework of a hybrid coupled dual porosity and discrete fracture model. The model is completed by considering several aspects of behaviour that are particularly important for study of CO_2 sequestration with ECBM recovery, most notably the geomechanical behaviour of coal related to CO_2 sequestration and ECBM recovery process.

The main objectives of this research are to:

i. Develop a theoretical framework for the multiphase transport of multicomponent gas in fractured rock under coupled thermal, hydraulic, gas/chemical and deformation behaviour, based on a hybrid coupled dual porosity and discrete fracture approach, focusing on the coals and CO_2 sequestration.

ii. Advance a coupled thermo-hydro-chemo-mechanical (THCM) model to integrate the new simulation capabilities described by the hybrid coupled dual porosity and discrete fracture model.

iii. Develop and implement appropriate relationships for describing the physical and chemical coal-gas interactions, enabling the application of the model to study CO_2 sequestration with ECBM recovery.

iv. Build and implement appropriate numerical algorithm to couple the discrete fracture and dual porosity model for the simulation of coal reservoirs.

v. Verify and validate the newly developed model to determine its suitability for studying the coupled processes governing the performance of CO_2 sequestration and ECBM recovery.

vi. Apply the developed model to investigate the response of a coal seam during CO_2 injection to enhance CBM recovery at field scale.

1.5 Research background

The current work has been carried out at the Geoenvironmental Research Centre at Cardiff University, where considerable research, including the development of the numerical computer code COMPASS (**C**ode for Modelling **PA**rtially **S**aturated **S**oils), has been performed prior to the study. This section provides the context to this work and is not intended to replace more detailed reviews of the literature in chapter 2, nor the theoretical formulation in chapter 3.

A theoretical model of coupled transient heat and moisture (TH) transfer in unsaturated soil was developed by Thomas (1985). The principle of conservation of mass was employed for moisture flow and conservation of energy was employed for heat transfer. In this model, moisture vapour transport was assumed to be diffusive following Philip and De Vries (1957) and De Vries (1958). Latent heat transfer was introduced following Luikov (1964). The non-linearity of material parameters was included in the works by Thomas (1987), Thomas (1988a) and Thomas (1988b). Revised time-stepping schemes were investigated under the mentioned coupled TH model by Thomas and Rees (1988) and Thomas and Rees (1990).

Following an experimental investigation into the behaviour of unsaturated sand surrounding a heating rod, Ewen and Thomas (1987) and Ewen and Thomas (1989) modified the vapour transfer diffusivities of the numerical model to simulate coupled heat and moisture transfer processes in unsaturated soil. A numerical simulation in terms of moisture content and temperature was carried out by Ewen and Thomas (1989) including vapour transport via a diffusive mechanism.

Thomas and King (1991) presented a theoretical heat and moisture formulation cast in terms of capillary potential and temperature and found good agreement with the Ewen and Thomas (1987) experiments. Thomas and Sansom (1995) extended this formulation to include elevated pore air pressures and validated via comparison to experimental works on sand and clay. This formulation was presented in three-dimensions including work on pre and postprocessing, visualisation and parallel computation by Sloper (1997) and Thomas *et al.* (1998).

Mechanical behaviour and deformation was introduced examining seasonal ground movements by Thomas and Rees (1993), with an isothermal coupled hydro-mechanical numerical model presented by Thomas *et al.* (1992) utilising the non-linear elastic state-

surface approach proposed by Lloret and Alonso (1985). This model was applied to seasonal ground movements in the work presented by Thomas and Zhou (1995). An elasto-plastic coupled Thermo-Hydro-Mechanical (THM) model was presented by Thomas and He (1995) using the elasto-plastic model of Alonso *et al.* (1990).

Ramesh (1996) applied the THM model to simulate temperature, moisture and void ratio distributions of montmorillonite subjected to heating/hydration. The work also involved the investigation of the isothermal volume change behaviour of compacted kaolinite in suction controlled tests. Thomas and He (1998) and Thomas and Cleall (1999) extended the THM model to include highly expansive behaviour. Using the developed model, numerical simulations of large scale experiments were presented by Mitchell (2002), Thomas *et al.* (2003), Melhuish (2005) and Cleall *et al.* (2006), including an investigation into the microstructure behaviour of bentonite when re-saturating.

Chemical processes were first introduced as non-reactive chemical transport for a single species in the liquid phase (Thomas and Cleall 1997). Hashm (1999) developed the model for two-dimensional coupled moisture and multicomponent reactive chemical transport by linking the non-reactive transport code with the geochemical model, MINTEQA2 (Allison *et al.* 1991). The model was applied to simulate a series of leaching cell experiments to study the migration/sorption behaviour of some of the heavy metals. Seetharam (2003) developed the multicomponent reactive transport module of the coupled THCM model. The geochemical reactions were calculated by the geochemical model, MINTEQA2, using a time splitting scheme to solve the transport and reaction equations. The coupled THCM model was used to simulate the reactive transport of chemicals in compacted bentonite under heating and hydration (Seetharam *et al.* 2006; Cleall *et al.* 2007).

A number of theoretical and computational developments followed that focused mainly on the behaviour of compacted bentonite as the buffer in a geological nuclear waste repository, in addition to the modelling of the large scale THM behaviour of the repository. Singh (2007) presented an experimental and numerical investigation on the heat and moisture transfer in compacted bentonite and kaolinite, with special attention to the vapour transfer in compacted clays. Modifications to the existing vapour theory were suggested and implemented in the existing THM formulation. Siddiqua (2008) presented an investigation into the effects of elevated temperatures (343 to 473 K) on the THM processes in the model. A gas transfer equation for thermo-osmotic effect was developed to account for elevated temperatures.

Vardon (2009) extended the COMPASS model to accommodate three-dimensional THM behaviour in a geological repository, including the development of a high-performance computing algorithm using both multi-threaded and message-passing programming paradigms. These developments allowed simulations to be completed in significantly less time. The model was utilised for simulating the THM behaviour of a large-scale experiment, carried out at an underground research laboratory in Sweden.

Thomas *et al.* (2011) presented the inclusion of biological aspects to the coupled THCM model. The early developments in this area include some biological impacts on coupled transport behaviour in unsaturated porous media. The THCMB model incorporates the biodegradation kinetics of organic substrates.

To include both equilibrium and kinetically controlled chemical reactions, Sedighi (2011) linked the transport module in the COMPASS code with an advanced geochemical model, PHREEQC, version 2.0. The extended THCM model was applied to simulate the transport and fate of multicomponent chemicals in the liquid phase in clays. Subsequently, the combined effects of electrochemical and thermal diffusion potentials on the reactive transport were investigated by Thomas *et al.* (2012). Masum (2012) developed the geochemical model for multicomponent gas transport, including an extension of the coupling with PHREEQC for gas reactivity. The multicomponent gas formulation was developed under the assumption of an ideal gas.

An advanced laboratory facility was designed by Hadi Mosleh (2014) to investigate the interactions between coal and various gas species and assess the influence of effective stress and sorption-induced strain on coal permeability variations and gas flow behaviour. Hosking (2014) further developed the theoretical framework to consider the reactive transport of high pressure gas mixtures in fractured rock under coupled hydraulic, gas/chemical and deformation behaviour, based on a dual porosity approach, in which the behaviour of a non-ideal gas mixture at high pressure is considered, with application of the model to investigate gas transport and displacement in coal at the laboratory scale.

More recently, Zagorščak (2017) presented a comprehensive investigation into the underlying coupled processes in coal in response to high pressure gas injection. This was achieved by developing a new high-pressure gas experimental facility and conducting a series of experimental tests together with theoretical and numerical modelling of coupled

gas/chemical/-mechanical behaviour based on single porosity approach under isothermal conditions.

The accuracy of theoretical and numerical implementation in COMPASS for a wide variety of test cases involving coupled moisture, air, and heat transfer and deformation has already been explored in previous works (King 1991; Thomas and Sansom 1995; Cleall 1998). Further verification tests for developments to the COMPASS model of coupled thermal, hydraulic and mechanical behaviour, as presented by Thomas and He (1995), Thomas and Sansom (1995), Thomas and He (1998), Thomas et al. (1998), and Cleall (1998), were performed by Mitchell (2002). A number of verification and validation tests of the multicomponent gas module have been undertaken and presented by Masum (2012). Hosking (2014) has performed a series of tests to verify multicomponent reactive gas module in fractured rock, including high pressure gas transport.

Many deep rock formations are highly heterogenous with well-developed natural fracture networks at multiple orientations and may also have hydraulic fractures induced by permeability stimulation. it is neither practical nor advantageous to model numerous pre-existing fractures individually and explicitly. Generally, the large-scale fractures provide the main conduits for fluid flow and dominate the flow behaviour. Therefore, only the large-scale fractures need to be represented explicitly, which is achieved in this work using a discrete fracture model. The natural fracture network, composed of micro-fractures, and the rock matrix itself are modelled using a dual porosity model.

From the above, although the theoretical and numerical modelling platform have been developed and advanced, its efficiency and capabilities to investigate the reactive transport of high pressure gas in fractured rock under coupled thermo-hydro-chemical-mechanical conditions are inadequate, it is necessary to improve the capabilities of computational platform to explore the coupled physical and chemical processes in complex fractured rock, including study of the CBM recovery and CO_2 sequestration.

1.6 Scope and limitations

The scope of the work undertaken in this thesis, and in particular the limitations that are anticipated, are listed below:

i. Numerical approximation is used to find a solution to the system of coupled differential equations. In particular, the finite-element method is used to provide a spatial solution and the finite-difference method used to provide a temporal solution.

ii. A hybrid dual continuum and discrete fracture modelling approach is employed to model fractured rock. The hybrid model includes three domains: a matrix continuum, a fracture continuum and a set of discrete fractures, which have distinct material parameters.

iii. Mass and heat exchange, i.e. the flow and heat interactions between the domains, is described by including coupling terms in the governing equations, and the discrete fractures only interact with the fracture continuum.

iv. Geochemical reactions between the pore fluid and solid phase are assumed to only occur in the matrix continuum.

v. Constitutive relationships for coal deformation by physical and chemical mechanisms are developed for linear-elastic behaviour, i.e. all strains are fully recoverable.

1.7 Overview of the thesis

A brief description of each chapter in this thesis is provided below.

Chapter 2 presents a selective review of the current literature most relevant to the remainder of the thesis. A review of the state-of-the-art techniques for modelling coupled transport processes in fractured rock is included. Beyond this, the focus of the review is laid on the current understanding of thermo-hydro-chemo-mechanical behaviour in coal during gas injection and transport, which is informed by the findings from recent experimental and computational modelling studies.

The theoretical formulation for the coupled thermal, hydraulic, chemical and mechanical behaviour of fractured rock is described in chapter 3. The fractured rock is considered to have multi-scale fractures, including a well-developed small-scale fracture network with multiple orientations and a sparse network of large-scale fractures. The small-scale fracture network and porous rock matrix are treated as distinct, overlapping continua with properties

representing those of the discrete pore regions. The large-scale fractures are considered using a lower-dimensional domain. The formulations for the fracture continuum, matrix continuum and large-scale fractures are handled separately using dual porosity and discrete fracture models based on appropriate assumptions. The development of the governing equations for multicomponent gas transport, water transfer, heat transport, and deformation in fractured rock is presented. Specific attention is given to thermal-hydro-mechanical behaviour of coal interacting with reactive (sorptive) gases.

Chapter 4 summarises the numerical formulation for solving the governing equations, including the time splitting approach used to couple the transport terms with the mass exchange terms. In addition, the numerical algorithm used to couple the discrete fracture model and dual porosity model is detailed in this chapter.

A series of verification tests are presented in chapter 5 to ensure that the solution algorithm of the model is correct. Numerical simulation results are compared with the benchmarks provided by analytical solutions or alternative numerical solutions. The tests performed are selective and largely specific to the present work, since it is noted that the numerical model has previously been verified for a number of test cases involving coupled moisture flow, heat transfer and gas/chemical transport.

Chapter 6 deals with the validation and application of the developed theoretical and numerical models, including comparisons with experimental and field data. This allows an in-depth examination of the validity of the underlying theory describing the material behaviour and processes involved in the major coal-gas interactions during high pressure gas injection and transport in coal.

A set of numerical simulations are presented in chapter 7, as extensions of chapter 6, to evaluate the coupled processes involved during primary CBM recovery and CO_2-ECBM recovery. The roles of hydraulic fracturing in CO_2-ECBM process are also explored through a designed simulation scenario with simple hydraulic fracture layout in this chapter.

Concluding remarks and suggestions for further research are provided in chapter 8.

1.8 References

Allison, J. D., Brown, D. S. and Novo-Gradac, K. J. (1991). *MINTEQA2/PRODEFA2, a geochemical assessment model for environmental systems: version 3.0 user's manual*. Environmental Research Laboratory, Office of Research and Development, US.

Alonso, E. E., Gens, A. and Josa, A. (1990). A constitutive model for partially saturated soils. *Géotechnique* **40**(3):405-430.

Bachu, S. and Shaw, J. (2003). Evaluation of the CO_2 Sequestration Capacity in Alberta's Oil and Gas Reservoirs at Depletion and the Effect of Underlying Aquifers. *Journal of Canadian Petroleum Technology* **42**(09).

Briefing, U. S. (2013). International energy outlook 2013. *US Energy Information Administration*.

Bui, M., Adjiman, C. S., Bardow, A., Anthony, E. J., Boston, A., Brown, S., Hackett, L. A. (2018). Carbon capture and storage (CCS): the way forward. *Energy & Environmental Science* **11**(5):1062-1176.

Busch, A. and Gensterblum, Y. (2011). CBM and CO_2-ECBM related sorption processes in coal: a review. *International Journal of Coal Geology* **87**(2):49-71.

Chattaraj, S., Mohanty, D., Kumar, T. and Halder, G. (2016). Thermodynamics, kinetics and modeling of sorption behaviour of coalbed methane–a review. *Journal of Unconventional Oil and Gas Resources* **16**:14-33.

Cleall, P., Seetharam, S. and Thomas, H. (2007). Inclusion of some aspects of chemical behavior of unsaturated soil in thermo/hydro/chemical/mechanical models. II: Application and transport of soluble salts in compacted bentonite. *Journal of engineering mechanics* **133**(3):348-356.

Cleall, P. J., Melhuish, T. A. and Thomas, H. R. (2006). Modelling the three-dimensional behaviour of a prototype nuclear waste repository. *Engineering Geology* **85**(1-2):212-220.

Davis, T. L., Landrø, M. and Wilson, M. (2019). *Geophysics and Geosequestration*. Cambridge University Press.

De Vries, D. (1958). Simultaneous transfer of heat and moisture in porous media. *Eos, Transactions American Geophysical Union* **39**(5):909-916.

Ewen, J. and Thomas, H. (1987). The thermal probe—a new method and its use on an unsaturated sand. *Geotechnique* **37**(1):91-105.

Ewen, J. and Thomas, H. (1989). Heating unsaturated medium sand. *Geotechnique* **39**(3):455-470.

Fan, C., Elsworth, D., Li, S., Zhou, L., Yang, Z. and Song, Y. (2019). Thermo-hydro-mechanical-chemical couplings controlling CH4 production and CO_2 sequestration in enhanced coalbed methane recovery. *Energy* **173**:1054-1077.

Fujioka, M., Yamaguchi, S. and Nako, M. (2010). CO_2-ECBM field tests in the Ishikari Coal Basin of Japan. *International Journal of Coal Geology* **82**(3-4):287-298.

Global, C. (2012). Institute (2012) The global status of CCS: 2012. *Global CCS Institute, Canberra, Australia*.

Gu, F. (2009). Reservoir and geomechanical coupled simulation of CO_2 sequestration and enhanced coalbed methane recovery.

Hadi Mosleh, M. (2014). *An experimental investigation of flow and reaction processes during gas storage and displacement in coal.* Cardiff University.

Hashm, A. A. (1999). *A study of the transport of a selection of heavy metals in unsaturated soil.* University of Wales. Cardiff.

Hosking, L. (2014). *Reactive transport modelling of high pressure gas flow in coal*. Cardiff University.

Hoteit, H., Fahs, M. and Soltanian, M. R. (2019). Assessment of CO_2 Injectivity During Sequestration in Depleted Gas Reservoirs. *Geosciences* **9**(5):199.

IEA. (2018). *World energy out look 2018*. International Energy Agency.

IPCC. (2018). *Global Warming of 1.5 °C: special report*. Intergovernmental Panel on Climate Change.

Keles, C., Vasilikou, F., Ripepi, N., Agioutantis, Z. and Karmis, M. (2019). Sensitivity analysis of reservoir conditions and gas production mechanism in deep coal seams in Buchanan County, Virginia. *Simulation Modelling Practice and Theory* **94**:31-42.

Komarova, I. (2012). Carbon-dioxide storage in the subsurface: a fully coupled analysis of transport phenomena and solid deformation.

Lin, J., Ren, T., Wang, G. and Nemcik, J. (2018). Simulation investigation of N_2-injection enhanced gas drainage: Model development and identification of critical parameters. *Journal of Natural Gas Science and Engineering* **55**:30-41.

Liu, H., Were, P., Li, Q., Gou, Y. and Hou, Z. (2017). Worldwide status of CCUS technologies and their development and challenges in China. *Geofluids* **2017**.

Lloret, A. and Alonso, E. eds. (1985). *State surfaces for partially saturated soils*. Proceedings of the 11th International Conference on Soil Mechanics and Foundation Engineering, San Francisco, Calif.

Luikov, A. V. (1964). Heat and mass transfer in capillary-porous bodies. In: *Advances in heat transfer*. Vol. 1. Elsevier, pp. 123-184.

MacDowell, N., Florin, N., Buchard, A., Hallett, J., Galindo, A., Jackson, G., Fennell, P. (2010). An overview of CO_2 capture technologies. *Energy & Environmental Science* **3**(11):1645-1669.

Masoudian, M. S. (2016). Multiphysics of carbon dioxide sequestration in coalbeds: A review with a focus on geomechanical characteristics of coal. *Journal of Rock Mechanics and Geotechnical Engineering* **8**(1):93-112.

Masum, S. A. (2012). *Modelling of reactive gas transport in unsaturated soil. A coupled thermo-hydro-chemical-mechanical approach.* Cardiff University.

Mavor, M. J., Gunter, W. D. and Robinson, J. R. eds. (2004). *Alberta multiwell micro-pilot testing for CBM properties, enhanced methane recovery and CO_2 storage potential*. *SPE Annual Technical Conference and Exhibition.* Society of Petroleum Engineers.

Mavor, M. J., Gunter, W. D., Robinson, J. R., Law, D. H. and Gale, J. eds. (2002). *Testing for CO_2 sequestration and enhanced methane production from coal*. SPE Gas Technology Symposium. Society of Petroleum Engineers.

Melhuish, T. A. (2005). *An investigation of the three-dimensional thermo/hydro/mechanical behaviour of large scale in-situ experiments.* Ph. D. thesis, Cardiff University, Wales, UK.

Mitchell, H. (2002). *An investigation into the thermo/hydro/mechanical interactions involved in high level nuclear waste disposal.* Ph.D thesis, University of Wales, Cardiff, UK.

Moore, T. A. (2012). Coalbed methane: a review. *International Journal of Coal Geology* **101**:36-81.

Mukherjee, M. and Misra, S. (2018). A review of experimental research on Enhanced Coal Bed Methane (ECBM) recovery via CO_2 sequestration. *Earth-Science Reviews* **179**:392-410.

Pan, Z., Ye, J., Zhou, F., Tan, Y., Connell, L. D. and Fan, J. (2018). CO_2 storage in coal to enhance coalbed methane recovery: a review of field experiments in China. *International Geology Review* **60**(5-6):754-776.

Philip, J. and De Vries, D. (1957). Moisture movement in porous materials under temperature gradients. *Eos, Transactions American Geophysical Union* **38**(2):222-232.

Pini, R. (2009). *Enhanced coal bed methane recovery finalized to carbon dioxide storage.* Ph. D. thesis, ETH Zurich.

Ramesh, A. D. (1996). *Modelling the thermo/hydraulic/mechanical behaviour of unsaturated soil using an elasto-plastic constitutive relationship.* University of Wales. Cardiff, UK.

Reeves, S., Taillefert, A., Pekot, L. and Clarkson, C. (2003). *The Allison Unit CO_2–ECBM Pilot: A Reservoir Modeling Study, Topical Report, US Department of Energy*. DE-FC26-0NT40924.

Reeves, S. R. (2005). The Coal-Seq project: key results from field, laboratory, and modeling studies. In: *Greenhouse Gas Control Technologies 7*. Elsevier, pp. 1399-1403.

Ritchie, H. and Roser, M. (2017). CO_2 and Greenhouse Gas Emissions. Our world in data.

Sedighi, M. (2011). *An investigation of hydro-geochemical processes in coupled thermal, hydraulic, chemical and mechanical behaviours of unsaturated soils.* Ph. D. thesis, Cardiff University, Wales, UK.

Seetharam, S., Cleall, P. and Thomas, H. (2006). Modelling some aspects of ion migration in a compacted bentonitic clay. *Engineering geology* **85**(1-2):221-228.

Seetharam, S. C. (2003). *An investigation of the thermo/hydro/chemical/mechanical behaviour of unsaturated soils.* Ph. D. thesis, Cardiff University, Wales, UK.

Siddiqua, S. (2008). *An investigation of the influence of elevated temperatures on the thermal-hydraulic-mechanical response of unsaturated soils.* Ph. D. thesis, Cardiff University, Wales, UK.

Singh, R. M. (2007). *Experimental and numerical investigation of heat and mass movement in unsaturated clays*. Ph. D. thesis, Cardiff University, Wales, UK.

Stevens, S. H., Kuuskraa, V. A., Gale, J. and Beecy, D. (2001). CO_2 injection and sequestration in depleted oil and gas fields and deep coal seams: worldwide potential and costs. *Environmental Geosciences* **8**(3):200-209.

Thomas, H. (1985). Modelling two-dimensional heat and moisture transfer in unsaturated soils, including gravity effects. *International journal for numerical and analytical methods in geomechanics* **9**(6):573-588.

Thomas, H. (1988a). The influence of non-linear thermal parameters on moisture content distributions in unsaturated soil. *International journal for numerical methods in engineering* **26**(1):263-279.

Thomas, H. (1988b). A nonlinear analysis of two-dimensional heat and moisture transfer in partly saturated soil. *International journal for numerical and analytical methods in geomechanics* **12**(1):31-44.

Thomas, H. and Cleall, P. eds. (1997). *Chemico-osmotic effects on the behaviour of unsaturated expansive clays*. Proc Int Conf on Geoenvironmental Engineering, Cardiff.

Thomas, H. and Cleall, P. (1999). Inclusion of expansive clay behaviour in coupled thermo hydraulic mechanical models. *Engineering Geology* **54**(1-2):93-108.

Thomas, H., Cleall, P., Chandler, N., Dixon, D. and Mitchell, H. (2003). Water infiltration into a large-scale in-situ experiment in an underground research laboratory. *Géotechnique* **53**(2):207-224.

Thomas, H. and He, Y. (1995). Analysis of coupled heat, moisture and air transfer in a deformable unsaturated soil. *Geotechnique* **45**(4):677-689.

Thomas, H., Rees, S. and Sloper, N. (1998). Three-dimensional heat, moisture and air transfer in unsaturated soils. *International Journal for Numerical and Analytical Methods in Geomechanics* **22**(2):75-95.

Thomas, H. and Zhou, Z. (1995). A comparison of field measured and numerically simulated seasonal ground movement in unsaturated clay. *International journal for numerical and analytical methods in geomechanics* **19**(4):249-265.

Thomas, H., Zhou, Z. and He, Y. eds. (1992). *Analysis of consolidation of unsaturated soils*. Proc. 2nd Czechoslovak Conf. on Numer. Methods in Geomech., Prague.

Thomas, H. R. (1987). Nonlinear analysis of heat and moisture transer in unsaturated soil. *Journal of engineering mechanics* **113**(8):1163-1180.

Thomas, H. R. and He, Y. (1998). Modelling the behaviour of unsaturated soil using an elastoplastic constitutive model. *Géotechnique* **48**(5):589-603.

Thomas, H. R. and King, S. D. (1991). Coupled temperature/capillary potential variations in unsaturated soil. *Journal of engineering mechanics* **117**(11):2475-2491.

Thomas, H. R. and Rees, S. W. (1993). The numerical simulation of seasonal soil drying in an unsaturated clay soil. *International Journal for Numerical and Analytical Methods in Geomechanics* **17**(2):119-132.

Thomas, H. R. and Sansom, M. R. (1995). Fully coupled analysis of heat, moisture, and air transfer in unsaturated soil. *Journal of Engineering Mechanics* **121**(3):392-405.

Thomas, H. R., Sedighi, M. and Vardon, P. J. (2012). Diffusive reactive transport of multicomponent chemicals under coupled thermal, hydraulic, chemical and mechanical conditions. *Geotechnical and Geological Engineering* **30**(4):841-857.

Thomas, H. R., Seetharam, S. C. and Vardon, P. J. (2011). On the inclusion of some biological impacts and influences in coupled transport phenomena in unsaturated soil. *Geotechnical and Geological Engineering* **29**(2):181-191.

van Bergen, F., Krzystolik, P., van Wageningen, N., Pagnier, H., Jura, B., Skiba, J., Kobiela, Z. (2009). Production of gas from coal seams in the Upper Silesian Coal Basin in Poland in

the post-injection period of an ECBM pilot site. *International Journal of Coal Geology* **77**(1-2):175-187.

van Bergen, F., Pagnier, H. and Krzystolik, P. (2006). Field experiment of enhanced coalbed methane-CO_2 in the upper Silesian basin of Poland. *Environmental Geosciences* **13**(3):201-224.

Vardon, P. J. (2009). *Three-dimensional Numerical Investigation of the Thermo-hydro-mechanical Behaviour of a Large-scale Prototype Repository*. Cardiff University.

White, C. M., Smith, D. H., Jones, K. L., Goodman, A. L., Jikich, S. A., LaCount, R. B., Schroeder, K. T. (2005). Sequestration of carbon dioxide in coal with enhanced coalbed methane recovery a review. *Energy & Fuels* **19**(3):659-724.

White, C. M., Strazisar, B. R., Granite, E. J., Hoffman, J. S. and Pennline, H. W. (2003). Separation and capture of CO_2 from large stationary sources and sequestration in geological formations—coalbeds and deep saline aquifers. *Journal of the Air & Waste Management Association* **53**(6):645-715.

Wong, S., Law, D., Deng, X., Robinson, J., Kadatz, B., Gunter, W. D., Zhiqiang, F. (2007). Enhanced coalbed methane and CO_2 storage in anthracitic coals—micro-pilot test at South Qinshui, Shanxi, China. *International Journal of Greenhouse Gas Control* **1**(2):215-222.

Zagorščak, R. (2017). *An investigation of coupled processes in coal in response to high pressure gas injection.* Ph. D. thesis, Cardiff University, Wales, UK.

2

Literature review

2.1 Introduction

Among options for the geological sequestration of CO_2, its potential utilisation for ECBM recovery has been the subject of extensive research activities in recent decades, which have investigated the properties and behaviour of coalbeds via both numerical, experimental, and field investigations. The fundamental basis of this work is associated with the coupled physical, chemical, and mechanical behaviour of coal seams during gas injection and transport. This chapter provides a state-of-the-art review on the coupled processes caused by gas-coal interactions, including the main findings and developments from experimental, theoretical, and numerical investigations.

An overview of the structural characterisation of coal is presented in section 2.2. This includes a description of its complex pore structure and cleat system, which are relevant to the physical and chemical properties of coal. The discussion is intended to provide an introduction of the fundamental aspects related to this work before they are covered in more detail in the remaining sections.

Section 2.3 presents a detailed literature review on the interactions between coal and gases, including findings from both experiments and modelling studies of gas adsorption onto coal and adsorption-induced swelling. The effects of various parameters on gas sorption properties of coal are discussed. The adsorption isotherm models used to describe gas adsorption behaviour are also reviewed. In addition, the results of the coal matrix deformation induced by gas adsorption are summarized and provided in this section.

Developments relevant to fluid transport in coal are reviewed in section 2.4. The key factors controlling the transport properties of coal and the mechanisms involved in gas flow are

discussed, including diffusion in the coal matrix and advective-diffusive flow in the fracture system. The factors influencing gas diffusion behaviour in the porous matrix and models developed to describe diffusion behaviour are summarised in this section. The relative permeability and absolute permeability are key parameters for fluid flow in coal, thus, the focal points are specific to the main findings from experimental and modelling studies on coal permeability.

Section 2.5 deals with a brief review on the computational modelling approaches related to the CO_2 storage and enhanced CBM recovery in coal with specific focus on CO_2 sequestration. In this section, the general modelling approaches applied to characterise flow and transport in fractured geological media is firstly reviewed, followed by an overview of thermo-hydro-chemo-mechanical analyses related to CO_2 sequestration and CO_2-ECBM recovery.

Finally, a summary and the concluding remarks of this chapter are given in section 2.6.

2.2 Structural characterisation of coal

Coalbeds are highly heterogeneous. This heterogeneity is usually characterised by two distinct porosity systems, namely, a well-defined and almost uniformly distributed network of natural fractures and porous matrix blocks containing a multiscale pore structure between the fractures (Harpalani and Chen 1997; Shi and Durucan 2005b; White *et al.* 2005). Both pore volume and pore frequency vary with coal rank. According to the study of Gan *et al.* (1972), in lower-rank coals (carbon content less than 75%) the porosity is primarily due to the presence of macropore (>50nm). In coals having a carbon content in the range of 76-84%, about 80% of the total open pore volume is due to micro and transitional pores, whereas micropores are predominant in coals of higher carbon content. Other studies, however, have not necessarily confirmed this relation. For example, Nie *et al.* (2015) performed low-pressure nitrogen gas adsorption and scanning electron microscopy and found that the number of mesopores within the lower rank coals decreases with increasing coal rank and the coalification mainly affects the mesopore structure. For the higher rank coals, as the coalification effect increases, the mesopore size diminishes and the number of micropores increases.

The pore structure of the coal matrix is highly heterogeneous, ranging from a few nanometres to over a micrometre (Cai *et al.* 2013; Pant *et al.* 2015). The International Union of Pure and Applied Chemistry (IUPAC) divided coal pores into three categories: micropores (<2 nm), mesopores (2-50 nm) and macropores (>50 nm). It has been estimated that about 95% of the internal coal surface area resides in micropores, which provides the potentially available adsorption sites with a strong affinity to certain gases, such as CO_2 and CH_4 (Shi and Durucan 2003). The pore volumes at different scales in the coal matrix are nonuniform. A few studies report that the porous matrix has a bidisperse pore size distribution (Ruckenstein *et al.* 1971; Gan *et al.* 1972; Zou *et al.* 2013; Pant *et al.* 2015). Gan *et al.* (1972) studied the nature of the porosity in American coals and found that the pore volumes with size less than 1.2 nm and greater than 30 nm account for a large proportion of the total pore volume. However, multi-modal pore volume distributions were observed for all coals studied in the work of Clarkson and Bustin (1999a). Pant *et al.* (2015) analyses the pore sizes present in the coal structure using mercury intrusion porosimetry. The results indicate that coal has a bimodal porous structure with a primary mode in the range of 5–10 nm and a secondary mode in the range of 2–10 μm.

Many studies show that the pore structure characterisation of the coal matrix is changed by gas adsorption/desorption (e.g. Gathitu *et al.* 2009; Liu *et al.* 2010a; Liu *et al.* 2015a; Liu *et al.* 2018; Wang *et al.* 2018; Zhang *et al.* 2019). For example, Liu *et al.* (2015a) investigated the effect of the CO_2 sequestration process on the pore structure of 4 different ranks of coal samples; each type of coal was pre-treated by a solution of supercritical CO_2 and it was observed that the $ScCO_2$-H_2O-coal reaction mainly affects the micropores, which led to an increased fraction of micropores in the $ScCO_2$ treated coal samples. Similarly, Zhang *et al.* (2019) reported that supercritical CO_2-water treatment of high-volatile bituminous coal samples enlarged the pore and throat size, increased the numbers of pores and throats, and improved pore network connectivity.

Natural occurring fractures in coal, also known as cleats, are highly important physical attributes. The cleat systems available at each coalification stage are quite different to each other, and are well developed in low volatile bituminous coals and poorly formed in lowest ranking and anthracite coals (Sampath *et al.* 2017). Coal contains two distinct sets of natural fractures, as shown in Figure 2.1. The dominant fracture system, termed face cleat, is comprised of well-developed, widely spaced, nearly parallel fissures, which are usually

continuous throughout the coal seam. The secondary fracture system, termed butt cleat, is perpendicular to the face cleat and is characterized by less well-developed fractures of limited length, also roughly parallel, and often terminating at a face cleat. Both sets of cleats, face and butt, are nominally vertical, perpendicular to the bedding planes (Laubach *et al.* 1998; Seidle 2011).

Cleats and other natural fractures are the primary flow conduits in a coal seam and contain most of the moveable water but little adsorbed gas. Some coals initially have free gas present in the cleats, while others are completely water saturated (Seidle 2011). The spacing and aperture of the cleats are two important properties that have an immense impact on the transport of fluid through coalbeds. Cleat spacing for both face and butt cleats ranges from fractions of a millimetre to centimetres, with numerous visible fractures typically present in coal cores (Laubach *et al.* 1998). For instance, Bustin (1997) reported fracture spacings from 0.02 to 5 mm in high-volatile to low-volatile bituminous rank samples of Upper Permian coals from the Sydney Basin of Australia. Dawson and Esterle (2010) found that cleat spacing was inversely proportional to cleat height (i.e. the less frequent the cleats, the greater the length of any individual cleat).

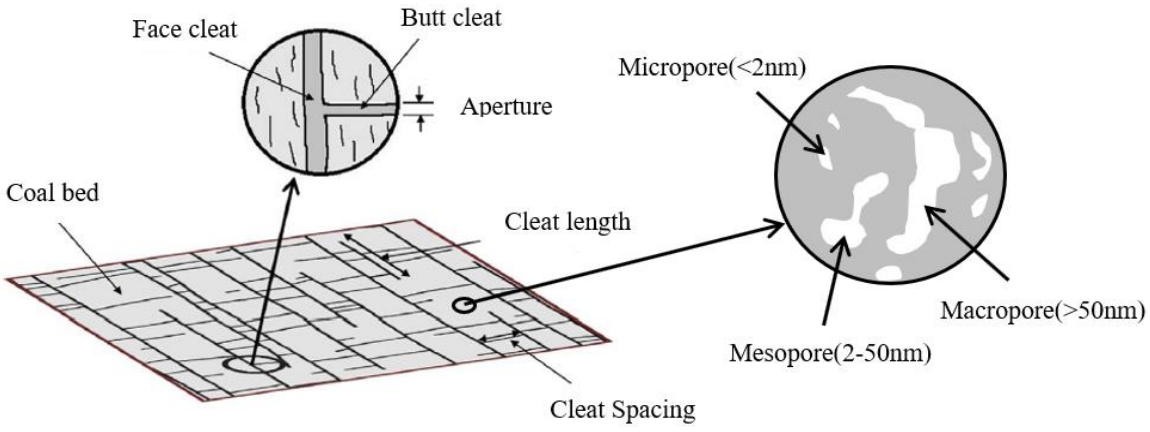

Figure 2.1 Schematic illustration of the natural fractures in coal (adapted from Sampath *et al.* 2017).

Most information on cleat aperture, i.e. the width of the opening, is based on outcrop studies and/or microscopic examination of coal samples without confining pressure (Laubach *et al.* 1998). Laubach *et al.* (1998) found a power law relationship between cumulative cleat frequency and aperture width from San Juan Basin core studies. Due to different power law constants for each core, the application of this relationship to in-situ coals is limited (Seidle 2011). The cleat aperture may be determined either from direct or indirect measurements.

The apertures obtained from direct measurements are mechanical apertures, while the apertures from indirect measurements are hydraulic apertures. They are back calculated using the cubic law from permeability (Reiss 1980). Mechanical apertures are generally greater than the corresponding hydraulic apertures due to the influences of wall roughness, tortuosity, contact area and fracture shape (Gu and Chalaturnyk 2010).

2.3 Gas adsorption and induced coal swelling

Gas adsorption/desorption and induced coal deformation are particularly important aspects of coal-gas interactions, which can have a considerable impact on the gas transport and storage behaviour. The adsorption/desorption capacity of coal for various gas species and the stability of the adsorbed gases can be affected by a number of factors, such as coal composition, gas properties, water, pressure, temperature. Various models have been proposed to predict the adsorption capacity and deformation. In this section, a combined review of the current findings and understanding of the coal-gas interaction is presented, including the insights from the related experimental, theoretical, and modelling studies.

2.3.1 Gas adsorption in coal

Gas adsorption and desorption, or simply gas sorption, is a process in which gas molecules interact with the surface of an adsorbent. A detailed description of gas adsorption phenomena can be found in across the literature (e.g. Do 1998; Ozdemir 2005; White *et al.* 2005). Adsorption processes are generally subdivided, according to the energies of interaction involved, into chemical sorption (chemisorption) and physical sorption (physisorption). In chemisorption, the adsorbate becomes bound to specific sorption sites on the solid surface by a direct chemical bond, typically involving monolayer formation. Physisorption generally occurs due to van der Waals and electrostatic interactions between the adsorbate molecules and the adsorbent surface, and can involve either monolayer or multilayer surface coverage, depending on the type of sorbent and sorbate investigated. Physical adsorption is a reversible process because there is no chemical bond between adsorbate molecules and the solid surface (Ozdemir 2005; White *et al.* 2005).

2.3.1.1 Models to predict gas adsorption capacity

Detailed reviews are available on the experimental estimation of gas adsorption in the work of Busch and Gensterblum (2011) and Mukherjee and Misra (2018), covering the gas adsorption measurement techniques, experimental conditions, and important results. During CO_2 sequestration in deep coal seams, the in-situ pressure and temperature can be high enough so that CO_2 is in a supercritical state (exceeding 31 °C and 7.38 MPa), therefore, more recent experimental tests on coal adsorption capacity are focused on high pressure adsorption (Busch *et al.* 2003; Siemons and Busch 2007; Gensterblum *et al.* 2013; Gensterblum *et al.* 2014; Tang and Ripepi 2017; Zagorščak 2017). The experimental measurements are usually modelled using theoretical formulations to compare the experimental results with theoretical assumptions. The adsorption of a given gas on a particular solid can be represented by an adsorption isotherm, which accounts for the relationships between the gas storage capacity of coal and pressure at a fixed temperature.

To date many gas adsorption isotherm models have been developed to describe the pure- and mixed-gas adsorption on coal under given conditions, and various adsorption mechanisms of gases on coals have been suggested. Adsorption on the surface with a monolayer, a multilayer, and a pore filling mechanism have most commonly appeared in the literature (Ozdemir 2005; Perera *et al.* 2012b; Masoudian Saadabad 2013; Zhang *et al.* 2016b; Liu *et al.* 2019a).

The Langmuir model is the most widely used model because of the fewer parameters required. The mechanism described by the Langmuir model is a dynamic equilibrium between adsorbed and free phases (Langmuir 1918); it is assumed that the adsorbate molecules are adsorbed on a fixed number of well-defined, localised sites, each of which can hold only one adsorbate molecule, with the adsorbent surface being energetically homogeneous for adsorption. A number of studies have investigated the sorption of CO_2 and multi-component gas mixtures in coal using the Langmuir model (e.g. Busch *et al.* 2004; Gensterblum *et al.* 2009). The BET model is an extension of the Langmuir model and introduces multilayer adsorption (Ozdemir 2005; Masoudian Saadabad 2013). These models are generally applied to describe the adsorption on a single flat surface or on a pore surface with larger radii pores, which are not applicable to microporous adsorbents in which the pore sizes are only few molecules wide. The application of the BET equation for supercritical fluid adsorption cannot be explained physically as there is unlikely to be a

multilayer formation in coal. Dubinin theory links the gas sorption to the mechanism of volume filling and considers both pressure and temperature effects (Clarkson *et al.* 1997). Two equations have been developed based on this theory: Dubinin-Radushkevich (D-R) and Dubinin-Astakhov (D-A) equations. The D-A equation is the general form of Dubinin theory.

Injected CO_2 has a strong tendency to displace adsorbed CH_4 leading to mixed-gas adsorption, with a few models having been proposed to describe the mixed-gas adsorption on coal (Pan and Connell 2009). Similar to the Langmuir model, the extended Langmuir model is widely used to show the adsorption behaviour of mixed gas. It is assumed that there is no interaction among the adsorbed molecules and that the adsorbate is a linear combination of each pure adsorbed gas. The ideal adsorbed solution model is for mixed-gas adsorption only, developed by Myers and Prausnitz (1965) by analogising adsorption to the Raoult's Law for vapor-liquid equilibrium. The adsorbed solution is assumed to be ideal and all activity coefficients in the adsorbed phase are unity (Clarkson and Bustin 2000). In addition, the two-dimensional equation of state (EOS) representation of the multicomponent adsorption isotherm was also investigated by DeGance (1992). This is analogous to the popular three-dimensional cubic EOS used in vapor–liquid equilibrium calculations. It assumes that the adsorbent is thermodynamically inert and the adsorbent surface is made up of many homogeneous sub-regions (Pan and Connell 2009). Yang *et al.* (2010) employed the quenched solid density functional theory (QSDFT) to study methane adsorption on coal at geological conditions. In recent years, the molecular simulation approach is applied to the adsorption isotherms of CH_4 and CO_2 in coal and shale gas systems (Mosher *et al.* 2013; Zhang *et al.* 2016a).

2.3.1.2 Factors affecting gas sorption

Gas adsorption capacity of any coal seam can be affected by a number of factors, such as coal rank, moisture content, temperature, pressure, and adsorbing gas species. Many experimental and theoretical studies have been conducted to research the effects of these factors on the gas adsorption capacity. Here, some parameters that can affect the adsorption capacity are summarised:

Moisture content: water in coal seams exists mostly as free water in fractures and adsorbed water in the coal matrix (Busch and Gensterblum 2011). Many studies have shown water content has a significant impact on gas adsorption in the coal matrix (e.g. Levy *et al.* 1997;

Clarkson and Bustin 2000; Crosdale *et al.* 2008; Day *et al.* 2008c; Ozdemir and Schroeder 2009; Pan *et al.* 2010b; Švábová *et al.* 2012; Gensterblum *et al.* 2013; Romanov *et al.* 2013; Gensterblum *et al.* 2014; Gupta *et al.* 2015; Teng *et al.* 2016b). A negative effect of moisture on gas adsorption in coals is demonstrated in most experimental observations. Pan et al. (2010b) conducted a series of experiments to investigate the effect of moisture on the gas sorption rate for Australian coal and found that the water in the coal matrix causes a profound reduction in the adsorption capacity of both CO_2 and CH_4, as shown in Figure 2.2. An explanation for this phenomena is given by Day *et al.* (2008c). In coal, the unbalanced distribution of ionic charges leads to a few adsorption sites that are polarised, and water molecules get attached to those polar sites via hydrogen bonding to reduce the sorption sites for CH_4 and CO_2. On the other hand, CO_2 and CH_4 sorption depends on pore characteristics. Narrow pores are filled up while larger pores are partially filled. The effect of moisture on the reduction of adsorbed volume is more prominent for CH_4 compared to that for CO_2, as reported by Day *et al.* (2008c), and the moisture-induced reduction in CO_2 and CH_4 sorption capacity decreases with increasing coal rank (Gensterblum *et al.* 2013).

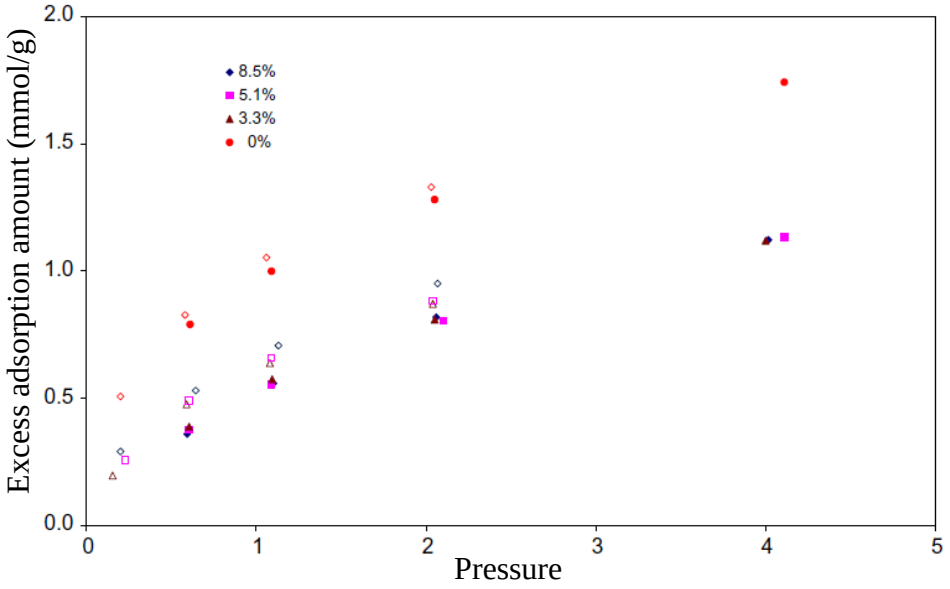

Figure 2.2 CO_2 adsorption isotherms on coal with different moisture content, solid symbol: adsorption; empty symbol: desorption (Pan *et al.* 2010b).

To investigate the magnitude and interplay of the moisture effect on gas adsorption and CBM production, approximate relationships have been developed. These relationships have been validated by comparison with a selection of literature data (Ettinger *et al.* 1958; Chen *et al.* 2012). Ettinger *et al.* (1958) proposed a linear relationship between the gas adsorption

capacity and the moisture content. This linear relationship is valid for high rank coals, but it may not be applicable for some low rank coals. Crosdale *et al.* (2008) observed a nonlinear relationship between the moisture content and the gas adsorption capacity by analysing CH_4 adsorption at a variety of moisture contents in a low rank coal from Huntly Coalfield in the North Island of New Zealand. A power law equation was used to describe the experimental data. An exponential decay equation is proposed by Chen *et al.* (2012) to quantify the moisture effect on the gas adsorption capacity, the gas effective diffusivity, and the coal swelling strain, which is applicable to both high and low rank coals provided the respective empirical coefficients can be defined.

Gas type: the adsorption capacity of coal highly depends on the type of the adsorbing gas. Coal in general has a higher adsorption tendency for CO_2 compared to other gases such as CH_4 and N_2, on a unit concentration basis and at a particular pressure, as intermolecular forces between the hydrocarbons of CO_2 and the coal are much stronger (e.g. Krooss *et al.* 2002; Day *et al.* 2008a; Ottiger *et al.* 2008; Pone *et al.* 2009; Li *et al.* 2010; Pini *et al.* 2010; Gensterblum *et al.* 2013; Perera 2017). There is not a consensus on the reasons why coal shows higher adsorption affinity for CO_2 when compared with CH_4. Sakurovs *et al.* (2010) proposed that sorption capacity is proportional to critical temperature of the considered phase. CO_2 has a critical temperature (31.1 °C) close to most of the conducted experimental temperatures compared with that of CH_4 (-81.9 °C), resulting in a higher sorption capacity of CO_2 over CH_4. Cui *et al.* (2004) suggest that coal can present a selective sorption behaviour since CO_2 will be adsorbed more compared to CH_4 and N_2 for most pore size ranges due to its lower kinetic diameter. Harpalani *et al.* (2006) attributed the higher CO_2 sorption over CH_4 in coal to a higher boiling point of CO_2 (-78.5 °C) than that of CH_4 (-161.5 °C), the adsorption affinity of CO_2 is higher than that of CH_4.

Temperature and pressure: the effect of temperature and pressure on gas adsorption in coal has been studied extensively (Levy *et al.* 1997; Krooss *et al.* 2002; Busch *et al.* 2004; Bae and Bhatia 2006; Crosdale *et al.* 2008; Li *et al.* 2010; Zhang *et al.* 2011; Pan *et al.* 2012; Cai *et al.* 2014; Wu *et al.* 2016; Zhu *et al.* 2019). Because gas adsorption is an exothermic process, high temperature can decrease the gas capacity (Zhang *et al.* 2016b) (Figure 2.3). A nearly linear reduction in CH_4 adsorption capacity was reported as temperature increases based on sorption experiments carried out under low pressure conditions (< 5 MPa) (Levy *et al.* 1997), with a similar result reported by Zhu *et al.* (2019). Kross et al (2002) found the

effect of temperature on gas adsorption is more complicated at high pressure (> 10 MPa) through experimental tests. The study of Li *et al.* (2010) indicates that the temperature dependence of CO_2 excess sorption on coals at high-pressures (> 20 MPa) becomes marginal. According to the Langmuir isotherm equation, an increase of pressure can in general increase the gas adsorption capacity. However, Li et al. (2010) reported that CO_2 adsorption volume increased with pressure reaching a maximum value at around the critical pressure, and then started to decline.

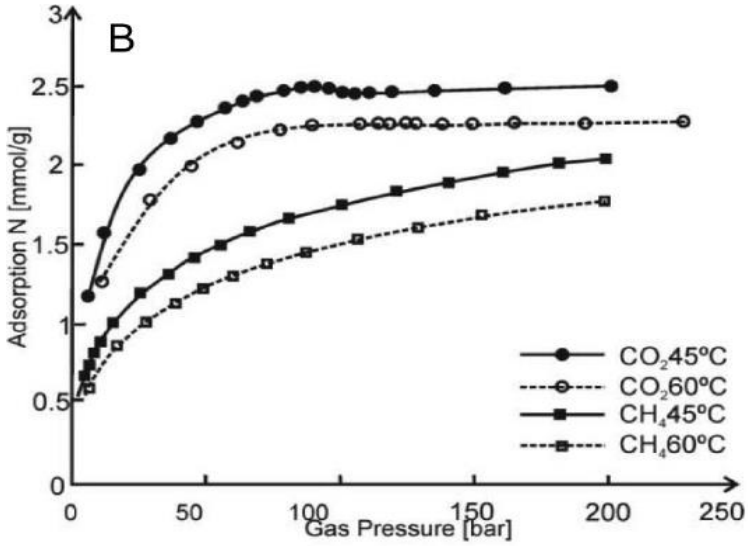

Figure 2.3 Adsorption capacity vs gas pressure at two different temperatures (Chattaraj *et al.* 2016).

A few mathematical models present the relationship between gas adsorption capacity and temperature via the temperature dependent Langmuir pressure, based on the van't Hoff equation (Busch and Gensterblum 2011; Qu *et al.* 2012; Chattaraj *et al.* 2016). In the classic Langmuir isotherm model, the Langmuir volume constant and Langmuir pressure constant are considered to be temperature independent. When considering effect of temperature, the Langmuir pressure constant is expressed as a function of temperature and heat of adsorption (Chattaraj *et al.* 2016; Ye *et al.* 2016). Tang *et al.* (2015) introduced the isosteric heat of adsorption, renamed the mean isosteric heat of adsorption, as a means to evaluate the adsorption affinity of CH_4 on coal, it was found that the mean isosteric heat of adsorption is independent of the temperature within a certain temperature range. Wang and Tang (2018) utilise a dual-site Langmuir model to describe supercritical CH_4 adsorption behaviour in anthracite and analyse the corresponding thermodynamic characteristics. The proposed model not only accurately describes measured adsorption isotherms under elevated

pressures (up to 17 MPa) and temperatures (up to 352.55 K), and interprets all observed adsorption phenomena, but also can extrapolate the adsorbed gas content and the total gas content at subsurface conditions beyond test conditions.

Confined stress: most historical experiments were performed using powdered coal samples to estimate the gas adsorption capacity, in which rapid gas sorption can be realised due to the greater exposure of internal surface area. Nonetheless, both CBM production and CO_2 storage take place within intact coal seam blocks with a complex porosity system including cleats, such that it is necessary to use coal samples confined at representative in-situ confining stress for reliable evaluation of the sorption capacity. Pone *et al.* (2009) studied the sorption capacities of CO_2 and methane for an intact bituminous coal sample for sample under confining stress as well as in powdered form. The application of 6.9 and 13.8 MPa of confining stress contributed to 39 and 64% CO_2 sorption capacity reduction. Similarly, 85 and 91% CH_4 uptake capacity reduction was observed at those confining stresses. Hol *et al.* (2011) investigated effects of the stress state within the coal on CO_2 sorption and observed that CO_2 sorption capacity of coal samples was reduced, with another such investigation also included in Liu *et al.* (2016).

2.3.2 Sorption-induced swelling/shrinkage of coal

It is a well-known phenomenon that coal swells upon adsorption and shrinks upon desorption of gaseous or liquid solvents. Larsen (2004) presented an explanation for the swelling process, whereby the coal matrix behaves as a glassy polymer at room temperature and the cross-linked macromolecular structure of the coal is effectively “frozen” in place. As the temperature rises, a transition takes place and the coal polymers change from a glassy to a rubbery state. The presence of CO_2 reduces the glass transition temperature of coal, promoting the transition from a glassy solid state to a rubbery state and thereby changing the molecular structure of coal. Karacan (2003, 2007) states that penetration of CO_2 in coal causes structural changes and rearrangements. Coal responds to the penetration of gases by altering its structure to a more stable structure, resisting further penetration of CO_2. However, Pan and Connell (2007) suggested that swelling of coal upon gas adsorption is due to energy balance, with the change in surface energy of coal during adsorption being balanced by elastic energy alteration, resulting in volume changes. The quantification of adsorption-induced swelling is important to understand the behaviour of coal in the course of CBM extraction as well as for gas injection for ECBM recovery. Many researchers have conducted

experiments and presented theoretical models for quantifying the sorption induced strain of coal, with the relevant results summarised in the following subsections.

2.3.2.1 Measurements of coal swelling/shrinkage

A large number of experimental investigations have been conducted to investigate the swelling/shrinkage behaviour of coal and to quantify the uniaxial or volumetric strains due to adsorption/desorption of gases in confined and unconfined conditions. A summary of the test conditions and measured swelling/shrinkage strains of coal for sorptive gases such as CH_4, CO_2 and N_2 has been shown by Gu and Chalaturnyk (2010), Vishal *et al.* (2016) and Mukherjee and Misra (2018), where experimental conditions and relevant details of coal swelling experiments performed by various researchers are covered. For example, Ceglarska-Stefańska and Czapliński (1993) investigated the coal expansion in CO_2 at 298 K using a gas-flame coal, a gas-coking coal, and an anthracite coal. Differential swelling was measured in directions parallel to the bedding plane (maximum linear strain 0.65 %) and perpendicular to the bedding plane (maximum linear strain 0.92 %)at pressures around 4.8 MPa. Ceglarska-Stefańska and Brzóska (1998) measured the expansion and contraction of "dry" coal and "prewetted" coal (water vapour pre-adsorbed) caused by adsorption and desorption. The results showed that during adsorption the "dry" coal underwent a lower extensional strain course than the "pre-wetted" coal and both "dry" and "pre-wetted" coals experienced an increased and then a decreased strain course during desorption. The volumetric changes of the coal matrix were monitored for four different gases (CH_4, N_2, CO_2 and He) on a sample from the South Island, New Zealand, in the work of George and Barakat (2001). The results showed that swelling due to adsorption was 2.16 % with CO_2, 0.38 % with CH_4, and 0.17 % with N_2, while there was a negligible compression of coal with He. The volume shrinkage of coal was less during desorption resulting in a permanent strain, with a similar observation found by Ottiger *et al.* (2008), while swelling was found to be isotropic and fully reversible in Ottiger *et al.* (2008).

Chikatamarla *et al.* (2004) conducted a series of volumetric swelling and shrinkage experiments on coals from the Western Canadian Sedimentary Basin, using N_2, CH_4, CO_2, and H_2S and showed H_2S resulted in the maximum volumetric strain in comparison with CO_2, CH_4, and N_2. The swelling and shrinkage (strain) in the coal samples resulting from the adsorption of N_2, CH_4, CO_2, and a mixture of gases was measured by Robertson (2005); it was shown that sorption-induced strains were reversible, with such a result also reported

by Battistutta *et al.* (2010). The experimental results presented by Mazumder *et al.* (2006) indicated that the swelling of coal is rank dependent, with volumetric swelling strain decreasing with coal rank. Measurements by Siemons and Busch (2007) showed that, generally, volumetric change seems to be different between dry coals and coals containing water. No specific trend was observed for the coals containing water, whilst for the dry coals the increase in coal volume decreased at low rank and increased again at higher rank.

Day *et al.* (2008b) described an apparatus capable of directly observing by an optical method swelling of coal exposed to CO_2 and other gases. With this setup, the CO_2-induced swelling of three Australian bituminous coals at pressures up to 15 MPa was measured. All three coals showed similar behaviour, with swelling increasing as a function of pressure up to about 8 to 10 MPa, after which no further increase in swelling was observed. Significant anisotropy was observed; swelling in the plane perpendicular to the bedding plane was always substantially higher than in the parallel plane. The swelling in these coals was completely reversible with each sample returning to its original dimensions after the gas was removed, even after multiple exposures. Similar results have been presented in Anggara *et al.* (2014) and Hol and Spiers (2012). Pone *et al.* (2010) evaluated the characterisation of lithotype specific deformation, and strain behaviour during CO_2 uptake at simulated in-situ stress conditions using X-ray computed tomography. Through alternating positive and negative strain values along the sample length during compression, sorption and desorption were observed, respectively, and it was emphasised that both localised compression/compaction and expansion of coal occur during CO_2 sequestration. The gas-induced swelling behaviour of four moist Australian coals was examined by Day *et al.* (2011), the results showed that swelling was greater for CO_2 than CH_4, with lower rank coals swelling more than high rank coal. The presence of moisture significantly reduced the amount of additional swelling compared to dry coals; however, the degree to which the swelling of the coals was affected by moisture was dependent on the rank of the coal. Laboratory measurements of swelling in four unconstrained Australian bituminous and sub-bituminous coals in CO_2, CH_4, and various mixtures of the two gases at pressures up to about 15 MPa were presented in Day *et al.* (2012), showing that in mixtures of CO_2 and CH_4 swelling was less than pure CO_2 but more than pure CH_4.

2.3.2.2 Models to predict coal swelling/shrinkage

Theoretical coal swelling models with simple mathematical forms are of great importance in permeability modelling. The strain resulting from adsorption is not linear with pressure but exhibits a curvilinear form that is steeper at a low pressure, becoming flatter at a higher pressure, resembling the sorption isotherm in shape (Levine 1996). The Langmuir-like equation is extensively used to describe the measured swelling behaviour (e.g. Levine 1996; Palmer and Mansoori 1996; Robertson 2005; Wu *et al.* 2010a; Zagorščak 2017):

$$\varepsilon_s = \frac{\varepsilon_L u_g}{u_L + u_g} \tag{2.1}$$

where ε_s is the volumetric swelling strain, $\varepsilon_L$is the maximum swelling strain when fitting with the Langmuir like equation, u_g is gas pressure and u_L is the Langmuir pressure for the swelling isotherm.

Although the Langmuir-like equation is most commonly used to theoretically describe the deformation of coal induced by the adsorption of gas, it cannot accurately predict total strain under high pressure. Experiments performed by Hol and Spiers (2012) show that the total strain increases monotonically with CO_2 at pressures between 0 and 20 MPa, then decreases as the gas pressure keeps increasing (> 20 MPa). The measured swelling strain as a result of adsorption consists of two effects: the swelling due to gas adsorption and the net compression due to the effective stress. Many published works presenting swelling strain measurements do not allow for the effects of compression and simply shows the measured strain, in which the mechanical strain and swelling strain are not separated (Pan and Connell 2012).

Pan and Connell (2007) present a theoretical model to describe adsorption-induced coal swelling at adsorption and strain equilibrium. This model applies an energy balance approach, which assumes that the surface energy change caused by adsorption is equal to the elastic energy change of the coal solid. A structure applied by (Scherer 1986) for modelling glass swelling caused by adsorption of water and its vapour was applied to describe the cross-linked coal structure. The elastic modulus of the coal, gas adsorption isotherm, and other measurable parameters, including coal density and porosity, are required in this model. When using the Langmuir adsorption model to describe the surface potential, the Pan and Connell coal swelling model is expressed as:

$$\varepsilon_s = RTV_L ln\left(1 + b_L u_g\right)\frac{\rho_s}{E_s} f(x, v_s) - \frac{u_g}{E_s}(1 - 2v_s) \tag{2.2}$$

where R is the universal gas constant, T is the temperature, ε_s is the swelling strain, V_L is Langmuir adsorption volume, ρ_s is the density for the coal solid, E_s is the Young's modulus for the coal solid, x is a coal structure parameter, and v_s is the Poisson's ratio for the coal solid. f is a function describing coal structure, as:

$$f(x, v_s) = \frac{[2(1 - v_s) - (1 + v_s)cx][3 - 5v_s - 4(1 - 2v_s)cx]}{(3 - 5v_s)(2 - 3cx)} \tag{2.3}$$

where c is a constant which equals to 1.2, and x is related to the porosity of micropores.

The Pan and Connell model is applied to match experimental observations of swelling, and results showed that this model is able to describe the differences in swelling behaviour with respect to gas species and at very high gas pressures, where the coal swelling ratio reaches a maximum then decreases (as described above). Clarkson *et al.* (2010) extended the Pan and Connell model to incorporate multicomponent adsorption by using the same set of coal property parameters and mixed-gas adsorption isotherms. Results showed the Pan and Connell model can accurately describe experimental measurements of coal swelling for mixed gas (Clarkson *et al.* 2010). However, this model contains solid-grain and pore structure geometry parameters that are not easy to determine, and anisotropic deformation is not considered.

The quenched solid density functional theory (QSDFT) was by Yang *et al.* (2010) employed to study CH_4 adsorption on coal at geological conditions. The main focus of this work was on coal deformation in the course of adsorption that may result in either expansion/swelling or contraction, depending upon the pressure, temperature, and pore size.

A comprehensive framework that enables the calculation of a macroscopic strain caused by adsorption of a fluid at the pore surface of a porous medium was developed by Vandamme *et al.* (2010) using a thermodynamic approach. Within this framework, the surface stress and macroscopic deformation are linked by extending poromechanics to surface energy to interpret how the surface stress is modified by adsorption. In this approach, the effects induced by the surface stress are conceptualised as a pre-stress and an initial pore pressure, implying these two stresses have to be applied against the effects induced by the surface stress in order to prevent any deformation and any porosity change with respect to the reference configuration.

Liu and Harpalani (2013) proposed a new theoretical technique to model the volumetric changes in the coal matrix during gas desorption or adsorption using the elastic properties, sorption parameters, and physical properties of coal. The proposed model was based on the theory of changes in surface energy as a result of sorption. It was assumed that the surface energy of the coal solid matrix decreases with adsorption of CH_4, and the resulting swelling of the solid is proportional to the decrease in surface energy. The compression effect was considered in this model.

The model derived by Liu and Harpalani (2013) differs from that of Pan and Connell (2007), which is based on the energy balance approach, assuming that the surface energy change caused by adsorption is equal to the change in the elastic energy of the coal solid. The proposed model is based on the theory of changes in surface energy, where the linear deformation of the solid coal is directly proportional to the change in the surface energy. Compared with the model derived by Pan and Connell (2007), the advantage of the proposed model lies in avoiding the solid-grain and pore structure geometry parameters, thus reducing the number of input parameters and the associated uncertainties. However, when considering fractured porous media, such models fail to describe the flow-mechanical response of adsorptive dual porosity media.

2.3.3 Relationship between strains and adsorbed gas volume

There is limited information available on the relationship between strains and the amount of gas adsorption. Several studies showed that the swelling strains of coal due to the adsorption of gases were positively correlated to the adsorbed volume of gas. Sawyer *et al.* (1990) used a linear relationship between the swelling strain and total adsorbed amount, Seidle and Huitt (1995) also employed a linear relationship with gas content to describe the behaviour of matrix shrinkage. The linear relationship between the swelling strain and total adsorbed amount is supported by some experimental studies (Harpalani and Chen 1995; Chikatamarla *et al.* 2004; Cui *et al.* 2007).

Ceglarska-Stefaríska (1994) reported that the rate of gas adsorption exceeded the rate of expansion and similarly the gas desorption was faster than the coal contraction. During the initial period (about 30 minutes) of the contact of sorbate molecules with coal, the main adsorption stage occurred. Up to 60% of the total amount of the gas was adsorbed at this stage and no change in sample dimensions was observed. Day *et al.* (2008b) combined

volumetric swelling data for two of the coals with gas adsorption results previously measured for these coals and observed that swelling was roughly proportional to the amount of CO_2 adsorbed up to intermediate pressures, but at high pressures, the relationship was no longer linear; adsorption continued to increase but swelling did not. The swelling of coals by supercritical gases and its relationship to sorption were discussed in Day *et al.* (2010). The amount of gas sorption and swelling in coal were found to be related according to a simple quadratic polynomial expression. The same relationship held for all of the coals and all gases investigated in this study, which indicated that swelling can be accurately predicted from the condensed volume of the gas adsorbed, regardless of the type of coal or gas.

2.4 Gas transport behaviour in coalbeds

Gas transport is an important process for CO_2 injection and achieving successful ECBM recovery under given operational conditions. As described in section 2.2, coal is a naturally fractured porous medium, usually characterised by a dual porosity system. The gas transport and storage regime between injection and production wells can be described by three different processes: adsorption/desorption, diffusion, and convection. For primary CBM recovery, pressure depletion initiated at the production well causes CH_4 to desorb in pores of the coal matrix before diffusing through the coal matrix to reach the cleat system (fracture network), where the majority of bulk flow occurs in coal seams. The CO_2 undergoes the opposite process. The adsorption/desorption behaviour have been reviewed in the previous section, hence, the focus of this section is specifically on the particular transport processes in the coal matrix and fracture system.

2.4.1 Diffusion in coal matrix

The multi-scale characterisation of coal structure together with gas adsorption leads to unusual diffusion behaviour, which is of particular interest. Over past decades, a great number of experiments have been conducted to investigate the diffusion properties of gas in coal. To quantify the adsorption/desorption-diffusion process, sorption kinetics data is obtained by monitoring gas adsorption after pressure steps as part of gravimetric, manometric, or other sorption experiments.

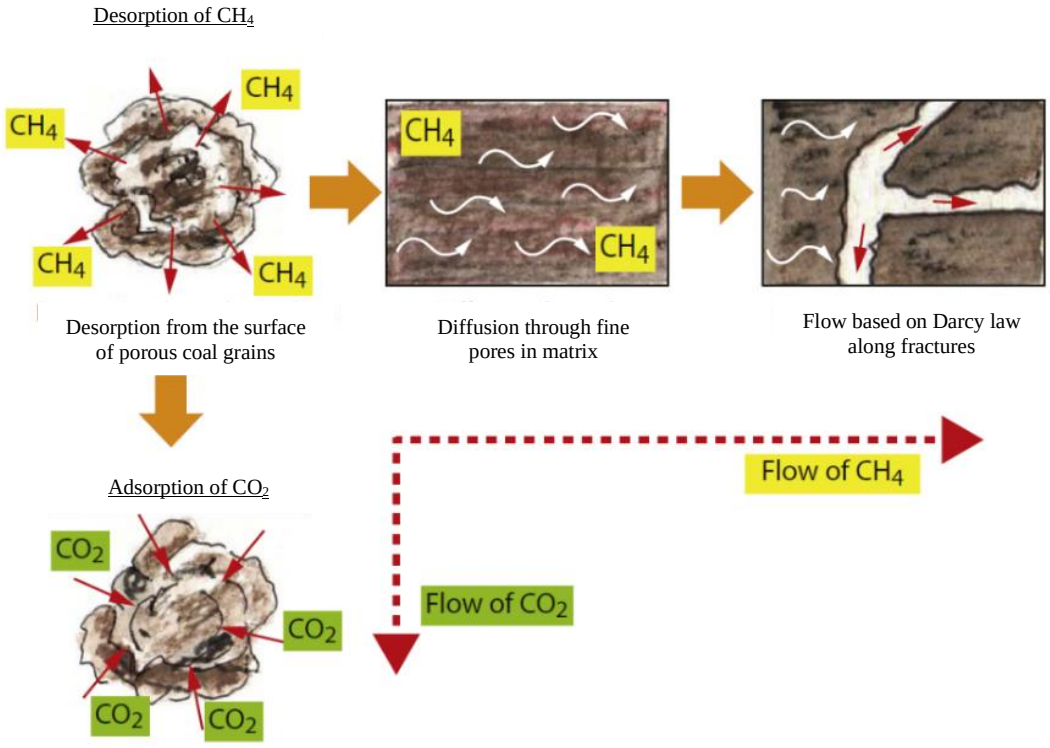

Figure 2.4 Schematic illustration of gas transportation in coal during CO_2-ECBM recovery (Mukherjee and Misra 2018).

Nandi and Walker Jr (1975) studied the diffusion of CH_4 in anthracite and high volatile bituminous coals at initial gas pressures up to about 2.76 MPa, adopting the particle adsorption technique. The results indicated that the diffusivity exhibited an increasing trend with increasing CH_4 concentration at high values of CH_4 sorption, and calculated diffusion coefficients were seen to increase sharply with decreasing average particle size. To study the diffusion mechanisms of CH_4, He and ethane in coal, Smith and Williams (1984) devised a constant-pressure, counter-diffusion experiment using several samples of a subbituminous coal from the Fruitland formation, USA. For CH_4 at pressures larger than > 0.2 MPa in bituminous coal, it appeared that bulk diffusion was dominant. At lower pressures, diffusion appeared to be in the transition region where the number of molecule/pore wall and molecule/molecule collisions are on the same order. This change from bulk to Knudsen diffusion with decreasing pressure is expected since the mean free path of the gas is increasing. For anthracite coal, the gas-phase CH_4 diffusion is primarily by bulk diffusion.

Crosdale *et al.* (1998) performed investigations of desorption rate using selected bright and dull coal samples in a high-pressure microbalance. The results indicated bright, vitrinite-rich coals usually have the slowest desorption rates which is associated with their highly

microporous structure. However, the occurrence of rapid desorption in bright coals may be related to the development of an extensive, unmineralised fracture systems. The kinetic experiments by Marecka and Mianowski (1998) showed that the availability of the pore structure of high rank coal changes during the crushing process in a similar way for the sorption of both CO_2 and CH_4, with CO_2 penetrating the structure of the micropores more easily.

Cui *et al.* (2004) examined the diffusivities of three different gases (CH_4, CO_2, N_2) and observed that CO_2 has a highest apparent micropore diffusivity compared to these of CH_4 and CO_2 due to its smallest kinetic diameter; similar findings are reported by Busch *et al.* (2004), Pone *et al.* (2009), (Charrière *et al.* 2010), (Cai *et al.* 2014). Busch *et al.* (2004) conducted experiments on six different grain size fractions, ranging from < 0.063 to ~3 mm, using a volumetric experimental setup. CO_2 sorption was consistently faster than CH_4 sorption under all experimental conditions and adsorption rates decreased with increasing grain size for all experimental conditions. Pone *et al.* (2009) quantified the time-dependent gas diffusion parameters using the volumetric method with a mathematical analysis of the pressure-decay data and found CO_2 diffused through the coal faster than CH_4. It was found that the overall gas movement, specifically diffusion, is hindered by confining stresses and takes place at rates significantly less than in unconfined powdered coal.

Gas transport in the coal matrix is strongly influenced by matrix moisture and temperature (Clarkson and Bustin 1999b; Busch *et al.* 2004; Charrière *et al.* 2010; Pan *et al.* 2010b; Salmachi and Haghighi 2012; Švábová *et al.* 2012; Cai *et al.* 2014; Meng and Li 2016). Clarkson and Bustin (1999b) found CO_2 diffusivity calculated via numerical and analytical models is larger than CH_4 diffusivity for dry coal. In addition, CH_4 diffusivity obtained using the models for wet coal are smaller than the model diffusivity obtained from dry coal. The experimental measurement performed by Pan *et al.* (2010b) on an Australian coal indicated that moisture content has a negative effect on the diffusion rate and this effect is stronger for CH_4 than for CO_2. Similarly, Busch *et al.* (2004) reported that sorption rates for both CO_2 and CH_4 in moist coals were reduced by a factor of more than 2 with respect to dry coals and the impact of moisture content on the diffusion rate was found to be stronger for CH_4 than that on CO_2. Nevertheless, it was found that equilibration times for measurements at 45°C are significantly shorter than those at 32°C, indicating that gas diffusion rates are positively related with temperature. Meng and Li (2016) measured the diffusion coefficient

of CH_4 at temperatures of 20 ℃, 30 ℃ and 40 ℃ and found the diffusion coefficient increased logarithmically with temperature.

There is no consensus yet on whether gas diffusion coefficients increase or decrease with rising pressure. Some experimental results indicate a negative correlation between diffusion coefficient and pressure (Cui *et al.* 2004; Pone *et al.* 2009; Pillalamarry *et al.* 2011; Švábová *et al.* 2012; Bhowmik and Dutta 2013; Wang and Liu 2016), whilst in other experiments it was found that the diffusion coefficient increases with rising pressure (Clarkson and Bustin 1999b; Charrière *et al.* 2010; Cai *et al.* 2014; Meng and Li 2016). The experiments by Siemons *et al.* (2007) indicate that the "fast" sorption occurs at lower pressures and dominates the sorption process. However, as the pressure increases, the "slow" sorption sites become increasingly dominant until slow sorption is the only sorption mechanism. This variation may be due to the selected models, coal, and experimental conditions (Staib *et al.* 2013).

Naveen *et al.* (2017) found that for the pressure range investigated, variation of the coefficient of diffusion followed a dual nature with a stable trend at pressures above 3.5 MPa and an increasing trend for lower pressures. The dynamic relation between sorption-diffusion reveals that the coefficient of diffusion significantly depends on the pore structure and pore size distribution, exhibiting a negative relationship with pressure variation. Han *et al.* (2013) predicted effective diffusion coefficients of CH_4 and CO_2 increase unexpectedly with the increase of the sample size. Zhao *et al.* (2017) conducted desorption experiments to obtain the diffusion coefficient at given times, and it was observed that in the initial stage the diffusion coefficient decreased rapidly with time, and the decay rate then became slower. It was found by Tan *et al.* (2018) that the effective macropore diffusivity increased with gas pressure and effective micropore coefficient decreased with gas pressure. The effective diffusivity showed differences among samples and directions, demonstrating coal heterogeneity and anisotropy both have a significant impact on gas diffusion behaviour.

In order to obtain the diffusion properties of gas in the coal matrix, the approach applied in most experiments is conversion of kinetic data into diffusion rates, using elapsed time during the adsorption/desorption with analytical or numerical models to estimate diffusion coefficients. Thus, an appropriate diffusion model is required. The various mathematical models of gas diffusion in coal have been reviewed by Zhao *et al.* (2019). There are two

widely used diffusion models, i.e. the unipore diffusion (UD) model and the bidisperse diffusion (BD) model.

The UD model is the simpler of the two and was developed based on Fick's second law, representing the coal particle as one homogeneous and isotropic sphere, with gas diffusion under the concentration gradient between the exterior and interior of the sphere. Only one characteristic diffusion coefficient is required for UD model. Some researchers stated that the UD model is sufficient to describe the dynamic adsorption-diffusion process in coals (Pone *et al.* 2009; Charrière *et al.* 2010; Švábová *et al.* 2012). The study of Clarkson and Bustin (1999b) discussed the unipore and bidisperse transport models for dull and bright coals of different pore size distributions, concluding that a one parameter model such as UD model may be adequate for some bright coals. However, for most coals with a multimodal pore distribution, one characteristic diffusion coefficient does not adequately capture the sorption kinetics.

By contrast, the BD model with two characteristic diffusion coefficients is capable to describe the diffusion process in coals with multimodal porosity (Smith and Williams 1984; Clarkson and Bustin 1999b; Shi and Durucan 2003; Busch *et al.* 2004; Cui *et al.* 2004). The BD model was first proposed by Ruckenstein *et al.* (1971) and then extended to model gas flow and transport by Smith and Williams (1984) for the study of CH_4 desorption from coals. It was later improved as a numerical model by Clarkson and Bustin (1999b) by considering the effect of nonlinear sorption in the micropores and a time-dependent pressure. This model assumes the pore size distribution in coal is bimodal and two-stage gas diffusion occurs in the coal matrix, i.e. a fast macropore diffusion stage and a slow micropore diffusion stage. The key issues for the BD model are how to determine a reasonable representation of the multi-scale pore structure for numerical models. Both UD model and BD model are restricted to a specific geometry of coal particle, i.e. spherical. Besides, the dependence of the diffusion coefficient on the concentration, position, and temperature is not revealed. The assumption of constant diffusion coefficient is therefore not true for the real gas adsorption-diffusion behaviour in coal (Zhao *et al.* 2019).

More recently, the dispersive diffusion model, also called the stretched exponential model, was developed and has been applied to gas diffusion in coal (Staib *et al.* 2015). It assumes a distribution of characteristic times for diffusion and avoids the arbitrary separation of pore size distributions. To explain the dependence of diffusion on experimental time, some

studies have introduced time-dependent diffusion coefficients into the original analytical UD model (Dong *et al.* 2017; Zhao *et al.* 2019). Though the measured values of gas adsorption/desorption are generally controlled by two processes: the adsorption/desorption process (adsorption/ desorption characteristics of the coal) and the diffusion process (diffusion of gas through coal matrix), these two processes are generally lumped together in gas adsorption kinetic studies. In addition, application of these diffusion models to field work is not trivial because of their complex mathematical calculations and the difficulty in determining the modelling parameters of coal. At present, there are no unified models for the characterisation of gas diffusion in coal, therefore, more efforts are required to study the transport processes of gas in the coal matrix.

2.4.2 Flow in fracture system

Fluid flow inside the fractures is assumed to be laminar and viscous and is usually described by Darcy's law. Multiphase flow occurs at reservoir conditions for both primary and enhanced CBM recovery processes. These processes are generally controlled by the effective permeabilities to water and gas rather than the absolute permeability (Zhang *et al.* 2015). The effective permeability is often expressed as a function of relative permeability and absolute permeability.

Relative permeability, or the ratio of effective permeability to absolute permeability, has been studied extensively. For example, Ham and Kantzas (2011) investigated the relative permeabilities of two coal samples from Grande Prairie and Goldsource Mines using three gases (He, CH_4 and CO_2) at three different operating pressures (100, 300, 400 psi) with a constant overburden pressure of 800 psi. The experimental results showed that the relative permeabilities were typically very low for all gases and high for water. Coal relative permeabilities to gas and water were dependent on the gas species and the operational pressures. Durucan *et al.* (2013) carried out laboratory experiments on seven European coals of different ranks using the unsteady state method to measure gas-water relative permeabilities due to its operational simplicity. The impact of factors such as wettability, absolute permeability, and overburden pressure on coal relative permeability were assessed. Considerable variation in the shapes of the relative permeability curves for different rank coals was observed, mainly attributed to heterogeneity of coal, both in terms of composition and cleat-matrix configuration. It was observed that, when the matrix effect is more predominant then the curves tend to be spread over a wider saturation range and are less

linear, while if the effect of the large cleats dominates, the relative permeability curves become straighter and narrower.

Relative permeability is often expressed as a function of wetting phase saturation, upon which it is strongly dependent (Chen *et al.* 2013). A commonly used method to obtain the relative permeability model is through integration from the capillary pressure model. Many capillary models are available in the literature based on the experimental data of core flooding on different porous media with different fluids (e.g. Brooks and Corey 1966; Van Genuchten 1980; Li and Horne 2001; Lomeland *et al.* 2008). Among these capillary pressure models, the Brooks–Corey model (1966) and the van Genuchten model (1980) are the two most widely used models. However, the validity of these models for coal reservoirs has not been examined in detail, leading to uncertainty in their validity since they were derived for conventional porous media.

Bogdanov *et al.* (2003) and Alonso *et al.* (2013) discussed how to apply the van Genuchten model to fractured media. Local equilibrium is assumed and the water pressure, air pressure, and the capillary pressure are continuous whilst the air entry pressure of the van Genuchten model differs between the fractures and porous matrix. Shen *et al.* (2011) proposed an empirical model for predicting relative permeability to water and gas in coals, applying multiple regression analysis on experimental data from five coals with different ranks. Recently, Chen *et al.* (2013) developed a relative permeability model specific for coals. They considered the fracture geometry by applying the matchstick model, instead of the bundle of capillary tubes model that is often used as the conceptual model for conventional porous media, to derive the relative permeability model. In addition, the effect of porosity change on relative permeability for coal is considered by introducing a residual phase saturation model and a shape factor as functions of the permeability ratio. In the improved model, the relative permeability is dependent on both the phase saturation and the porosity (or permeability) change.

It is commonly assumed that the contribution of flow in the coal matrix to bulk flow can be neglected compared to that of cleat system (Gu and Chalaturnyk 2006; Pan and Connell 2012). The intrinsic permeability of coal is therefore directly related to a range of fracture characteristics, which may include pore size and connectivity, wall roughness, aperture, tortuosity, and the degree of mineral infill (Pan and Connell 2012). During CBM extraction and CO_2 sequestration, the absolute permeability of coal reservoirs is not a constant but

changes significantly due to the changes of stress-strain which result from the alternations of in-situ conditions such as pressures, gas sorption, and temperature (Gu and Chalaturnyk 2006).

Research on coal permeability behaviour has been performed in recent decades, initially due to its important role in CBM production and increasingly due to the potential for CO_2 sequestration with ECBM recovery. In contrast to conventional gas reservoirs, most studies on the permeability evolution of coalbeds during CO_2 sequestration are mainly focused on how effective stress and gas adsorption induced swelling/shrinkage influence permeability.

Early experimental studies have found coal permeability was significantly sensitive to effective stress (Somerton *et al.* 1975; McKee *et al.* 1988; Seidle *et al.* 1992), The permeability was observed to show an exponential relationship with effective stress. However, the effect of gas adsorption induced deformation on the coal permeability change was neglected by using non-adsorptive gases or by keeping the gas pressure constant. Harpalani and Schraufnagel (1990) studied the impact of matrix shrinkage and compressibility on the coal permeability via injecting He, CH_4, and CO_2 under triaxial stress conditions, with the confining stress kept constant and effective stress changes realised by altering the gas pressure. The results indicated that the permeability of coal to He decreased with reducing gas pressure while the coal permeability to CH_4 and CO_2 increased with decreasing gas pressure in spite of the increased effective stress, this can be attributed to effect of coal swelling caused by gas adsorption.

Robertson (2005) investigated the influence of coal swelling on the permeability change. Four different gases (He, N_4, CH4, and CO_2) were injected into coal samples and the permeability was monitored in real time for selected pressure increments after equilibrium flow had been established. The experiments demonstrated that even under controlled stress conditions, the injection of adsorptive gas reduced the coal permeability when injected gas pressure is lower and a permeability rebound was observed at a higher injected gas pressure. This observed switch in behaviour is presumably due to the dependence of coal swelling on the gas pressure, with coal swelling diminishing at higher pressures, as discussed in section 2.3. Furthermore, the CO_2 injection displayed a stronger effect compared to CH_4 and N_2. Similar experiments have been performed by other researchers (e.g. Pini *et al.* 2009; Wang *et al.* 2010).

Pan *et al.* (2010a) measured gas permeability of coal cores using a triaxial test arrangement at a series of pore pressures up to 13 MPa for CH_4, CO_2 and He with confining pressures up to 20 MPa. The results showed that permeability decreases significantly with confining pressure and pore pressure, and the permeability decline with pore pressure is a direct result of adsorption-induced coal swelling, as shown in Figure 2.5(a-c). The role of effective stress coefficient in the evaluation of permeability change in adsorbing gases was presented by Chen *et al.* (2011) through a series of experiments conducted for coal samples using both non-adsorbing (He) and adsorbing gases (CH_4, CO_2). The permeability reduction from He experiments was then used to calibrate the subsequent experiments using adsorbing gas species.

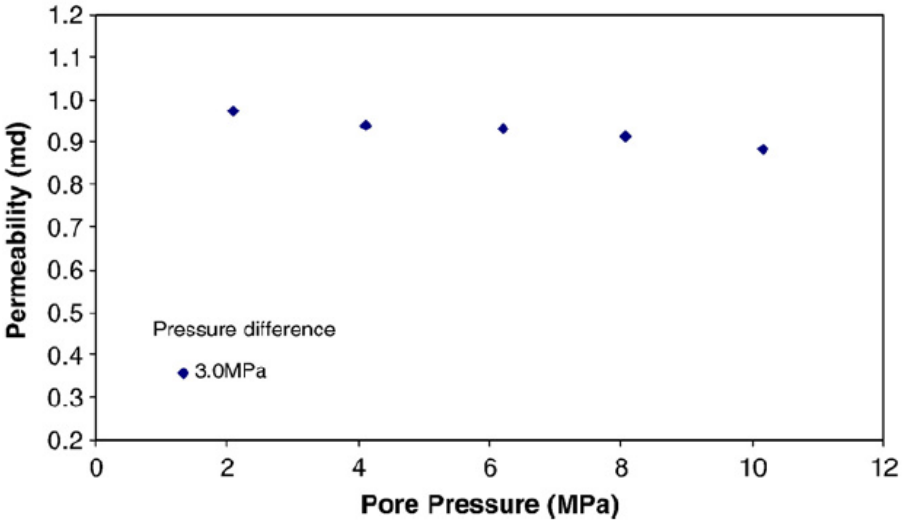

(a)

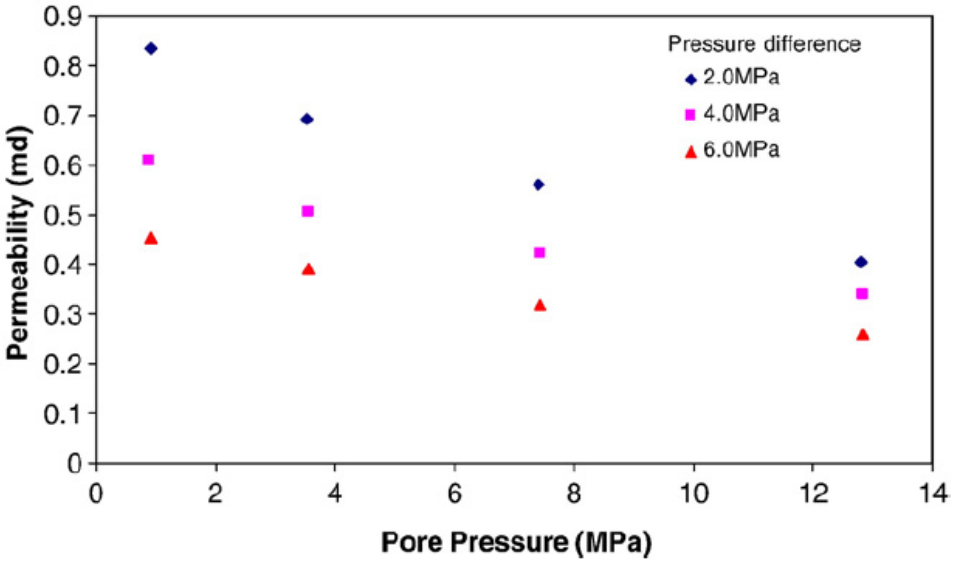

(b)

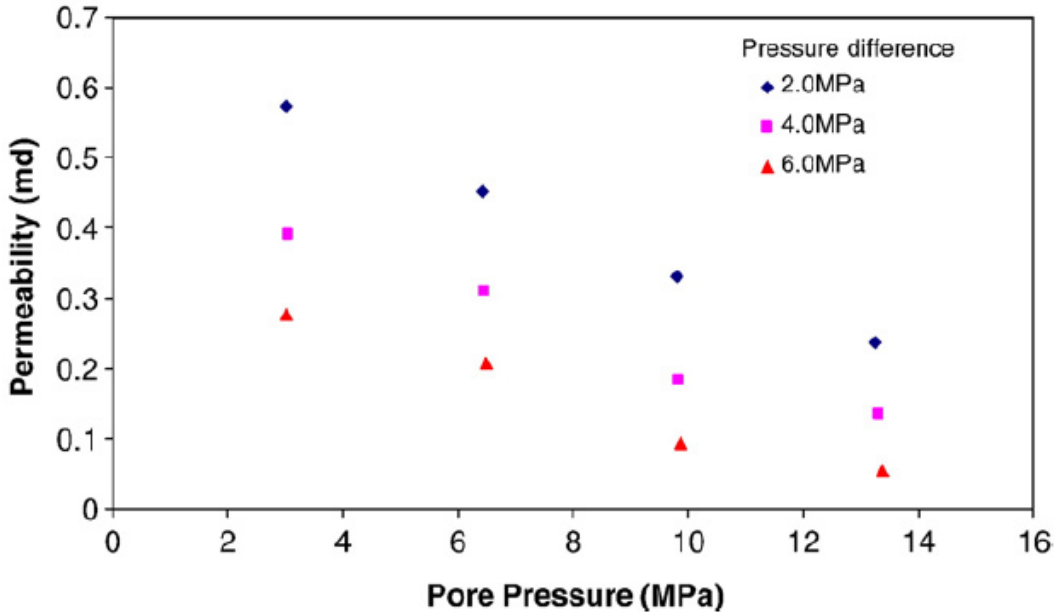

(c)

Figure 2.5 Permeability measured using (a) He, (b) CH_4 and (c) CO_2 by Pan *et al.* (2010a).

Comparison between the measured permeability data and the calibrated results demonstrated that the effective stress coefficient could play an important role in the evaluation of permeability change in adsorbing gases. Mitra *et al.* (2012) developed an experimental technique to estimate the variation of permeability with pore pressure under stress-strain-controlled conditions best replicating the in-situ behaviour of coal through applying stress vertically and horizontally on coal sample. The permeability of coal increased continuously with decrease in pressure, with the rate of increase accelerating at low pressures. The primary reason for the increase appeared to be the decrease in horizontal stress resulting from the sorption-induced volumetric strain, or the so called matrix shrinkage effect.

The effect of temperature on coal permeability was investigated by Perera *et al.* (2012a) using a triaxial apparatus at five different injection pressures (between 8–13 MPa) under two different confining pressure (20 and 24 MPa) and at five different temperatures (between 25-70 °C). It was observed that there was a clear increase in CO_2 permeability with increasing temperature for any confining pressure at high injecting pressures (more than 10 MPa). However, for low injection pressures (less than 9 MPa), the temperature effect was less apparent. With increasing injection pressure, CO_2 permeability decreased at low temperatures (less than around 40 °C), and increases at high temperatures (more than 50 °C). On the one hand, the adsorption behaviour of gas is influenced by temperature, increase temperature can reduce the adsorbed amount of gas, leading to decrease in coal swelling.

On the other hand, the temperature increase can induced coal expansion, resulting in increase in coal porosity and permeability. However, there was no noticeable temperature effect on N_2 permeability as it does not create any swelling effect in coal matrix.

Coal seams are subjected to in-situ stresses and the adsorption and strain are strongly coupled. Espinoza *et al.* (2014) present a set of triaxial testing measurements on 38 mm diameter fractured sub-bituminous/bituminous coal cores exposed to CO_2. The fluid uptake, adsorption-induced strains and stresses, and the impact on permeability were simultaneously measured. The results suggested that order of magnitude changes of reservoir permeability observed in the field are linked to the sorption-induced change of Terzaghi's effective horizontal stress under a laterally constrained displacement condition. Niu *et al.* (2019) conducted a series of corresponding permeability tests for coals of different ranks under a range of adsorption pressures (2-10 MPa), moisture states (dry and wet), temperatures (35-65 °C), and effective stresses (3-10 MPa). According to Niu *et al.* (2019), coal matrix swelling induced by CO_2 adsorption narrows the cleat width and reduces the permeability of a coal reservoir, especially for supercritical CO_2. Injecting CO_2 into wet coal was observed to cause a higher permeability loss rate than the dry coal, probably due to the combined influences of CO_2 adsorption swelling, moisture-induced swelling, and water blocking effect. Analysis of the permeability contribution ratio indicated that the coal rank, CO_2 adsorption, and effective stress variation are the main controlling factors for the reservoir permeability, followed by the moisture, with the influence of the temperature being quite weak by comparison (Niu *et al.* 2019).

A wide range of models have been developed to predict coal permeability evolution, which broadly fall into two categories: analytical permeability models and coupled permeability models (Gu and Chalaturnyk 2006). Liu *et al.* (2011a) and Pan and Connell (2012) presented a thorough review of analytical coal permeability models, including model comparison and validation. Liu *et al.* (2011a) classified the major analytical models into two groups: permeability models under conditions of uniaxial strain and permeability models under conditions of constant stress. The uniaxial strain boundary condition is where strain within the horizontal plane is zero but vertical strain may occur; this boundary conditions is assumed in many prevalent permeability models (Gray 1987; Seidle *et al.* 1992; Palmer and Mansoori 1996; Pekot and Reeves 2003; Cui and Bustin 2005; Shi and Durucan 2005a; Clarkson *et al.* 2008). In addition, the constant stress boundary conditions have been widely

employed during derivation of permeability models, where the stress due to the weight of the overburden geology does not change. Models that can be applied to the stress controlled boundary conditions were developed (Robertson and Christiansen 2006; Connell *et al.* 2010; Liu and Rutqvist 2010; Liu *et al.* 2010d; Izadi *et al.* 2011; Ma *et al.* 2011).

The permeability models mentioned above assume isotropic permeability behaviour. A few models have been proposed to describe anisotropic permeability; Gu and Chalaturnyk (2010) developed a permeability model used for reservoir and geomechanical coupled simulation, in which a discontinuous coal mass (containing cleats and matrix) is as an equivalent continuum elastic medium and the anisotropy of coalbeds in permeability, matrix shrinkage/swelling due to gas desorption/adsorption, thermal expansion due to temperature change, and mechanical parameters, are all included. Liu *et al.* (2010c) presented a permeability model to define the evolution of gas sorption-induced permeability anisotropy under the full spectrum of mechanical conditions spanning prescribed in-situ stresses through constrained displacement. In the model, gas sorption induced coal directional permeabilities are linked into directional strains through an elastic modulus reduction ratio, which represents the partitioning of total strain for an equivalent porous coal medium between the fracture system and the matrix. Wu *et al.* (2010b) extended their previous work to define the evolution of gas sorption-induced permeability anisotropy under variable stresses and constrained displacement boundary conditions.

In addition to analytical permeability models, coupled permeability models have also proposed to predict the changes in coal permeability (Zhang *et al.* 2008; Gu and Chalaturnyk 2010; Liu *et al.* 2010c). These models are used in reservoir and geomechanical coupled simulations. For example, Zhang *et al.* (2008) implemented a general porosity and permeability model into a coupled gas flow and coal deformation finite element model to evaluate the influence of sorption-induced coal matrix deformation on the evolution of porosity and permeability of fractured coal seams.

Recently, a number of permeability models have been developed for more complicated conditions (e.g. Qu *et al.* 2012; Li *et al.* 2016; Teng *et al.* 2016a). Qu *et al.* (2012) developed a fully coupled thermal, hydrogeological and mechanical (THM) model to evaluate the evolution of coal permeability under variable pressure and temperature. It was found that the variation in temperature affects coal permeability via thermal expansion and sorption-induced swelling. A thermally sensitive permeability model including matrix permeability

and fracture permeability was proposed to describe the coal-gas interactions under variable temperature. It describes the impact of thermal expansion, thermal fracturing, the change of matrix sorption capacity, and the thermal volatilisation of fracture surfaces on coal permeability (Teng *et al.* 2016a).

Most models consider the matrix deformation to be equal to the fracture deformation. However, some studies have shown that only part of the matrix deformation contributes to the fracture deformation. Connell *et al.* (2010) and Liu and Rutqvist (2010) established permeability models in which the sorption deformation only partly applied to the fractures. More recently, the concept of an internal swelling coefficient has been introduced to quantify the contribution of adsorption-induced matrix deformation to fracture aperture and coal permeability (Guo *et al.* 2014; Lu *et al.* 2016; Zhou *et al.* 2016; Liu *et al.* 2017b; Zagorščak 2017). Although these permeability models can match the history data well, the emphasis of these models is laid on the change in fracture porosity; hence, the effects of changes in the microporous coal matrix are ignored and the fundamental mechanism of permeability or porosity variation during coal expansion is not revealed. Also, the impact of coal matrix-fracture compartment interactions on the evolution of coal permeability has not been incorporated appropriately. Swelling is the major technical barrier that is currently limiting utilisation of coal seams for CO_2 sequestration with ECBM recovery, because the permeability is reduced significantly mainly attributed to coal matrix-fracture compartment interactions, it is necessary to improve understanding of matrix-fracture interactions during coal swelling.

2.5 Modelling of CO_2 storage and enhanced coalbed methane recovery

A wide range of experimental and theoretical studies have been performed to investigate the complex interactions occurring in CO_2 sequestration with-ECBM recovery. Different from conventional reservoirs, gas flow within coal seams is a complex physical and chemical process coupling solid deformation, gas adsorption/desorption, gas transport, water flow, and thermal transport, as shown in Figure 2.6. The overall behaviour depends strongly on these process interactions and, combined with the complex structure of coal, this presents a considerable modelling challenge. The aim of this section is to review the current state-of-the-art in relation to coupled model development and application in this area.

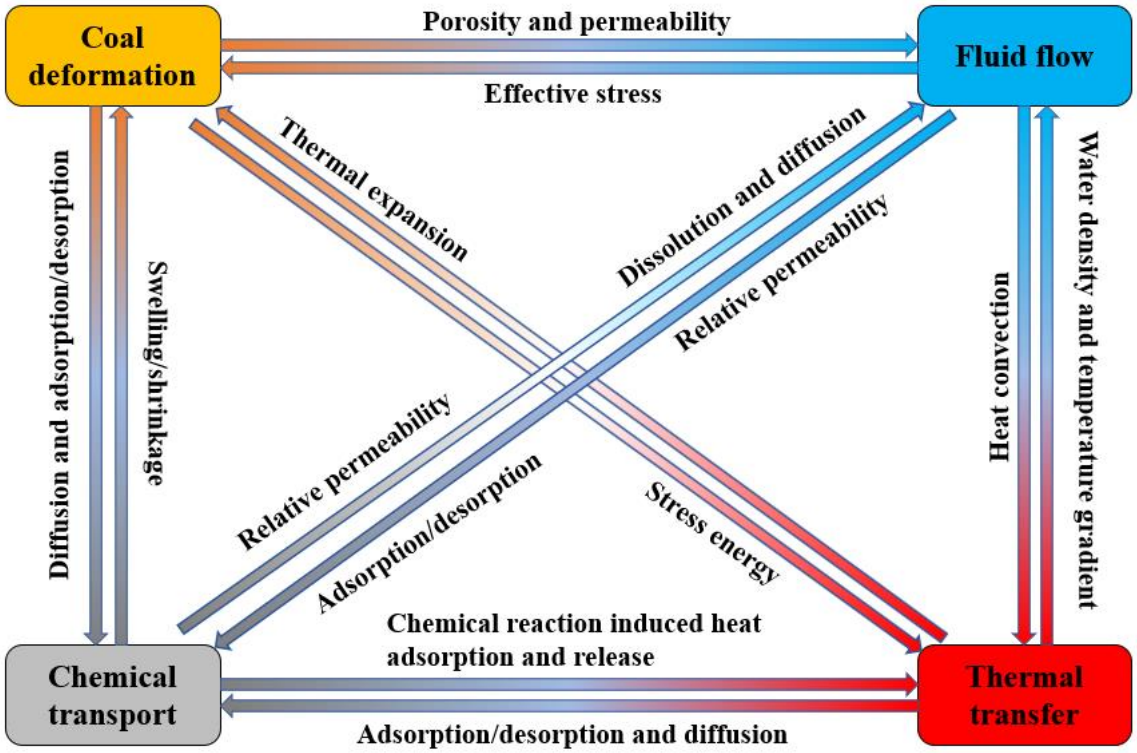

Figure 2.6 Cross-coupling in coal-gas interaction during CO_2 sequestration with ECBM recovery.

2.5.1 Conceptual models for representation of fractured porous media

Fractures in porous media are discontinuities in the form of narrow zones that are locally approximately planar and have distinctly different characteristics than the porous medium (Watanabe 2011; Berre *et al.* 2018). Fractures provide the most likely pathway for the transmission of fluid and heat and their hydraulic and transport behaviour are quite distinct to the rock matrix itself. Although the rock matrix may be impervious, or essentially impervious, to flow, it can play a primary role for the retardation of fluid, chemicals, or for heat storage. It seems impossible to set up a model that is an exact representation of reality, however, a few conceptual models have been developed that are able to reflect the occurrence and significance of both fractures and pore spaces within the rock matrix. The optimal choice of model concept strongly depends on the scale of the problem, the geological characteristics of the area of investigation, and the purpose of the simulation (Dietrich *et al.* 2005).

In general, the following conceptual models exist for fractured rock modelling, as illustrated in Figure 2.6:

- Equivalent continuum model
- Multi-continuum model
- Discrete fracture matrix model
- Discrete fracture network model

The first is the equivalent continuum approach that treats a fractured rock as an equivalent porous medium with fractures represented by adjusting the bulk permeability. A homogenisation process is performed to obtain averaged rock properties that represent the fracture network and matrix blocks (Wu *et al.* 2004). This approach is simple but less accurate, especially for problems with a large permeability contrast between the fractures and rock matrix (Hao *et al.* 2013). The equivalent continuum approach is applicable to fractured media when a representative elementary volume (REV) can be identified.

The multi-continuum approach represents a fractured porous medium as two or more overlapping continua, and was originally proposed by Barenblatt *et al.* (1960) and then widely improved and applied to predict the flow and transport in fractured reservoirs (e.g.Warren and Root 1963; Gerke and Genuchten 1993; Wu *et al.* 2011; Hosking *et al.* 2017). Dual continuum models, also known as dual porosity models (DP), are the most prevalent form of multi-continuum model, having been implemented in many reservoir simulators. This approach is able to express the different characteristics of the fractures and rock matrix. The fracture continuum generally covers the conductive part, whereas the matrix continuum generally provides the storage capacity. The fracture network and porous matrix are modelled as distinct, overlapping continua with interaction via a non-equilibrium mass exchange term. Based on the treatment of flow mechanisms within the porous matrix block, dual porosity model can be grouped into two different categories: dual porosity/single permeability (DPSP) models and dual porosity/dual permeability (DPDP) models. The key difference is that the DPSP model only considers bulk fluid flow within the fracture continuum. Local fluid flow occurs between the matrix element and the overlapping fracture element, with matrix elements acting as a sink or source for fluid flow within the adjacent fractures. By comparison, in the DPDP model, all matrix elements are connected with each other and are assumed to be permeable, hence, the matrix continuum provides both flow channels and whilst also acting as a sink or source for fluid flow in the fractures (Hill and Thomas 1985; Lee *et al.* 1999; Šimůnek and van Genuchten 2008; Al-Kobaisi *et al.* 2009; Hosking *et al.* 2017). Conventional DP models are appropriate for reservoirs with highly

connected small-scale fractures, but may not provide accurate solutions for cases of high-localised anisotropy and struggle to account for the presence of multi-scale fractures (Moinfar *et al.* 2011).

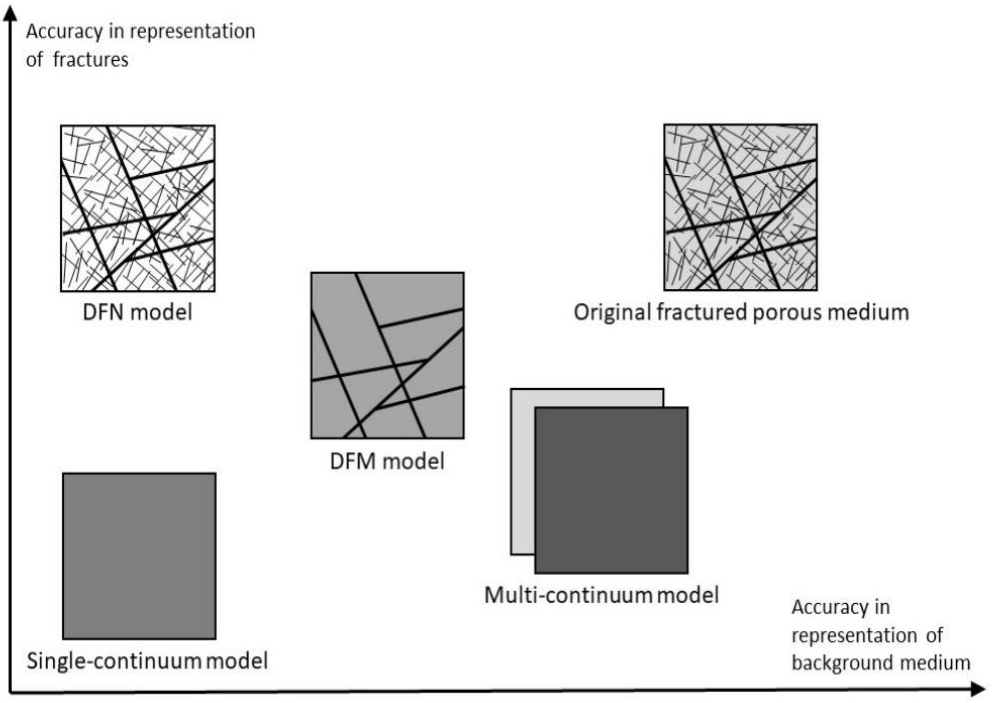

Figure 2.6 Conceptual models for modelling of a fractured porous medium (Berre *et al.* 2018).

To overcome the reliance of DP models on the presence of an idealised regular fracture topology, the discrete fracture matrix (DFM) model attempts to represent the effect of individual fractures explicitly, allowing for a more accurate and realistic description of the fracture network and its associated flow dynamics (Jiang and Younis 2016). Over recent decades, DFM models have received significant attention. They have been introduced for single-phase flow (Noorishad and Mehran 1982; Baca *et al.* 1984) and two-phase flow (Kim and Deo 2000; Karimi-Fard and Firoozabadi 2003), combining the finite element method and unstructured grids. In practice, explicit processing of fractures with a conforming mesh requires a large number of elements, which can become very computationally costly as fracture network complexity and problem scale increase. Recently, Li and Lee (2006), Lee et al. (2001), Norbeck et al.(2014), and Moinfar et al. (2012) developed and improved an embedded discrete fracture model that can represent the effect of each fracture explicitly using a structured grid, disregarding the requirement for the simulation mesh to conform with the fracture geometry. In principle, all the fractures within the domain can be

incorporated, but in practice it is not feasible to retain an explicit representation of all fractures because of the associated high computational expense. Therefore, DFM models are lose effectiveness and efficiency in their description of fractured porous media with complex fracture systems, especially when a large number of small-scale fractures exist (Berre *et al.* 2018).

The network of fractures, disregarding the host medium, is commonly referred to as a discrete fracture network (DFN). In a DFN model, all fluid is assumed to be contained within the fracture network, which is represented by a lattice. Strictly speaking, this is not a model of a fractured porous medium since the material in-between the fractures is considered impermeable. In particular, DFN flow models are appropriate for porous media where the entire porosity and permeability is due to fractures that can be explicitly represented. This gives an accurate representation of dynamics in fractures, which can be of use in multi-physics coupling, such as reactive flows and mechanical deformation (Berre *et al.* 2018).

Coal is a naturally fractured dual porosity reservoir, typically consisting of a micro-porous matrix and natural fractures (cleats). Connected fractures dominate bulk flow patterns, and their representation is therefore a critical part of model design. In recent years, the treatment of hydraulic fracturing has been considered an effective means to enhance the CO_2 injectivity of coal (van Bergen *et al.* 2009). Therefore, a modelling framework capable of efficiently handling multiscale fractures is particularly valuable for this application.

In order to achieve a balance between accurate representation, computational efficiency, and field application, improved approaches have been presented in the literature (Lee *et al.* 2001; Gong 2007; Maier and Geiger 2013; Moinfar *et al.* 2013; Jiang and Younis 2016; Norbeck *et al.* 2016; Li *et al.* 2017; Wang *et al.* 2017; Xu *et al.* 2017b; Zhu *et al.* 2017; Rueda *et al.* 2018; Liu *et al.* 2019b; Xu *et al.* 2019). A hierarchical fracture modelling approach was developed by Lee et al.(2001) in which the different scale fractures are modelled distinctly using a structured grid. Norbeck et al (2014) adopted a hierarchical approach for the matrix-fracture mass transfer component of the model to ensure that the fracture propagation problem remained tractable in terms of numerical efficiency. Wang *et al*.(2017) developed a comprehensive model that couples embedded discrete fractures, multiple interacting continua, and geomechanics to accurately simulate the fluid flow in shale gas reservoirs with multiscale fractures, with similar models also presented in the works of Wu *et al.* (2014), Chai *et al.* (2016) and Jiang and Younis (2016). Rueda (2018), Moinfar *et al* (2013), Maier

and Geiger (2013), and Li *et al* (2017) developed integrated DFM and DP models for fluid flow in fractured media, whereby large-scale hydraulic fractures are described by an embedded discrete fracture method, whilst middle-scale and small-scale natural fractures are modelled using the dual continuum approach. Zhu *et al*. (2017) presenetd a coupled discrete fracture and discrete dual continuum model to simulate fluid flow in fractured systems, with sparse small-scale fractures modelled using a discrete dual continuum approach, which is different from the conventional DPDP models. In the hybrid approach, the establishment of the link between the fine-scale discrete fracture network and the corresponding continuum-type model is a critical aspect. Compared to conventional models, hybrid models that can effectively integrate the DFM model with continuum-type approachs are a promising direction towards the accuracy and efficient modelling of natrually fractured reservoirs with a complex fracture system (Jiang and Younis 2016; Rueda *et al.* 2018).

2.5.2 Coupled simulation of CO_2 sequestration and CBM recovery

As shown in Figure 2.5, CO_2 sequestration with ECBM recovery typically involves complex thermal-hydraulic-chemical-mechanical (THCM) processes. For instance, geomechanics may have significant effects on the porosity and permeability of the formation, which in turn affect flow and transport processes. The fluid phases may be compressible, such that their mass density and dynamic viscosity may vary depending on the reservoir pressure and temperature.

There are relatively few models appropriate for CBM recovery simulation where a fully coupled simulation method is applied. Rutqvist *et al.* (2002) presented a thermal-hydraulic-mechanical coupled model to analysis multiphase fluid flow, heat transfer, and deformation in fractured porous rock using the equivalent continuum approach, achieving a solution by jointly executing the TOUGH2 and FLAC3D computer codes. A similar coupled THCM model has been developed by Taron *et al.* (2009). However, their model employed a multi-continuum approach, with multiphase fluid behaviour coupled with the mechanical response in one continuum via dual porosity poroelasticity and thermodynamically controlled fluid compressibility. The gas adsorption behaviour was neglected in these two models.

Zhao *et al*. (2004) presented a nonlinear coupled model to simulate CBM production. In the application of their model, the physical mechanisms of solid deformations and gas seepage in fractured rock were investigated. The flows and deformations in the matrix and fractures

were considered separately and the dual permeability changes with in-situ stress were described with different permeability models for each continuum. Connell (2009) developed a coupled numerical mode for gas drainage from coal seams. The modelling approach involved coupling the existing coal seam gas reservoir simulator, SIMED II, with the geomechanical simulator, FLAC3D. Whilst SIMED II was used to simulate gas migration in a hypothetical coal seam and a series of production scenarios, FLAC3D simulated the geomechanical response of the coal and the adjacent non-coal geological formations to fluid pressure and gas content changes imported from SIMED II.

Gu and Chalaturnyk (2010) established a coupled geomechanical model for coalbed reservoir simulation. In the formulation, the discontinuous coal mass (containing cleats and porous matrix) was considered as an equivalent continuum elastic medium considering the anisotropy of coalbeds with regards to permeability, matrix shrinkage/swelling due to gas desorption/adsorption, thermal expansion due to temperature change, and mechanical parameters. The implementation procedure for an explicit sequential coupled model using the developed theory in combination with industrial simulators was detailed, and its application in the study of pressure depletion for CBM production was demonstrated. Zhu *et al.* (2011) developed a coupled model of coal deformation, gas transport and thermal transport to investigate the complex coal and gas interactions under variable temperatures. Thararoop *et al.* (2012) has presented a compositional dual-porosity, dual-permeability CBM simulator, in which the CBM reservoir is treated as a dual porosity, dual-permeability system. The numerical model incorporated the effects of water presence in the coal matrix and the phenomena of coal shrinkage and swelling.

Liu *et al.* (2015b) reported that the effective stress law for multi-porosity media was more suitable for CBM reservoirs and proposed a coupled gas flow and coal deformation model with the Klinkenberg effect. A fully coupled thermal-hydraulic-mechanical model (THM). including coal deformation, gas seepage, water seepage, and thermal transport governing equations was presented in Li *et al.* (2016). The coal mass was treated as a dual porosity and single permeability medium, whilst CBM migration was considered as a combined process of desorption, diffusion and seepage. The dynamic evolution model of permeability serving as the coupled term for the THM model was developed under the combined influence of stress, water pressure, gas pressure, gas adsorption/desorption, and temperature. Bertrand *et al.* (2017) develoepd a hydro-mechanical model for CBM production. The model was

developed based on a dual-continuum approach due to the particular structure of coal. This fully coupled hydro-mechanical model captures the sorption-induced volumetric strain or the dependence of permeability on fracture aperture, which evolves with the stress state.

In addition to the CBM models described above, several coupled numerical models have been developed to describe the thermal-hydraulic-chemical-mechanical (THCM) behaviour during CO_2-ECBM recovery (Connell and Detournay 2009; Ozdemir 2009; Wu *et al.* 2010a; Thararoop *et al.* 2012; Wei and Zhang 2013; Hosking *et al.* 2017; Ma *et al.* 2017a; Fan *et al.* 2018; Vishal *et al.* 2018; Chen *et al.* 2019a; Fan *et al.* 2019a; Fan *et al.* 2019b; Fang *et al.* 2019). Ozdemir (2009) developed a single continuum model to predict CBM production and CO_2 sequestration in a coal seam, in which only two phase flow was considered while the thermal and mechanical effects were not accounted for. Wu *et al.* (2010a) presented a novel isothermal dual poroelastic model to quantify the dynamics of CO_2 injection into coal. The model separately accommodated ideal gas flow and transport in the coal matrix and fracture systems as well as the role of dual porosity mechanical deformation. Fan *et al.* (2019b) explored the fully coupled thermo-hydro-mechanical-chemical (THMC) response of CO_2-ECBM recovery ,considering the coupling relationships of competitive sorption of ideal binary gas and dissolved gas in water, two phase gas and water transport, thermal expansion and non-isothermal gas sorption, and coal deformation, assuming local thermal equilibrium.

Despite the progress made in coupled modelling of CO_2 sequestration with ECBM recovery, there remain opportunities to improve our current theoretical understanding of the coupled phenomena, whilst also improving the manner in which multiscale heterogeneity is handled in numerical simulations. for example, many existing models neglect the real gas effect. In addition, heat transport mechanism is different in the characteristic times between conduction of heat in the porous blocks and forced convection in the fracture network, a feature that motivates an analysis that allows for local thermal non-equilibrium. In many existing dual poroelastic models, the elastic parameters adopted only pertain to deformation of the porous matrix block, or are lumped to describe deformation of the matrix blocks and fractures as a whole. The former characterisation neglects the important impact of fracture deformation which should be substantially larger than the matrix deformation because of its greater compressibility, whilst the latter neglects the significant differences between the matrix and fracture deformations.

For complex fluid flow systems, coupled models must consider a full range of behaviour, including multiphase flow (gas and water), phase changes (from liquid to gas and vice versa), multi-component chemical transport (CH_4, CO_2, N_2), multiscale and distinct pore structure (porous matrix and fracture), and local non thermal equilibrium, enabling the study of geoenergy applications such as CBM recovery and CO_2 sequestration.

2.6 Conclusions

Studies of CO_2 sequestration with ECBM recovery ranging from experimental to theoretical and numerical modelling have been carried out in recent decades, as reviewed in this chapter. The overview has covered the structural characterisation of coal, as well as our current understanding of coal-gas interactions and transport behaviour of fluids in both the coal matrix and natural fracture network. An analysis of the conceptual models for representing fractured porous media and in particular the models developed for coupled simulation of CO_2 sequestration and CBM recovery has been provided.

Coalbeds are highly heterogeneous. This heterogeneity is usually characterised by two distinct porosity systems, namely, a well-developed network of natural fractures (cleats) and the porous matrix blocks containing a multiscale pore structure. It has been estimated that about 95% internal coal surface resides in micropores, which inherently provide the potentially available sorption sites with a strong affinity to certain gases, such as CO_2 and CH_4. Cleats and other natural fractures are the primary flow conduits in a coal seam and contain most of the moveable water but only a small fraction of adsorbed gas. The spacing and aperture of the coal cleats are two important properties that have a dominant impact on the fluid transport regime.

Gas adsorption/desorption and the associated coal deformation are two particularly important aspects of coal-gas interactions. The adsorption/desorption capacity of coal for various gas species and the stability of the adsorbed gases can be affected by a number of factors, such as moisture content, pressure, and temperature. Many models have been proposed to predict the adsorption capacity and coal swelling. However, most of these models is not able to elaborate the nature of the underlying physical and chemical processes involved under in situ conditions.

Fluid flow inside the fractures is assumed to be laminar and viscous, and is usually described by Darcy's law, with a key dependence on the relative permeability and absolute permeability. Conventional relative permeability models developed for porous media should be modified when used for fractured reservoirs. Although a large number of permeability models have been presented and can match the history data well, the emphasis of these models is laid on the change in fracture porosity; the effects of changes in the microporous coal matrix are ignored and the fundamental mechanism of permeability or porosity variation during coal expansion is not revealed. Also, the impact of coal matrix-fracture compartment interactions on the evolution of coal permeability has not been incorporated appropriately.

There are several conceptual models for fractured rock modelling, which have been developed and applied under a wide range of conditions with varying levels of accuracy. Currently, treatments to increase the CBM production and overcome the injectivity loss of CO_2 have been applied in field tests, such as hydraulic fracturing. These treatments affect the transport behaviour significantly, however, many conventional reservoir simulators are unable to handle this problem, which need to be improved.

Compared to conventional models, hybrid models that can effectively integrate the discrete fracture-matrix model with the dual continuum approach are a promising direction toward the accuracy and efficient modelling of naturally fractured reservoirs with a complex fracture system. The discrete fracture matrix model attempts to represent the effect of individual fractures explicitly, allowing for a more accurate and realistic description of the fracture network, which can be used to describe the large scale fractures. Dual porosity model represents the fracture network and porous matrix are modelled as distinct, overlapping continua with interaction via a non-equilibrium mass exchange term, which is used to represent the natured fractured network.

Different from conventional reservoirs, gas flow within coal seams is a complex physical and chemical process coupling solid deformation, gas desorption, gas movement, water flow, and thermal transport. The literature remains some way off a comprehensive description of fluid flow within coal seams. It is necessary to develop a fully coupled reservoir simulator that is capable to deal with nonisothermal, multiphase, multicomponent flow with the consideration of rock deformation, which are the focus of newly developed model in this work.

2.7 References

Al-Kobaisi, M., Kazemi, H., Ramirez, B., Ozkan, E. and Atan, S. (2009). A critical review for proper use of water/oil/gas transfer functions in dual-porosity naturally fractured reservoirs: part II. *SPE Reservoir Evaluation & Engineering* **12**(02):211-217.

Alonso, E., Zandarín, M. and Olivella, S. (2013). Joints in unsaturated rocks: thermo-hydro-mechanical formulation and constitutive behaviour. *Journal of Rock Mechanics and Geotechnical Engineering* **5**(3):200-213.

Anggara, F., Sasaki, K., Rodrigues, S. and Sugai, Y. (2014). The effect of megascopic texture on swelling of a low rank coal in supercritical carbon dioxide. *International Journal of Coal Geology* **125**:45-56.

Baca, R., Arnett, R. and Langford, D. (1984). Modelling fluid flow in fractured-porous rock masses by finite-element techniques. *International Journal for Numerical Methods in Fluids* **4**(4):337-348.

Bae, J.-S. and Bhatia, S. K. (2006). High-pressure adsorption of methane and carbon dioxide on coal. *Energy & Fuels* **20**(6):2599-2607.

Barenblatt, G., Zheltov, I. P. and Kochina, I. (1960). Basic concepts in the theory of seepage of homogeneous liquids in fissured rocks [strata]. *Journal of applied mathematics and mechanics* **24**(5):1286-1303.

Battistutta, E., Van Hemert, P., Lutynski, M., Bruining, H. and Wolf, K.-H. (2010). Swelling and sorption experiments on methane, nitrogen and carbon dioxide on dry Selar Cornish coal. *International Journal of Coal Geology* **84**(1):39-48.

Berre, I., Doster, F. and Keilegavlen, E. (2018). Flow in fractured porous media: A review of conceptual models and discretization approaches. *arXiv preprint arXiv:1805.05701*.

Bertrand, F., Cerfontaine, B. and Collin, F. (2017). A fully coupled hydro-mechanical model for the modeling of coalbed methane recovery. *Journal of Natural Gas Science and Engineering* **46**:307-325.

Bhowmik, S. and Dutta, P. (2013). Adsorption rate characteristics of methane and CO_2 in coal samples from Raniganj and Jharia coalfields of India. *International Journal of Coal Geology* **113**:50-59.

Bogdanov, I., Mourzenko, V., Thovert, J.-F. and Adler, P. (2003). Two-phase flow through fractured porous media. *Physical Review E* **68**(2):026703.

Brooks, R. H. and Corey, A. T. (1966). Properties of porous media affecting fluid flow. *Journal of the irrigation and drainage division* **92**(2):61-90.

Busch, A. and Gensterblum, Y. (2011). CBM and CO_2-ECBM related sorption processes in coal: a review. *International Journal of Coal Geology* **87**(2):49-71.

Busch, A., Gensterblum, Y. and Krooss, B. M. (2003). Methane and CO_2 sorption and desorption measurements on dry Argonne premium coals: pure components and mixtures. *International Journal of Coal Geology* **55**(2-4):205-224.

Busch, A., Gensterblum, Y., Krooss, B. M. and Littke, R. (2004). Methane and carbon dioxide adsorption–diffusion experiments on coal: upscaling and modeling. *International Journal of Coal Geology* **60**(2):151-168.

Bustin, R. (1997). Importance of fabric and composition on the stress sensitivity of permeability in some coals, northern Sydney basin, Australia: relevance to coalbed methane exploitation. *AAPG bulletin* **81**(11):1894-1908.

Cai, Y., Liu, D., Pan, Z., Yao, Y., Li, J. and Qiu, Y. (2013). Pore structure and its impact on CH_4 adsorption capacity and flow capability of bituminous and subbituminous coals from Northeast China. *Fuel* **103**:258-268.

Cai, Y., Pan, Z., Liu, D., Zheng, G., Tang, S., Connell, L. D., Zhou, Y. (2014). Effects of pressure and temperature on gas diffusion and flow for primary and enhanced coalbed methane recovery. *Energy Exploration & Exploitation* **32**(4):601-619.

Ceglarska-Stefańska, G. and Brzóska, K. (1998). The effect of coal metamorphism on methane desorption. *Fuel* **77**(6):645-648.

Ceglarska-Stefańska, G. and Czapliński, A. (1993). Correlation between sorption and dilatometric processes in hard coals. *Fuel* **72**(3):413-417.

Ceglarska-Stefaríska, G. (1994). Effect of gas pressure in methane induced swelling on the porous structure of coals. In: *Studies in Surface Science and Catalysis*. Vol. 87. Elsevier, pp. 671-677.

Chai, Z., Yan, B., Killough, J. and Wang, Y. eds. (2016). *Dynamic embedded discrete fracture multi-continuum model for the simulation of fractured shale reservoirs*. International Petroleum Technology Conference. International Petroleum Technology Conference.

Charrière, D., Pokryszka, Z. and Behra, P. (2010). Effect of pressure and temperature on diffusion of CO_2 and CH_4 into coal from the Lorraine basin (France). *International Journal of Coal Geology* **81**(4):373-380.

Chattaraj, S., Mohanty, D., Kumar, T. and Halder, G. (2016). Thermodynamics, kinetics and modeling of sorption behaviour of coalbed methane–a review. *Journal of Unconventional Oil and Gas Resources* **16**:14-33.

Chen, D., Pan, Z., Liu, J. and Connell, L. D. (2012). Modeling and simulation of moisture effect on gas storage and transport in coal seams. *Energy & Fuels* **26**(3):1695-1706.

Chen, D., Pan, Z., Liu, J. and Connell, L. D. (2013). An improved relative permeability model for coal reservoirs. *International Journal of Coal Geology* **109**:45-57.

Chen, M., Hosking, L. J., Sandford, R. J. and Thomas, H. R. (2019). Dual porosity modelling of the coupled mechanical response of coal to gas flow and adsorption. *International Journal of Coal Geology*.

Chen, Z., Pan, Z., Liu, J., Connell, L. D. and Elsworth, D. (2011). Effect of the effective stress coefficient and sorption-induced strain on the evolution of coal permeability: experimental observations. *International Journal of Greenhouse Gas Control* **5**(5):1284-1293.

Chikatamarla, L., Cui, X. and Bustin, R. M. eds. (2004). *Implications of volumetric swelling/shrinkage of coal in sequestration of acid gases*. Proceedings of the International Coalbed Methane Symposium, Tuscaloosa, AL.

Clarkson, C. and Bustin, R. (1999a). The effect of pore structure and gas pressure upon the transport properties of coal: a laboratory and modeling study. 1. Isotherms and pore volume distributions. *Fuel* **78**(11):1333-1344.

Clarkson, C. and Bustin, R. (1999b). The effect of pore structure and gas pressure upon the transport properties of coal: a laboratory and modeling study. 2. Adsorption rate modeling. *Fuel* **78**(11):1345-1362.

Clarkson, C. and Bustin, R. (2000). Binary gas adsorption/desorption isotherms: effect of moisture and coal composition upon carbon dioxide selectivity over methane. *International Journal of Coal Geology* **42**(4):241-271.

Clarkson, C., Bustin, R. and Levy, J. (1997). Application of the mono/multilayer and adsorption potential theories to coal methane adsorption isotherms at elevated temperature and pressure. *Carbon* **35**(12):1689-1705.

Clarkson, C. R., Jordan, C. L., Gierhart, R. R. and Seidle, J. P. (2008). Production data analysis of coalbed-methane wells. *SPE Reservoir Evaluation & Engineering* **11**(02):311-325.

Clarkson, C. R., Pan, Z., Palmer, I. D. and Harpalani, S. (2010). Predicting sorption-induced strain and permeability increase with depletion for coalbed-methane reservoirs. *Spe Journal* **15**(01):152-159.

Connell, L. (2009). Coupled flow and geomechanical processes during gas production from coal seams. *International Journal of Coal Geology* **79**(1):18-28.

Connell, L. and Detournay, C. (2009). Coupled flow and geomechanical processes during enhanced coal seam methane recovery through CO_2 sequestration. *International Journal of Coal Geology* **77**(1):222-233.

Connell, L. D., Lu, M. and Pan, Z. (2010). An analytical coal permeability model for tri-axial strain and stress conditions. *International Journal of Coal Geology* **84**(2):103-114.

Crosdale, P. J., Beamish, B. B. and Valix, M. (1998). Coalbed methane sorption related to coal composition. *International Journal of Coal Geology* **35**(1-4):147-158.

Crosdale, P. J., Moore, T. A. and Mares, T. E. (2008). Influence of moisture content and temperature on methane adsorption isotherm analysis for coals from a low-rank, biogenically-sourced gas reservoir. *International Journal of Coal Geology* **76**(1-2):166-174.

Cui, X. and Bustin, R. M. (2005). Volumetric strain associated with methane desorption and its impact on coalbed gas production from deep coal seams. *Aapg Bulletin* **89**(9):1181-1202.

Cui, X., Bustin, R. M. and Chikatamarla, L. (2007). Adsorption-induced coal swelling and stress: Implications for methane production and acid gas sequestration into coal seams. *Journal of Geophysical Research* **112**(B10).

Cui, X., Bustin, R. M. and Dipple, G. (2004). Selective transport of CO_2, CH_4, and N_2 in coals: insights from modeling of experimental gas adsorption data. *Fuel* **83**(3):293-303.

Dawson, G. and Esterle, J. (2010). Controls on coal cleat spacing. *International Journal of Coal Geology* **82**(3-4):213-218.

Day, S., Duffy, G., Sakurovs, R. and Weir, S. (2008a). Effect of coal properties on CO_2 sorption capacity under supercritical conditions. *International Journal of Greenhouse Gas Control* **2**(3):342-352.

Day, S., Fry, R. and Sakurovs, R. (2008b). Swelling of Australian coals in supercritical CO_2. *International Journal of Coal Geology* **74**(1):41-52.

Day, S., Fry, R. and Sakurovs, R. (2011). Swelling of moist coal in carbon dioxide and methane. *International Journal of Coal Geology* **86**(2):197-203.

Day, S., Fry, R. and Sakurovs, R. (2012). Swelling of coal in carbon dioxide, methane and their mixtures. *International Journal of Coal Geology* **93**:40-48.

Day, S., Fry, R., Sakurovs, R. and Weir, S. (2010). Swelling of coals by supercritical gases and its relationship to sorption. *Energy & Fuels* **24**(4):2777-2783.

Day, S., Sakurovs, R. and Weir, S. (2008c). Supercritical gas sorption on moist coals. *International Journal of Coal Geology* **74**(3-4):203-214.

DeGance, A. E. (1992). Multicomponent high-pressure adsorption equilibria on carbon substrates: theory and data. *Fluid Phase Equilibria* **78**:99-137.

Dietrich, P., Helmig, R., Sauter, M., Hötzl, H., Köngeter, J. and Teutsch, G. (2005). *Flow and transport in fractured porous media*. Springer Science & Business Media.

Do, D. D. (1998). *Adsorption analysis: equilibria and kinetics*. Imperial college press London.

Dong, J., Cheng, Y., Liu, Q., Zhang, H., Zhang, K. and Hu, B. (2017). Apparent and true diffusion coefficients of methane in coal and their relationships with methane desorption capacity. *Energy & Fuels* **31**(3):2643-2651.

Durucan, S., Ahsan, M., Syed, A., Shi, J.-Q. and Korre, A. (2013). Two phase relative permeability of gas and water in coal for enhanced coalbed methane recovery and CO_2 storage. *Energy Procedia* **37**:6730-6737.

Espinoza, D., Vandamme, M., Pereira, J.-M., Dangla, P. and Vidal-Gilbert, S. (2014). Measurement and modeling of adsorptive–poromechanical properties of bituminous coal cores exposed to CO_2: Adsorption, swelling strains, swelling stresses and impact on fracture permeability. *International Journal of Coal Geology* **134**:80-95.

Ettinger, I., Lidin, G., Dmitriev, A. and Zhupakhina, E. (1958). Systematic Handbook for the Determination of the Methane Content of Coal Seams from the Seam Pressure of the Gas and the Methane Capacity of the Coal. *Institute of Mining, Academy of Sciences, USSR, US Bureau of Mines Translation* (1505).

Fan, C., Elsworth, D., Li, S., Chen, Z., Luo, M., Song, Y. and Zhang, H. (2019a). Modelling and optimization of enhanced coalbed methane recovery using CO_2/N_2 mixtures. *Fuel* **253**:1114-1129.

Fan, C., Elsworth, D., Li, S., Zhou, L., Yang, Z. and Song, Y. (2019b). Thermo-hydro-mechanical-chemical couplings controlling CH4 production and CO_2 sequestration in enhanced coalbed methane recovery. *Energy* **173**:1054-1077.

Fan, Y., Deng, C., Zhang, X., Li, F., Wang, X. and Qiao, L. (2018). Numerical study of CO_2-enhanced coalbed methane recovery. *International Journal of Greenhouse Gas Control* **76**:12-23.

Fang, H., Sang, S. and Liu, S. (2019). The coupling mechanism of the thermal-hydraulic-mechanical fields in CH4-bearing coal and its application in the CO2-enhanced coalbed methane recovery. *Journal of Petroleum Science and Engineering*.

Gan, H., Nandi, S. and Walker, P. (1972). Nature of the porosity in American coals. *Fuel* **51**(4):272-277.

Gathitu, B. B., Chen, W.-Y. and McClure, M. (2009). Effects of coal interaction with supercritical CO_2: physical structure. *Industrial & Engineering Chemistry Research* **48**(10):5024-5034.

Gensterblum, Y., Busch, A. and Krooss, B. M. (2014). Molecular concept and experimental evidence of competitive adsorption of H_2O, CO_2 and CH_4 on organic material. *Fuel* **115**:581-588.

Gensterblum, Y., Merkel, A., Busch, A. and Krooss, B. M. (2013). High-pressure CH4 and CO2 sorption isotherms as a function of coal maturity and the influence of moisture. *International Journal of Coal Geology* **118**:45-57.

Gensterblum, Y., Van Hemert, P., Billemont, P., Busch, A., Charriere, D., Li, D., Wolf, K.-H. (2009). European inter-laboratory comparison of high pressure CO_2 sorption isotherms. I: Activated carbon. *Carbon* **47**(13):2958-2969.

George, J. S. and Barakat, M. (2001). The change in effective stress associated with shrinkage from gas desorption in coal. *International Journal of Coal Geology* **45**(2-3):105-113.

Gerke, H. and Genuchten, M. v. (1993). Evaluation of a first-order water transfer term for variably saturated dual-porosity flow models. *Water Resources Research* **29**(4):1225-1238.

Gong, B. (2007). *Effective models of fractured systems*.

Gray, I. (1987). Reservoir engineering in coal seams: Part 1-The physical process of gas storage and movement in coal seams. *SPE Reservoir Engineering* **2**(01):28-34.

Gu, F. and Chalaturnyk, R. (2006). Numerical simulation of stress and strain due to gas sorption/desorption and their effects on in situ permeability of coalbeds. *Journal of Canadian Petroleum Technology* **45**(10).

Gu, F. and Chalaturnyk, R. (2010). Permeability and porosity models considering anisotropy and discontinuity of coalbeds and application in coupled simulation. *Journal of Petroleum Science and Engineering* **74**(3-4):113-131.

Guo, P., Cheng, Y., Jin, K., Li, W., Tu, Q. and Liu, H. (2014). Impact of effective stress and matrix deformation on the coal fracture permeability. *Transport in porous media* **103**(1):99-115.

Gupta, S., Helmig, R. and Wohlmuth, B. (2015). Non-isothermal, multi-phase, multi-component flows through deformable methane hydrate reservoirs. *Computational Geosciences* **19**(5):1063-1088.

Ham, Y. S. and Kantzas, A. eds. (2011). *Relative permeability of coal to gas (Helium, Methane, and Carbon Dioxide) and water: results and experimental limitations*. Canadian Unconventional Resources Conference. Society of Petroleum Engineers.

Han, F., Busch, A., Krooss, B. M., Liu, Z. and Yang, J. (2013). CH_4 and CO_2 sorption isotherms and kinetics for different size fractions of two coals. *Fuel* **108**:137-142.

Hao, Y., Fu, P. and Carrigan, C. R. eds. (2013). *Application of a dual-continuum model for simulation of fluid flow and heat transfer in fractured geothermal reservoirs*. Proceedings, 38th Workshop On Geothermal Reservoir Engineering, vol SGP-TR-198. Stanford University, Stanford, California.

Harpalani, S. and Chen, G. (1995). Estimation of changes in fracture porosity of coal with gas emission. *Fuel* **74**(10):1491-1498.

Harpalani, S. and Chen, G. (1997). Influence of gas production induced volumetric strain on permeability of coal. *Geotechnical & Geological Engineering* **15**(4):303-325.

Harpalani, S., Prusty, B. K. and Dutta, P. (2006). Methane/CO_2 sorption modeling for coalbed methane production and CO2 sequestration. *Energy & Fuels* **20**(4):1591-1599.

Harpalani, S. and Schraufnagel, R. A. (1990). Shrinkage of coal matrix with release of gas and its impact on permeability of coal. *Fuel* **69**(5):551-556.

Hill, A. and Thomas, G. eds. (1985). *A new approach for simulating complex fractured reservoirs*. Middle east oil technical conference and exhibition. Society of Petroleum Engineers.

Hol, S., Peach, C. J. and Spiers, C. J. (2011). Applied stress reduces the CO_2 sorption capacity of coal. *International Journal of Coal Geology* **85**(1):128-142.

Hol, S. and Spiers, C. J. (2012). Competition between adsorption-induced swelling and elastic compression of coal at CO_2 pressures up to 100MPa. *Journal of the Mechanics and Physics of Solids* **60**(11):1862-1882.

Hosking, L. J., Thomas, H. R. and Sedighi, M. (2017). A dual porosity model of high-pressure gas flow for geoenergy applications. *Canadian Geotechnical Journal* **55**(6):839-851.

Izadi, G., Wang, S., Elsworth, D., Liu, J., Wu, Y. and Pone, D. (2011). Permeability evolution of fluid-infiltrated coal containing discrete fractures. *International Journal of Coal Geology* **85**(2):202-211.

Jiang, J. and Younis, R. M. (2016). Hybrid coupled discrete-fracture/matrix and multicontinuum models for unconventional-reservoir simulation. *SPE Journal* **21**(03):1,009-001,027.

Karacan, C. Ö. (2003). Heterogeneous sorption and swelling in a confined and stressed coal during CO_2 injection. *Energy & Fuels* **17**(6):1595-1608.

Karacan, C. Ö. (2007). Swelling-induced volumetric strains internal to a stressed coal associated with CO_2 sorption. *International Journal of Coal Geology* **72**(3):209-220.

Karimi-Fard, M. and Firoozabadi, A. (2003). *Numerical Simulation of Water Injection in Fractured Media Using the Discrete Fractured Model and the Galerkin Method. SPEREE 6 (2): 117–126*. SPE-83633-PA.

Kim, J. G. and Deo, M. D. (2000). Finite element, discrete-fracture model for multiphase flow in porous media. *AIChE Journal* **46**(6):1120-1130.

Krooss, B. v., Van Bergen, F., Gensterblum, Y., Siemons, N., Pagnier, H. and David, P. (2002). High-pressure methane and carbon dioxide adsorption on dry and moisture-equilibrated Pennsylvanian coals. *International Journal of Coal Geology* **51**(2):69-92.

Langmuir, I. (1918). The adsorption of gases on plane surfaces of glass, mica and platinum. *Journal of the American Chemical society* **40**(9):1361-1403.

Larsen, J. W. (2004). The effects of dissolved CO_2 on coal structure and properties. *International Journal of Coal Geology* **57**(1):63-70.

Laubach, S., Marrett, R., Olson, J. and Scott, A. (1998). Characteristics and origins of coal cleat: a review. *International Journal of Coal Geology* **35**(1):175-207.

Lee, J., Choi, S.-U. and Cho, W. (1999). A comparative study of dual-porosity model and discrete fracture network model. *KSCE Journal of Civil Engineering* **3**(2):171-180.

Lee, S. H., Lough, M. and Jensen, C. (2001). Hierarchical modeling of flow in naturally fractured formations with multiple length scales. *Water resources research* **37**(3):443-455.

Levine, J. R. (1996). Model study of the influence of matrix shrinkage on absolute permeability of coal bed reservoirs. *Geological Society, London, Special Publications* **109**(1):197-212.

Levy, J. H., Day, S. J. and Killingley, J. S. (1997). Methane capacities of Bowen Basin coals related to coal properties. *Fuel* **76**(9):813-819.

Li, D., Liu, Q., Weniger, P., Gensterblum, Y., Busch, A. and Krooss, B. M. (2010). High-pressure sorption isotherms and sorption kinetics of CH_4 and CO_2 on coals. *Fuel* **89**(3):569-580.

Li, K. and Horne, R. N. (2001). An experimental and analytical study of steam/water capillary pressure. *SPE Reservoir Evaluation & Engineering* **4**(06):477-482.

Li, L. and Lee, S. H. eds. (2006). *Efficient field-scale simulation for black oil in a naturally fractured reservoir via discrete fracture networks and homogenized media*. International oil & gas conference and exhibition in China. Society of Petroleum Engineers.

Li, S., Fan, C., Han, J., Luo, M., Yang, Z. and Bi, H. (2016). A fully coupled thermal-hydraulic-mechanical model with two-phase flow for coalbed methane extraction. *Journal of Natural Gas Science and Engineering* **33**:324-336.

Li, W., Dong, Z. and Lei, G. (2017). Integrating Embedded Discrete Fracture and Dual-Porosity, Dual-Permeability Methods to Simulate Fluid Flow in Shale Oil Reservoirs. *Energies* **10**(10):1471.

Liu, C., Wang, G., Sang, S., Gilani, W. and Rudolph, V. (2015a). Fractal analysis in pore structure of coal under conditions of CO_2 sequestration process. *Fuel* **139**:125-132.

Liu, C., Wang, G., Sang, S. and Rudolph, V. (2010a). Changes in pore structure of anthracite coal associated with CO2 sequestration process. *Fuel* **89**(10):2665-2672.

Liu, H.-H. and Rutqvist, J. (2010). A new coal-permeability model: internal swelling stress and fracture–matrix interaction. *Transport in Porous Media* **82**(1):157-171.

Liu, H., Sang, S., Liu, S., Wu, H., Lan, T., Xu, H. and Ren, B. (2019a). Supercritical-CO_2 Adsorption Quantification and Modeling for a Deep Coalbed Methane Reservoir in the Southern Qinshui Basin, China. *ACS Omega* **4**(7):11685-11700.

Liu, J., Chen, Z., Elsworth, D., Miao, X. and Mao, X. (2010b). Evaluation of stress-controlled coal swelling processes. *International journal of coal geology* **83**(4):446-455.

Liu, J., Chen, Z., Elsworth, D., Miao, X. and Mao, X. (2010c). Linking gas-sorption induced changes in coal permeability to directional strains through a modulus reduction ratio. *International Journal of Coal Geology* **83**(1):21-30.

Liu, J., Chen, Z., Elsworth, D., Qu, H. and Chen, D. (2011). Interactions of multiple processes during CBM extraction: a critical review. *International Journal of Coal Geology* **87**(3-4):175-189.

Liu, J., Spiers, C. J., Peach, C. J. and Vidal-Gilbert, S. (2016). Effect of lithostatic stress on methane sorption by coal: Theory vs. experiment and implications for predicting in-situ coalbed methane content. *International Journal of Coal Geology* **167**:48-64.

Liu, J., Wang, J., Gao, F., Leung, C. F. and Ma, Z. (2019b). A fully coupled fracture equivalent continuum-dual porosity model for hydro-mechanical process in fractured shale gas reservoirs. *Computers and Geotechnics* **106**:143-160.

Liu, Q., Cheng, Y., Zhou, H., Guo, P., An, F. and Chen, H. (2015b). A mathematical model of coupled gas flow and coal deformation with gas diffusion and klinkenberg effects. *Rock Mechanics and Rock Engineering* **48**(3):1163-1180.

Liu, S. and Harpalani, S. (2013). A new theoretical approach to model sorption-induced coal shrinkage or swelling. *AAPG bulletin* **97**(7):1033-1049.

Liu, S., Ma, J., Sang, S., Wang, T., Du, Y. and Fang, H. (2018). The effects of supercritical CO_2 on mesopore and macropore structure in bituminous and anthracite coal. *Fuel* **223**:32-43.

Liu, T., Lin, B. and Yang, W. (2017). Impact of matrix–fracture interactions on coal permeability: model development and analysis. *Fuel* **207**:522-532.

Lomeland, F., Ebeltoft, E. and Hammervold Thomas, W. eds. (2008). *A new versatile capillary pressure correlation*. Paper SCA 2008-08 presented at the International Symposium of the Society of Core Analysts held in Abu Dhabi, UAE.

Lu, S., Cheng, Y. and Li, W. (2016). Model development and analysis of the evolution of coal permeability under different boundary conditions. *Journal of Natural Gas Science and Engineering* **31**:129-138.

Ma, Q., Harpalani, S. and Liu, S. (2011). A simplified permeability model for coalbed methane reservoirs based on matchstick strain and constant volume theory. *International Journal of Coal Geology* **85**(1):43-48.

Ma, T., Rutqvist, J., Oldenburg, C. M. and Liu, W. (2017). Coupled thermal–hydrological–mechanical modeling of CO_2-enhanced coalbed methane recovery. *International Journal of Coal Geology* **179**:81-91.

Maier, C. and Geiger, S. eds. (2013). *Combining unstructured grids, discrete fracture representation and dual-porosity models for improved simulation of naturally fractured reservoirs*. SPE Reservoir Characterization and Simulation Conference and Exhibition. Society of Petroleum Engineers.

Marecka, A. and Mianowski, A. (1998). Kinetics of CO_2 and CH_4 sorption on high rank coal at ambient temperatures. *Fuel* **77**(14):1691-1696.

Masoudian Saadabad, M. (2013). Chemo-hydro-mechanical aspects of CO_2 sequestration in deep coal seams.

Mazumder, S., Karnik, A. A. and Wolf, K.-H. A. (2006). Swelling of coal in response to CO_2 sequestration for ECBM and its effect on fracture permeability. *Spe Journal* **11**(03):390-398.

McKee, C. R., Bumb, A. C. and Koenig, R. A. (1988). Stress-dependent permeability and porosity of coal.

Meng, Y. and Li, Z. (2016). Experimental study on diffusion property of methane gas in coal and its influencing factors. *Fuel* **185**:219-228.

Mitra, A., Harpalani, S. and Liu, S. (2012). Laboratory measurement and modeling of coal permeability with continued methane production: Part 1–Laboratory results. *Fuel* **94**:110-116.

Moinfar, A., Narr, W., Hui, M.-H., Mallison, B. T. and Lee, S. H. eds. (2011). *Comparison of discrete-fracture and dual-permeability models for multiphase flow in naturally fractured reservoirs*. SPE reservoir simulation symposium. Society of Petroleum Engineers.

Moinfar, A., Varavei, A., Sepehrnoori, K. and Johns, R. T. eds. (2012). *Development of a novel and computationally-efficient discrete-fracture model to study IOR processes in naturally fractured reservoirs*. SPE Improved Oil Recovery Symposium. Society of Petroleum Engineers.

Moinfar, A., Varavei, A., Sepehrnoori, K. and Johns, R. T. eds. (2013). *Development of a coupled dual continuum and discrete fracture model for the simulation of unconventional reservoirs*. SPE reservoir simulation symposium. Society of Petroleum Engineers.

Mosher, K., He, J., Liu, Y., Rupp, E. and Wilcox, J. (2013). Molecular simulation of methane adsorption in micro-and mesoporous carbons with applications to coal and gas shale systems. *International Journal of Coal Geology* **109**:36-44.

Mukherjee, M. and Misra, S. (2018). A review of experimental research on Enhanced Coal Bed Methane (ECBM) recovery via CO_2 sequestration. *Earth-Science Reviews* **179**:392-410.

Myers, A. L. and Prausnitz, J. M. (1965). Thermodynamics of mixed-gas adsorption. *AIChE Journal* **11**(1):121-127.

Nandi, S. P. and Walker Jr, P. L. (1975). Activated diffusion of methane from coals at elevated pressures. *Fuel* **54**(2):81-86.

Naveen, P., Asif, M., Ojha, K., Panigrahi, D. and Vuthaluru, H. B. (2017). Sorption kinetics of CH4 and CO_2 diffusion in coal: Theoretical and experimental study. *Energy & fuels* **31**(7):6825-6837.

Nie, B., Liu, X., Yang, L., Meng, J. and Li, X. (2015). Pore structure characterization of different rank coals using gas adsorption and scanning electron microscopy. *Fuel* **158**:908-917.

Niu, Q., Cao, L., Sang, S., Zhou, X. and Liu, S. (2019). Experimental study of permeability changes and its influencing factors with CO_2 injection in coal. *Journal of Natural Gas Science and Engineering* **61**:215-225.

Noorishad, J. and Mehran, M. (1982). An upstream finite element method for solution of transient transport equation in fractured porous media. *Water Resources Research* **18**(3):588-596.

Norbeck, J., Huang, H., Podgorney, R. and Horne, R. eds. (2014). *An integrated discrete fracture model for description of dynamic behavior in fractured reservoirs*. Proceedings of the 39th Workshop on Geothermal Reservoir Engineering, Stanford.

Norbeck, J. H., McClure, M. W., Lo, J. W. and Horne, R. N. (2016). An embedded fracture modeling framework for simulation of hydraulic fracturing and shear stimulation. *Computational Geosciences* **20**(1):1-18.

Ottiger, S., Pini, R., Storti, G. and Mazzotti, M. (2008). Competitive adsorption equilibria of CO_2 and CH_4 on a dry coal. *Adsorption* **14**(4):539-556.

Ozdemir, E. (2005). *Chemistry of the adsorption of carbon dioxide by Argonne premium coals and a model to simulate CO_2 sequestration in coal seams.* University of Pittsburgh.

Ozdemir, E. (2009). Modeling of coal bed methane (CBM) production and CO_2 sequestration in coal seams. *International Journal of Coal Geology* **77**(1-2):145-152.

Ozdemir, E. and Schroeder, K. (2009). Effect of moisture on adsorption isotherms and adsorption capacities of CO_2 on coals. *Energy & Fuels* **23**(5):2821-2831.

Palmer, I. and Mansoori, J. eds. (1996). *How permeability depends on stress and pore pressure in coalbeds: a new model*. SPE Annual Technical Conference and Exhibition. Society of Petroleum Engineers.

Pan, J., Hou, Q., Ju, Y., Bai, H. and Zhao, Y. (2012). Coalbed methane sorption related to coal deformation structures at different temperatures and pressures. *Fuel* **102**:760-765.

Pan, Z. and Connell, L. D. (2007). A theoretical model for gas adsorption-induced coal swelling. *International Journal of Coal Geology* **69**(4):243-252.

Pan, Z. and Connell, L. D. (2009). Comparison of adsorption models in reservoir simulation of enhanced coalbed methane recovery and CO_2 sequestration in coal. *International journal of greenhouse gas control* **3**(1):77-89.

Pan, Z. and Connell, L. D. (2012). Modelling permeability for coal reservoirs: a review of analytical models and testing data. *International Journal of Coal Geology* **92**:1-44.

Pan, Z., Connell, L. D. and Camilleri, M. (2010a). Laboratory characterisation of coal reservoir permeability for primary and enhanced coalbed methane recovery. *International Journal of Coal Geology* **82**(3-4):252-261.

Pan, Z., Connell, L. D., Camilleri, M. and Connelly, L. (2010b). Effects of matrix moisture on gas diffusion and flow in coal. *Fuel* **89**(11):3207-3217.

Pant, L. M., Huang, H., Secanell, M., Larter, S. and Mitra, S. K. (2015). Multi scale characterization of coal structure for mass transport. *Fuel* **159**:315-323.

Pekot, L. and Reeves, S. eds. (2003). *Modeling the effects of matrix shrinkage and differential swelling on coalbed methane recovery and carbon sequestration*. Paper 0328, proc. 2003 International Coalbed Methane Symposium. University of Alabama. Citeseer.

Perera, M., Ranjith, P., Choi, S. and Airey, D. (2012a). Investigation of temperature effect on permeability of naturally fractured black coal for carbon dioxide movement: An experimental and numerical study. *Fuel* **94**:596-605.

Perera, M. S. A. (2017). Influences of CO2 Injection into Deep Coal Seams: A Review. *Energy & Fuels* **31**(10):10324-10334.

Perera, M. S. A., Ranjith, P., Choi, S., Airey, D. and Weniger, P. (2012b). Estimation of gas adsorption capacity in coal: a review and an analytical study. *International Journal of Coal Preparation and Utilization* **32**(1):25-55.

Pillalamarry, M., Harpalani, S. and Liu, S. (2011). Gas diffusion behavior of coal and its impact on production from coalbed methane reservoirs. *International Journal of Coal Geology* **86**(4):342-348.

Pini, R., Ottiger, S., Burlini, L., Storti, G. and Mazzotti, M. (2009). Role of adsorption and swelling on the dynamics of gas injection in coal. *Journal of Geophysical Research: Solid Earth* **114**(B4).

Pini, R., Ottiger, S., Burlini, L., Storti, G. and Mazzotti, M. (2010). Sorption of carbon dioxide, methane and nitrogen in dry coals at high pressure and moderate temperature. *International Journal of Greenhouse Gas Control* **4**(1):90-101.

Pone, J. D. N., Halleck, P. M. and Mathews, J. P. (2009). Sorption capacity and sorption kinetic measurements of CO_2 and CH_4 in confined and unconfined bituminous coal. *Energy & Fuels* **23**(9):4688-4695.

Pone, J. D. N., Halleck, P. M. and Mathews, J. P. (2010). 3D characterization of coal strains induced by compression, carbon dioxide sorption, and desorption at in-situ stress conditions. *International Journal of Coal Geology* **82**(3-4):262-268.

Qu, H., Liu, J., Chen, Z., Wang, J., Pan, Z., Connell, L. and Elsworth, D. (2012). Complex evolution of coal permeability during CO_2 injection under variable temperatures. *International Journal of Greenhouse Gas Control* **9**:281-293.

Reiss, L. H. (1980). *The reservoir engineering aspects of fractured formations*. Editions Technip.

Robertson, E. P. (2005). *Measurement and modeling of sorption-induced strain and permeability changes in coal*. Idaho National Laboratory (INL).

Robertson, E. P. and Christiansen, R. L. (2006). *A permeability model for coal and other fractured, sorptive-elastic media*. Idaho National Laboratory (INL).

Romanov, V. N., Hur, T.-B., Fazio, J. J., Howard, B. H. and Irdi, G. A. (2013). Comparison of high-pressure CO_2 sorption isotherms on Central Appalachian and San Juan Basin coals. *International Journal of Coal Geology* **118**:89-94.

Ruckenstein, E., Vaidyanathan, A. and Youngquist, G. (1971). Sorption by solids with bidisperse pore structures. *Chemical Engineering Science* **26**(9):1305-1318.

Rueda, J., Mejia, E. and Roehl, D. (2018). Integrated discrete fracture and dual porosity-Dual permeability models for fluid flow in deformable fractured media. *Journal of Petroleum Science and Engineering*.

Rutqvist, J., Wu, Y.-S., Tsang, C.-F. and Bodvarsson, G. (2002). A modeling approach for analysis of coupled multiphase fluid flow, heat transfer, and deformation in fractured porous rock. *International Journal of Rock Mechanics and Mining Sciences* **39**(4):429-442.

Sakurovs, R., Day, S. and Weir, S. (2010). Relationships between the critical properties of gases and their high pressure sorption behavior on coals. *Energy & Fuels* **24**(3):1781-1787.

Salmachi, A. and Haghighi, M. (2012). Temperature effect on methane sorption and diffusion in coal: application for thermal recovery from coal seam gas reservoirs. *The APPEA Journal* **52**(1):291-300.

Sampath, K., Perera, M., Ranjith, P., Matthai, S., Rathnaweera, T., Zhang, G. and Tao, X. (2017). CH 4 CO_2 gas exchange and supercritical CO_2 based hydraulic fracturing as CBM production-accelerating techniques: A review. *Journal of CO_2 Utilization* **22**:212-230.

Sawyer, W., Paul, G. and Schraufnagel, R. eds. (1990). *Development and application of a 3-D coalbed simulator*. Annual technical meeting. Petroleum Society of Canada.

Scherer, G. W. (1986). Dilatation of porous glass. *Journal of the American Ceramic Society* **69**(6):473-480.

Seidle, J. (2011). *Fundamentals of coalbed methane reservoir engineering*. PennWell Books.

Seidle, J., Jeansonne, M. and Erickson, D. eds. (1992). *Application of matchstick geometry to stress dependent permeability in coals*. SPE rocky mountain regional meeting. Society of Petroleum Engineers.

Seidle, J. R. and Huitt, L. eds. (1995). *Experimental measurement of coal matrix shrinkage due to gas desorption and implications for cleat permeability increases*. International meeting on petroleum Engineering. Society of Petroleum Engineers.

Shen, J., Qin, Y., Wang, G. X., Fu, X., Wei, C. and Lei, B. (2011). Relative permeabilities of gas and water for different rank coals. *International Journal of Coal Geology* **86**(2-3):266-275.

Shi, J.-Q. and Durucan, S. (2005a). A model for changes in coalbed permeability during primary and enhanced methane recovery. *SPE Reservoir Evaluation & Engineering* **8**(04):291-299.

Shi, J. and Durucan, S. (2003). A bidisperse pore diffusion model for methane displacement desorption in coal by CO_2 injection☆. *Fuel* **82**(10):1219-1229.

Shi, J. and Durucan, S. (2005b). CO_2 storage in deep unminable coal seams. *Oil & gas science and technology* **60**(3):547-558.

Siemons, N. and Busch, A. (2007). Measurement and interpretation of supercritical CO_2 sorption on various coals. *International Journal of Coal Geology* **69**(4):229-242.

Siemons, N., Wolf, K.-H. A. and Bruining, J. (2007). Interpretation of carbon dioxide diffusion behavior in coals. *International Journal of Coal Geology* **72**(3-4):315-324.

Šimůnek, J. and van Genuchten, M. T. (2008). Modeling nonequilibrium flow and transport processes using HYDRUS. *Vadose Zone Journal* **7**(2):782-797.

Smith, D. M. and Williams, F. L. (1984). Diffusional effects in the recovery of methane from coalbeds. *Society of Petroleum Engineers Journal* **24**(05):529-535.

Somerton, W. H., Söylemezoğlu, I. and Dudley, R. eds. (1975). *Effect of stress on permeability of coal*. International journal of rock mechanics and mining sciences & geomechanics abstracts. Elsevier.

Staib, G., Sakurovs, R. and Gray, E. M. A. (2013). A pressure and concentration dependence of CO_2 diffusion in two Australian bituminous coals. *International Journal of Coal Geology* **116**:106-116.

Staib, G., Sakurovs, R. and Gray, E. M. A. (2015). Dispersive diffusion of gases in coals. Part I: Model development. *Fuel* **143**:612-619.

Švábová, M., Weishauptová, Z. and Přibyl, O. (2012). The effect of moisture on the sorption process of CO_2 on coal. *Fuel* **92**(1):187-196.

Tan, Y., Pan, Z., Liu, J., Kang, J., Zhou, F., Connell, L. D. and Yang, Y. (2018). Experimental study of impact of anisotropy and heterogeneity on gas flow in coal. Part I: Diffusion and adsorption. *Fuel* **232**:444-453.

Tang, X. and Ripepi, N. (2017). High pressure supercritical carbon dioxide adsorption in coal: Adsorption model and thermodynamic characteristics. *Journal of CO_2 Utilization* **18**:189-197.

Tang, X., Wang, Z., Ripepi, N., Kang, B. and Yue, G. (2015). Adsorption affinity of different types of coal: mean isosteric heat of adsorption. *Energy & Fuels* **29**(6):3609-3615.

Taron, J., Elsworth, D. and Min, K.-B. (2009). Numerical simulation of thermal-hydrologic-mechanical-chemical processes in deformable, fractured porous media. *International Journal of Rock Mechanics and Mining Sciences* **46**(5):842-854.

Teng, T., Wang, J., Gao, F., Ju, Y. and Jiang, C. (2016a). A thermally sensitive permeability model for coal-gas interactions including thermal fracturing and volatilization. *Journal of Natural Gas Science and Engineering* **32**:319-333.

Teng, T., Wang, J., Gao, F., Ju, Y. and Xia, T. (2016b). Impact of water film evaporation on gas transport property in fractured wet coal seams. *Transport in Porous Media* **113**(2):357-382.

Thararoop, P., Karpyn, Z. T. and Ertekin, T. (2012). Development of a multi-mechanistic, dual-porosity, dual-permeability, numerical flow model for coalbed methane reservoirs. *Journal of Natural Gas Science and Engineering* **8**:121-131.

van Bergen, F., Krzystolik, P., van Wageningen, N., Pagnier, H., Jura, B., Skiba, J., Kobiela, Z. (2009). Production of gas from coal seams in the Upper Silesian Coal Basin in Poland in the post-injection period of an ECBM pilot site. *International Journal of Coal Geology* **77**(1-2):175-187.

Van Genuchten, M. T. (1980). A closed-form equation for predicting the hydraulic conductivity of unsaturated soils 1. *Soil science society of America journal* **44**(5):892-898.

Vandamme, M., Brochard, L., Lecampion, B. and Coussy, O. (2010). Adsorption and strain: The CO_2-induced swelling of coal. *Journal of the Mechanics and Physics of Solids* **58**(10):1489-1505.

Vishal, V., Mahanta, B., Pradhan, S., Singh, T. and Ranjith, P. (2018). Simulation of CO_2 enhanced coalbed methane recovery in Jharia coalfields, India. *Energy* **159**:1185-1194.

Vishal, V., Sudhakaran, A., Tiwari, A. K., Pradhan, S. P. and Singh, T. (2016). A review summary on multiple aspects of coal seam sequestration. In: *Geologic Carbon Sequestration*. Springer, pp. 161-182.

Wang, G., Wei, X., Wang, K., Massarotto, P. and Rudolph, V. (2010). Sorption-induced swelling/shrinkage and permeability of coal under stressed adsorption/desorption conditions. *International Journal of Coal Geology* **83**(1):46-54.

Wang, K., Liu, H., Luo, J., Wu, K. and Chen, Z. (2017). A comprehensive model coupling embedded discrete fractures, multiple interacting continua, and geomechanics in shale gas reservoirs with multiscale fractures. *Energy & Fuels* **31**(8):7758-7776.

Wang, Y. and Liu, S. (2016). Estimation of pressure-dependent diffusive permeability of coal using methane diffusion coefficient: laboratory measurements and modeling. *Energy & Fuels* **30**(11):8968-8976.

Wang, Z., Cheng, Y., Zhang, K., Hao, C., Wang, L., Li, W. and Hu, B. (2018). Characteristics of microscopic pore structure and fractal dimension of bituminous coal by cyclic gas adsorption/desorption: An experimental study. *Fuel* **232**:495-505.

Wang, Z. and Tang, X. (2018). New insights from supercritical methane adsorption in coal: gas resource estimation, thermodynamics, and engineering application. *Energy & fuels* **32**(4):5001-5009.

Warren, J. and Root, P. J. (1963). The behavior of naturally fractured reservoirs. *Society of Petroleum Engineers Journal* **3**(03):245-255.

Watanabe, N. (2011). Finite element method for coupled thermo-hydro-mechanical processes in discretely fractured and non-fractured porous media.

Wei, Z. and Zhang, D. (2013). A fully coupled multiphase multicomponent flow and geomechanics model for enhanced coalbed-methane recovery and CO_2 storage. *SPE Journal* **18**(03):448-467.

White, C. M., Smith, D. H., Jones, K. L., Goodman, A. L., Jikich, S. A., LaCount, R. B., Schroeder, K. T. (2005). Sequestration of carbon dioxide in coal with enhanced coalbed methane recovery a review. *Energy & Fuels* **19**(3):659-724.

Wu, S., Tang, D., Li, S., Chen, H. and Wu, H. (2016). Coalbed methane adsorption behavior and its energy variation features under supercritical pressure and temperature conditions. *Journal of Petroleum Science and Engineering* **146**:726-734.

Wu, Y.-S., Li, J., Ding, D., Wang, C. and Di, Y. (2014). A generalized framework model for the simulation of gas production in unconventional gas reservoirs. *SPE Journal* **19**(05):845-857.

Wu, Y.-S., Liu, H. and Bodvarsson, G. (2004). A triple-continuum approach for modeling flow and transport processes in fractured rock. *Journal of Contaminant Hydrology* **73**(1-4):145-179.

Wu, Y., Liu, J., Chen, Z., Elsworth, D. and Pone, D. (2011). A dual poroelastic model for CO_2-enhanced coalbed methane recovery. *International Journal of Coal Geology* **86**(2):177-189.

Wu, Y., Liu, J., Elsworth, D., Chen, Z., Connell, L. and Pan, Z. (2010a). Dual poroelastic response of a coal seam to CO_2 injection. *International Journal of Greenhouse Gas Control* **4**(4):668-678.

Wu, Y., Liu, J., Elsworth, D., Miao, X. and Mao, X. (2010b). Development of anisotropic permeability during coalbed methane production. *Journal of Natural Gas Science and Engineering* **2**(4):197-210.

Xu, J., Sun, B. and Chen, B. (2019). A hybrid embedded discrete fracture model for simulating tight porous media with complex fracture systems. *Journal of Petroleum Science and Engineering* **174**:131-143.

Xu, Y., Cavalcante Filho, J. S., Yu, W. and Sepehrnoori, K. (2017). Discrete-fracture modeling of complex hydraulic-fracture geometries in reservoir simulators. *SPE Reservoir Evaluation & Engineering* **20**(02):403-422.

Yang, K., Lu, X., Lin, Y. and Neimark, A. V. (2010). Deformation of coal induced by methane adsorption at geological conditions. *Energy & Fuels* **24**(11):5955-5964.

Ye, Z., Chen, D., Pan, Z., Zhang, G., Xia, Y. and Ding, X. (2016). An improved Langmuir model for evaluating methane adsorption capacity in shale under various pressures and temperatures. *Journal of Natural Gas Science and Engineering* **31**:658-680.

Zagorščak, R. (2017). *An investigation of coupled processes in coal in response to high pressure gas injection.* Ph. D. thesis, Cardiff University, Wales, UK.

Zhang, G., Ranjith, P., Perera, M., Lu, Y. and Choi, X. (2019). Quantitative Analysis of Micro-structural Changes in a Bituminous Coal After Exposure to Supercritical CO_2 and Water. *Natural Resources Research*:1-22.

Zhang, H., Liu, J. and Elsworth, D. (2008). How sorption-induced matrix deformation affects gas flow in coal seams: a new FE model. *International Journal of Rock Mechanics and Mining Sciences* **45**(8):1226-1236.

Zhang, J., Clennell, M. B., Liu, K., Dewhurst, D. N., Pervukhina, M. and Sherwood, N. (2016a). Molecular dynamics study of CO2 sorption and transport properties in coal. *Fuel* **177**:53-62.

Zhang, J., Feng, Q., Zhang, X., Wen, S. and Zhai, Y. (2015). Relative permeability of coal: a review. *Transport in Porous Media* **106**(3):563-594.

Zhang, L., Aziz, N., Ren, T. X. and Wang, Z. (2011). Influence of temperature on coal sorption characteristics and the theory of coal surface free energy. *Procedia Engineering* **26**:1430-1439.

Zhang, X. G., Ranjith, P. G., Perera, M. S. A., Ranathunga, A. S. and Haque, A. (2016b). Gas Transportation and Enhanced Coalbed Methane Recovery Processes in Deep Coal Seams: A Review. *Energy & Fuels* **30**(11):8832-8849.

Zhao, W., Cheng, Y., Jiang, H., Wang, H. and Li, W. (2017). Modeling and experiments for transient diffusion coefficients in the desorption of methane through coal powders. *International Journal of Heat and Mass Transfer* **110**:845-854.

Zhao, W., Cheng, Y., Pan, Z., Wang, K. and Liu, S. (2019). Gas diffusion in coal particles: A review of mathematical models and their applications. *Fuel* **252**:77-100.

Zhou, Y., Li, Z., Yang, Y., Zhang, L., Qi, Q., Si, L. and Li, J. (2016). Improved porosity and permeability models with coal matrix block deformation effect. *Rock Mechanics and Rock Engineering* **49**(9):3687-3697.

Zhu, C.-j., Ren, J., Wan, J., Lin, B.-q., Yang, K. and Li, Y. (2019). Methane adsorption on coals with different coal rank under elevated temperature and pressure. *Fuel* **254**:115686.

Zhu, L., Liao, X., Chen, Z. and Mu, L. eds. (2017). *Development of a Coupled Discrete Dual Continuum and Discrete Fracture Model for the Simulation of Naturally Fractured Reservoirs*. SPE Reservoir Characterisation and Simulation Conference and Exhibition. Society of Petroleum Engineers.

Zhu, W., Wei, C., Liu, J., Qu, H. and Elsworth, D. (2011). A model of coal–gas interaction under variable temperatures. *International Journal of Coal Geology* **86**(2):213-221.

Zou, M., Wei, C., Zhang, M., Shen, J., Chen, Y. and Qi, Y. (2013). Classifying coal pores and estimating reservoir parameters by nuclear magnetic resonance and mercury intrusion porosimetry. *Energy & Fuels* **27**(7):3699-3708.

3

Theoretical Formulation

3.1 Introduction

The formulation presented in this chapter considers non-isothermal, multiphase, multicomponent flow through elastically deformable fractured rock with multiscale fractures. It accounts for non-isothermal fluid-solid interactions relevant to carbon dioxide (CO_2) sequestration in coal with enhanced coalbed methane (ECBM) recovery.

General aspects of the theoretical formulation are presented in section 3.2, including an introduction to the approach taken to describe the different domains in this work (matrix continuum, fracture continuum, and discrete fractures), in addition to the basic assumptions and the primary variables of the formulation. In section 3.3, the governing equations for multicomponent reactive gas transport are derived based on the principle of mass conservation, with transport behaviour in large-scale fractures represented explicitly. Multiple transport mechanisms are incorporated and the coupling between the different pore domains is introduced. An equilibrium sorption approach is adopted to deal with reactions between the gas and solid phases (i.e. adsorption-desorption). The total content of each component is considered as sum of the bulk and adsorbed phase.

The governing equations describing water transfer in different pore domains are presented in section 3.4 based on the principle of mass conservation. This is followed in section 3.5 by the corresponding derivation of the governing equation for heat transfer on the basis of the energy conservation principle. In this section, heat transfer in the different domains is considered by means of the local thermal non-equilibrium theory. Heat conduction, convection are identified as the main mechanisms of transfer. The Joule–Thomson cooling effect due to gas expansion is incorporated.

The mechanical behaviour of fractured rock is presented in section 3.6. The governing equation for deformation is derived considering stress equilibrium and the effective stress law within the framework of dual poroelastic theory. Both the matrix and fracture deformations are considered along with the effects of various physical and chemical mechanisms of deformation. In addition, the changes in the porosity and permeability in a fractured rock due to thermal effects, fluid pressure, and adsorption-desorption-induced swelling-shrinkage are described. A new porosity and permeability model is derived in section 3.7, followed by the description of mechanical behaviour of fracture in section 3.8.

Finally, a summary of the theoretical formulation is presented in section 3.9.

3.2 Theoretical formulation – general aspects

Figure 3.1 shows the development process of integrating the dual continuum and discrete fracture models. This new numerical model comprises three different media: (i) the matrix continuum with relatively large porosity and low permeability, (ii) the fracture continuum with intermediate porosity and permeability, and (iii) the discrete fractures with relatively high permeability and low porosity. Each medium is considered to be a three-phase system, consisting of a solid skeleton, pore water and pore gas, to which appropriate material parameters are assigned to produce the overall behaviour equivalent to that observed in the respective pore regions of a fractured rock.

Figure 3.2 shows the flow connectivity between the pore regions in the new model. For CO_2 sequestration, fluid firstly flows from the injection well into the hydraulic fractures and then spread to the natural fracture network, subsequently leaking into the coal matrix. ECBM recovery follows the reverse process. Flows between the three media are described with mass exchange terms.

The governing equations are expressed in terms of primary variables, with each variable having three different values at any analysis point. Gas concentrations are expressed as a vector of any number of components present in the system, with each component being treated as a primary variable in this formulation. The governing equations for deformation are expressed in terms of the displacement vector. The primary variables used in this formulation are:

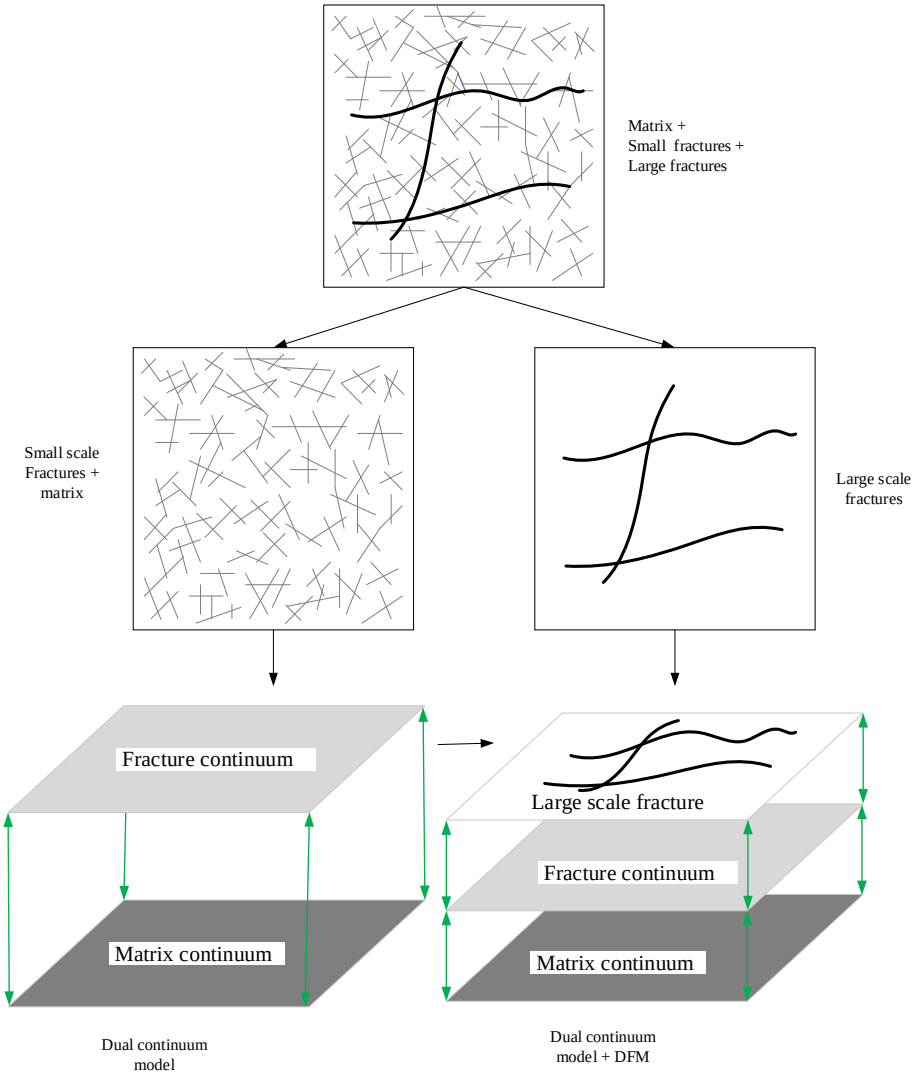

Figure 3.1 The development process for the integrated dual continuum and discrete fracture model.

1) Gas concentrations in the natural fracture continuum (c_{f}^{i}, where i can be 1 to $\mathrm{n_g}$ components);
2) Gas concentrations in the matrix continuum (c_{m}^{i});
3) Gas concentrations in the discrete hydraulic fractures (c_{F}^{i});
4) Temperature in the natural fracture continuum (T_{f});
5) Temperature in the matrix continuum (T_{m});
6) Temperature in the discrete hydraulic fractures (T_{F});
7) Pore water pressure in the natural fracture continuum (u_{lf});

8) Pore water pressure in the matrix continuum (u_{lm});

9) Pore water pressure in discrete hydraulic fractures (u_{lF});

10) Displacement ($\mathbf{u}_{\mathrm{s}}$).

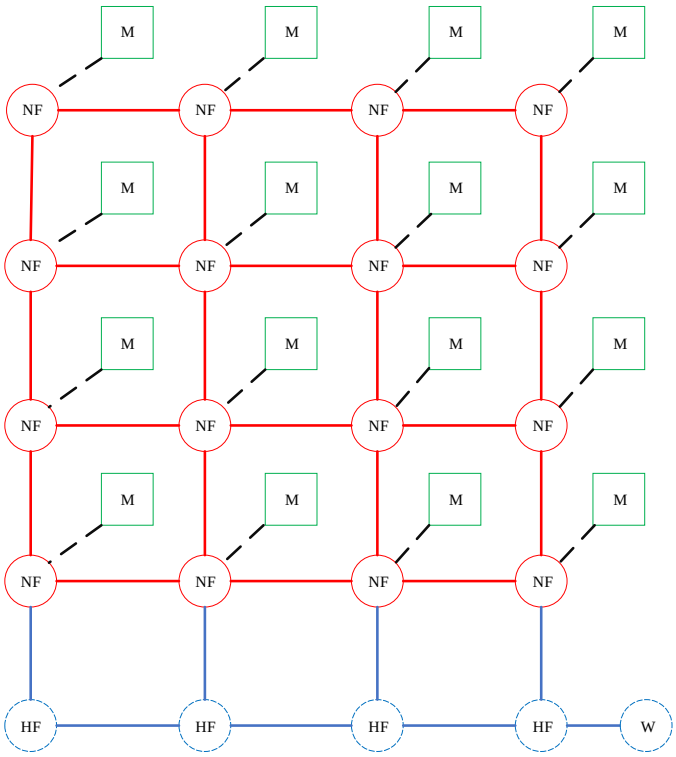

Figure 3.2 Schematic illustration of flow connectivity between the pore regions in the new model (W: injection well, DF: discrete hydraulic fractures, FC: natural fracture continuum, and MC: matrix continuum).

The new theoretical formulation provides an advanced tool for the study of non-isothermal, multiphase, multicomponent flow in deformable fractured geomaterials for geoenergy applications, based on the following assumptions:

1) The medium is treated as a multiphase system of solid, liquid, and gas; hence, voids are filled partially with liquid water, and partially with gas;

2) Each phase is continuous and each spatial point in the mixture is assumed to be occupied simultaneously by a material point of every phase;

3) The distinct natural fracture network and rock matrix are homogenous and isotropic;

4) Gas is free phase in natural fractures and discrete hydraulic fractures, whereas gas in the rock matrix is free or adsorbed with adsorption following a Langmiur isotherm;

5) The fractured rock is in local thermal non-equilibrium (LTNE);
6) Deformation of both the rock matrix and fractures is linearly elastic;
7) Hydraulic fractures are treated as lower dimensional objects with all variables uniform in the lateral direction; hence fluid flow occurs only in the longitudinal direction;
8) Gravity is ignored.

In the following sections, the pore regions (fracture continuum, matrix continuum, and discrete hydraulic fractures) will be denoted by subscripts $\alpha = \mathrm{f},\ \mathrm{m},\ \mathrm{F}$, respectively, and the solid and fluid phases (gas and water) will be denoted by subscripts $\beta = \mathrm{s},\ \mathrm{g},\ \mathrm{l}$, respectively. When only fracture and matrix continua are considered, they will be labelled by subscripts $\kappa = \mathrm{f},\ \mathrm{m}$. The gas component is labelled by superscripts $i = 1, 2\ 3\ \ldots . n_g$.

3.3 Multicomponent gas transport

Pore gas is composed of a gas mixture described in terms of a set of chemical components, which are assigned the properties of the chemical species. Sink-source terms are presented for phase transformation, chemical reactions, exchange between different pore regions, and external contributions (Masum 2012; Hosking 2014). The governing equations for multicomponent reactive pore gas flow have been derived based on the principle of conservation of mass for the fracture and matrix continua. Following the work of Hosking (2014), the mass balance equation for the i^{th} gas component in a unsaturated system can be expressed mathematically as:

$$\frac{\partial}{\partial t}\left(\theta_{\mathrm{g}\alpha} c_{\alpha}^{i} \delta V\right) = -\delta V \nabla \cdot \boldsymbol{J}_{\mathrm{g}\alpha}^{i} - \delta V \Gamma_{\mathrm{g}\alpha}^{i} - \delta V R_{\mathrm{g}\alpha}^{i} \tag{3.1}$$

where $\theta_{\mathrm{g}\alpha}$is the volumetric gas content in pore region α, c_{α}^{i} represents the concentration of i^{th} gas component, δV is the elemental volume, t is the time, ∇ is the gradient operator, $\mathbf{J}_{\mathrm{g}\alpha}^{i}$ is the total flux, $\Gamma_{\mathrm{g}\alpha}^{i}$ is the sink-source term for mass exchange between different pore regions, and $R_{\mathrm{g}\alpha}^{i}$ represents the sink-source term for geochemical reactions.

The volumetric gas content of the natural fracture network and rock matrix can be expressed in terms of the degree of gas saturation and porosity in each continuum, given as:

$$\theta_{\mathrm{g}\kappa} = n_{\kappa} S_{\mathrm{g}\kappa} \tag{3.2}$$

For large-scale hydraulic fractures, porosity is considered to be unity, thus, the volumetric gas content is equal to gas saturation:

$$\theta_{\mathrm{gF}} = S_{\mathrm{gF}} \tag{3.3}$$

where n_{κ} are the porosities of the fracture and matrix continua, respectively, and S_{κ} and S_{F} are the degrees of gas saturation.

In this work, mechanical behaviour is described explicitly and so the increment of elemental volume cannot be removed from equation (3.1). Substituting equation (3.3) into equation (3.1) and expanding the term on the left side of equation (3.1), noting that $\frac{\partial \delta V}{\delta V \partial t} = \frac{\partial \varepsilon_v}{\partial t}$, equation (3.1) can be rewritten for the fracture and matrix continua as:

$$n_{\kappa} S_{\mathrm{g}\kappa} \frac{\partial c_{\kappa}^{i}}{\partial t} + n_{\kappa} c_{\kappa}^{i} \frac{\partial S_{\mathrm{g}\kappa}}{\partial t} + \theta_{\mathrm{g}\kappa} c_{\kappa}^{i} \frac{\partial n_{\kappa}}{\partial t} + \theta_{\mathrm{g}\kappa} c_{\kappa}^{i} n_{\kappa} \frac{\partial \varepsilon_v}{\partial t} = -\nabla \cdot \mathbf{J}_{\mathrm{g}\kappa}^{i} - \Gamma_{\mathrm{g}\kappa}^{i} - R_{\mathrm{g}\kappa}^{i} \tag{3.4}$$

where ε_v is the volumetric strain, which is detailed in section 3.6. The third term on the left-hand side of equation (3.5) shows the effect of pore volume change on gas flow, which is presented in section 3.7.

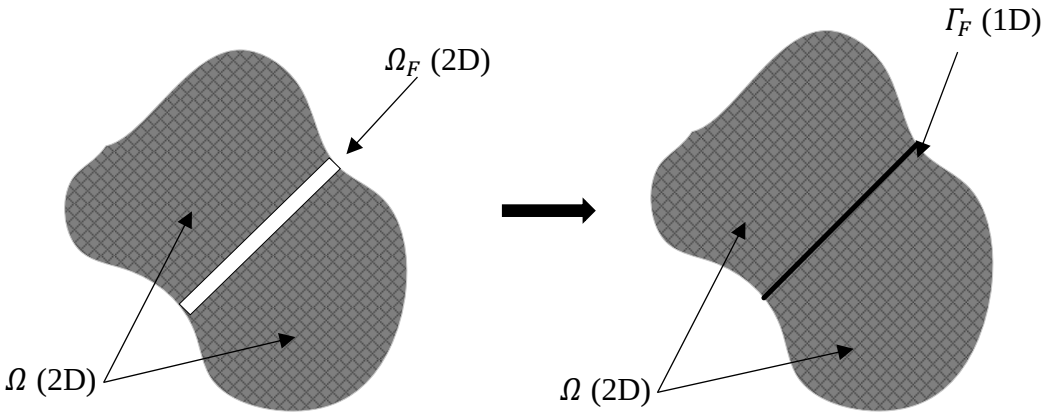

Figure 3.3 Schematic representation of the discrete fracture matrix approach.

For a hydraulic fracture, due to its high aspect ratio with its thickness orders of magnitude lower than its length, it is treated as lower dimensional objects, as shown in Figure 3.3. Equation (3.1) is reduced to a lower dimensional form, giving:

$$w S_{\mathrm{gF}} \frac{\partial c_{\mathrm{F}}^{i}}{\partial t} + w c_{\mathrm{F}}^{i} \frac{\partial S_{\mathrm{gF}}}{\partial t} + S_{\mathrm{gF}} c_{\mathrm{F}}^{i} \frac{\partial w}{\partial t} = -w \nabla_{l} \cdot \mathbf{J}_{\mathrm{gF}}^{i} - w \Gamma_{\mathrm{gF}}^{i} - w R_{\mathrm{gF}}^{i} \tag{3.5}$$

where w is the hydraulic fracture aperture, ∇_l is the lower dimensional gradient operator, for example, if $\nabla = \frac{\partial}{\partial x'} + \frac{\partial}{\partial y'}$, ∇_l can be expressed as $\nabla_l = \frac{\partial}{\partial x'}$, $x' - y'$ are local coordinate, details of which are given in next chapter.

Due to the complex pore structure and multiscale pore sizes, fluid flow in unconventional gas reservoirs is a complex physical process (Pant *et al.* 2015). Each pore region shows different flow behaviour characterised by various transport mechanisms. The transport mechanisms of multicomponent gas are discussed in the following sections.

3.3.1 Gas transport in the matrix continuum

Gas transport in coal matrix is a diffusion-dominated process, which is driven by the concentration gradient. Due to the small fracture spacing of coal matrix, the transport mode of gas in coal matrix is diffusion into or from fracture network (Chen *et al*. 2019a; Chen *et al*. 2019b; Hosking *et al*. 2019), the governing equation for gas transport in coal matrix can be written as:

$$n_{\mathrm{m}} S_{\mathrm{gm}} \frac{\partial c_{\mathrm{m}}^{i}}{\partial t} + n_{\kappa} c_{\mathrm{m}}^{i} \frac{\partial S_{\mathrm{gm}}}{\partial t} + \theta_{\mathrm{gm}} c_{\mathrm{m}}^{i} \frac{\partial n_{\mathrm{m}}}{\partial t} + \theta_{\mathrm{gm}} c_{\mathrm{m}}^{i} n_{\mathrm{m}} \frac{\partial \varepsilon_{v}}{\partial t} = -\Gamma_{\mathrm{gm}}^{i} - R_{\mathrm{gm}}^{i} \qquad (3.6)$$

where Γ_{gm}^{i} mass exchange between matrix continuum and fracture regions, which will be give in section 3.3.4, R_{gm}^{i} represents the sink-source term due to geochemical reactions. Due to the majority of the available adsorbent surface area in coal matrix, most of the gas is stored in the adsorbed phase in matrix, therefore, gas adsorption-desorption is considered as the sink/source of free phase gas, expressed as:

$$R_{gm}^{i} = \frac{\partial R_{gm \rightarrow ad}^{i}}{\partial t} \qquad (3.7)$$

where $R_{\mathrm{gm} \rightarrow ad}^{i}$ is the adsorbed amount of i^{th} gas component.

Equilibrium or kinetic models can be applied to describe gas adsorption behaviour in coal (Wu *et al.* 2010a; Wu *et al.* 2014; Bertrand *et al.* 2017; Hosking *et al.* 2017; Chen *et al.* 2019b). Since the dynamic adsorption process is not the focus of this work, equilibrium sorption is adopted. The extended Langmuir isotherm has been suggested as a valid model to describe the adsorbed amount of gas (Chaback *et al.* 1996; Clarkson and Bustin 2000; Merkel *et al.* 2015), given by the following expression:

$$R^i_{\mathrm{gm}\rightarrow ad} = \rho_s V^i \tag{3.8}$$

where ρ_s is coal density; V^i is the adsorbed concentration, given as:

$$V^i = \frac{V_L^i Z_{\mathrm{m}} R T_{\mathrm{m}} b_L^i c_{\mathrm{m}}^i}{Z_{\mathrm{m}} R T_{\mathrm{m}} \sum_{i=1}^{n} b_L^i c_{\mathrm{m}}^i + 1} \tag{3.9}$$

where R is the universal gas constant, T_{m} is temperature of the matrix continuum, and Z_{m} gas compressibility factor, V_L^i is the Langmuir volume constant and b_L^i is the affinity equilibrium constant, which is calculated as the reciprocal of Langmuir pressure constant P_L^i:

$$b_L^i = \frac{1}{P_L^i} \tag{3.10}$$

In the classic Langmuir model, V_L^i and b_L^i are temperature independent, however, experimental studies show that the temperature independent Langmuir model could not accurately describe the experimental data (e.g. Krooss *et al.* 2002; Sakurovs *et al.* 2008; Tang and Ripepi 2016; Guan *et al.* 2018). Do and Wang (1998) presented the following temperature dependent form of the adsorption capacity, V_L^i:

$$V_L^i = V_{L0}^i \exp\left(-\Phi^i T_{\mathrm{m}}\right) \tag{3.11}$$

Similarly, the affinity equilibrium constant, b_L^i, can be expressed as a function of temperature, heat of adsorption, and the universal gas constant as (Do and Wang 1998; Ye *et al.* 2016):

$$b_L^i = b_{L\infty}^i \exp\left(\frac{E_{in}^i}{RT}\right) \tag{3.12}$$

where V_{L0}^i is the theoretical maximum adsorption capacity for the adsorbent, Φ^i is a reduction coefficient related with temperature increase, E_{in}^i is the interaction energy between the adsorbate and the adsorbent, and $b_{L\infty}^i$ is the affinity at infinite temperature.

Real gas behaviour may approach the conceptual model of an ideal gas at low pressures and high temperatures. However, the ideal gas law does not accurately describe the pressure-volume-temperature characteristics of gas under the majority of conditions (Dake 1983). An equation of state (EoS) is applied to describe the real gas compressibility behaviour in present work, which provides an approach to estimating the volumetric behaviour of gases

and liquids as a function of temperature and pressure (Poling *et al.* 2001). Generally, the compressibility factor Z is used to illustrate the deviations of the behaviour of real gases from ideal gas behaviour, which is defined as the ratio of the actual molar volume V_{mm}^{r} to the ideal gas molar volume V_{mm}^{i}. The EoS proposed by Peng and Robinson (1976) (PR-EoS) has been widely applied because of its accuracy and less input parameters (Wei and Sadus 2000; Hosking 2014). PR-EoS expresses the bulk gas pressure as:

$$\mathrm{u_{gm}} = \frac{RT_{\mathrm{m}}}{V_{\mathrm{mm}}^{r} - b_{\mathrm{mm}}} - \frac{a_{\mathrm{mm}}}{{V_{\mathrm{mm}}^{r}}^{2} + 2b_{\mathrm{mm}}V_{\mathrm{mm}}^{r} - {b_{\mathrm{mm}}}^{2}} \tag{3.13}$$

Where $\mathrm{u_{gm}}$ is gas pressure in matrix continuum, V_{mm}^{r} is the real gas molar volume in matrix continuum, b_{mm} is the effective volume of the molecules contained in one mole of bulk gas and a_{mm} is a coefficient accounting for the intermolecular interactions in the mixture.

The mixture parameters b_{mm} and a_{mm} in equation (3.13) are defined using the van der Waals mixing rules (Kwak and Mansoori 1986), given as:

$$a_{\mathrm{mm}} = \sum_{i=1}^{n_g}\sum_{j=1}^{n_g} x_{\mathrm{gm}}^{i}\, x_{\mathrm{gm}}^{j}\left(1 - \omega_{\mathrm{gm}}^{ij}\right)\sqrt{a_{\mathrm{mm}}^{i} a_{\mathrm{mm}}^{j}} \tag{3.14}$$

$$b_{\mathrm{mm}} = \sum_{i=1}^{n_g} x_{\mathrm{gm}}^{i} b_{\mathrm{mm}}^{i} \tag{3.15}$$

where $\omega_{\mathrm{gm}}^{ij}$ is a binary gas interaction parameter to account for interactions between the molecules of components i and j and a_{mm}^{i} and b_{mm}^{i} are the pure component factors for intermolecular interactions and effective volume, respectively.

3.3.2 Gas transport in fracture continuum

Compared to the matrix continuum, the fracture continuum has a higher permeability. The micro-fractures are well-developed with a pore size significantly larger than the mean free path of molecules, therefore, the transport mechanism is dominated by advective flow and diffusion can be neglected. The advective mass flux of the i^{th} pore gas component is written as:

$$\mathrm{J}_{\mathrm{gf}}^{i} = x_{\mathrm{f}}^{i} c_{\mathrm{f}}^{t} \mathbf{v}_{\mathrm{gf}} \tag{3.16}$$

where x_{gf}^{i} is molar fraction in the gas phase of component *i* in the fracture continuum, $\mathbf{v}_{\mathrm{gf}}$ is the advective flow velocity and c_{gf}^{t} is the total gas concentration, which is equal to the sum of the concentrations of the individual gas components, giving:

$$c_{\mathrm{f}}^{t} = \sum_{i=1}^{n_g} c_{\mathrm{f}}^{i} \tag{3.17}$$

The molar fraction x_{f}^{i} is defined as:

$$x_{\mathrm{f}}^{i} = \frac{c_{\mathrm{f}}^{i}}{c_{\mathrm{f}}^{t}} \tag{3.18}$$

Based on Darcy's law, the flow velocity can be expressed as:

$$\mathbf{v}_{\mathrm{gf}} = -\frac{K_{\mathrm{f}} K_{\mathrm{rgf}}}{\mu_{\mathrm{gf}}} \nabla u_{\mathrm{gf}} \tag{3.19}$$

where K_{f} is the intrinsic permeability, K_{rgf} is the relative permeability to gas in the natural fracture network, μ_{gf} is the gas mixture viscosity, and u_{gf} is the pore gas pressure, which for real gas is given as:

$$u_{\mathrm{gf}} = Z_{\mathrm{f}} R T_{\mathrm{f}} c_{\mathrm{f}}^{t} \tag{3.20}$$

where T_{f} is temperature of the fracture continuum and Z_{f} gas compressibility factor, which can be calculated in the manner provided by PR-EoS.

The relative permeability curve for two phase flow in fractures is generally different from that in porous media, and comparatively less studies have been conducted in this area. Bogdanov *et al.* (2003) proposed a simple model for the relative permeability of a gas phase flowing in rough walled fractures:

$$K_{\mathrm{rgf}} = (1 - S_{\mathrm{lf}})^{N} \tag{3.21}$$

where N is the power exponent for the relative permeability in fractures.

Substitution of equations (3.17) to (3.19) into equation (3.16) leads to the mass flux in the fracture continuum, written as:

$$\mathrm{J}_{\mathrm{gf}}^{i} = -c_{\mathrm{f}}^{i} \frac{K_{\mathrm{f}} K_{\mathrm{rgf}}}{\mu_{\mathrm{gf}}} \nabla u_{\mathrm{gf}} \tag{3.22}$$

3.3.3 Gas transport in discrete hydraulic fractures

Similar to the fluid flow in natural fractures, the gas flux in discrete hydraulic fractures is written as:

$$\mathrm{J}_{\mathrm{gF}}^{i} = x_{\mathrm{F}}^{i} c_{\mathrm{F}}^{t} \mathbf{v}_{\mathrm{gF}} \tag{3.23}$$

where x_{F}^{i} is the molar fraction in the gas phase of component *i* in the discrete fractures, $\mathbf{v}_{\mathrm{gF}}$ is the average velocity of gas flow along the fractures, and c_{F}^{t} is the total gas concentration, which is equal to the sum of the concentrations of the individual gas components, giving:

$$c_{\mathrm{F}}^{t} = \sum_{i=1}^{n_g} c_{\mathrm{F}}^{i} \tag{3.24}$$

The molar fraction x_{F}^{i} is defined as:

$$x_{\mathrm{F}}^{i} = \frac{c_{\mathrm{F}}^{i}}{c_{\mathrm{F}}^{t}} \tag{3.25}$$

If it is assumed that the fluid flow along the fracture obeys Poiseuille's law, then $\mathbf{v}_{\mathrm{gF}}$ can be described by the well-known cubic law function of the fracture aperture and fluid viscosity (Pouya 2015):

$$\mathbf{v}_{\mathrm{gF}} = -\frac{K_{\mathrm{rgF}} w^2}{12\mu_{\mathrm{gF}}} \nabla_l u_{\mathrm{gF}} \tag{3.26}$$

where K_{rgF} is the relative permeability to gas in the discrete fracture network, which can be calculated with equation (3.21), μ_{gF} is the gas mixture viscosity, and u_{gF} is the pore gas pressure, expressed as:

$$u_{\mathrm{gF}} = Z_{\mathrm{F}} R T_{\mathrm{F}} c_{\mathrm{F}}^{t} \tag{3.27}$$

where T_{F} is temperature in the discrete fracture and Z_{F} gas compressibility factor, which can be obtained in the manner provided by PR-EoS.

Substitution of equations (3.24) to (3.27) into equation (3.23) leads to the mass flux in discrete fractures, written as:

$$\mathrm{J}_{\mathrm{gF}}^{i} = -\theta_{\mathrm{gF}} c_{\mathrm{F}}^{i} \frac{K_{\mathrm{rgF}} w^2}{12\mu_{\mathrm{gF}}} \nabla_l u_{\mathrm{gF}} \tag{3.28}$$

3.3.4 Mass exchange

Gas transport in an unsaturated fractured rock is described in this work using three distinct equations, as per equation (3.1), which are coupled by a sink/source term, Γ^i. In this section, the mechanisms that control the magnitude and the rate of the mass exchange processes are discussed and the mass exchange term is derived.

Mass exchange may take place between any two pore regions, as shown in Figure 3.4(a). However, due to the lower permeability of the rock matrix compared to the natural fracture network, the fluid in the larger hydraulic fractures has a preference to penetrate into the natural fractures (Chen *et al*. 2019a). Hence, the mass exchange rate between the matrix continuum and the hydraulic fractures is lower than that between the fracture continuum and the hydraulic fractures. Thus, in present study, the large-scale fractures are considered to be coupled with the surrounding fracture continuum, and the matrix continuum only has mass exchange with natural fractures, as shown in Figure 3.4(b).

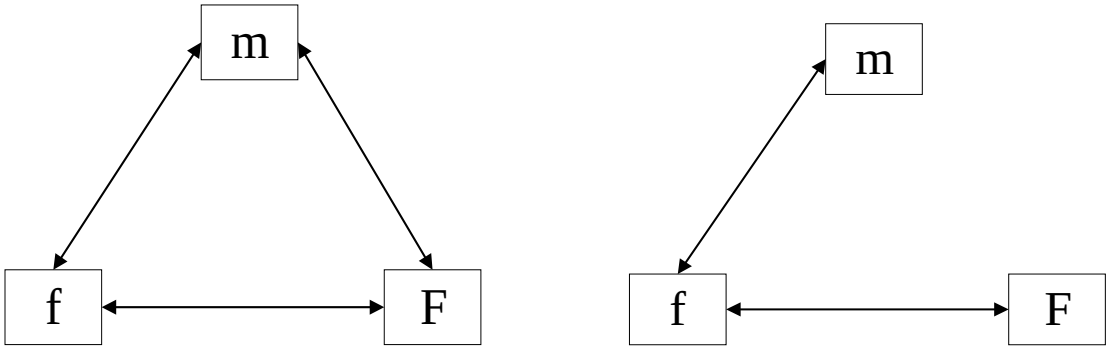

Figure 3.4 Schematic of mass exchange in a fracture rock showing: (a) the coupling between the discrete fracture and dual continuum medium, and (b) the simplified fracture-matrix mass exchange process adopted in this work.

It follows from the above that the mass exchange term in equations (3.4) and (3.5) can be expressed as:

$$\Gamma^i_{\mathrm{gm}} = \Gamma^i_{\mathrm{gfm}} \tag{3.29}$$

$$\Gamma^i_{\mathrm{gf}} = -\Gamma^i_{\mathrm{gfm}} + \Gamma^i_{\mathrm{gfF}} \tag{3.30}$$

$$\Gamma^i_{\mathrm{gF}} = -\Gamma^i_{\mathrm{gfF}} \tag{3.31}$$

where Γ^i_{gfm} represents the mass transfer between the dual continua and Γ^i_{gfF} represents mass exchange between the fracture continuum and the hydraulic fractures.

Mass exchange between the dual continua is determined by assuming that a quasi-steady state pore gas pressure distribution prevails in the matrix blocks, whereby the mass exchange process becomes a function of the averaged fracture and matrix pressures or concentrations (Gerke and Genuchten 1993). The mass exchange term for pore gas presented here includes components due to diffusive flow, which can be expressed as a linear function of the difference between the average pore gas concentrations in the fracture and matrix continua. The resulting mass exchange term for the pore gas component is expressed as:

$$\Gamma^i_{\mathrm{gfm}} = \sigma_{\mathrm{gD}}\left(c^i_{\mathrm{f}} - c^i_{\mathrm{m}}\right) \tag{3.32}$$

where σ_{gD} is the first order mass exchange coefficient for diffusion of the i^{th} gas component, for gas diffusion induced leak-off flow, σ_{gD} is given by:

$$\sigma_{\mathrm{gD}} = \frac{\delta}{l^2} D^i_{\mathrm{gm}} \tag{3.33}$$

where δ is a factor related to the geometry of the matrix blocks, D^i_{gm} is the effective diffusion coefficient of the i^{th} gas component and l is the typical thickness of a matrix block.

Considering the adsorption behaviour of gas phase in solid, the sorption time is generally introduced to represents mass exchange of gas phase between two continua (Chen M et al. 2019a; Lee et al. 2019):

$$\frac{1}{\tau^i} = \frac{\delta}{l^2} D^i_{\mathrm{gm}} \tag{3.34}$$

Substitution of equations (3.34) into equation (3.32) yields:

$$\Gamma^i_{\mathrm{gfm}} = \frac{1}{\tau^i}\left(c^i_{\mathrm{f}} - c^i_{\mathrm{m}}\right) \tag{3.35}$$

where τ^i is the sorption time of i^{th} gas component.

3.3.5 Governing equations for multicomponent gas transport

The transport mechanisms of multicomponent pore gas in a dual porosity medium were described in section 3.3.1, and mass transfer between the different pore regions was described in section 3.3.2. The governing equations for multicomponent pore gas transport

are now assembled using the components of the equations given in the previous sections. The final equations are presented in terms of the primary variables.

Before giving the governing equations, it is useful to express the partial derivative in the second term on the right hand side of equation (3.4) and (3.5) in terms of the temporal derivative of the degree of water saturation according the closure relation $S_{g\alpha} + S_{l\alpha} = 1$, as:

$$\frac{\partial S_{g\alpha}}{\partial t} = -\frac{\partial S_{l\alpha}}{\partial t} \tag{3.36}$$

Neglecting the effects of osmotic suction and adsorbed liquid water, the liquid saturation, S_l, is assumed to be a function of capillary pressure, giving:

$$S_{l\alpha} = S_{l\alpha}(s_\alpha) \tag{3.37}$$

$$s_\alpha = u_{g\alpha} - u_{l\alpha} \tag{3.38}$$

where s_α is the capillary pressure, describing the difference in pressure across the interface between two immiscible fluids.

Substituting equation (3.37) and (3.38) into equation (3.36) and applying the real gas law gives:

$$\frac{\partial S_{g\alpha}}{\partial t} = \frac{\partial S_{l\alpha}}{\partial s_\alpha}\frac{\partial u_{l\alpha}}{\partial t} - R\frac{\partial S_{l\alpha}}{\partial s_\alpha}\sum_{i=1}^{n_g}\left(Z_\alpha T_\alpha \frac{\partial c_\alpha^i}{\partial t} + Z_\alpha c_\alpha^i \frac{\partial T_\alpha}{\partial t} + T_\alpha c_\alpha^i \frac{\partial Z_\alpha}{\partial t}\right) \tag{3.39}$$

In this work, Z_α is updated in each time step using the equation of state (EoS) proposed by Peng and Robinson (1976), details of which are provided in section 3.7.6. The temporal derivative of the compressibility factor, i.e. $\frac{\partial Z_\alpha}{\partial t}$, has not been considered. Equation (3.39) therefore reduces to:

$$\frac{\partial S_{g\alpha}}{\partial t} = \frac{\partial S_{l\alpha}}{\partial s_\alpha}\frac{\partial u_{l\alpha}}{\partial t} - R\frac{\partial S_{l\alpha}}{\partial s_\alpha}\sum_{j=1}^{n_g}\left(Z_\alpha T_\alpha \frac{\partial c_\alpha^j}{\partial t} + Z_\alpha c_\alpha^j \frac{\partial T_\alpha}{\partial t}\right) \tag{3.40}$$

The partial derivative of the degree of saturation with respect to capillary pressure in equation (3.39) is defined using the gradient the curve produced by the van Genuchten equation in this study. The capillary pressure-saturation relationship is described as (Van Genuchten 1980):

$$S_{\mathrm{l}\alpha e} = \frac{S_{\mathrm{l}\alpha} - S_{\mathrm{l}\alpha r}}{S_{\mathrm{l}\alpha \max} - S_{\mathrm{l}\alpha r}} = \left(1 + \left|\frac{s_\alpha}{p_{0\alpha}}\right|^{\gamma_\alpha}\right)^{-\psi_\alpha} \tag{3.41}$$

where $S_{\mathrm{l}\alpha e}$ is the effective water saturation, $S_{\mathrm{l}\alpha\max}$ is the maximum water saturation, $S_{\mathrm{l}\alpha r}$ are the residual water saturation, γ_α and ψ_α ($\psi_\alpha = 1 - 1/\gamma_\alpha$) are constants based on the water retention characteristics and $p_{0\alpha}$ is a characteristic pressure. Estimates of $p_{0\alpha}$ are given below.

Equation (3.41) is applied both in the rock matrix and fracture domains. Due to the assumption of local continuity, the water pressure, gas pressure, and capillary pressure in the fracture continuum and discrete hydraulic fractures are continuous along the surfaces of hydraulic fractures. However, the parameters $p_{0\alpha}$ and γ_α selected are generally different for three pore domains (Bogdanov *et al.* 2003). Particularly, if the Laplace law is applied, the capillary pressure across the interface between two fluids is inversely proportional to the meniscus radius, which is of the order of the typical pore size. If the fractures are considered as large pores, it may be expected that:

$$\frac{p_{0\mathrm{f}}}{p_{0\mathrm{m}}} \approx \sqrt{\frac{K_{\mathrm{m}}}{K_{\mathrm{f}}}} = k \qquad \rightarrow \qquad p_{0\mathrm{f}} = k p_{0\mathrm{m}} \tag{3.42}$$

Generally, k has a small value due to the contrasting permeability between the matrix and fracture domains, hence, $p_{0\mathrm{f}}$ is smaller than $p_{0\mathrm{m}}$, resulting in sharp saturation contrasts, the fracture domain drains freely even at low capillary pressures.

Substituting equation (3.40) into the right hand side of the mass balance equations (3.4) and (3.5) and replacing the total gas flux on right hand side with equations (3.22) and (3.28), whilst taking account of equations (3.35) for mass exchange and replacing $\frac{\partial \varepsilon_v}{\partial t} = \mathbf{m}^{\boldsymbol{T}} \boldsymbol{B} \frac{\partial \mathbf{u}_{\mathrm{s}}}{\partial t}$, gives the governing equations for multicomponent pore gas transport in a discretely fractured porous medium, expressed in a simplified form as:

$$\sum_{j=1}^{n_g} C_{\mathrm{c_m c_m}} \frac{\partial c_{\mathrm{m}}^j}{\partial t} + \sum_{j=1}^{n_g} C_{\mathrm{c_m c_f}} \frac{\partial c_{\mathrm{f}}^j}{\partial t} + C_{\mathrm{c_m l_m}} \frac{\partial u_{\mathrm{lm}}}{\partial t} + C_{\mathrm{c_m l_f}} \frac{\partial u_{\mathrm{lf}}}{\partial t} + C_{\mathrm{c_m T_m}} \frac{\partial T_{\mathrm{m}}}{\partial t} + C_{\mathrm{c_m T_f}} \frac{\partial T_{\mathrm{f}}}{\partial t}$$

$$+ C_{\mathrm{c_m}\mathbf{u}_{\mathrm{s}}} \frac{\partial \mathbf{u}_{\mathrm{s}}}{\partial t} = Q_{\mathrm{c_m}}^i \tag{3.43}$$

$$\sum_{j=1}^{n_g} C_{\mathrm{c_f c_m}} \frac{\partial c_{\mathrm{m}}^j}{\partial t} + \sum_{j=1}^{n_g} C_{\mathrm{c_f c_f}} \frac{\partial c_{\mathrm{f}}^j}{\partial t} + C_{\mathrm{c_f l_m}} \frac{\partial u_{\mathrm{lm}}}{\partial t} + C_{\mathrm{c_f l_f}} \frac{\partial u_{\mathrm{lf}}}{\partial t} + C_{\mathrm{c_f T_m}} \frac{\partial T_{\mathrm{m}}}{\partial t} + C_{\mathrm{c_f T_f}} \frac{\partial T_{\mathrm{f}}}{\partial t} + C_{\mathrm{c_f u_s}} \frac{\partial \mathbf{u}_{\mathrm{s}}}{\partial t} = \nabla \cdot \left(\sum_{j=1}^{n_g} K_{\mathrm{c_f c_f}} \nabla c_{\mathrm{f}}^j \right) + \nabla \cdot \left(K_{\mathrm{c_f T_f}} \nabla T_{\mathrm{f}} \right) + Q_{\mathrm{gf}}^i \quad (3.44)$$

$$\sum_{j=1}^{n_g} C_{\mathrm{c_F c_F}} \frac{\partial c_{\mathrm{F}}^j}{\partial t} + C_{\mathrm{c_F l_F}} \frac{\partial u_{\mathrm{lF}}}{\partial t} + C_{\mathrm{c_F T_F}} \frac{\partial T_{\mathrm{F}}}{\partial t} = \nabla_l \cdot \left(\sum_{j=1}^{n_g} K_{\mathrm{c_F c_F}} \nabla_l c_{\mathrm{F}}^j \right) + \nabla_l \cdot \left(K_{\mathrm{c_F T_F}} \nabla_l T_F \right) + Q_{\mathrm{c_F}}^i \quad (3.45)$$

The coefficients of primary variables in equations (3.43) – (3.45) are summarised in appendix A.

3.4 Water transfer

Application of the principle of conservation of mass demands that the time derivative of the liquid content is equal to the spatial gradient of the liquid flux. With the inclusion of a sink-source term allowing for mass exchange between different pore domains this can be expressed mathematically as (Bear 2012):

$$\frac{\partial}{\partial t}(\theta_{\mathrm{l}\alpha} \rho_{\mathrm{l}} \delta V) = -\delta V \nabla \cdot (\rho_{\mathrm{l}} \mathbf{v}_{\mathrm{l}\alpha}) + \delta V \rho_{\mathrm{l}} \Gamma_{\mathrm{l}\alpha} \quad (3.46)$$

where $\theta_{\mathrm{l}\alpha}$ is the volumetric water content in each medium, ρ_{l} is the density of water, $\mathbf{v}_{\mathrm{l}\alpha}$ is the velocity of water, and $\Gamma_{\mathrm{l}\alpha}$ is the sink-source term for mass exchange of water between the different pore domains.

Similar to volumetric gas content, the volumetric water content of the fracture network and rock matrix can be expressed in terms of the degree of saturation and the porosity in each continuum, given as:

$$\theta_{\mathrm{l}\kappa} = n_{\kappa} S_{\mathrm{l}\kappa} \quad (3.47)$$

The volumetric water content in hydraulic fractures is equal to the degree of water saturation based on the assumption of unit porosity, written as:

$$\theta_{\mathrm{lF}} = S_{\mathrm{lF}} \tag{3.48}$$

where $S_{\mathrm{l\kappa}}$ and S_{lF} are the degree of gas saturation in the respective pore domains.

Substitution of equation (3.47) into equation (3.46) and expanding the term on the left-hand side yields:

$$n_{\kappa} S_{\mathrm{l\kappa}} \frac{\partial \rho_{\mathrm{l}}}{\partial t} + n_{\kappa} \rho_{\mathrm{l}} \frac{\partial S_{\mathrm{l\kappa}}}{\partial t} + \rho_{\mathrm{l}} S_{\mathrm{l\kappa}} \frac{\partial n_{\kappa}}{\partial t} + \rho_{\mathrm{l}} S_{\mathrm{l\kappa}} n_{\kappa} \frac{\partial \varepsilon_{v}}{\partial t} = -\nabla \cdot (\rho_{\mathrm{l}} \mathbf{v}_{\mathrm{l\kappa}}) + \rho_{\mathrm{l}} \Gamma_{\mathrm{l\kappa}} \tag{3.49}$$

For the discrete hydraulic fractures, a similar approach to multicomponent gas transport is used for derivation of the mass balance equation, giving:

$$w S_{\mathrm{lF}} \frac{\partial \rho_{\mathrm{l}}}{\partial t} + w \rho_{\mathrm{l}} \frac{\partial S_{\mathrm{lF}}}{\partial t} + S_{\mathrm{lF}} \rho_{\mathrm{l}} \frac{\partial w}{\partial t} = -w \nabla_{l} \cdot (\rho_{\mathrm{l}} \mathbf{v}_{\mathrm{lF}}) - w \rho_{\mathrm{l}} \Gamma_{\mathrm{lF}} \tag{3.50}$$

3.4.1 Mechanisms of water transfer

In the present work, the flow of liquid water due to gravitational, thermal, chemical and electrical gradients has been neglected, and the total water potential is considered as the driving force for water flow. According to Darcy's law, the rate of flow of water due to a water potential can be expressed as (Bear 2012):

$$\mathbf{v}_{\mathrm{l}\alpha} = -\mathbf{k}_{\mathrm{l}\alpha} \nabla u_{\mathrm{l}\alpha} \tag{3.51}$$

where $\mathbf{k}_{\mathrm{l}\alpha}$ the unsaturated hydraulic conductivity.

Water flow in fractured rock is usually considered to be a laminar process with the unsaturated hydraulic conductivity given by:

$$\mathrm{k}_{\mathrm{l}\alpha} = \frac{K_{\mathrm{rl}\alpha} K_{\alpha}}{\mu_{\mathrm{l}\alpha}} \tag{3.52}$$

where K_{α} is the intrinsic permeability, $K_{\mathrm{rl}\alpha}$ is the relative permeability to water, and $\mu_{\mathrm{l}\alpha}$ is the absolute water viscosity. For hydraulic fractures, the permeability can be expressed as (Pouya 2015) :

$$K_{\mathrm{F}} = \frac{w^2}{12} \tag{3.53}$$

The relative permeability of an unsaturated medium to water can be evaluated based on the degree of saturation, the most widely used van Genuchten model (Van Genuchten 1980) is employed in this study:

$$K_{\mathrm{rl}\alpha} = {S_{\mathrm{l}\alpha\mathrm{e}}}^{1/2}\left[1-\left(1-{S_{\mathrm{l}\alpha\mathrm{e}}}^{1/\psi_\alpha}\right)^{\psi_\alpha}\right]^2 \tag{3.54}$$

Variation of the absolute viscosity in equation (3.52) with temperature is described using the following relationship presented by Kaye and Laby (1973), which is valid for $273K < T_\alpha < 373K$:

$$\mu_{\mathrm{l}\alpha} = 661.2(T_\alpha - 229)^{-1.562}\times 10^{-3} \pm 0.5\% \tag{3.55}$$

3.4.2 Mass exchange term for water

Hydraulic fractures are coupled with the surrounding natural fracture continuum and the matrix continuum only interacts with the natural fracture continuum. The mass exchange terms in equation (3.49) and (3.50) can then be expressed as:

$$\Gamma_{\mathrm{lm}} = \Gamma_{\mathrm{lfm}} \tag{3.56}$$

$$\Gamma_{\mathrm{lf}} = -\Gamma_{\mathrm{lfm}} + \Gamma_{\mathrm{lfF}} \tag{3.57}$$

$$\Gamma_{\mathrm{lF}} = -\Gamma_{\mathrm{lfF}} \tag{3.58}$$

The approach to calculate the mass exchange terms for water flow follows that presented for multicomponent gas, presented in section 3.3.2. Accordingly, the pore water pressure distribution in the rock matrix is assumed to be quasi-steady state, and the mass exchange process becomes a function of the averaged fracture and matrix pressures. Different from the exchange of multicomponent gas, which was analogous to a combination of advective and diffusive processes, the mass exchange term for water presented here is a purely advective process, and the water exchange rate is expressed as a linear function of the difference between the average pore water pressures in the fracture and matrix continua (Barenblatt *et al.* 1960; Warren and Root 1963), giving:

$$\Gamma_{\mathrm{lfm}} = \sigma_{\mathrm{lv}}(u_{\mathrm{lf}} - u_{\mathrm{lm}}) \tag{3.59}$$

where σ_{lv} is the first order mass exchange coefficient for water, expanded using a similar approach to pore gas exchange, giving:

$$\sigma_{\mathrm{lv}} = \Omega_l \frac{\delta}{l^2} K_{\mathrm{m}} \tag{3.60}$$

Substitution of equation (3.60) into equation (3.59) produces:

$$\Gamma_{\mathrm{lfm}} = \Omega_l \frac{\delta}{l^2} K_{\mathrm{m}}(u_{\mathrm{lf}} - u_{\mathrm{lm}}) \tag{3.61}$$

3.4.3 Governing equations for water transfer

To give the governing equations for water transfer, the equations for flow and mass exchange are incorporated into the mass conservation equations (3.49) and (3.50). The resulting equation is then expanded in terms of the primary variables.

The degree of saturation in each pore region is defined as a function of the capillary pressure, thus, the temporal derivative of degree of saturation in equations (3.49) and (3.50) can be expressed in terms of the primary variables, as:

$$\frac{\partial S_{\mathrm{l}\alpha}}{\partial t} = -\frac{\partial S_{\mathrm{l}\alpha}}{\partial s_\alpha}\frac{\partial u_{\mathrm{l}\alpha}}{\partial t} + R\frac{\partial S_{\mathrm{l}\alpha}}{\partial s_\alpha}\sum_{i=1}^{n_g}\left(Z_\alpha T_\alpha \frac{\partial c_\alpha^i}{\partial t} + Z_\alpha c_\alpha^i \frac{\partial T_\alpha}{\partial t}\right) \tag{3.62}$$

The temporal derivative of water density can be transformed as:

$$\frac{\partial \rho_{\mathrm{l}}}{\partial t} = \frac{\partial \rho_{\mathrm{l}}}{\partial u_{\mathrm{l}}}\frac{\partial u_{\mathrm{l}}}{\partial t} = \rho_{\mathrm{l}} c_{\mathrm{l}} \frac{\partial u_{\mathrm{l}}}{\partial t} - \rho_{\mathrm{l}} \alpha_{\mathrm{lT}} \frac{\partial T_{\mathrm{l}}}{\partial t} \tag{3.63}$$

where $c_{\mathrm{l}} = \frac{1}{\rho_{\mathrm{l}}}\frac{\partial \rho_{\mathrm{l}}}{\partial u_{\mathrm{l}}}$, is water compressibility, $\alpha_{\mathrm{lT}} = -\frac{1}{\rho_{\mathrm{l}}}\frac{\partial \rho_{\mathrm{l}}}{\partial T_{\mathrm{l}}}$, is thermal expansion coefficient of water.

Substituting equations (3.62) and (3.63) into the left-hand side of equations (3.49) and (3.50) and substituting $\mathbf{v}_{\mathrm{l}\alpha}$ from equation (3.51), and $\Gamma_{\mathrm{l}\alpha}$ from equation (3.61) into the right-hand side gives the governing equations for water transfer in a discretely fractured porous medium. The governing equations can be represented in a simplified form as:

$$\sum_{j=1}^{n_g}\left(C_{\mathrm{l_m c_m}}\frac{\partial c_{\mathrm{m}}^j}{\partial t}\right) + \sum_{j=1}^{n_g}\left(C_{\mathrm{l_m c_f}}\frac{\partial c_{\mathrm{f}}^j}{\partial t}\right) + C_{\mathrm{l_m l_m}}\frac{\partial u_{\mathrm{lm}}}{\partial t} + C_{\mathrm{l_m l_f}}\frac{\partial u_{\mathrm{lf}}}{\partial t} + C_{\mathrm{l_m T_m}}\frac{\partial T_{\mathrm{m}}}{\partial t} + C_{\mathrm{l_m T_f}}\frac{\partial T_{\mathrm{f}}}{\partial t} + C_{\mathrm{l_m}\mathbf{u}_{\mathrm{s}}}\frac{\partial \mathbf{u}_{\mathrm{s}}}{\partial t} = -\nabla\cdot\left(K_{\mathrm{l_m l_m}}\nabla u_{\mathrm{lm}}\right) + Q_{\mathrm{l_m}} \tag{3.64}$$

$$\sum_{j=1}^{n_g}\left(C_{\mathrm{l_f c_m}}\frac{\partial c_{\mathrm{m}}^j}{\partial t}\right) + \sum_{j=1}^{n_g}\left(C_{\mathrm{l_f c_f}}\frac{\partial c_{\mathrm{f}}^j}{\partial t}\right) + C_{\mathrm{l_f l_m}}\frac{\partial u_{\mathrm{lm}}}{\partial t} + C_{\mathrm{l_f l_f}}\frac{\partial u_{\mathrm{lf}}}{\partial t} + C_{\mathrm{l_f T_m}}\frac{\partial T_{\mathrm{m}}}{\partial t} + C_{\mathrm{l_f T_f}}\frac{\partial T_{\mathrm{f}}}{\partial t} + C_{\mathrm{l_f}\mathbf{u}_{\mathrm{s}}}\frac{\partial \mathbf{u}_{\mathrm{s}}}{\partial t} = -\nabla\cdot\left(K_{\mathrm{l_f l_f}}\nabla u_{\mathrm{lf}}\right) + Q_{\mathrm{l_f}} \tag{3.65}$$

$$C_{\mathrm{l_F l_F}}\frac{\partial u_{\mathrm{lF}}}{\partial t} + \sum_{i=1}^{n_g}\left(C_{\mathrm{l_F c_F}}\frac{\partial c_{\mathrm{F}}^i}{\partial t}\right) + C_{\mathrm{l_F T_F}}\frac{\partial T_{\mathrm{F}}}{\partial t} = -\nabla_l\cdot\left(K_{\mathrm{l_F l_F}}\nabla_l u_{\mathrm{lF}}\right) + Q_{\mathrm{l_F}} \tag{3.66}$$

The coefficients of primary variables in equations (3.64) – (3.66) are summarised in appendix A.

3.5 Heat transfer

Several non-isothermal effects resulting from geological CO_2 sequestration are evaluated in this section. These include the Joule-Thomson (heating and cooling) effect, exothermic gas dissolution, exothermic gas adsorption, endothermic gas desorption, heat changes associated with concomitant water vaporisation, frictional energy losses, conductive heat exchange between the injected fluid and the surrounding reservoir fluids and rock, and heat supply due to thermal expansion of the solid skeleton (Han *et al.* 2010; Mathias *et al.* 2014). Among these thermal effects, Joule - Thomson effect and heat exchange due to differences in temperature between the injected fluids and surrounding rock usually govern the thermal effects during CO_2 sequestration (Chen *et al.* 2018) .

A local thermal non-equilibrium (LTNE) approach is applied to allow parameterisation for the pore space and fractures separately, considering heat transfer between the different domains linked to mass transfer. Due to slow fluid flow in the rock matrix, any temperature difference between the solid grains and fluid in the rock matrix pores reaches thermal equilibrium relatively quickly and heat transfer between solid grains and matrix fluid is ignored. There is no heat exchange between the phases in individual domain, in other words, different phases always have the same temperature in each pore domain.

The principle of conservation of energy is applied to form the general equations of heat transfer, stating that the time rate of the total internal energy in any volume must be equal to the heat flux across the boundary, plus the mechanical work and energy supply. The general form of energy balance equation can be expressed as (Bird *et al.* 2007):

$$\frac{\partial\left(n_\beta \rho_\beta U_\beta\right)}{\partial t} = -\nabla \cdot \boldsymbol{J}_\beta - \nabla \cdot W_\beta + q_\beta \tag{3.67}$$

where n_β is the volume fraction of β phase, U_β is specific internal energy of β phase, ρ_β is density of β phase, $\boldsymbol{J}_\beta$ is the heat flux, W_β is mechanical flux, and q_β is the heat source, accounting for heat transfer between different pore domains and heat supply, for example through geochemical reactions.

In general, the heat flux, $\boldsymbol{J}_\beta$, includes contributions from advective and conductive transport mechanisms, given as:

$$\boldsymbol{J}_\beta = \boldsymbol{J}_{\beta adv} + \boldsymbol{J}_{\beta con} \tag{3.68}$$

where $\boldsymbol{J}_{adv}$ and $\boldsymbol{J}_{con}$ are the advective and conductive components of flux, respectively, which are given as:

$$\boldsymbol{J}_{\beta adv} = -\rho_\beta U_\beta \mathbf{v}_\beta \tag{3.69}$$

$$\boldsymbol{J}_{\beta con} = -\lambda_\beta \nabla T_\beta \tag{3.70}$$

where $\mathbf{v}_\beta$ is velocity of β phase and λ_β is thermal conductivity of β phase. For the solid phase, only the conductive flux is considered, i.e. $\boldsymbol{J}_{sadv} = 0$.

The mechanical heat flux accounts for the heat energy change in the course of the bulk deformation of β phase. For the water and solid phases, due to their small compressibility, the mechanical heat flux can be neglected (Rutqvist *et al.* 2001), i.e.:

$$W_\mathrm{s} = W_\mathrm{l} = 0 \tag{3.71}$$

In contrast, the gas phase is highly compressible and the mechanical work during gas compression or expansion can affect system temperature, giving:

$$W_\mathrm{g} = \quad u_\mathrm{g} \mathrm{v}_\mathrm{g} \tag{3.72}$$

where u_g is the stress tensor of gas phase.

Substituting equations (3.68) to (3.72) into equation (3.67) yields the general forms the energy balance equations for the different phases:

$$\frac{\partial\left(n_\beta \rho_\beta U_\beta\right)}{\partial t} = -\nabla \cdot \left(\rho_\beta U_\beta \mathbf{v}_\beta\right) - \nabla \cdot W_\beta + \nabla \cdot \left(\lambda_\beta \nabla T_\beta\right) + q_\beta \tag{3.73}$$

Expanding the term on the left-hand side and the first term on the right-hand side of equation (3.73) produces:

$$U_\beta \frac{\partial\left(n_\beta \rho_\beta\right)}{\partial t} + n_\beta \rho_\beta \frac{\partial U_\beta}{\partial t} + \rho_\beta \mathbf{v}_\beta \cdot \nabla U_\beta = -U_\beta \nabla \cdot \left(\rho_\beta \mathbf{v}_\beta\right) - \nabla \cdot W_\beta + \nabla \cdot \left(\lambda_\beta \nabla T_\beta\right) + q_\beta \tag{3.74}$$

By applying mass conversation, it is obtained:

$$n_\beta \rho_\beta \frac{\partial U_\beta}{\partial t} = -\rho_\beta \mathbf{v}_\beta \cdot \nabla U_\beta - \nabla \cdot W_\beta + \nabla \cdot \left(\lambda_\beta \nabla T_\beta\right) + q_\beta \tag{3.75}$$

With the assumption that there is no work done for the solid and water phases, the internal energy can be approximated by specific heat capacity and temperature change, which can be expressed as:

$$dU_\mathrm{s} \approx C_{ps} dT_\mathrm{s} \tag{3.76}$$

$$dU_\mathrm{l} \approx C_{p\mathrm{l}} dT_\mathrm{l} \tag{3.77}$$

where C_{ps} and $C_{p\mathrm{l}}$ are the specified heat capacities of the solid phase and water phase and T_s and T_l are the temperatures of solid phase and water phase, respectively.

For a thermodynamically open system, the internal energy, U_g, has a relation with specific enthalpy (Ziabakhsh-Ganji and Kooi 2014):

$$U_\mathrm{g} = H_\mathrm{g} - \frac{u_\mathrm{g}}{\rho_\mathrm{g}} \tag{3.78}$$

$$dH_\mathrm{g} = C_{p\mathrm{g}} dT_\mathrm{g} - \mu_{JT} C_{p\mathrm{g}} du_\mathrm{g} \tag{3.79}$$

where H_g specific enthalpy, μ_{JT} is Joule–Thomson coefficient, T_g is the temperature of gas phase, $C_{p\mathrm{g}}$ is the specified heat capacities of the gas phase.

The following thermodynamic relation is used to calculate the constant pressure specific heat capacity:

$$C_{p\mathrm{g}\alpha} = DC_{p\mathrm{g}\alpha} + C^0_{p\mathrm{g}\alpha} \tag{3.80}$$

where $DC_{p\mathrm{g}\alpha}$ is the departure function of specific heat capacity, which is defined as the difference between the specific heat capacity for an ideal gas, $C^0_{p\mathrm{g}\alpha}$, and that in real case for any temperature and pressure. In current work, PR-EoS is applied to calculate the departure function of specific heat capacity. The ideal gas specific heat capacity is qualified using a polynomial function with coefficient presented by Poling *et al.* (2001). The thermodynamic relation of the Joule-Thomson cooling coefficient is expressed as (Ziabakhsh-Ganji and Kooi 2014):

$$\mu_\mathrm{JT} = -\frac{1}{C_{p\mathrm{g}\alpha}} \left[\frac{T_\mathrm{g} \left(\partial u_\mathrm{gm} / T_\mathrm{m}\right)_{V^r_{\mathrm{m}\alpha}}}{\left(\partial u_\mathrm{gm} / V^r_{\mathrm{m}\alpha}\right)_{T_\mathrm{m}}} + V^r_{\mathrm{m}\alpha} \right] \tag{3.81}$$

Inserting equations (3.76) to (3.79) into equation (3.75) and ignoring the effect of solid deformation, the heat energy equations for the three phases can be obtained, as:

$$n_{\mathrm{s}}\rho_{\mathrm{s}}C_{ps}\frac{\partial T_{\mathrm{s}}}{\partial t} = \nabla\cdot(\lambda_{\mathrm{s}}\nabla T_{\mathrm{s}}) \ + q_{\mathrm{s}} \tag{3.82}$$

$$n_{\mathrm{l}}\rho_{\mathrm{l}}C_{p\mathrm{l}}\frac{\partial T_{\mathrm{l}}}{\partial t} = -\rho_{\mathrm{l}}C_{p\mathrm{l}}\mathbf{v}_{\mathrm{l}}\cdot\nabla T_{\mathrm{l}} - \nabla\cdot(\lambda_{\mathrm{l}}\nabla T_{\mathrm{l}}) \ + q_{\mathrm{l}} \tag{3.83}$$

$$n_{\mathrm{g}}\rho_{\mathrm{g}}C_{p\mathrm{g}}\frac{\partial T_{\mathrm{g}}}{\partial t} - \left(n_{\mathrm{g}}\rho_{\mathrm{g}}C_{p\mathrm{g}}\mu_{JT} + n_{\mathrm{g}}\right)\frac{\partial u_{\mathrm{g}}}{\partial t} = -\rho_{\mathrm{g}}C_{p\mathrm{g}}\mathbf{v}_{\mathrm{g}}\left(\nabla T_{\mathrm{g}} - \mu_{JT}\nabla u_{\mathrm{g}}\right) - \nabla\cdot\left(\lambda_{\mathrm{g}}\nabla T_{\mathrm{g}}\right) + q_{\mathrm{g}} \tag{3.84}$$

Equations (3.82) to (3.84) describe the heat transfer of each phase. The heat transport equation of each medium can be obtained by summing up the heat energy equations of the three phases.

3.5.1 Heat transfer in the matrix continuum

The governing equation for heat transfer in the rock matrix is obtained by summing the energy balance equations over each of the phases (Hosking *et al.* 2019). It is assumed that the fluid velocity in the rock matrix is low enough that the solid grains and the fluid in the rock matrix remain at local thermal equilibrium, i.e. $T_{\mathrm{s}} = T_{\mathrm{l,m}} = T_{\mathrm{g,m}} = T_{\mathrm{m}}$, giving:

$$\left(\rho_{\mathrm{m}}C_{\mathrm{pm}}\right)_{\mathrm{eff}}\frac{\partial T_{\mathrm{m}}}{\partial t} - n_{\mathrm{m}}S_{\mathrm{gm}}\left(\rho_{\mathrm{gm}}C_{\mathrm{pgm}}\mu_{\mathrm{JT}} + 1\right)\frac{\partial u_{\mathrm{gm}}}{\partial t} = \nabla\cdot(\lambda_{\mathrm{em}}\nabla T_{\mathrm{m}}) - \left(S_{\mathrm{lm}}\rho_{\mathrm{l}}C_{\mathrm{pl}}\mathbf{v}_{\mathrm{lm}} + S_{\mathrm{gm}}\rho_{\mathrm{gm}}C_{\mathrm{pgm}}\mathbf{v}_{\mathrm{gm}}\right)\cdot\nabla T_{\mathrm{m}} + S_{\mathrm{gm}}\rho_{\mathrm{gm}}C_{\mathrm{pgm}}\mathbf{v}_{\mathrm{gm}}\mu_{\mathrm{JT}}\cdot\nabla u_{\mathrm{gm}} + q_{\mathrm{m}} \tag{3.85}$$

where T_{m} is the matrix temperature, $\left(\rho_{\mathrm{m}}C_{\mathrm{pm}}\right)_{\mathrm{eff}}$ and λ_{em} are the effective specific heat capacity and the effective the average thermal conductivity of the matrix, respectively.

The effective specific heat capacity can be obtained from the density and specific heat capacities of all components within rock matrix as (Gupta *et al.* 2015):

$$\left(\rho_{\mathrm{m}}C_{\mathrm{pm}}\right)_{\mathrm{eff}} = (1 - n_{\mathrm{m}} - n_{\mathrm{f}})\left(\rho_{\mathrm{s}}C_{\mathrm{ps}} + \rho_{\mathrm{a}}C_{\mathrm{pa}}\right) + \theta_{\mathrm{lm}}\rho_{\mathrm{l}}C_{\mathrm{pl}} + \theta_{\mathrm{gm}}\rho_{\mathrm{gm}}C_{\mathrm{pgm}} \tag{3.86}$$

where C_{pa} and ρ_a the specific heat capacities of the adsorbed phase gas, ρ_{gm} is the density of the gas mixture, and C_{pgm} is specific heat capacity of the gas mixture, which can be calculated as:

$$\rho_{\mathrm{gm}} = \sum_{i=1}^{n_g} x_{\mathrm{m}}^{i} c_{\mathrm{m}}^{t} M^{i} \tag{3.87}$$

$$C_{p\mathrm{gm}} = \sum_{i=1}^{n_g} X_{\mathrm{m}}^{i} C_{p\mathrm{gm}}^{i} \tag{3.88}$$

where M^i is the molar mass of i^{th} gas component and X_{m}^{i} is the mass fraction of i^{th} gas component, which is calculated as:

$$X_{\mathrm{m}}^{i} = \frac{x_{\mathrm{m}}^{i} M^{i}}{\sum_{i=1}^{n_g} x_{\mathrm{m}}^{i} M^{i}} \tag{3.89}$$

Unlike the effective specific heat capacity, for which an arithmetic mean is used, the effective thermal conductivity is obtained based on the geometric mean of the thermal conductivities of the three phases was adopted (Sass *et al.* 1971):

$$\lambda_{\mathrm{me}} = \lambda_{\mathrm{s}}^{(1-n_{\mathrm{m}}-n_{\mathrm{f}})} \lambda_{\mathrm{l}}^{n_{\mathrm{m}} S_{\mathrm{lm}}} \lambda_{\mathrm{g}}^{n_{\mathrm{m}}(1-S_{\mathrm{lm}})} = \lambda_{sat}^{S_{\mathrm{lm}}} \lambda_{dry}^{(1-S_{\mathrm{lm}})} \tag{3.90}$$

where λ_{s}, λ_{l} and λ_{g} are the thermal conductivities of the solid, water and gas phases, respectively, and λ_{sat} and λ_{dry} are the thermal conductivities of the fully saturated and fully dried material, which can be obtained through:

$$\lambda_{sat} = \lambda_{\mathrm{s}}^{(1-n_m)} \lambda_{\mathrm{l}}^{n_m} \tag{3.91}$$

$$\lambda_{dry} = \lambda_{\mathrm{s}}^{(1-n_m)} \lambda_{\mathrm{g}}^{n_m} \tag{3.92}$$

$$\lambda_g = \sum_{i=1}^{n_g} \mathrm{X}_{\alpha \mathrm{i}} \lambda_{\mathrm{g}}^{i} \tag{3.93}$$

3.5.2 Heat transfer in the fracture continuum

Similarly, the governing equation for heat transfer in the fracture continuum can be obtained by combining the energy balances for the fluid in the natural fracture network, written as:

$$\begin{aligned} \left(\rho_{\mathrm{f}} C_{\mathrm{pf}}\right)_{\mathrm{eff}} \frac{\partial T_{\mathrm{f}}}{\partial t} - n_{\mathrm{f}} S_{gf} \left(\rho_{\mathrm{gf}} C_{\mathrm{pgf}} \mu_{\mathrm{JT}} + 1\right) \frac{\partial u_{\mathrm{gf}}}{\partial t} = \nabla \cdot \left(\lambda_{\mathrm{ef}} \nabla T_{\mathrm{f}}\right) \\ - \left(S_{\mathrm{lf}} \rho_{\mathrm{l}} C_{\mathrm{pl}} \mathbf{v}_{lf} + S_{\mathrm{gf}} \rho_{\mathrm{gf}} C_{\mathrm{pgf}} \mathbf{v}_{\mathrm{gf}}\right) \cdot \nabla T_{\mathrm{f}} + S_{\mathrm{gf}} \rho_{\mathrm{gf}} C_{\mathrm{pgf}} \mathbf{v}_{\mathrm{gf}} \mu_{\mathrm{JT}} \cdot \nabla u_{\mathrm{gf}} + q_{\mathrm{f}} \end{aligned} \tag{3.94}$$

where T_{f} is the fracture continuum temperature, $\left(\rho_{\mathrm{f}} C_{\mathrm{pf}}\right)_{\mathrm{eff}}$ and λ_{ef} are the effective specific heat capacity and the effective thermal conductivity of the fracture continuum, respectively, expressed as:

$$\left(\rho_{\mathrm{f}} C_{\mathrm{pf}}\right)_{\mathrm{eff}} = \theta_{\mathrm{lf}} \rho_{\mathrm{l}} \mathrm{C}_{\mathrm{pl}} + \theta_{\mathrm{gf}} \rho_{\mathrm{gf}} C_{\mathrm{pgf}} \tag{3.95}$$

where ρ_{gf} is the density of the gas mixture and C_{pgf} is its specific heat capacity, given by:

$$\rho_{\mathrm{gf}} = \sum_{i=1}^{n_g} x_{\mathrm{f}}^{i} c_{\mathrm{f}}^{t} M^{i} \tag{3.96}$$

$$C_{\mathrm{pgf}} = \sum_{i=1}^{n_g} X_{\mathrm{f}}^{i} C_{\mathrm{pgf}}^{i} \tag{3.97}$$

where X_{f}^{i} is the mass fraction of i^{th} gas component, which is calculated as:

$$X_{\mathrm{f}}^{i} = \frac{x_{\mathrm{f}}^{i} M^{i}}{\sum_{i=1}^{n_g} x_{\mathrm{f}}^{i} M^{i}} \tag{3.98}$$

An effective thermal conductivity based on the geometric mean of the thermal conductivities of the three phases is again adopted (Sass *et al.* 1971):

$$\lambda_{\mathrm{ef}} = \lambda_{\mathrm{l}}^{n_{\mathrm{f}} S_{\mathrm{lf}}} \lambda_{\mathrm{g}}^{n_{\mathrm{f}}(1-S_{\mathrm{lf}})} = \lambda_{sat}^{S_{\mathrm{lf}}} \lambda_{dry}^{(1-S_{\mathrm{lf}})} \tag{3.99}$$

where λ_s, λ_w and λ_g are the thermal conductivities of solid, water and gas phases, respectively, and λ_{sat} and λ_{dry} are the thermal conductivities of the fully saturated and fully dried material, which can be obtained through:

$$\lambda_{sat} = \lambda_{\mathrm{l}}^{n_{\mathrm{f}}} \tag{3.100}$$

$$\lambda_{dry} = \lambda_{\mathrm{g}}^{n_{\mathrm{f}}} \tag{3.101}$$

$$\lambda_{\mathrm{g}} = \sum_{i=1}^{n_g} X_{\mathrm{f}}^{i} \lambda_{\mathrm{g}}^{i} \tag{3.102}$$

3.5.3 Heat transfer in discrete hydraulic fractures

Using a similar approach, the governing equation for heat transfer through the fluid in the discrete hydraulic fractures can be obtained, as:

$$w\left(\rho_{\mathrm{F}}C_{\mathrm{pF}}\right)_{\mathrm{eff}}\frac{\partial T_{\mathrm{F}}}{\partial t}-wS_{\mathrm{gF}}\left(\rho_{\mathrm{gF}}C_{\mathrm{pgF}}\mu_{\mathrm{JT}}+1\right)\frac{\partial u_{\mathrm{gF}}}{\partial t}=\nabla\cdot\left(w\boldsymbol{\lambda}_{\mathrm{eF}}\nabla T_{\mathrm{F}}\right)$$

$$-\left(wS_{\mathrm{lF}}\rho_{\mathrm{l}}C_{\mathrm{pl}}\mathbf{v}_{\mathrm{lF}}+wS_{\mathrm{gF}}\rho_{\mathrm{gF}}C_{\mathrm{pgF}}\mathbf{v}_{\mathrm{gF}}\right)\cdot\nabla T_{\mathrm{F}}+wS_{\mathrm{gF}}\rho_{\mathrm{gF}}C_{\mathrm{pgF}}\mathbf{v}_{\mathrm{gF}}\mu_{\mathrm{JT}}\cdot\nabla u_{\mathrm{gF}}+q_{\mathrm{F}} \quad (3.103)$$

where T_{F} is the hydraulic fracture temperature, $\left(\rho_{\mathrm{F}}C_{\mathrm{pF}}\right)_{\mathrm{eff}}$ and λ_{eF} are the effective specific heat capacity and the effective the average thermal conductivity of the hydraulic fractures, respectively, expressed as:

$$\left(\rho_F C_{pF}\right)_{\mathrm{eff}}=S_{\mathrm{lF}}\rho_{\mathrm{l}}C_{\mathrm{pl}}+S_{\mathrm{gF}}\rho_{\mathrm{gF}}C_{\mathrm{pgF}} \quad (3.104)$$

where ρ_{gF} is the density of the gas mixture and C_{pgF} is its specific heat capacity, given by:

$$\rho_{\mathrm{gF}}=\sum_{i=1}^{n_g}x_{\mathrm{F}}^{i}c_{\mathrm{F}}^{t}M^{i} \quad (3.105)$$

$$C_{\mathrm{pgF}}=\sum_{i=1}^{n_g}X_{\mathrm{F}}^{i}C_{\mathrm{pgF}}^{i} \quad (3.106)$$

where X_{F}^{i} is the mass fraction of i^{th} gas component, which is calculated as:

$$X_{\mathrm{F}}^{i}=\frac{x_{\mathrm{F}}^{i}M^{i}}{\sum_{i=1}^{n_g}x_{\mathrm{F}}^{i}M^{i}} \quad (3.107)$$

An effective thermal conductivity based on the geometric mean of the thermal conductivities of the three phases is again adopted (Sass *et al.* 1971):

$$\lambda_{\mathrm{ef}}=\lambda_{\mathrm{l}}^{S_{\mathrm{lF}}}\lambda_{\mathrm{g}}^{(1-S_{\mathrm{lF}})}=\lambda_{sat}^{S_{\mathrm{lF}}}\lambda_{dry}^{(1-S_{\mathrm{lF}})} \quad (3.108)$$

where λ_s, λ_{l} and λ_{g} are the thermal conductivities of solid, water and gas phases, respectively, and λ_{sat} and λ_{dry} are the thermal conductivities of the fully saturated and fully dried material, which can be obtained through:

$$\lambda_{sat}=\lambda_{l}^{S_{\mathrm{lF}}} \quad (3.109)$$

$$\lambda_{dry}=\lambda_{g}^{S_{\mathrm{gF}}} \quad (3.110)$$

$$\lambda_{\mathrm{g}}=\sum_{i=1}^{n_g}X_{\mathrm{F}}^{i}\lambda_{\mathrm{g}}^{i} \quad (3.111)$$

3.5.4 Heat exchange

As the temperatures of the rock matrix and natural fractures are considered separately by using the local thermal non-equilibrium (LTNE) model, the heat source in equations (3.85), (3.94) and (3.103) originate from two types, namely, heat transfer between the domains and internal or external heat supply, as:

$$q_{\mathrm{m}} = q_{\mathrm{fm}} + q_{\mathrm{ms}} \tag{3.112}$$

$$q_{\mathrm{f}} = -q_{\mathrm{fm}} + q_{\mathrm{fF}} + q_{\mathrm{fs}} \tag{3.113}$$

$$q_{\mathrm{F}} = -\mathrm{q}_{\mathrm{fF}} + q_{\mathrm{Fs}} \tag{3.114}$$

where q_{fm} and q_{fF} represent the heat transfer between the dual continua and between the fracture continuum and hydraulic fracture domain, respectively, and q_{ms}, q_{fs} and q_{Fs} are heat source terms, for example due to geochemical reactions.

For consistency, it has been assumed that the temperature in natural fractures is identical to that in hydraulic fractures. No heat transfer occurs between the fracture continuum and discrete fractures, hence, only thermal transfer between the dual continua is considered in this work. Heat transfer is separated into two processes, namely, heat transfer between the rock matrix and fracture fluid by conduction through the fracture surfaces, and heat transfer by advection through mass exchange between the continua (Heinze and Hamidi 2017), given as:

$$q_{\mathrm{fm}} = h_{\mathrm{T}} A_{\mathrm{fm}} (T_{\mathrm{f}} - T_{\mathrm{m}}) + \left(\Gamma_{\mathrm{lfm}} C_{pl} + \Gamma_{\mathrm{gfm}} C_{pg}\right)(T_{\mathrm{f}} - T_{\mathrm{m}}) \tag{3.115}$$

where h_T is the heat transfer coefficient between the fracture and matrix continua, and A_{fm} is the interfacial fracture-matrix specific area, which can be estimated based on the geometric relation between the natural fractures and the rock matrix. The first term on the right-hand side of equation (3.115) represents the heat exchange between matrix and fracture continua by conduction through the fracture surfaces, and the second term represents heat transfer by advection through the mass exchange term (Hao *et al.* 2013). Both h_T and A_{fm} are important parameters, influencing fracture-matrix interactions. The heat transfer coefficient is typically calculated by harmonic averaging of the matrix-fracture thermal conductivity (Hao *et al.* 2013):

$$h_{\mathrm{T}} = \frac{\lambda_{\mathrm{em}} \lambda_{\mathrm{ef}}}{l\lambda_{\mathrm{ef}} + w\lambda_{\mathrm{em}}} \tag{3.116}$$

The interfacial fracture-matrix specific area is derived using geometrical considerations for an aperture w and a matrix block length l_b (Heinze and Hamidi 2017):

$$A_{\mathrm{fm}} = \frac{8l_b}{(2l_b + w)^2} \tag{3.117}$$

3.5.5 Governing equations for heat transport

To obtain the governing differential equations for heat transfer, the real gas law has been substituted into the energy conservation equations (3.85), (3.194) and (3.103), yielding the following presented in terms of the primary variables:

$$C_{\mathrm{T_m T_m}} \frac{\partial T_{\mathrm{m}}}{\partial t} + \sum_{j=1}^{n_g} C_{\mathrm{T_m c_m}} \frac{\partial c_{\mathrm{m}}^{j}}{\partial t} = \nabla \cdot \left(K_{\mathrm{T_m T_m}} \nabla T_{\mathrm{m}}\right) + K_{\mathrm{T_m T_m}}^{\mathrm{v}} \nabla T_{\mathrm{m}} + \sum_{j=1}^{n_g} \mathrm{K}_{\mathrm{T_m c_m}}^{\mathrm{v}} \nabla c_{\mathrm{m}}^{j} + Q_{\mathrm{T_m}} \tag{3.118}$$

$$C_{T_{\mathrm{f}} T_{\mathrm{f}}} \frac{\partial T_{\mathrm{f}}}{\partial t} + \sum_{j=1}^{n_g} C_{T_{\mathrm{f}} c_{\mathrm{f}}} \frac{\partial c_{\mathrm{f}}^{j}}{\partial t} = \nabla \cdot \left(K_{T_{\mathrm{f}} T_{\mathrm{f}}} \nabla T_{\mathrm{f}}\right) + K_{T_{\mathrm{f}} T_{\mathrm{f}}}^{\mathrm{v}} \nabla T_{\mathrm{f}} + \sum_{j=1}^{n_g} K_{T_{\mathrm{f}} c_{\mathrm{f}}}^{\mathrm{v}} \nabla c_{\mathrm{f}}^{j} + Q_{T_{\mathrm{f}}} \tag{3.119}$$

$$C_{\mathrm{T_F T_F}} \frac{\partial T_F}{\partial t} + \sum_{j=1}^{n_g} C_{\mathrm{T_F c_F}} \frac{\partial c_{\mathrm{F}}^{j}}{\partial t} = \nabla_l \cdot \left(K_{\mathrm{T_F T_F}} \nabla T_{\mathrm{F}}\right) + K_{\mathrm{T_F T_F}}^{\mathrm{v}} \nabla_l T_{\mathrm{F}} + \sum_{j=1}^{n_g} K_{\mathrm{T_F c_F}}^{\mathrm{v}} \nabla_l c_{\mathrm{F}}^{j} + Q_{\mathrm{T_F}} \tag{3.120}$$

The coefficients of primary variables in equations (3.118) – (3.120) are summarised in appendix A.

3.6 Deformation

The deformation behaviour of fractured rock is represented in this work by using dual poroelastic theory. The three basic principles of poroelastic theory, namely, the stress equilibrium, strain-displacement, and strain-stress relations are used. The current formulation considers a positive sign convention for tensile stress, while fluid pressure is positive for compression. The mechanical behaviour described in this section is related to

the dual continuum system only, the deformation of hydraulic fracture will be handled separately in section 3.8.

3.6.1 Effective stress

Biot's poroelastic theory is used to describe the fluid-solid coupling of a single porosity system and is here extended to dual porosity media. Based on the principle of effective stress, the relationship between changes in total stress and effective stress can be written as (Pao and Lewis 2002; Chen et al. 2019):

$$d\boldsymbol{\sigma} = d\boldsymbol{\sigma}^{e} + \tilde{\mathfrak{b}}_1 \boldsymbol{m} du_{\mathrm{m}} + \tilde{\mathfrak{b}}_2 \mathbf{m} du_{\mathrm{f}} \tag{3.121}$$

where $\boldsymbol{\sigma}$ is the total stress tensor, $\boldsymbol{\sigma}^{e}$ is the effective stress tensor, $\mathbf{m}$ is a vector with $\mathbf{m}^{\boldsymbol{T}} = (1,1,1,0,0,0)$ and $(1,1,0)$ for three- and two-dimensional problems, respectively. $\tilde{\mathfrak{b}}_1$ and $\tilde{\mathfrak{b}}_2$ are the Biot's effective stress coefficients of the matrix and matrix, respectively. And u_{m} and u_{f} are the effective average pore pressures.

For unsaturated fractured rock, the effective average pore pressure is weighted by the saturations for both the matrix and fractures systems (Lewis and Schrefler 1998; Pao and Lewis 2002):

$$u_{\mathrm{m}} = S_{\mathrm{lm}} u_{\mathrm{lm}} + S_{\mathrm{gm}} u_{\mathrm{gm}} \tag{3.122}$$

$$u_{\mathrm{f}} = S_{\mathrm{lf}} u_{\mathrm{lf}} + S_{\mathrm{gf}} u_{\mathrm{gf}} \tag{3.123}$$

The Biot's effective stress coefficients, $\tilde{\mathfrak{b}}_1$ and $\tilde{\mathfrak{b}}_2$, are expressed as (Pao and Lewis 2002; Chen *et al.* 2019):

$$\tilde{\mathfrak{b}}_1 = \frac{c_{\mathrm{m}}}{c} - \frac{c_{\mathrm{s}}}{c} \tag{3.124}$$

$$\tilde{\mathfrak{b}}_2 = 1 - \frac{c_{\mathrm{m}}}{c} \tag{3.125}$$

where $c = 3(1-v)/E$ is the compressibility of bulk fractured porous media, c_{s} is the elastic compressibility of the solid constituent, $c_{\mathrm{m}} = 3(1-v)/E_{\mathrm{m}}$ is the elastic drained compressibility of the porous matrix, v are the Possion's ratio, E is the bulk Young's modulus, E_{m} is the Young's modulus, which can be obtained from the experiments performed on specimens an order of magnitude larger than the spacing of the matrix pores but devoid of fracture.

3.6.2 Elastic constitutive relationships

The deformation of rocks is generally divided into mechanical deformation due to effective stress, thermal expansion, and adsorption-desorption-induced matrix swelling-shrinkage. Assuming thermal expansion-contraction and matrix swelling-shrinkage are isotropic and reversible, the total strain for a non-isothermal rock can be given in an incremental form as (Chen M et al. 2019a; Hosking et al. 2019):

$$d\boldsymbol{\varepsilon} = d\boldsymbol{\varepsilon}^{e} + \frac{1}{3}\mathbf{m}d\varepsilon^{s} + \frac{1}{3}\mathbf{m}d\varepsilon^{T} \tag{3.126}$$

where $\boldsymbol{\varepsilon}$ is the total strain vector, $\boldsymbol{\varepsilon}^{e}$ is the elastic strain vector, ε^{s} is the sorption-induced volumetric strain, and ε^{T} is thermal expansion-contraction strain.

The component of strain due to gas adsorption-desorption and temperature is expressed as:

$$d\varepsilon^{s} = \sum_{j=1}^{n_g} A_{\mathrm{s}}^{j}\, dc_{\mathrm{m}}^{j} \tag{3.127}$$

$$d\varepsilon^{T} = A_T dT_{\mathrm{m}} \tag{3.128}$$

where A_s^i and A_T are two coefficients related to adsorption-induced swelling and thermal deformation, details of which will be provided in section 3.6.3.

Substituting equations (122) to (3.128) into equation (3.121) and rearranging gives:

$$d\boldsymbol{\sigma} = \boldsymbol{D}_{\mathrm{e}}\left(d\boldsymbol{\varepsilon} - \frac{1}{3}\mathbf{m}\sum_{j=1}^{n_g} A_s^{j}\, dc_{\mathrm{m}}^{j} - \frac{1}{3}\mathbf{m}A_T dT_{\mathrm{m}}\right) + \mathbf{m}\tilde{\mathrm{b}}_1 du_{\mathrm{m}} + \mathbf{m}\tilde{\mathrm{b}}_2 du_{\mathrm{f}} \tag{3.129}$$

where $\boldsymbol{D}_{\mathrm{e}}$ is the elasticity matrix.

The strain is related to displacement, expressed as:

$$d\boldsymbol{\varepsilon} = \mathbf{B}d\mathbf{u}_{\mathrm{s}} \tag{3.130}$$

where $\mathbf{B}$ is the strain-displacement matrix and $\boldsymbol{d}\mathbf{u}_{\mathrm{s}}$ is a vector of the incremental displacement.

Considering the local equilibrium condition, the stress equilibrium equation without considering body forces is given as:

$$\mathbf{B}^{\boldsymbol{T}} d\boldsymbol{\sigma} = 0 \tag{3.131}$$

where

$$\mathbf{B}^{\boldsymbol{T}} = \begin{bmatrix} \frac{\partial}{\partial x} & 0 & 0 & \frac{\partial}{\partial y} & 0 & \frac{\partial}{\partial z} \\ 0 & \frac{\partial}{\partial y} & 0 & \frac{\partial}{\partial x} & \frac{\partial}{\partial z} & 0 \\ 0 & 0 & \frac{\partial}{\partial z} & 0 & \frac{\partial}{\partial y} & \frac{\partial}{\partial x} \end{bmatrix}$$

3.6.3 Thermal and adsorption-desorption-induced swelling-shrinkage

It has been shown that the total strain includes mechanical strain, thermal strain and adsorption-induced swelling strain. The thermal strain caused by temperature increases or decreases can be defined as:

$$\varepsilon^T = \alpha_T (T - T_0) \tag{3.132}$$

where α_T is thermal expansion coefficient.

Some geomaterials, for example coal, swell when exposed to adsorptive fluid, such as CO_2. This deformation behaviour can no longer be described using the conventional stress-strain relation. It should be recognised that the porous medium without its fluids does not only contain the solid matrix, but also the solid–fluid interface (i.e., the interface between the solid matrix and the pore space), which provides a large amount of available sites for fluid adsorption (Gor *et al.* 2017; Zhang 2018). In the surface science literature, the adsorption-induced deformation of materials is considered to arise from the properties of the solid surface being altered upon fluid adsorption. If the surface is deformable, the solid surface can be stretched through increasing interatomic bonds between solid atoms at a constant number of solid atoms, as shown in Figure 3.5. The surface stress is generally introduced to quantify the work of stretching the existing surface, which provides a basis for estimating the deformation related to adsorption behaviour. The results of recent studies show that the surface stress effect is analogous to the effect of matrix pore pressure on the macroscopic volumetric strain (Vandamme *et al.* 2010; Nikoosokhan *et al.* 2012; Zhang 2018), and surface variation is only related to the micro-porosity change of the matrix if the microstructure of the porous matrix is idealized as uniformly distributed mono-sized spherical pores, which corresponds to a macroscopically isotropic poroelastic media.

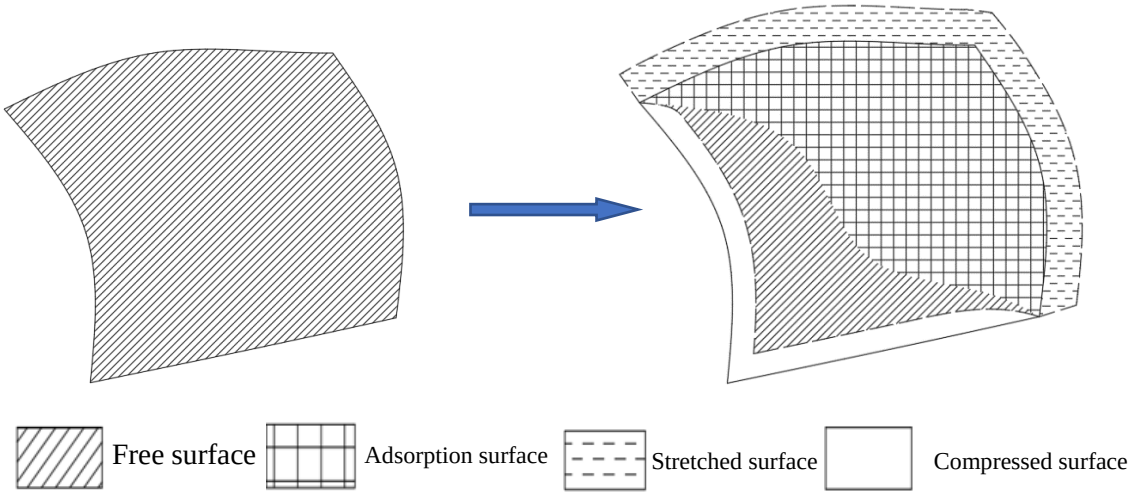

Figure 3.5 Schematic of a deformable internal surface (solid line denotes boundary of undeformed surface and dashed line denotes boundary of deformed surface).

Following the work of Chen *et al.* (2019b), the surface stress of the solid-fluid interface is conceptualized as a pre-pressure u_a acting in the porous matrix, which implies that a pre-pressure u_a has to be applied against the effects induced by the surface stress change resulting from gas adsorption in order to prevent any deformation and porosity change with respect to the reference configuration. The pre-pressure u_a is related with surface stress change, as:

$$u_a = \xi \Delta\sigma^s \tag{3.133}$$

where ξ is a constant material parameter representing the correlations between changes in the adsorption area of the matrix pore and in porosity of the matrix (Nikoosokhan *et al.* 2013). $\Delta\sigma^s$ is the change in surface stress due to gas adsorption. For the case of a pure gas, the change in surface stress can be obtained according to the Gibbs-Duhem relation (Nikoosokhan *et al.* 2012; Chen *et al.* 2019b):

$$\Delta\sigma^s = -\int_{u_{g0}}^{u_g} \Gamma \bar{V}_b \, du_{\mathrm{gm}} \tag{3.134}$$

where Γ is the number of moles of fluid molecules adsorbed per unit area of the fluid-solid interface, and $\bar{V}_b = RT/u_{\mathrm{gm}}$ is the molar volume of the bulk fluid. If the fluid adsorption obeys a Langmuir isotherm, the change of surface stress is written as:

$$\Delta\sigma^s = -\Gamma^{max} RT \ln\left(1 + b_L u_{\mathrm{gm}}\right) \tag{3.135}$$

where Γ^{max} is the Langmuir adsorption constant, representing the adsorption capacity of fluid per unit adsorption surface.

For the case of a gas mixture, the change in surface stress can be expressed as (Zhang 2018):

$$\Delta\sigma^s = -\frac{RT_{\mathrm{m}}\sum_{i=1}^{n_g}\Gamma_i^{max}b_{Li}x_i}{\sum_{i=1}^{n_g}b_{Li}x_i}\ln\left(1+u_{\mathrm{gm}}\sum_{i=1}^{n_g}b_{Li}x_i\right) \tag{3.136}$$

Similar to the pore fluid pressure, the volumetric strain induced by surface stress change can be expressed as:

$$\varepsilon^s = -\frac{\tilde{\mathrm{b}}_1 u_a}{K_b} \tag{3.137}$$

where $K_b = 1/c$ is the bulk modulus of fractured porous media.

3.6.4 Governing equation for deformation

Substituting equations (3.137) and (3.138) into equation (136) and applying the real gas law to the u_m and u_f, the governing equation can be written in concise form as:

$$\sum_{j=1}^{n_g} C_{\mathbf{u}_{\mathrm{s}}\mathrm{c}_{\mathrm{m}}} dc_{\mathrm{m}}^j + \sum_{j=1}^{n_g} C_{\mathbf{u}_{\mathrm{s}}\mathrm{c}_{\mathrm{f}}} dc_{\mathrm{f}}^j + C_{\mathbf{u}_{\mathrm{s}}\mathrm{l}_{\mathrm{m}}} du_{\mathrm{lm}} + C_{\mathbf{u}_{\mathrm{s}}\mathrm{l}_{\mathrm{f}}} du_{\mathrm{lf}} +$$

$$C_{\mathbf{u}_{\mathrm{s}}\mathrm{T}_{\mathrm{m}}} dT_{\mathrm{m}} + C_{\mathbf{u}_{\mathrm{s}}\mathrm{T}_{\mathrm{m}}} dT_{\mathrm{f}} + C_{\mathbf{u}_{\mathrm{s}}\mathbf{u}_{\mathrm{s}}} d\mathbf{u}_{\mathrm{s}} = 0 \tag{3.138}$$

The coefficients of primary variables in equations (3.138) are summarised in appendix A.

3.7 Porosity and permeability of the fracture and matrix continuum

To be able to use the governing field equations in previous section, explicit expression of porosity, permeability and fracture aperture are required. For the fracture and matrix continua, the mechanical response is shown in terms of porosity and permeability, while the aperture of large scale fracture is applied to describe the mechanical response of hydraulic fractures in current work. The descriptions of porosity and permeability of dual porosity media are presented in this section, and the mechanical behaviour of large scale is given next.

The porosity of each continuum can be defined as:

$$n_{\kappa} = \frac{V_{\kappa}}{V} \tag{3.139}$$

where V is the bulk volume and V_k is the pore volume of each continuum.

Thus, the porosity change of a deforming rock mass can be expressed as:

$$dn_{\kappa} = d\left(\frac{V_{\kappa}}{V}\right) = \frac{dV_{\kappa}}{V} - n_{\kappa}\frac{dV}{V} \tag{3.140}$$

It can be seen from equation (3.140) that the increase in porosity is due to the increase in the pore volume minus the increase in the bulk volume (Lewis and Pao 2002). Considering small strain, the second expression on the right-hand side of equation (3.140) can be approximated as the volumetric strain of the bulk volume:

$$\frac{dV}{V} \approx \frac{dV}{V_0} = d\varepsilon_v \tag{3.141}$$

whereV_0 is the initial bulk volume.

To establish the constitutive links between the porosity changes and the primary field variables, the two additional equations are required to calculate two unknowns $\frac{dV_k}{V}$. Consider a representative volume of the fractured porous medium subjected to the principal stresses, internal pore pressure and thermal stresses, as shown in Figure 3.6. For the sake of simplicity, the principal stress σ_2, the stress component normal to the page is not shown in Figure 3.6.

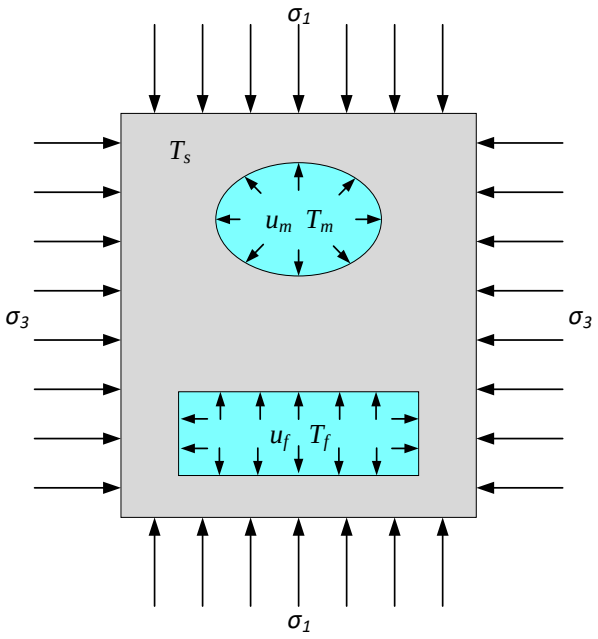

Figure 3.6 A representative volume of the fractured rock subjected to stress conditions.

It is assumed that the rock is homogeneous and isotropic and the deformation is considered to be elastic and small. The strains can be expressed as linear combinations of the stresses within the elastic range of deformation, therefore, the equilibrium of a representative volume loaded under both mechanical stress and thermal stresses can be separated into two stress states (Nur and Byerlee 1971; Gelet 2011). Figure 3.7 shows the thermo-mechanical loading decomposition. The mechanical stresses are represented by the principal stresses and fluid pressures for pore fluid and fractured fluid, while the thermal stresses are represented by the temperatures of solid and fluids in the matrix pore and fractures.

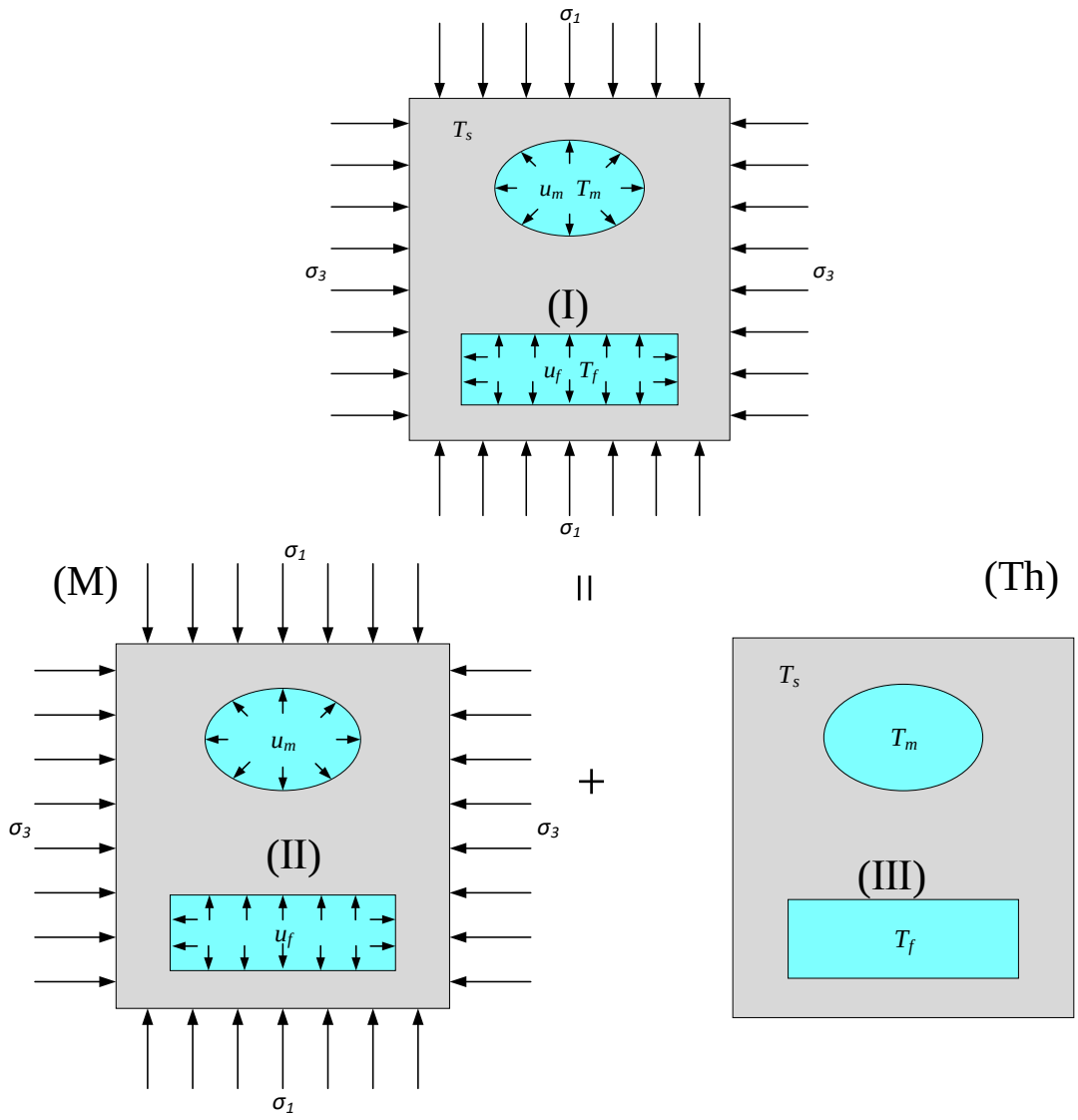

Figure 3.7 Total load decomposition of a representative fractured rock volume.

Deviatoric strains, which measure angular distortion rather than stretching, make no contribution to volumetric change, thus, only the stress causing volumetric change needs to be considered. It would be useful to have a way of excluding the deviatoric stress that acts

at the point in question (Jaeger *et al.* 2009). To do this, the stress tensor is decomposed into an isotropic (or hydrostatic) part and a deviatoric part, as shown in Figure 3.8. The hydrostatic part includes an isotropic hydrostatic stress, an internal matrix pressure, and an internal fracture pressure. The isotropic part of the stress is defined as the mean value of the three principal stresses:

$$\bar{\sigma} = \frac{\sigma_1 + \sigma_2 + \sigma_3}{3} \tag{3.142}$$

Considering the bulk volumetric change in the case V:

$$dV = V[cd\bar{\sigma} - (c_{\mathrm{m}} - c_{\mathrm{s}})du_{\mathrm{m}} - (c - c_{\mathrm{m}})du_{\mathrm{f}}] \tag{3.143}$$

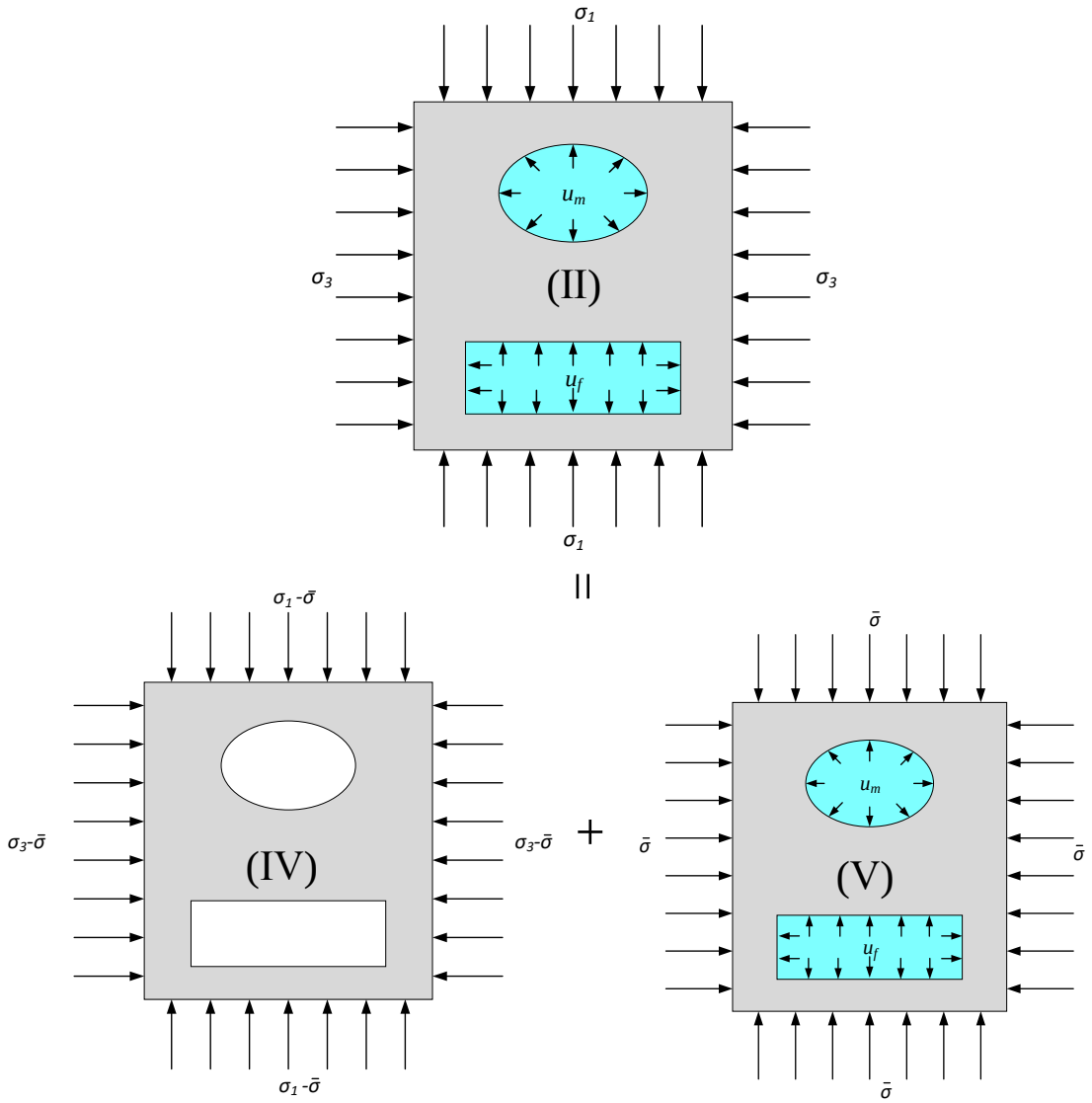

Figure 3.8 Mechanical stress decomposition of a representative fractured rock volume.

However, the micropore volume change, dV_{m}, and fracture volume change, dV_{f}, cannot be calculated in case V.

Additional equations are required to calculate the unknown pore volume change. Consider another two stress state cases VI and VII, as shown in Figure 3.9, stress state case VI corresponds to an equal external and internal matrix pressure of u_{m}, and stress state case VII corresponds to an equal external and internal fracture pressure of u_{m} and null pore pressure.

In stress state case VI, the volumetric change for bulk volume dV^{*}, pore volume $dV_m{}^{*}$, and fracture volume $V_{\mathrm{f}}{}^{*}$are expressed as:

$$dV^{*} = Vc_{\mathrm{s}}du_{\mathrm{m}} \tag{3.144}$$

$$dV_{\mathrm{m}}{}^{*} = n_{\mathrm{m}}Vc_{\mathrm{s}}du_{\mathrm{m}} \tag{3.145}$$

$$dV_{\mathrm{f}}{}^{*} = n_{\mathrm{f}}Vc_{\mathrm{s}}du_{\mathrm{f}} \tag{3.146}$$

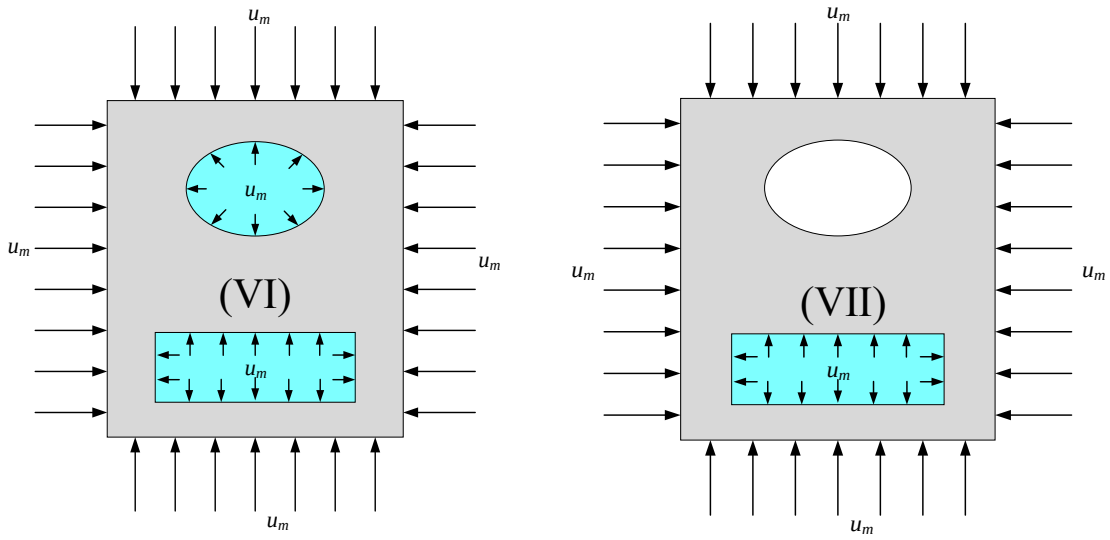

Figure 3.9 Stress cases VI: equal external and internal matrix pressure and Stress cases VII: equal external and internal fracture pressure and null matrix pressure.

In stress state case VI, the volumetric change for bulk volume $dV^{**}$and fracture volume $dV_{\mathrm{f}}{}^{**}$are expressed as:

$$dV^{**} = Vc_{\mathrm{m}}du_{\mathrm{m}} \tag{3.147}$$

$$dV_{\mathrm{f}}{}^{**} = n_{\mathrm{f}}Vc_{\mathrm{m}}du_{\mathrm{m}} \tag{3.148}$$

However, the micropore volume change, $dV_{\mathrm{m}}{}^{**}$cannot be calculated in case stress state case VI.

Applying Betty's reciprocity theorem to case V and VI and, case V and VII, and case VI and VII, it can be shown that:

$$(dV - dV_{\mathrm{m}} - dV_{\mathrm{f}})du_{\mathrm{m}} = V(c_s d\bar{\sigma} - n_{\mathrm{m}}c_{\mathrm{s}}du_{\mathrm{m}} - n_{\mathrm{f}}c_{\mathrm{s}}du_{\mathrm{f}})du_{\mathrm{m}} \tag{3.149}$$

$$(dV - dV_{\mathrm{f}})du_{\mathrm{m}} = Vc_{\mathrm{m}}du_{\mathrm{m}}d\bar{\sigma} - \ dV_{\mathrm{m}}{}^{**}du_{\mathrm{m}} - n_{\mathrm{f}}Vc_{\mathrm{m}}du_{\mathrm{m}}du_{\mathrm{f}} \tag{3.150}$$

$$Vc_{\mathrm{s}}du_{\mathrm{m}}du_{\mathrm{m}} - n_{\mathrm{f}}Vc_s du_{\mathrm{m}}du_{\mathrm{m}} = Vc_m du_{\mathrm{m}}du_{\mathrm{m}} - \ dV_{\mathrm{m}}{}^{**}du_{\mathrm{m}} - n_{\mathrm{f}}Vc_m du_{\mathrm{m}}du_{\mathrm{m}} \tag{3.151}$$

Solving equation (3.149) to (3.151) for dV_{m} and dV_{f}, and replacing dV with equation (3.143) gives:

$$\frac{dV_{\mathrm{f}}}{V} = (c - c_{\mathrm{m}})d\bar{\sigma} + n_{\mathrm{f}}(c_s - c_{\mathrm{m}})du_{\mathrm{m}} - [c - (1 + n_{\mathrm{f}})c_{\mathrm{m}}]du_{\mathrm{f}} \tag{3.152}$$

$$\frac{dV_{\mathrm{m}}}{V} = (c_m - c_s)d\bar{\sigma} + [(1 - n_{\mathrm{f}})c_m - (1 + n_{\mathrm{m}} - n_{\mathrm{f}})]du_{\mathrm{m}} - n_{\mathrm{f}}(c_{\mathrm{m}} - c_s)du_{\mathrm{f}} \tag{3.153}$$

$$\frac{dV}{V} = cd\bar{\sigma} - (c_m - c_s)du_{\mathrm{m}} - (c - c_m)du_{\mathrm{f}} \tag{3.154}$$

To obtain consistent equations for flow and deformation, it is necessary to eliminate the term $d\bar{\sigma}$ in the above equations. This can be achieved by substituting equation (3.154) into equations (3.152) and (3.153) and noting that the volumetric strain $d\varepsilon_v = dV/V$, hence:

$$\frac{dV_{\mathrm{m}}}{V} = \tilde{\mathrm{b}}_1 d\varepsilon_v + (\tilde{\mathrm{b}}_1 - n_{\mathrm{m}})c_s du_{\mathrm{m}} - (\tilde{\mathrm{b}}_1 - n_{\mathrm{f}})(c_m - c_s)(du_{\mathrm{f}} - du_{\mathrm{m}}) \tag{3.155}$$

$$\frac{dV_{\mathrm{f}}}{V} = \tilde{\mathrm{b}}_2 d\varepsilon_v + (\tilde{\mathrm{b}}_2 - n_{\mathrm{f}})c_s du_{\mathrm{f}} - (\tilde{\mathrm{b}}_2 - n_{\mathrm{f}})(c_m - c_s)(du_{\mathrm{m}} - du_{\mathrm{f}}) \tag{3.156}$$

Recent studies show that the effect of deformation resulting from adsorption-induced swelling on fracture and pore volume is characterised by two ways: global strain and local strain (Liu *et al.* 2011b; Peng *et al.* 2014; Zhang *et al.* 2018; Wei *et al.* 2019). Before uniform global deformation occurs, the adsorption induced deformation is localized in the vicinity of fracture, i.e. local strain, The matrix expansion will narrow the fracture space. When the global deformation takes place, the matrix-fracture compartment interaction still exists because of pressure difference between coal matrix and fracture. Following our previous work of Chen *et al.* (2019), it is assumed that the effect of global swelling strain on porosity

evolution is analogous to that pore gas pressure. Considering the effect of surface stress change due to gas adsorption, the fluid pressure, u_m, should be modified as u_{m}^{a} ($= u_{\mathrm{m}} - u_a$). Replacing $u_m$with u_a equation (3.155) and (156) and incorporating the local swelling effect gives:

$$\frac{dV_{\mathrm{m}}}{V} = \tilde{\mathrm{b}}_1 d\varepsilon_v + (\tilde{\mathrm{b}}_1 - n_{\mathrm{m}})c_s du_{\mathrm{m}}^{a} - (\tilde{\mathrm{b}}_1 - n_{\mathrm{f}})(c_m - c_s)(du_{\mathrm{f}} - du_{\mathrm{m}}^{a}) + d\varepsilon_{sl} \quad (3.157)$$

$$\frac{dV_{\mathrm{f}}}{V} = \tilde{\mathrm{b}}_2 d\varepsilon_v + (\tilde{\mathrm{b}}_2 - n_{\mathrm{f}})c_s du_{\mathrm{f}} - (\tilde{\mathrm{b}}_2 - n_{\mathrm{f}})(c_m - c_s)(du_{\mathrm{m}}^{a} - du_{\mathrm{f}}) - d\varepsilon_{sl} \quad (3.158)$$

Where ε_{sl} is the local swelling strain. In this study, it is assumed that the local swelling is linearly proportional to global swelling:

$$\varepsilon_{sl} = \Lambda \varepsilon^{s} \quad (3.159)$$

where Λ is the ratio of local swelling to global swelling, which can be obtained by matching the experimental results of coal swelling and permeability.

Substitution of equations (3.156) and (3.157) into equation (3.140) yields:

$$dn_{\mathrm{m}} = (\tilde{\mathrm{b}}_1 - n_{\mathrm{m}})d\varepsilon_v + (\tilde{\mathrm{b}}_1 - n_{\mathrm{m}})c_s du_{\mathrm{m}}^{a} - (\tilde{\mathrm{b}}_2 - n_{\mathrm{f}})(c_m - c_s)(du_{\mathrm{f}} - du_{\mathrm{m}}^{a}) + d\varepsilon_{sl} \quad (3.160)$$

$$dn_{\mathrm{f}} = (\tilde{\mathrm{b}}_2 - n_{\mathrm{f}})d\varepsilon_v + (\tilde{\mathrm{b}}_2 - n_{\mathrm{f}})c_s du_{\mathrm{f}} - (\tilde{\mathrm{b}}_2 - n_{\mathrm{f}})(c_m - c_s)(du_{\mathrm{m}}^{a} - du_{\mathrm{f}}) - d\varepsilon_{sl} \quad (3.161)$$

According to equations (3.160) and (3.161), the pore and fracture volume change per unit of bulk volume in a fractured porous medium is due to four components on the right-hand side. The first term denotes the pore and fracture volume change due to a change in the overall bulk volume of materials. It depends on the overall bulk compressibility of the material, and its contribution is weighted by the effective stress coefficients (modified Biot's coefficients) in front of the volumetric strain. The second term shows the pore and fracture volume change caused by a change in the fluid pressure occupying the pores or fractures. It depends on the grain compressibility of the solid constituent. The last two terms represent the matrix-fracture interaction due to the pressure difference between the pore regions can also contribute to changes in the pore and fracture volume and adsorption-induced swelling effect. It is responsible for the internal deformation of the material. It worth noting that even in cases where the solid constituent is incompressible and the bulk volume is constrained, there is still a pore volume change due to the last two terms.

Equations (3.160) and (3.161) can reduce to the equation of a single porosity system if one of the fluid pressure fields does not exist, or if both fluid pressures reach equilibrium, which is consistent with the framework of poroelastic theory. Equations (3.160) and (3.161) provide a capacity to analyse the fracture-matrix interaction. Introducing the approximations $\frac{d(\ )}{dt} \approx \frac{\partial(\ )}{\partial t}$ yields the partial derivative of porosities with respect to time, as:

$$\frac{\partial n_{\mathrm{m}}}{\partial t} = (\tilde{\mathrm{b}}_1 - n_{\mathrm{m}})\frac{\partial \varepsilon_v}{\partial t} + (\tilde{\mathrm{b}}_1 - n_{\mathrm{m}})c_s\frac{\partial u_{\mathrm{m}}^a}{\partial t} - (\tilde{\mathrm{b}}_2 - n_{\mathrm{f}})(c_{\mathrm{m}} - c_s)\left(\frac{\partial u_{\mathrm{f}}}{\partial t} - \frac{\partial u_{\mathrm{m}}^a}{\partial t}\right) + \frac{\partial \varepsilon_{sl}}{\partial t} \tag{3.162}$$

$$\frac{\partial n_{\mathrm{f}}}{\partial t} = (\tilde{\mathrm{b}}_2 - n_{\mathrm{f}})\frac{\partial \varepsilon_v}{\partial t} + (\tilde{\mathrm{b}}_2 - n_{\mathrm{f}})c_s\frac{\partial u_{\mathrm{f}}}{\partial t} - (\tilde{\mathrm{b}}_2 - n_{\mathrm{f}})(c_{\mathrm{m}} - c_s)\left(\frac{\partial u_{\mathrm{m}}^a}{\partial t} - \frac{\partial u_{\mathrm{f}}}{\partial t}\right) - \frac{\partial \varepsilon_{sl}}{\partial t} \tag{3.163}$$

The permeability varies with porosity, which can be described by the widely used cubic relationship between permeability and porosity (e.g. Cui and Bustin 2005; Zhang *et al.* 2008), given as:

$$\frac{K_{\kappa}}{K_{\kappa 0}} = \left(\frac{n_{\kappa}}{n_{\kappa 0}}\right)^3 \tag{3.164}$$

where $K_{\kappa 0}$ is the initial permeability and $n_{\kappa 0}$ is the initial porosity of the matrix and fracture system, respectively.

3.8 Mechanical behaviour in discrete fractures

The fracture system properties depend largely on the reservoir stress field. Two distinct mechanisms are generally applied to describe the variation of fracture aperture, the first being the variation of normal effective stress acting on the surface of the fracture and resulting in relative displacements between the surfaces of the fracture, directly altering the fracture aperture as shown in Figure 3.10a. The second is the shear stress acting along the fracture, which is likely to make the fracture walls slide relative to each other and may cause a change in the fracture aperture through normal dilation, as shown in Figure 3.10b (Huang and Ghassemi 2015; Chen *et al*,2019b; Moradi *et al.* 2017). Fracture initiation as well as the propagation and mechanisms related to rock failure are not addressed in this work.

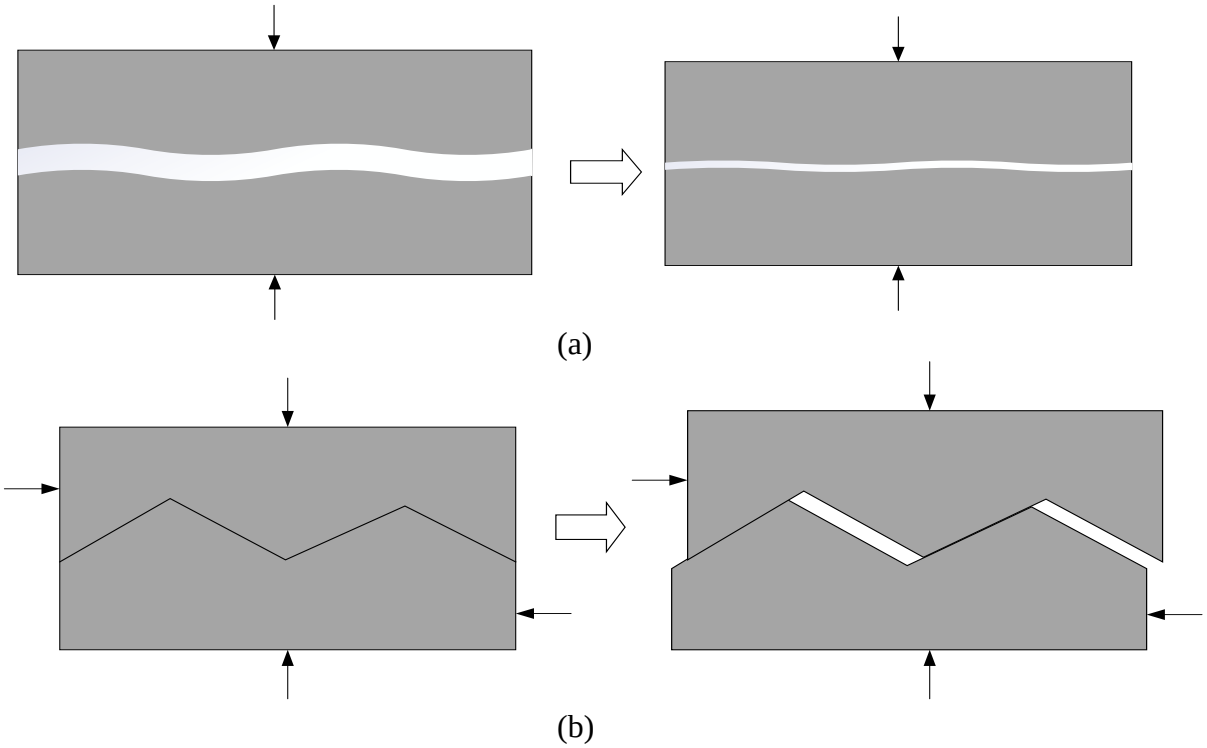

(a)

(b)

Figure 3.10 Fracture deformation, (a) normal displacement by effective normal stress, and (b) normal displacement by shear dilation (adapted from Huang and Ghassemi 2015).

The fracture opening or closure in the normal direction is controlled by the normal effective stress and normal fracture stiffness. A hyperbolic model developed by Bandis et al. (1983) and Barton *et al.* (1985) is widely used to describe the relation between normal effective stress and the response of fracture aperture in normal closure. Figure 3.11 shows the relationship between normal stress and fracture aperture, formulated as:

$$\Delta w_n = \frac{\sigma_n' w_{nmax}}{\sigma_n' + K_{n0} w_{nmax}} \tag{3.165}$$

where w_{nmax} is the maximum closure of the fracture aperture, K_{n0} is the initial normal fracture stiffness, and σ_n' is the effective normal stress acting on the fracture. Normal fracture stiffness is a measure of the fracture's sensitivity to normal stress and can be calculated as (Bandis *et al.* 1983):

$$K_n = \frac{d\sigma_n'}{dw_n} = K_{n0}\left[1 - \frac{\sigma_n'}{K_{n0} w_{nmax} + \sigma_n'}\right]^{-2} \tag{3.166}$$

The effective normal stress acting at the fracture surface is defined as (Liu *et al.* 2019b):

$$\sigma_n' = \sigma_n + \tilde{\mathfrak{b}} u_{\mathrm{F}} \tag{3.167}$$

where u_{F} is the fluid pressure in large scale fractures.

For a fracture, the bulk modulus is much less than the solid bulk modulus, the Biot coefficient $\tilde{\mathfrak{b}}$ is usually identified as unity (Tao *et al.* 2011), and the effective stress is given by:

$$\sigma_n' = \sigma_n + u_{\mathrm{F}} \tag{3.168}$$

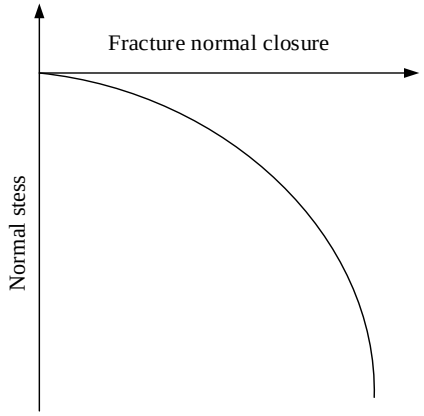

Figure 3.11 Fracture aperture evolution under normal stress.

The shear dilation-induced normal displacement of fractures has been observed in experiments (Barton *et al.* 1985), however, shear dilation does not always occur when shear stress is applied to the fracture. Before reaching the shear strength, τ_c, only tangential displacement caused by shear stress occurs and no normal displacement is observed. Shear dilation starts to trigger normal dilation when the shear stress reaches the shear strength, τ_c, as shown in Figure 3.12. The shear dilation, w_s, induced by an associated shear displacement, $u_{s,d}$, is given as (Gu *et al.* 2014):

$$w_s = u_{s,d}\tan\varphi \tag{3.169}$$

where φ is the dilation angle.

It can be seen from Figure 3.12 that the tangential displacement that generates shear dilation is a function of shear stress and shear stiffness of the fractures, as follows:

$$u_{s,a} = \frac{|\tau| - \tau_c}{K_t} \tag{3.170}$$

where K_t is the shear stiffness of fractures. Due to presence of fractures, the normal stiffness K_n and shear stiffness K_t are much lower than those of intact rock matrix, this is why the fractured reservoir is more stress sensitive than that without any fracture (Gu *et al.* 2014).

When the shear stress reaches the yield limit, the plastic deformation of fractured rock is generated, as shown in Figure 3.12, and a different constitutive relation should be used to correlate the normal displacement and stress field. To determine the peak shear stress $\sigma_{\mathrm{s-peak}}$, here the Mohr-Coulomb criterion is adopted widely in literatures (Gu *et al.* 2014; Gan and Elsworth 2016; Moradi *et al.* 2017), formulated as:

$$\sigma_{\mathrm{s-peak}} = \sigma_{\mathrm{n}} \tan \Phi_a \tag{3.171}$$

where Φ_a is the internal friction angle, the cohesion strength is ignored because it is usually zero in rock.

The normal displacement w_{s-ap} caused by the additional shear displacement after the point of the peak shear stress is given as(Gu *et al.* 2014; Moradi *et al.* 2017):

$$w_{s-ap} = \frac{\sigma_{\mathrm{n}} - \sigma_{\mathrm{s-peak}}}{K_n(\sigma_{\mathrm{n}}) \tan \varphi} \tag{3.172}$$

The following relations can be summarized for the fracture aperture under compression:

$$w = \begin{cases} w_0 - \dfrac{\sigma_n' w_{nmax}}{\sigma_n' + K_{n0} w_{nmax}} & \tau \le \tau_c \\ w_0 - \dfrac{\sigma_n' w_{nmax}}{\sigma_n' + K_{n0} w_{nmax}} + \dfrac{\tau - \tau_c}{K_t} \tan \varphi & \tau_c \le \tau < \sigma_{\mathrm{s-peak}} \\ w_0 - \dfrac{\sigma_n' w_{nmax}}{\sigma_n' + K_{n0} w_{nmax}} + \dfrac{\tau - \tau_c}{K_t} \tan \varphi + \dfrac{\sigma_{\mathrm{n}} - \sigma_{\mathrm{s-peak}}}{K_n(\sigma_{\mathrm{n}}) \tan \varphi} & \tau = \sigma_{\mathrm{s-peak}} \end{cases} \tag{3.173}$$

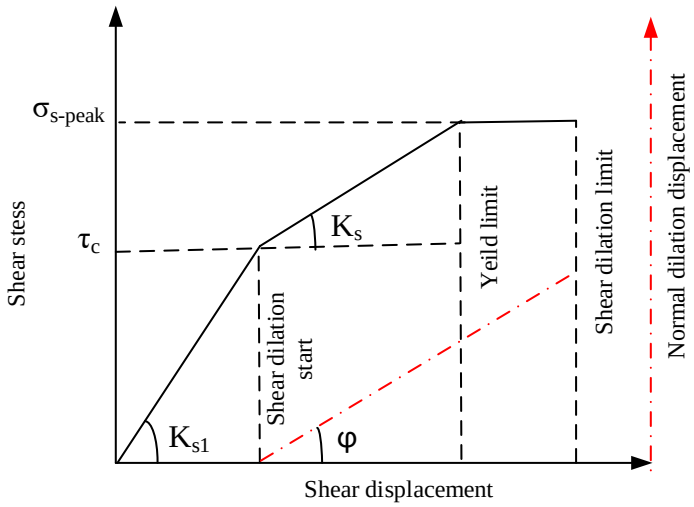

Figure 3.12 Normal dilation displacement of a facture under shear stress.

The fracture is usually represented using a local coordinate system, as illustrated in Figure 3.13. In order to update the fracture aperture, the stress field calculated in the global coordinate system should be converted into the local coordinate system along the fracture, as:

$$\sigma_n = \sigma_{xx}\sin^2\varphi_o - 2\sigma_{xy}\sin\varphi_o\cos\varphi_o + \sigma_{yy2}\cos^2\varphi_o \tag{3.174}$$

$$\tau_n = -(\sigma_{xx} - \sigma_{yy})\sin\varphi_o\cos\varphi_o + \sigma_{xy}\cos 2\varphi_o \tag{3.175}$$

where φ_o is the orientation of the fracture.

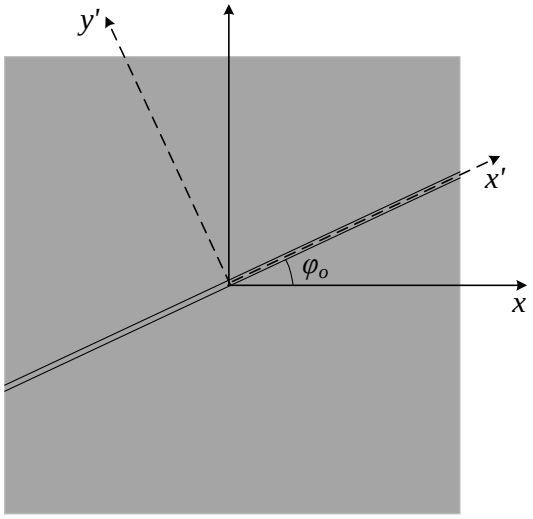

Figure 3.13 Transformation between the x'-y' local coordinate system (dash line) and x-y global coordinate system (solid line).

3.9 Conclusions

In this chapter, the flow and mechanical behaviour of fractured rock has been represented using a hybrid coupled dual continuum and discrete fracture approach. The small-scale natural fracture network and porous rock matrix have been treated as distinct, overlapping continua and are handled with dual continuum model and large-scale fractures have been modelled using a lower-dimensional medium and represented as discrete fractures, different domains are interacted via mass and heat exchange processes.

The governing equations have been derived based upon the law of mass conservation for multicomponent gas flow and water transfer, transport properties including saturation, relative permeability and real gas effect involved in multiphase flow have been considered.

The thermal transfer model has been developed based on the local thermal non-equilibrium with the Joule-Thomson cooling effect being considered. The equilibrium sorption model is adopted, and the extended Langmuir isotherm has been modified to describe the adsorbed amount of multicomponent gas by introduction of temperature dependent Langmuir constants.

Based on dual porosity thermoporoelastic theory, the deformation behaviour of fractured porous media has been represented in which adsorption-desorption induced swelling-shrinkage behaviour is considered by the introduction of surface stress. Mechanical behaviour in discrete fractures have been discussed in this chapter, the variation of fracture aperture due to normal effective stress acting on the surface of the fracture and shear stress acting along the fracture is described. A new porosity-permeability model has been derived that considers the mechanical, thermal response, and gas-solid interaction. In particular, the matrix-fracture compartment interaction is included in this porosity-permeability model, which provides a tool to investigate the structural change of coal.

3.10 References

Bandis, S., Lumsden, A. and Barton, N. eds. (1983). *Fundamentals of rock joint deformation*. International Journal of Rock Mechanics and Mining Sciences & Geomechanics **20**: 249-268.

Barenblatt, G., Zheltov, I. P. and Kochina, I. (1960). Basic concepts in the theory of seepage of homogeneous liquids in fissured rocks [strata]. *Journal of applied mathematics and mechanics* **24**(5):1286-1303.

Barton, N., Bandis, S. and Bakhtar, K. eds. (1985). *Strength, deformation and conductivity coupling of rock joints*. International journal of rock mechanics and mining sciences & geomechanics abstracts. Elsevier.

Bear, J. (2012). *Hydraulics of groundwater*. Courier Corporation.

Bertrand, F., Cerfontaine, B. and Collin, F. (2017). A fully coupled hydro-mechanical model for the modeling of coalbed methane recovery. *Journal of Natural Gas Science and Engineering* **46**:307-325.

Bird, R. B., Stewart, W. E. and Lightfoot, E. N. (2007). *Transport phenomena*. John Wiley & Sons.

Bogdanov, I., Mourzenko, V., Thovert, J.-F. and Adler, P. (2003). Two-phase flow through fractured porous media. *Physical Review E* **68**(2):026703.

Chaback, J., Morgan, W. and Yee, D. (1996). Sorption of nitrogen, methane, carbon dioxide and their mixtures on bituminous coals at in-situ conditions. *Fluid Phase Equilibria* **117**(1-2):289-296.

Chen, M., Hosking, L. J., Sandford, R. J. and Thomas, H. R. (2019). Dual porosity modelling of the coupled mechanical response of coal to gas flow and adsorption. *International Journal of Coal Geology* **205**:115-125.

Chen, M., Hosking, L.J., Sandford, R.J. and Thomas, H.R. (2019a). Numerical analysis of improvements to CO_2 injectivity in coal seams through stimulated fracture connection to the injection well. *Rock mechanics and rock engineering* (under review).

Chen, M., Hosking, L.J., Sandford, R.J. and Thomas, H.R. (2019b). A coupled compressible flow and geomechanics model for dynamic fracture aperture during carbon sequestration in coal. *International Journal for Numerical and Analytical Methods in Geomechanics* (under review).

Chen, M., Hosking, L. J. and Thomas, H. R. eds. (2018). Non-isothermal Gas Flow During Carbon Sequestration in Coalbeds. *The International Congress on Environmental Geotechnics.* Springer.

Clarkson, C. and Bustin, R. (2000). Binary gas adsorption/desorption isotherms: effect of moisture and coal composition upon carbon dioxide selectivity over methane. *International Journal of Coal Geology* **42**(4):241-271.

Cui, X. and Bustin, R. M. (2005). Volumetric strain associated with methane desorption and its impact on coalbed gas production from deep coal seams. *Aapg Bulletin* **89**(9):1181-1202.

Dake, L. P. (1983). *Fundamentals of reservoir engineering*. Elsevier.

Do, D. and Wang, K. (1998). A new model for the description of adsorption kinetics in heterogeneous activated carbon. *Carbon* **36**(10):1539-1554.

Gan, Q. and Elsworth, D. (2016). A continuum model for coupled stress and fluid flow in discrete fracture networks. *Geomechanics and Geophysics for Geo-Energy and Geo-Resources* **2**(1):43-61.

Gelet, R. (2011). *Thermo-hydro-mechanical study of deformable porous media with double porosity in local thermal non-equilibrium.* Université de Grenoble.

Gerke, H. and Genuchten, M. v. (1993). Evaluation of a first-order water transfer term for variably saturated dual-porosity flow models. *Water Resources Research* **29**(4):1225-1238.

Gor, G. Y., Huber, P. and Bernstein, N. (2017). Adsorption-induced deformation of nanoporous materials—A review. *Applied Physics Reviews* **4**(1):011303.

Gu, S., Liu, Y. and Chen, Z. (2014). Numerical study of dynamic fracture aperture during production of pressure-sensitive reservoirs. *International Journal of Rock Mechanics and Mining Sciences* **70**:229-239.

Guan, C., Liu, S., Li, C., Wang, Y. and Zhao, Y. (2018). The temperature effect on the methane and CO_2 adsorption capacities of Illinois coal. *Fuel* **211**:241-250.

Gupta, S., Helmig, R. and Wohlmuth, B. (2015). Non-isothermal, multi-phase, multi-component flows through deformable methane hydrate reservoirs. *Computational Geosciences* **19**(5):1063-1088.

Han, W. S., Stillman, G. A., Lu, M., Lu, C., McPherson, B. J. and Park, E. (2010). Evaluation of potential nonisothermal processes and heat transport during CO_2 sequestration. *Journal of Geophysical Research: Solid Earth* **115**(B7).

Hao, Y., Fu, P. and Carrigan, C. R. eds. (2013). *Application of a dual-continuum model for simulation of fluid flow and heat transfer in fractured geothermal reservoirs*. Proceedings, 38th Workshop On Geothermal Reservoir Engineering, vol SGP-TR-198. Stanford University, Stanford, California.

Heinze, T. and Hamidi, S. (2017). Heat transfer and parameterization in local thermal non-equilibrium for dual porosity continua. *Applied Thermal Engineering* **114**:645-652.

Hosking, L. (2014). *Reactive transport modelling of high pressure gas flow in coal.* Ph. D. thesis, Cardiff University, Wales, UK.

Hosking, L. J., Thomas, H. R. and Sedighi, M. (2017). A dual porosity model of high-pressure gas flow for geoenergy applications. *Canadian Geotechnical Journal* **55**(6):839-851.

Hosking, L.J., Chen, M., Sandford, R.J. and Thomas, H.R. (2019). Analysis of coupled dual porosity thermo-hydro-chemo-mechanical behaviour during CO_2 injection in coal. *Geomechanics for Energy and the Environment* (under review).

Huang, J. and Ghassemi, A. (2015). A poroelastic model for evolution of fractured reservoirs during gas production. *Journal of Petroleum Science and Engineering* **135**:626-644.

Jaeger, J. C., Cook, N. G. and Zimmerman, R. (2009). *Fundamentals of rock mechanics*. John Wiley & Sons.

Kaye, G. and Laby, T. (1973). Tables of Chemical Constants. Longman, Harlow.

Krooss, B. v., Van Bergen, F., Gensterblum, Y., Siemons, N., Pagnier, H. and David, P. (2002). High-pressure methane and carbon dioxide adsorption on dry and moisture-equilibrated Pennsylvanian coals. *International Journal of Coal Geology* **51**(2):69-92.

Kwak, T. and Mansoori, G. (1986). Van der Waals mixing rules for cubic equations of state. Applications for supercritical fluid extraction modelling. *Chemical engineering science* **41**(5):1303-1309.

Lewis, R. and Pao, W. (2002). Numerical simulation of three-phase flow in deforming fractured reservoirs. *Oil & Gas Science and Technology* **57**(5):499-514.

Lewis, R. and Schrefler, B. (1998). The finite element method in the static and dynamic deformation and consolidation of porous media. John Wiley & Sons, Chichester, UK.

Liu, J., Wang, J., Chen, Z., Wang, S., Elsworth, D. and Jiang, Y. (2011). Impact of transition from local swelling to macro swelling on the evolution of coal permeability. *International Journal of Coal Geology* **88**(1):31-40.

Liu, J., Wang, J., Gao, F., Leung, C. F. and Ma, Z. (2019). A fully coupled fracture equivalent continuum-dual porosity model for hydro-mechanical process in fractured shale gas reservoirs. *Computers and Geotechnics* **106**:143-160.

Masum, S. A. (2012). *Modelling of reactive gas transport in unsaturated soil. A coupled thermo-hydro-chemical-mechanical approach.* Ph. D. thesis, Cardiff University, Wales, UK.

Mathias, S. A., McElwaine, J. N. and Gluyas, J. G. (2014). Heat transport and pressure buildup during carbon dioxide injection into depleted gas reservoirs. *Journal of Fluid Mechanics* **756**:89-109.

Merkel, A., Gensterblum, Y., Krooss, B. M. and Amann, A. (2015). Competitive sorption of CH_4, CO_2 and H_2O on natural coals of different rank. *International Journal of Coal Geology* **150**:181-192.

Moradi, M., Shamloo, A. and Dezfuli, A. D. (2017). A sequential implicit discrete fracture model for three-dimensional coupled flow-geomechanics problems in naturally fractured porous media. *Journal of Petroleum Science and Engineering* **150**:312-322.

Nikoosokhan, S., Brochard, L., Vandamme, M., Dangla, P., Pellenq, R. J. M., Lecampion, B. and Fen-Chong, T. (2013). CO_2 Storage in Coal Seams: Coupling Surface Adsorption and Strain.115-132.

Nikoosokhan, S., Brochard, L., Vandamme, M., Dangla, P., Pellenq, R. J. M., Lecampion, B. and Fen-Chong, T. (2012). CO_2 Storage in Coal Seams: Coupling Surface Adsorption and Strain. *Geomechanics in CO_2 Storage Facilities*:115-132.

Nur, A. and Byerlee, J. D. (1971). An exact effective stress law for elastic deformation of rock with fluids. *Journal of Geophysical Research* **76**(26):6414-6419.

Pant, L. M., Huang, H., Secanell, M., Larter, S. and Mitra, S. K. (2015). Multi scale characterization of coal structure for mass transport. *Fuel* **159**:315-323.

Pao, W. K. and Lewis, R. W. (2002). Three-dimensional finite element simulation of three-phase flow in a deforming fissured reservoir. *Computer methods in applied mechanics and engineering* **191**(23-24):2631-2659.

Peng, D.-Y. and Robinson, D. B. (1976). A new two-constant equation of state. *Industrial & Engineering Chemistry Fundamentals* **15**(1):59-64.

Peng, Y., Liu, J., Wei, M., Pan, Z. and Connell, L. D. (2014). Why coal permeability changes under free swellings: New insights. *International Journal of Coal Geology* **133**:35-46.

Poling, B. E., Prausnitz, J. M. and O'connell, J. P. (2001). *The properties of gases and liquids*. Mcgraw-hill New York.

Pouya, A. (2015). A finite element method for modeling coupled flow and deformation in porous fractured media. *International Journal for Numerical and Analytical Methods in Geomechanics* **39**(16):1836-1852.

Rutqvist, J., Börgesson, L., Chijimatsu, M., Kobayashi, A., Jing, L., Nguyen, T., Tsang, C.-F. (2001). Thermohydromechanics of partially saturated geological media: governing equations and formulation of four finite element models. *International journal of rock mechanics and mining sciences* **38**(1):105-127.

Sakurovs, R., Day, S., Weir, S. and Duffy, G. (2008). Temperature dependence of sorption of gases by coals and charcoals. *International Journal of Coal Geology* **73**(3-4):250-258.

Sass, J., Lachenbruch, A. H. and Munroe, R. J. (1971). Thermal conductivity of rocks from measurements on fragments and its application to heat-flow determinations. *Journal of geophysical research* **76**(14):3391-3401.

Tang, X. and Ripepi, N. (2016). Temperature-dependent Langmuir model in the coal and methane sorption process: Statistical relationship. *Trans. Soc. Min. Metall. Explor.* **340**:61-69.

Tao, Q., Ghassemi, A. and Ehlig-Economides, C. A. (2011). A fully coupled method to model fracture permeability change in naturally fractured reservoirs. *International Journal of Rock Mechanics and Mining Sciences* **48**(2):259-268.

Van Genuchten, M. T. (1980). A closed-form equation for predicting the hydraulic conductivity of unsaturated soils 1. *Soil science society of America journal* **44**(5):892-898.

Vandamme, M., Brochard, L., Lecampion, B. and Coussy, O. (2010). Adsorption and strain: The CO_2-induced swelling of coal. *Journal of the Mechanics and Physics of Solids* **58**(10):1489-1505.

Warren, J. and Root, P. J. (1963). The behavior of naturally fractured reservoirs. *Society of Petroleum Engineers Journal* **3**(03):245-255.

Wei, M., Liu, J., Elsworth, D., Li, S. and Zhou, F. (2019). Influence of gas adsorption induced non-uniform deformation on the evolution of coal permeability. *International Journal of Rock Mechanics and Mining Sciences* **114**:71-78.

Wei, Y. S. and Sadus, R. J. (2000). Equations of state for the calculation of fluid-phase equilibria. *AIChE Journal* **46**(1):169-196.

Wu, Y.-S., Li, J., Ding, D., Wang, C. and Di, Y. (2014). A generalized framework model for the simulation of gas production in unconventional gas reservoirs. *SPE Journal* **19**(05):845-857.

Wu, Y., Liu, J., Elsworth, D., Chen, Z., Connell, L. and Pan, Z. (2010). Dual poroelastic response of a coal seam to CO_2 injection. *International Journal of Greenhouse Gas Control* **4**(4):668-678.

Ye, Z., Chen, D., Pan, Z., Zhang, G., Xia, Y. and Ding, X. (2016). An improved Langmuir model for evaluating methane adsorption capacity in shale under various pressures and temperatures. *Journal of Natural Gas Science and Engineering* **31**:658-680.

Zhang, H., Liu, J. and Elsworth, D. (2008). How sorption-induced matrix deformation affects gas flow in coal seams: a new FE model. *International Journal of Rock Mechanics and Mining Sciences* **45**(8):1226-1236.

Zhang, S., Liu, J., Wei, M. and Elsworth, D. (2018). Coal permeability maps under the influence of multiple coupled processes. *International Journal of Coal Geology*.

Zhang, Y. (2018). Mechanics of adsorption–deformation coupling in porous media. *Journal of the Mechanics and Physics of Solids* **114**:31-54.

Ziabakhsh-Ganji, Z. and Kooi, H. (2014). Sensitivity of Joule–Thomson cooling to impure CO_2 injection in depleted gas reservoirs. *Applied Energy* **113**:434-451.

4

Numerical Formulation

4.1 Introduction

In this chapter, a numerical algorithm has been developed to achieve a solution to the highly coupled governing equations for coupled thermal-hydraulic-gas-mechanical behaviour presented in the previous chapter. A finite element method (FEM) is employed to spatially discretise the equations whilst a finite difference method (FDM) is used to achieve temporal discretisation. A sequential non-iterative approach (SNIA) has also been implemented in order to couple the flow processes with the sink/source terms for the mass exchange process, details of which are also provided in this chapter.

Section 4.2 deals with the spatial discretisation of the governing equations for flow and deformation via the Galerkin weighted residual method. Section 4.3 describes the general representation of the matrix form of the governing equations along with the details of the temporal discretisation. A backward finite difference mid-interval time-stepping algorithm is used to achieve temporal discretisation in this work. The description of the SNIA used to handle coupling of the transport and sink/source terms is presented in section 4.4. Finally, the conclusions of this chapter are provided in section 4.5.

4.2 Spatial discretisation

In the present study, the Galerkin weighted residual method is employed to spatially discretise the governing equations. This method is a widely accepted tool for spatial discretisation in numerical techniques and details on this method can be found in the literature (e.g.Zienkiewicz *et al.* 2005). The approximate solution to sets of nonlinear partial different equations can be obtained via this method along with appropriate boundary and

initial conditions. Previous studies by Thomas and co-workers have found the Galerkin weighted residual method to be an effective method for the type of highly coupled governing equations presented in the previous chapter (e.g. Thomas and He 1995; Thomas *et al.* 1998; Vardon 2009; Masum 2012; Hosking 2014; Zagorščak 2017).

Spatial discretisation of the governing equations using the Galerkin finite element method is presented in an abbreviated form. The spatial discretisation for the formulation for multicomponent gas transport is presented, followed by the spatial discretisation of water flow and heat transfer following the procedures presented for gas transport. The spatial discretisation of the deformation variables is finally presented.

Based on the Galerkin weighted residual method, the primary variables (unknowns) and their spatial derivatives are approximated using shape functions. For an element with n_{node} nodes, this gives:

$$\omega_\alpha \approx \widehat{\omega}_\alpha = \sum_{s=1}^{n_{node}} N_{s\alpha}\omega_{s\alpha} \tag{4.1}$$

$$\nabla\widehat{\omega}_\alpha = \sum_{s=1}^{n_{node}} (\nabla N_{s\alpha})\omega_{s\alpha} \tag{4.2}$$

where ω_α represents any of the primary variables in medium α out of c_α^i, $u_{l\alpha}$, T_α and $\mathbf{u}_s$, $N_{s\alpha}$ is the shape function, the subscript s is the node indicator for the element, and the symbol $\widehat{\ }$ denotes the approximate value of the primary variable. It is noteworthy that the shape function used in the fracture and matrix continua is different from that in the large fracture domain in subsequent section. For the sake of simplification, N_s is used to denote the shape function for the fracture and matrix continua and N_{sF} is used for the large fracture domain.

4.2.1 Spatial discretisation of governing equations for multicomponent gas transport

In the previous chapter, the governing equations for multicomponent gas transport in the three coupled media were presented in a general form for n_g components. As the process for spatial discretisation remains the same for each component of a multi-gas system in each domain, it is unnecessary to present the derivation process for all components. Hence, this section only considers the i^{th} component. The governing equations for the i^{th} component

transport in matrix continuum, fracture continuum and discrete fractures can be expressed as:

$$-\sum_{j=1}^{n_g} C_{\mathrm{c_m c_m}} \frac{\partial \hat{c}_{\mathrm{m}}^{j}}{\partial t} - \sum_{j=1}^{n_g} C_{\mathrm{c_m c_f}} \frac{\partial \hat{c}_{\mathrm{f}}^{j}}{\partial t} - C_{\mathrm{c_m l_m}} \frac{\partial \hat{u}_{\mathrm{lm}}}{\partial t} - C_{\mathrm{c_m l_f}} \frac{\partial \hat{u}_{\mathrm{lf}}}{\partial t} - C_{\mathrm{c_m T_m}} \frac{\partial \hat{T}_{\mathrm{m}}}{\partial t} - C_{\mathrm{c_m T_f}} \frac{\partial \hat{T}_{\mathrm{f}}}{\partial t} - C_{\mathrm{c_m \mathbf{u}_s}} \frac{\partial \hat{\mathbf{u}}_{\mathrm{s}}}{\partial t} + Q_{\mathrm{c_m}}^{i} = R_{\Omega,\mathrm{m}} \tag{4.3}$$

$$-\sum_{j=1}^{n_g} C_{\mathrm{c_f c_m}} \frac{\partial \hat{c}_{\mathrm{m}}^{j}}{\partial t} - \sum_{j=1}^{n_g} C_{\mathrm{c_f c_f}} \frac{\partial \hat{c}_{\mathrm{f}}^{j}}{\partial t} - C_{\mathrm{c_f l_m}} \frac{\partial \hat{u}_{\mathrm{lm}}}{\partial t} - C_{\mathrm{c_f l_f}} \frac{\partial \hat{u}_{\mathrm{lf}}}{\partial t} - C_{\mathrm{c_f T_m}} \frac{\partial \hat{T}_{\mathrm{m}}}{\partial t} - C_{\mathrm{c_f T_f}} \frac{\partial \hat{T}_{\mathrm{f}}}{\partial t} - C_{\mathrm{c_f \mathbf{u}_s}} \frac{\partial \mathbf{u}_{\mathrm{s}}}{\partial t} + \nabla \cdot \left(\sum_{j=1}^{n_g} K_{\mathrm{c_f c_f}} \nabla c_{\mathrm{f}}^{j} \right) + \nabla \cdot \left(K_{\mathrm{c_f T_f}} \nabla T_{\mathrm{f}} \right) + Q_{\mathrm{c_f}}^{i} = R_{\Omega,\mathrm{f}} \tag{4.4}$$

$$-\sum_{j=1}^{n_g} C_{\mathrm{c_F c_F}} \frac{\partial \hat{c}_{\mathrm{F}}^{j}}{\partial t} - C_{\mathrm{c_F l_F}} \frac{\partial \hat{u}_{\mathrm{lF}}}{\partial t} - C_{\mathrm{c_F T_F}} \frac{\partial \hat{T}_{\mathrm{F}}}{\partial t} + \nabla_l \cdot \left(\sum_{j=1}^{n_g} K_{\mathrm{c_F c_F}} \nabla \hat{c}_{\mathrm{F}}^{j} \right) + \nabla_l \cdot \left(K_{\mathrm{c_F T_F}} \nabla \hat{T}_F \right) + Q_{\mathrm{c_F}}^{i} = R_{\Omega,\mathrm{F}} \tag{4.5}$$

where the residual error, $R_{\Omega,\mathrm{m}}$, $R_{\Omega,\mathrm{f}}$ and $R_{\Omega,\mathrm{F}}$ are introduced as a result of the substitution of the approximate values of the primary variables in place of the actual values.

The last terms on the left-hand side of equations (4.3) - (4.5) denote the sink/source term for mass exchange between media. Due to usage of the SNIA, the exchange process in equation (4.3) - (4.5) is handled only after the convergence in the solution of the transport equations has been achieved. Section 4.4 presents a description of the numerical treatment of mass exchange with the SNIA. The governing equations for the i^{th} component transport without mass exchange term is expressed as:

$$-\sum_{j=1}^{n_g} C_{\mathrm{c_m c_m}} \frac{\partial \hat{c}_{\mathrm{m}}^{j}}{\partial t} - \sum_{j=1}^{n_g} C_{\mathrm{c_m c_f}} \frac{\partial \hat{c}_{\mathrm{f}}^{j}}{\partial t} - C_{\mathrm{c_m l_m}} \frac{\partial \hat{u}_{\mathrm{lm}}}{\partial t} - C_{\mathrm{c_m l_f}} \frac{\partial \hat{u}_{\mathrm{lf}}}{\partial t} - C_{\mathrm{c_m T_m}} \frac{\partial \hat{T}_{\mathrm{m}}}{\partial t} - C_{\mathrm{c_m T_f}} \frac{\partial \hat{T}_{\mathrm{f}}}{\partial t} - C_{\mathrm{c_m \mathbf{u}_s}} \frac{\partial \hat{\mathbf{u}}_{\mathrm{s}}}{\partial t} = R_{\Omega,\mathrm{m}} \tag{4.6}$$

$$-\sum_{j=1}^{n_g} C_{\mathrm{c_f c_m}} \frac{\partial \hat{c}_{\mathrm{m}}^{j}}{\partial t} - \sum_{j=1}^{n_g} C_{\mathrm{c_f c_f}} \frac{\partial \hat{c}_{\mathrm{f}}^{j}}{\partial t} - C_{\mathrm{c_f l_m}} \frac{\partial \hat{u}_{\mathrm{lm}}}{\partial t} - C_{\mathrm{c_f l_f}} \frac{\partial \hat{u}_{\mathrm{lf}}}{\partial t} - C_{\mathrm{c_f T_m}} \frac{\partial \hat{T}_{\mathrm{m}}}{\partial t} - C_{\mathrm{c_f T_f}} \frac{\partial \hat{T}_{\mathrm{f}}}{\partial t}$$

$$-C_{\mathrm{c_f u_s}} \frac{\partial \mathbf{u}_{\mathrm{s}}}{\partial t} + \nabla \cdot \left(\sum_{j=1}^{n_g} K_{\mathrm{c_f c_f}} \nabla \hat{c}_{\mathrm{f}}^{j} \right) + \nabla \cdot \left(K_{\mathrm{c_f T_f}} \nabla \hat{T}_{\mathrm{f}} \right) = R_{\Omega,\mathrm{f}} \quad (4.7)$$

$$-\sum_{j=1}^{n_g} C_{\mathrm{c_F c_F}} \frac{\partial \hat{c}_{\mathrm{F}}^{j}}{\partial t} - C_{\mathrm{c_F l_F}} \frac{\partial \hat{u}_{\mathrm{lF}}}{\partial t} - C_{\mathrm{c_F T_F}} \frac{\partial \hat{T}_{\mathrm{F}}}{\partial t}$$

$$+\nabla_l \cdot \left(\sum_{j=1}^{n_g} K_{\mathrm{c_F c_F}} \nabla \hat{c}_{\mathrm{F}}^{j} \right) + \nabla_l \cdot \left(K_{\mathrm{c_F T_F}} \nabla_l \hat{T}_F \right) = R_{\Omega,\mathrm{F}} \quad (4.8)$$

As the approximated form is not the exact solution of equation (4.1), it contains a residual error which can be given as:

$$R_{\Omega,\alpha} = \omega_\alpha - \widehat{\omega}_\alpha \quad (4.9)$$

In the Galerkin weighted residual approach, this residual over the entire element domain Ω^e is attempted to be minimised using the shape functions N_r as weighting coefficients, as:

$$\int_{\Omega^e} N_r R_{\Omega,\alpha} d\Omega = 0 \quad (4.10)$$

where Ω is the element area or volume. Substituting equation (4.10) into equations (4.6)-(4.8) produces:

$$\int_{\Omega} N_r \left[\begin{array}{l} -\sum_{j=1}^{n_g} C_{\mathrm{c_m c_m}} \frac{\partial \hat{c}_{\mathrm{m}}^{j}}{\partial t} - \sum_{j=1}^{n_g} C_{\mathrm{c_m c_f}} \frac{\partial \hat{c}_{\mathrm{f}}^{j}}{\partial t} - C_{\mathrm{c_m l_m}} \frac{\partial \hat{u}_{\mathrm{lm}}}{\partial t} - \\ C_{\mathrm{c_m l_f}} \frac{\partial \hat{u}_{\mathrm{lf}}}{\partial t} - C_{\mathrm{c_m T_m}} \frac{\partial \hat{T}_{\mathrm{m}}}{\partial t} - C_{\mathrm{c_m T_f}} \frac{\partial \hat{T}_{\mathrm{f}}}{\partial t} - C_{\mathrm{c_m u_s}} \frac{\partial \hat{\mathbf{u}}_{\mathrm{s}}}{\partial t} \end{array} \right] d\Omega = 0 \quad (4.11)$$

$$\int_{\Omega} N_r \left[\begin{array}{c} -\sum_{j=1}^{n_g} C_{\mathrm{c_f c_m}} \frac{\partial \hat{c}_{\mathrm{m}}^{j}}{\partial t} - \sum_{j=1}^{n_g} C_{\mathrm{c_f c_f}} \frac{\partial \hat{c}_{\mathrm{f}}^{j}}{\partial t} - C_{\mathrm{c_f l_m}} \frac{\partial \hat{u}_{\mathrm{lm}}}{\partial t} - C_{\mathrm{c_f l_f}} \frac{\partial \hat{u}_{\mathrm{lf}}}{\partial t} - C_{\mathrm{c_f T_m}} \frac{\partial \hat{T}_{\mathrm{m}}}{\partial t} \\ -C_{\mathrm{c_f T_f}} \frac{\partial \hat{T}_{\mathrm{f}}}{\partial t} - C_{\mathrm{c_f u_s}} \frac{\partial \hat{\mathbf{u}}_{\mathrm{s}}}{\partial t} + \nabla \cdot \left(\sum_{j=1}^{n_g} K_{\mathrm{c_f c_f}} \nabla \hat{c}_{\mathrm{f}}^{j} \right) + \nabla \cdot \left(K_{\mathrm{c_f T_f}} \nabla \hat{T}_{\mathrm{f}} \right) \end{array} \right] d\Omega$$

$$= 0 \quad (4.12)$$

$$\int_{\Omega} N_r \begin{bmatrix} -\sum_{j=1}^{n_g} C_{\mathrm{c_F c_F}} \frac{\partial \hat{c}_{\mathrm{F}}^{j}}{\partial t} - C_{\mathrm{c_F l_F}} \frac{\partial \hat{u}_{\mathrm{lF}}}{\partial t} - C_{\mathrm{c_F T_F}} \frac{\partial \hat{T}_{\mathrm{F}}}{\partial t} \\ +\nabla_l \cdot \left(\sum_{j=1}^{n_g} K_{\mathrm{c_F c_F}} \nabla \hat{c}_{\mathrm{F}}^{j} \right) + \nabla_l \cdot \left(K_{\mathrm{c_F T_F}} \nabla \hat{T}_F \right) \end{bmatrix} d\Omega = 0 \qquad (4.13)$$

Using the theory of integration by parts, the weak form of equations (4.11) - (4.13) can be obtained. The eighth and ninth term of equation (4.12) can be expressed as:

$$\int_{\Omega} N_r \nabla \cdot \left(\sum_{j=1}^{n_g} K_{\mathrm{c_f c_f}} \nabla \hat{c}_{\mathrm{f}}^{j} \right) d\Omega = \int_{\Omega} \nabla \cdot \left(N_r \sum_{j=1}^{n_g} K_{\mathrm{c_f c_f}} \nabla \hat{c}_{\mathrm{f}}^{j} \right) d\Omega - \int_{\Omega} \left(\sum_{j=1}^{n_g} K_{\mathrm{c_f c_f}} \nabla \hat{c}_{\mathrm{f}}^{j} \right) \nabla N_r d\Omega \qquad (4.14)$$

$$\int_{\Omega} N_r \nabla \cdot \left(K_{\mathrm{c_f T_f}} \nabla \hat{T}_{\mathrm{f}} \right) d\Omega = \int_{\Omega} \nabla \cdot \left(N_r K_{\mathrm{c_f T_f}} \nabla \hat{T}_{\mathrm{f}} \right) d\Omega - \int_{\Omega} K_{\mathrm{c_f T_f}} \nabla \hat{T}_{\mathrm{f}} \nabla N_r d\Omega \qquad (4.15)$$

The fourth and fidth term of equation (4.13) can be expressed as:

$$\int_{\Omega} N_r \nabla_l \cdot \left(\sum_{j=1}^{n_g} K_{\mathrm{c_F c_F}} \nabla_l \hat{c}_{\mathrm{F}}^{j} \right) d\Omega = \int_{\Omega} \nabla_l \cdot \left(N_r \sum_{j=1}^{n_g} K_{\mathrm{c_F c_F}} \nabla_l \hat{c}_{\mathrm{F}}^{j} \right) d\Omega - \int_{\Omega} \left(\sum_{j=1}^{n_g} K_{\mathrm{c_F c_F}} \nabla_l \hat{c}_{\mathrm{F}}^{j} \right) \nabla_l N_r d\Omega \qquad (4.16)$$

$$\int_{\Omega} N_r \nabla_l \cdot \left(K_{\mathrm{c_F T_F}} \nabla_l \hat{T}_F \right) d\Omega = \int_{\Omega} \nabla_l \cdot \left(N_r K_{\mathrm{c_F T_F}} \nabla \hat{T}_F \right) d\Omega - \int_{\Omega} K_{\mathrm{c_F T_F}} \nabla_l \hat{T}_F \nabla_l N_r d\Omega \qquad (4.17)$$

Inserting equations (4.14) and (4.15) into equation (4.12) and equations (4.16) and (4.17) into equation (4.13) gives:

$$\int_{\Omega}\left[\begin{array}{c} N_r\left[\begin{array}{c} -\sum_{j=1}^{n_g} C_{\mathrm{c_f c_m}}\frac{\partial \hat{c}_{\mathrm{m}}^{j}}{\partial t}-\sum_{j=1}^{n_g} C_{\mathrm{c_f c_f}}\frac{\partial \hat{c}_{\mathrm{f}}^{j}}{\partial t}-C_{\mathrm{c_f l_m}}\frac{\partial \hat{u}_{\mathrm{lm}}}{\partial t} \\ -C_{\mathrm{c_f l_f}}\frac{\partial \hat{u}_{\mathrm{lf}}}{\partial t}-C_{\mathrm{c_f T_m}}\frac{\partial \hat{T}_{\mathrm{m}}}{\partial t}-C_{\mathrm{c_f T_f}}\frac{\partial \hat{T}_{\mathrm{f}}}{\partial t}-C_{\mathrm{c_f u_s}}\frac{\partial \hat{\mathbf{u}}_{\mathrm{s}}}{\partial t} \end{array}\right]+ \\ \nabla\cdot\left[N_r\sum_{j=1}^{n_g} K_{\mathrm{c_f c_f}}\widehat{\nabla}c_{\mathrm{f}}^{j}\right]-\sum_{j=1}^{n_g} K_{\mathrm{c_f c_f}}\widehat{\nabla}c_{\mathrm{f}}^{j}\,\nabla N_r \\ +\nabla\cdot\left[N_r K_{\mathrm{c_f T_f}}\nabla\hat{T}_{\mathrm{f}}\right]-K_{\mathrm{c_f T_f}}\nabla\hat{T}_{\mathrm{f}}\nabla N_r \end{array}\right]d\Omega=0 \tag{4.18}$$

$$\int_{\Omega}\left[\begin{array}{c} N_r\left[-\sum_{j=1}^{n_g} C_{\mathrm{c_F c_F}}\frac{\partial \hat{c}_{\mathrm{F}}^{j}}{\partial t}-C_{\mathrm{c_F l_F}}\frac{\partial \hat{u}_{\mathrm{lF}}}{\partial t}-C_{\mathrm{c_F T_F}}\frac{\partial \hat{T}_{\mathrm{F}}}{\partial t}\right]+ \\ \nabla_l\cdot\left[N_r\sum_{j=1}^{n_g} K_{\mathrm{c_F c_F}}\nabla_l\hat{c}_{\mathrm{F}}^{j}\right]-\sum_{j=1}^{n_g} K_{\mathrm{c_F c_F}}\nabla_l\hat{c}_{\mathrm{F}}^{j}\,\nabla N_r \\ +\nabla_l\cdot\left[N_r K_{\mathrm{c_F T_F}}\nabla_l\hat{T}_F\right]-K_{\mathrm{c_F T_F}}\nabla_l\hat{T}_F\nabla_l N_r \end{array}\right]d\Omega=0 \tag{4.19}$$

Using the Gauss-Green divergence theorem (Zienkiewicz *et al.* 2005), the second order differential terms can be reduced to first order terms and surface integrals are introduced for all elements in the domain. On adjacent elements, the surface integrals cancel each other to leave only the contributions at the domain boundary. Applying the divergence theorem and rearranging the terms in equation (4.18) and (4.19) yields:

$$\begin{aligned}\int_{\Omega}&\left[\begin{array}{c} N_r\left[\begin{array}{c} -\sum_{j=1}^{n_g} C_{\mathrm{c_f c_m}}\frac{\partial \hat{c}_{\mathrm{m}}^{j}}{\partial t}-\sum_{j=1}^{n_g} C_{\mathrm{c_f c_f}}\frac{\partial \hat{c}_{\mathrm{f}}^{j}}{\partial t}-C_{\mathrm{c_f l_m}}\frac{\partial \hat{u}_{\mathrm{lm}}}{\partial t} \\ -C_{\mathrm{c_f l_f}}\frac{\partial \hat{u}_{\mathrm{lf}}}{\partial t}-C_{\mathrm{c_f T_m}}\frac{\partial \hat{T}_{\mathrm{m}}}{\partial t}--C_{\mathrm{c_f T_f}}\frac{\partial \hat{T}_{\mathrm{f}}}{\partial t}-C_{\mathrm{c_f u_s}}\frac{\partial \hat{\mathbf{u}}_{\mathrm{s}}}{\partial t}\end{array}\right]+ \\ -\sum_{j=1}^{n_g} K_{\mathrm{c_f c_f}}\widehat{\nabla}c_{\mathrm{f}}^{j}\,\nabla N_r-K_{\mathrm{c_f T_f}}\nabla\hat{T}_{\mathrm{f}}\nabla N_r \end{array}\right]d\Omega \\ &+\int_{\Gamma^e} N_r\left[\sum_{j=1}^{n_g} K_{\mathrm{c_f c_f}}\widehat{\nabla}c_{\mathrm{f}}^{j}+K_{\mathrm{c_f c_f}}\nabla\hat{T}_{\mathrm{f}}\right]\underline{n}\,d\Gamma^e=0\end{aligned} \tag{4.20}$$

$$\int_{\Omega}\left[\begin{array}{l} N_r\left[-\sum_{j=1}^{n_g} C_{\mathrm{c_F c_F}}\frac{\partial \hat{c}_{\mathrm{F}}^{j}}{\partial t} - C_{\mathrm{c_F l_F}}\frac{\partial \hat{u}_{\mathrm{lF}}}{\partial t} - C_{\mathrm{c_F T_F}}\frac{\partial \hat{T}_{\mathrm{F}}}{\partial t}\right] + \\ \quad -\sum_{j=1}^{n_g} K_{\mathrm{c_F c_F}}\nabla \hat{c}_{\mathrm{F}}^{j}\,\nabla N_r - K_{\mathrm{c_F T_F}}\nabla \hat{T}_F \nabla N_r \end{array}\right] d\Omega$$

$$+\int_{\Gamma^e} N_r\left[\sum_{j=1}^{n_g} K_{\mathrm{c_F c_F}}\nabla_l \hat{c}_{\mathrm{F}}^{j} + K_{\mathrm{c_F c_F}}\nabla_l \hat{c}_{\mathrm{F}}^{j}\right]\underline{n}\, d\Gamma^e = 0 \tag{4.21}$$

where $\Gamma^e$and is the element boundary surface and $\underline{n}$ is the direction cosine normal to the surface,

By introducing and expanding expressions for the derivatives of the primary variables, equations (4.11), (4.20) and (4.21) are rewritten using vector notation as:

$$\sum_{j=1}^{n_g}\int_{\Omega^e}\left[C_{\mathrm{c_m c_m}}\boldsymbol{N}_s{}^T\boldsymbol{N}_s\right]d\Omega^e\frac{\partial \boldsymbol{c}_{\mathrm{m}}^{j}}{\partial t} + \sum_{j=1}^{n_g}\int_{\Omega^e}\left[C_{\mathrm{c_m c_f}}\boldsymbol{N}_s{}^T\boldsymbol{N}_s\right]d\Omega^e\frac{\partial \boldsymbol{c}_{\mathrm{f}}^{j}}{\partial t}$$

$$+\int_{\Omega^e}\left[C_{\mathrm{c_m l_m}}\boldsymbol{N}_s{}^T\boldsymbol{N}_s\right]d\Omega^e\frac{\partial \boldsymbol{u}_{\mathrm{lm}}}{\partial t} + \int_{\Omega^e}\left[C_{\mathrm{c_m l_f}}\boldsymbol{N}_s{}^T\boldsymbol{N}_s\right]d\Omega^e\frac{\partial \boldsymbol{u}_{\mathrm{lf}}}{\partial t}$$

$$+\int_{\Omega^e}\left[C_{\mathrm{c_m T_m}}\boldsymbol{N}_s{}^T\boldsymbol{N}_s\right]d\Omega^e\frac{\partial \boldsymbol{T}_{\mathrm{m}}}{\partial t} + +\int_{\Omega^e}\left[C_{\mathrm{c_m T_f}}\boldsymbol{N}_s{}^T\boldsymbol{N}_s\right]d\Omega^e\frac{\partial \boldsymbol{T}_{\mathrm{f}}}{\partial t}$$

$$+\int_{\Omega^e}\left[C_{\mathrm{c_m u_s}}\boldsymbol{N}_s{}^T\boldsymbol{N}_s\right]d\Omega^e\frac{\partial \mathbf{u}_{\mathrm{s}}}{\partial t} = 0 \tag{4.22}$$

$$\sum_{j=1}^{n_g}\int_{\Omega^e}\left[C_{\mathrm{c_f c_m}}\boldsymbol{N}_s{}^T\boldsymbol{N}_s\right]d\Omega^e\frac{\partial \boldsymbol{c}_{\mathrm{m}}^{j}}{\partial t} + \sum_{j=1}^{n_g}\int_{\Omega^e}\left[C_{\mathrm{c_f c_f}}\boldsymbol{N}_s{}^T\boldsymbol{N}_s\right]d\Omega^e\frac{\partial \boldsymbol{c}_{\mathrm{f}}^{j}}{\partial t}$$

$$+\int_{\Omega^e}\left[C_{\mathrm{c_f l_m}}\boldsymbol{N}_s{}^T\boldsymbol{N}_s\right]d\Omega^e\frac{\partial \boldsymbol{u}_{\mathrm{lm}}}{\partial t} + \int_{\Omega^e}\left[C_{\mathrm{c_f l_f}}\boldsymbol{N}_s{}^T\boldsymbol{N}_s\right]d\Omega^e\frac{\partial \boldsymbol{u}_{\mathrm{lf}}}{\partial t}$$

$$+\int_{\Omega^e}\left[C_{\mathrm{c_f T_m}}\boldsymbol{N}_s{}^T\boldsymbol{N}_s\right]d\Omega^e\frac{\partial \boldsymbol{T}_{\mathrm{m}}}{\partial t} + +\int_{\Omega^e}\left[C_{\mathrm{c_f T_f}}\boldsymbol{N}_s{}^T\boldsymbol{N}_s\right]d\Omega^e\frac{\partial \boldsymbol{T}_{\mathrm{f}}}{\partial t}$$

$$+\int_{\Omega^e}\left[C_{\mathrm{c_f u_s}}\boldsymbol{N}_s{}^T\boldsymbol{N}_s\right]d\Omega^e\frac{\partial \mathbf{u}_{\mathrm{s}}}{\partial t} + \sum_{j=1}^{n_g}\int_{\Omega^e}\left[K_{\mathrm{c_f c_f}}\nabla\boldsymbol{N}_s{}^T\nabla\boldsymbol{N}_s\right]d\Omega^e\boldsymbol{c}_{\mathrm{f}}^{j}$$

$$+\int_{\Omega^e}\left[K_{\mathrm{c_f T}_f}\nabla\boldsymbol{N}_s{}^T\nabla\boldsymbol{N}_s\right]d\Omega^e\boldsymbol{T}_{\mathrm{f}} - \int_{\Gamma^e}\boldsymbol{N}_s{}^T\left[f_{\mathrm{g,f}}^{j}\right]\underline{n}\, d\Gamma^e = 0 \tag{4.23}$$

$$\sum_{j=1}^{n_g}\int_{\Gamma^{Fe}}\left[C_{\mathrm{c_F c_F}}\boldsymbol{N}_{sF}{}^{T}\boldsymbol{N}_{sF}\right]d\Gamma^{Fe}\frac{\partial \boldsymbol{c}_{\mathrm{F}}^{j}}{\partial t}+\int_{\Gamma^{Fe}}\left[C_{\mathrm{c_F l_F}}\boldsymbol{N}_{sF}{}^{T}\boldsymbol{N}_{sF}\right]d\Gamma^{Fe}\frac{\partial \boldsymbol{u}_{\mathrm{lF}}}{\partial t}$$
$$+\int_{\Gamma^{Fe}}\left[C_{\mathrm{c_F T_F}}\boldsymbol{N}_{sF}{}^{T}\boldsymbol{N}_{sF}\right]d\Gamma^{Fe}\frac{\partial \boldsymbol{T}_{\mathrm{F}}}{\partial t}+\sum_{j=1}^{n_g}\int_{\Gamma^{Fe}}\left[K_{\mathrm{c_F c_F}}\nabla_l\boldsymbol{N}_{sF}{}^{T}\nabla_l\boldsymbol{N}_{sF}\right]d\Gamma^{Fe}\boldsymbol{c}_{\mathrm{F}}^{j}$$
$$+\int_{\Gamma^{Fe}}\left[K_{\mathrm{c_F c_F}}\nabla_l\boldsymbol{N}_{sF}{}^{T}\nabla_l\boldsymbol{N}_{sF}\right]d\Gamma^{Fe}\boldsymbol{T}_{\mathrm{F}}-\boldsymbol{N}_{sF}{}^{T}\left[f_{\mathrm{g,F}}^{j}\right]\Big|_{L_1}^{L_2}=0 \qquad (4.24)$$

where $f_{\mathrm{g,f}}^{j}$ and $f_{\mathrm{g,F}}^{j}$ is the approximate pore gas flux normal to the boundary surface, $\boldsymbol{N}_s$ and $\boldsymbol{N}_{sF}$ are the shape function for both continua and the terms $\boldsymbol{c}_{\alpha}^{j}$, $\boldsymbol{u}_{\mathrm{l}\alpha}$, $\boldsymbol{T}_{\alpha}$ and $\mathbf{u}_{\mathrm{s}}$ are the vectors of the gas concentrations, pore water pressure, temperature and displacement at nodes, respectively.

The computational domains can be represented by a mesh of 1-D, 2-D and/or 3-D basic elements (geometric units) such as lines, triangles, quadrilaterals, tetrahedrons, hexahedra and pyramids. The determination of the most appropriate element type for a particular problem depends on several factors, such as domain geometry, required accuracy, computational costs, etc. (Watanabe 2011; Kolditz 2013). Domains composed of a porous matrix, natural fracture network and discrete large fractures can be discretised using a combination of multiple element types. In this work, discrete large fractures are idealized as lower-dimensional geometric objects and can be represented by, for example, lines in two-dimensional space. The lower-dimensional interface elements are used to discretise the large fracture domain. It is assumed that the flow variables (gas concentration, water pressure and temperature) are continuous over the fracture continuum and large scale fracture domain, i.e. $c_{\mathrm{f}}^{j}=c_{\mathrm{F}}^{j}$, $u_{\mathrm{lf}}=u_{\mathrm{lF}}$ and $T_{\mathrm{f}}=T_{\mathrm{F}}$. Thus, the discrete fracture elements must be located on the edges of continuum elements with both kind of elements sharing the same nodes, as shown in Figure 4.1. The coupling between the two flow systems is achieved by using the principle of superposition, which has been applied in many works (e.g. Baca *et al.* 1984; Karimi-Fard and Firoozabadi 2003; Watanabe 2011; Zhang *et al.* 2013). By using the principle of superposition, the mass/heat exchange term between the fracture continuum and large fracture domain can balance off and no explicit calculation for mass exchange is required (Chen et al. 2019). Before superimposition of two discretised flow equations, the local coordinate system should be transformed into the global coordinate system. The

transformation relation between the two sets of coordinate systems is achieved by the rotation matrix (Huang and Ghassemi 2015):

$$\mathbf{R} = \begin{bmatrix} \cos\varphi_o & \sin\varphi_o \\ -\sin\varphi_o & \cos\varphi_o \end{bmatrix} \tag{4.25}$$

where φ_o is the angle between the positive x-axis in the global coordinate and the positive x'-axis in the local coordinate, as shown in Figure 3.13.

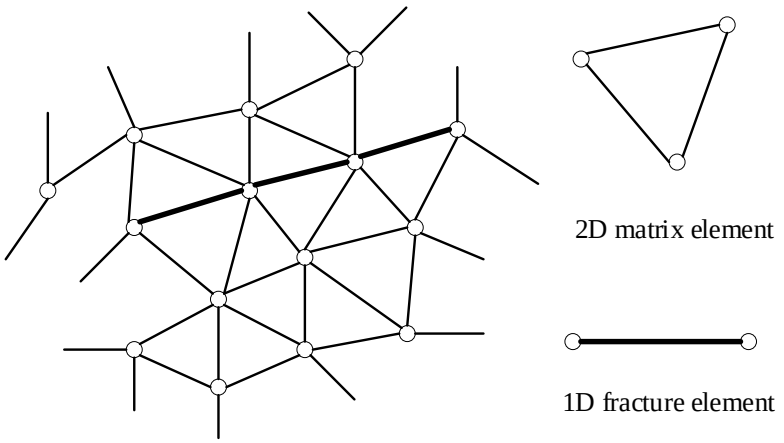

Figure 4.1 Mesh schematics of a fracture model, with the matrix and fracture continua discretised using 2D elements and a large fracture discretised using line elements.

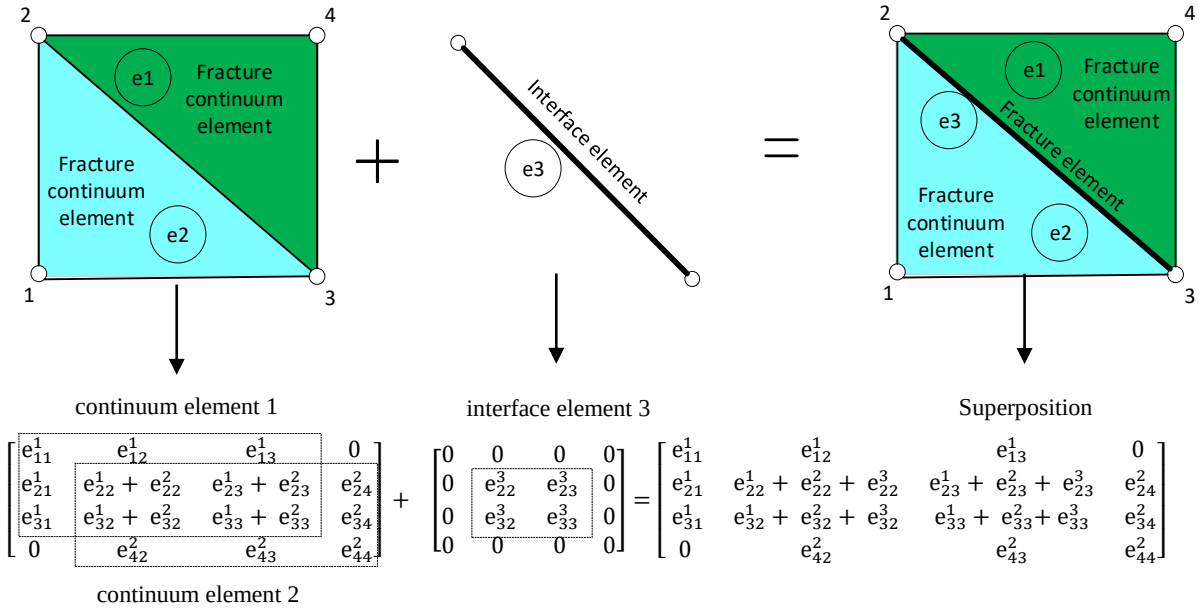

Figure 4.2 Assembly process of the matrix and fracture equations into the stiffness matrix (Chen et al. 2019).

After superimposing the two discretised equations of the weak forms for the transport systems in the fracture continuum and large fracture domain, as show in Figure 4.2, the finite

element formulations of the governing equations can be reduced and rewritten in a concise matrix notation. For the matrix continuum this yields:

$$\sum_{j=1}^{n_g} \mathbf{C}_{\mathrm{c_m c_m}} \frac{\partial \boldsymbol{c}_{\mathrm{m}}^{j}}{\partial t} + \sum_{j=1}^{n_g} \mathbf{C}_{\mathrm{c_m c_f}} \frac{\partial \boldsymbol{c}_{\mathrm{f}}^{j}}{\partial t} + \mathbf{C}_{\mathrm{c_m l_m}} \frac{\partial \boldsymbol{u}_{\mathrm{lm}}}{\partial t} + \mathbf{C}_{\mathrm{c_m l_f}} \frac{\partial \boldsymbol{u}_{\mathrm{lf}}}{\partial t} + \mathbf{C}_{\mathrm{c_m T_m}} \frac{\partial \boldsymbol{T}_{\mathrm{m}}}{\partial t}$$

$$+\mathbf{C}_{\mathrm{c_m T_f}} \frac{\partial \boldsymbol{T}_{\mathrm{f}}}{\partial t} + \mathbf{C}_{\mathrm{c_m u_s}} \frac{\partial \mathbf{u}_{\mathrm{s}}}{\partial t} = \mathbf{f}_{\mathrm{g,m}}^{j} \qquad (4.26)$$

where for a matrix domain with n_{elem} elements:

$$\mathbf{C}_{\mathrm{c_m c_m}} = \sum_{e=1}^{n_{elem}} \int_{\Omega^e} \left[C_{\mathrm{c_m c_m}} \boldsymbol{N}_s{}^T \boldsymbol{N}_s \right] d\Omega^e \qquad (4.26a)$$

$$\mathbf{C}_{\mathrm{c_m c_f}} = \sum_{e=1}^{n_{elem}} \int_{\Omega^e} \left[C_{\mathrm{c_m c_f}} \boldsymbol{N}_s{}^T \boldsymbol{N}_s \right] d\Omega^e \qquad (4.26b)$$

$$\mathbf{C}_{\mathrm{c_m l_m}} = \sum_{e=1}^{n_{elem}} \int_{\Omega^e} \left[C_{\mathrm{c_m l_m}} \boldsymbol{N}_s{}^T \boldsymbol{N}_s \right] d\Omega^e \qquad (4.26c)$$

$$\mathbf{C}_{\mathrm{c_m l_f}} = \sum_{e=1}^{n_{elem}} \int_{\Omega^e} \left[C_{\mathrm{c_m l_f}} \boldsymbol{N}_s{}^T \boldsymbol{N}_s \right] d\Omega^e \qquad (4.26d)$$

$$\mathbf{C}_{\mathrm{c_m T_m}} = \sum_{e=1}^{n_{elem}} \int_{\Omega^e} \left[C_{\mathrm{c_m T_m}} \boldsymbol{N}_s{}^T \boldsymbol{N}_s \right] d\Omega^e \qquad (4.26e)$$

$$\mathbf{C}_{\mathrm{c_m T_f}} = \sum_{e=1}^{n_{elem}} \int_{\Omega^e} \left[C_{\mathrm{c_m T_f}} \boldsymbol{N}_s{}^T \boldsymbol{N}_s \right] d\Omega^e \qquad (4.26f)$$

$$\mathbf{C}_{\mathrm{c_m u_s}} = \sum_{e=1}^{n_{elem}} \int_{\Omega^e} \left[C_{\mathrm{c_m u_s}} \boldsymbol{N}_s{}^T \boldsymbol{N}_s \right] d\Omega^e \qquad (4.26g)$$

$$\mathbf{f}_{\mathrm{g,m}}^{j} = 0.0 \qquad (4.26h)$$

For the fracture domain comprising the fracture continuum with n_{elem} elements and the discrete fracture domain with n_{eleF} lower dimensional interface elements:

$$\sum_{j=1}^{n_g} \mathbf{C}_{\mathrm{c_f c_m}}^{\mathrm{fF}} \frac{\partial \boldsymbol{c}_{\mathrm{m}}^{j}}{\partial t} + \sum_{j=1}^{n_g} \mathbf{C}_{\mathrm{c_f c_f}}^{\mathrm{fF}} \frac{\partial \boldsymbol{c}_{\mathrm{f}}^{j}}{\partial t} + \mathbf{C}_{\mathrm{c_f l_m}}^{\mathrm{fF}} \frac{\partial \boldsymbol{u}_{\mathrm{lm}}}{\partial t} + \mathbf{C}_{\mathrm{c_f l_f}}^{\mathrm{fF}} \frac{\partial \boldsymbol{u}_{\mathrm{lf}}}{\partial t} + \mathbf{C}_{\mathrm{c_f T_m}}^{\mathrm{fF}} \frac{\partial \boldsymbol{T}_{\mathrm{m}}}{\partial t}$$

$$+\mathbf{C}^{\mathrm{fF}}_{\mathrm{c_f T_f}}\frac{\partial \boldsymbol{T}_{\mathrm{f}}}{\partial t}+\mathbf{C}^{\mathrm{fF}}_{\mathrm{c_f u_s}}\frac{\partial \mathbf{u}_{\mathrm{s}}}{\partial t}+\sum_{j=1}^{n_g}\mathbf{K}^{\mathrm{fF}}_{\mathrm{c_f c_f}}\boldsymbol{c}^{j}_{\mathrm{m}}+\mathbf{K}^{\mathrm{fF}}_{\mathrm{c_f T_f}}\boldsymbol{T}_{\mathrm{f}}=\mathbf{f}^{j}_{\mathrm{g,fF}} \qquad (4.27)$$

where:

$$\mathbf{C}^{\mathrm{fF}}_{\mathrm{c_f c_m}}=\sum_{e=1}^{n_{elem}}\int_{\Omega^e}\left[C_{\mathrm{c_f c_m}}\boldsymbol{N}_s{}^T\boldsymbol{N}_s\right]d\Omega^e \qquad (4.27a)$$

$$\mathbf{C}^{\mathrm{fF}}_{\mathrm{c_f c_f}}=\sum_{e=1}^{n_{elem}}\int_{\Omega^e}\left[C_{\mathrm{c_f c_f}}\boldsymbol{N}_s{}^T\boldsymbol{N}_s\right]d\Omega^e+\sum_{e=1}^{n_{eleF}}\int_{\Gamma^{Fe}}\left[C_{\mathrm{c_F c_F}}\boldsymbol{N}_{sF}{}^T\mathbf{R}^T\mathbf{R}\boldsymbol{N}_{sF}\right]d\Gamma^{Fe} \qquad (4.27b)$$

$$\mathbf{C}^{\mathrm{fF}}_{\mathrm{c_f l_m}}=\sum_{e=1}^{n_{elem}}\int_{\Omega^e}\left[C_{\mathrm{c_f l_m}}\boldsymbol{N}_s{}^T\boldsymbol{N}_s\right]d\Omega^e \qquad (4.27c)$$

$$\mathbf{C}^{\mathrm{fF}}_{\mathrm{c_f l_f}}=\sum_{e=1}^{n_{elem}}\int_{\Omega^e}\left[C_{\mathrm{c_f l_f}}\boldsymbol{N}_s{}^T\boldsymbol{N}_s\right]d\Omega^e+\sum_{e=1}^{n_{eleF}}\int_{\Gamma^{Fe}}\left[C_{\mathrm{c_f l_F}}\boldsymbol{N}_{sF}{}^T\mathbf{R}^T\mathbf{R}\boldsymbol{N}_{sF}\right]d\Gamma^{Fe} \qquad (4.27d)$$

$$\mathbf{C}^{\mathrm{fF}}_{\mathrm{c_f T_m}}=\sum_{e=1}^{n_{elem}}\int_{\Omega^e}\left[C_{\mathrm{c_f T_m}}\boldsymbol{N}_s{}^T\boldsymbol{N}_s\right]d\Omega^e \qquad (4.27e)$$

$$\mathbf{C}^{\mathrm{fF}}_{\mathrm{c_f T_f}}=\sum_{e=1}^{n_{elem}}\int_{\Omega^e}\left[C_{\mathrm{c_f T_f}}\boldsymbol{N}_s{}^T\boldsymbol{N}_s\right]d\Omega^e+\sum_{e=1}^{n_{eleF}}\int_{\Gamma^{Fe}}\left[C_{\mathrm{c_F T_F}}\boldsymbol{N}_{sF}{}^T\mathbf{R}^T\mathbf{R}\boldsymbol{N}_{sF}\right]d\Gamma^{Fe} \qquad (4.27f)$$

$$\mathbf{C}^{\mathrm{fF}}_{\mathrm{c_f u_s}}=\sum_{e=1}^{n_{elem}}\int_{\Omega^e}\left[C_{\mathrm{c_f u_s}}\boldsymbol{N}_s{}^T\boldsymbol{N}_s\right]d\Omega^e \qquad (4.27g)$$

$$\mathbf{K}^{\mathrm{fF}}_{\mathrm{c_f c_f}}=\sum_{e=1}^{n_{elem}}\int_{\Omega^e}\left[K_{\mathrm{c_f c_f}}\nabla\boldsymbol{N}_s{}^T\nabla\boldsymbol{N}_s\right]d\Omega^e+\sum_{e=1}^{n_{eleF}}\int_{\Gamma^{Fe}}\left[K_{\mathrm{c_F c_F}}\nabla_l\boldsymbol{N}_{sF}{}^T\mathbf{R}^T\mathbf{R}\nabla_l\boldsymbol{N}_{sF}\right]d\Gamma^{Fe} \qquad (4.27h)$$

$$\mathbf{K}^{\mathrm{fF}}_{\mathrm{c_f T_f}}=\sum_{e=1}^{n_{elem}}\int_{\Omega^e}\left[K_{\mathrm{c_f T_f}}\nabla\boldsymbol{N}_s{}^T\nabla\boldsymbol{N}_s\right]d\Omega^e+\sum_{e=1}^{n_{eleF}}\int_{\Gamma^{Fe}}\left[K_{\mathrm{c_F T_F}}\nabla_l\boldsymbol{N}_{sF}{}^T\mathbf{R}^T\mathbf{R}\nabla_l\boldsymbol{N}_{sF}\right]d\Gamma^{Fe} \qquad (4.27i)$$

$$\mathbf{f}^{j}_{\mathrm{g,fF}}=\sum_{e=1}^{n_{elem}}\int_{\Gamma^e}\boldsymbol{N}_s{}^T\left[f^{j}_{\mathrm{g,f}}\right]\underline{n}d\Gamma^e+f^{j}_{\mathrm{g,F}}\boldsymbol{N}_f^T\Big|_{L_1}^{L_2} \qquad (4.27j)$$

where L_1 and L_2 denote the endpoints of the interface element.

4.2.2 Spatial discretisation of governing equations for water transfer

The procedure for spatial discretisation for multicomponent gas transport equations can be replicated for the water flow variables, $u_{\mathrm{l}\alpha}$. Substitution of the approximate values of water pressure into governing equations for water transfer yields:

$$-\sum_{j=1}^{n_g}\left(C_{\mathrm{l_m c_m}}\frac{\partial \hat{c}_{\mathrm{m}}^{j}}{\partial t}\right)-\sum_{j=1}^{n_g}\left(C_{\mathrm{l_m c_f}}\frac{\partial \hat{c}_{\mathrm{f}}^{j}}{\partial t}\right)-C_{\mathrm{l_m l_m}}\frac{\partial \hat{u}_{\mathrm{lm}}}{\partial t}-C_{\mathrm{l_m l_f}}\frac{\partial \hat{u}_{\mathrm{lf}}}{\partial t}-C_{\mathrm{l_m T_m}}\frac{\partial \hat{T}_{\mathrm{m}}}{\partial t}-C_{\mathrm{l_m T_f}}\frac{\partial \hat{T}_{\mathrm{f}}}{\partial t}$$
$$-C_{\mathrm{l_m u_s}}\frac{\partial \hat{\mathbf{u}}_{\mathrm{s}}}{\partial t}+\nabla\cdot\left(K_{\mathrm{l_m l_m}}\nabla\hat{u}_{\mathrm{lm}}\right)=0 \qquad (4.28)$$

$$-\sum_{j=1}^{n_g}\left(C_{\mathrm{l_f c_m}}\frac{\partial \hat{c}_{\mathrm{m}}^{j}}{\partial t}\right)-\sum_{j=1}^{n_g}\left(C_{\mathrm{l_f c_f}}\frac{\partial \hat{c}_{\mathrm{f}}^{j}}{\partial t}\right)-C_{\mathrm{l_f l_m}}\frac{\partial \hat{u}_{\mathrm{lm}}}{\partial t}-C_{\mathrm{l_f l_f}}\frac{\partial \hat{u}_{\mathrm{lf}}}{\partial t}-C_{\mathrm{l_f T_m}}\frac{\partial \hat{T}_{\mathrm{m}}}{\partial t}-C_{\mathrm{l_f T_f}}\frac{\partial \hat{T}_{\mathrm{f}}}{\partial t}$$
$$-C_{\mathrm{l_f u_s}}\frac{\partial \hat{\mathbf{u}}_{\mathrm{s}}}{\partial t}+\nabla\cdot\left(K_{\mathrm{l_f l_f}}\nabla\hat{u}_{\mathrm{lf}}\right)=0 \qquad (4.29)$$

$$-C_{\mathrm{l_F l_F}}\frac{\partial \hat{u}_{\mathrm{lF}}}{\partial t}-\sum_{i=1}^{n_g}\left(C_{\mathrm{l_F c_F}}\frac{\partial \hat{c}_{\mathrm{F}}^{i}}{\partial t}\right)-C_{\mathrm{l_F T_F}}\frac{\partial \hat{T}_{\mathrm{F}}}{\partial t}+\nabla_l\cdot\left(K_{\mathrm{l_F l_F}}\nabla\hat{u}_{\mathrm{lF}}\right)=0 \qquad (4.30)$$

Application of Galerkin weighted residual approach and the Gauss-Green divergence theorem to equations (4.28) – (4.30), it can be obtained:

$$\int_{\Omega}\left[N_r\begin{bmatrix}-\sum_{j=1}^{n_g}C_{\mathrm{l_m c_m}}\frac{\partial \hat{c}_{\mathrm{m}}^{j}}{\partial t}-\sum_{j=1}^{n_g}C_{\mathrm{l_m c_f}}\frac{\partial \hat{c}_{\mathrm{f}}^{j}}{\partial t}-C_{\mathrm{l_m l_m}}\frac{\partial \hat{u}_{\mathrm{lm}}}{\partial t}\\ -C_{\mathrm{l_m l_f}}\frac{\partial \hat{u}_{\mathrm{lf}}}{\partial t}-C_{\mathrm{l_m T_m}}\frac{\partial \hat{T}_{\mathrm{m}}}{\partial t}-C_{\mathrm{l_m T_f}}\frac{\partial \hat{T}_{\mathrm{f}}}{\partial t}-C_{\mathrm{l_m u_s}}\frac{\partial \hat{\mathbf{u}}_{\mathrm{s}}}{\partial t}\\ -K_{\mathrm{l_m l_m}}\widehat{\nabla}\hat{u}_{\mathrm{lm}}\nabla N_r\end{bmatrix}+\right]d\Omega$$
$$+\int_{\Gamma}N_r\left[K_{\mathrm{l_m l_m}}\nabla\hat{u}_{\mathrm{lm}}\right]\underline{n}\,d\Gamma=0 \qquad (4.31)$$

$$\int_{\Omega}\left[N_r\begin{bmatrix}-\sum_{j=1}^{n_g}C_{\mathrm{l_f c_m}}\frac{\partial \hat{c}_{\mathrm{m}}^{j}}{\partial t}-\sum_{j=1}^{n_g}C_{\mathrm{l_f c_f}}\frac{\partial \hat{c}_{\mathrm{f}}^{j}}{\partial t}-C_{\mathrm{l_f l_m}}\frac{\partial \hat{u}_{\mathrm{lm}}}{\partial t}\\ -C_{\mathrm{l_f l_f}}\frac{\partial \hat{u}_{\mathrm{lf}}}{\partial t}-C_{\mathrm{l_f T_m}}\frac{\partial \hat{T}_{\mathrm{m}}}{\partial t}-C_{\mathrm{l_f T_f}}\frac{\partial \hat{T}_{\mathrm{f}}}{\partial t}-C_{\mathrm{l_f u_s}}\frac{\partial \hat{\mathbf{u}}_{\mathrm{s}}}{\partial t}\\ -K_{\mathrm{l_f l_f}}\widehat{\nabla}\hat{u}_{\mathrm{lf}}\nabla N_r\end{bmatrix}+\right]d\Omega+\int_{\Gamma}N_r\left[K_{\mathrm{l_f l_f}}\nabla\hat{u}_{\mathrm{lf}}\right]\underline{n}\,d\Gamma$$
$$=0 \qquad (4.32)$$

$$\int_{\Omega}\left[N_r\left[-\sum_{j=1}^{n_g} C_{\mathrm{l_F c_F}}\frac{\partial \hat{c}_{\mathrm{F}}^{j}}{\partial t} - C_{\mathrm{l_F l_F}}\frac{\partial \hat{u}_{\mathrm{lF}}}{\partial t} - C_{\mathrm{l_F T_F}}\frac{\partial \hat{T}_{\mathrm{F}}}{\partial t}\right] + \right.$$
$$\left. -K_{\mathrm{l_F l_F}}\nabla_l \hat{u}_{\mathrm{lF}}\nabla_l N_r\right] d\Omega + \int_{\Gamma} N_r\left[K_{\mathrm{l_F l_F}}\nabla_l \hat{u}_{\mathrm{lF}}\right]\underline{n}\, d\Gamma$$
$$= 0 \qquad (4.33)$$

Introducing the approximated primary variables into equations (4.31) - (4.33) and expanding expressions for the derivatives of the primary variables, equations (4.31) - (4.33) are rewritten using vector notation as:

$$\sum_{j=1}^{n_g}\int_{\Omega^e}\left[C_{\mathrm{l_m c_m}}\boldsymbol{N}_s{}^T\boldsymbol{N}_s\right]d\Omega^e\frac{\partial \boldsymbol{c}_{\mathrm{m}}^{j}}{\partial t} + \sum_{j=1}^{n_g}\int_{\Omega^e}\left[C_{\mathrm{l_m c_f}}\boldsymbol{N}_s{}^T\boldsymbol{N}_s\right]d\Omega^e\frac{\partial \boldsymbol{c}_{\mathrm{f}}^{j}}{\partial t}$$
$$+\int_{\Omega^e}\left[C_{\mathrm{l_m l_m}}\boldsymbol{N}_s{}^T\boldsymbol{N}_s\right]d\Omega^e\frac{\partial \boldsymbol{u}_{\mathrm{lm}}}{\partial t} + \int_{\Omega^e}\left[C_{\mathrm{l_m l_f}}\boldsymbol{N}_s{}^T\boldsymbol{N}_s\right]d\Omega^e\frac{\partial \boldsymbol{u}_{\mathrm{lf}}}{\partial t}$$
$$+\int_{\Omega^e}\left[C_{\mathrm{l_m T_m}}\boldsymbol{N}_s{}^T\boldsymbol{N}_s\right]d\Omega^e\frac{\partial \boldsymbol{T}_{\mathrm{m}}}{\partial t} + +\int_{\Omega^e}\left[C_{\mathrm{l_m T_f}}\boldsymbol{N}_s{}^T\boldsymbol{N}_s\right]d\Omega^e\frac{\partial \boldsymbol{T}_{\mathrm{f}}}{\partial t}$$
$$+\int_{\Omega^e}\left[C_{\mathrm{l_m u_s}}\boldsymbol{N}_s{}^T\boldsymbol{N}_s\right]d\Omega^e\frac{\partial \mathbf{u}_{\mathrm{s}}}{\partial t} + \int_{\Omega^e}\left[K_{\mathrm{l_m l_m}}\nabla\boldsymbol{N}_s{}^T\nabla\boldsymbol{N}_s\right]d\Omega^e\boldsymbol{u}_{\mathrm{lm}}$$
$$-\int_{\Gamma^e}\boldsymbol{N}_s{}^T\left[f_{\mathrm{l,m}}\right]\underline{n}\, d\Gamma^e = 0 \qquad (4.34)$$

$$\sum_{j=1}^{n_g}\int_{\Omega^e}\left[C_{\mathrm{l_f c_m}}\boldsymbol{N}_s{}^T\boldsymbol{N}_s\right]d\Omega^e\frac{\partial \boldsymbol{c}_{\mathrm{m}}^{j}}{\partial t} + \sum_{j=1}^{n_g}\int_{\Omega^e}\left[C_{\mathrm{l_f c_f}}\boldsymbol{N}_s{}^T\boldsymbol{N}_s\right]d\Omega^e\frac{\partial \boldsymbol{c}_{\mathrm{f}}^{j}}{\partial t}$$
$$+\int_{\Omega^e}\left[C_{\mathrm{l_f l_m}}\boldsymbol{N}_s{}^T\boldsymbol{N}_s\right]d\Omega^e\frac{\partial \boldsymbol{u}_{\mathrm{lm}}}{\partial t} + \int_{\Omega^e}\left[C_{\mathrm{l_f l_f}}\boldsymbol{N}_s{}^T\boldsymbol{N}_s\right]d\Omega^e\frac{\partial \boldsymbol{u}_{\mathrm{lf}}}{\partial t}$$
$$+\int_{\Omega^e}\left[C_{\mathrm{l_f T_m}}\boldsymbol{N}_s{}^T\boldsymbol{N}_s\right]d\Omega^e\frac{\partial \boldsymbol{T}_{\mathrm{m}}}{\partial t} + +\int_{\Omega^e}\left[C_{\mathrm{l_f T_f}}\boldsymbol{N}_s{}^T\boldsymbol{N}_s\right]d\Omega^e\frac{\partial \boldsymbol{T}_{\mathrm{f}}}{\partial t}$$
$$+\int_{\Omega^e}\left[C_{\mathrm{l_f u_s}}\boldsymbol{N}_s{}^T\boldsymbol{N}_s\right]d\Omega^e\frac{\partial \mathbf{u}_{\mathrm{s}}}{\partial t} + \int_{\Omega^e}\left[K_{\mathrm{l_f l_f}}\nabla\boldsymbol{N}_s{}^T\nabla\boldsymbol{N}_s\right]d\Omega^e\boldsymbol{u}_{\mathrm{lf}}$$
$$-\int_{\Gamma^e}\boldsymbol{N}_s{}^T\left[f_{\mathrm{l,f}}\right]\underline{n}\, d\Gamma^e = 0 \qquad (4.35)$$

$$\sum_{j=1}^{n_g}\int_{\Gamma^{Fe}}\left[C_{\mathrm{l_F c_F}}\boldsymbol{N}_{sF}{}^{T}\boldsymbol{N}_{sF}\right]d\Gamma^{Fe}\frac{\partial \boldsymbol{c}_{\mathrm{F}}^{j}}{\partial t}+\int_{\Gamma^{Fe}}\left[C_{\mathrm{l_F l_F}}\boldsymbol{N}_{sF}{}^{T}\boldsymbol{N}_{sF}\right]d\Gamma^{Fe}\frac{\partial \boldsymbol{u}_{\mathrm{lF}}}{\partial t}$$
$$+\int_{\Gamma^{Fe}}\left[C_{\mathrm{l_F T_F}}\boldsymbol{N}_{sF}{}^{T}\boldsymbol{N}_{sF}\right]d\Gamma^{Fe}\frac{\partial \boldsymbol{T}_{\mathrm{F}}}{\partial t}+\int_{\Gamma^{Fe}}\left[K_{\mathrm{l_F l_F}}\nabla_{l}\boldsymbol{N}_{sF}{}^{T}\nabla_{l}\boldsymbol{N}_{sF}\right]d\Gamma^{Fe}\boldsymbol{u}_{\mathrm{lF}}$$
$$-\boldsymbol{N}_{sF}{}^{T}\left[f_{\mathrm{l,F}}\right]\Big|_{L_1}^{L_2}=0 \qquad (4.36)$$

The finite element formulations of the governing equation for water transfer in matrix continuum can be rewritten in a concise matrix notation, given as:

$$\sum_{j=1}^{n_g}\mathbf{C}_{\mathrm{l_m c_m}}\frac{\partial \boldsymbol{c}_{\mathrm{m}}^{j}}{\partial t}+\sum_{j=1}^{n_g}\mathbf{C}_{\mathrm{l_m c_f}}\frac{\partial \boldsymbol{c}_{\mathrm{f}}^{j}}{\partial t}+\mathbf{C}_{\mathrm{l_m l_m}}\frac{\partial \boldsymbol{u}_{\mathrm{lm}}}{\partial t}+\mathbf{C}_{\mathrm{l_m l_f}}\frac{\partial \boldsymbol{u}_{\mathrm{lf}}}{\partial t}+\mathbf{C}_{\mathrm{l_m T_m}}\frac{\partial \boldsymbol{T}_{\mathrm{m}}}{\partial t}+$$
$$\mathbf{C}_{\mathrm{l_m T_f}}\frac{\partial T_{\mathrm{f}}}{\partial t}+\mathbf{C}_{\mathrm{l_m u_s}}\frac{\partial \mathbf{u}_{\mathrm{s}}}{\partial t}+\mathbf{K}_{\mathrm{l_m l_m}}\boldsymbol{u}_{\mathrm{lm}}=\mathbf{f}_{\mathrm{lm}} \qquad (4.37)$$

where:

$$\mathbf{C}_{\mathrm{l_m c_m}}=\sum_{e=1}^{n_{elem}}\int_{\Omega^e}\left[C_{\mathrm{l_m c_m}}\boldsymbol{N}_s{}^{T}\boldsymbol{N}_s\right]d\Omega^e \qquad (4.37a)$$

$$\mathbf{C}_{\mathrm{l_m c_f}}=\sum_{e=1}^{n_{elem}}\int_{\Omega^e}\left[C_{\mathrm{l_m c_f}}\boldsymbol{N}_s{}^{T}\boldsymbol{N}_s\right]d\Omega^e \qquad (4.37b)$$

$$\mathbf{C}_{\mathrm{l_m l_m}}=\sum_{e=1}^{n_{elem}}\int_{\Omega^e}\left[C_{\mathrm{l_m l_m}}\boldsymbol{N}_s{}^{T}\boldsymbol{N}_s\right]d\Omega^e \qquad (4.37c)$$

$$\mathbf{C}_{\mathrm{l_m l_f}}=\sum_{e=1}^{n_{elem}}\int_{\Omega^e}\left[C_{\mathrm{l_m l_f}}\boldsymbol{N}_s{}^{T}\boldsymbol{N}_s\right]d\Omega^e \qquad (4.37d)$$

$$\mathbf{C}_{\mathrm{l_m T_m}}=\sum_{e=1}^{n_{elem}}\int_{\Omega^e}\left[C_{\mathrm{l_m T_m}}\boldsymbol{N}_s{}^{T}\boldsymbol{N}_s\right]d\Omega^e \qquad (4.37e)$$

$$\mathbf{C}_{\mathrm{l_m T_f}}=\sum_{e=1}^{n_{elem}}\int_{\Omega^e}\left[C_{\mathrm{l_m T_f}}\boldsymbol{N}_s{}^{T}\boldsymbol{N}_s\right]d\Omega^e \qquad (4.37f)$$

$$\mathbf{C}_{\mathrm{l_m u_s}} = \sum_{e=1}^{n_{elem}} \int_{\Omega^e} \left[C_{\mathrm{l_m u_s}} \boldsymbol{N}_s{}^T \boldsymbol{N}_s \right] d\Omega^e \tag{4.37g}$$

$$\mathbf{K}_{\mathrm{l_m l_m}} = \sum_{e=1}^{n_{elem}} \int_{\Omega^e} \left[K_{\mathrm{l_m l_m}} \nabla \boldsymbol{N}_s{}^T \nabla \boldsymbol{N}_s \right] d\Omega^e \tag{4.37h}$$

$$\mathbf{f}_{\mathrm{l,m}} = \sum_{e=1}^{n_{elem}} \int_{\Gamma^e} \boldsymbol{N}_s{}^T \left[f_{\mathrm{l,m}} \right] \underline{n} d\Gamma^e \tag{4.37i}$$

Based on the principle of superposition, the finite element formula of governing equations for water transfer in fracture continuum and discrete fracture domain are combined, the following is obtained:

$$\sum_{j=1}^{n_g} \mathbf{C}^{\mathrm{fF}}_{\mathrm{l_f c_m}} \frac{\partial \boldsymbol{c}^j_{\mathrm{m}}}{\partial t} + \sum_{j=1}^{n_g} \mathbf{C}^{\mathrm{fF}}_{\mathrm{l_f c_f}} \frac{\partial \boldsymbol{c}^j_{\mathrm{f}}}{\partial t} + \mathbf{C}^{\mathrm{fF}}_{\mathrm{l_f l_m}} \frac{\partial \boldsymbol{u}_{\mathrm{lm}}}{\partial t} + \mathbf{C}^{\mathrm{fF}}_{\mathrm{l_f l_f}} \frac{\partial \boldsymbol{u}_{\mathrm{lf}}}{\partial t} + \mathbf{C}^{\mathrm{fF}}_{\mathrm{l_f T_m}} \frac{\partial \boldsymbol{T}_{\mathrm{m}}}{\partial t} + \mathbf{C}^{\mathrm{fF}}_{\mathrm{l_f T_f}} \frac{\partial \boldsymbol{T}_{\mathrm{f}}}{\partial t} + \mathbf{C}^{\mathrm{fF}}_{\mathrm{l_f u_s}} \frac{\partial \mathbf{u}_{\mathrm{s}}}{\partial t} + \mathbf{K}^{\mathrm{fF}}_{\mathrm{l_f l_f}} \boldsymbol{u}_{lf} = \mathbf{f}_{\mathrm{l,fF}} \tag{4.38}$$

where

$$\mathbf{C}^{\mathrm{fF}}_{\mathrm{l_f c_m}} = \sum_{e=1}^{n_{elem}} \int_{\Omega^e} \left[C_{\mathrm{l_f c_m}} \boldsymbol{N}_s{}^T \boldsymbol{N}_s \right] d\Omega^e \tag{4.38a}$$

$$\mathbf{C}^{\mathrm{fF}}_{\mathrm{l_f c_f}} = \sum_{e=1}^{n_{elem}} \int_{\Omega^e} \left[C_{\mathrm{l_f c_f}} \boldsymbol{N}_s{}^T \boldsymbol{N}_s \right] d\Omega^e + \sum_{e=1}^{n_{eleF}} \int_{\Gamma^{Fe}} \left[C_{\mathrm{l_F c_F}} \boldsymbol{N}_{sF}{}^T \mathbf{R}^T \mathbf{R} \boldsymbol{N}_{sF} \right] d\Gamma^{Fe} \tag{4.38b}$$

$$\mathbf{C}^{\mathrm{fF}}_{\mathrm{l_f l_m}} = \sum_{e=1}^{n_{elem}} \int_{\Omega^e} \left[C_{\mathrm{l_f c_m}} \boldsymbol{N}_s{}^T \boldsymbol{N}_s \right] d\Omega^e \tag{4.38c}$$

$$\mathbf{C}^{\mathrm{fF}}_{\mathrm{l_f l_f}} = \sum_{e=1}^{n_{elem}} \int_{\Omega^e} \left[C_{\mathrm{l_f l_f}} \boldsymbol{N}_s{}^T \boldsymbol{N}_s \right] d\Omega^e + \sum_{e=1}^{n_{eleF}} \int_{\Gamma^{Fe}} \left[C_{\mathrm{l_F l_F}} \boldsymbol{N}_{sF}{}^T \mathbf{R}^T \mathbf{R} \boldsymbol{N}_{sF} \right] d\Gamma^{Fe} \tag{4.38d}$$

$$\mathbf{C}^{\mathrm{fF}}_{\mathrm{l_f T_m}} = \sum_{e=1}^{n_{elem}} \int_{\Omega^e} \left[C_{\mathrm{l_f T_m}} \boldsymbol{N}_s{}^T \boldsymbol{N}_s \right] d\Omega^e \tag{4.38e}$$

$$\mathbf{C}^{\mathrm{fF}}_{\mathrm{l_f T_f}} = \sum_{e=1}^{n_{elem}} \int_{\Omega^e} \left[C_{\mathrm{l_f T_f}} \boldsymbol{N}_s{}^T \boldsymbol{N}_s\right] d\Omega^e + \sum_{e=1}^{n_{eleF}} \int_{\Gamma^{Fe}} \left[C_{\mathrm{l_F T_F}} \boldsymbol{N}_{sF}{}^T \mathbf{R}^T \mathbf{R} \boldsymbol{N}_{sF}\right] d\Gamma^{Fe} \qquad (4.38f)$$

$$\mathbf{C}^{\mathrm{fF}}_{\mathrm{l_f u_s}} = \sum_{e=1}^{n_{elem}} \int_{\Omega^e} \left[C_{\mathbf{l_u s},\mathrm{f}} \boldsymbol{N}_s{}^T \boldsymbol{N}_s\right] d\Omega^e \qquad (4.38g)$$

$$\mathbf{K}^{\mathrm{fF}}_{\mathrm{l_f l_f}} = \sum_{e=1}^{n_{elem}} \int_{\Omega^e} \left[K_{\mathrm{l_f l_f}} \nabla \boldsymbol{N}_s{}^T \nabla \boldsymbol{N}_s\right] d\Omega^e + \sum_{e=1}^{n_{eleF}} \int_{\Gamma^{Fe}} \left[K_{\mathrm{l_F l_F}} \nabla_l \boldsymbol{N}_{sF}{}^T \mathbf{R}^T \mathbf{R} \nabla_l \boldsymbol{N}_{sF}\right] d\Gamma^{Fe} \qquad (4.38h)$$

$$\mathbf{f}_{\mathrm{l,fF}} = \sum_{e=1}^{n_{elem}} \int_{\Gamma^e} \boldsymbol{N}_s{}^T \left[f_{\mathrm{l,f}}\right] \underline{n} d\Gamma^e + f_{\mathrm{l,F}} \boldsymbol{N}_f^T \Big|_{L_1}^{L_2} \qquad (4.38i)$$

where $\mathbf{f}_{\mathrm{l},\alpha}$ is the approximate total pore water flux normal to the boundary surface.

4.2.3 Spatial discretisation of governing equations for heat transfer

Similarly, considering the sink/source term for heat exchange between continua suing the SNIA and substitution of the approximate values of temperature into governing equations for heat transfer yields:

$$\sum_{j=1}^{n_g} C_{\mathrm{T_m c_m}} \frac{\partial \hat{c}_{\mathrm{m}}^j}{\partial t} + C_{\mathrm{T_m T_m}} \frac{\partial \hat{T}_{\mathrm{m}}}{\partial t} = \nabla \cdot \left(K_{\mathrm{T_m T_m}} \nabla \hat{T}_{\mathrm{m}}\right) + K^{\mathrm{v}}_{\mathrm{T_m T_m}} \nabla \hat{T}_{\mathrm{m}} + \sum_{j=1}^{n_g} \mathrm{K}^{\mathrm{v}}_{\mathrm{T_m c_m}} \nabla \hat{c}_{\mathrm{m}}^j \qquad (4.39)$$

$$\sum_{j=1}^{n_g} C_{T_{\mathrm{f}} c_{\mathrm{f}}} \frac{\partial \hat{c}_{\mathrm{f}}^j}{\partial t} + C_{T_{\mathrm{f}} T_{\mathrm{f}}} \frac{\partial \hat{T}_{\mathrm{f}}}{\partial t} = \nabla \cdot \left(K_{T_{\mathrm{f}} T_{\mathrm{f}}} \nabla \hat{T}_{\mathrm{f}}\right) + K^{\mathrm{v}}_{T_{\mathrm{f}} T_{\mathrm{f}}} \nabla \hat{T}_{\mathrm{f}} + \sum_{j=1}^{n_g} K^{\mathrm{v}}_{T_{\mathrm{f}} c_{\mathrm{f}}} \nabla \hat{c}_{\mathrm{f}}^j \qquad (4.40)$$

$$\sum_{j=1}^{n_g} C_{\mathrm{T_F c_F}} \frac{\partial \hat{c}_{\mathrm{F}}^j}{\partial t} + C_{\mathrm{T_F T_F}} \frac{\partial \hat{T}_F}{\partial t} = \nabla_l \cdot \left(K_{\mathrm{T_F T_F}} \nabla \hat{T}_{\mathrm{F}}\right) + K^{\mathrm{v}}_{\mathrm{T_F T_F}} \nabla_l \hat{T}_{\mathrm{F}} + \sum_{j=1}^{n_g} K^{\mathrm{v}}_{\mathrm{T_F c_F}} \nabla_l \hat{c}_{\mathrm{F}}^j \qquad (4.41)$$

Using the Galerkin weighted residual approach and integrating over the element area, equations (4.39) – (4.41) become:

$$\int_{\Omega}\left[N_r\left[\begin{array}{c}-\sum_{j=1}^{n_g} C_{\mathrm{T_m c_m}}\frac{\partial \hat{c}_{\mathrm{m}}^{j}}{\partial t}-C_{\mathrm{T_m T_m}}\frac{\partial \hat{T}_{\mathrm{m}}}{\partial t}\\ +\sum_{j=1}^{n_g} K_{\mathrm{T_m c_m}}^{\mathrm{v}}\nabla \hat{c}_{\mathrm{m}}^{j}+K_{\mathrm{T_m T_m}}^{\mathrm{v}}\nabla \hat{T}_{\mathrm{m}}\end{array}\right]+\right.\left.\begin{array}{c}\\ -K_{\mathrm{T_m T_m}}\widehat{\nabla}\hat{T}_{\mathrm{m}}\nabla N_r\end{array}\right]d\Omega+\int_{\Gamma} N_r\left[K_{\mathrm{T_m T_m}}\nabla \hat{T}_{\mathrm{m}}\right]\underline{n}\,d\Gamma=0 \quad (4.42)$$

$$\int_{\Omega}\left[N_r\left[\begin{array}{c}-\sum_{j=1}^{n_g} C_{T_{\mathrm{f}}c_{\mathrm{f}}}\frac{\partial \hat{c}_{\mathrm{f}}^{j}}{\partial t}-C_{T_{\mathrm{f}}c_{\mathrm{f}}}\frac{\partial \hat{T}_{\mathrm{f}}}{\partial t}\\ +\sum_{j=1}^{n_g} \mathrm{K}_{\mathrm{T_f c_f}}^{\mathrm{v}}\nabla \hat{c}_{\mathrm{f}}^{j}+K_{\mathrm{T_f T_f}}^{\mathrm{v}}\nabla \hat{T}_{\mathrm{f}}\end{array}\right]+\right.\left.\begin{array}{c}\\ -K_{T_{\mathrm{f}}T_{\mathrm{f}}}\nabla \hat{T}_{\mathrm{f}}\nabla N_r\end{array}\right]d\Omega+\int_{\Gamma} N_r\left[K_{\mathrm{T_f T_f}}\nabla \hat{T}_{\mathrm{f}}\right]\underline{n}\,d\Gamma=0 \quad (4.43)$$

$$\int_{\Omega}\left[N_r\left[\begin{array}{c}-\sum_{j=1}^{n_g} C_{\mathrm{T_F c_F}}\frac{\partial \hat{c}_{\mathrm{F}}^{j}}{\partial t}-C_{\mathrm{T_F T_F}}\frac{\partial \hat{T}_{F}}{\partial t}\\ +\sum_{j=1}^{n_g} K_{\mathrm{T_F c_F}}^{\mathrm{v}}\nabla_l \hat{c}_{\mathrm{F}}^{j}+K_{\mathrm{T_F T_F}}^{\mathrm{v}}\nabla_l \hat{T}_{\mathrm{F}}\end{array}\right]+\right.\left.\begin{array}{c}\\ -K_{\mathrm{T_F T_F}}\nabla_l \hat{T}_{\mathrm{F}}\nabla_l N_r\end{array}\right]d\Omega+\int_{\Gamma} N_r\left[K_{\mathrm{T_F T_F}}\nabla_l \hat{T}_{\mathrm{F}}\right]\underline{n}\,d\Gamma=0 \quad (4.44)$$

Introducing and expanding expressions for the derivatives of the primary variables, equations (4.42) - (4.44) are rewritten using vector notation as:

$$\begin{aligned}\sum_{j=1}^{n_g}\int_{\Omega^e}\left[C_{\mathrm{T_m c_m}}\boldsymbol{N}_s{}^{T}\boldsymbol{N}_s\right]d\Omega^e\frac{\partial \boldsymbol{c}_{\mathrm{m}}^{j}}{\partial t}+\int_{\Omega^e}\left[C_{\mathrm{T_m T_m}}\boldsymbol{N}_s{}^{T}\boldsymbol{N}_s\right]d\Omega^e\frac{\partial \boldsymbol{T}_{\mathrm{m}}}{\partial t}\\ +\int_{\Omega^e}\left[K_{\mathrm{T_m T_m}}\nabla\boldsymbol{N}_s{}^{T}\nabla\boldsymbol{N}_s\right]d\Omega^e\boldsymbol{T}_{\mathrm{m}}-\int_{\Omega^e}\left[K_{\mathrm{T_m T_m}}^{\mathrm{v}}\boldsymbol{N}_s{}^{T}\nabla\boldsymbol{N}_s\right]d\Omega^e\boldsymbol{T}_{\mathrm{m}}\\ -\sum_{j=1}^{n_g}\int_{\Omega^e}\left[K_{\mathrm{T_m c_m}}^{\mathrm{v}}\boldsymbol{N}_s{}^{T}\nabla\boldsymbol{N}_s\right]d\Omega^e\boldsymbol{c}_{\mathrm{m}}^{j}-\int_{\Gamma^e}\boldsymbol{N}_s{}^{T}\left[f_{\mathrm{T,m}}\right]\underline{n}\,d\Gamma^e=0\end{aligned} \quad (4.45)$$

$$\sum_{j=1}^{n_g}\int_{\Omega^e}\left[C_{T_{\mathrm{f}}c_{\mathrm{f}}}\boldsymbol{N}_s{}^T\boldsymbol{N}_s\right]d\Omega^e\frac{\partial \boldsymbol{c}_{\mathrm{f}}^j}{\partial t}+\int_{\Omega^e}\left[C_{T_{\mathrm{f}}c_{\mathrm{f}}}\boldsymbol{N}_s{}^T\boldsymbol{N}_s\right]d\Omega^e\frac{\partial \boldsymbol{T}_{\mathrm{f}}}{\partial t}+\int_{\Omega^e}\left[K_{T_{\mathrm{f}}T_{\mathrm{f}}}\nabla\boldsymbol{N}_s{}^T\nabla\boldsymbol{N}_s\right]d\Omega^e\boldsymbol{T}_{\mathrm{f}}$$
$$-\int_{\Omega^e}\left[K^{\mathrm{v}}_{\mathrm{T_f T_f}}\boldsymbol{N}_s{}^T\nabla\boldsymbol{N}_s\right]d\Omega^e\boldsymbol{T}_{\mathrm{f}}-\sum_{j=1}^{n_g}\int_{\Omega^e}\left[K^{\mathrm{v}}_{\mathrm{T_f c_f}}\boldsymbol{N}_s{}^T\nabla\boldsymbol{N}_s\right]d\Omega^e\boldsymbol{c}_{\mathrm{f}}^j$$
$$-\int_{\Gamma^e}\boldsymbol{N}_s{}^T\left[f_{\mathrm{T,f}}\right]\underline{n}\,d\Gamma^e=0 \tag{4.46}$$

$$\sum_{j=1}^{n_g}\int_{\Gamma^{Fe}}\left[C_{\mathrm{T_F c_F}}\boldsymbol{N}_{sF}{}^T\boldsymbol{N}_{sF}\right]d\Gamma^{Fe}\frac{\partial \boldsymbol{c}_{\mathrm{F}}^j}{\partial t}+\int_{\Gamma^{Fe}}\left[C_{\mathrm{T_F T_F}}\boldsymbol{N}_{sF}{}^T\boldsymbol{N}_{sF}\right]d\Gamma^{Fe}\frac{\partial \boldsymbol{T}_{\mathrm{F}}}{\partial t}$$
$$+\int_{\Gamma^{Fe}}\left[K_{\mathrm{t_F t_F}}\nabla_l\boldsymbol{N}_{sF}{}^T\nabla_l\boldsymbol{N}_{sF}\right]d\Gamma^{Fe}\boldsymbol{T}_{\mathrm{F}}-\int_{\Omega^e}\left[K^{\mathrm{v}}_{\mathrm{T_F T_F}}\boldsymbol{N}_{sF}{}^T\nabla_l\boldsymbol{N}_{sF}\right]d\Gamma^{Fe}\boldsymbol{T}_{\mathrm{F}}$$
$$-\sum_{j=1}^{n_g}\int_{\Omega^e}\left[K^{\mathrm{v}}_{\mathrm{T_F c_F}}\boldsymbol{N}_{sF}{}^T\nabla_l\boldsymbol{N}_{sF}\right]d\Gamma^{Fe}\boldsymbol{c}_{\mathrm{F}}^j-\boldsymbol{N}_{sF}{}^T\left[f_{\mathrm{T,F}}\right]\Big|_{L_1}^{L_2}=0 \tag{4.47}$$

The spatial discretisation of the governing equations for the heat transfer in terms of primary variables T_α for a matrix continuum domain is given as:

$$\sum_{j=1}^{n_g}\mathbf{C}_{\mathrm{T_m c_m}}\frac{\partial \boldsymbol{c}_{\mathrm{m}}^j}{\partial t}+\mathbf{C}_{\mathrm{T_m T_m}}\frac{\partial \boldsymbol{T}_{\mathrm{m}}}{\partial t}+\sum_{j=1}^{n_g}\mathbf{K}^{\mathrm{v}}_{\mathrm{T_m c_m}}\boldsymbol{c}_{\mathrm{m}}^j+\left(\mathbf{K}_{\mathrm{T_m T_m}}+\mathbf{K}^{\mathrm{v}}_{\mathrm{T_m T_m}}\right)\boldsymbol{T}_{\mathrm{m}}=\mathbf{f}_{\mathrm{T,m}} \tag{4.48}$$

where:

$$\mathbf{C}_{\mathrm{T_m c_m}}=\sum_{e=1}^{n_{elem}}\int_{\Omega^e}\left[C_{\mathrm{T_m c_m}}\boldsymbol{N}_s{}^T\boldsymbol{N}_s\right]d\Omega^e \tag{4.48a}$$

$$\mathbf{C}_{\mathrm{T_m T_m}}=\sum_{e=1}^{n_{elem}}\int_{\Omega^e}\left[C_{\mathrm{T_m T_m}}\boldsymbol{N}_s{}^T\boldsymbol{N}_s\right]d\Omega^e \tag{4.48b}$$

$$\mathbf{K}^{\mathrm{v}}_{\mathrm{T_m c_m}}=\sum_{e=1}^{n_{elem}}\int_{\Omega^e}\left[-K^{\mathrm{v}}_{\mathrm{T_m c_m}}\boldsymbol{N}_s{}^T\nabla\boldsymbol{N}_s\right]d\Omega^e \tag{4.48c}$$

$$\mathbf{K}_{\mathrm{T_m T_m}}=\sum_{e=1}^{n_{elem}}\int_{\Omega^e}\left[K_{\mathrm{T_m T_m}}\nabla\boldsymbol{N}_s{}^T\nabla\boldsymbol{N}_s\right]d\Omega^e \tag{4.48d}$$

$$\mathbf{K}^{\mathrm{v}}_{\mathrm{T_m T_m}} = \sum_{e=1}^{n_{elem}} \int_{\Omega^e} \left[-K^{\mathrm{v}}_{\mathrm{T_m T_m}} \boldsymbol{N}_s{}^T \nabla \boldsymbol{N}_s\right] d\Omega^e \tag{4.48e}$$

$$\mathbf{f}_{\mathrm{T,m}} = \sum_{e=1}^{n_{elem}} \int_{\Gamma^e} \boldsymbol{N}_s{}^T \left[f_{\mathrm{T,m}}\right] \underline{n} d\Gamma^e \tag{4.48f}$$

Application of principle of superposition, the discretisation of governing equations for heat transfer in fracture continuum and large fracture domains is obtained:

$$\sum_{j=1}^{n_g} \mathbf{C}^{\mathrm{fF}}_{\mathrm{T_f c_f}} \frac{\partial \boldsymbol{c}^j_{\mathrm{f}}}{\partial t} + \mathbf{C}^{\mathrm{fF}}_{\mathrm{T_f T_f}} \frac{\partial \boldsymbol{T}_{\mathrm{f}}}{\partial t} + \mathbf{K}^{\mathrm{v}}_{\mathrm{T_f c_f}} \boldsymbol{c}^j_{\mathrm{f}} + \left(\mathbf{K}^{\mathrm{fF}}_{\mathrm{T_f T_f}} + \mathbf{K}^{\mathrm{v}}_{\mathrm{T_f T_f}}\right) \boldsymbol{T}_{\mathrm{f}} = \mathbf{f}_{\mathrm{T,fF}} \tag{4.49}$$

where:

$$\mathbf{C}^{\mathrm{fF}}_{\mathrm{T_f c_f}} = \sum_{e=1}^{n_{elem}} \int_{\Omega^e} \left[C_{\mathrm{T_f c_f}} \boldsymbol{N}_s{}^T \boldsymbol{N}_s\right] d\Omega^e + \sum_{e=1}^{n_{eleF}} \int_{\Gamma^{Fe}} \left[C_{\mathrm{T_F c_F}} \boldsymbol{N}_{sF}{}^T \mathbf{R}^T \mathbf{R} \boldsymbol{N}_{sF}\right] d\Gamma^{Fe} \tag{4.49a}$$

$$\mathbf{C}^{\mathrm{fF}}_{\mathrm{T_f T_f}} = \sum_{e=1}^{n_{elem}} \int_{\Omega^e} \left[C_{\mathrm{T_f T_f}} \boldsymbol{N}_s{}^T \boldsymbol{N}_s\right] d\Omega^e + \sum_{e=1}^{n_{eleF}} \int_{\Gamma^{Fe}} \left[C_{\mathrm{T_F T_F}} \boldsymbol{N}_{sF}{}^T \mathbf{R}^T \mathbf{R} \boldsymbol{N}_{sF}\right] d\Gamma^{Fe} \tag{4.49b}$$

$$\mathbf{K}^{\mathrm{v}}_{\mathrm{T_f c_f}} = \sum_{e=1}^{n_{elem}} \int_{\Omega^e} \left[-K^{\mathrm{v}}_{\mathrm{T_f c_f}} \boldsymbol{N}_s{}^T \nabla \boldsymbol{N}_s\right] d\Omega^e + \sum_{e=1}^{n_{eleF}} \int_{\Gamma^{Fe}} \left[-K^{\mathrm{v}}_{\mathrm{T_F c_F}} \boldsymbol{N}_{sF}{}^T \mathbf{R}^T \mathbf{R} \nabla \boldsymbol{N}_{sF}\right] d\Gamma^{Fe} \tag{4.49c}$$

$$\mathbf{K}^{\mathrm{fF}}_{\mathrm{T_f T_f}} = \sum_{e=1}^{n_{elem}} \int_{\Omega^e} \left[K_{\mathrm{T_f T_f}} \nabla \boldsymbol{N}_s{}^T \nabla \boldsymbol{N}_s\right] d\Omega^e + \sum_{e=1}^{n_{eleF}} \int_{\Gamma^{Fe}} \left[K_{\mathrm{T_F T_F}} \nabla \boldsymbol{N}_s{}^T \boldsymbol{N}_{sF}{}^T \mathbf{R}^T \mathbf{R} \nabla \boldsymbol{N}_{sF}\right] d\Gamma^{Fe} \tag{4.49d}$$

$$\mathbf{K}^{\mathrm{v}}_{\mathrm{T_f T_f}} = \sum_{e=1}^{n_{elem}} \int_{\Omega^e} \left[-K^{\mathrm{v}}_{\mathrm{T_f T_f}} \boldsymbol{N}_s{}^T \nabla \boldsymbol{N}_s\right] d\Omega^e + \sum_{e=1}^{n_{eleF}} \int_{\Gamma^{Fe}} \left[-K^{\mathrm{v}}_{\mathrm{T_F T_F}} \boldsymbol{N}_s{}^T \boldsymbol{N}_{sF}{}^T \mathbf{R}^T \mathbf{R} \nabla \boldsymbol{N}_{sF}\right] d\Gamma^{Fe} \tag{4.49e}$$

$$\mathbf{f}_{\mathrm{T,fF}} = \sum_{e=1}^{n_{elem}} \int_{\Gamma^e} \boldsymbol{N}_s{}^T \left[f_{\mathrm{T,f}}\right] \underline{n} d\Gamma^e + f_{\mathrm{T,F}} \boldsymbol{N}^T_{sF} \Big|_{L_1}^{L_2} \tag{4.49f}$$

where $\mathbf{f}_{\mathrm{T,fF}}$ is the approximate total pore water flux normal to the boundary surface.

4.2.4 Spatial discretisation of governing equations for deformation

The general method of spatial discretisation for displacement variables is the same as for flow variables, as described in section 4.2.1. The governing equation for displacement, with substitution from equations (4.1) and (4.2), can be expressed using the shape functions as:

$$\sum_{j=1}^{n_g} C_{\mathbf{u}_s \mathrm{c}_m} d\hat{c}_{\mathrm{m}}^{j} + \sum_{j=1}^{n_g} C_{\mathbf{u}_s \mathrm{c}_f} d\hat{c}_{\mathrm{f}}^{j} + C_{\mathbf{u}_s \mathrm{l}_m} d\hat{u}_{\mathrm{lm}} + C_{\mathbf{u}_s \mathrm{l}_f} d\hat{u}_{\mathrm{lf}} + C_{\mathbf{u}_s \mathrm{T}_m} d\hat{T}_{\mathrm{m}} + C_{\mathbf{u}_s \mathrm{T}_f} d\hat{T}_{\mathrm{f}} + C_{\mathbf{u}_s \mathbf{u}_s} d\hat{\mathbf{u}}_{\mathrm{s}} = R_{\Omega} \qquad (4.50)$$

Application of the Galerkin weighted residual method is intended to minimise error over the element domain Ω^e using the shape functions, N_r, as weighting coefficients, which yields:

$$\int_{\Omega^e} N_r \left[\sum_{j=1}^{n_g} C_{\mathbf{u}_s \mathrm{c}_m} d\hat{c}_{\mathrm{m}}^{j} + \sum_{j=1}^{n_g} C_{\mathbf{u}_s \mathrm{c}_f} d\hat{c}_{\mathrm{f}}^{j} + C_{\mathbf{u}_s \mathrm{l}_m} d\hat{u}_{\mathrm{lm}} + C_{\mathbf{u}_s \mathrm{l}_f} d\hat{u}_{\mathrm{lf}} + C_{\mathbf{u}_s \mathrm{T}_m} d\hat{T}_m + C_{\mathbf{u}_s \mathrm{T}_f} d\hat{T}_f + C_{\mathbf{u}_s \mathbf{u}_s} d\hat{\mathbf{u}}_{\mathrm{s}} \right] d\Omega^e = 0 \qquad (4.51)$$

Integrating by parts and with substitution from section 3.6 yields the weak form, for example the first term becomes:

$$\begin{aligned} \int_{\Omega^e} N_r \, C_{\mathbf{u}_s \mathrm{c}_m} d\hat{c}_{\mathrm{m}}^{j} d\Omega^e &= \int_{\Omega^e} N_r \, \mathbf{B}^{\boldsymbol{T}} \left[\mathbf{m} \tilde{\mathfrak{b}}_1 S_{\mathrm{gm}} Z_{\mathrm{m}} R T_{\mathrm{m}} - \frac{1}{3} \boldsymbol{D}_{\mathrm{mf}} \mathbf{m} A_s^j \right] d\hat{c}_{\mathrm{m}}^{j} d\Omega^e \\ &= - \int_{\Omega^e} \mathbf{B}^{\boldsymbol{T}} N_r \left[\mathbf{m} \tilde{\mathfrak{b}}_1 S_{\mathrm{gm}} Z_{\mathrm{m}} R T_{\mathrm{m}} - \frac{1}{3} \boldsymbol{D}_{\mathrm{mf}} \mathbf{m} A_s^j \right] d\hat{c}_{\mathrm{m}}^{j} d\Omega^e \\ &+ \int_{\Omega^e} \mathbf{B}^{\boldsymbol{T}} \left[N_r \mathbf{m} \tilde{\mathfrak{b}}_1 S_{\mathrm{gm}} Z_{\mathrm{m}} R T_{\mathrm{m}} - \frac{1}{3} N_r \boldsymbol{D}_{\mathrm{mf}} \mathbf{m} A_s^j \right] d\hat{c}_{\mathrm{m}}^{j} d\Omega^e \end{aligned} \qquad (4.52)$$

where $\mathbf{B}^{\boldsymbol{T}} N_r$ can be expressed as:

$$\boldsymbol{P} = \begin{bmatrix} \frac{\partial N_r}{\partial x} & 0 & 0 & \frac{\partial N_r}{\partial y} & 0 & \frac{\partial N_r}{\partial z} \\ 0 & \frac{\partial N_r}{\partial y} & 0 & \frac{\partial N_r}{\partial x} & \frac{\partial N_r}{\partial z} & 0 \\ 0 & 0 & \frac{\partial N_r}{\partial z} & 0 & \frac{\partial N_r}{\partial y} & \frac{\partial N_r}{\partial x} \end{bmatrix} \qquad (4.53)$$

Following the same procedure as for the first term, the weak form of the remaining terms in equation (4.20) can be obtained, giving:

$$
\begin{aligned}
&-\int_{\Omega^e} \boldsymbol{P}\left[\mathbf{m}\tilde{\mathfrak{b}}_1 S_{gm} Z_m R T_m - \frac{1}{3}\boldsymbol{D}_{mf}\mathbf{m}\sum_{j=1}^{n_g} A_s^j\right] d\hat{c}_{\mathrm{m}}^j d\Omega^e \\
&\quad + \int_{\Omega^e} \mathbf{B}^{\boldsymbol{T}}\left[N_r\mathbf{m}\tilde{\mathfrak{b}}_1 S_{\mathrm{gm}} Z_{\mathrm{m}} R T_{\mathrm{m}} - \frac{1}{3}N_r\boldsymbol{D}_{\mathrm{mf}}\mathbf{m}\sum_{j=1}^{n_g} A_s^j\right] d\hat{c}_{\mathrm{m}}^j d\Omega^e \\
&\quad - \int_{\Omega^e} \boldsymbol{P}\left[\mathbf{m}\tilde{\mathfrak{b}}_2 S_{\mathrm{gf}} Z_{\mathrm{f}} R T_{\mathrm{f}}\right] d\hat{c}_{\mathrm{f}}^j d\Omega^e + \int_{\Omega^e} \mathbf{B}^{\boldsymbol{T}}\left[N_r\mathbf{m}\tilde{\mathfrak{b}}_2 S_{\mathrm{gf}} Z_{\mathrm{f}} R T_{\mathrm{f}}\right] d\hat{c}_{\mathrm{f}}^j d\Omega^e \\
&\quad - \int_{\Omega^e} \boldsymbol{P}[\mathbf{m}\tilde{\mathfrak{b}}_1 S_{\mathrm{lm}}] d\hat{u}_{\mathrm{lm}} d\Omega^e + \int_{\Omega^e} \mathbf{B}^{\boldsymbol{T}}[N_r\mathbf{m}\tilde{\mathfrak{b}}_1 S_{\mathrm{lm}}] d\hat{u}_{\mathrm{lm}} d\Omega^e \\
&\quad - \int_{\Omega^e} \boldsymbol{P}[\mathbf{m}\tilde{\mathfrak{b}}_2 S_{\mathrm{lf}}] d\hat{u}_{\mathrm{lf}} d\Omega^e + \int_{\Omega^e} \mathbf{B}^{\boldsymbol{T}}[N_r\mathbf{m}\tilde{\mathfrak{b}}_2 S_{\mathrm{lf}}] d\hat{u}_{\mathrm{lf}} d\Omega^e \\
&\quad - \int_{\Omega^e} \boldsymbol{P}\left[\mathbf{m}\tilde{\mathfrak{b}}_1 S_{\mathrm{gm}} Z_{\mathrm{m}} R \sum_{j=1}^{n_g} c_{\mathrm{m}}^j - \frac{1}{3}\boldsymbol{D}_{\mathrm{e}}\mathbf{m}A_T\right] d\hat{T}_{\mathrm{m}} d\Omega^e \\
&\quad + \int_{\Omega^e} \mathbf{B}^{\boldsymbol{T}}\left[N_r\mathbf{m}\tilde{\mathfrak{b}}_1 S_{\mathrm{gm}} Z_{\mathrm{m}} R \sum_{j=1}^{n_g} c_{\mathrm{m}}^j - \frac{1}{3}N_r\boldsymbol{D}_{\mathrm{mf}}\mathbf{m}A_T\right] d\hat{T}_{\mathrm{m}} d\Omega^e \\
&\quad - \int_{\Omega^e} \boldsymbol{P}\left[\mathbf{m}\tilde{\mathfrak{b}}_2\, S_{\mathrm{gf}} Z_{\mathrm{f}} R \sum_{j=1}^{n_g} c_{\mathrm{f}}^j\right] d\hat{T}_{\mathrm{f}} d\Omega^e \\
&\quad + \int_{\Omega^e} \mathbf{B}^{\boldsymbol{T}}\left[N_r\mathbf{m}\tilde{\mathfrak{b}}_2\, S_{\mathrm{gf}} Z_{\mathrm{f}} R \sum_{j=1}^{n_g} c_{\mathrm{gf}}^j\right] d\hat{T}_{\mathrm{f}} d\Omega^e - \int_{\Omega^e} \boldsymbol{P}[\boldsymbol{D}_{\mathrm{e}}\mathbf{B}] d\hat{\mathbf{u}}_{\mathrm{s}} d\Omega^e \\
&\quad + \int_{\Omega^e} \mathbf{B}^{\boldsymbol{T}}[N_r\boldsymbol{D}_{\mathrm{e}}\mathbf{B}] d\hat{\mathbf{u}}_{\mathrm{s}} d\Omega^e = 0
\end{aligned}
\tag{4.54}
$$

The Gauss-Green divergence theorem may be applied to equation (3.190), producing the surface integrals and yielding:

$$
\begin{aligned}
&-\int_{\Omega^e} \boldsymbol{P}\left[\mathbf{m}\tilde{\mathfrak{b}}_1 S_{\mathrm{gm}} Z_{\mathrm{m}} R T_{\mathrm{m}} - \frac{1}{3}\boldsymbol{D}_{\mathrm{mf}}\mathbf{m}\sum_{j=1}^{n_g} A_s^j\right] d\hat{c}_{\mathrm{m}}^j d\Omega^e \\
&\quad + \int_{\Gamma^e}\left[N_r\mathbf{m}\tilde{\mathfrak{b}}_1 S_{\mathrm{gm}} Z_{\mathrm{m}} R T_{\mathrm{m}} - \frac{1}{3}N_r\boldsymbol{D}_{\mathrm{mf}}\mathbf{m}\sum_{j=1}^{n_g} A_s^j\right] d\hat{c}_{\mathrm{m}}^j \underline{n} d\Gamma^e \\
&\quad - \int_{\Omega^e} \boldsymbol{P}\left[\mathbf{m}\tilde{\mathfrak{b}}_2 S_{\mathrm{gf}} Z_{\mathrm{f}} R T_{\mathrm{f}}\right] d\hat{c}_{\mathrm{f}}^j d\Omega^e + \int_{\Gamma^e}\left[N_r\mathbf{m}\tilde{\mathfrak{b}}_2 S_{\mathrm{gf}} Z_{\mathrm{f}} R T_{\mathrm{f}}\right] d\hat{c}_{\mathrm{f}}^j \underline{n} d\Gamma^e \\
&\quad - \int_{\Omega^e} \boldsymbol{P}[\mathbf{m}\tilde{\mathfrak{b}}_1 S_{\mathrm{lm}}] d\hat{u}_{\mathrm{lm}} d\Omega^e + \int_{\Gamma^e}[N_r\mathbf{m}\tilde{\mathfrak{b}}_1 S_{\mathrm{lm}}] d\hat{u}_{\mathrm{lm}}\underline{n} d\Gamma^e \\
&\quad - \int_{\Omega^e} \boldsymbol{P}[\mathbf{m}\tilde{\mathfrak{b}}_2 S_{\mathrm{lf}}] d\hat{u}_{\mathrm{lf}} d\Omega^e + \int_{\Gamma^e}[N_r\mathbf{m}\tilde{\mathfrak{b}}_2 S_{\mathrm{lf}}] d\hat{u}_{\mathrm{lf}}\underline{n} d\Gamma^e \\
&\quad - \int_{\Omega^e} \boldsymbol{P}\left[\mathbf{m}\tilde{\mathfrak{b}}_1 S_{\mathrm{gm}} Z_{\mathrm{m}} R\sum_{j=1}^{n_g} c_{\mathrm{m}}^j - \frac{1}{3}\boldsymbol{D}_{\mathrm{mf}}\mathbf{m}A_T\right] d\hat{T}_{\mathrm{m}} d\Omega^e \\
&\quad + \int_{\Gamma^e}\left[N_r\mathbf{m}\tilde{\mathfrak{b}}_1 S_{\mathrm{gm}} Z_{\mathrm{m}} R\sum_{j=1}^{n_g} c_{\mathrm{m}}^j - \frac{1}{3}N_r\boldsymbol{D}_{\mathrm{e}}\mathbf{m}A_T\right] d\hat{T}_{\mathrm{m}}\underline{n} d\Gamma^e \\
&-\int_{\Omega^e} \boldsymbol{P}\left[\mathbf{m}\tilde{\mathfrak{b}}_2 S_{\mathrm{gf}} Z_{\mathrm{f}} R\sum_{j=1}^{n_g} c_{\mathrm{f}}^j\right] d\hat{T}_{\mathrm{f}} d\Omega^e + \int_{\Gamma^e}\left[N_r\mathbf{m}\tilde{\mathfrak{b}}_2 S_{\mathrm{gf}} Z_{\mathrm{f}} R\sum_{j=1}^{n_g} c_{\mathrm{f}}^j\right] d\hat{T}_{\mathrm{f}}\underline{n} d\Gamma^e \\
&-\int_{\Omega^e} \boldsymbol{P}[\boldsymbol{D}_{\mathrm{e}}\mathbf{B}] d\hat{\mathbf{u}}_{\mathrm{s}} d\Omega^e + \int_{\Gamma^e}[N_r\boldsymbol{D}_{\mathrm{e}}\mathbf{B}] d\hat{\mathbf{u}}_{\mathrm{s}}\underline{n} d\Gamma^e = 0
\end{aligned}
\tag{4.55}
$$

The surface integrals in equation (4.55) may be simplified to:

$$
\int_{\Gamma^e} N_r \begin{bmatrix}
\left[\mathbf{m}\tilde{\mathfrak{b}}_1 S_{\mathrm{gm}} Z_{\mathrm{m}} R T_{\mathrm{m}} - \frac{1}{3}\boldsymbol{D}_{\mathrm{e}}\mathbf{m}\sum_{j=1}^{n_g} A_s^j\right] d\hat{c}_{\mathrm{m}}^j \\
\left[\mathbf{m}\tilde{\mathfrak{b}}_2 S_{\mathrm{gf}} Z_{\mathrm{f}} R T_{\mathrm{f}}\right] d\hat{c}_{\mathrm{f}}^j + [\mathbf{m}\tilde{\mathfrak{b}}_1 S_{\mathrm{lm}}] d\hat{u}_{\mathrm{lm}} \\
[\mathbf{m}\tilde{\mathfrak{b}}_2 S_{\mathrm{lf}}] d\hat{u}_{\mathrm{lf}} + \left[\mathbf{m}\tilde{\mathfrak{b}}_1 S_{\mathrm{gm}} Z_{\mathrm{m}} R\sum_{j=1}^{n_g} c_{\mathrm{m}}^j - \frac{1}{3}\boldsymbol{D}_{\mathrm{e}}\mathbf{m}A_T\right] d\hat{T}_{\mathrm{m}} \\
\left[\mathbf{m}\tilde{\mathfrak{b}}_2 S_{\mathrm{gf}} Z_{\mathrm{f}} R\sum_{i=1}^{n_g} c_{\mathrm{f}}^i\right] d\hat{T}_{\mathrm{f}} + [\boldsymbol{D}_{\mathrm{e}}\mathbf{B}] d\hat{\mathbf{u}}_{\mathrm{s}}
\end{bmatrix} \underline{n} d\Gamma^e
$$

$$
= \int_{\Gamma^e}\left[N_r\underline{\hat{T}_r}\right] d\Gamma^e \tag{4.56}
$$

where $\underline{\widehat{T_r}}$ is the external traction forces on the boundary Γ^e.

Substituting the shape function from equation (4.1) and equation (4.56) into equation (4.55) yields:

$$\int_{\Omega^e} \boldsymbol{P}\left[\mathbf{m}\tilde{\mathfrak{b}}_1 S_{\mathrm{gm}} Z_{\mathrm{m}} R T_{\mathrm{m}} - \frac{1}{3}\boldsymbol{D}_{\mathrm{mf}}\mathbf{m}\sum_{j=1}^{n_g} A_s^j\right]\boldsymbol{N}d\Omega^e d\boldsymbol{c}_{\mathrm{m}}^j + \int_{\Omega^e}\boldsymbol{P}\left[\mathbf{m}\tilde{\mathfrak{b}}_2 S_{\mathrm{gf}} Z_{\mathrm{f}} R T_{\mathrm{f}}\right]\boldsymbol{N}d\Omega^e\, d\boldsymbol{c}_{\mathrm{f}}^j$$
$$+ \int_{\Omega^e}\boldsymbol{P}[\mathbf{m}\tilde{\mathfrak{b}}_1 S_{\mathrm{lm}}]\boldsymbol{N}d\Omega^e d\boldsymbol{u}_{\mathrm{lm}} + \int_{\Omega^e}\boldsymbol{P}[\mathbf{m}\tilde{\mathfrak{b}}_2 S_{\mathrm{lf}}]\boldsymbol{N}d\Omega^e d\boldsymbol{u}_{\mathrm{lf}}$$
$$+ \int_{\Omega^e}\boldsymbol{P}\left[\mathbf{m}\tilde{\mathfrak{b}}_1 S_{\mathrm{gm}} Z_{\mathrm{m}} R\sum_{j=1}^{n_g} c_{\mathrm{m}}^j - \frac{1}{3}\boldsymbol{D}_{\mathrm{e}}\mathbf{m}A_T\right]\boldsymbol{N}d\Omega^e\, d\boldsymbol{T}_{\mathrm{m}}$$
$$+ \int_{\Omega^e}\boldsymbol{P}\left[\mathbf{m}\tilde{\mathfrak{b}}_2\, S_{\mathrm{gf}} Z_{\mathrm{f}} R\sum_{j=1}^{n_g} c_{\mathrm{f}}^j\right]\boldsymbol{N}d\Omega^e d\boldsymbol{T}_{\mathrm{f}} + \int_{\Omega^e}[\boldsymbol{P}\boldsymbol{D}_{\mathrm{e}}\mathbf{P}^{\boldsymbol{T}}]d\Omega^e d\mathbf{u}_{\mathrm{s}}$$
$$= \int_{\Gamma^e}\left[N_r\underline{\widehat{T_r}}\right]d\Gamma^e \tag{4.57}$$

Equation (4.57) must be used in incremental form for transient analysis, found by multiplying the constants by the gradient of time. Doing this and expressing in concise matrix form yields:

$$\sum_{j=1}^{n_g}\mathbf{C}_{\mathbf{u}_{\mathrm{s}}\mathrm{c}_{\mathrm{m}}}\frac{\partial\boldsymbol{c}_m^j}{\partial t} + \sum_{j=1}^{n_g}\mathbf{C}_{\mathbf{u}_{\mathrm{s}}\mathrm{c}_{\mathrm{f}}}\frac{\partial\boldsymbol{c}_{\mathrm{f}}^j}{\partial t} + C_{\mathbf{u}_{\mathrm{s}}\mathrm{l}_{\mathrm{m}}}\frac{\partial\boldsymbol{u}_{\mathrm{lm}}}{\partial t} + C_{\mathbf{u}_{\mathrm{s}}\mathrm{l}_{\mathrm{f}}}\frac{\partial\boldsymbol{u}_{\mathrm{lf}}}{\partial t}$$
$$+ C_{\mathbf{u}_{\mathrm{s}}\mathrm{T}_{\mathrm{m}}}\frac{\partial\boldsymbol{T}_{\mathrm{m}}}{\partial t} + C_{\mathbf{u}_{\mathrm{s}}\mathrm{T}_{\mathrm{f}}}\frac{\partial\boldsymbol{T}_{\mathrm{f}}}{\partial t} + \mathbf{C}_{\mathbf{u}_{\mathrm{s}}\mathbf{u}_{\mathrm{s}}}\frac{\partial\mathbf{u}_{\mathrm{s}}}{\partial t} = \mathbf{f}_{\mathbf{u}_{\mathrm{s}}} \tag{4.58}$$

$$\mathbf{C}_{\mathbf{u}_{\mathrm{s}}\mathrm{c}_{\mathrm{m}}} = \sum_{e=1}^{n_{elem}}\int_{\Omega^e}\boldsymbol{P}\left[\mathbf{m}\tilde{\mathfrak{b}}_1 S_{\mathrm{gm}} Z_{\mathrm{m}} R T_{\mathrm{m}} - \frac{1}{3}\boldsymbol{D}_{\mathrm{e}}\mathbf{m}A_s^j\right]\boldsymbol{N}d\Omega^e \tag{4.58a}$$

$$\mathbf{C}_{\mathbf{u}_{\mathrm{s}}\mathrm{c}_{\mathrm{f}}} = \sum_{e=1}^{n_{elem}}\int_{\Omega^e}\boldsymbol{P}\left[\mathbf{m}\tilde{\mathfrak{b}}_2 S_{\mathrm{gf}} Z_{\mathrm{f}} R T_{\mathrm{f}}\right]\boldsymbol{N}d\Omega^e \tag{4.58b}$$

$$\boldsymbol{C}_{\mathbf{u}_{\mathrm{s}}\mathrm{l}_{\mathrm{m}}} = \sum_{e=1}^{n_{elem}}\int_{\Omega^e}\boldsymbol{P}[\mathbf{m}\tilde{\mathfrak{b}}_1 S_{\mathrm{lm}}]\boldsymbol{N}d\Omega^e \tag{4.58c}$$

$$\boldsymbol{C}_{\mathbf{u}_\mathrm{s}\mathrm{l}_\mathrm{f}} = \sum_{e=1}^{n_{elem}} \int_{\Omega^e} \boldsymbol{P}[\mathbf{m}\tilde{\mathrm{b}}_2 S_{\mathrm{lf}}]\boldsymbol{N}d\Omega^e \tag{4.58d}$$

$$\boldsymbol{C}_{\mathbf{u}_\mathrm{s}\mathrm{T}_\mathrm{m}} = \sum_{e=1}^{n_{elem}} \boldsymbol{P}\left[\mathbf{m}\tilde{\mathrm{b}}_1 S_{\mathrm{gm}} Z_\mathrm{m} R \sum_{j=1}^{n_g} c_\mathrm{m}^j - \frac{1}{3}\boldsymbol{D}_\mathrm{e}\mathbf{m}A_T\right]\boldsymbol{N}d\Omega^e \tag{4.58e}$$

$$\boldsymbol{C}_{\mathbf{u}_\mathrm{s}\mathrm{T}_\mathrm{f}} = \sum_{e=1}^{n_{elem}} \boldsymbol{P}\left[\mathbf{m}\tilde{\mathrm{b}}_2\, S_{\mathrm{gf}} Z_\mathrm{f} R \sum_{j=1}^{n_g} c_\mathrm{f}^j\right]\boldsymbol{N}d\Omega^e \tag{4.58f}$$

$$\mathbf{C}_{\mathbf{u}_\mathrm{s}\mathbf{u}_\mathrm{s}} = \sum_{e=1}^{n_{elem}} \int_{\Omega^e} [\boldsymbol{P}\boldsymbol{D}_{\mathrm{mf}}\mathbf{P}^{\boldsymbol{T}}]d\Omega^e \tag{4.58g}$$

$$\mathbf{f}_{\mathbf{u}_\mathrm{s}} = \sum_{e=1}^{n_{elem}} \int_{\Gamma^e} \left[N_r \underline{\widehat{T}_r}\right] d\Gamma^e \tag{4.58h}$$

4.3 Temporal discretisation

In order to determine the value of the primary variables over time, a numerical algorithm for temporal discretisation has been employed. In the present work, a fully implicit mid-interval backward-difference time-stepping algorithm is used. This has been found as a suitable solution for highly non-linear class of equations such as the current application problems (Thomas *et al.* 1998; Cook 2007).

Section 4.2 has developed a set of spatially discretised equations for multicomponent gas transport, water flow, heat transfer, and deformation. These equations can be presented in a matrix form, as shown in Figure 4.3. Using compact notation, the matrix equation in Figure 4.3 can conveniently be expressed as:

$$\boldsymbol{A}\phi + \boldsymbol{B}\frac{\partial \phi}{\partial t} + \mathbf{C} = \{\mathbf{0}\} \tag{4.59}$$

where $\boldsymbol{A}$, $\boldsymbol{B}$ and $\mathbf{C}$ are the matrices of coefficients and ϕ is the vector of variables.

$\boldsymbol{u}_{\mathrm{lf}}$, $\boldsymbol{T}_\mathrm{m}$, $\boldsymbol{T}_\mathrm{f}$ and $\mathbf{u}$ represent the time differentials of gas concentrations, water pressure, temperature, and deformation variables respectively. For convenience, the multicomponent system is represented by the superscript $1 \rightarrow \mathrm{n_g}$.

$$\begin{bmatrix} \mathbf{C}_{c_m c_m} & \mathbf{C}_{c_m c_f} & \mathbf{C}_{c_m l_m} & 0 & \mathbf{C}_{c_m T_m} & \mathbf{C}_{c_m T_f} & \mathbf{C}_{c_m u_s} \\ \mathbf{C}^{fF}_{c_f c_m} & \mathbf{C}^{fF}_{c_f c_f} & 0 & \mathbf{C}^{fF}_{c_f l_f} & \mathbf{C}^{fF}_{c_f T_m} & \mathbf{C}^{fF}_{c_f T_f} & \mathbf{C}^{fF}_{c_f u_s} \\ \mathbf{C}_{l_m c_m} & \mathbf{C}_{l_m c_f} & \mathbf{C}_{l_m l_m} & 0 & \mathbf{C}_{l_m T_m} & \mathbf{C}_{l_m T_f} & \mathbf{C}_{l_m u_s} \\ \mathbf{C}^{fF}_{l_f c_m} & \mathbf{C}^{fF}_{l_f c_f} & 0 & \mathbf{C}^{fF}_{l_f l_f} & \mathbf{C}^{fF}_{l_f T_m} & \mathbf{C}^{fF}_{l_f T_f} & \mathbf{C}^{fF}_{l_f u_s} \\ \mathbf{C}_{T_m c_m} & 0 & 0 & 0 & \mathbf{C}_{T_m T_m} & 0 & 0 \\ 0 & \mathbf{C}^{fF}_{T_f c_f} & 0 & 0 & 0 & \mathbf{C}^{fF}_{T_f T_f} & 0 \\ \mathbf{C}_{u_s c_m} & \mathbf{C}_{u_s c_f} & \mathbf{C}_{u_s l_m} & \mathbf{C}_{u_s l_f} & \mathbf{C}_{u_s T_m} & \mathbf{C}_{u_s T_f} & \mathbf{C}_{u_s u_s} \end{bmatrix} \times \begin{bmatrix} \dot{\boldsymbol{c}}_m^{1\to n_g} \\ \dot{\boldsymbol{c}}_f^{1\to n_g} \\ \dot{\boldsymbol{u}}_{lm} \\ \dot{\boldsymbol{u}}_{lf} \\ \dot{\boldsymbol{T}}_m \\ \dot{\boldsymbol{T}}_f \\ \dot{\mathbf{u}}_s \end{bmatrix} +$$

$$\begin{bmatrix} 0 & 0 & 0 & 0 & 0 & 0 & 0 \\ 0 & \mathbf{K}^{fF}_{c_f c_f} & 0 & 0 & 0 & \mathbf{K}^{fF}_{c_f T_f} & 0 \\ 0 & 0 & \mathbf{K}_{l_m l_m} & 0 & 0 & 0 & 0 \\ 0 & 0 & 0 & \mathbf{K}^{fF}_{l_f l_f} & 0 & 0 & 0 \\ \mathbf{K}^{v}_{T_m c_m} & 0 & 0 & 0 & \mathbf{K}_{T_m T_m} + \mathbf{K}^{v}_{T_m T_m} & 0 & 0 \\ 0 & \mathbf{K}^{v}_{T_f c_f} & 0 & 0 & 0 & \mathbf{K}^{fF}_{T_f T_f} + \mathbf{K}^{v}_{T_f T_f} & 0 \\ 0 & 0 & 0 & 0 & 0 & 0 & 0 \end{bmatrix} \times \begin{bmatrix} \boldsymbol{c}_m^{1\to n_g} \\ \boldsymbol{c}_f^{1\to n_g} \\ \boldsymbol{u}_{lm} \\ \boldsymbol{u}_{lf} \\ \boldsymbol{T}_m \\ \boldsymbol{T}_f \\ \mathbf{u}_s \end{bmatrix} + \begin{bmatrix} \mathbf{f}_{g,m}^{1\to n_g} \\ \mathbf{f}_{g,fF}^{1\to n_g} \\ \mathbf{f}_{l,m} \\ \mathbf{f}_{l,fF} \\ \mathbf{f}_{T,m} \\ \mathbf{f}_{T,fF} \\ \mathbf{f}_{u_s} \end{bmatrix} = \begin{bmatrix} 0 \\ 0 \\ 0 \\ 0 \\ 0 \\ 0 \\ 0 \end{bmatrix}$$

Figure 4.3 Matrix presentation of the numerical formulation.

As earlier reported, the fully implicit mid-interval backward-difference time-stepping algorithm is used for time discretisation of the spatially discretised governing equations, giving:

$$\boldsymbol{A}^{\phi_l}[(1-\Theta)\phi^{n} + \Theta\phi^{n+1}] + \boldsymbol{B}^{\phi_l}\left[\frac{\phi^{n+1}-\phi^{n}}{\Delta t}\right] + \mathbf{C}^{\phi_l} = \{\mathbf{0}\} \tag{4.60}$$

In equation (4.60), Θ is an integration constant equal to 1 for an implicit time integration scheme, 0.5 for a Crank-Nicholson scheme, and 0 for an explicit scheme. The superscript parameter $\boldsymbol{\phi_l}$ denotes the level at which the matrices $\boldsymbol{A}$, $\boldsymbol{B}$, and $\mathbf{C}$ are evaluated, and can be expressed in general as:

$$\phi_l = \varkappa(n+1) + (1-\varkappa)n \tag{4.61}$$

where $\varkappa$ is a constant, which controls the interval for which matrices $\boldsymbol{A}$, $\boldsymbol{B}$, and $\mathbf{C}$ are evaluated. In this work, a fully implicit, mid-interval algorithm is used, hence Θ and $\varkappa$ take the values of 1 and 0.5 respectively.

Substitution of these constants into equation (4.60) yields:

$$\boldsymbol{A}^{n+1/2}\phi^{\mathrm{n+1}} + \boldsymbol{B}^{n+1/2}\left[\frac{\phi^{\mathrm{n+1}} - \phi^{\mathrm{n}}}{\Delta t}\right] + \mathbf{C}^{n+1/2} = \{\mathbf{0}\} \tag{4.62}$$

Equation (4.62) can be rearranged to give:

$$\phi^{\mathrm{n+1}} = \left[\boldsymbol{A}^{n+1/2} + \frac{\boldsymbol{B}^{n+1/2}}{\Delta t}\right]^{-1}\left[\frac{\boldsymbol{B}^{n+1/2}\phi^{\mathrm{n}}}{\Delta t} - \mathbf{C}^{n+1/2}\right] \tag{4.63}$$

Equation (4.63) cannot be solved directly. To obtain the solution for $\phi^{\mathrm{n+1}}$, the values of the matrices of coefficient are required to be determined at the mid-interval and an iterative solution procedure is necessary. In the current work, a predictor-corrector algorithm is employed, described by the following steps:

i. Matrices $\boldsymbol{A}$, $\boldsymbol{B}$, and $\mathbf{C}$ are evaluated at time n, the first estimate is termed the predictor.

ii. The predictor and the previous time step are then used to calculate the $\boldsymbol{A}$, $\boldsymbol{B}$, and $\mathbf{C}$ at the mid-interval time $n + 1/2$, producing an estimate termed the corrector.

iii. Convergence is checked by either of the following conditions:

$$\left|\phi_{iC}^{n+1} - \phi_{(i-1)C}^{n+1}\right| < \boldsymbol{TL}_{abs} \tag{4.64}$$

$$\left|\frac{\phi_{iC}^{n+1} - \phi_{(i-1)C}^{n+1}}{\phi_{(i-1)C}^{n+1}}\right| < \boldsymbol{TL}_{rel} \tag{4.65}$$

where i is the iteration level, C denotes that the corrector value has been used, and $\boldsymbol{TL}_{abs}$ and $\boldsymbol{TL}_{rel}$ are the matrices of absolute and relative tolerances for each variable. The stress equilibrium is also checked to ensure the residual force is within a tolerance value. The residual force, ζ, can be obtained as (Owen 1980):

$$\int_{\Omega} \mathbf{P}^{\boldsymbol{T}} \Delta\boldsymbol{\sigma}\, d\Omega - \Delta F = \zeta \tag{4.66}$$

iv. If either the convergence criterion has not been satisfied or the residual stress is large in stage (iii), the algorithm returns to stage (ii) where the corrector becomes the new predictor. If convergence is achieved or the residual force stays within the tolerance limit, the algorithm moves to the next time step where the process repeats.

The number of iterations required to achieve convergence depends on a number of factors, such as the simulation conditions, the variable gradients, material parameters, and the size of the time step. In order to improve the efficiency of the solution procedure, a variable

timestep is allowed. If the number of iterations exceeds a specified value, the timestep is reduced by a factor. Conversely, if fewer iterations than specified are required to achieve convergence, the timestep is increased by a factor.

This model has been incorporated in a computer code COMPASS, the **CO**de for **M**odelling **PA**rtially **S**aturated **S**oils, which has been incrementally developed at the Geoenvironmental Research Centre (GRC), Cardiff University (e.g. Thomas *et al.* 1998).

To solve numerically the set of nonlinear partial differential equations, appropriate boundary conditions are required. Thomas and He (1995) discussed various types of boundary conditions that can be adopted in the formulation, including:

i. Dirichlet condition (prescribed primary variable $\omega_\alpha = \omega_\alpha^*$ on boundaryΓ^d)
ii. Neumann condition (prescribed flux $J_\alpha = J_\alpha^*$, stress $\tilde{t} = \tilde{t}^*$ on boundary Γ^n, Γ^t)
iii. Cauchy condition (prescribed convection condition on boundary Γ^c)

4.4 Coupling between transport and exchange/reaction terms

As mentioned earlier in the chapter, the coupling of the transport term with the mass and heat exchange term is realised by using the sequential non-iterative approach (SNIA) in the governing flow equations. Time splitting methods have been proposed and applied successfully for coupling the transport model, i.e. COMPASS, with geochemical reaction models such as MINTEQA2 and PHREEQC (Seetharam 2003; Seetharam *et al.* 2007; Sedighi 2011; Masum 2012; Hosking 2014). Details about the coupling with external models have been provided in the cited literature. Since the mass and heat exchange between the fracture and matrix continua are incorporated into COMPASS modules, this section explains the SNIA used to couple these modules with the transport module.

Sequential methods have been developed to overcome the large computational cost associated with solving the transport and reaction terms simultaneously, which is referred to as the global implicit approach (KEE *et al.* 1985; Steefel and Lasaga 1994). The time splitting SNIA completes the transport stage and exchange stage sequentially in each timestep (Steefel and MacQuarrie 1996). In other words, the mass and heat exchange models are calculated after the transport equations are solved. A coupled solution at each timestep is obtained once the transport solution have achieved convergence and then been modified

for the mass and heat exchange, and then the analysis moves onto the next timestep and the procedure is repeated.

The convergence check performed after each iterative solution of the conservative transport equations can be expressed mathematically as (Steefel and MacQuarrie 1996):

$$\left(c_{g\alpha}^{i}\right)^{Transport} - \left(c_{g\alpha}^{i}\right)^{n} = L\left(\boldsymbol{J}_{c_{g\alpha}^{i}}\right)^{n} \tag{4.67}$$

where the superscript n denotes the time step and L is the spatial operator applying to the fluxes $\boldsymbol{J}_{c_{g\alpha}^{i}}$.

In equation (4.67), the changes in chemical concentrations associated with the transport processes are obtained using the values obtained from the previous time step, n. The new values are then modified to account for the inter-continua mass and heat exchange, giving the following expressions for chemical concentration, water pressure, and temperature:

$$\frac{\left(c_{g\alpha}^{i}\right)^{Exchange} - \left(c_{g\alpha}^{i}\right)^{Transport}}{\Delta t} = R_{gi}^{Ex} \tag{4.68}$$

$$\frac{\left(u_{w\alpha}\right)^{Exchange} - \left(u_{w\alpha}\right)^{Transport}}{\Delta t} = R_{l}^{Ex} \tag{4.69}$$

$$\frac{\left(T_{\alpha}\right)^{Exchange} - \left(T_{\alpha}\right)^{Transport}}{\Delta t} = R_{T}^{Ex} \tag{4.70}$$

where R_{gi}^{Ex} and R_{l}^{Ex} denote the rate of mass exchange between the fracture and matrix continua for the chemical component and pore water, respectively, and R_{T}^{Ex} denotes the rate of heat exchange between the fracture and matrix continua.

A flowchart of the entire process of coupling transport and mass/heat exchange with the SNIA is presented in Figure 4.4.

4.5 Conclusions

A numerical solution of the previously developed governing equations for coupled thermo-hydro-gas-mechanical behaviour has been developed in this chapter. The procedures to obtain the discretised form of the multicomponent gas transport, water flow, heat transfer and deformation equations have been described in detail. The Galerkin finite element method with hybrid dimensional elements has been used for the spatial discretisation of the

governing equations and a backward difference, mid-interval time stepping algorithm has been implemented for temporal discretisation.

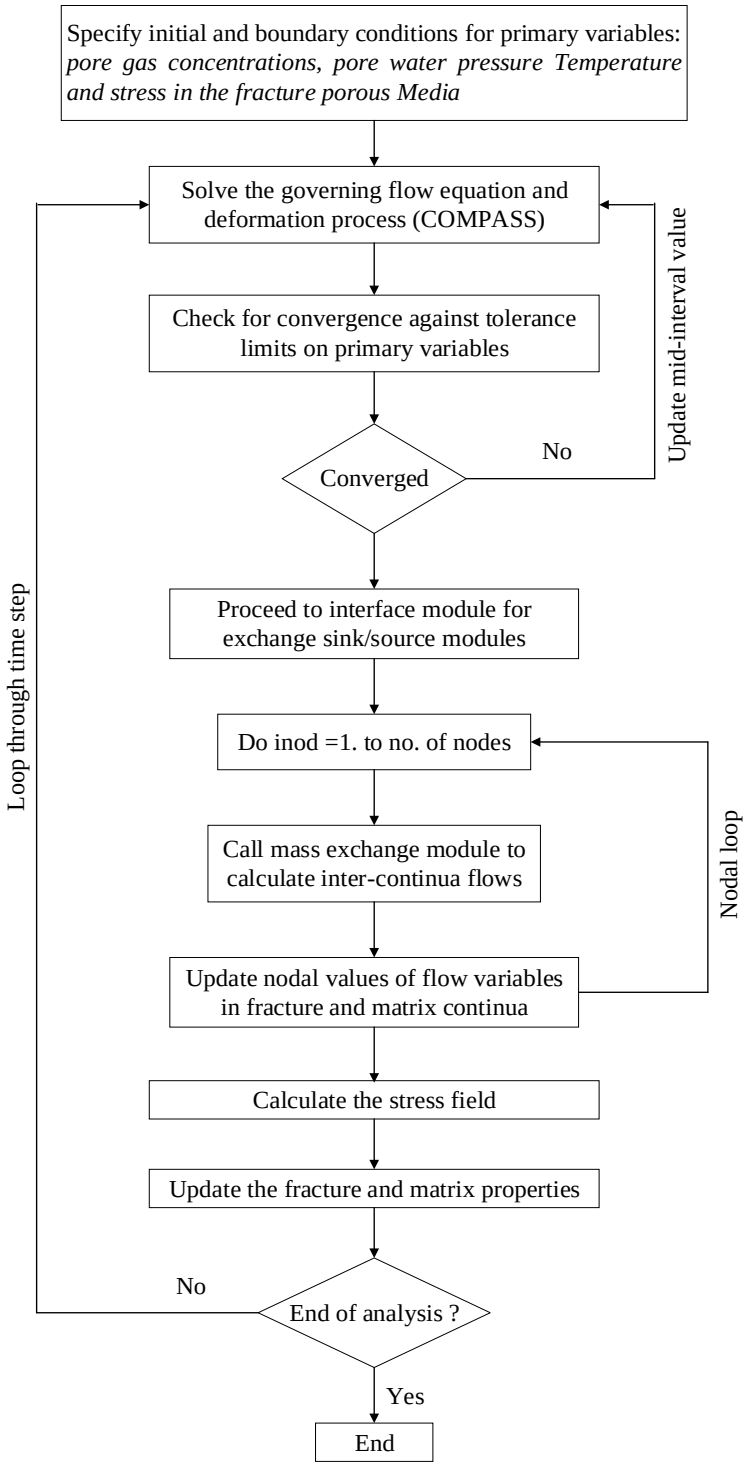

Figure 4.4 Flowchart of the sequential non-iterative approach (SNIA) adopted for coupling the transport and exchange/reaction modules in COMPASS (*after* Hosking 2014).

A sequential non-iterative approach (SNIA) has been adopted to couple the transport model with the sink/source terms from mass/heat exchange. The implementation of this coupling technique has been described in detail. The numerical formulation described in this chapter has been incorporated into an existing computer code COMPASS, which has been developed at the Geoenvironmental Research Centre, Cardiff University. The numerical solution calculated by COMPASS will be tested and compared with a series of benchmark in the next chapter for the purpose of verification.

4.6 References

Baca, R., Arnett, R. and Langford, D. (1984). Modelling fluid flow in fractured-porous rock masses by finite-element techniques. *International Journal for Numerical Methods in Fluids* **4**(4):337-348.

Chen, M., Hosking, L.J., Sandford, R.J. and Thomas, H.R. (2019b). A coupled compressible flow and geomechanics model for dynamic fracture aperture during carbon sequestration in coal. *International Journal for Numerical and Analytical Methods in Geomechanics* (under review).

Cook, R. D. (2007). *Concepts and applications of finite element analysis*. John Wiley & Sons.

Hosking, L. (2014). Reactive transport modelling of high pressure gas flow in coal. Ph.D Thesis, Cardiff University, Wales, UK.

Huang, J. and Ghassemi, A. (2015). A poroelastic model for evolution of fractured reservoirs during gas production. *Journal of Petroleum Science and Engineering* **135**:626-644.

Karimi-Fard, M. and Firoozabadi, A. (2003). *Numerical Simulation of Water Injection in Fractured Media Using the Discrete Fractured Model and the Galerkin Method. SPEREE 6 (2): 117–126*. SPE-83633-PA.

Kee, R. J., Petzold L. R., Smooke, M. D. and Grcar, J. F. (1985). Implicit methods in combustion and chemical kinetics modeling. In: *Multiple Time Scales*.113-144.

Kolditz, O. (2013). *Computational methods in environmental fluid mechanics*. Springer Science & Business Media.

Masum, S. A. (2012). *Modelling of reactive gas transport in unsaturated soil. A coupled thermo-hydro-chemical-mechanical approach.* Ph.D Thesis, Cardiff University, Wales, UK.

Owen, D. R. J. (1980). Finite elements in plasticity, theory and practice.

Sedighi, M. (2011). *An investigation of hydro-geochemical processes in coupled thermal, hydraulic, chemical and mechanical behaviours of unsaturated soils.* Ph.D Thesis, Cardiff University, Wales, UK.

Seetharam, S., Thomas, H. and Cleall, P. J. (2007). Coupled thermo/hydro/ chemical/ mechanical model for unsaturated soils—Numerical algorithm. *International Journal for Numerical Methods in Engineering* **70**(12):1480-1511.

Seetharam, S. C. (2003). *An investigation of the thermo/hydro/chemical/mechanical behaviour of unsaturated soils.* Cardiff University.

Steefel, C. I. and Lasaga, A. C. (1994). A coupled model for transport of multiple chemical species and kinetic precipitation/dissolution reactions with application to reactive flow in single phase hydrothermal systems. *American Journal of science* **294**(5):529-592.

Steefel, C. I. and MacQuarrie, K. T. (1996). Approaches to modeling of reactive transport in porous media. *Reviews in Mineralogy and Geochemistry* **34**(1):85-129.

Thomas, H. and He, Y. (1995). Analysis of coupled heat, moisture and air transfer in a deformable unsaturated soil. *Geotechnique* **45**(4):677-689.

Thomas, H., Rees, S. and Sloper, N. (1998). Three-dimensional heat, moisture and air transfer in unsaturated soils. *International Journal for Numerical and Analytical Methods in Geomechanics* **22**(2):75-95.

Vardon, P. J. (2009). *Three-dimensional Numerical Investigation of the Thermo-hydro-mechanical Behaviour of a Large-scale Prototype Repository*. Ph.D Thesis, Cardiff University, Wales, UK.

Watanabe, N. (2011). Finite element method for coupled thermo-hydro-mechanical processes in discretely fractured and non-fractured porous media.

Zagorščak, R. (2017). *An investigation of coupled processes in coal in response to high pressure gas injection.* Ph. D. thesis, Cardiff University, Wales, UK.

Zhang, N., Yao, J., Huang, Z. and Wang, Y. (2013). Accurate multiscale finite element method for numerical simulation of two-phase flow in fractured media using discrete-fracture model. *Journal of Computational Physics* **242**:420-438.

Zienkiewicz, O. C., Taylor, R. L. and Zhu, J. Z. (2005). *The finite element method: its basis and fundamentals*.

5

Model Verification

5.1 Introduction

This chapter presents a series of verification tests that have been carried out as part of the research to examine the accuracy of the implementation of the theoretical and numerical formulations in the model and to explore whether the solution algorithm is correct. The verification benchmarks, simulation conditions and results achieved for a range of tests have been described. The verification tests presented in this chapter are closely related with application of the newly developed hybrid model for the investigation of coupled thermo-hydro-gas/chemical-mechanical behaviour of coal during CBM production and CO_2 sequestration.

Section 5.2 presents a verification test to evaluate the implementation of variably saturated flow in a dual-permeability system. The simulations consider two overlaying continua at the macroscopic level, namely, a fracture pore system and a less permeable matrix pore system. Variably saturated flow in the matrix and fracture pore system is described with the Richards's equation. Results are compared with those presented by Kolditz *et al.* (2016) using the numerical code OpenGeoSys (OGS) and S1D_DUAL.

The verification test presented in section 5.3 is applied to examine the gas flow with adsorption/desorption in an isothermal single porosity system. A nonlinear adsorption isotherm is considered in this simulation. To show the effect of gas adsorption behaviour on gas transport, a simulation case without considering gas adsorption is performed as well. The results are compared with the analytical solution derived by Wu *et al.* (2014) to verify that the predicted gas pressure profile follows that expected for transient flow with and without adsorption.

Verification tests for assessing the accuracy of the implementation of the heat transfer equation are presented in section 5.4. Since these tests are concerned with examining the heat advection and conduction mechanisms, the heat exchange between different media is not taken into consideration and the verification test is simplified as heat transport in a single porosity system. This simplification allows comparison to be made with the results obtained using the analytical solution for advective-conductive transport presented by Kolditz *et al.* (2016). In addition, a verification test of the Joule-Thomson cooling processes is performed in this section, with the analytical solution derived by Mathias *et al.* (2010) providing a benchmark for this test.

The aim of section 5.5 is to verify that the numerical model is capable to solve the stress equilibrium equation for an elastic problem. The simulation considers the elastic response outside a cylindrical hole in an infinite elastic medium subjected to a uniform in-situ stress field far from the hole. An analytical solution given by the classical Kirsch solution (e.g. Jaeger *et al.* 2009) for the radial and tangential stress distributions in the vicinity of the cylindrical hole is utilised for this verification exercise.

In section 5.6, two test cases are presented to demonstrate the general capability of the newly developed modelling approach and finite element technique in COMPASS. The test considers flow in porous media with a discrete fracture. This test is conducted to examine the principle of superposition used to deal with thermal, hydraulic and chemical flow problems in the porous medium with discrete fractures. The results are compared with numerical modelling studies presented by Strack (1982).

Section 5.7 deal with the verification of coupled thermo-hydro-mechanical behaviour. Three verification tests are presented in order to check the theoretical components included in the governing equation and constitutive relationships for the flow and deformation behaviour. The first verification exercise considers 1-D consolidation of dual porosity media to examine the coupling between flow and mechanical deformation, with the results of the model compared with analytical solutions provided by Bai and Elsworth (2000). In the second verification, the results of modelling the mechanical behaviour of fractures are examined via similar simulations reported by Moradi *et al.* (2017) and Gu *et al.* (2014). The third verification focuses on the thermo-hydro-mechanical tests induced by thermal loading. This analysis is restricted to a local thermal equilibrium model. The reliability of implementation

of the coupled thermo-hydro-mechanical model into the finite element code is verified by comparison with the analytical solutions by McTigue (1986).

Finally, section 5.8 and 5.9 provides a summary and conclusions from the verification tests.

5.2 Variably saturated flow in a dual permeability system (Test I)

A multiphase, multicomponent transport model is presented in the current work, as discussed in chapter 3. The verification exercises for multicomponent gas transport in fractured rock have been completed by Hosking (2014) and Masum (2012), hence, the verification exercise in this section focuses on the isothermal multiphase flow in fractured rock with uniformly distributed natural fractures. The fractured rock is treated as a dual permeability system. The flow processes in the rock mass are governed by the dual continuum Richards' equations in one dimension, the transport mechanism is governed by viscous flow, details of which are provided in Kolditz *et al.* (2016). Additional transfer terms are introduced to couple flow between dual continua, expressed as:

$$\Gamma_{lfm} = 0.01 * \Lambda^* \frac{K_m}{\mu_l}\left(u_{lf} - u_{lm}\right) \tag{5.1}$$

where Λ^* is the first-order exchange coefficient.

The hydraulic properties of the fracture and matrix pore systems are described with the widely used van Genuchten model (Van Genuchten 1980). The results obtained using COMPASS are compared with those by the dual permeability model OGS and S1D_DUAL.

5.2.1 Simulation conditions

The numerical simulation was performed for a 60 cm long vertical column, which was spatially discretised into 200 equally sized 4-noded quadrilateral elements. The initial and boundary conditions are given in Figure 5.1.

Both the fracture and matrix continua are prescribed a linear pressure gradient as the initial condition, varying from -27440 Pa at the top boundary to -21560 Pa at the bottom boundary. Identical boundary conditions are defined for both continua, with a fixed pressure prescribed at the top boundary and free drainage at the bottom. No flux occurs on the lateral boundaries. A summary of the material parameters used in this verification is provided in Table 5.1, which are chosen from the work of Kolditz *et al.* (2016).

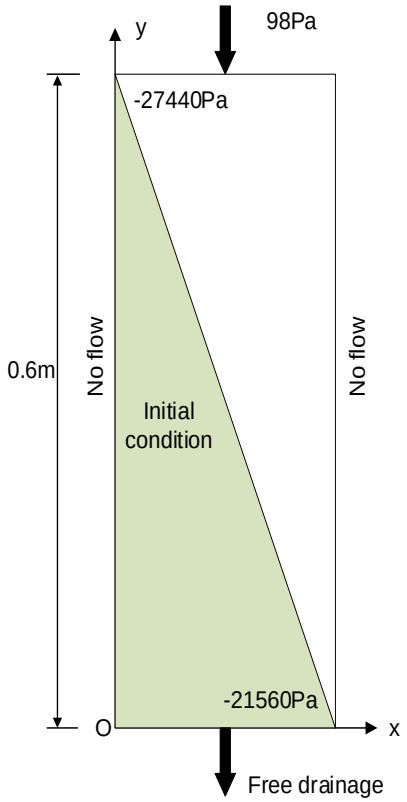

Figure 5.1 Model domain with initial and boundary conditions.

5.2.2 Results and discussion

Figure 5.2 shows the water pressure distributions in the column at the time of 30 min. The corresponding results of OGS and S1D DUAL are collected from the work of Kolditz *et al.* (2016), which are given in Figure 5.2. The pressure fronts in the matrix calculated by COMPASS are illustrated by solid lines and those of the fracture by dashed lines. Due to high permeability of the fracture continuum, the pressure front moves toward the bottom more quickly than for the matrix continuum.

It can be observed that there is a close agreement between the results of the numerical simulation with the benchmarks provided by Kolditz *et al.* (2016), indicating that the dual continuum model and capillary pressure-saturation model have been implemented successfully into the transport model in COMPASS.

Table 5.1 Material parameters used in Test I (Kolditz et al. 2016).

Material parameters	**Relationship/value**
Porosity, n_{f} (-)	0.03
Residual water saturation, S_{lr} (-)	0.0833
Maximum water saturation, S_l (-)	1.0
Van Genuchten parameter, $1/p_0$ (1/m)	5.6
Van Genuchten parameter, γ (-)	2.68
Saturated permeability, K_{f} (m^2)	1.09×10^{-11}
Porosity, n_{m} (-)	0.47
Residual water saturation, S_{lr} (-)	0.0
Maximum water saturation, S_l (-)	1.0
Van Genuchten parameter, $1/p_0$ (1/m)	1.8
Van Genuchten parameter, γ (-)	1.8
Saturated permeability, K_{m}(m^2)	2.32×10^{-13}
Transfer coefficient, α^*($1/\mathrm{m}^2$)	200

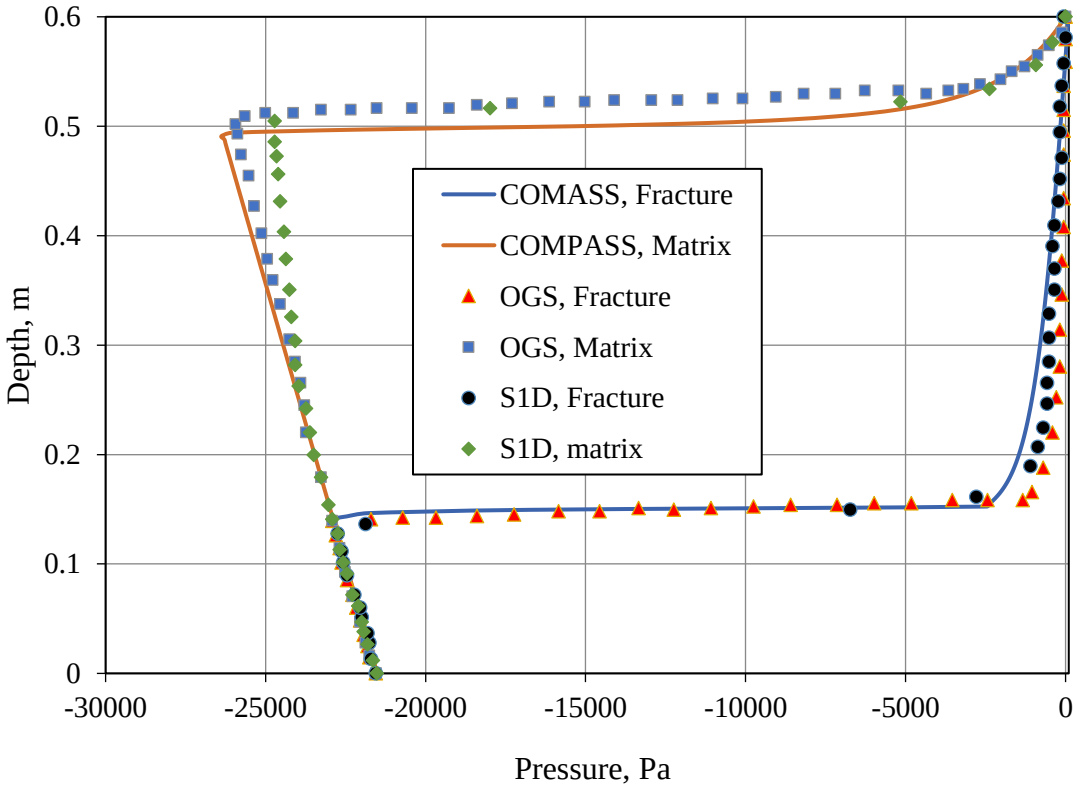

Figure 5.2 Comparison of the pressure distribution after 30 min obtained using COMPASS with the results from two different codes.

5.3 Transient flow of heat (Test III)

Non-isothermal flow is considered in the current work. Heat transport generally occurs due to conduction and convection. In addition, when compressible fluid is considered, the temperature can be disturbed due to fluid expansion, known as the Joule-Thomson cooling effect caused by high pressure gas expansion and viscous heat dissipation, as discussed in chapter 3.5. The verification exercises presented in this section examine conductive-convective transport of heat and the Joule-Thomson cooling effect. In the first verification, pure convection and combined conductive-convective transport are considered separately to show the difference between the transport mechanisms. The results obtained from the numerical model are compared with those from the analytical solution presented by Ogata and Banks (1961). The aim of the second verification is to assess the accuracy of the numerical model in predicting the temperature change caused by the Joule-Thomson cooling effect, with the analytical solution derived by Mathias *et al.* (2010) providing a benchmark for this test.

5.3.1 Heat conduction and convection (Test III-a)

Considering heat transport in single phase by advection and conduction, the heat transport equation (3.92) in chapter 3 can be simplified as:

$$c_p \rho \frac{\partial T}{\partial t} = -c_p \rho \mathbf{v} \cdot \nabla T + \nabla \cdot (\lambda \nabla T) \qquad (5.2)$$

where c_p is specific heat capacity, ρ is density, T is temperature, $\mathbf{v}$ is advection velocity and λ is thermal conductivity.

In order to evaluate the reliability of the solution algorithms for advective flow, a simulation case in which the conduction part of the heat transport process was avoided by minimizing the thermal conductivity of the fluid has been carried out, i.e. the second term on the right-hand side of equation (5.4) is neglected.

5.3.1.1 Simulation conditions

This simulation shows 1D heat transport by conduction and convection in a 100 m long fracture. There is no rock matrix surrounding the fracture considered, as shown in Figure 5.3. The fracture is fully saturated with water, flowing with constant velocity at 3.0×10^{-7} m/s. The simulation domain is discretised into 400 equally sized quadrilateral elements and

the simulation is run for 5.0×10^8 s. Figure 5.3 shows a summary of the initial and boundary conditions that are applied to the domain. The initial temperature of whole domain is 0 ℃, and boundary conditions are prescribed for a fixed temperature of 1 ℃ at the left boundary. The material properties used in this verification is provided in Table 5.3, which are chosen from Kolditz *et al.* (2016).

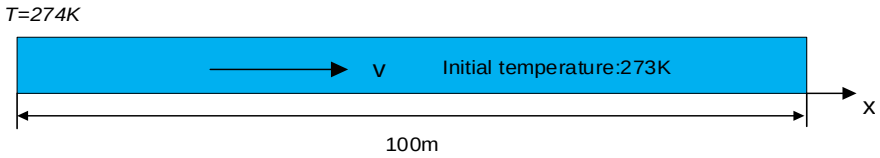

Figure 5.3 A fracture fully saturated with flowing water at constant velocity and a constant temperature at the left boundary.

Table 5.2 Material parameters used in Test III-a (Kolditz et al. 2016).

Material parameters	**Relationship/value**
Density of water, ρ (kg/m^3)	1000
Specific heat capacity, c_p(J/K/kg)	4000
Thermal conductivity of water, λ(W/m/K)	0.6
Water velocity, v (m/s)	3×10^{-7}

5.3.1.2 Results and discussion

The temperature breakthrough curves for conductive-advective transport and only convective heat transport at the end of the fracture at $x = 100$ m have been obtained using the numerical approach and analytical solution by Ogata and Banks (1961), as shown in Figure 5.4 and Figure 5.5. Compared with pure convective heat transport, the inclusion of heat conduction produces a smoother breakthrough curve. It can be seen that the numerical results show acceptable agreement with the analytical solution, especially when the conductive part of the heat transport is incorporated. These results indicate that these heat transport mechanisms have been correctly implemented in the model.

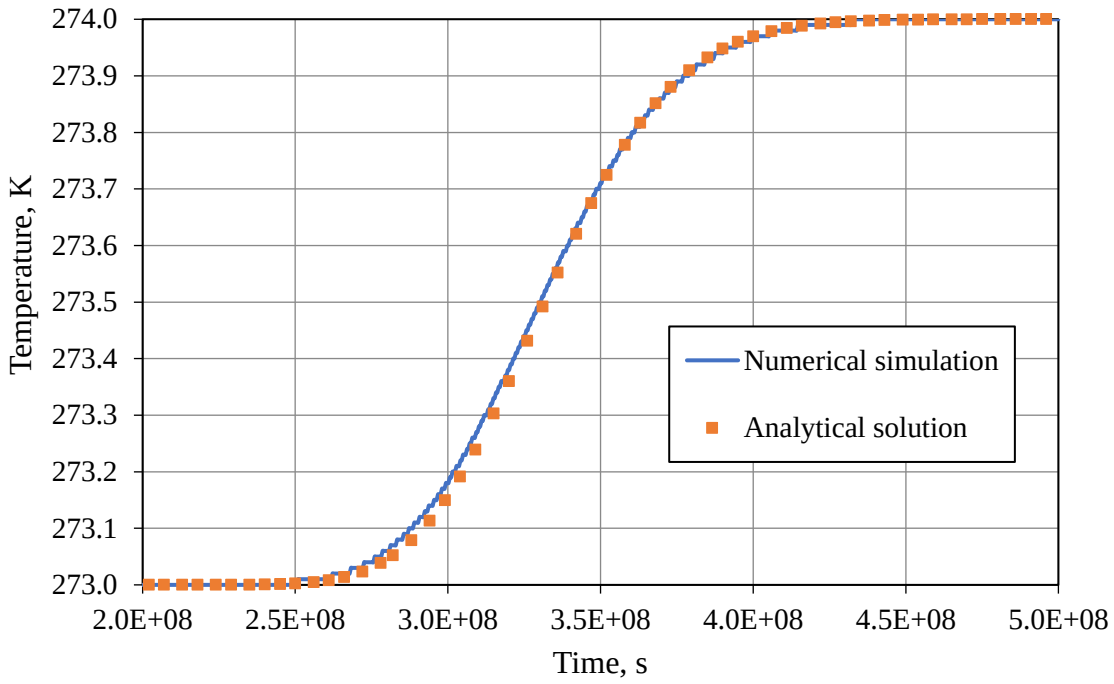

Figure 5.4 Temperature breakthrough curve at $x = 100$ m for conductive-advective heat transport.

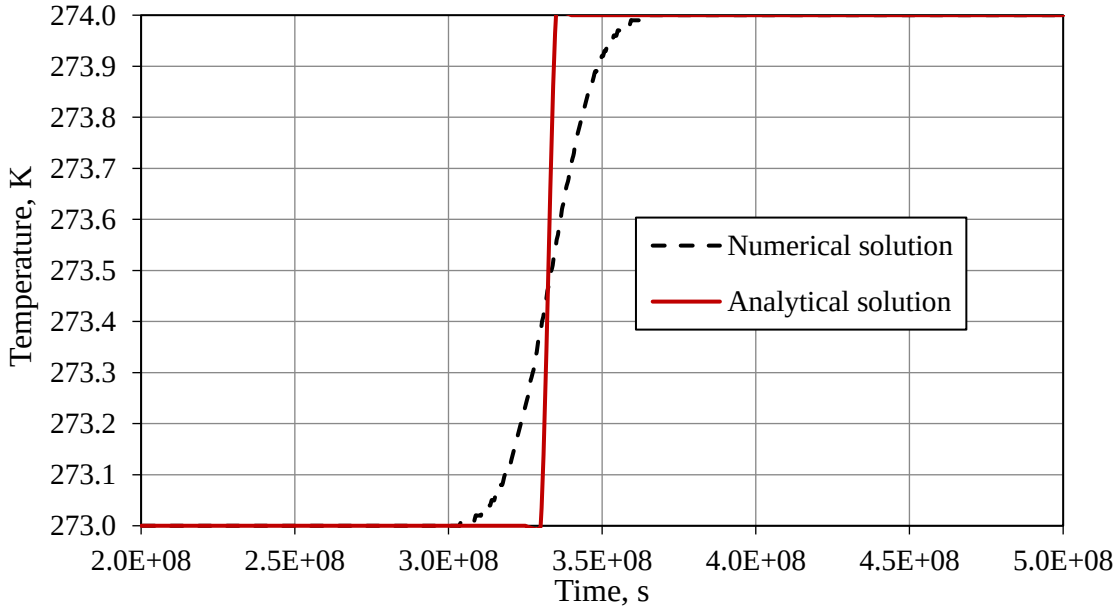

Figure 5.5 Temperature breakthrough curve at $x = 100$ m for only advective heat transport.

5.3.2 Joule-Thomson cooling effect (Test III-b)

The process of coupled fluid flow and heat transport in fractured porous media has been discussed in section 3.5. In contrast to the majority of liquids, most notably water, gas is highly compressible. Flow of gas in permeable media is not an isothermal process because there is a temperature change resulting from the Joule-Thomson cooling effect. This section presents an exercise to test this coupling process, as predicted by the numerical model. The fracture and matrix continua are lumped together and treated as a single porosity medium. Assuming the rock and fluid to be in a local thermal equilibrium with no adsorption-desorption taking place, the heat transport problem can then be written as:

$$\left[(1-n)\rho_s C_{ps} + n\rho_f C_{pf}\right]\frac{\partial T}{\partial t} - n\left(\rho_f C_{pf}\mu_{JT} + 1\right)\frac{\partial u_f}{\partial t} = -\rho_f C_{pf}\boldsymbol{v}\cdot\left(\nabla T - \mu_{JT}\nabla u_f\right) + \nabla\cdot\left[\left((1-n)\lambda_s + n\lambda_f\right)\nabla T\right] \quad (5.3)$$

where n is the porosity, C_{ps} and C_{pf} are the specific heat capacity of solid phase and gas phase, respectively, ρ_s and ρ_f are the rock density and fluid density, λ_s and λ_f are thermal conductivity of solid and gas phase, μ_{JT} is the Joule-Thomas coefficient used to examine how T changes with u_f, and $\mathbf{v}$ is the velocity of fluid flow, which is described by Darcy's law.

The benchmark analytical solution for Joule-Thomson cooling during gas injection into depleted oil and gas reservoirs has been derived by Mathias *et al.* (2010) by assuming the transport properties to be constant and uniform, the flow field to be steady state, and by ignoring thermal conduction(e.g. Ziabakhsh-Ganji and Kooi 2014). Details of the analytical solution derivation can are provided by Mathias *et al.* (2010).

5.3.2.1 Simulation conditions

A simple one-dimensional radial domain is chosen to represent a homogenous and isotropic gas reservoir with radial geometry similar to that illustrated in Figure 5.15. The domain has a 1000 m radius with a thickness of 50 m. An injection well is located at the centre of domain and the fluid flows outward from the injection well in a radially symmetric pattern. A highly refined one dimensional radially symmetric mesh is designed to capture the area around the injection well where the temperature change due to the Joule-Thomson effect is expected to be large, as shown in Figure 5.6. The simulation presented here considers injection of a gas (CO_2) at a constant rate of 3 kg/s. The thermophysical properties are constant and the thermal

conduction is nullified in order to reproduce the results with the analytical solution. The initial temperature of the reservoir is 318 K. The model parameters are chosen from Mathias *et al.* (2010), as given in Table 5.3.

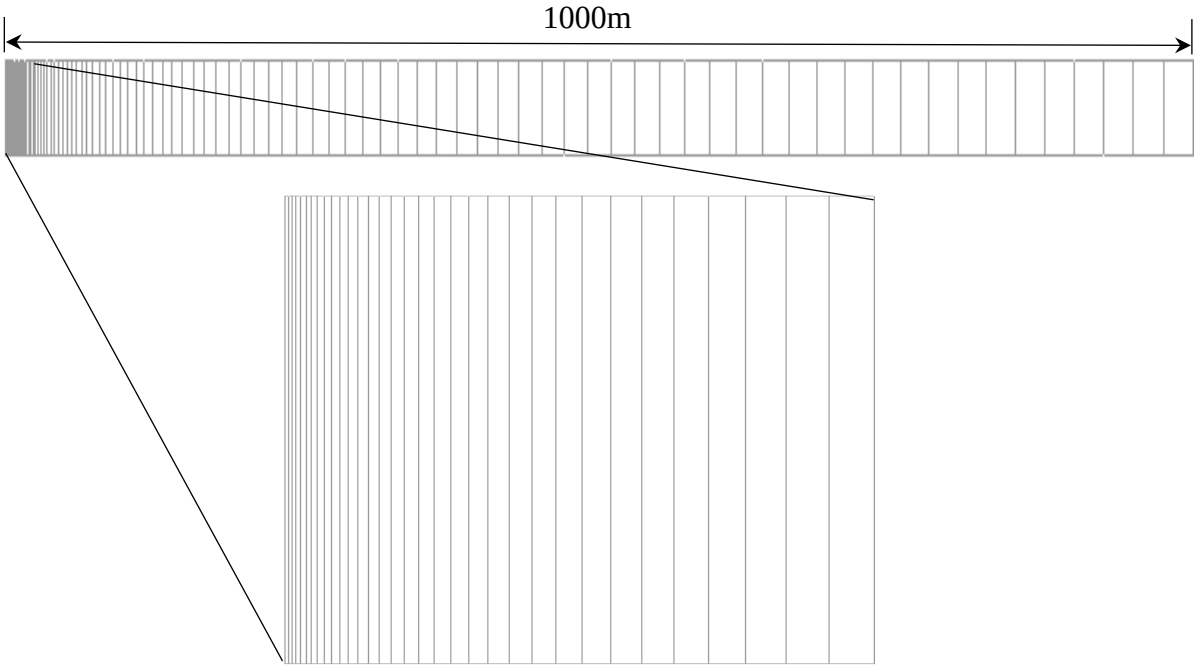

Figure 5.6 Refined mesh schematic for one dimensional radial domain.

Table 5.3 Material parameters used in Test III-b (Mathias et al.2010).

Material parameters	**Relationship/value**
Porosity, n (-)	0.3
Permeability, K (m^2)	5×10^{-15}
Rock density, ρ_s (kg/m^3)	2600
Specific heat capacity of rock, C_{ps} (J/K/kg)	1000
Gas injection rate (kg/s)	3
Well radius (m)	0.05
Gas density, ρ_f (kg/m^3)	109
Specific heat capacity of fluid, c_{pf} (J/K/kg)	798
Joule-Thomson coefficient, μ_{JT} (K/Pa)	9.13×10^{-6}

5.3.2.2 Results and discussion

Figure 5.7 shows the temperature profile over the first 100 m radial distance from the well at simulation times of 90 days and 1 year. It can be observed that gas injection can lead to a fall of temperature because the pressure decreases with a high gradient. The model shows a good agreement with the analytical solution provided by Mathias *et al.* (2010), which supports the verification of the implementation of Joule-Thomson cooling in the numerical model.

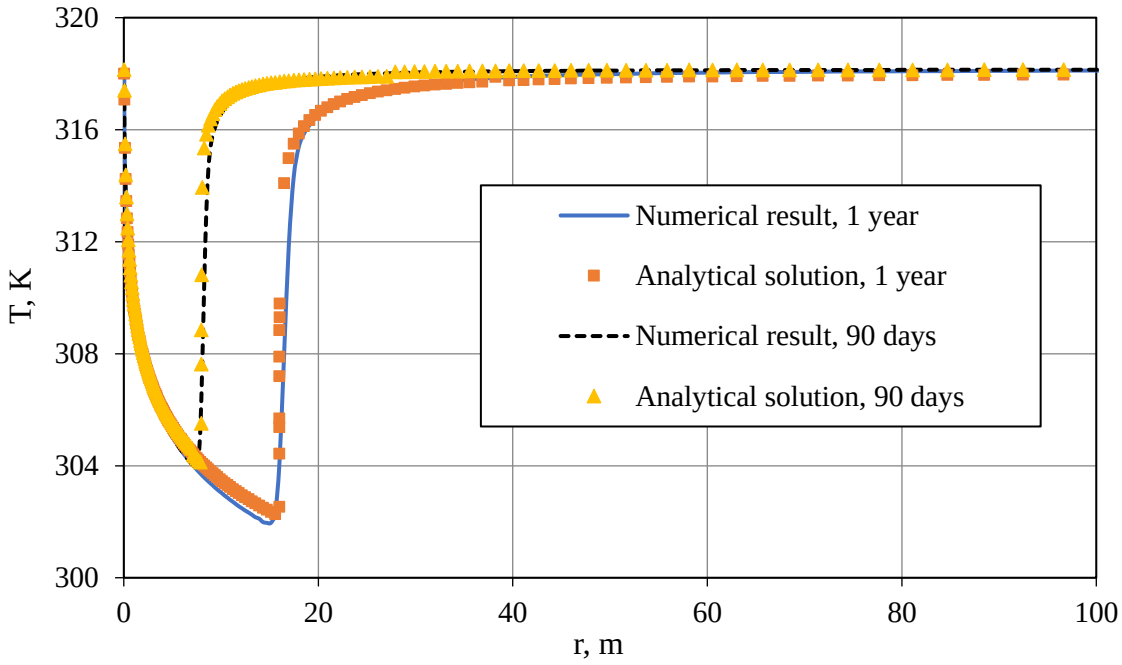

Figure 5.7 Comparison between results from the developed numerical model and the analytical solution by Mathias *et al.* (2010).

5.4 Elastic deformation behaviour (Test IV)

A hollow cylinder problem is one of the most important problems for deep geoenergy engineering applications, representing the circular cross section due to wellbore drilling for applications such as geological carbon sequestration, unconventional oil and gas production. In this section, this problem is simplified as a cylindrical hole in an infinite rock mass subjected to a uniform state of stress far from the hole, as shown in Figure 5.8. The problem tests the isotropic elastic material model under compression for an axisymmetric geometry. The radial and tangential stress distributions outsides the circular hole are given by the

classical Kirsch solution (Jaeger *et al.* 2009),which are used here as the benchmark in this exercise.

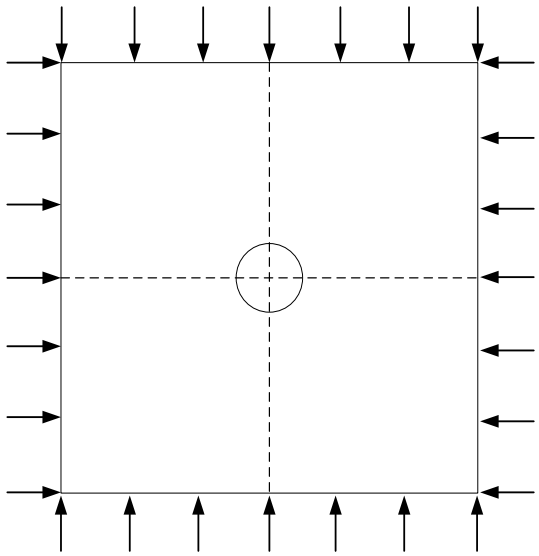

Figure 5.8 Cylindrical hole in an infinite elastic medium (in plain view).

5.4.1 Simulation conditions

An axisymmetric model with the axis of symmetry aligned with the hole axis is considered, as shown in Figure 5.9. A circular hole with a radius of 1 m is drilled in an infinite body under a uniform compressive stress of 30 MPa. A radial mesh is produced with increasing mesh size away from the hole. A total of 100 4-noded quadrilateral axisymmetric elements are used in this mesh, similar to that shown in Figure 5.6. The outer boundary is selected at 10m from the hole centre. The material parameters used in this verification test are given in Table 5.5.

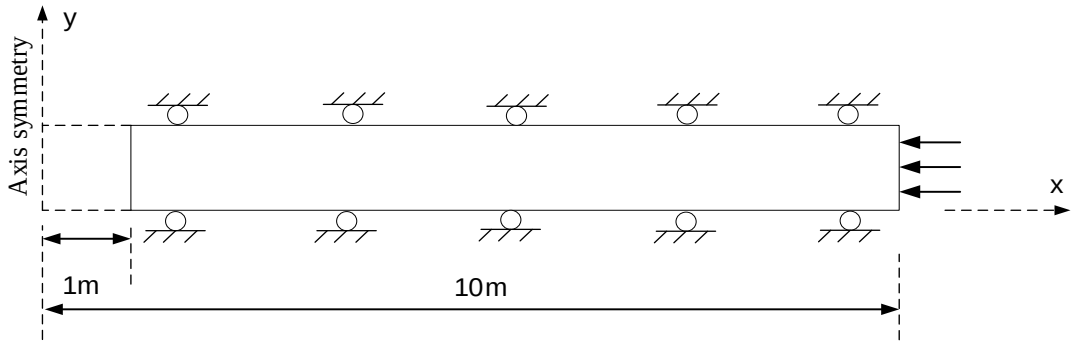

Figure 5.9 Geometry and boundary conditions for the axisymmetric model used in Test IV.

Table 5.4 Material parameters used in Test IV.

Material parameters	Relationship/value
Young's modulus, K(GPa)	10
Poisson's ratio, v (-)	0.2

5.4.2 Results and discussion

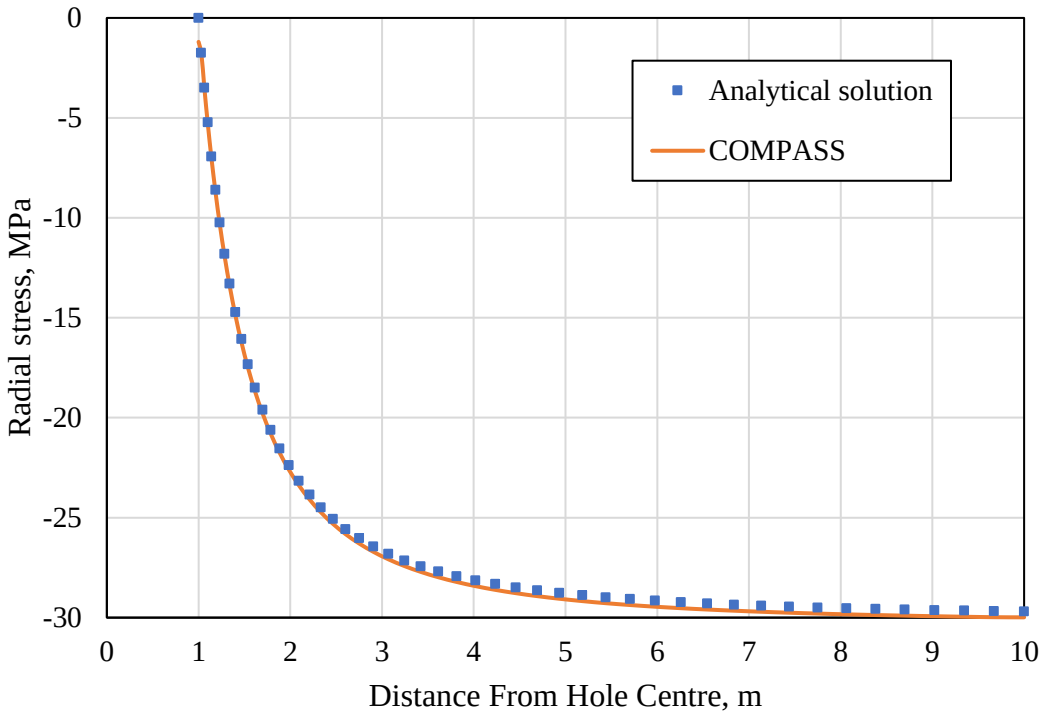

Figure 5.10 Comparison of radial stress distributions for Test IV.

Figure 5.10 and Figure 5.11 plot the radial stress and tangential stress with respect to radial distance. It can be seen that the radial stress increases along the radial distance and reaches the in situ stress of 30 MPa. The radial tangential stress distributions displays a different pattern, with the maximum tangential stress occurring at the wall of the hole being double the in situ stress and decreasing along the radial distance. As can be seen, the results from COMPASS are very similar to those predicted by the classical Kirsch solution, hence, these two plots demonstrate the correctness of the implementation of the model for deformation.

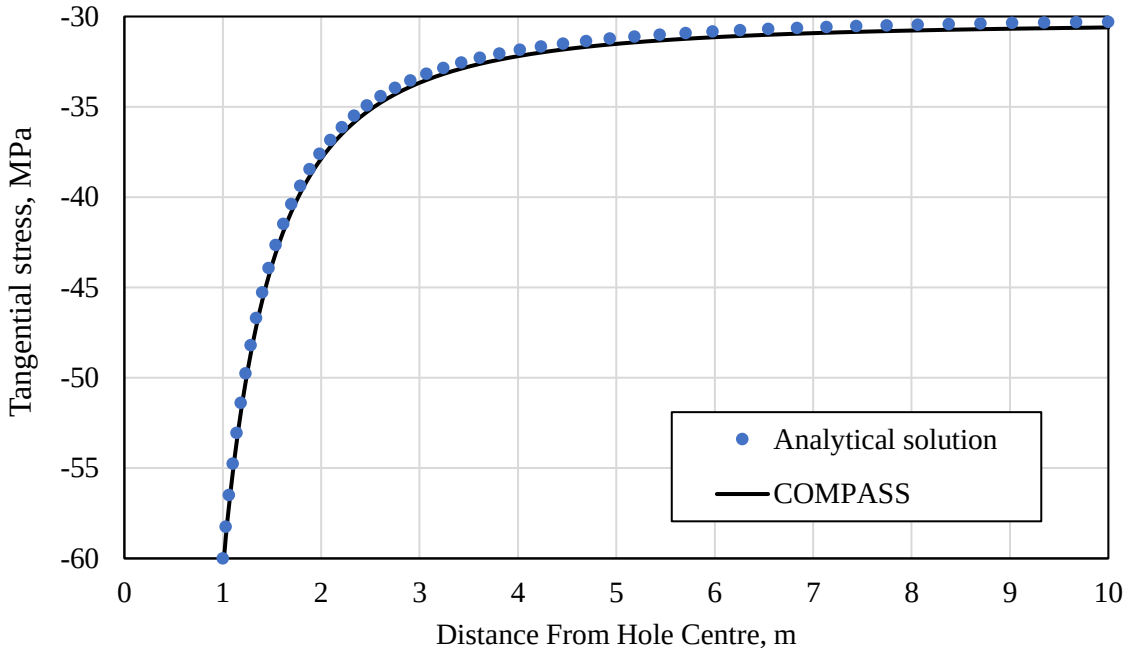

Figure 5.11 Comparison of tangential stress distributions for Test IV.

5.5 Flow in a porous medium with discrete fractures (Test V)

In this section, the discrete fracture-matrix model is employed to investigate the flow behaviour of a large-scale fracture, which is included using the newly introduced finite element techniques described in chapter 4 of this work. The test is used to verify the principle of superposition used to develop the hybrid model as well as the implementation of line element approach. Isothermal steady flow in a porous medium with a single embedded fracture at the centre of the domain is considered. The analytical solution derived by Strack (1982) is used as the benchmark for calculation of the pressure distribution in an infinite domain.

The fluid flow equations are specialised for a porous medium with discrete fractures by introducing the applicable flow law. Darcy's law is applied to the porous medium, whereas flow in the individual fracture is assumed to be laminar along the fracture surface, with the Poiseuille equation being applicable. This example illustrates the disturbance of the uniform flow in porous media due to the presence of a fracture.

5.5.1 Simulation conditions

A 2-D infinite horizontal plane of a porous medium with an embedded fracture is considered, with the middle point of the fracture placed at the centre of the plane. In the numerical model, this plane is set up in a finite space as a square with length of 10 m. The fracture geometry is illustrated in Figure 5.12. It has a length of 2 m and is inclined at an angle of 45º, represented as a 1-D hydraulic path. The domain is spatially discretised using an unstructured grid of 3-noded triangular elements and sixline elements are connected end-to-end to represent the fracture. Both types of element share the nodes. The prescribed pressures at the lateral boundaries are 496465 Pa and −496465 Pa, respectively. Zero flux is assigned to the top and bottom boundaries. It is assumed that the fracture aperture does not vary and has a constant value even at the endpoints. The material properties used in the numerical simulation are collected from Kolditz *et al.* (2016), as listed in Table 5.5.

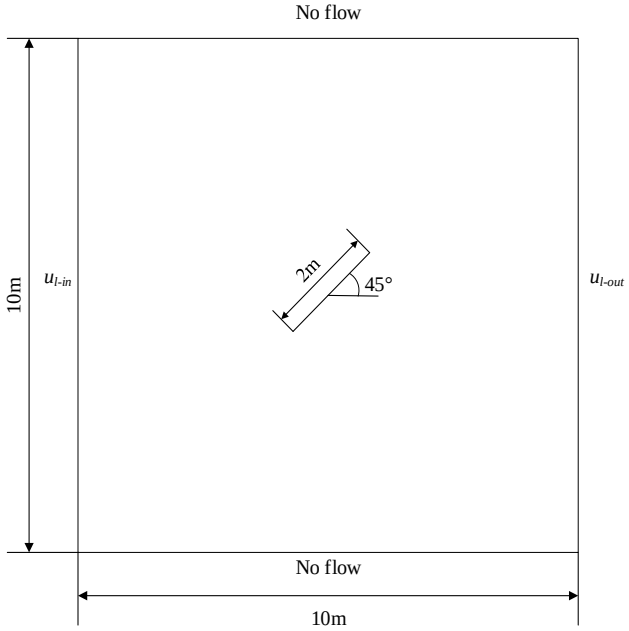

Figure 5.12 Computational domain showing the discrete fracture and boundary conditions.

Table 5.5 Material parameters used in Test V-b (Kolditz *et al.* 2016).

Material parameters	Relationship/value
Fracture aperture, w (m)	0.05
Fracture hydraulic conductivity, k_{lF} (m/s)	1×10^{-3}
Porous medium hydraulic conductivity, k_{lm} (m/s)	1×10^{-5}
Fracture length (m)	2

5.5.2 Results and discussion

To compare with the analytical solution, a numerical solution has been obtained by solving the steady state fluid flow problem in a hybrid system of a discrete fracture model and continuum model (porous medium). A comparison of the analytical solution and the predicted numerical result for the pressure profile along a diagonal line from the bottom-left to the top-right of the domain is shown in Figure 5.13. It can be observed that although the fracture geometry is idealised in the numerical solution, the results show a good agreement with the analytical solution, demonstrating the correctness of the implementation of the approach adopted for the hybrid computational model.

Figure 5.14 shows the pressure distribution obtained by the numerical model. Due to its higher hydraulic conductivity, the fracture becomes the flow path of least resistance, effectively diverting flow into and through the fracture, thus, lateral uniform flow is disturbed in the vicinity of the inclined fracture. In addition, the high hydraulic conductivity of the fracture reduces the pressure gradient along the fracture.

5.6 Coupled thermo-hydro-mechanical behaviour (Test VI)

This section evaluates the correctness of the numerical implementation in describing coupled thermo-hydro-mechanical behaviour. Three verification tests are considered. In section 5.7.1, the hydro-mechanical coupling is examined by the consolidation analysis for single phase fluid flow in a single deformable medium, with the analytical solution provided in Bai and Elsworth (2000) being used to assess the numerical solution. A verification test for fracture deformation is presented in section 5.7.2, with the numerical results being compared with those published in the literature (Gu *et al.* 2014; Moradi *et al.* 2017). In section 5.7.3, a test is presented to compare the analytical and numerical solutions in order to verify the coupling between temperature, flow, and deformation by considering the thermal contributions in the fully coupled thermo-hydro-mechanical model. The analytical solution of a partially coupled thermo-hydro-mechanical model proposed by Selvadurai and Suvorov (2017) is used as the benchmark in the exercise.

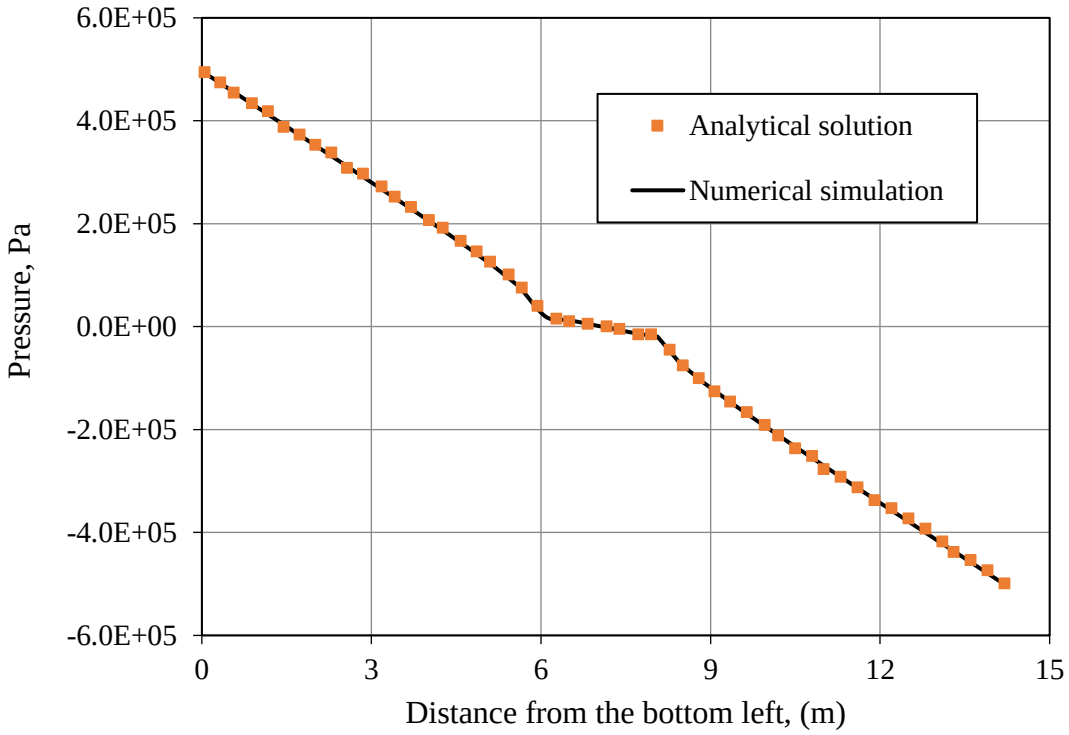

Figure 5.13 Pressure profile along a diagonal line from the bottom-left to the top-right.

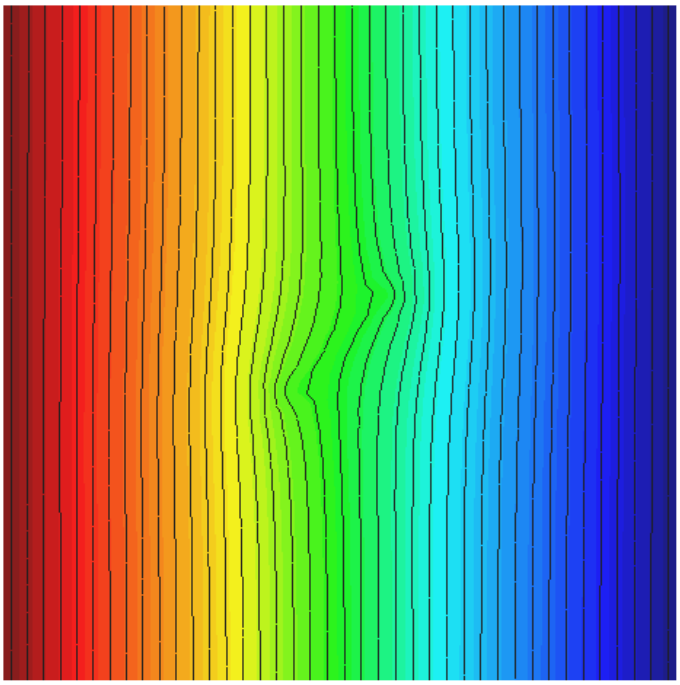

Figure 5.14 Pressure distribution obtained by the numerical simulation for Test V.

5.7 Gas flow with and without adsorption (Test II)

In many cases of gas production or CO_2 sequestration, gas desorption-adsorption behaviour can influence fluid transport. Hence, the exercise presented in this section considers gas transport involving adsorption behaviour. As discussed in chapter 3, it is assumed that adsorption is an equilibrium reaction and can be described by a nonlinear Langmiur isotherm. Since this exercise is mainly concerned with the verification of transient flow of gas with adsorption behaviour, the system is treated as a single porosity medium. Furthermore, the flow obeys Darcy's law. This allows the focus of the analysis to remain on the relevant aspects of the formulation.

Considering a single porosity medium saturated with a single ideal gas component, the gas flow equation (3.61) incorporating gas adsorption under isothermal condition is simplified as:

$$\frac{\partial\left(nc+\rho_s\frac{V_{\mathrm{L}}b_{\mathrm{L}}u}{b_{\mathrm{L}}u+1}\right)}{\partial t}=\nabla\cdot\left(c\frac{K}{\mu}\nabla u\right) \tag{5.4}$$

where u is gas pressure, and n and K are the porosity and intrinsic permeability of the single porosity medium, respectively. The gas pressure u is obtained according to the ideal gas law:

$$u=cRT \tag{5.5}$$

The results obtained using the numerical model are compared with an analytical solution derived by Wu *et al.* (2014) for a radial system with a constant injection source. The approximate analytical solutions and the details about the analytical solution derivation are included in work of Wu *et al.* (2014) and Wu and Pruess (1998). Only the verification results are presented in this section.

5.7.1 Simulation conditions

The numerical simulation considers single phase isothermal transient gas flow in a radially infinite system with a constant gas mass injection rate. An axisymmetric domain is selected with a thickness of 1 m, as shown in Figure 5.15, with a radius raised to up to 10 m so that the response is not influenced by the finite boundary conditions within the analysis time.

The initial and boundary conditions used in the numerical simulation are given in the Figure 5.15 Schematic of the simulation domain and initial and boundary conditions used in Test

II. Nitrogen (N_2) is selected as the injected gas. The domain is initially saturated with N_2 at 0.1 MPa. The gas is injected with a constant mass rate of 1.0×10^{-5} kg/s, and no flow flux is prescribed at the external boundary. Since it is assumed in this exercise that the gas behaves as an ideal gas, the compressibility factor, Z , is set to 1.0. The simulation is performed under isothermal conditions with a constant temperature of 298 K. Table 5.6 lists the material parameters used in this verification exercise, which are selected from Wu and Pruess (1998).

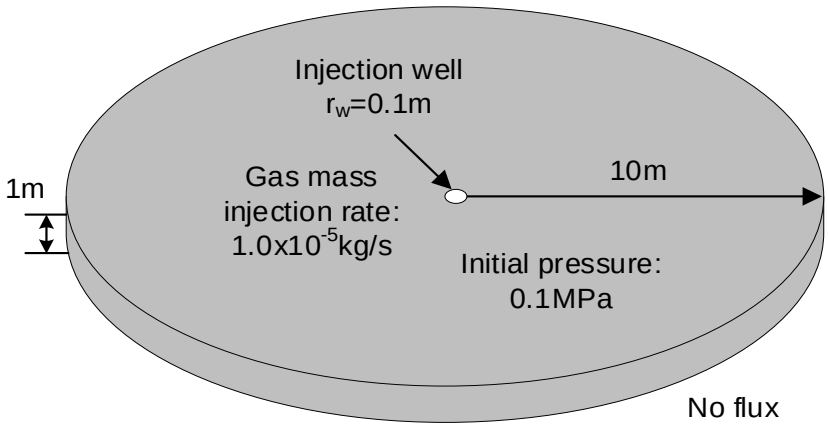

Figure 5.15 Schematic of the simulation domain and initial and boundary conditions used in Test II.

Table 5.6 Material parameters used in Test II.

Material parameters	**Relationship/value**
Porosity, n_f (-)	0.3
Permeability, K (m^2)	1.0×10^{-15}
Gas viscosity, μ (Pa·s)	1.84×10^{-5}
Temperature, T (K)	298
Langmiur volume constnat, V_L (mol/kg)	0.6465
Langmiur volume constnat, b_L (Pa^{-1})	1.0×10^{-6}
Density of material, ρ_s (kg/m^3)	1250

5.7.2 Results and discussion

Two verification tests, one with and one without adsorption, are performed to show the effect of adsorption on gas transport. Figure 5.16 shows the radial pressure distributions at 1 day, which were obtained using the numerical model and analytical solution.

It is noted that the change in gas pressure in the test involving adsorption is slower, which is the expected result since adsorption decreases the amount of free gas and effectively retards flow. As shown in Figure 5.16, the results obtained from the numerical and analytical approaches show a good correlation, implying that the transport and adsorption processes have been implemented correctly.

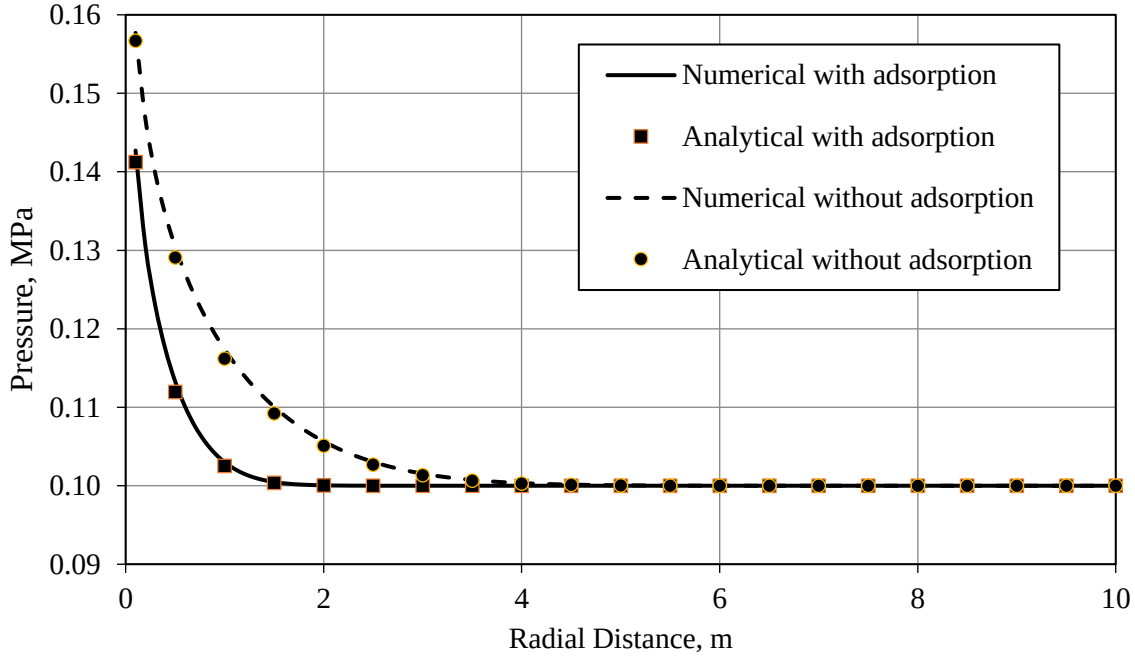

Figure 5.16 Comparison of gas pressure profiles with and without adsorption calculated using the numerical and the analytical solutions in a radially infinite system at 1 day.

5.7.3 1-D consolidation (Test VI-a)

The problem of consolidation, in which a porous layer of rock or soil is subjected to an instantaneously applied normal load at its upper surface, is an important problem in geotechnical engineering. The subject of the theory of consolidation is the simultaneous deformation of the porous material and the flow of the pore fluid. Mechanical compression generates a fluid pressure response, while pressure storage and dissipation modify the mechanical condition via the effective stress (Jaeger *et al.* 2009; Kolditz *et al.* 2016). The consolidation process is used in this section to test the coupled deformation and flow behaviour. Currently, an analytical solution is only available for the problem of consolidation for a single porosity medium. To compare the numerical solution with analytical solution, it is assumed that the fracture spacing within the fractured rock is very large and the normal stiffness of the fractures is very high, hence, the response of the dual

porosity medium resembles that of a single-porosity medium. Considering an elastic porous system saturated with fluid, the differential equations for flow and effective stress within a poroelastic framework under isothermal condition may be expressed as:

$$[nc_{\mathrm{l}} + (\tilde{\mathfrak{b}} - n)c_{\mathrm{s}}]\frac{\partial u_{\mathrm{l}}}{\partial t} + \tilde{\mathfrak{b}}\mathbf{m}^{T}\boldsymbol{B}\frac{\partial \mathbf{u}_{\mathrm{s}}}{\partial t} = \nabla \cdot (\mathrm{k_l}\,\nabla u_{\mathrm{l}}) \tag{5.6}$$

$$d\boldsymbol{\sigma} = d\boldsymbol{\sigma}^{e} + \tilde{\mathfrak{b}}\mathbf{m}du_{\mathrm{l}} \tag{5.7}$$

The analytical solutions of 1-D consolidation derived by Bai and Elsworth (2000) for evolution of pressure and displacement are adopted as benchmarks for the verification test.

5.7.3.1 Simulation and conditions

A 1-D column is selected for the consolidation analysis. The length of column is set at 1 m. At the initial time, a uniform compressive load of 1 MPa is applied on the top surface, as shown in Figure 5.17. Displacement constraints are assigned to the bottom boundary and lateral displacements are restricted horizontally, hence, only vertical displacement is allowed within the column. No-flow lateral boundary conditions prevail in the column, except on the top surface, where fluid may exit freely from the column. The initial pore pressure is 0 Pa. 2-D plane strain finite elements are used to simulate this 1-D situation. The simulation domain is spatially discretised using 50 equally sized 4-noded quadrilateral elements. The basic parameters required in the numerical simulation are chosen from Bai and Elsworth (2000), as listed in Table 5.7. Pressure and displacement are monitored in time.

Table 5.7 Material parameters used in Test VI-a (Bai and Elsworth 2000).

Material parameters	**Relationship/value**
Young's modulus, E (MPa)	2.4
Poisson's ratio, v (-)	0.2
Hydraulic conductivity, $\mathrm{k_l}$ (m/s)	5.381×10^{-7}
Porosity, n (-)	0.02
Fluid bulk modulus, ${c_{\mathrm{l}}}^{-1}$ (MPa)	0.1183
Biot coefficient, $\tilde{\mathfrak{b}}$ (-)	0.8929
Solid grain bulk modulus, ${c_{\mathrm{s}}}^{-1}$ (MPa)	12.445
Loading stress (MPa)	1.0

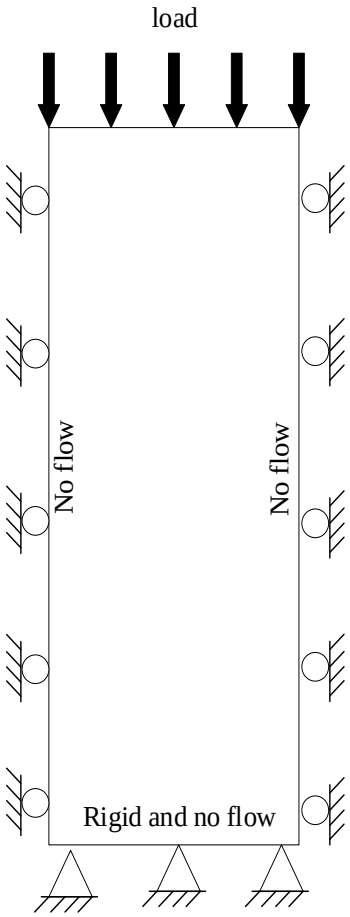

Figure 5.17 Schematic of the 1-D column consolidation and boundary conditions used in verification Test VI-a.

5.7.3.2 Results and discussion

The temporal evolution of displacement at the top surface is monitored in this numerical simulation. It can be seen from the Figure 5.18 that there is a good agreement between the analytical and numerical results. Figure 5.19 presents the comparison of pressure dissipation along the column between the analytical and numerical solutions at times of 0.005 s, 0.05 s, 0.5 s and 1 s, showing a close agreement between the two solutions.

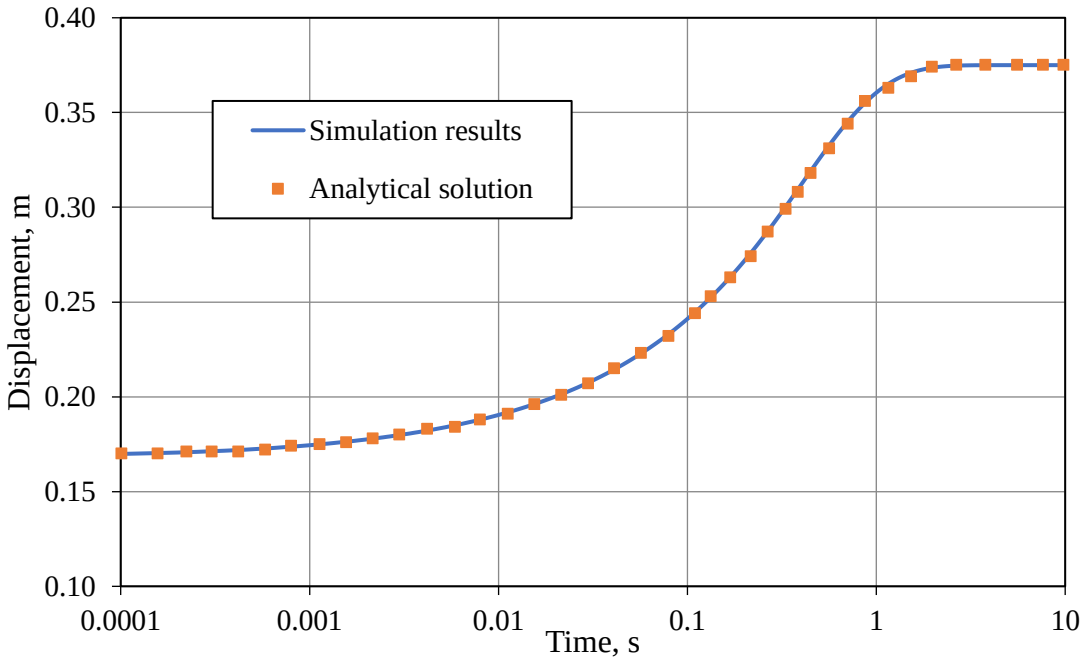

Figure 5.18 Comparison of temporal displacement between the analytical solution and the numerical model for Test VI-a.

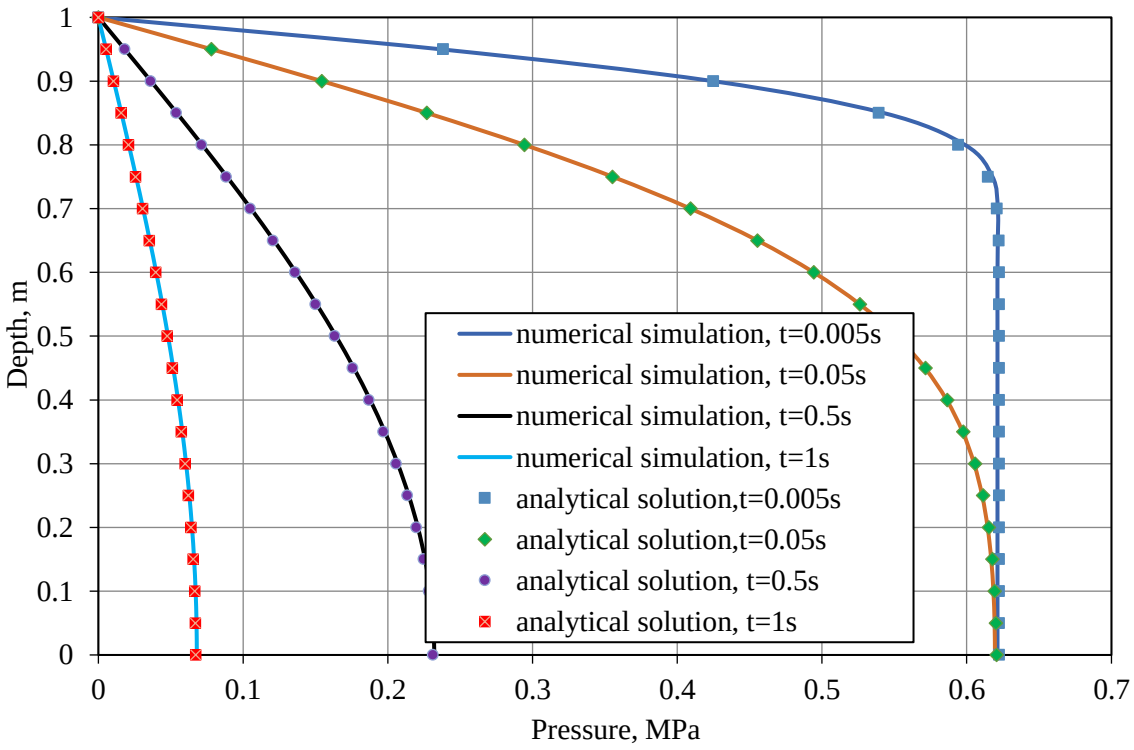

Figure 5.19 Pore pressures distributions obtained using the analytical solution and predicted by the numerical model for verification Test VI-a.

It is worth mentioning that for the hydro-mechanical coupling process, when the load is applied on the top surface of column the pore pressure instantaneously increases to the maximum from the initial zero pore pressure, however, the increase of pore pressure is lower than the applied stress. This is because the solid grains are assumed to be compressible and the Biot coefficient is less than one. With the dissipation of pore pressure, the mechanical condition of the column is altered via effective stress, displacement occurs and increases gradually to the maximum corresponding to the dissipation of fluid pressure in the column.

5.7.4 The effect of pressure on fracture aperture (Test VI-b)

In fractured reservoirs, the fracture opening or closure induced by the variation of pressure and in situ stress has a considerable effect on the flow behaviour. In the current work, deformation of the natural fracture network is described in terms changes in the fracture continuum porosity, whereas the mechanical behaviour of large-scale hydraulic fractures is represented explicitly, as discussed in section 3.7.4. Two distinct mechanisms cause the fracture aperture to change, i.e. variation of normal stress applied to the fracture and shear dilation caused by shear stress acting along the fracture. The former is generally represented by the well-known Barton and Bandis equation (Bandis *et al.* 1983; Barton *et al.* 1985) and the latter is calculated with shear stiffness and shear dilation angle. The verification test presented in this section is used to examine the accuracy of the implementation of the mechanical model for fracture deformation in the numerical model. Since this exercise is mainly concerned with verification of the mechanical model for fracture deformation, small-scale natural fractures are neglected. The fracture-matrix fluid transport model, which has been verified in section 5.6, is employed to model flow behaviour in the fracture system and porous medium (matrix). The results obtained using the developed model at steady state are compared with the results of a numerical modelling study published by Gu *et al.* (2014) and Moradi *et al.* (2017).

5.7.4.1 Simulation conditions

A horizontal well-pair pattern with one producer and one injector is simulated. Four separate fractures are located between the two wells, as follows: (a) fracture length is 200 m, interconnecting the two well bores, (b) fracture length is 100 m, connected with the injection wellbore, (c) fracture length is 100 m, connected with the production wellbore, and (d) fracture length is 100 m without a connection to either wellbore, as shown in Fig. 9. The

displacements at the left and bottom sides are constrained in the horizontal and vertical directions, respectively. Isotropic in situ stresses of 20 MPa are applied on the top and the right sides, the initial pressure is 10 MPa, and the injection and production wells operate at constant pressure of 20 MPa and 10 MPa, respectively. It is assumed that the four fractures have the same properties initially. The no-load aperture of fractures is set to 0.25 mm and the maximum normal fracture closure is 0.24 mm. A single component fluid with a compressibility of 5.39×10^{-9} Pa^{-1} is selected. The input data used for the verification test are listed in Table 5.8, which are chosen from the work of Moradi et al. (2017). The matrix domain is spatially discretised using quadrilateral elements and fractures are represented with line elements. The calculation time is set to 1 year until the model reaches steady state flow.

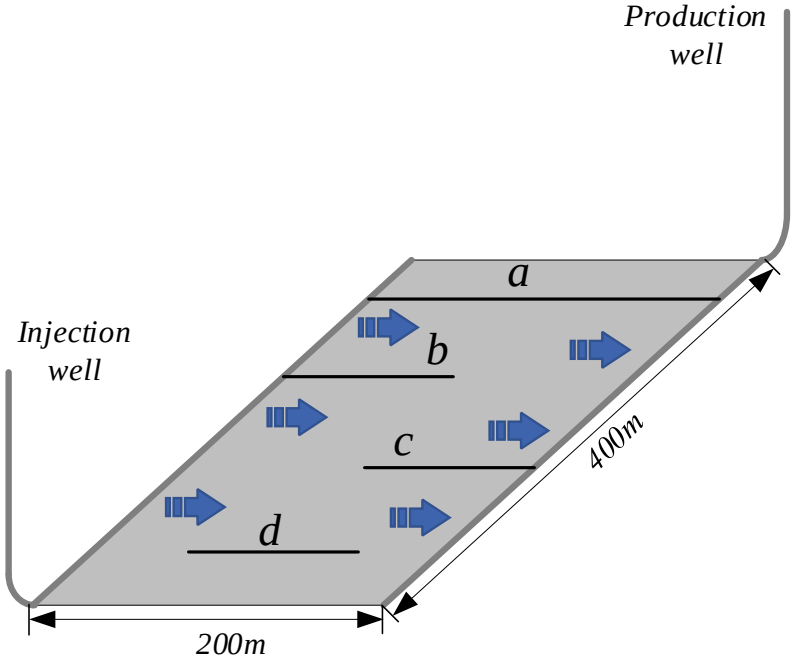

Figure 5.20 Schematic of fracture distribution between two horizontal wells for Test VI-b.

5.7.4.2 Results and discussion

A comparison of fracture apertures at the steady state condition obtained in the present work and in the works by Gu et al.(2014) and Moradi et al.(2017) is shown in Figure 5.21. The variation in each fracture aperture along the width of the domain is almost linear, which is because the pressure change between the injection and production wells is likewise approximately linear. This test verifies the interaction between the pressure field and the fracture deformation field. It can be seen that there is a good agreement between the two sets

of results, demonstrating that the mechanical model of fracture deformation developed in this work has been accurately implemented in the numerical model.

Table 5.8 Material parameters used in Test VI-b Moradi et al.(2017).

Material parameters	**Relationship/value**
Young's modulus, E (GPa)	5.8
Poisson's ratio, v (-)	0.3
Matrix permeability, K_{m} (m^2)	5.0×10^{-14}
Porosity, n (-)	0.15
Fluid viscosity, μ (Pa·s)	1.8e-4
Biot coefficient, $\tilde{\mathfrak{b}}$ (-)	0.83
Initial normal stiffness, K_{n0} (GPa/s)	120
Shear stiffness, K_t (GPa/s)	120
No-load fracture aperture, w_0 (mm)	0.25
Internal friction angle, Φ (°)	25
Shear dilation angle, φ (°)	5
Shear strength, τ_c (MPa)	5

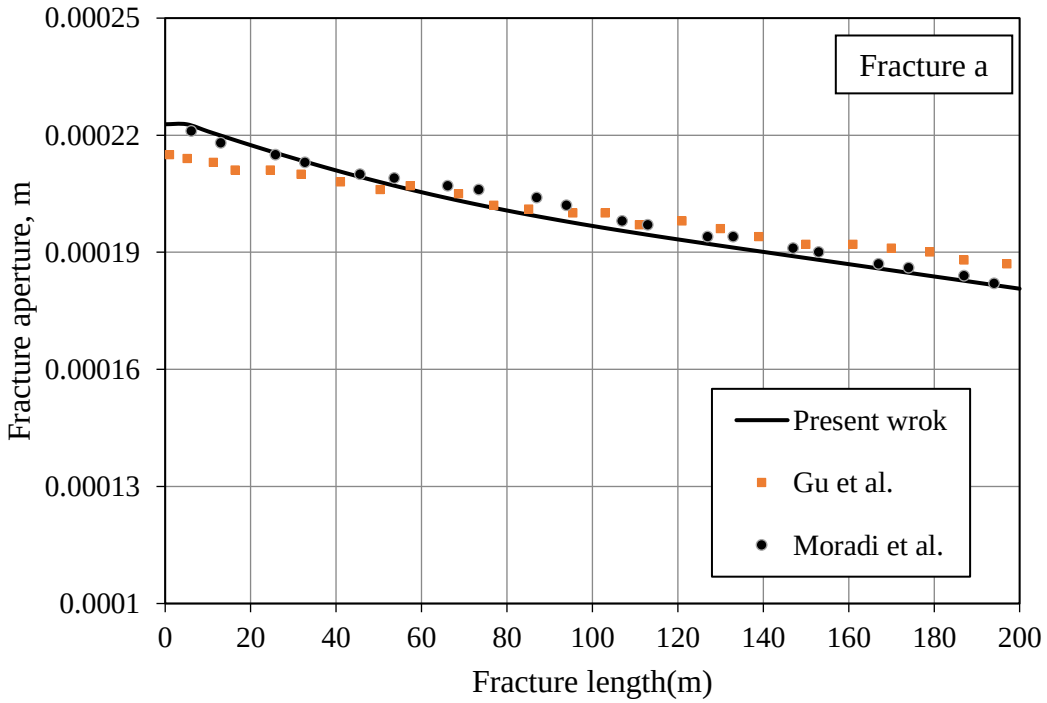

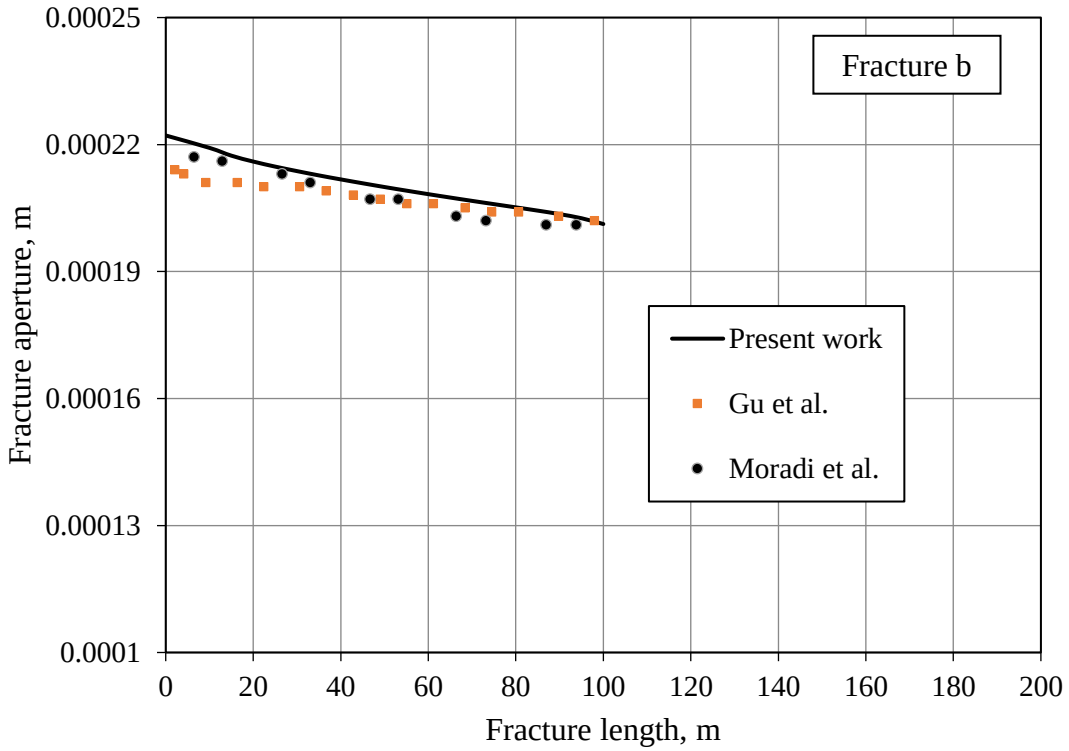
Fracture b
Present work
Gu et al.
Moradi et al.
Fracture aperture, m
0.00025
0.00022
0.00019
0.00016
0.00013
0.0001
0
20
40
60
80
100
120
140
160
180
200
Fracture length, m

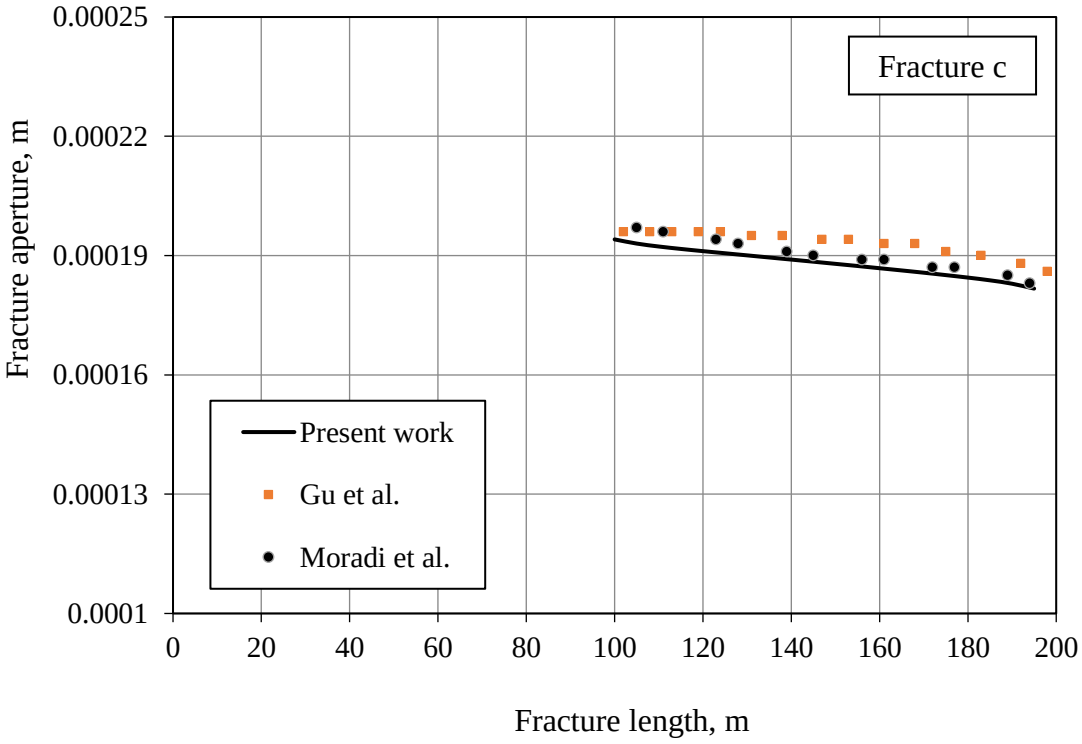
Fracture c
Present work
Gu et al.
Moradi et al.
Fracture aperture, m
0.00025
0.00022
0.00019
0.00016
0.00013
0.0001
0
20
40
60
80
100
120
140
160
180
200
Fracture length, m

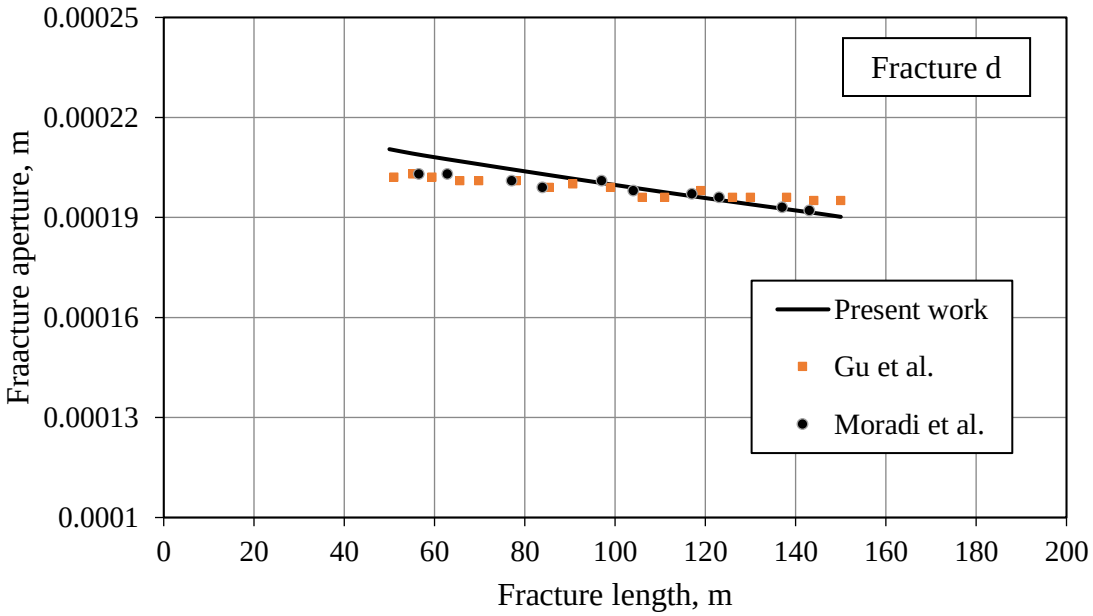

Figure 5.21 Comparison of fracture apertures predicted by the current numerical model with the numerical modelling study presented by Gu *et al.* (2014) and (Gu *et al.* 2014); Moradi *et al.* (2017).

5.7.5 Thermo-hydro-elastic response of rock under thermal loading (Test VI-c)

The accurate implementation of the coupled hydro-mechanical model of isothermal, fluid saturated porous media has been verified in the previous section 5.7.1. However, non-isothermal media can be encountered in engineering applications. Heat transfer in a liquid-saturated geological medium initiates coupled thermal-hydraulic-mechanical phenomena, referred to as thermohydroelasticity (Noorishad *et al.* 1984). The verification exercise presented in this section is to test the accuracy of the numerical model for predicting coupled thermal-hydraulic-mechanical behaviour. Analytical results provided by Selvadurai and Suvorov (2017) for a partially coupled thermo-hydro-mechanical model are used as a benchmark to examine the correct implementation of the numerical model. The following simplifications provide the basis for the derivation of the analytical solution by Selvadurai and Suvorov (2017): (i) the coupled thermo-mechanical constitutive law is proposed for a single porosity medium in thermal equilibrium, (ii) the medium is fully saturated with single phase fluid, and (iii) heat convection is neglected in the heat transport equation. In other words, to be consistent with the fundamentals of the theory for saturated thermoelastic porous media presented by Selvadurai and Suvorov (2017), the volume of fractures is assumed to be zero and the convection term in the heat transfer equation is excluded.

5.7.5.1 Simulation conditions

This verification test considers a one-dimensional poroelastic column that is restrained from movement at the bottom surface, as shown in Figure 5.22. The initial thermo-hydro-mechanical state and boundary conditions are also illustrated in Figure 5.22. The initial thermal equilibrium is fixed at T_{ini} = 323 K and the initial pressure is set at $u_{l\text{ini}}$ = 0 Pa. The initial equilibrium stress is fixed at 0 Pa. For deformation, displacement constraints are assigned to the bottom boundary, and lateral displacements are restricted horizontally so that only vertical (uniaxial) displacement is allowed within the column. For fluid flow, zero pressure is imposed at the top and the bottom boundaries, where fluid may exit freely from the column. No hydraulic flux boundary conditions prevail on both lateral sides. A fixed temperature of 273 K is assigned to the top surface and no lateral thermal flux is imposed on the sides. The column is subjected to a temperature change of 50 K suddenly applied to the column at t = 0 s. It should be noted that the specification of a temperature change of 50 K is purely for the purpose of the computational simulations and no phase transformations are allowed to occur. The basic parameters used in the simulation are selected from Selvadurai and Suvorov (2017), as listed in Table 5.9.

Table 5.9 Material parameters used in Test VI-c (Selvadurai and Suvorov 2017).

Material parameters	**Relationship/value**
Compressibility of the porous matrix, c_{m} (GPa^{-1})	0.2
Poisson's ratio, v (-)	0.3
Matrix permeability, K_{m} (m^2)	6.0×10^{-19}
Porosity, n (-)	0.25
Fluid viscosity, μ (Pa·s)	1.0e-3
Biot coefficient, $\tilde{\mathfrak{b}}$ (-)	0.75
Compressibility of solid, c_{s} (GPa^{-1})	0.05
Fluid compressibility, c_{l} (GPa^{-1})	0.4545
Effective thermal conductivity, λ_{e} (W/m/K)	1.62
Effective specific heat capacity, $\left(\rho C_p\right)_{\text{e}}$ (J/K/ m^3)	1.0×10^{6}
Thermal expansion coefficient of solid, α_T (1/K)	8.3×10^{-6}
Thermal expansion coefficient of fluid, α_T (1/K)	6.9×10^{-5}

5.7.5.2 Results and discussion

Figure 5.23 shows the time-dependent temperature profile within the column at selected times of 1 day, 10 days, 100 days and 365 days. The temperature of column is increased to 323 K at time t = 0 s and the temperature at the upper surface is restrained at 273 K. The time-dependent reduction of temperature at the insulated end of the column is illustrated in Figure 5.24. Given sufficient time, the temperature will reduce to 273K, i.e. the initial temperature.

The distribution of pore fluid pressure within the one-dimensional column is shown in Figure 5.25. The sudden increase of temperature leads to a sudden change in pore fluid pressure. In the beginning, the pore fluid pressure profile is positive along the column and the value of pore pressure decreases with increasing time. Eventually, the pore pressure can become negative as the temperature of the column decays, as shown in Figure 5.25. The effect of the pressure decay is also demonstrated in Figure 5.26 for the bottom of the column as a result of a change in temperature corresponding to Figure 5.24.

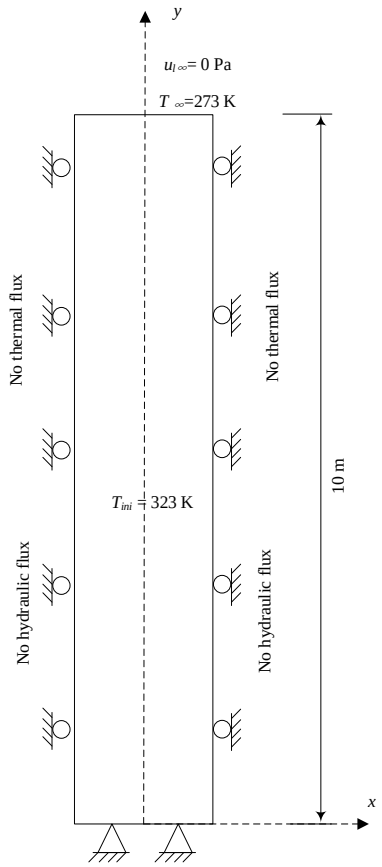

Figure 5.22 Schematic of the domain and the initial and boundary conditions for Test VI-c.

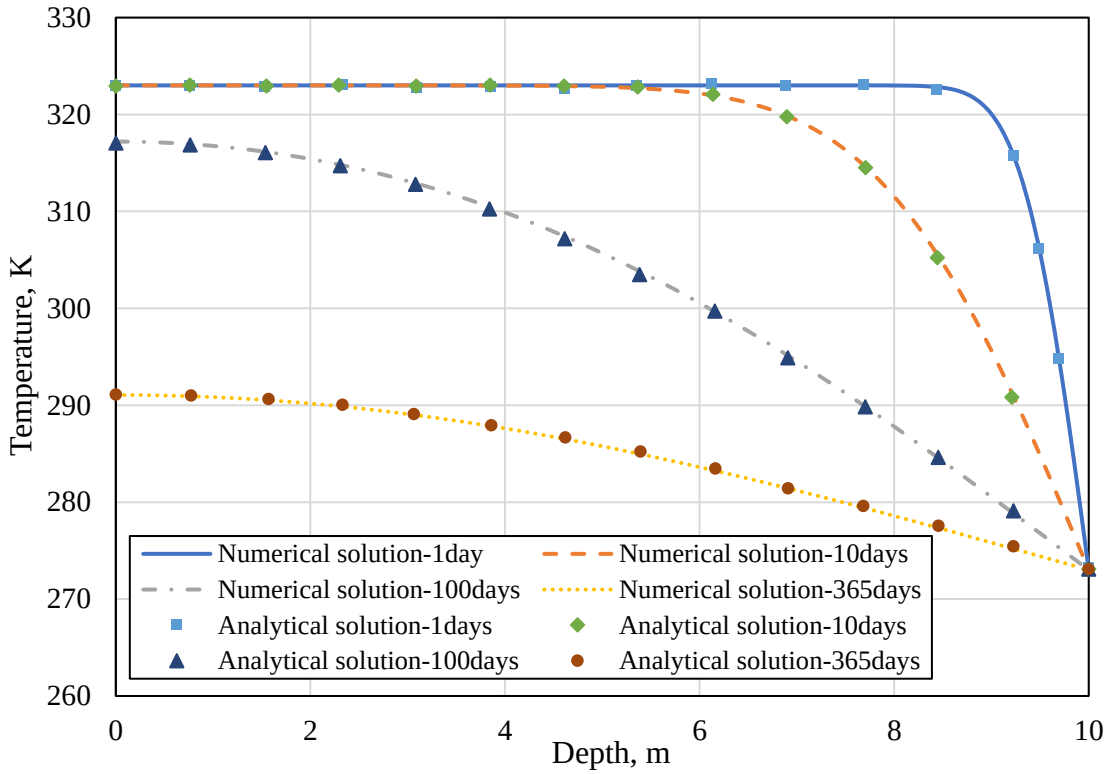

Figure 5.23 Temperature distribution at selected times within the column subjected to an initial temperature change of 50 K.

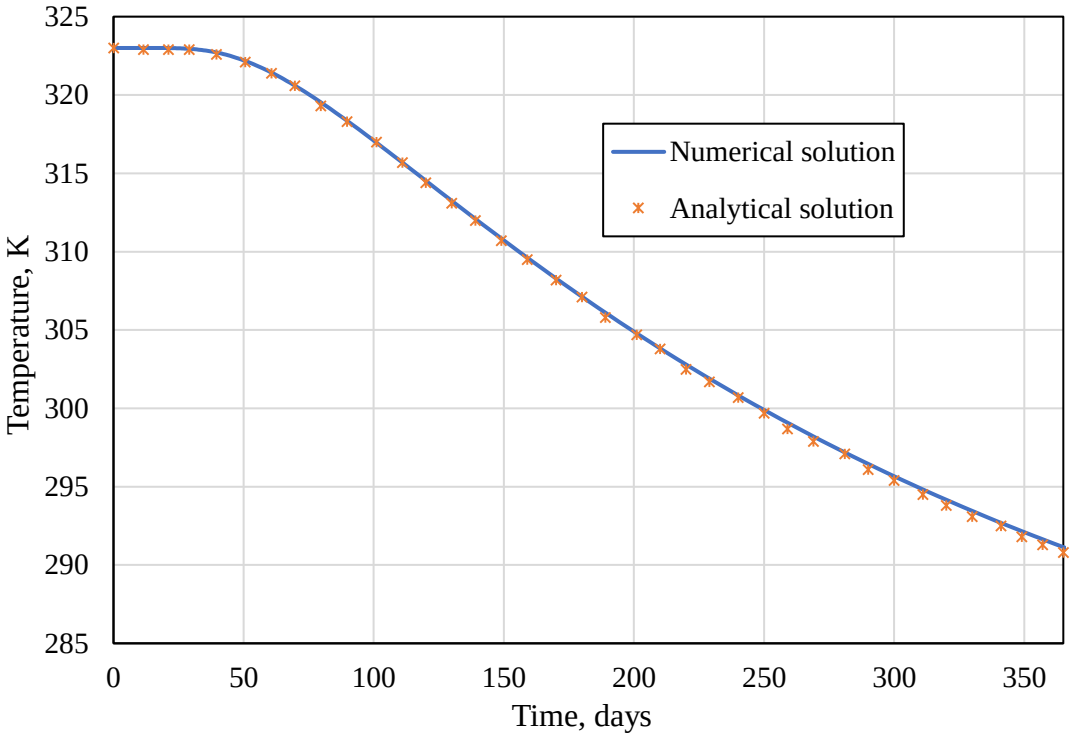

Figure 5.24 Evolution of temperature with time at the bottom of the column.

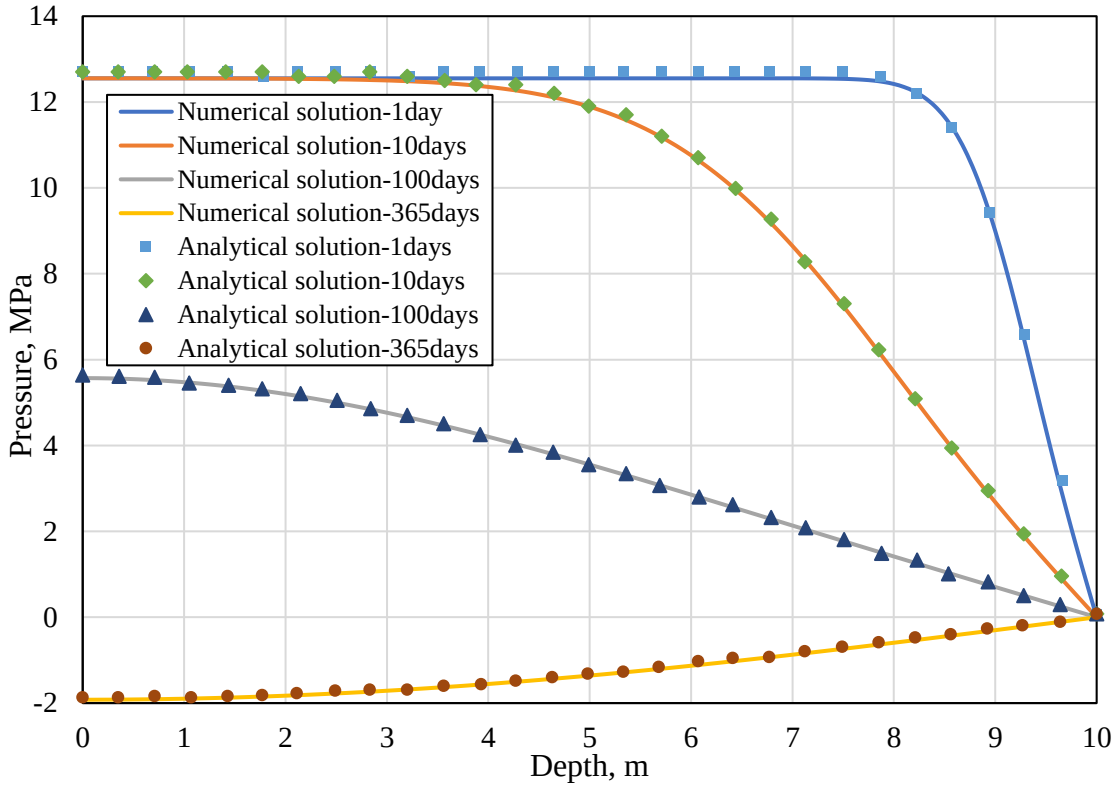

Figure 5.25 Pressure distribution at selected times within the column subjected to the temperature change of 50 K.

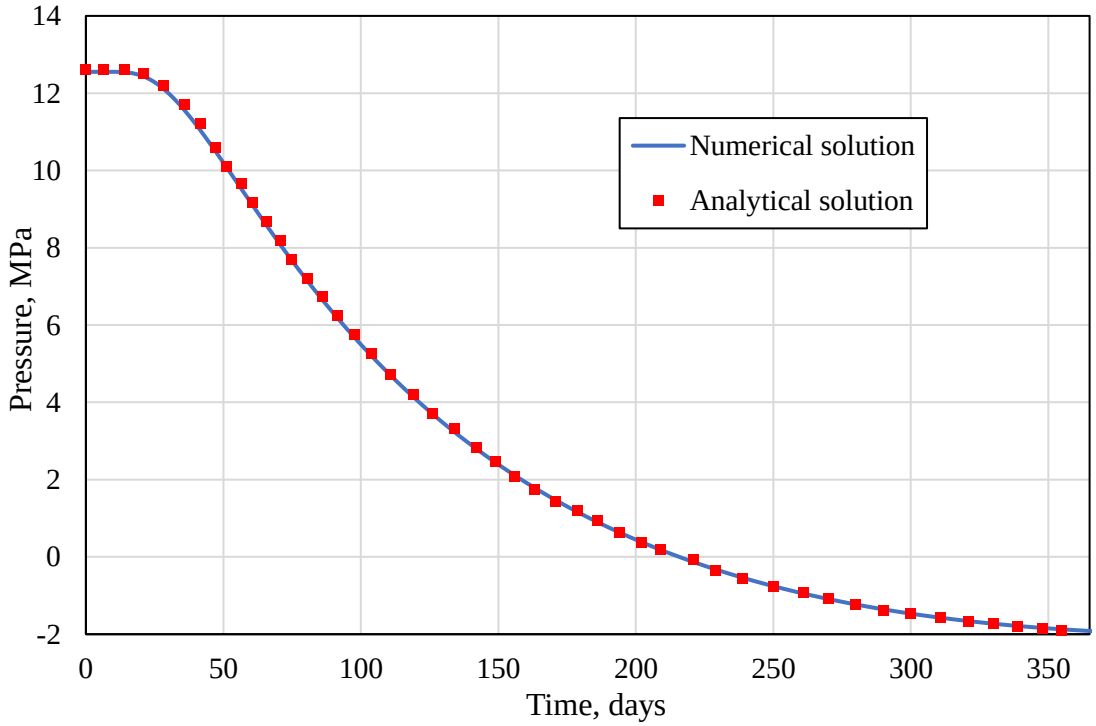

Figure 5.26 Pressure evolution with time at the bottom of the column.

Figure 5.27 illustrates the axial displacement of the one-dimensional poroelastic column. The sudden increase of temperature causes a positive rise of displacement, which is indicative of the thermal expansion of the column. Although the initial displacement changes linearly along the axis, the nonlinear distributions of temperature and pore pressure along the column result in nonlinear change in displacement. As the temperature decays according to the typical variations shown in Figure 5.24, the poroelastic column contracts and ultimately the axial displacement reduces to zero. The variation in pressure with time is demonstrated in Figure 5.28 for the upper surface of the column.

The computational results are consistent with the trends predicted by the analytical results. In combination with the previous section, the exercise described in this section has served to verify the coupling between the heat transport, fluid flow and mechanical modules in the numerical model.

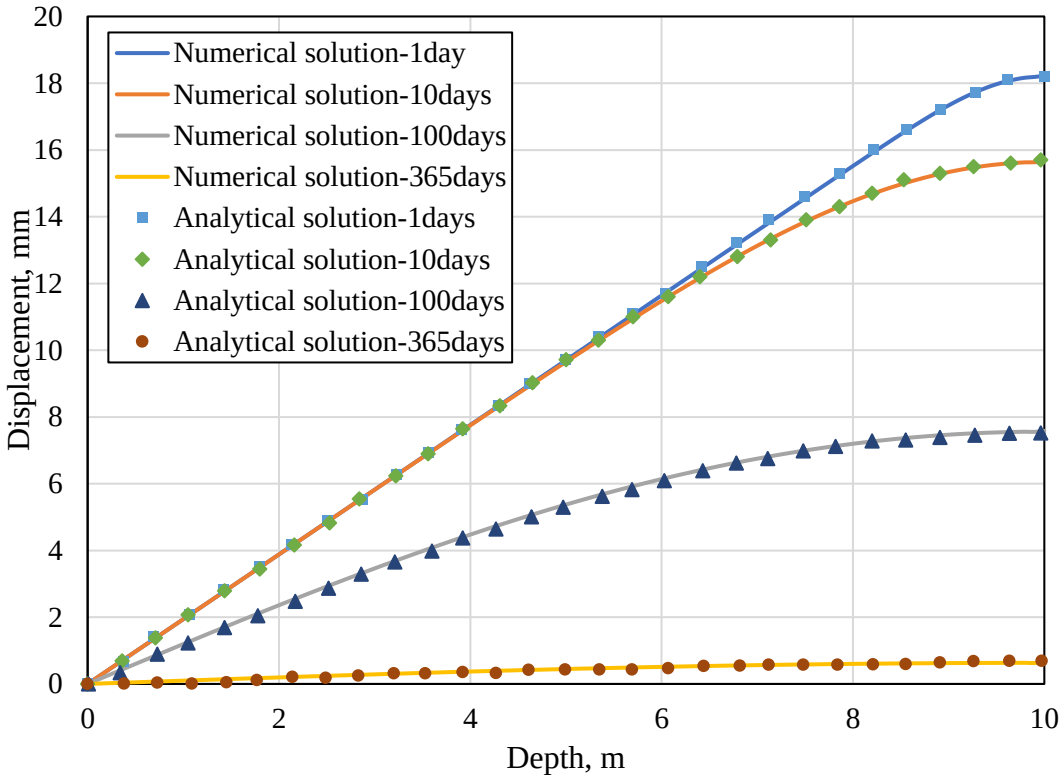

Figure 5.27 Displacement distribution inside the column subjected to the temperature change of 50 K.

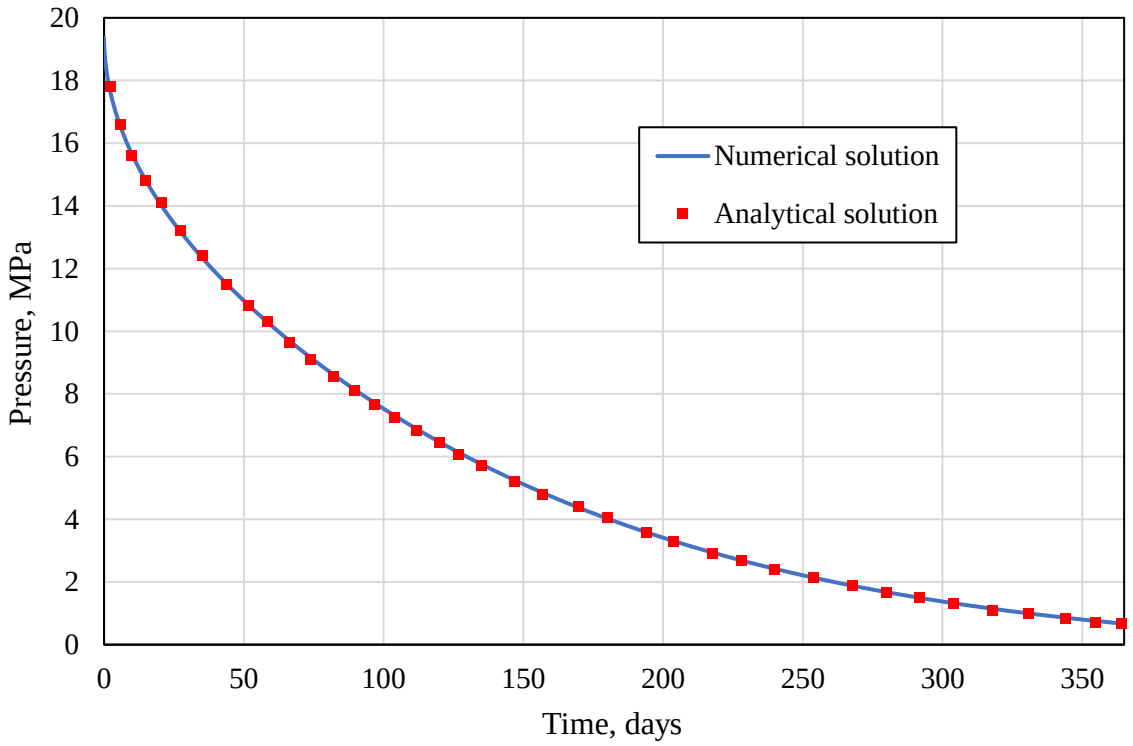

Figure 5.28 Pressure evolution of the column surface with time.

5.8 Specific conclusions

A set of verification exercises have been presented in this chapter, which were performed to evaluate the major components of the developed numerical model of coupled transport and deformation behaviour in fractured rock. The major focus of these exercises has been on verifying that the key components describing non-isothermal, multiphase flow in elastically deformable rock with multiscale fractures have been correctly implemented in the model. The main results of each of these exercises are summarised below.

A verification test was performed to examine the ability of the numerical model to describe isothermal unsaturated flow in fractured rock, which was treated as a dual permeability system. The numerical simulation considered a column with nonuniform initial pressure distribution. The simulation results for the pressure in the domain have been compared with numerical studies from the OGS and S1D_DUAL simulation code presented in the literature. The predicted results showed a good agreement with the benchmarks provided, indicating the governing equations for variably saturated flow in a dual permeability system have been correctly implemented in the numerical model.

A verification exercise considering gas transport with adsorption has been presented to ensure the gas pressure profile predicted by the numerical model follows that expected by analytical solutions. Two verification tests, one with and one without adsorption, were performed to show the effect of adsorption on gas transport. The simulations were performed for an axisymmetric domain. The simulation results reflect that adsorption decreases the amount of free gas and retards flow. The predicted gas pressure distribution was in a close agreement with the analytical solutions considered, which provided the quantitative benchmark for the test.

The implementation of the heat transport formulation has been evaluated by two verification exercises, including conductive-convective heat transport and the Joule-Thomson cooling effect. Pure convection and combined conductive-convective transport have been considered separately to show the different heat transport mechanisms. The temperature change caused by the Joule-Thomson cooling effect during compressible fluid flow has been shown. Comparisons have been made against analytical solutions for conductive-convective transport, pure convection, and the Joule-Thomson cooling effect. The results have shown that the inclusion of heat conduction can produce a smoother breakthrough curve compared with purely convective heat transport, and that the injection of high pressure gas can lead to a fall of temperature as fluid pressure decreases with a high gradient. The predicted results obtained from the numerical model have been found to match well with the analytical solutions adopted as benchmarks for the tests. As a result, it can be concluded that the heat transport mechanisms have been successfully implemented in the numerical model.

To verify that the numerical model is able to solve the stress equilibrium equation for an elastic problem, a verification test was considered concerned with the elastic response outside of a cylindrical hole in an infinite elastic medium subjected to a uniform in situ stress field far from the hole. The problem tested the isotropic elastic material model, the plane-strain condition and axisymmetric geometry. An analytical solution for the radial and tangential stress distributions in the vicinity of the cylindrical hole served as the benchmark for this verification exercise. The numerical results for radial stress and tangential stress with respect to radial distance produced a close agreement with the analytical solution, hence, the accuracy of the implementation of the model for deformation was successfully verified.

A verification test has been presented to examine the newly introduced modelling approach and finite element technique used to handle discrete fractures. This test provided a

verification for the implementation of the line element approach, on the other hand, it was also used to verify the principle of superposition adopted for development of the hybrid model, considering the problem of isothermal steady state flow in a porous medium with a single embedded fracture in the centre of the domain. The predicted steady state pressure profile has been compared with the analytical solution considered. A good agreement between numerical solutions and benchmarks provided by literature and analytical solution has been observed. This test demonstrated the correctness of the implementation of the approach adopted for the hybrid-dimensional computational model.

A set of simulations were completed to assess the thermo-hydro-mechanical coupling in the numerical model. To evaluate the accuracy of the numerical model in describing the coupled thermo-hydro-mechanical behaviour, three verification tests were presented in this section. The hydro-mechanical coupling was examined by the consolidation analysis for single phase fluid flow in a single porosity deformable medium, with an analytical solution used as the benchmark for this exercise. The simulation results for fracture deformation have been compared with those presented in the literature. A test was conducted to compare the analytical and numerical solutions to verify the coupling between temperature, flow and deformation by considering the thermal contributions in the fully coupled thermo-hydro-mechanical model. The comparison between simulation solution and benchmark showed an excellent agreement, demonstrating the accurate implementation of thermo-hydro-mechanical coupling in the numerical model.

The verification exercises presented in this chapter have provided an evaluation of the numerical implementation of the theoretical framework for non-isothermal unsaturated flow in deformable fractured rock. Further confidence in the accuracy of the implementation of the theoretical and numerical formulations has been achieved through the exercises presented. The application and validation of the model is presented in the following chapters.

5.9 General conclusions

The purpose of this chapter has been to evaluate the soundness of the implementation of the theoretical and numerical formulations. This has been pursued by breaking down the numerical model into component parts in order to verify the specific developments presented in chapters 3 and 4. The correlations achieved between the numerical results and the

benchmarks considered have given confidence that mathematically correct results were computed by the numerical model when predicting multiphase flow, gas flow with adsorption, heat transport, elastic deformation, and thermal-hydraulic-mechanical coupling. The findings of this chapter facilitate an application of the proposed numerical model for the purpose of validation via the simulation of experimental work or field trials. Hence, the validity of the proposed numerical model will be the subject of the next chapter.

5.10 References

Bai, M. and Elsworth, D. eds. (2000). *Coupled processes in subsurface deformation, flow, and transport*. American Society of Civil Engineers **20**: 249-268.

Bandis, S., Lumsden, A. and Barton, N. eds. (1983). *Fundamentals of rock joint deformation*. International Journal of Rock Mechanics and Mining Sciences & Geomechanics **20**: 249-268.

Barton, N., Bandis, S. and Bakhtar, K. eds. (1985). *Strength, deformation and conductivity coupling of rock joints*. International journal of rock mechanics and mining sciences & geomechanics abstracts.

Gu, S., Liu, Y. and Chen, Z. (2014). Numerical study of dynamic fracture aperture during production of pressure-sensitive reservoirs. *International Journal of Rock Mechanics and Mining Sciences* **70**:229-239.

Hosking, L. (2014). *Reactive transport modelling of high pressure gas flow in coal.* Ph.D Thesis, Cardiff University, Wales, UK.

Jaeger, J. C., Cook, N. G. and Zimmerman, R. (2009). *Fundamentals of rock mechanics*. John Wiley & Sons.

Kolditz, O., Shao, H., Wang, W. and Bauer, S. (2016). *Thermo-hydro-mechanical-chemical processes in fractured porous media: modelling and benchmarking*. Springer.

Masum, S. A. (2012). *Modelling of reactive gas transport in unsaturated soil. A coupled thermo-hydro-chemical-mechanical approach.* Ph.D Thesis, Cardiff University, Wales, UK.

Mathias, S. A., Gluyas, J. G., Oldenburg, C. M. and Tsang, C.-F. (2010). Analytical solution for Joule–Thomson cooling during CO_2 geo-sequestration in depleted oil and gas reservoirs. *International Journal of Greenhouse Gas Control* **4**(5):806-810.

McTigue, D. (1986). Thermoelastic response of fluid-saturated porous rock. *Journal of Geophysical Research: Solid Earth* **91**(B9):9533-9542.

Moradi, M., Shamloo, A. and Dezfuli, A. D. (2017). A sequential implicit discrete fracture model for three-dimensional coupled flow-geomechanics problems in naturally fractured porous media. *Journal of Petroleum Science and Engineering* **150**:312-322.

Noorishad, J., Tsang, C. and Witherspoon, P. (1984). Coupled thermal-hydraulic-mechanical phenomena in saturated fractured porous rocks: Numerical approach. *Journal of Geophysical Research: Solid Earth* **89**(B12):10365-10373.

Ogata, A. and Banks, R. (1961). *A solution of the differential equation of longitudinal dispersion in porous media: fluid movement in earth materials*. US Government Printing Office.

Selvadurai, A. P. and Suvorov, A. (2017). *Thermo-poroelasticity and geomechanics*. Cambridge University Press.

Strack, O. D. (1982). *Assessment of effectiveness of geologic isolation systems. Analytic modeling of flow in a permeable fissured medium*. Pacific Northwest Lab.

Van Genuchten, M. T. (1980). A closed-form equation for predicting the hydraulic conductivity of unsaturated soils 1. *Soil science society of America journal* **44**(5):892-898.

Wu, Y.-S., Li, J., Ding, D., Wang, C. and Di, Y. (2014). A generalized framework model for the simulation of gas production in unconventional gas reservoirs. *SPE Journal* **19**(05):845-857.

Wu, Y.-S. and Pruess, K. (1998). Gas flow in porous media with Klinkenberg effects. *Transport in porous media* **32**(1):117-137.

Ziabakhsh-Ganji, Z. and Kooi, H. (2014). Sensitivity of Joule–Thomson cooling to impure CO_2 injection in depleted gas reservoirs. *Applied Energy* **113**:434-451.

6

Model Validation and Application

6.1 Introduction

This chapter presents a series of validation tests as part of the research to examine the ability of the proposed model and constitutive relationships in chapters 3 and 4 to interpret processes in practical applications. Experimental and field data published in the literature is used as a benchmark to evaluate the capabilities of model related to gas flow and interactions in coal.

In section 6.2, the effects of factors including temperature and pressure on the gas adsorption capacity are discussed with the developed constitutive relationship (ref. section 3.3), which is useful to estimate the gas content under in-situ conditions. Gas adsorption in coal is temperature dependent and is assumed to obey Langmuir theory. The fundamentals of gas adsorption characteristics on coal with varying temperature and pressure are discussed.

The theoretical model has been developed based on the thermodynamic approach to predict the adsorption-induced swelling. Sets of relevant experimental data are selected to compare with the results obtained using the developed theoretical model. The relationship between adsorption and swelling is discussed in section 6.3. A new permeability model has been derived to describe the variation of coal permeability due to effective stress and swelling/shrinkage. The main objective of section 6.3 is to examine this newly developed approach via comparisons between the results of the adopted permeability model and experimental results. In addition, mechanisms for permeability change of coal exposed to adsorptive gases are analysed. The coupling relationship between swelling strain and the amount of adsorbed gas in coal is also discussed. A numerical simulation is then presented to analyse the gas flow behaviour and structural changes of coal during CO_2 injection into a

coal core at the laboratory scale. An in-depth discussion on the processes and behaviour involved is provided.

Section 6.4 presents a numerical simulation of CBM recovery, with the results calibrated using the field production data from Palmer and Mansoori (1996). The experimental results are presented in terms of the gas production rate, water production rate, and bottom hole pressure. A sensitivity analysis with respect to key input modelling parameters for CBM production is then carried out. Finally, the impacts of different physical parameters on CBM extraction are discussed based on the simulation results.

Finally, the specific conclusions and general conclusions of this chapter are summarised in section 6.5 and 6.6.

6.2 Effects of temperature on adsorption characteristics

The adsorption characteristics of coal are important in determining the in-situ CBM content and the amount of the CO_2 that coal seams can store in place. As discussed in the literature review, the adsorption characteristics of coal are affected by many parameters, including temperature and pressure. In this work, a theoretical model is proposed to quantitatively describe the effects of these factors on the gas adsorption behaviour of coal. The purpose of this section is to examine the ability of the proposed theoretical model to predict the influence of temperature and pressure at a certain range of temperature. Published data in the literature is used to validate the model. The ability of the model to describe the combined effects of temperature and pressure on adsorption in coal are examined in this section.

6.2.1 Experimental results of gas adsorption

Guan *et al.* (2018) experimentally measured the CH_4 and CO_2 sorption capacities of coal taken from a coal mine in the Illinois Basin, USA, with tests conducted at various temperatures. In order to measure the gas adsorption capacity of pulverised coal, the coal blocks were broken into lumps and then pulverised and sieved through a 60–80 mesh sieve to obtain the desired powder size. Prior to the experiment, the pulverised sample was dried and maintained moisture free. The dry powder sample was separated into two groups for the CH_4 and CO_2 sorption processes, respectively, to enable a comparison between the two gases under the same experimental conditions (Guan *et al.* 2018). The temperature was set with

10 K intervals between 283.15 K and 313.15 K in the experiments. The results of adsorption behaviour of CO_2 and CH_4 at selected temperature are shown in Figure 6.1 and Figure 6.2.

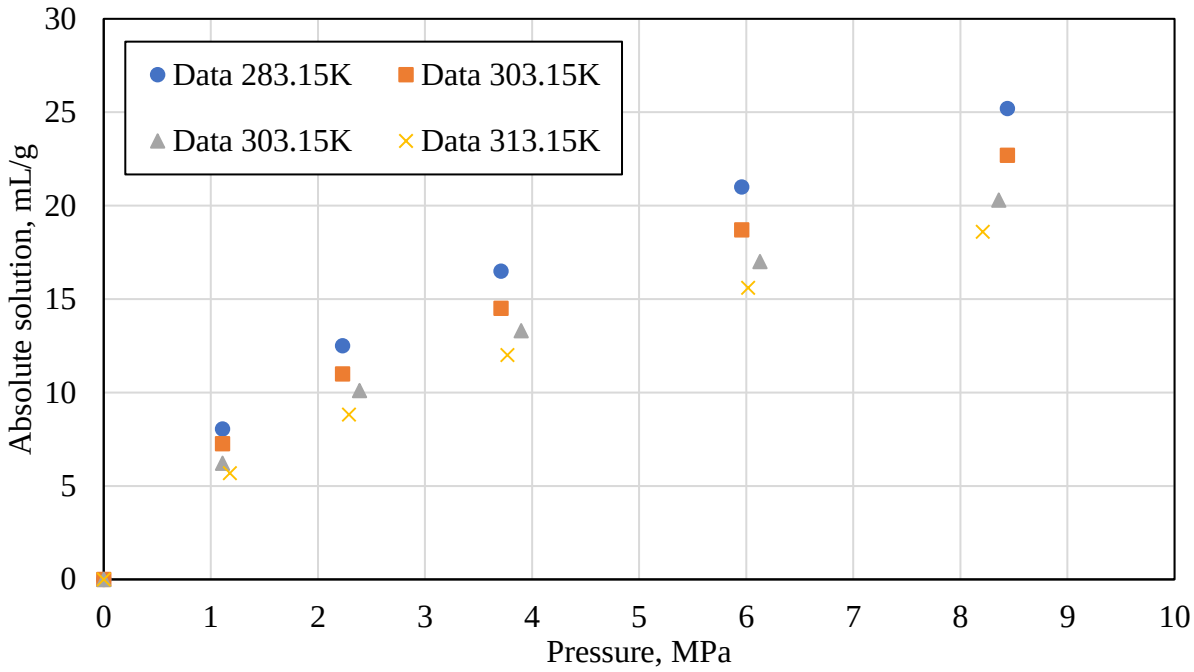

Figure 6.1 Adsorption isotherms for CH_4 on coal at selected temperatures (Guan *et al.* 2018).

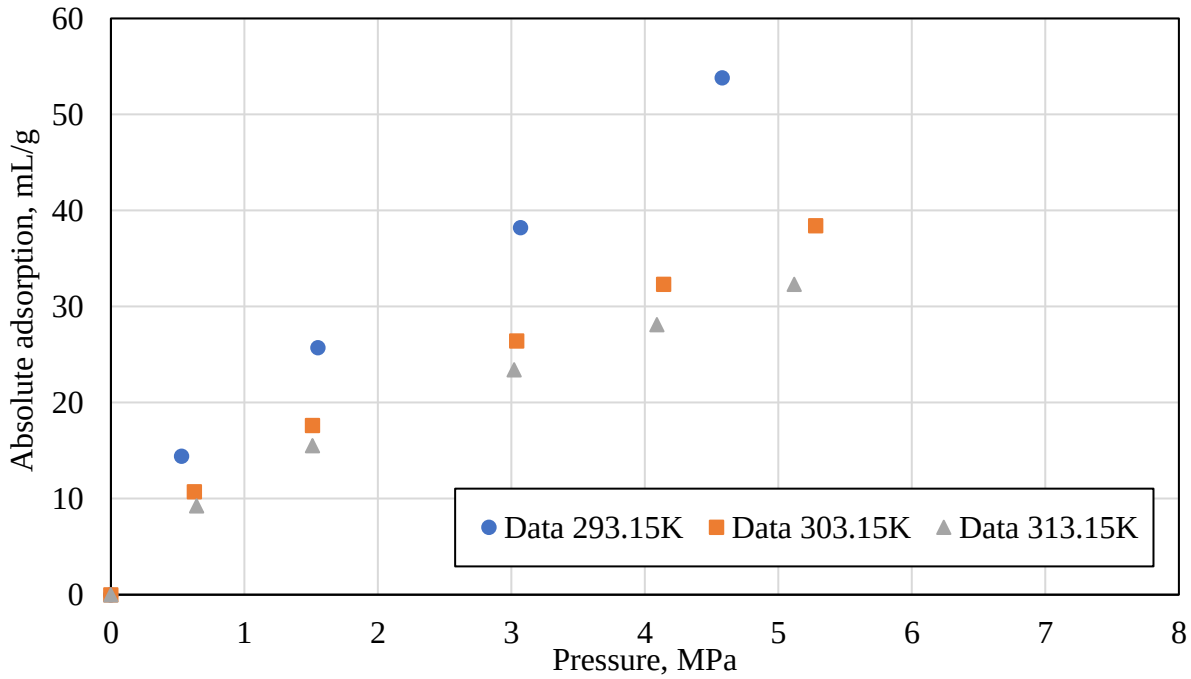

Figure 6.2 Adsorption isotherms for CO_2 on coal at selected temperatures (Guan *et al.* 2018).

6.2.2 Material parameters and matching results

For convenience, the temperature dependent adsorption model expressed in equations (3.9) to (3.12) in chapter 3 is rewritten as follows:

$$V = \frac{V_L\, exp(-\Phi \Delta T)\, b_L u_g}{b_L u_g + 1} \tag{6.1}$$

$$V_L = V_{L0} \exp(-\Phi T) \tag{6.2}$$

$$b_L = b_{L\infty} \exp\left(\frac{E_{in}}{RT}\right) \tag{6.3}$$

where V_{L0} is the theoretical maximum adsorption capacity for the adsorbent, Φ is a reduction coefficient related with temperature increase, E_{in} is the interaction energy between the adsorbate and the adsorbent, and $b_{L\infty}$ is the affinity at infinite temperature.

The parameters required to model the effect of temperature on gas adsorption behaviour are obtained through matching experimental data. A summary of the material parameters is provided in Table 6.1, these parameters are obtained by matching the experimental measurement.

Table 6.1 Parameters used for modified Langmuir isotherm model.

	Material parameters	**Relationship/value**
CH_4	Maximum adsorption capacity, V_L (mL/g)	36.91
	Reduction coefficient, Φ (K^{-1})	0.00833
	Interaction energy, E_{in} ($J\cdot mol^{-1}$)	9238
	Affinity at infinite temperature, $b_{L\infty}$ (MPa^{-1})	1/194
CO_2	Maximum adsorption capacity, V_L (mL/g)	75.82
	Reduction coefficient, Φ (K^{-1})	0.02339
	Interaction energy, E_{in} ($J\cdot mol^{-1}$)	5266
	Affinity at infinite temperature, $b_{L\infty}$ (MPa^{-1})	1/23

The results of modelling the temperature dependent adsorption behaviour for CO_2 and CH_4 are presented in Figure 6.3 and 6.4, respectively. CO_2 displays higher adsorption capacity compared with CH_4, and temperature shows a negative impact on the amount of gas adsorbed onto the coal. The decreased amount of gas adsorption as temperature increases

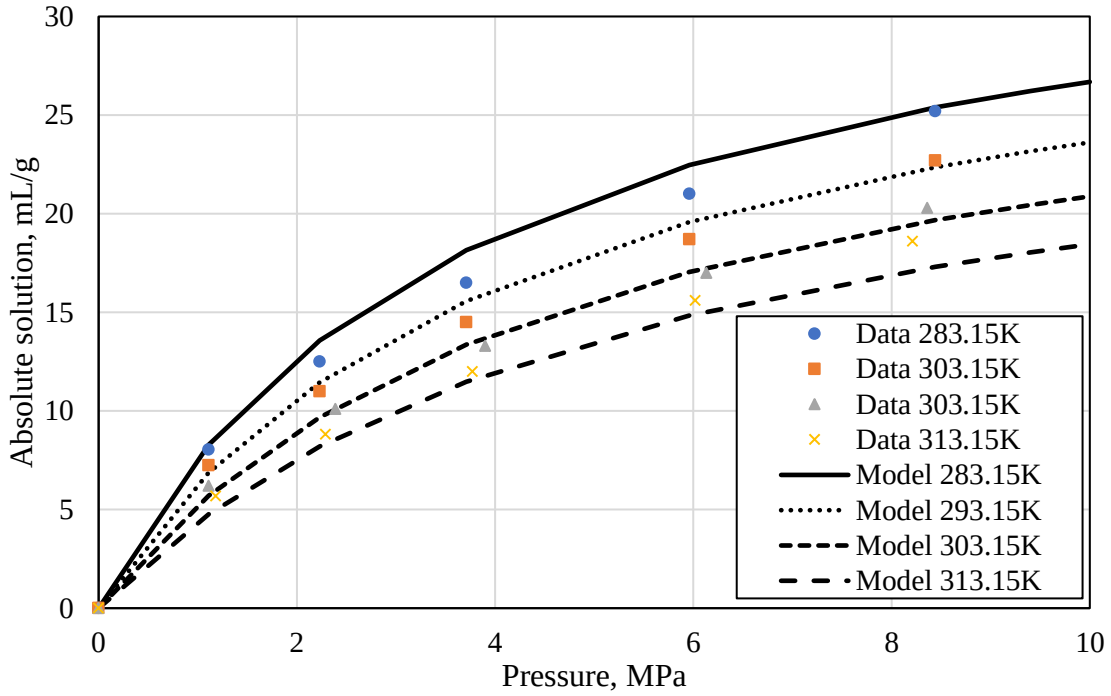

Figure 6.3 Comparison between experimental data and model prediction of CH_4 adsorption.

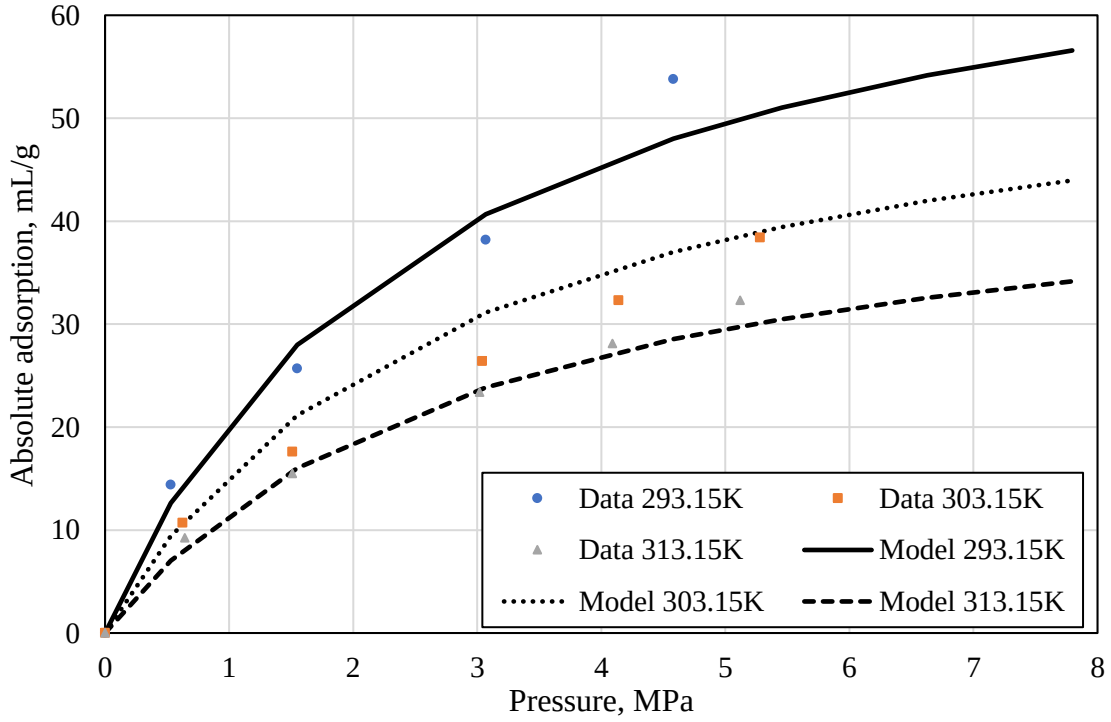

Figure 6.4 Comparison between experimental data and model prediction of CO_2 adsorption.

may be because gas adsorption is an exothermic process, such that increasing the temperature would result in a lower amount of adsorption at higher temperatures (Ye *et al.* 2016). It is shown that there is a good fit between the experimental measurements and the results predicted by the proposed exponential relation.

6.3 Mechanical response of coal to adsorptive gases

Coal permeability is a key controlling factor for coalbed reservoirs, especially for the process of CO_2-enhanced coalbed methane recovery. The permeability of coal reservoirs is not only sensitive to changes in effective stress but also additional changes due to gas adsorption (Somerton *et al.* 1975; Pan and Connell 2012). Coal shrinks with desorption and swells with gas adsorption, leading to a geomechanical stress response and changing the permeability. In order to predict coal permeability accurately, the coal permeability model must represent the mechanisms leading to observed flow behaviour. In section 3.7, a theoretical model was proposed to describe the deformation behaviour of coal interacting with adsorptive fluid using a surface stress approach. This section examines the performance of the constitutive relationship for deformation involving gas adsorption behaviour. Two sets of experimental data from core Anderson 01 (Robertson 2005) and core No. 01 (Pan *et al.* 2010a) are used to evaluate the developed deformation model and permeability model. The developed deformation model is then applied to investigate the coupling relationship between adsorption-induced swelling and the amount of gas adsorbed on coal. Finally, to improve understanding of the dynamic mechanical response to adsorptive gas transport in coal, the dynamics of coal porosity and permeability are analysed.

6.3.1 Experimental results of coal deformation and permeability

To validate the applicability of the deformation model developed in this work, two sets of experimental data (Robertson 2005; Pan *et al.* 2010a) are used to compare with the predicted results from the model. The coal samples studied in Robertson's experiment (2005) were of a subbituminous coal from the Anderson seam of the Power River Basin, USA. The small samples, with a diameter of 2 inches, used to measure strain were taken from the larger blocks and then dried. All measurements were done at a constant temperature of 26.67 ℃ using an optical method. The sorption-induced strain data versus pressure were collected for pure gases (CO_2, CH_4, N_2) and for a gas mixture (49% CO_2 and 51% N_2). Figure 6.5 shows

the data resulting from these experiments. Cores used to measure permeability were drilled parallel to the bedding plane from the same coal blocks. The inlet and outlet faces of the core used in the permeability measurements presented clear cleat systems. A series of experiments was conducted in which the pore pressure was varied while holding the confining pressure constant. The description of the permeability measurement process was detailed by Robertson (2005). Results of varying pore pressure and gas composition for the coal core are shown in Figure 6.6.

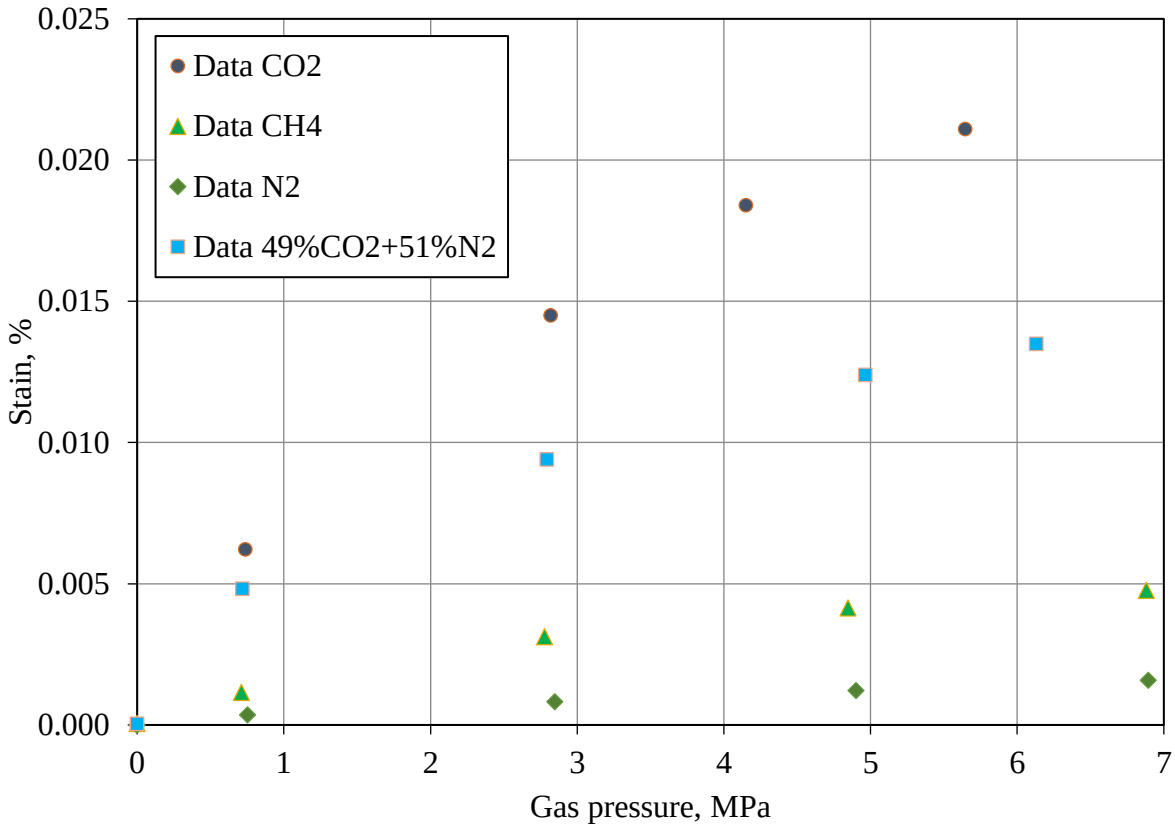

Figure 6.5 Experimental results of swelling strain induced by adsorption of CO_2, CH_4, N_2 and their mixture (Robertson 2005).

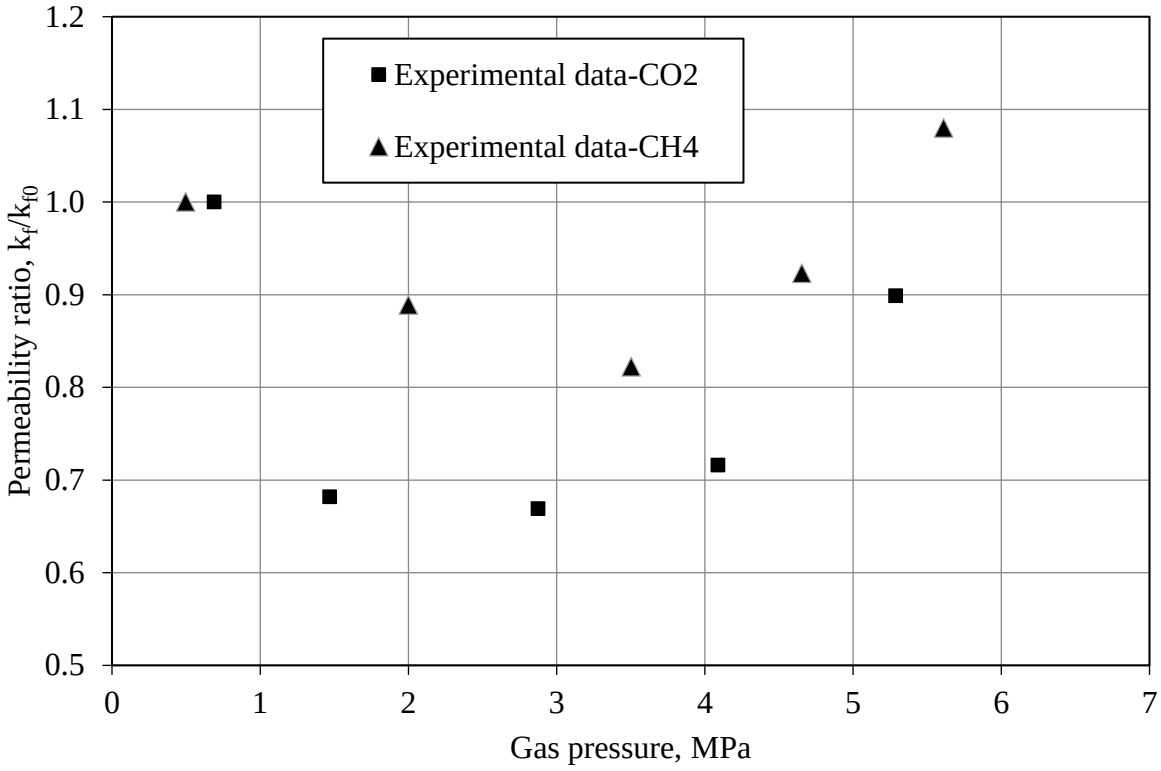

Figure 6.6 Experimental results of coal permeability for the flow of CO_2 and CH_4 versus pressure at different differential pressure by Robertson (2005).

To estimate the effects of swelling and effective stress on permeability, Pan *et al.* (2010a) conducted a series of measurements of gas adsorption, coal permeability, and core strain on an Australian core sample from the southern Sydney basin using a triaxial cell. The coal sample was bituminous coal from the Bulli seam and cored to 4.5 cm in diameter and 10.55 cm in length. Three gases were used; He, CH_4 and CO_2. All measurements were conducted at 45 °C. Gas permeability, adsorption, swelling, and geomechanical properties of coal cores at a series of pore pressures and for CH_4, CO_2 and He with pore pressures up to 13 MPa and confining pressures up to 20 MPa were recorded. Swelling displacements were measured simultaneously with gas adsorption at a constant effective stress, which was controlled by tracking the pore pressure. The CH_4 and CO_2 adsorption-induced coal swelling strain results are shown in Figure 6.7. The permeability measured using CO_2 and CH_4 at different differential pressures (confining pressure minus injection pressure) are shown in Figure 6.8 and Figure 6.9, respectively.

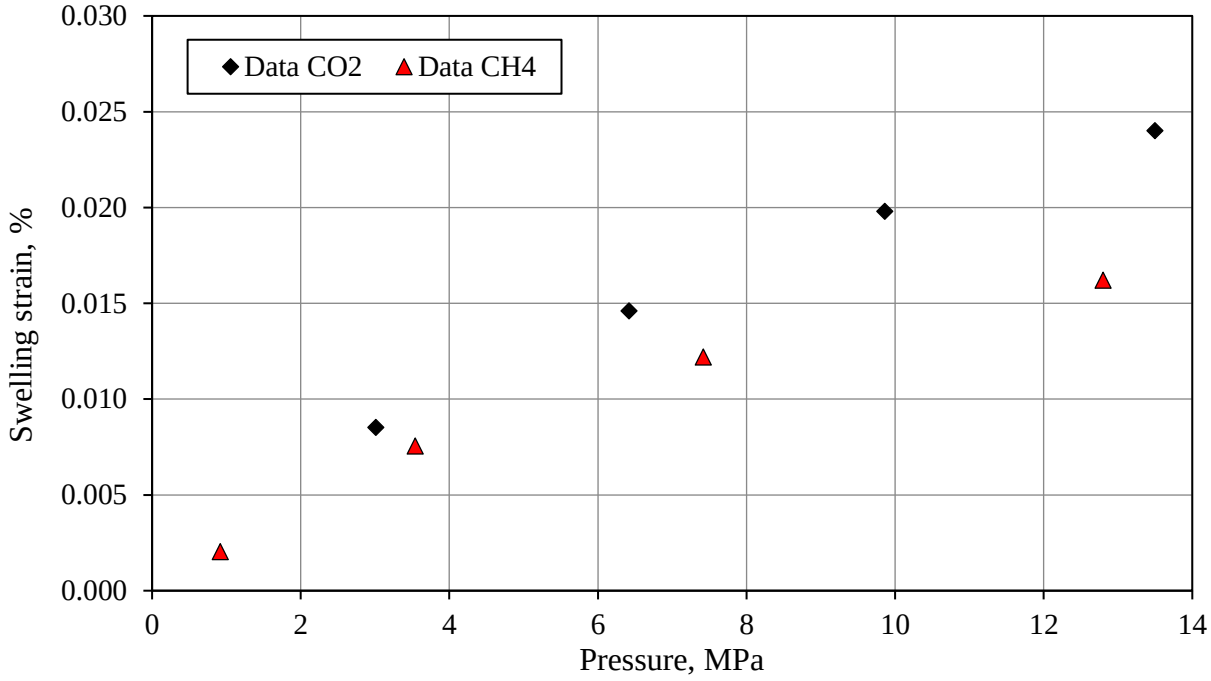

Figure 6.7 Experimental results of CH_4 and CO_2 adsorption-induced swelling (Pan *et al.* 2010a).

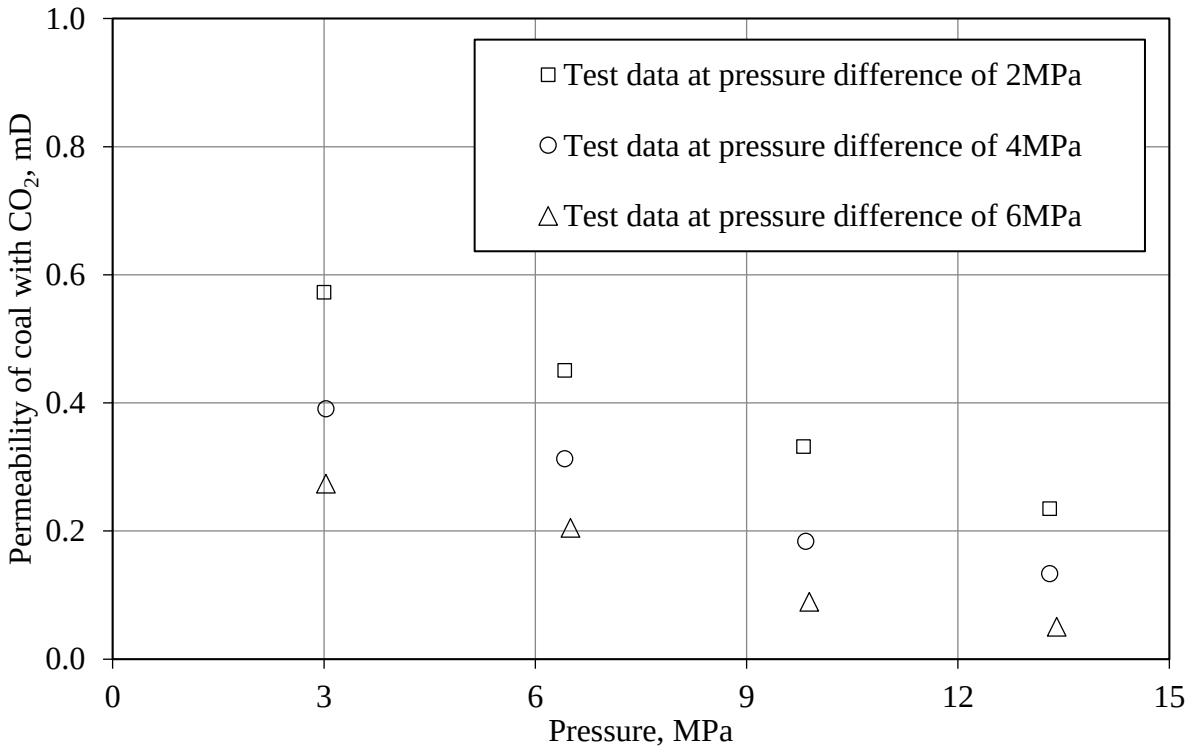

Figure 6.8 Experimental results of coal permeability with CO_2 versus pressure at different differential pressures (Pan et al.2010).

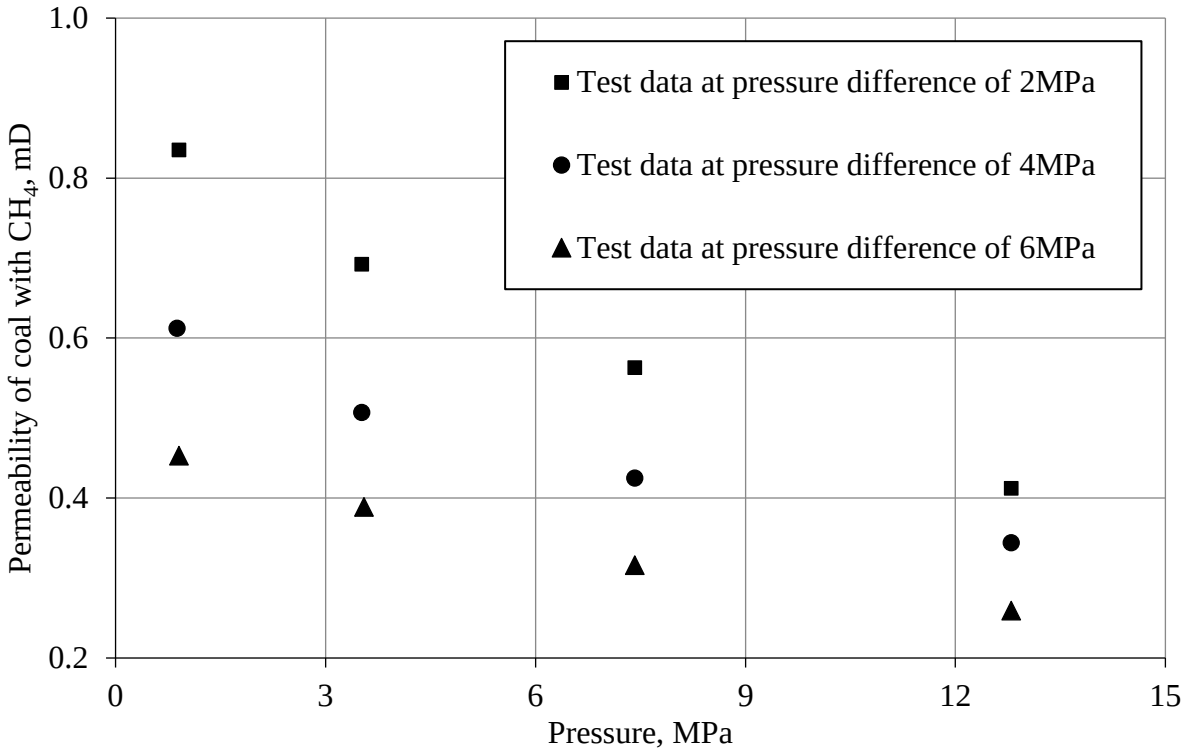

Figure 6.9 Experimental results of coal permeability with CH_4 versus pressure at different differential pressures (Pan et al 2010).

6.3.2 Matching of experimental data

According to the analysis presented in section 3.7, the total strain is a summation of deformation resulting from effective stress and adsorption-induced swelling, as:

$$\varepsilon_v = \varepsilon_v^e + \varepsilon_v^s = \frac{\bar{\sigma}}{K} - \frac{\tilde{\mathrm{b}}_1 u_a}{K} \tag{6.4}$$

where $\bar{\sigma} = -(\sigma_{11} + \sigma_{22} + \sigma_{33})/3 + \tilde{\mathrm{b}}_1 u_m + \tilde{\mathrm{b}}_2 u_f$ is the mean effective stress.

It is recalled that the pre-pressure u_a is related with the surface stress change, calculated as:

$$u_a = \pi RT \ln(1 + b_L u_{\mathrm{m}}) \tag{6.5}$$

Thus, the total strain for pure gas can be obtained by substitution of equation (6.5) into equation (6.4), given as:

$$\varepsilon_v = \frac{\bar{\sigma} + \pi RT \ln(1 + b_L u_{\mathrm{m}})}{K} \tag{6.6}$$

where $\pi = \tilde{\mathrm{b}}_1 \xi \Gamma^{max}$, which can be viewed as a Langmuir constant for surface stress, representing the effect of changes in coal structure on the adsorbed amount of gas. It can be obtained by matching the experimental measurements.

Coal deformation induced by the adsorption of binary gas mixture (CO_2 and N_2) can be calculated as:

$$\varepsilon_v = \frac{\bar{\sigma} + \dfrac{\pi_{CO_2} B_{L_{CO_2}} x_{CO_2} + \pi_{N_2} B_{L_{N_2}} x_{N_2}}{B_{L_{CO_2}} x_{CO_2} + B_{L_{N_2}} x_{N_2}} RT \ln\left[1 + \left(B_{L_{CO_2}} x_{CO_2} + B_{L_{N_2}} x_{N_2}\right) u_{\mathrm{m}}\right]}{K} \tag{6.7}$$

where x_{CO_2} and x_{N_2} are the gas fractions in the gas mixture.

The coal has two distinct pore structures, i.e. the porous matrix and facture network. Since the coal fracture permeability is typically in the region of 8 to 9 orders of magnitude larger than that in the porous matrix, providing the preferential channels for fluid flow in coal reservoirs, the contribution of the porous matrix to the coal permeability can be neglected (Seidle *et al.* 1992; Cui and Bustin 2005). Therefore, the evolution of total permeability is predicted using the porosity-permeability model derived in section 3.7.5, given by:

$$\Delta n_{\mathrm{f}} = (\tilde{\mathrm{b}}_2 - n_{\mathrm{f}})\Delta\varepsilon_v + (\tilde{\mathrm{b}}_2 - n_{\mathrm{f}}) c_s \Delta u_{\mathrm{f}} - (\tilde{\mathrm{b}}_2 - n_{\mathrm{f}})(c_{\mathrm{m}} - c_{\mathrm{s}})(\Delta u_{\mathrm{m}}^a - \Delta u_{\mathrm{f}}) - \Delta\varepsilon_{al} \tag{6.8}$$

Rearranging equation (6.8) produces:

$$n_{\mathrm{f}} = \frac{n_{\mathrm{f0}} + \tilde{\mathrm{b}}_2 \Delta\varepsilon_v + \tilde{\mathrm{b}}_2 c_s \Delta u_{\mathrm{f}} - \tilde{\mathrm{b}}_2 (c_{\mathrm{m}} - c_{\mathrm{s}})(\Delta u_{\mathrm{m}}^a - \Delta u_{\mathrm{f}}) - \Delta\varepsilon_{al}}{[1 + \Delta\varepsilon_v + c_s \Delta u_{\mathrm{f}} + (c_{\mathrm{m}} - c_{\mathrm{s}})(\Delta u_{\mathrm{m}}^a - \Delta u_{\mathrm{f}})]} \tag{6.9}$$

Based on the assumption of small strain, the fracture porosity equation can be simplified as:

$$n_{\mathrm{f}} = n_{\mathrm{f0}} + \tilde{\mathrm{b}}_2 \Delta\varepsilon_v + \tilde{\mathrm{b}}_2 c_{\mathrm{s}} \Delta u_{\mathrm{f}} - \tilde{\mathrm{b}}_2 (c_{\mathrm{m}} - c_{\mathrm{s}})(\Delta u_{\mathrm{m}}^a - \Delta u_{\mathrm{f}}) - \Delta\varepsilon_{al} \tag{6.10}$$

By applying the cubic law between porosity and permeability, the fracture permeability equation is expressed as:

$$\frac{K_{\mathrm{f}}}{K_{\mathrm{f0}}} = \left\{1 + \frac{1}{n_{\mathrm{f0}}}[\tilde{\mathrm{b}}_2 \Delta\varepsilon_v + \tilde{\mathrm{b}}_2 c_s \Delta u_{\mathrm{f}} - \tilde{\mathrm{b}}_2 (c_{\mathrm{m}} - c_{\mathrm{s}})\Delta(u_{\mathrm{m}}^a - u_{\mathrm{f}}) - \Delta\varepsilon_{al}]\right\}^3 \tag{6.11}$$

Equations (6.6), (6.7) and (6.11) are used to match the experimental results from Robertson (2005) and Pan *et al.* (2010a). Table 6.2 lists the matching parameters used to validate the developed models for coal deformation. The mechanical properties of coal are chosen from the work of Robertson (2005) and Pan *et al.* (2010a). The Langmuir constants are obtained by matching the experimental data.

Table 6.2 Summary of the matching parameters for swelling model.

Material parameters	**Relationship/value**	
	Robertson (2005)	**Pan *et al.* (2010a)**
Bulk modulus of coal, K (GPa)	1.1	1.6
Bulk modulus of coal grains, K_s (GPa)	3.6	29.1
Bulk modulus of coal matrix, K_m (GPa)	2.8	21.3
Temperature, T (K)	300	308
Langmuir constant, π_{CO_2} (mol m^{-3})	1.6e4	1.17e4
Langmuir constant, B_{CO_2} (MPa^{-1})	0.88	0.19
Langmuir constant, π_{CH_4} (mol m^{-3})	4.3e3	6.04e3
Langmuir constant, B_{CH_4} (MPa^{-1})	0.67	0.34
Langmuir constant, π_{N_2} (mol m^{-3})	2.8e3	-
Langmuir constant, B_{N_2} (MPa^{-1})	0.29	-
Biot's coefficient, b (-)	0.7	0.945

It can be seen from Figure 6.10 and Figure 6.11 that the model results compare well with the experimental measurement for both pure gas and mixed gas, indicating that the developed swelling model is able to describe the deformation behaviour when adsorptive fluids are involved. Different gases cause distinct deformation behaviour, hence, the coal deformation involving gas adsorption is species dependent. Both coals exhibited the largest strain when adsorbing CO_2 compared to the swelling strain induced by CH_4 and N_2 adsorption. The decrease of CO_2 fraction in the gas mixture reduces coal swelling. This is because coal has a greater preference to adsorb CO_2 ahead of CH_4 and N_2, and the solid surface that provides the adsorption sites for gas molecule is stretched significantly, leading to a significant decrease in surface stress and an increase in adsorption stress, as shown in Figure 6.12. The adsorption stress induced by CO_2 adsorption is considerably larger than that by CH_4 and N_2.

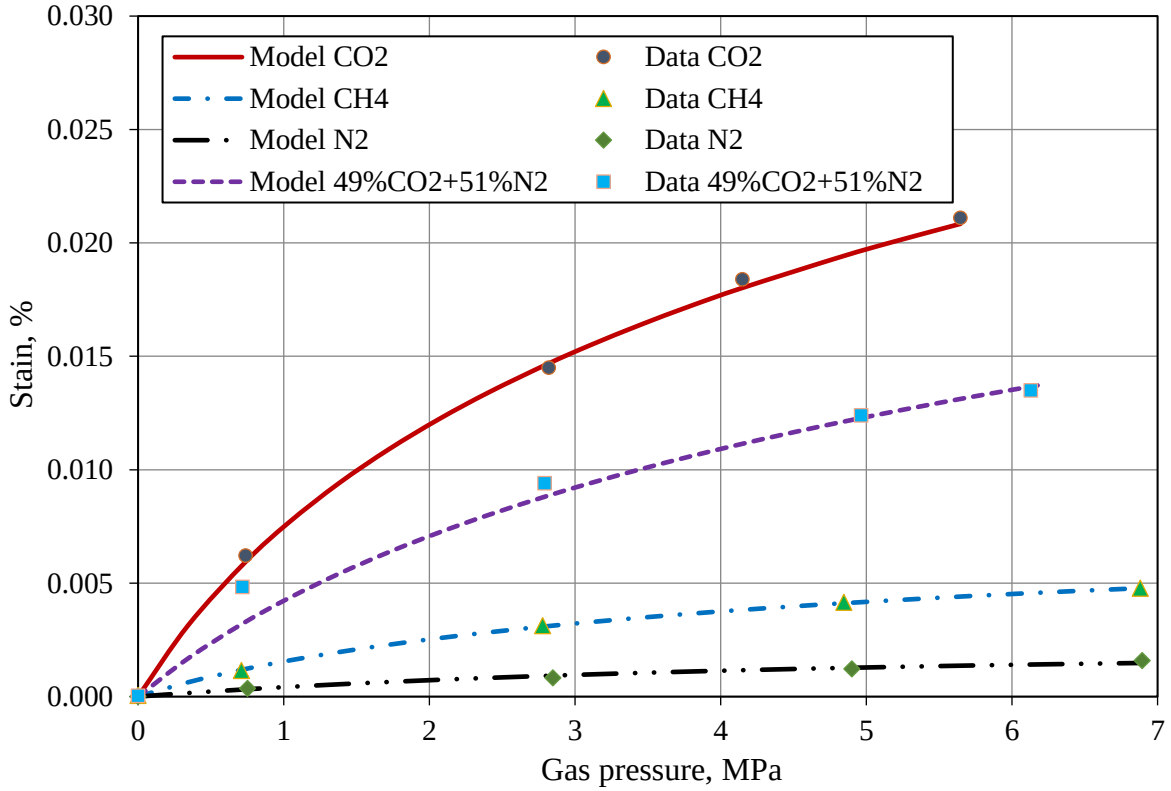

Figure 6.10 Comparison between the experimental data from Robertson (2005) and predicted swelling strain.

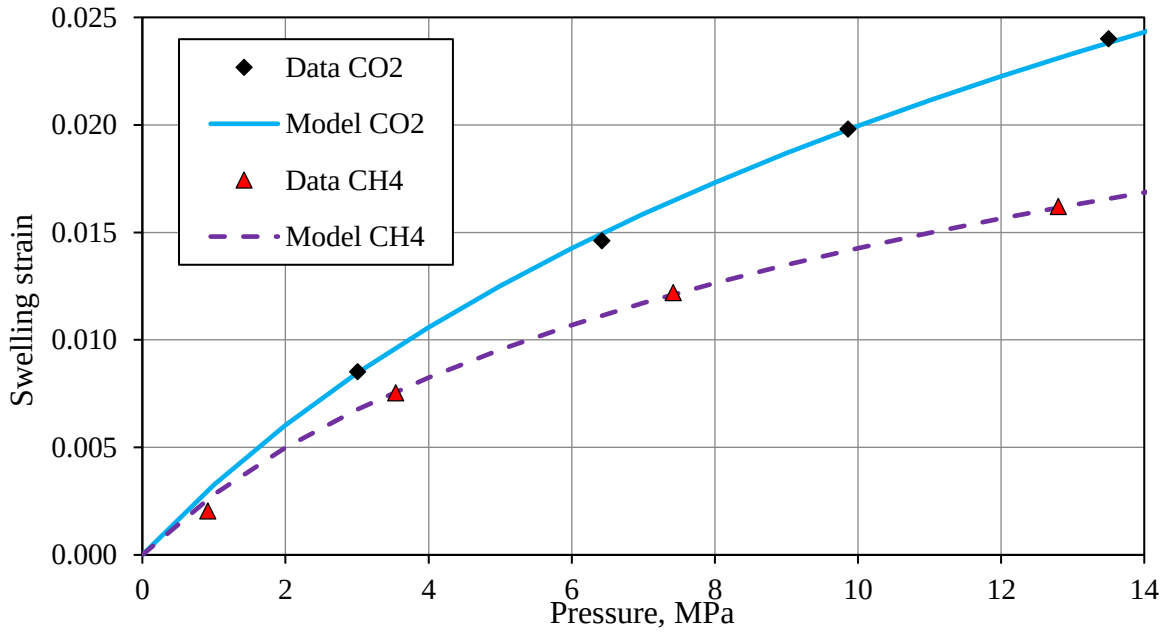

Figure 6.11 Comparison of model predicted swelling strain with experimental data from Pan *et al.* (2010a).

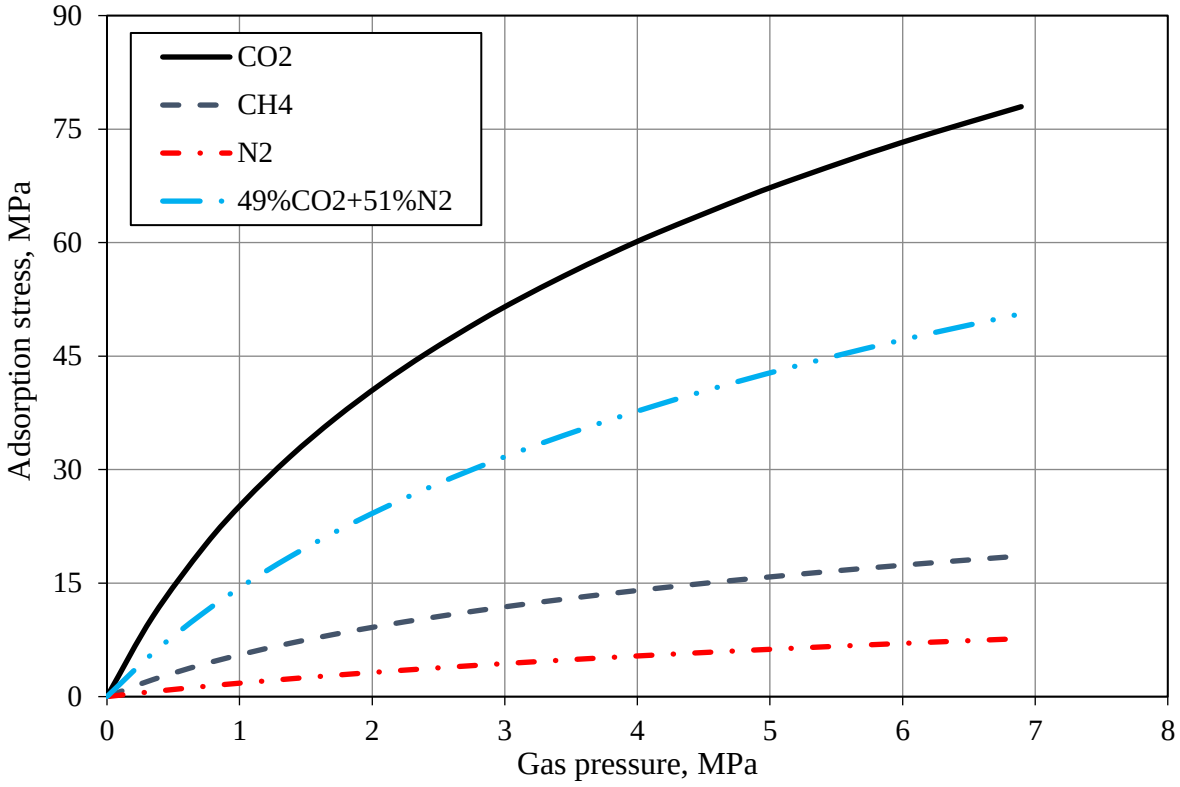

Figure 6.12 Adsorption stress change due to adsorption for different gases used in experiment by Robertson (2005).

Figure 6.13 compares the computed responses with the experimental data of coal from the Anderson seam of the Power River Basin. Table 6.3 provides the matching parameters used to validate the developed models for porosity and permeability change. It is shown that the model has captured the nonlinear permeability ratio curve. The permeability results for both CO_2 and CH_4 exhibit a similar evolution pattern. As pore gas pressure increases, the permeability initially decreases because of larger sorption-induced strain. As pore pressure continues to increase, the permeability starts to redound due to the competing effects between sorption-induced strain and effective stress. When the pore gas pressure reaches a larger value, the effect of sorption-induced strain was overcome by the opposite-acting strain caused by the elastic properties of the coal at higher pore pressures (Robertson 2005). As expected, the permeability with CO_2 shows a larger decrease due to the larger swelling strain.

Table 6.3 Fitting parameters of swelling model.

Material Parameters	Values	
	Robertson (2005)	**Pan et al. (2010)**
Bulk modulus of coal, K (GPa)	1.1	1.6
Bulk modulus of coal grains, K_s (GPa)	3.6	29.1
Bulk modulus of coal matrix, K_m (GPa)	2.8	21.3
Temperature, T (K)	300	308
Initial porosity, n_{f0} (-)	0.013	0.014
Biot's coefficient, $\tilde{b}_2$	0.6	0.925
Biot's coefficient, $\tilde{b}_1$ (-)	0.1	0.02
Langmuir constant, B_{CO_2} (MPa^{-1})	0.88	0.19
Langmuir constant, π_{CO_2} (mol m^{-3})	1.6e4	1.17e4
Ratio of local swelling to global swelling for CO_2, Λ (-)	0.25	0.14
Langmuir constant, B_{CH_4} (MPa^{-1})	0.67	0.34
Langmuir constant, π_{CH_4} (mol m^{-3})	4.3e3	6.04e3
Ratio of local swelling to global swelling for CH_4, Λ (-)	0.92	0.96

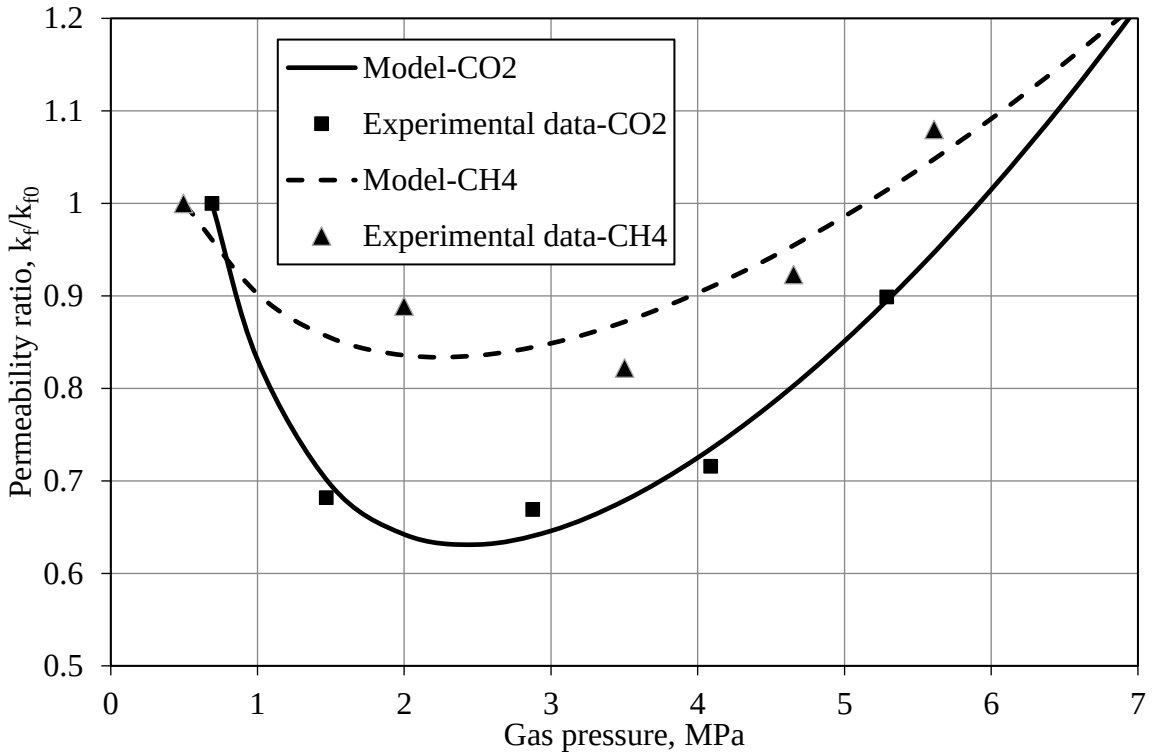

Figure 6.13 Comparison of the model predictions with the test data by Robertson (2005) for permeability of coal with CO_2 and CH_4 versus pressure.

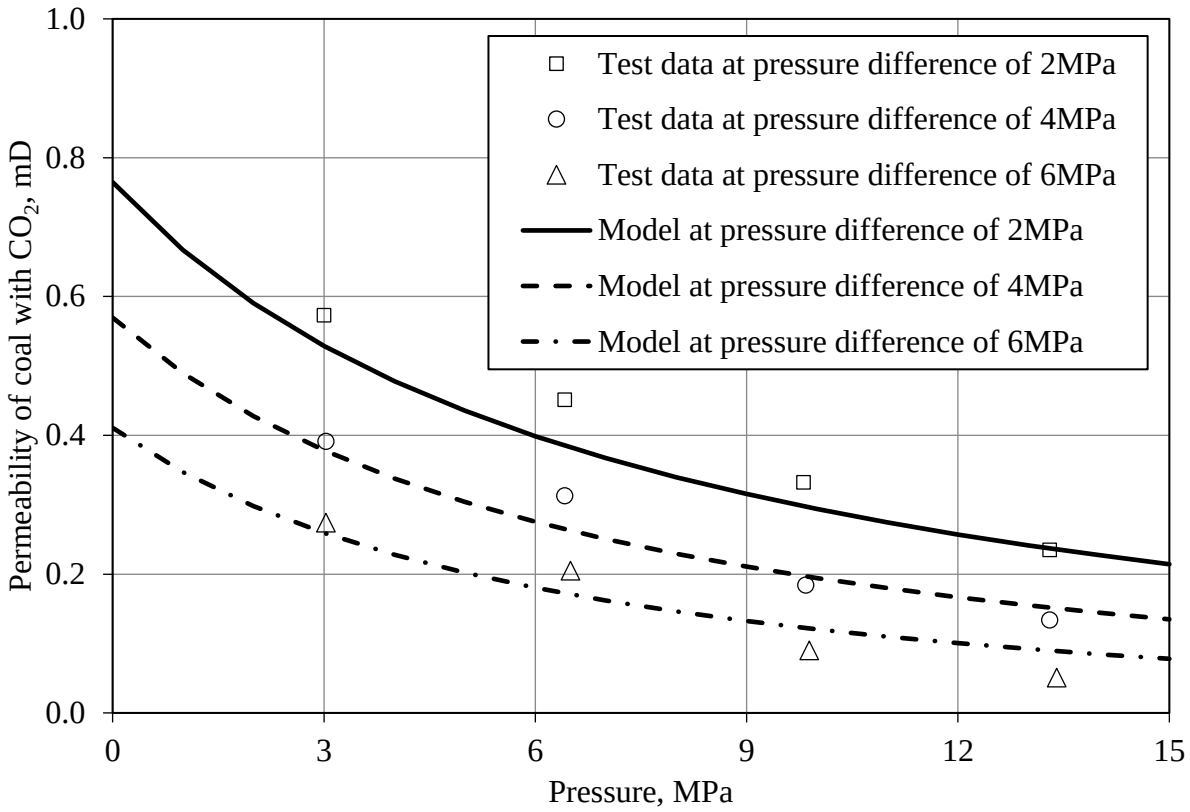

Figure 6.14 Comparison of the model predictions with the test data by Pan *et al.* (2010a) for permeability of coal with CO_2 versus pressure at different differential pressures.

Comparisons of the permeabilities measured in the laboratory with those predicted by the model for CO_2 and CH_4 are shown in Figure 6.14 and Figure 6.15, respectively. The material parameters are again those given in Table 6.3. It can be seen from the comparison that there are differences between the permeabilities for the different gas species. Although the permeability decreases with increasing pore pressure under a constant pressure difference for both gases, the permeability measured using CO_2 is lower than that measured using CH_4, with the declines with CO_2 being larger than those with CH_4, possibly due to the higher swelling effect associated with CO_2 adsorption. In addition, the impact of effective stress on the permeability is worth highlighting. At constant pore pressure, a larger the pressure difference leads to lower permeability. Since the tests were performed at constant pore pressure during experimental measurement, the change in pressure difference was achieved by varying the confining pressure (Pan *et al.* 2010a), with a larger pressure difference leading to lower permeability.

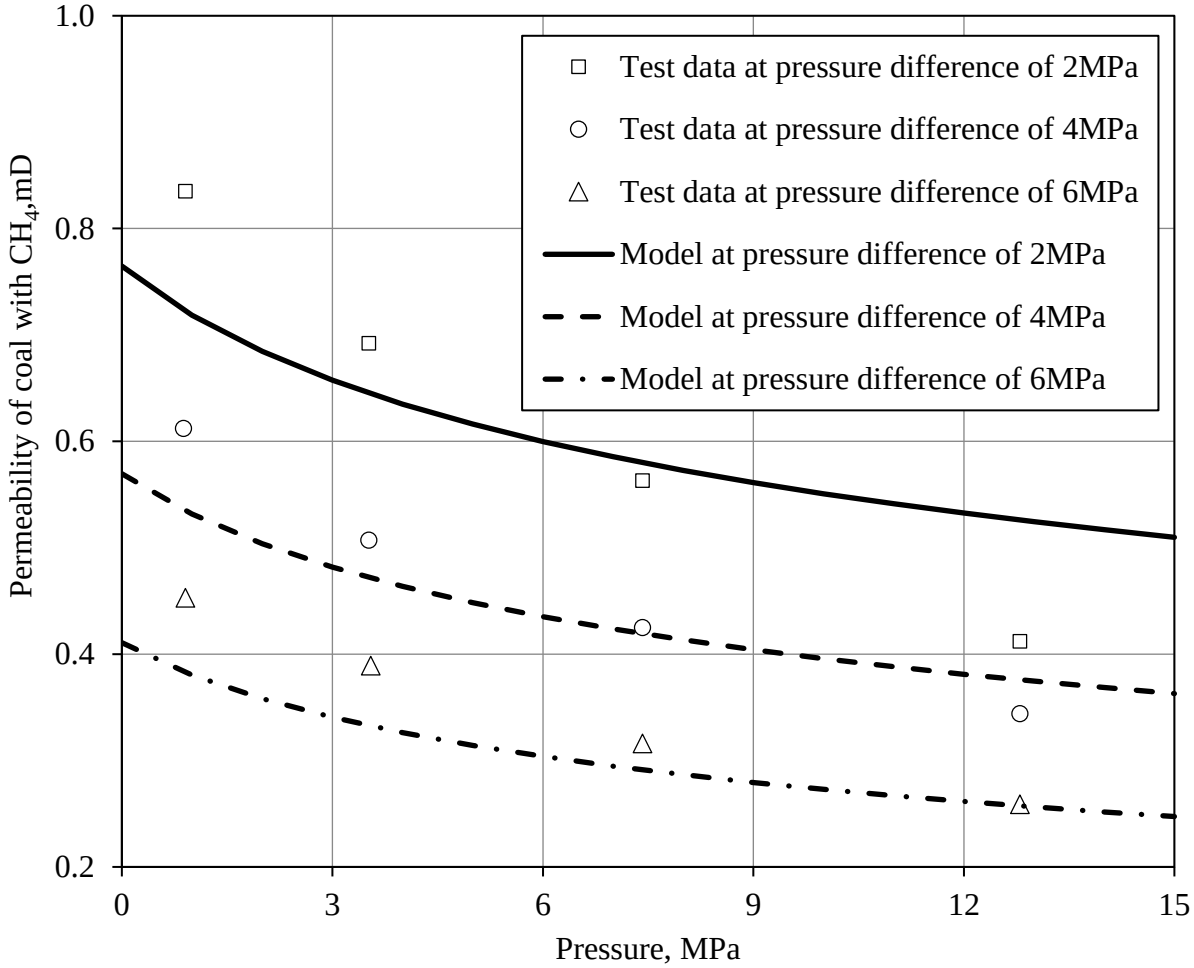

Figure 6.15 Comparison of the model predictions with the test data by Pan *et al.* (2010a) for permeability of coal with CH_4 versus pressure at different differential pressure.

6.3.3 The coupling between adsorption and swelling

The relationship between swelling deformation and the amount of gas adsorption has usually been assumed to be linear (e.g. Sawyer *et al.* 1990; Harpalani and Chen 1995; Seidle and Huitt 1995; Cui and Bustin 2005) with a sraightforward application in permeability models. However, more recent studies show a non-linear (s-shaped) relationship between adsorption-induced swelling strain and absolute adsorption (Hol and Spiers 2012; Zhang 2018).

According to the Langmuir isotherm, the pressure is treated as a funcion of adsorption amount, written as:

$$u_{\mathrm{m}} = \frac{V}{b_L(V_L - V)} \tag{6.12}$$

Substitution of equation (6.12) into equation (6.5) yields:

$$\frac{u_a}{\pi RT} = \ln\left(\frac{1}{1 - V/V_L}\right) \tag{6.13}$$

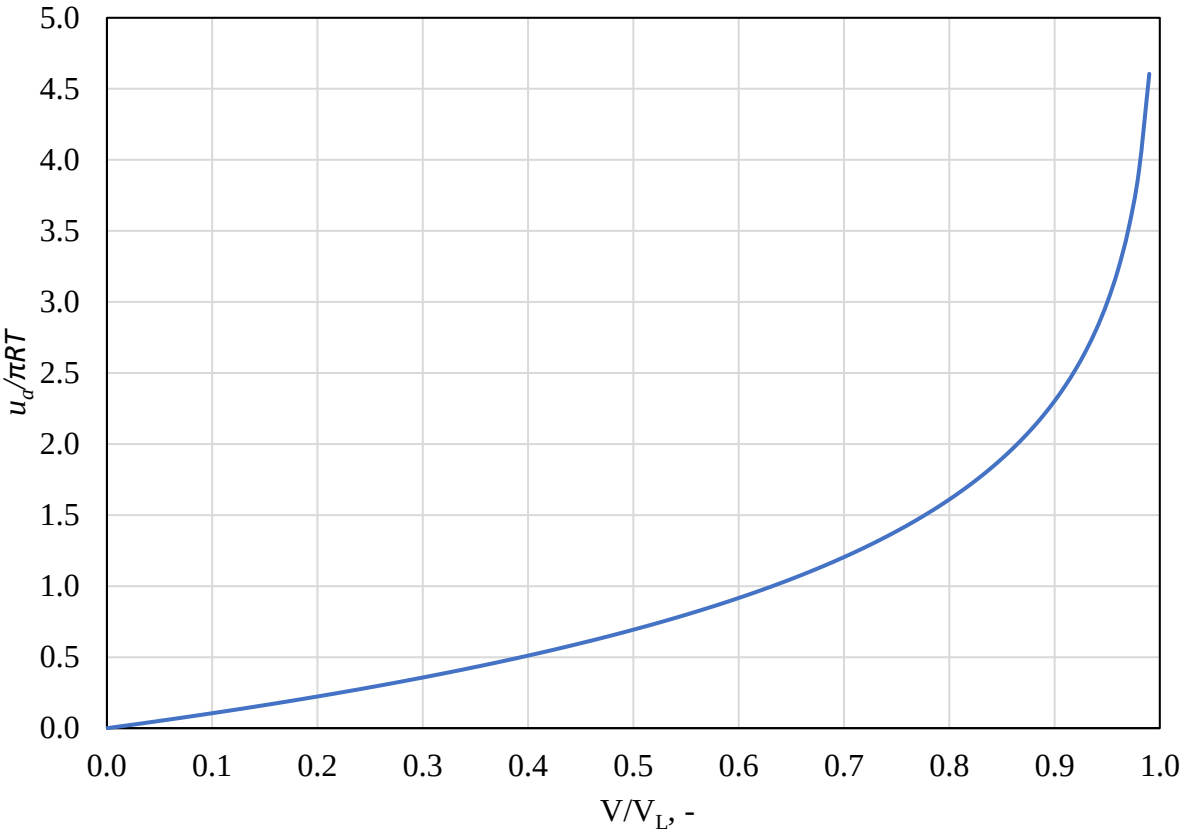

Figure 6.16 Relationship between the adsorption-induced swelling stress and normalised adsorption amount.

It can be seen from Figure 6.16 that if gas adsorption follows the Langmiur isotherm, the adsorption-induced swelling stress shows an nonlinear relation with the normalised adsorption amount, espeically when the amount of gas adsorption exceeds half of the gas adsorption capacity, i.e. $V/V_L > 0.5$, where the increase of adsorption-induced swelling with adsorption amount is dramatic. Nevertheless, when $V/V_L < 0.5$, the adsorption-induced swelling is approximately linear.

6.3.4 Dynamics of coal porosity and permeability

In the previous sections, aspects of the formulation related to gas adsorption and deformation behaviour of coal were examined. Whist the overall trends of the predicted deformation and permeability curves are consistent with those observed in experiments, all of the results used

as benchmarks were for an equilibrium state, such that the dynamic characteristics of the mechanical response were not clear. In this section, a series of numerical simulations are performed to investigate the impact of adsorption on flow behaviour during CO_2 injection into a coal core at the laboratory scale. This includes an in-depth discussion on the processes and behaviour involved. The results presented in this section have been published and can be found in Chen *et al.* (2019a).

6.3.4.1 Model domain and material parameters

A cylindrical geometry (100 mm in length and 50 mm in width) confined by constant stress is selected for the numerical simulation, as shown in Figure 6.17a. Due to the symmetry, the cylindrical coal sample can be simplified as the 2D model shown in Figure 6.17b. Boundary conditions corresponding to the conditions shown in Figure 6.17b are required for this coupled problem. For coal deformation, a vertical constraint is applied to the outflow boundary while a constant confining stress is applied to the right and inflow boundaries. The left side of the model is fixed horizontally. For gas flow, a zero-flux boundary is applied to the right and left boundaries of the domain. For gas flow in the matrix continuum, zero-flux conditions are specified for all boundaries of the model. The initial pressure for both the fracture and matrix continua is 0.1 MPa, the injected pressure is set 7 MPa.

Three measuring points with an equal spacing of 30 mm are set to monitor the variations of the gas pressures and permeability, i.e. A (12,80), B (12, 50) and C (12, 20). The parameters for simulations are listed in Table 6.4, some of which are chosen from the validation tests presented above, with others selected from the literature (Gensterblum *et al.* 2010; Peng *et al.* 2014; Zhang *et al.* 2018). In this simulation, the selected fracture porosity is higher than the matrix porosity. This is taken as reasonable since Robertson and Christiansen (2006) present a photograph of the coal sample used, in which clearly-defined fractures can be seen. A time-dependent injection pressure is specified at the top surface as an inflow boundary to the fracture continuum for the gas transport model, a constant loading speed is assumed, and the characteristic time for equilibrium fracture pressure is set 2500 seconds.

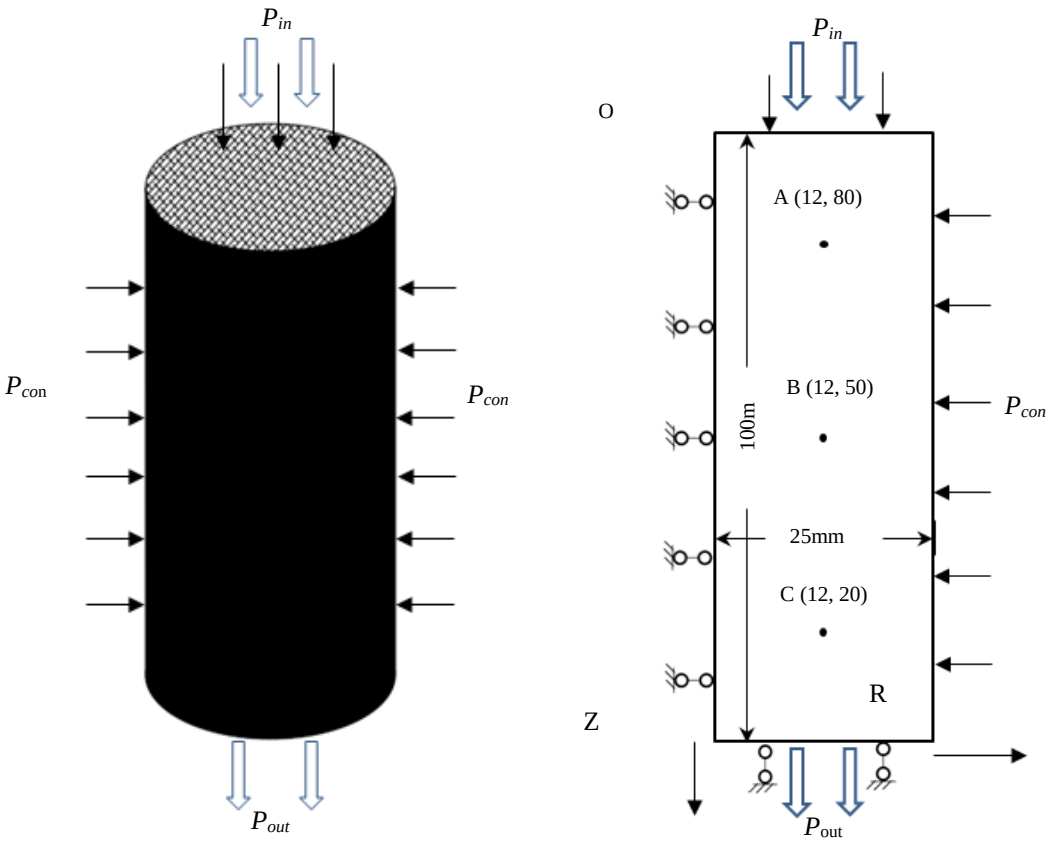

(a) Laboratory coal sample (b) 2-D model

Figure 6.17 Geometry and boundary conditions of the numerical model under constant confining stress.

6.3.4.2 Simulation results and discussion

Figure 6.18 depicts the distribution of the gas pressure in the fracture and matrix continua along the coal sample after the equilibrium state is reached. The high pressure is located at the gas inlet of the coal sample, deceasing gradually to the gas outlet pressure. For the matrix porosity, the high-pressure area shows larger matrix porosity. The matrix porosity increases from 1% to about 7% with the increase of gas pressure from 0.1 MPa to 7 MPa. However, the increase of matrix porosity tends to be slow with increase in the gas pressure. The fracture porosity displays a different pattern from the matrix porosity. The fracture porosity across most of the core is less than the initial value and decreases to the minimum at the location where the pressure is approximately 2.2 MPa.

Table 6.4 Parameters input in the numerical simulation.

Material Parameters	Value
Bulk modulus of coal, K (GPa)	1.1
Modulus of coal matrix, K_m (GPa)	2.8
Modulus of solid grains, K_s (GPa)	3.6
Poisson's ratio, v (-)	0.35
Initial porosity of fracture, n_{f0} (-)	0.013
Initial porosity of matrix, n_{m0} (-)	0.01
Initial fracture permeability, K_{f0} (m^2)	8.5e-14
Density of coal matrix, ρ_c (kg/m^3)	1400
Viscosity of gas, μ (Pa·s)	1.84e-5
Langmuir volume constant, V_L (m^3/kg)	0.035
Langmuir pressure constant, B (MPa^{-1})	0.88
Langmuir constant, π_{CO_2} (mol m^{-3})	1.6e4
Temperature, T (K)	300
Ratio of local swelling to global swelling for CO_2, Λ (-)	0.25
Sorption time, $\mathscr{L}$ (s)	2.0e5

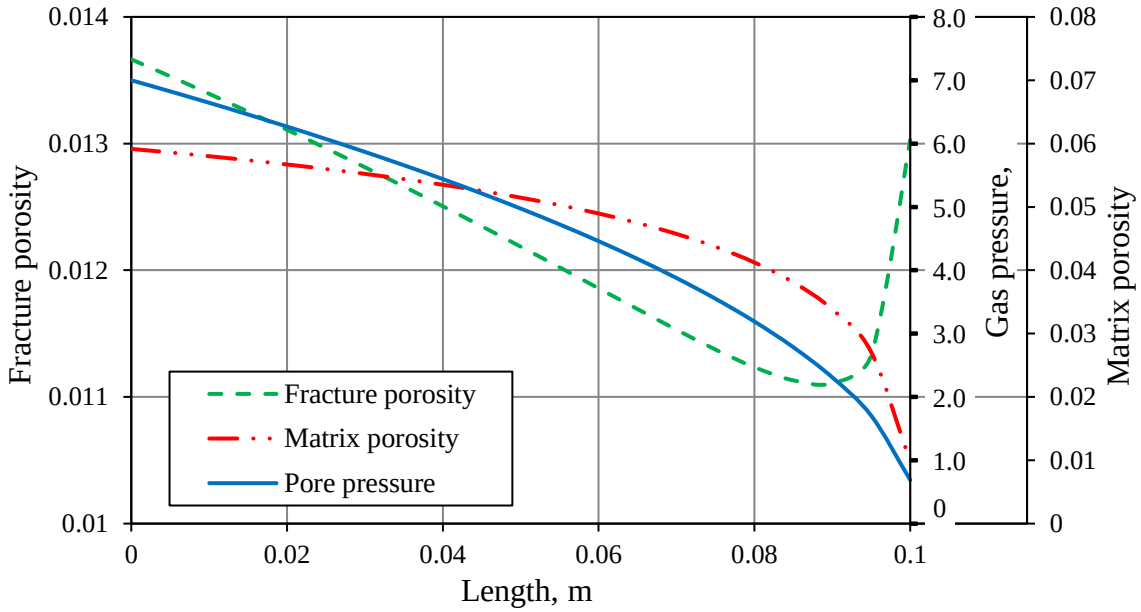

Figure 6.18 Spatial distribution of the gas pressure and porosities in the coal sample under equilibrium state.

In order to better understand the variation of gas pressures in the fracture and matrix continua with equilibrium time, three monitoring points are set to explore the characteristics of gas flow. Due to the larger permeability of the fracture continuum, the fracture gas pressure rapidly increases and reaches the equilibrium state almost at the same time. The point closer to the gas inlet of the coal sample has higher gas pressures as shown in Figure 6.19. It can be seen that almost no gas diffuses into the coal matrix before the fracture gas pressure achieves equilibrium. There is a rapid increase in matrix gas pressure after equilibrium of the fracture gas pressure. While the equilibrium time for gas pressure in the matrix at these three monitoring points is different. The equilibrium time for point A is relatively shorter than the other two points, as expected since higher pressures in the fracture continuum promote gas diffusion into the coal matrix continuum and reduce the equilibrium time.

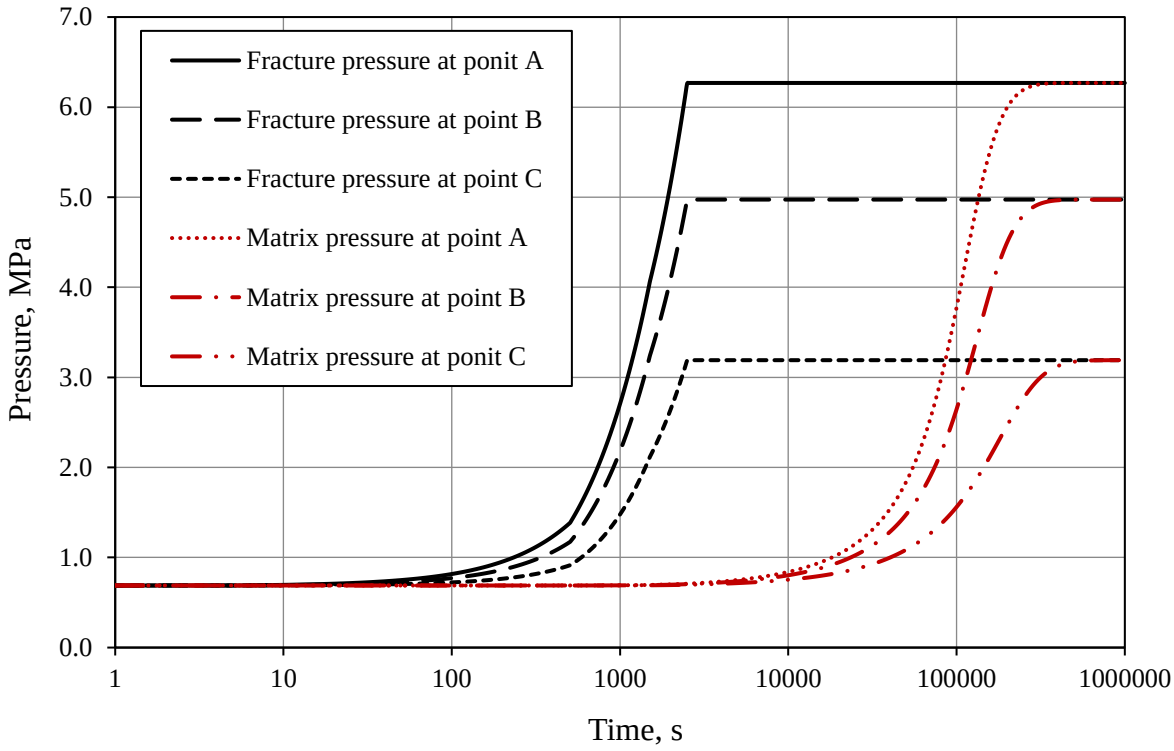

Figure 6.19 The evolution of gas pressures in fracture and matrix with time at three detection points.

The overall relationships between the simulation time and the evolving coal porosity and permeability are illustrated in Figure 6.20, Figure 6.21 and Figure 6.22. Figure 6.20 shows that the patterns of porosity variation with time at the three monitoring points are similar at early simulation times; the rapid increase in fracture gas pressure results in the decrease of effective stress and increase of fracture porosity, and fracture porosity change is controlled

by the first two terms in equation (3.160). Mass exchange between the fracture continuum and coal matrix continuum occurs with the increase in simulation time, leading to an increase in the gas pressure of the coal matrix continuum and therefore the amount of gas adsorption. In turn, the increase of the amount of adsorbed gas induces the increase in pressure difference between the coal matrix and fracture system and internal swelling deformation. The change in fracture volume due to internal deformation of the coal is competitive with that due to the bulk volume change induced by effective stress; that is, the terms representing fracture-matrix compartment interaction in equation (3.160) play a controlled role in the variation of fracture porosity. The volume occupied by the fractures is compressed. Therefore, the fracture porosity declines during this period of the simulation. The fracture porosity of point A shows an obvious rebound before reaching equilibrium compared with these of points B and C. This is because with the increase in gas pressure in the matrix continuum as a result of continuous diffusion of gas into the coal matrix, the change in fracture volume due to the internal deformation of coal is smaller than the change in bulk volume induced by effective stress; the fracture porosity is mainly affected by the effective stress when the gas pressure is larger. The pressures at points B and C are relatively lower and the impact of internal interactions on changes to the fracture volume are still dominant, and thus no rebounds are displayed. The permeability evolutions with equilibrium time at three detection points show the same trend as fracture porosity, as shown in Figure 6.21.

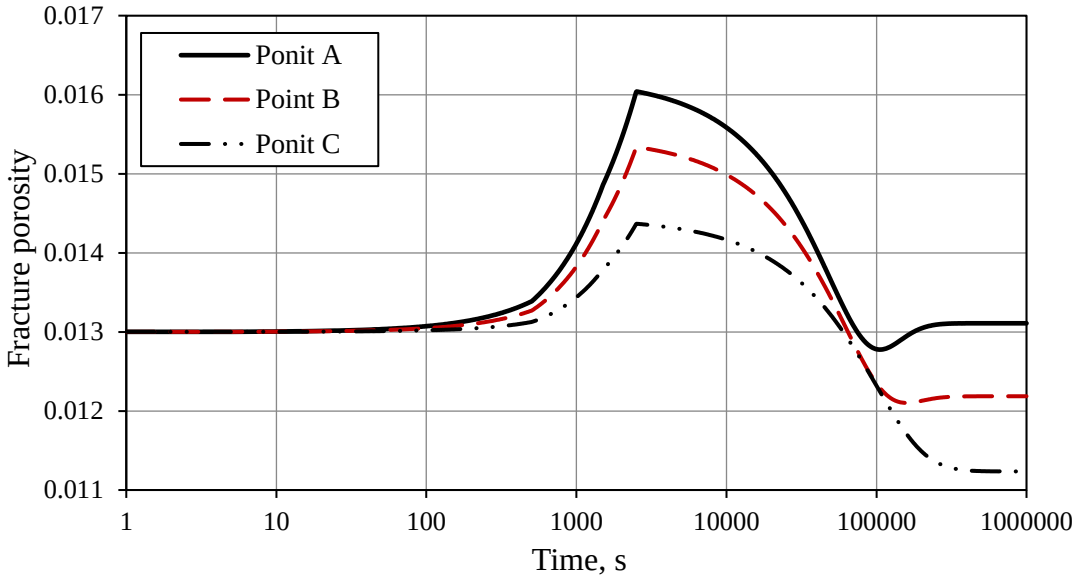

Figure 6.20 The evolution of fracture porosity with time at three detection points.

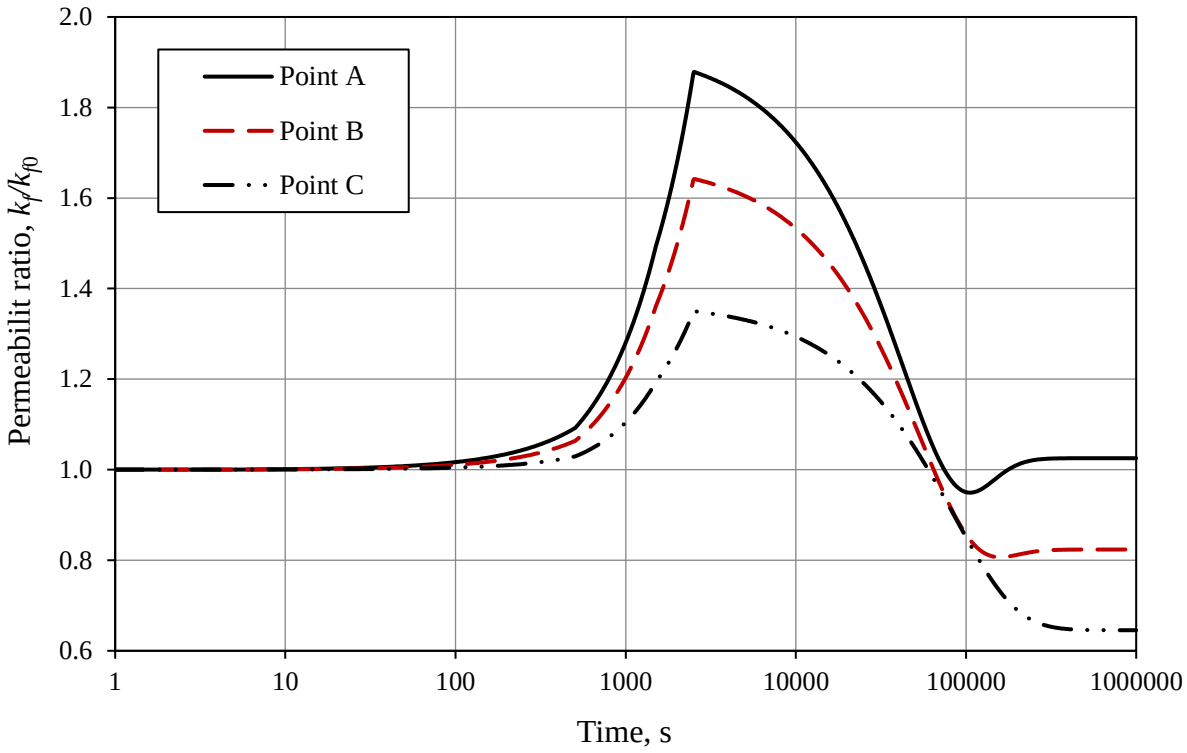

Figure 6.21 The evolution of fracture permeability with time at three detection points.

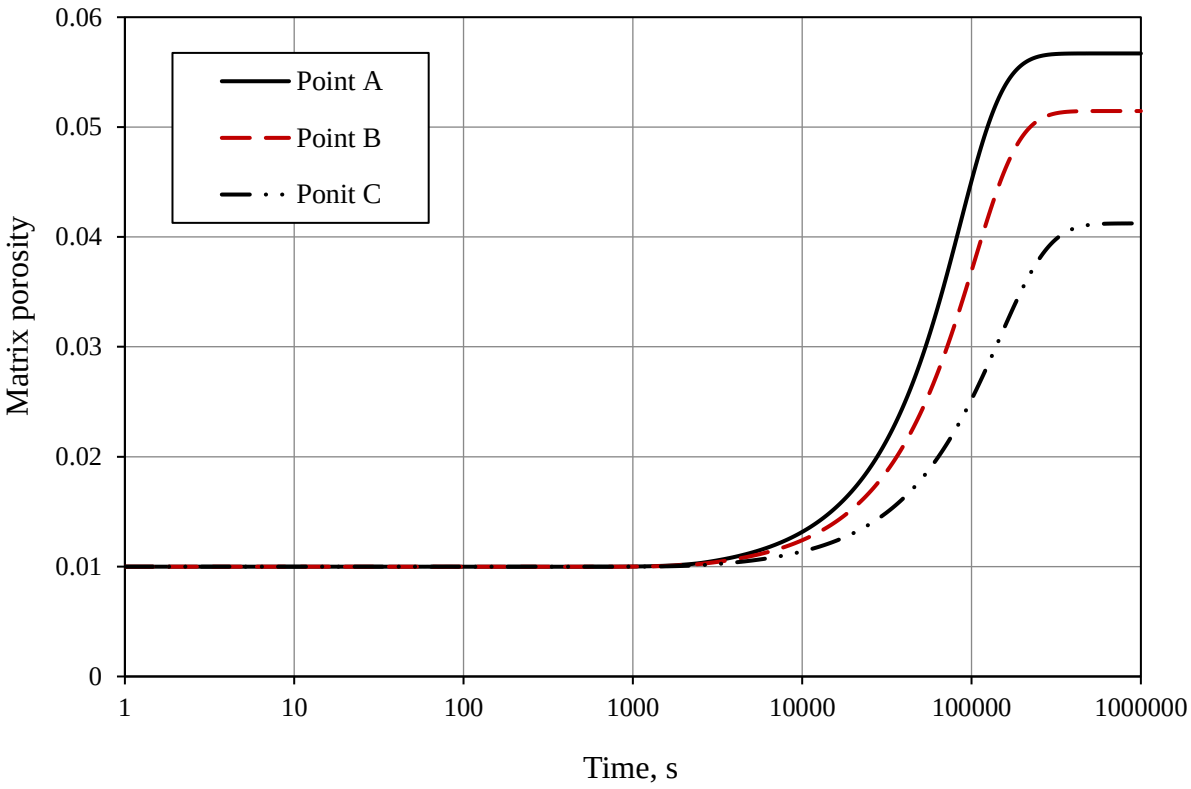

Figure 6.22 The evolution of matrix porosity with time at three detection points.

In previous studies, most of the focus has fallen on the fracture porosity and permeability; attempts to consider the variation of matrix porosity are limited. Figure 6.22 depicts how the matrix porosity varies with equilibrium time. Compared with the fracture porosity, CO_2 injection into coal has the potential to increase the microporosity significantly, with similar findings having been reported in the literature (Gathitu *et al.* 2009; Liu *et al.* 2010b). For example, the matrix porosity at point A increases from the initial porosity of 1% to about 5.5% at equilibrium state. It can be seen that the matrix porosity shows a similar pattern to the gas pressure in the matrix, illustrated in Figure 6.19. At the early stage, although the bulk gas pressure in the fracture network is higher than that in matrix system and matrix pores can be contracted, the increase in bulk volume caused by bulk gas pressure in the micropores can bring about an increase in micropore volume of the coal matrix at the same time. Thus, the porosity does not show an obvious decrease during the early period. As time increases, the bulk gas pressure in the matrix increases as a consequence of more gas diffusion into the coal matrix from the fracture network, leading to more gas being adsorbed onto internal walls of the coal and the larger influence of surface stress. Not only the increase of bulk volume and compression of solid constituent, but also the internal deformation makes contributions to changes in the matrix porosity; in other words, the three terms on the right-hand side of equation (3.160) have positive effects on the matrix porosity. Compared with the volumetric strain (three times the longitudinal strain) illustrated in Figure 6.10, it is interesting that the significant increase in microporosity seems to be an important reason for the occurrence of the swelling phenomenon during CO_2 injection into coal.

6.4 Prediction of CBM recovery performance including multi-phase flow

In the previous section, the capabilities of the developed model for describing the mechanical deformation and flow characteristics of a coal core have been examined by comparing the model predictions with experimental measurements. However, only single-phase flow was considered in these validation tests. To further validate the predictive capacity of the coupled model developed in this work, this section applies the coupled model to simulate the pressure depletion due to CBM recovery. This test examines the hydro-mechanical coupling, involving dual porosity multiphase flow, the new porosity and permeability model, adsorption behaviour, and deformation behaviour. After that, a

parameter sensitivity study is performed to investigate the influences of various parameters on gas production.

As shown in Figure 6.23, the San Juan Basin is located in southwest Colorado and northwest New Mexico, containing the second largest gas deposit in the United States (Ayers Jr 2003),. The Basin contains abundant coalbed gas in both the Menefee and the Fruitland formations, but commercial CBM production is from the Fruitland formation only (Ayers Jr 2003). The commercial production of Fruitland CBM in the San Juan Basin not only triggered worldwide exploration of CBM but has also contributed to numerical simulator development for coalbed reservoirs. Field data collected from CBM production in the San Juan Basin has been applied to examine the reliability of many developed models (Palmer and Mansoori 1996; Mavor and Vaughn 1998; Palmer and Vaziri 2004; Clarkson *et al.* 2007; Gierhart *et al.* 2007; Palmer 2009; Clarkson *et al.* 2010; Shi and Durucan 2010; Moore *et al.* 2011).

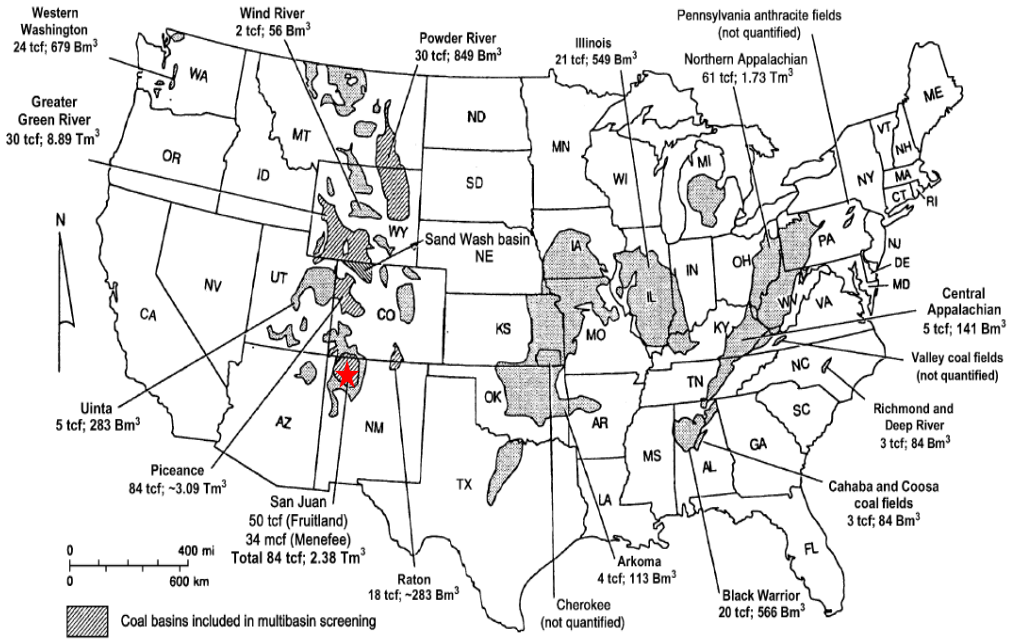

Figure 6.23 United States coal basins and coalbed-gas resources (Ayers Jr 2003).

The well analysed in this test is the boomer Fairway well located in the Fruitland formation of the San Juan Basin (Figure 6.24). The very strong gas production increase with time is a distinguished characteristic of boomer Fairway wells (Pan and Connell 2012) because of the well-cleated system and higher permeability of the Fruitland bituminous coals in the Fairway (Moore *et al.* 2011). Palmer and Mansoori (1996) presented CBM production data for

Boomer Fairway well B#1, as shown in Figure 6.25 to 6.27, which show the historical daily water production rate, gas production rate, and bottom hole pressure, respectively. A historical matching of the production data is performed to validate the predictive capacity of the model developed in this work.

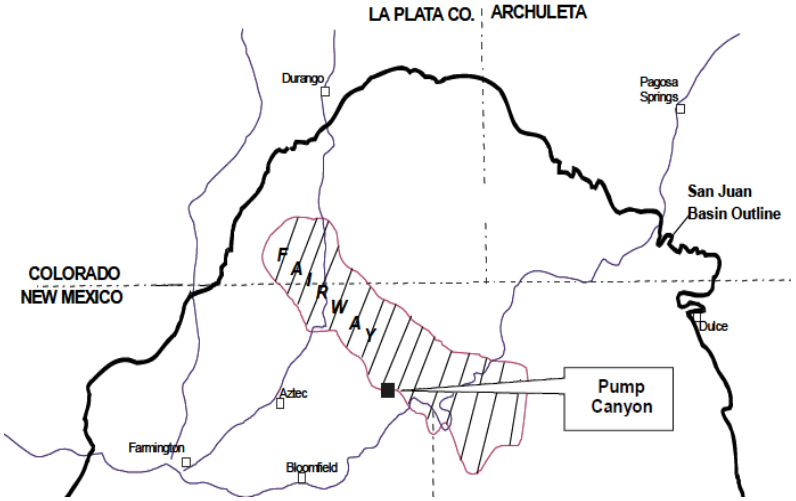

Figure 6.24 Map showing the location of Fairway in the San Juan Basin (Oudinot *et al.* 2011).

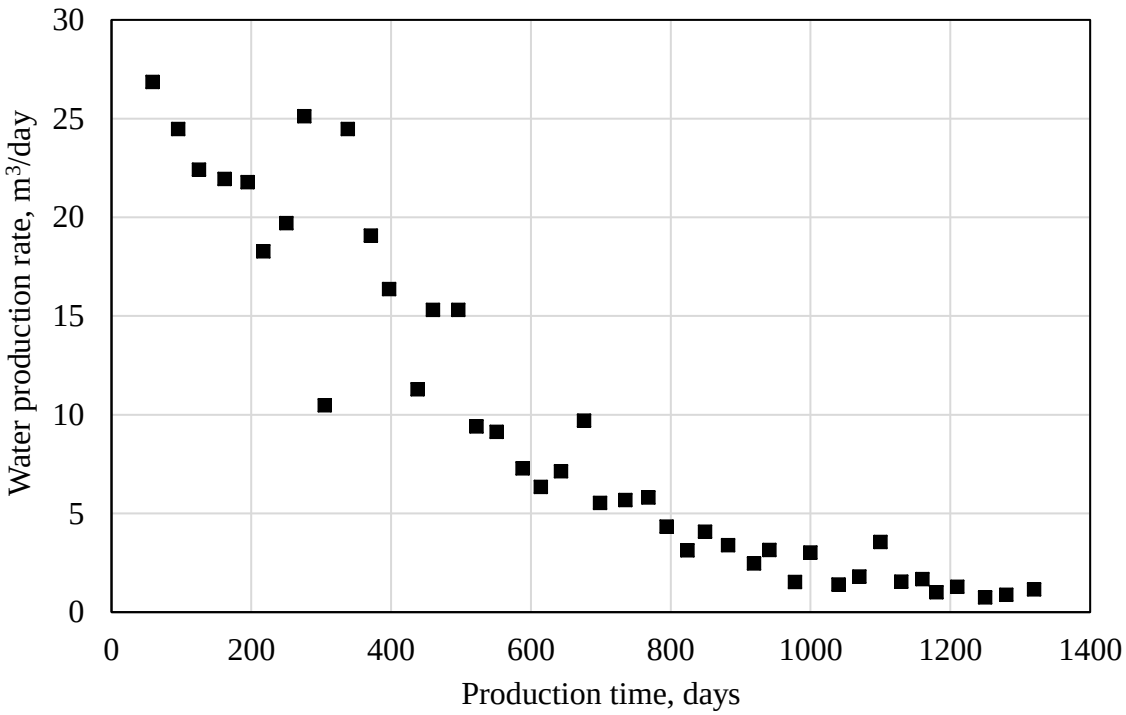

Figure 6.25 Water production performance of Fairway well B#1(Palmer and Mansoori 1996).

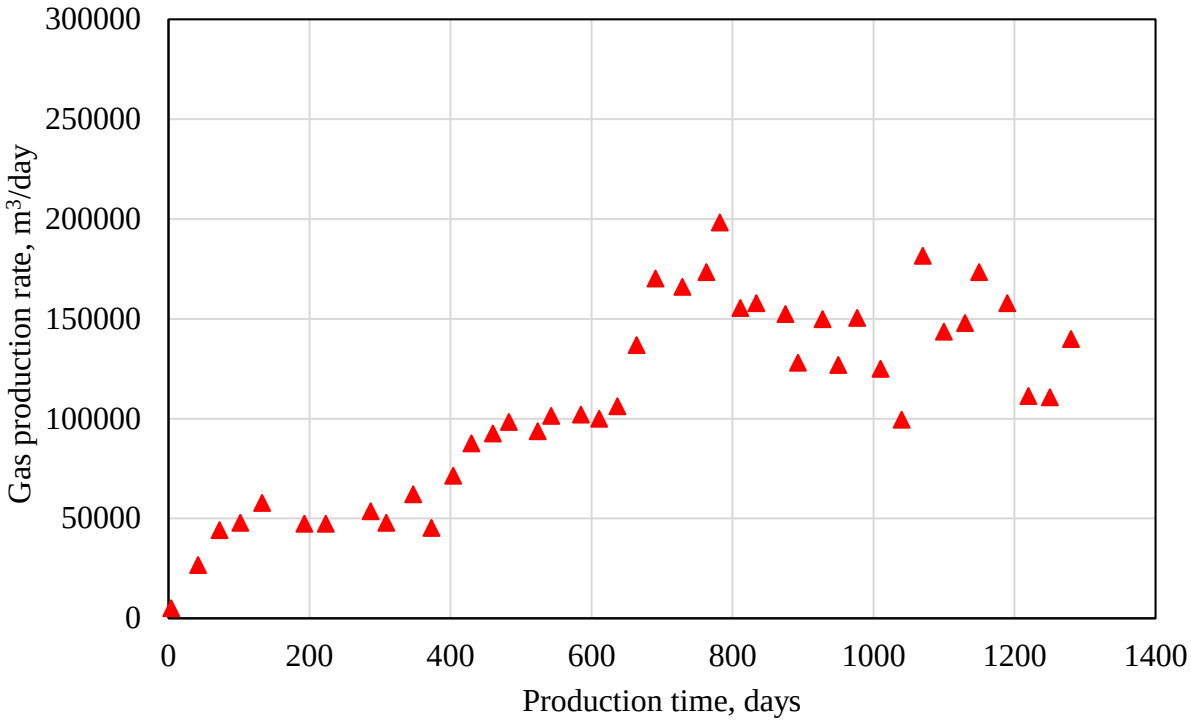

Figure 6.26 Gas production performance of Fairway well B#1 (Palmer and Mansoori 1996).

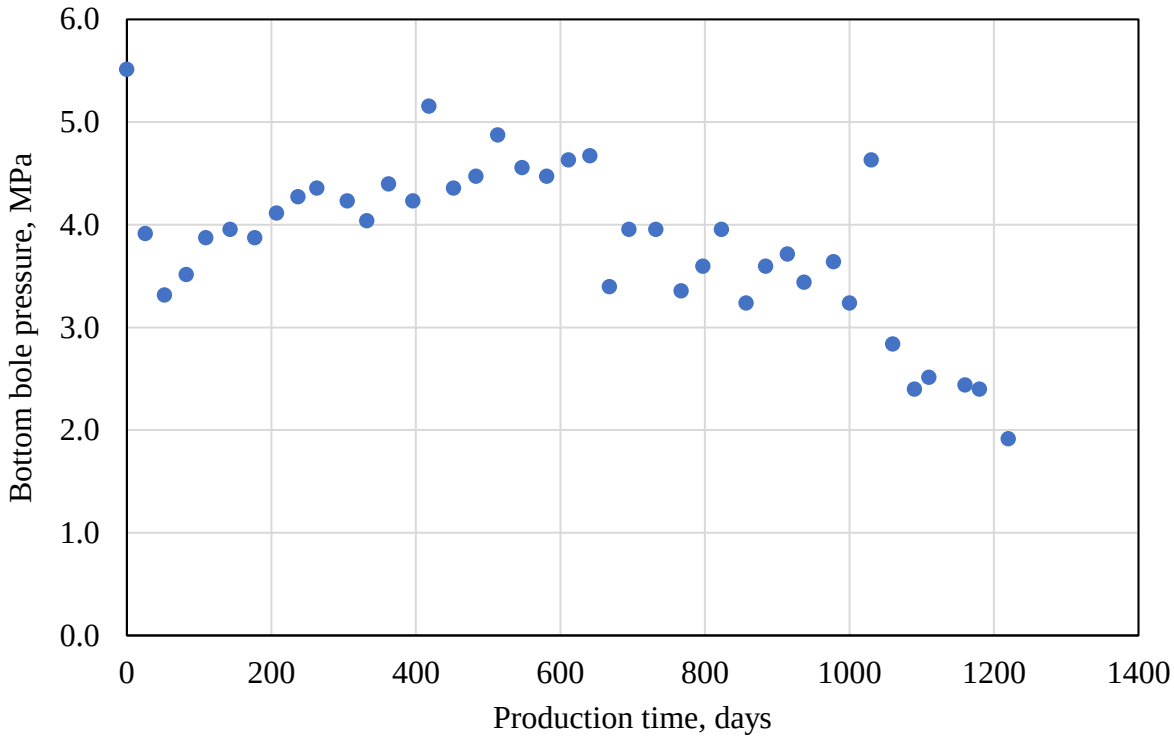

Figure 6.27 Bottomhole pressure for Fairway well B#1(Palmer and Mansoori 1996).

6.4.1 Model domain and material parameters

This section covers the modelling domain and material properties used in the validation test. The model domain is illustrated in Figure 6.28a, assuming that the coal seam is a horizontally infinite plane. The production well is located at the centre of the coalbed. According to symmetry, only a quarter of the coalbed, represented by the 300 m by 300 m simulation domain, is considered. The finite element domain is discretised using 4-noded isoparametric quadrilateral elements with a varying mesh size, with a highly defined grid prescribed in the area around the production well, as shown in Figure 6.29.

Table 6.5 lists the parameter values used for the numerical simulation. The material properties are either selected from a range of literature sources relevant to Fruitland coal, or are assumed or fitted. Compared to the other producing area of the San Juan Basin, the total coalbed thickness in the Fairway is relatively high in the order of 21 to 33.5 m (Zahner 1997; Moore *et al.* 2011; Shovkun and Espinoza 2017); the total thickness of 33 m used in the present work is the same as in the work of Zahner (1997).

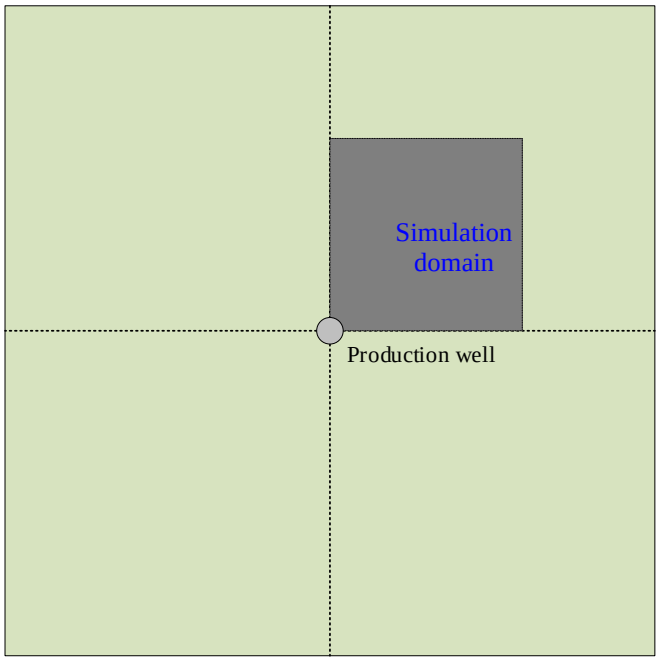

(a)

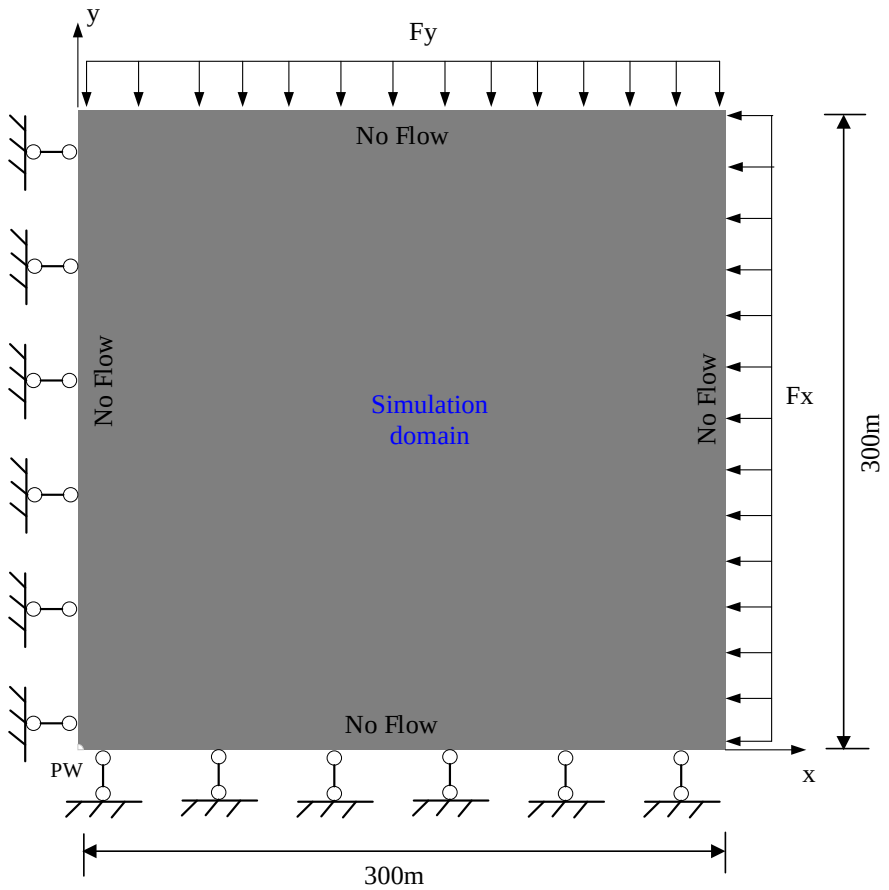

(b)

Figure 6.28 (a) Schematic of the geometric model for simulating CBM production, and (b) the defined boundary conditions.

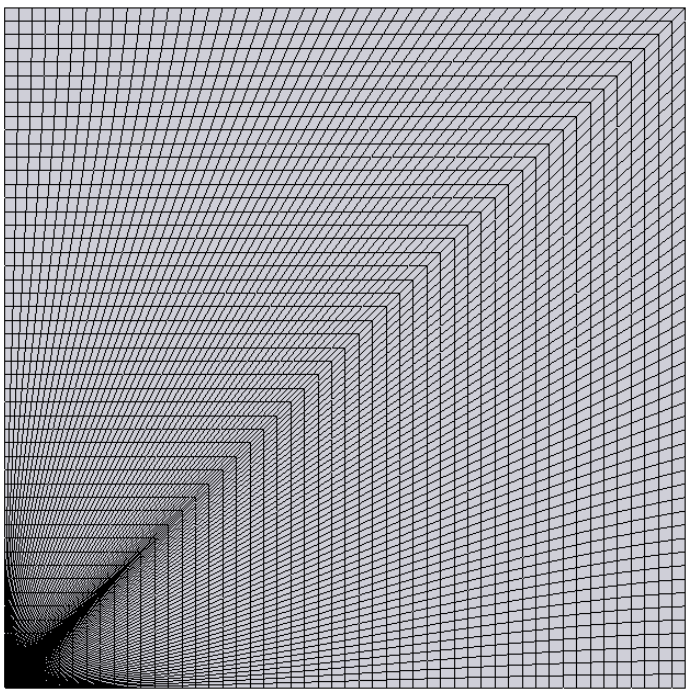

Figure 6.29 Model grid used in the numerical simulation.

Table 6.5 Parameters for the Boomer Fairway well validation test.

Material parameters	**Relationship/value**
Bulk modulus of coal, K (GPa)	2.1
Bulk modulus of coal matrix, K_{m} (Gpa)	14.3
Bulk modulus of coal grains, K_{s} (Gpa)	29.0
Poisson's ratio, v (-)	0.32
Biot's coefficient, b (-)	0.92
Coal density, ρ_s (kg/ m^3)	1485
Coal thickness (m)	33
Initial fracture porosity, n_{f0} (-)	0.0012
Initial matrix porosity, n_{m0} (-)	0.06
Initial permeability, K_{f0} (m^2)	3.0e-14
Temperature, T (K)	316
Langmuir volumetric strain constant, π_{CH_4} (mol m^{-3})	1.42e4
Langmuir pressure constant, B_{CH_4} (Mpa^{-1})	0.5
Langmuir volumetric adsorption constant, V_L (mol/kg)	0.63
Ratio of local swelling to global swelling, Λ (-)	0.2
Desorption time, $\mathscr{L}$ (day)	1.0
Initial reservoir pressure, u_{lf0} (MPa)	10.3
Initial water saturation, S_{lf0} (-)	0.99
Residual water saturation, S_{lr} (-)	0.25
Residual gas saturation, S_{gr} (-)	0.0
Saturation constant, γ (-)	2.3
Saturation constant, p_0 (MPa)	2.0
Water compressibility, c_{l} (MPa^{-1})	3.0e-10
Water viscosity, μ_{l} (Pa ·s)	1.0e-3
Gas viscosity, μ_{g} (Pa ·s)	1.1e-5

The coal density used in works by Zahner (1997), Mavor and Vaughn (1998), Clarkson *et al.* (2010), and Shovkun *et al.* (2016) ranges from 1400 to 1570 kg/m^3, within which a value of 1485 kg/m^3 is selected. Palmer and Vaziri (2004) analysed a set of permeability data from the San Juan Basin presented in Zahner (1997), Mavor and Vaughn (1998), Clarkson and McGovern (2003), by matching the permeability data using the Palmer–Mansoori model.

The fracture porosity was estimated between 0.05% to 0.5%, and in a similar study conducted by Moore *et al.* (2011), the initial cleat porosity in Fruitland coal was estimated in the range of 0.055% to 0.17%, showing a good agreement with independent values (0.04% to 0.14%) obtained through history matching of water production rates presented by Clarkson *et al.* (2010). An initial cleat porosity of 0.12% is used in this validation test. This is the same as in the work of Palmer (2009), is slightly larger than the value used by Palmer and Mansoori (1996) (0.085%) and Clarkson *et al.* (2012) (0.08%), but is restricted within the range presented by Palmer and Vaziri (2004) and Clarkson and McGovern (2003). There are few studies on the matrix porosity of Fruitland coal. Clarkson *et al.* (2010) performed a history match to performance of a Fruitland coal well using a combination of the Palmer–Mansoori model (1996) and Pan-Connell model (2007), estimating the matrix porosity to be 6.0%. A reservoir temperature of 43 ℃ is used in this simulation and is close to the 46 ℃ used by Clarkson *et al.* (2011) and Clarkson *et al.* (2012).

Palmer and Mansoori (1996) carried out a history match study on Fairway Boomer well No. 1 (B1) with three different types of pore pressure-dependent permeability behaviour, ranging from no rebound to strong rebound, as shown in Figure 6.30 (digitised from the original paper). The results indicated that the pore pressure–permeability relationship, which shows a significant permeability rebound at lower drawdown pressures (Case1), could best match the gas and water production and bottom hole pressure. Particular mechanical properties of Fruitland coals are also obtained by fitting pressure-dependent permeability behaviour, as presented by Palmer and Mansoori (1996) and compared with the values from the literature (Mavor and Vaughn 1998; Palmer and Vaziri 2004; Shi and Durucan 2004; Palmer 2009). The fitted Young's modulus and Poisson's ratio are 2.27 GPa and 0.32, respectively, which fall within the range of Young's modulus (2.0 to 2.9 GPa) presented by Palmer (2009), obtained by matching field data from the high-productivity Fairway in the San Juan basin, whilst the matched Poisson's ratio aligns with the values (0.3 to 0.46) presented by Palmer and Vaziri (2004). Biot's coefficient is often assumed to be 1 in weak rocks, because grain compressibility is much lower than bulk compressibility. Although coal is a weak rock, the grain compressibility is larger than expected (Palmer 2009), hence, the Biot coefficient and bulk modulii of coal grains and coal matrix are fitted to give values of 0.92, 29.0, and 14.3 GPa, respectively, yielding the result shown in Figure 6.31.

Figure 6.32 and Figure 6.33 show the adopted adsorption isotherm and adsorption-induced swelling strain curve with pressure. The parameters used to describe the adsorption behaviour are obtained by matching the gas production rate data. The fitted Langmuir volume is 0.63 mol/kg, which is supported by the values (0.43 to 1.2 mol/kg) presented in the work of Zahner (1997), Mavor and Vaughn (1998), Clarkson *et al.* (2011), Clarkson *et al.* (2012), Ibrahim and Nasr-El-Din (2015), Shovkun *et al.* (2016), and Shovkun and Espinoza (2017). The Langmuir pressure of Fruitland coal in the San Juan Basin is estimated between 2.0 to 6.1 MPa according to the studies of Palmer and Vaziri (2004) and Shovkun and Espinoza (2017), with a value of 2.0 MPa being used in the present work.

It is assumed that the coalbed is saturated with water in cleats and the coal matrix is water-free and dry (Bertrand *et al.* 2017), hence, the moisture effect on gas adsorption is neglected. It can be seen from the permeability rebound curve (Figure 6.30) that the initial reservoir pressure is 10.3 MPa (1600psia), which is close to the values used by Zahner (1997) (11 MPa) and Clarkson *et al.* (2011) (10 MPa). The initial absolute permeability in the Fairway is generally estimated to be larger than 10 md (Clarkson *et al.* 2010), and the fitted initial permeability is 13 md, which agrees with those of Palmer and Mansoori (1996) and Clarkson *et al.* (2012), whilst being lower than those of Clarkson *et al.* (2011), Shovkun *et al.* (2016), and (Shovkun and Espinoza 2017). In addition to absolute permeability, the effective permeability is also influenced by relative permeability changes; Figure 6.34 shows the gas-water two phase relative permeability curves adopted in this simulation, which are obtained through matching the production rate of water and gas.

The boundary conditions consist of zero fluid flux at the external boundaries, with the specified pressure for the production well evolving on a time curve according to the change in bottom hole pressure during production. The bottom hole pressure is represented by a fitting polynomial function in fourth order, as shown in Figure 6.35. The fixed gas pressure boundary were converted to the equivalent gas concentrations using the real gas law. The displacements at the left and bottom sides are constrained in the horizontal directions. The coalbed is assumed to be isotropic with a buried depth of 965 m (Zahner 1997); an overburden gradient of 22.6 kPa/m (Shovkun and Espinoza 2017), the total vertical stress is calculated as 22 MPa, and the isotropic horizonal stress is calculated as 11.8 MPa. An isotropic horizontal stress of 11.8 MPa is applied to the top and right sides.

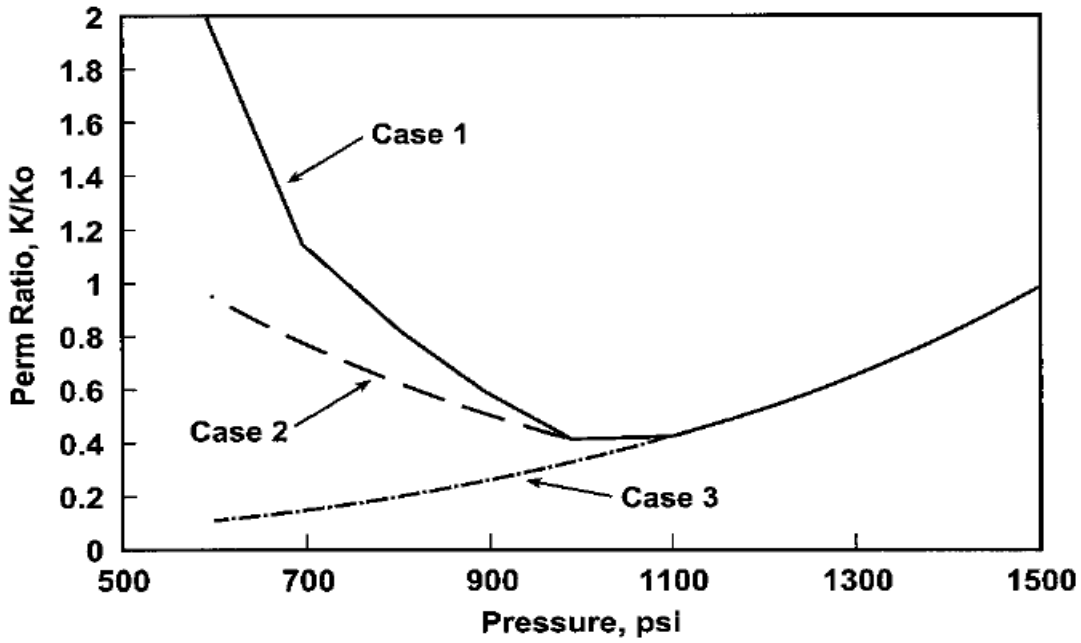

Figure 6.30 Three different types of pore pressure-dependent permeability behaviour used to match Well B1 primary production in Palmer and Mansoori (1996).

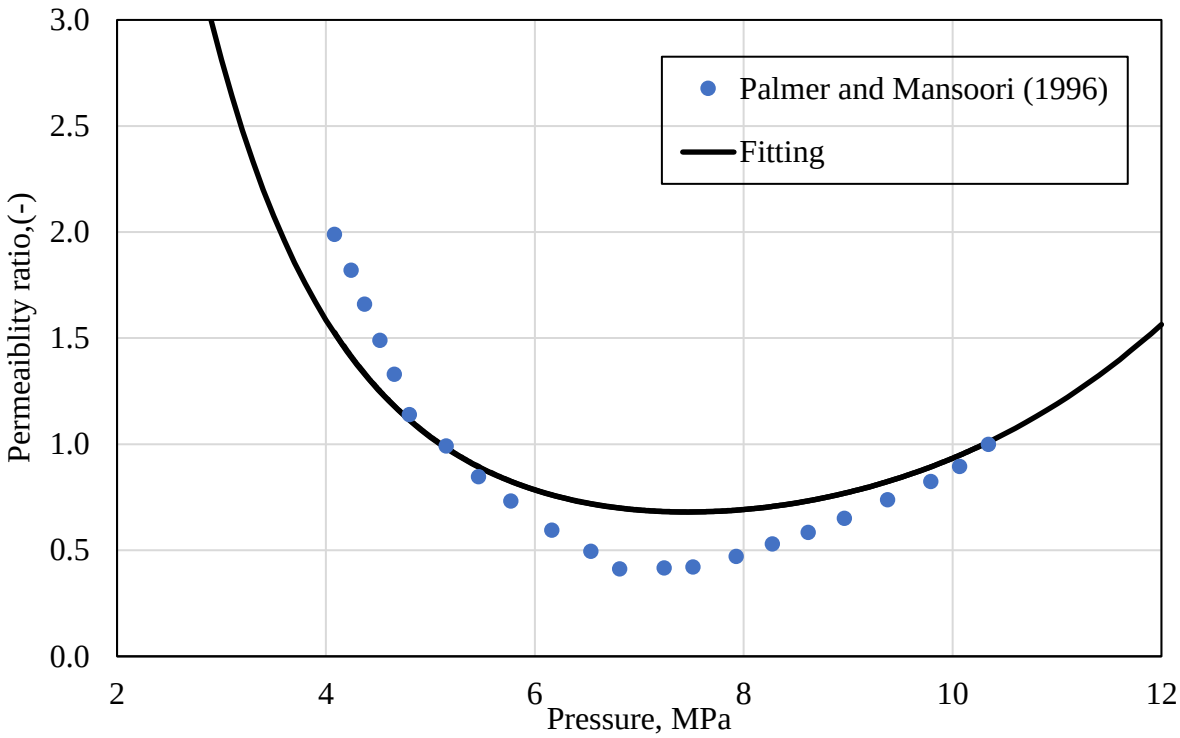

Figure 6.31 Fitted result of pressure-dependent permeability behaviour in Case 1.

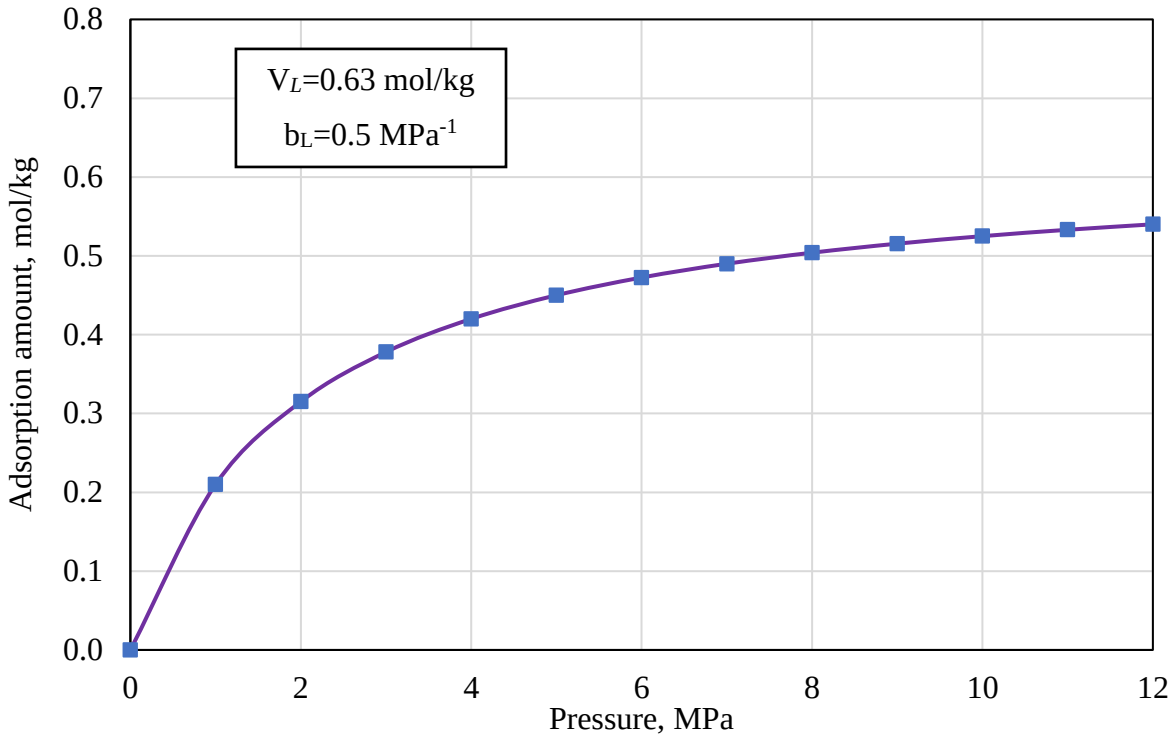

Figure 6.32 The Langmuir adsorption curve adopted in the validation test.

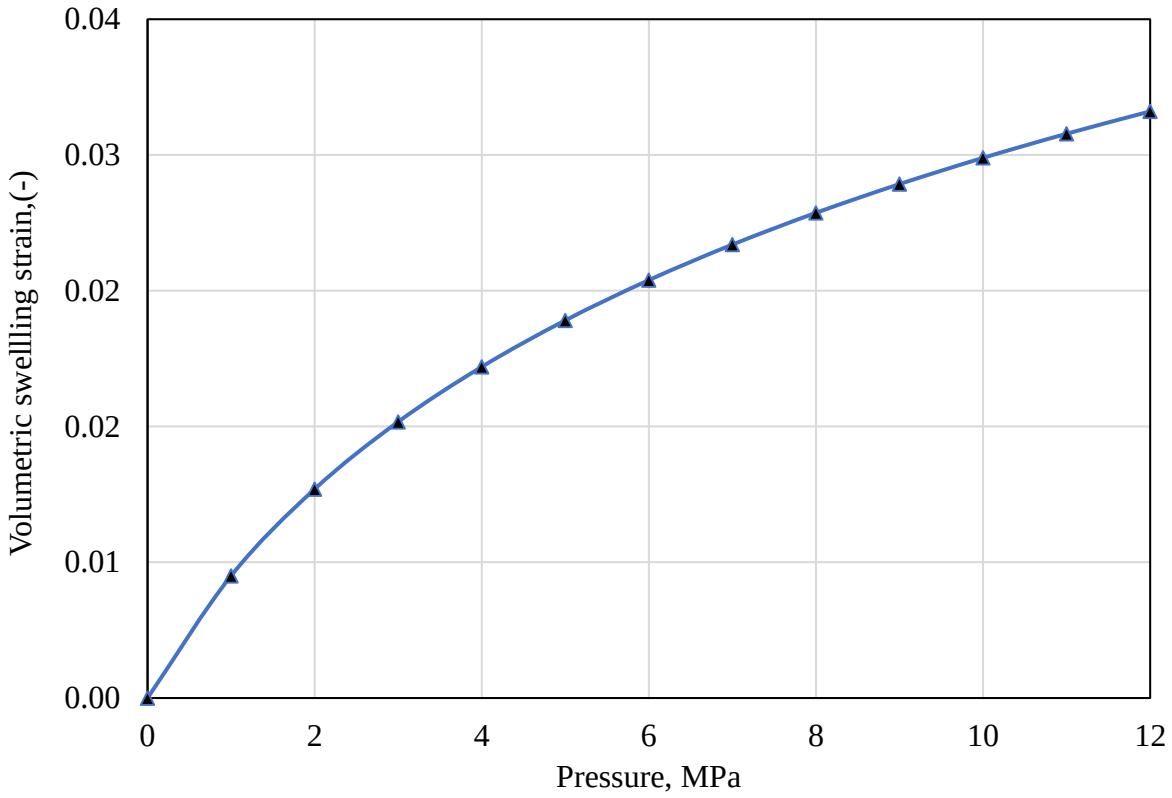

Figure 6.33 The volumetric swelling strain curve adopted in the validation test.

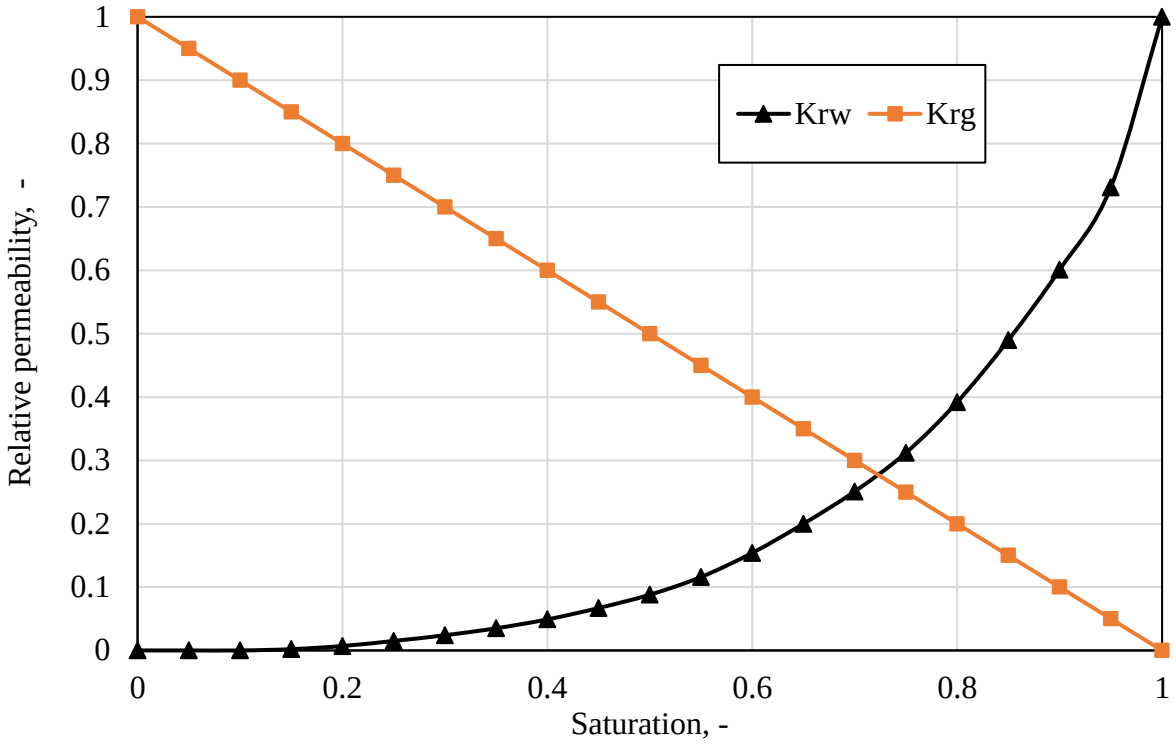

Figure 6.34 The gas-water two phase relative permeability curve adopted in the validation test.

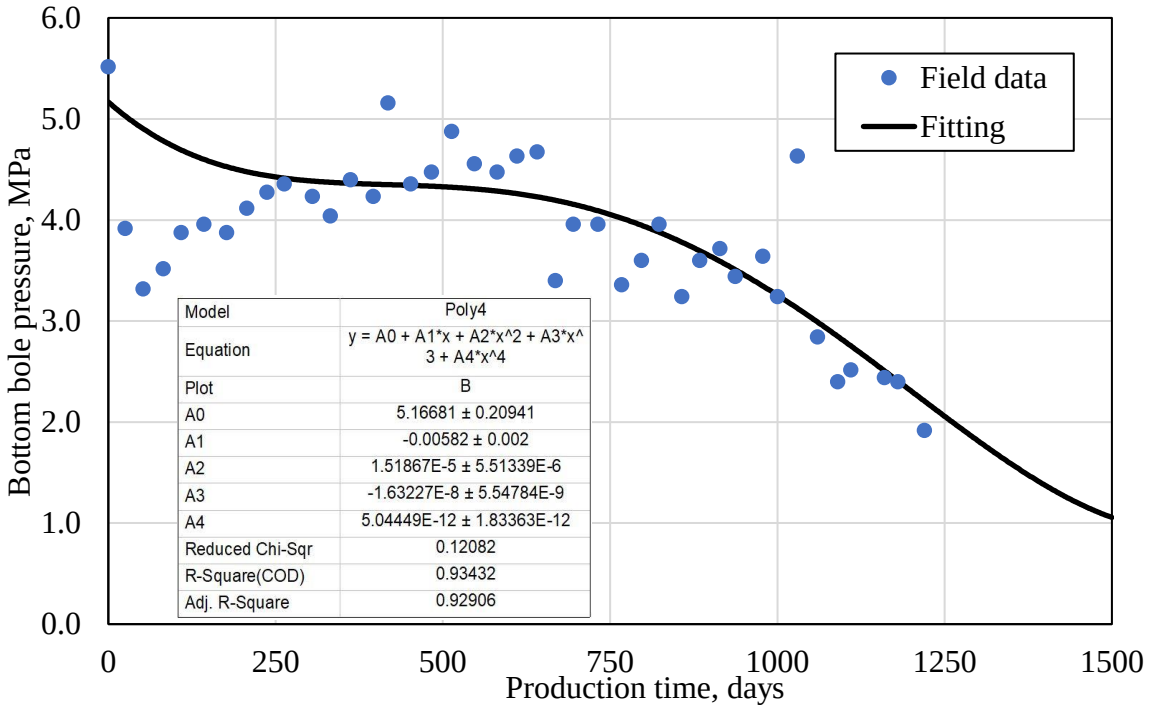

Figure 6.35 The fourth order polynomial function used to fit the bottom hole pressure data in the validation test.

6.4.2 History matching of field production data and discussion

It can be seen from Figure 6.36 and Figure 6.37 that the production performance predicted by the model achieved an acceptable agreement with the observations from the actual CBM well, especially for the gas production rate, which is indicative of the reliability and effectiveness of the model.

Figure 6.36 show the comparison of water production performance predicted by the proposed model with that of the actual CBM well. At the early stage, the bottom hole pressure is lower than the initial reservoir pressure and there is a relatively large pressure difference between production well and coal reservoir. In addition, the coal reservoir is almost saturated with water, and the relative permeability to water is higher, therefore, the water production rate at increases rapidly in the early stage. The underestimate of water production at this initial stage is caused by the higher water pressure boundary compared with the realistic value. With increasing water drainage, the water pressure and saturation decrease, and the water pressure gradient and water relative permeability decline; as a result, the water production rate gradually decreases with time.

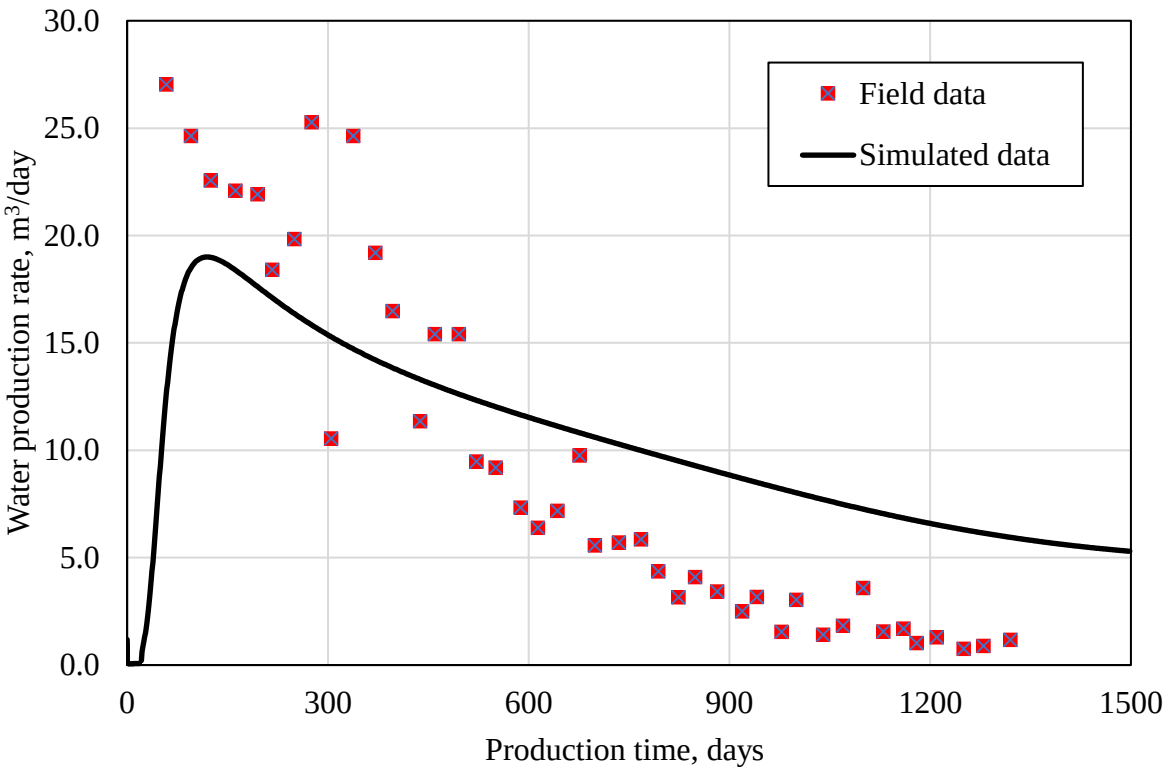

Figure 6.36 Comparison of the water production rate observed in in the Fruitland formation, San Juan Basin, with the rate predicted by the numerical model.

The comparison of gas production performance predicted by the proposed model with that of the actual CBM well is plotted in Figure 6.37. Contrary to the water production rate, the gas production rate initially is very low. This is because the cleat network of the coal reservoir provides the predominant channel for fluid flow, hence, when the cleat network is initially saturated with water, there is a lower gas relative permeability. With water drainage, the water saturation reduces gradually and the gas relative permeability increases. On the other hand, when the reservoir gas pressure is lower, the absolute permeability increases, as illustrated in Figure 6.31. Furthermore, there is significant gas desorption at low pressure conditions, as shown in Figure 6.32; as a consequence, the production rate of CBM increases gradually. After reaching the maximum, the production rate of CBM starts to decline due to lower reservoir pressure, which causes lower flow velocity and a reduction of diffusion from the coal matrix into the cleat network. It can be inferred that most CBM is extracted after dewatering.

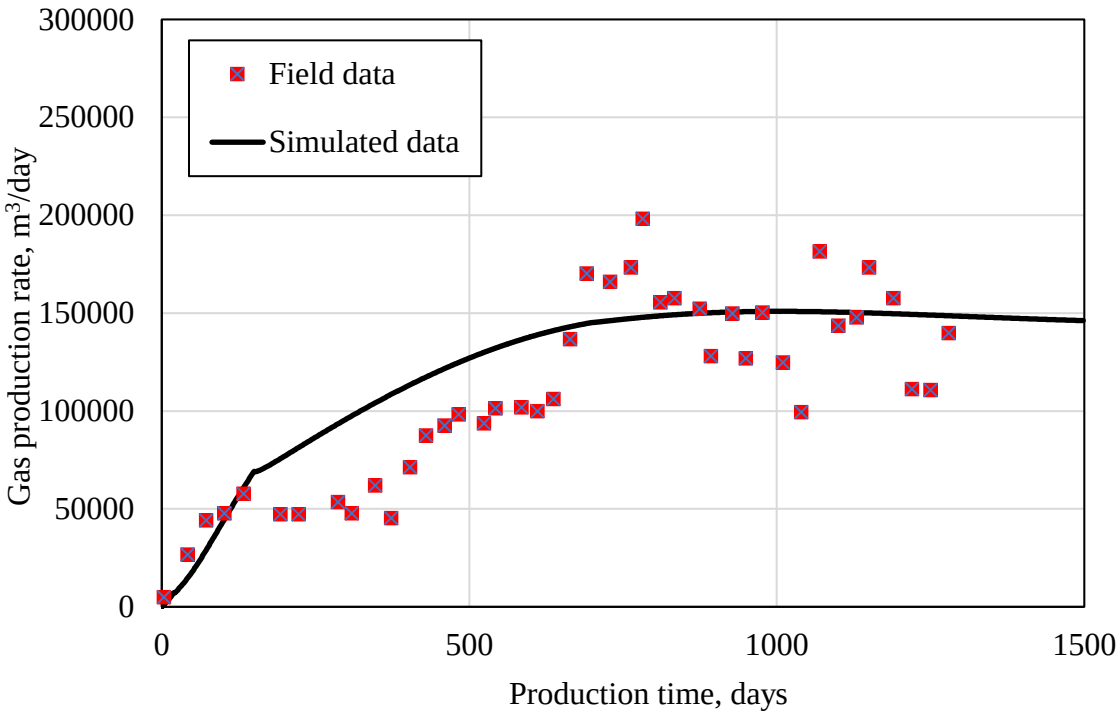

Figure 6.37 Comparison of the CBM production rate observed in in the Fruitland formation, San Juan Basin, with the rate predicted by the numerical model.

6.4.3 Parameteric sensitivity analysis

Due to the large number of modelling input parameters and the degree of uncertainty in determinng their values, a model sensitivity analysis is now provided. In this section, the

influence of key paramters on the gas production rate, such as initial reserovir permeability, initial water saturation, and the adsorption behaviour, are investiagted. The input parameters used in the simulations are same as those determined above, other than the parameters changed for the sensitivity analysis. Table 6.6 shows the various paramters that are studied to evaluate their influence on gas production.

Table 6.6 Set of parameters varied in simulations for the sensitivity analysis.

Material parameters	Values	Varied values
Initial permeability, K_{f0} (m^2)	3.0e-14	1.5e-14, 3.0e-15
Langmuir pressure constant, B_{CH_4} (Mpa^{-1})	0.5	0.35, 0.2
Desorption time, $\mathscr{L}$(day)	1.0	2.0, 3.0
Initial water saturation, S_{lf0} (-)	0.99	0.9, 0.8
Residual water saturation, S_{lr} (-)	0.25	0.2, 0.15

6.4.3.1 Influence of intial permeability

Coal permeability is one of the key parameters controlling the process of CBM extraction. In order to understand the impact of the initial permeability of coalbed reservoirs, a set of simulation tests with different initial permeabilities has been performed, yielding the results shown in Figure 6.38. It can be seen that, as expected, a higher initial permeability leads to a larger gas production rate. At the early stage, the increase of gas production rate is relatively larger in the simulation test with higher initial permeability. On the other hand, it can also be observed that the maximum gas production rate is not proportionate to that of intial permeability. For example, the maximum gas production rate with an initial permeability of 3.0e-14 m^2 is over 15 times larger than that for an initial permeability of 3.0e-15 m^2. When the initial permeability is lower, for cases known as tight reservoirs, the CBM is difficult extract using the traditional pressure depletion technique, and reservoir permeability stimulation may be used to promote CBM recovery. To enhance the gas production, additional treatments should be considered, such as CO_2 injection, hydraulic fracturing.

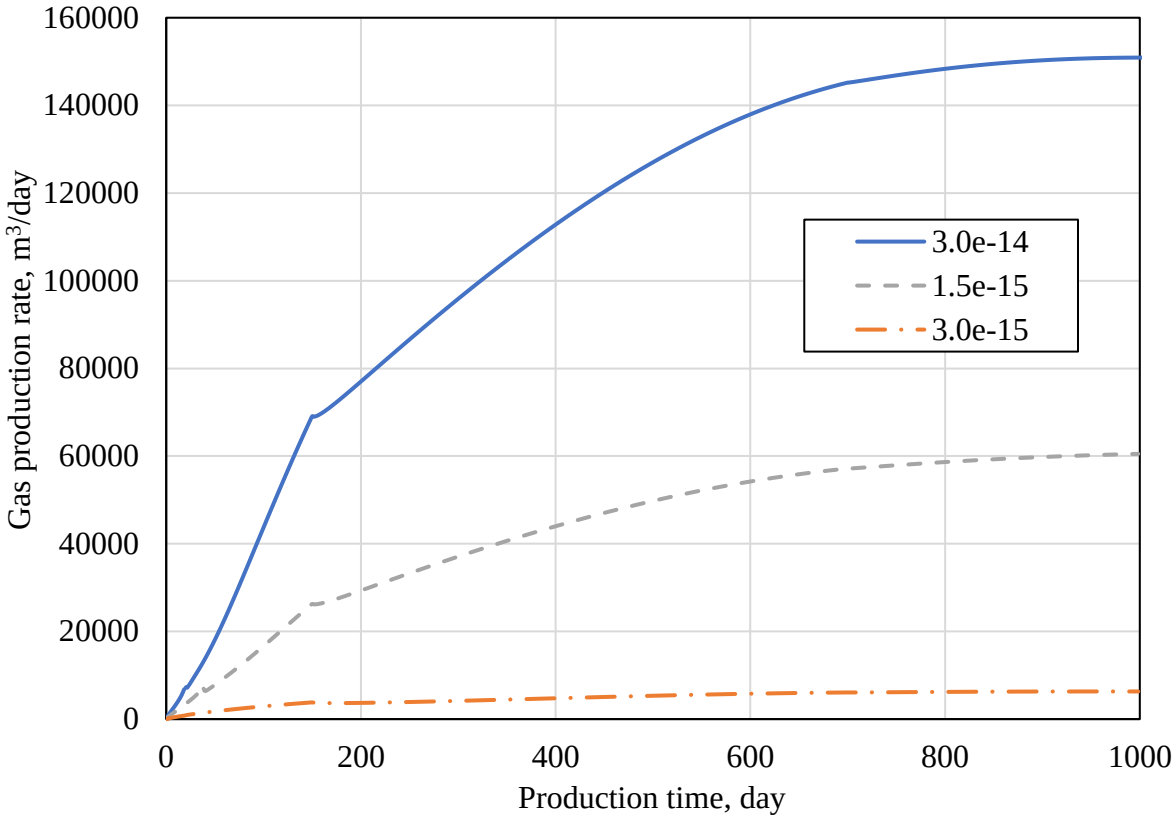

Figure 6.38 Impact of intial coal permeability on gas production.

6.4.3.2 Influence of intial saturation and residual saturation

The cleat system of coalbed reservirs are usually saturated or nearly saturated with water. The presnece of water has a significant effect on the gas prodcution process. To investigate this effect, two simulations are presented in this section for intial water saturations different from that used in the validation test . Figure 6.39 shows the comparison of simulation results for the selected initial degrees of water saturation. As expected, lower water satuation brings about a higher gas production rate because of the associated higher gas relative permeability. In addition, the maximum gas production rate for lower initial water saturation occurs earlier than that for higher initial saturation. Compared to the effect of initial water saturation, the residual water has little effect on the gas production rate, especially at the early stage of production, although the effect of residual saturation on production rate is comparable at later stages, as shown in Figure 6.40.

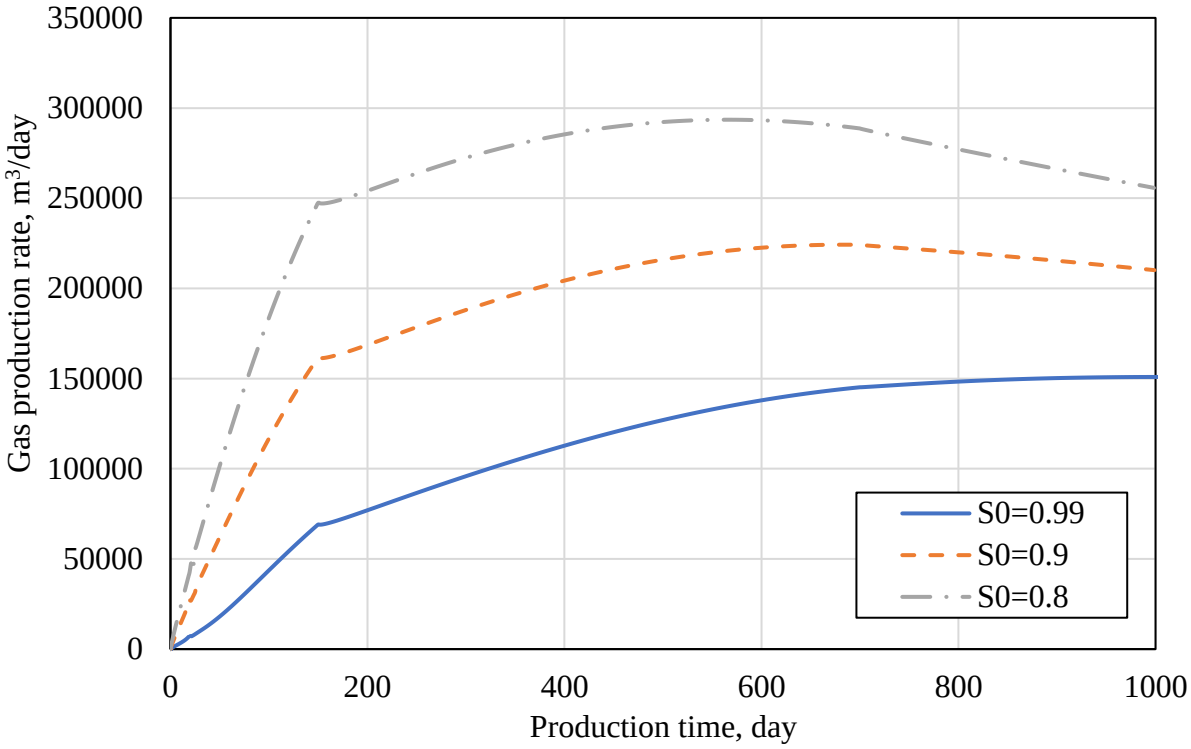

Figure 6.39 Impact of intial saturation condition on gas production.

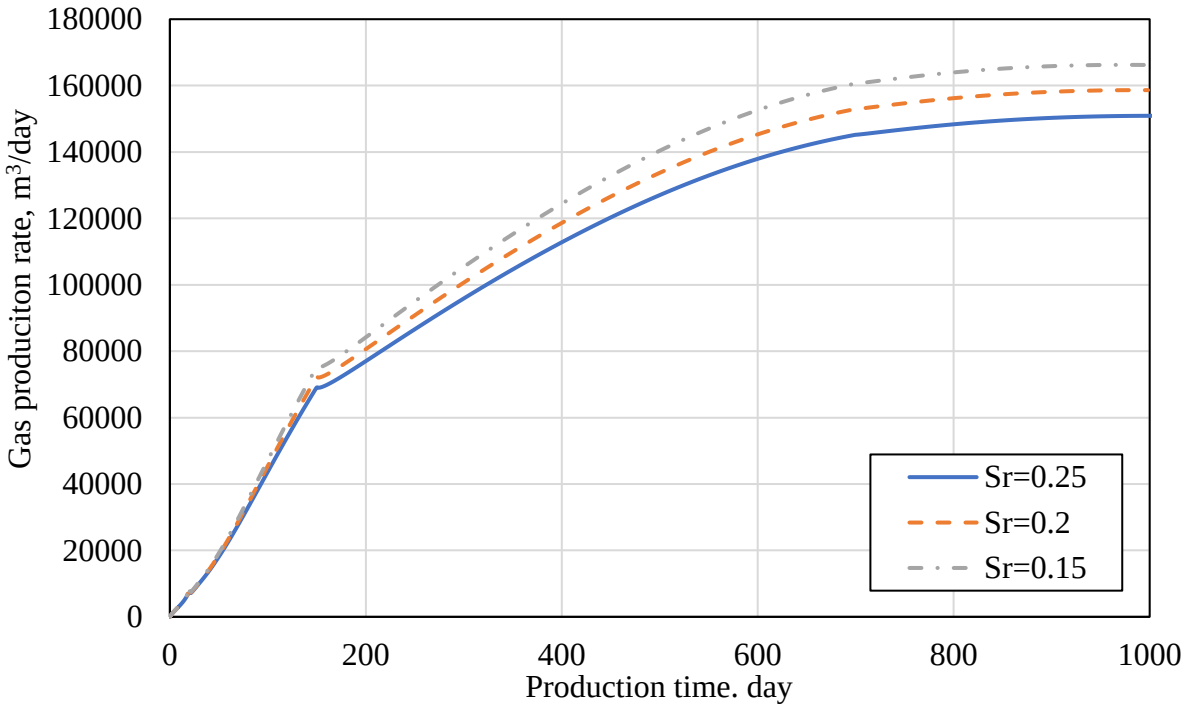

Figure 6.40 Impact of residual water saturation condition on gas production.

6.4.3.3 Influence of Langmuir pressure

Most CBM gas is stored in the adsorbed phase within the coal matrix, therefore, the adsorption behaviour of gas is expected to control gas production. In this work, the gas adsorption is described using the Langmuir isotherm. To analyse the impact of gas adsorption behaviour on gas production rate, different Langmuir pressure constants are used in the simulation tests. As shown in Figure 6.41, the higher Langmuir pressure constant resulted in a decrease in gas production rate. This behaviour can be explained in terms of the inverse relationship between the Langmuir pressure constant and the Langmuir pressure, at which half of the adsorption capacity is reached. Hence, the higher pressure constant implies a lower Langmuir pressure, whereby most gas desorption occurs in the low pressure range. On the contrary, the lower Langmuir pressure constant implies a higher Langmuir pressure, whereby gas desorption is more evenly spread across the full range of pressure depletion.

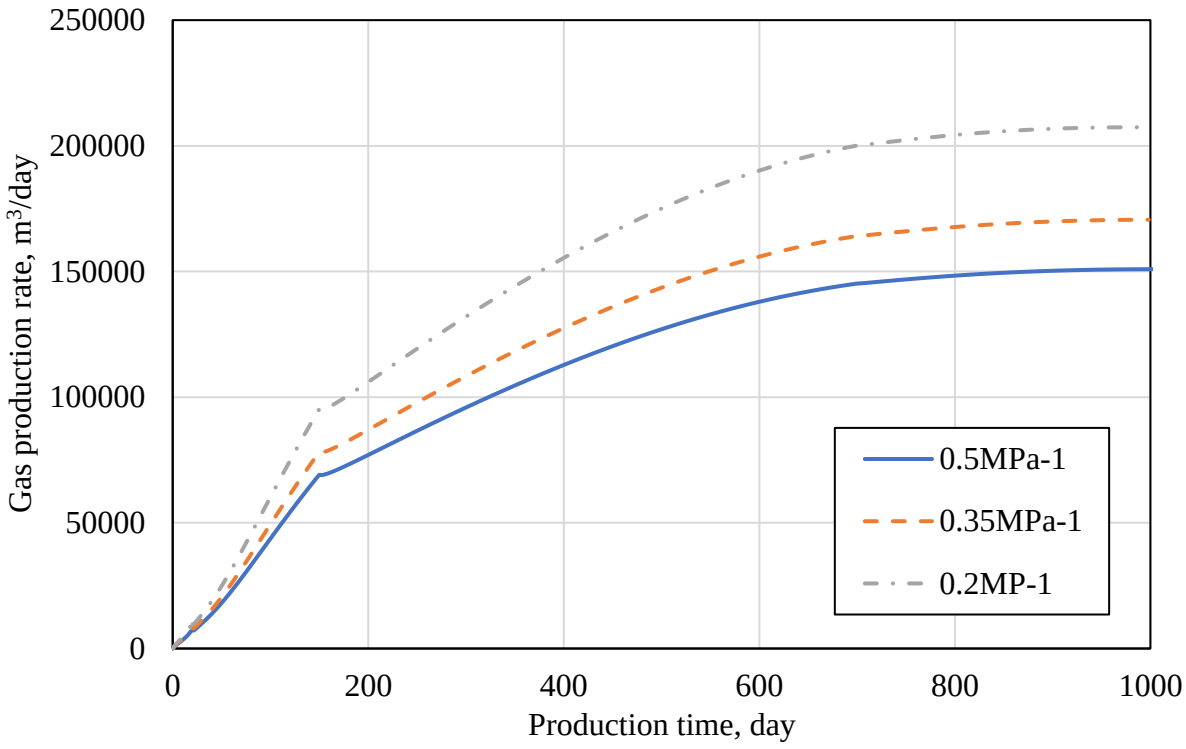

Figure 6.41 Impact of Langmuir pressure on gas production.

6.5 Specific conclusions

This chapter has examined the validity of the developed model and constitutive relationships used to describe gas flow and interactions in coal. This has been achieved by comparing the results calculated using the developed model with those observed in experimental studies published in the literature, as well as field data for CBM production. Meanwhile, the mechanical behaviour of coal due to gas transport and adsorption has been analysed. The developed dual poroelastic model was applied to investigate the dynamic characteristics of the mechanical response of coal during CO_2 injection into a coal core, typical of those tested at the laboratory scale.

The gas adsorption behaviour in coal is temperature dependent. In this work, the traditional Langmuir isotherm has been modified by proposing an exponential relation to represent the impact of temperature on the relevant parameters, i.e. the Langmuir adsorption capacity and Langmuir pressure. The predictions of the proposed exponential relation show an improved fit with experimental measurements. It is found that temperature shows a negative impact on the amount of gas adsorption in coal, which has been attributed to the fact that gas adsorption is an exothermic process and as such is restrained by increasing temperature.

The surface stress approach has been introduced in this work to analyse the deformation of solids due to interaction with adsorptive fluid. The performance of the developed deformation model involving gas adsorption behaviour is examined by comparing the predicted results with two sets of experimental data, one for pure gas and another for mixed gas, which were obtained from the literature. The results have shown that the developed swelling model is able to describe the deformation behaviour when adsorptive fluids are involved. It has also been observed that coal deformation involving gas adsorption is species dependent. Both coals were seen to exhibit the largest strain when adsorbing CO_2 compared to that induced by CH_4 and N_2 adsorption.

The coupling relationship between the amount of adsorbed gas and adsorption-induced swelling has been invetigated in this chapter. If the gas adsorption follows the Langmiur isotherm, the adsorption-induced swelling stress shows a non-linear relation with the normalised adsorption amount, espeically when the amount of gas adsorption exceeds half

of gas adsorption capacity. However, when $V/V_L < 0.5$, the adsorption-induced swelling is approximately linear.

The newly developed permeability model has been applied to match the permeabiliy data from experimental measurements conducted on coals of different ranks. It has been shown that the model is able to describe the nonlinear permeability curve. Moreover, the permeability changes in both experiments displayed different trends, indicating that the permeability model is capable of decribing the coal permeability evolution under different conditions.

The model developed in this study has provided a capacity to predict the evolution characteristics of the mechanical response of coal during gas flow and adsorption in laboratory core flood tests. It has been found that the structural change is significant during adsorptive gas transport in coal. The variation of fracture porosity is relatively complex as a result of the competing influence of effective stress and internal deformation. Compared to variation of the fracture porosity, adsorptive gas injection in coal has the potential to increase the microporosity of coal significantly, which seems to be an important reason for coal swelling and, contrary to the reduced fracture porosity, is beneficial for CO_2 storage.

The fully coupled model has been validated by comparing the simulated results for primary CBM recovery with historic production data obtained from the Boomer Fairway well located in the Fruitland formation, San Juan Basin, USA. The material properties used in the validation simulation are analysed in detail. The results have shown that the production performance from the proposed model can achieve an acceptable match compared with the actual field data of a CBM well, especially for the gas production rate, which has served to clarify the reliability of the model. Based on the history matching results, the impacts of the key parameters on the gas production rate, such as initial porosity, reservoir permeability, initial water saturation, and the adsorption behaviour of material, are investigated. Compared to the effects of water satuation and gas adsorption behaviour, the initial permeability exerts a siginificantly negative influence on the gas production rate. To enhance the gas production, additional treatments should be considered, such as CO_2 injection, hydraulic fracturing.

6.6 General conclusions

The aim of the validation exercises presented in this chapter has been to gain confidence in the ability of proposed theoretical model to predict the behaviour exhibited by coal during gas transport and interactions. Three important subsets of the numerical model were validated against experimental or field trial data, firstly, the temperature dependent adsorption characteristics, secondly, the mechanical response of coal to adsorptive gases, and finally the coupled processes in relation to CBM production. Favourable comparisons with the benchmarks considered were achieved in each case. It can be concluded that the proposed numerical model is able to correctly predict the coupled flow-adsorption-mechanical behaviour of coal under the conditions considered, thereby improving confidence in the validity of the numerical model for this application. With the success of the verification and validation tests presented in this and the previous chapters, the author has gained confidence in the integrity and soundness of the numerical model for further applications related to CO_2-ECBM recovery, which are presented in the next chapter.

6.7 References

Ayers Jr, W. B. (2003). Coalbed methane in the Fruitland Formation, San Juan Basin, western United States: A giant unconventional gas play.

Bertrand, F., Cerfontaine, B. and Collin, F. (2017). A fully coupled hydro-mechanical model for the modeling of coalbed methane recovery. *Journal of Natural Gas Science and Engineering* **46**:307-325.

Chen, M., Hosking, L. J., Sandford, R. J. and Thomas, H. R. (2019). Dual porosity modelling of the coupled mechanical response of coal to gas flow and adsorption. *International Journal of Coal Geology*.

Clarkson, C., Jordan, C., Ilk, D. and Blasingame, T. (2012). Rate-transient analysis of 2-phase (gas+ water) CBM wells. *Journal of Natural Gas Science and Engineering* **8**:106-120.

Clarkson, C. and McGovern, J. eds. (2003). *A new tool for unconventional reservoir exploration and development applications*. Proceedings of the 2003 International Coalbed Methane Symposium, University of Alabama, Tuscaloosa, Alabama, paper.

Clarkson, C. R., Jordan, C. L., Gierhart, R. R. and Seidle, J. P. eds. (2007). *Production data analysis of CBM wells*. Rocky Mountain Oil & Gas Technology Symposium. Society of Petroleum Engineers.

Clarkson, C. R., Pan, Z., Palmer, I. D. and Harpalani, S. (2010). Predicting sorption-induced strain and permeability increase with depletion for coalbed-methane reservoirs. *Spe Journal* **15**(01):152-159.

Clarkson, C. R., Rahmanian, M., Kantzas, A. and Morad, K. (2011). Relative permeability of CBM reservoirs: controls on curve shape. *International Journal of Coal Geology* **88**(4):204-217.

Cui, X. and Bustin, R. M. (2005). Volumetric strain associated with methane desorption and its impact on coalbed gas production from deep coal seams. *Aapg Bulletin* **89**(9):1181-1202.

Gathitu, B. B., Chen, W.-Y. and McClure, M. (2009). Effects of coal interaction with supercritical CO_2: physical structure. *Industrial & Engineering Chemistry Research* **48**(10):5024-5034.

Gensterblum, Y., Van Hemert, P., Billemont, P., Battistutta, E., Busch, A., Krooss, B., Wolf, K.-H. (2010). European inter-laboratory comparison of high pressure CO_2 sorption isotherms II: Natural coals. *International Journal of Coal Geology* **84**(2):115-124.

Gierhart, R. R., Clarkson, C. R. and Seidle, J. P. eds. (2007). *Spatial variation of San Juan Basin Fruitland coalbed methane pressure dependent permeability: Magnitude and functional form*. International petroleum technology conference. International Petroleum Technology Conference.

Guan, C., Liu, S., Li, C., Wang, Y. and Zhao, Y. (2018). The temperature effect on the methane and CO2 adsorption capacities of Illinois coal. *Fuel* **211**:241-250.

Harpalani, S. and Chen, G. (1995). Estimation of changes in fracture porosity of coal with gas emission. *Fuel* **74**(10):1491-1498.

Hol, S. and Spiers, C. J. (2012). Competition between adsorption-induced swelling and elastic compression of coal at CO_2 pressures up to 100MPa. *Journal of the Mechanics and Physics of Solids* **60**(11):1862-1882.

Ibrahim, A. F. and Nasr-El-Din, H. A. (2015). A comprehensive model to history match and predict gas/water production from coal seams. *International Journal of Coal Geology* **146**:79-90.

Liu, C., Wang, G., Sang, S. and Rudolph, V. (2010). Changes in pore structure of anthracite coal associated with CO_2 sequestration process. *Fuel* **89**(10):2665-2672.

Mavor, M. and Vaughn, J. (1998). Increasing coal absolute permeability in the San Juan Basin fruitland formation. *SPE Reservoir Evaluation & Engineering* **1**(03):201-206.

Moore, R. L., Loftin, D. F. and Palmer, I. D. eds. (2011). *History matching and permeability increases of mature coalbed methane wells in San Juan Basin*. SPE Asia pacific oil and gas conference and exhibition. Society of Petroleum Engineers.

Oudinot, A. Y., Koperna, G. J., Philip, Z. G., Liu, N., Heath, J. E., Wells, A., Wilson, T. (2011). CO_2 injection performance in the Fruitland coal fairway, San Juan Basin: results of a field pilot. *SPE Journal* **16**(04):864-879.

Palmer, I. (2009). Permeability changes in coal: analytical modeling. *International Journal of Coal Geology* **77**(1-2):119-126.

Palmer, I. and Mansoori, J. eds. (1996). How permeability depends on stress and pore pressure in coalbeds: a new model. *SPE Annual Technical Conference and Exhibition*. Society of Petroleum Engineers.

Palmer, I. and Vaziri, H. eds. (2004). Permeability changes in a CBM reservoir during production: an update, and implications for CO_2 injection. *Proceedings of the 2004 International Coalbed Methane Symposium*, University of Alabama, Tuscaloosa, Alabama, paper.

Pan, Z. and Connell, L. D. (2007). A theoretical model for gas adsorption-induced coal swelling. *International Journal of Coal Geology* **69**(4):243-252.

Pan, Z. and Connell, L. D. (2012). Modelling permeability for coal reservoirs: a review of analytical models and testing data. *International Journal of Coal Geology* **92**:1-44.

Pan, Z., Connell, L. D. and Camilleri, M. (2010). Laboratory characterisation of coal reservoir permeability for primary and enhanced coalbed methane recovery. *International Journal of Coal Geology* **82**(3-4):252-261.

Peng, Y., Liu, J., Wei, M., Pan, Z. and Connell, L. D. (2014). Why coal permeability changes under free swellings: New insights. *International Journal of Coal Geology* **133**:35-46.

Robertson, E. P. (2005). Measurement and modeling of sorption-induced strain and permeability changes in coal. *Idaho National Laboratory (INL)*.

Robertson, E. P. and Christiansen, R. L. (2006). A permeability model for coal and other fractured, sorptive-elastic media. *Idaho National Laboratory (INL)*.

Sawyer, W., Paul, G. and Schraufnagel, R. eds. (1990). Development and application of a 3-D coalbed simulator. *Annual technical meeting*. Petroleum Society of Canada.

Seidle, J., Jeansonne, M. and Erickson, D. eds. (1992). Application of matchstick geometry to stress dependent permeability in coals. *SPE rocky mountain regional meeting*. Society of Petroleum Engineers.

Seidle, J. R. and Huitt, L. eds. (1995). Experimental measurement of coal matrix shrinkage due to gas desorption and implications for cleat permeability increases. *International meeting on petroleum Engineering*. Society of Petroleum Engineers.

Shi, J.-Q. and Durucan, S. (2010). Exponential growth in San Juan Basin Fruitland coalbed permeability with reservoir drawdown: model match and new insights. *SPE Reservoir Evaluation & Engineering* **13**(06):914-925.

Shi, J. and Durucan, S. (2004). Drawdown induced changes in permeability of coalbeds: a new interpretation of the reservoir response to primary recovery. *Transport in porous media* **56**(1):1-16.

Shovkun, I., Espinoza, D. and Ramos, M. eds. (2016). Coupled reservoir simulation of geomechanics and fluid flow in organic-rich rocks: Impact of gas desorption and stress changes on permeability during depletion. *50th US Rock Mechanics/Geomechanics Symposium*. American Rock Mechanics Association.

Shovkun, I. and Espinoza, D. N. (2017). Coupled fluid flow-geomechanics simulation in stress-sensitive coal and shale reservoirs: Impact of desorption-induced stresses, shear failure, and fines migration. *Fuel* **195**:260-272.

Somerton, W. H., Söylemezoğlu, I. and Dudley, R. eds. (1975). Effect of stress on permeability of coal. *International journal of rock mechanics and mining sciences & geomechanics* **12**: 129-145.

Ye, Z., Chen, D., Pan, Z., Zhang, G., Xia, Y. and Ding, X. (2016). An improved Langmuir model for evaluating methane adsorption capacity in shale under various pressures and temperatures. *Journal of Natural Gas Science and Engineering* **31**:658-680.

Zahner, B. ed. (1997). Application of material balance to determine ultimate recovery of a San Juan Fruitland coal well. *SPE Annual Technical Conference and Exhibition*. Society of Petroleum Engineers.

Zhang, S., Liu, J., Wei, M. and Elsworth, D. (2018). Coal permeability maps under the influence of multiple coupled processes. *International Journal of Coal Geology* **167**:71-82.

Zhang, Y. (2018). Mechanics of adsorption–deformation coupling in porous media. *Journal of the Mechanics and Physics of Solids* **114**:31-54.

7

Coupled THCM behaviour during CO_2 sequestration with enhanced CBM recovery

7.1 Introduction

In this chapter, the model developed in this work is applied for predictive purposes, having been verified and validated by the series of tests presented in chapters 5 and 6. The gas production rates presented and analysed in the previous chapter for primary CBM recovery indicated that the CBM recovery of low permeability coal seams needed additional treatments to enhance CBM production, such as CO_2 injection, hydraulic fracturing. The simulations presented in this chapter deals with how CO_2 inection into coal and hydraulic fracuring treatment to enhance the CBM recovery from low permeability coal seams. The study of primary CBM recovery has also been included for comparison. The main objective of these simulations is to consider the coupled THCM behaviour in greater detail and to evaluate the major coupled processes involved during CO_2-ECBM recovery. The investigation is able to enhance the knowledge of the major processes occurring during CO_2-ECBM, especially the geomechanical behaviour involved in CO_2 sequestration with enhanced CH_4 recovery, and this is of practical importance to success of CO_2-ECBM in many low permeability coal seams.

The development of the numerical simulation scenario is discussed in section 7.2, including the descriptions of the model domain, injection scheme, material parameters, and initial and boundary conditions. A set of simulation cases is designed to investigate the coupled THCM behaviour occurring during CBM recovery and CO_2 enhanced CBM recovery. The role of hydraulic fracturing in the CO_2-ECBM recovery process is also explored through a simulation scenario in which a simple hydraulic fracture layout is adopted.

The results of the above simulation are presented in section 7.3. The temporal evolution and spatial distribution of field variables obtained in the numerical simulations are shown, such as gas pressure, temperature, porosity, and permeability. A discussion of the results is provided, which focuses on the gas transport, thermal, and mechanical behaviour for the field scale simulations considered. In particular, the efficiency of CO_2 injection with and without hydraulic fractures is evaluated and the implications for field practice are analysed in this section.

Finally, the major conclusions from the investigation presented in this chapter are given in section 7.4.

7.1.1 Simulation conditions and material parameters

This section covers the description of the modelling domain and material properties for CBM production and CO_2 sequestration in a coal seam. The CBM reservoir conditions used in the simulations are the same as those used for historical matching of field production data in the previous chapter (section 6.4). however, the initial coal permeability is set to be much lower than that used in historical match of field production to represent the low permeability characteristics of coal seams.

A typical five-well layout is usually designed for CO_2-ECBM recovery (Wong *et al.* 2007; Ma *et al.* 2017b), as shown in Figure 7.1, where the original single well for primary CBM recovery in the validation test is used as one of the corner producers (PW). Three new wells are drilled for other corner producers and a new CO_2 injection well (IW) is drilled at the centre of a near-square array composed of four production wells. Due to the lower permeability, a horizontal production area of 300 m × 300 m is used in this simulation. According to the symmetry, only a quarter of the reservoir domain, which is represented by a 150 m × 150 m area, is considered in a 2D plane strain model (Saliya *et al.* 2015). The simulation model is shown in Figure 7.2, in which the injection well is located at the left corner and the production well located at the top right corner. All wells are 0.1m in diameter.

In reality, coal seams are often characterised by low permeability and most of CBM is adsorbed onto the micropores of matrix (Zhang 2014). In order to enhance CO_2 injection and CBM recovery, permeability stimulation measures may be employed. Among these measures, hydraulic fracturing is regarded as an effective method for increasing CBM

production (e.g. Holditch *et al.* 1988; Chen *et al.* 2017; Xu *et al.* 2017a) and CO_2 injectivity (van Bergen *et al.* 2009; Fujioka *et al.* 2010). Therefore, a simulation scenario with hydraulic fractures is also considered. The purpose of this simulation is to investigate how hydraulic fractures affect gas production and CO_2 injection, therefore, it is assumed that the stimulated fractures are static without further propagation, although their aperture can vary due to variation of stress within coal seams. Figure 7.2 shows the hydraulic fracture pattern implemented in this investigation. Coal is a fractured rock with well-developed cleat network, including more continuous face cleats and less continuous butt cleats, the coal is easy to be cracked along the cleats, therefore, three intersected hydraulic fractures are selected (HF1, HF2, HF3), used to represent the stimulated fractures along the cleats in coal seams. Due to lack of information on the hydraulic induced fracture, a simple hydraulic fracture layout is used in simulation to show the influence of hydraulic fracturing

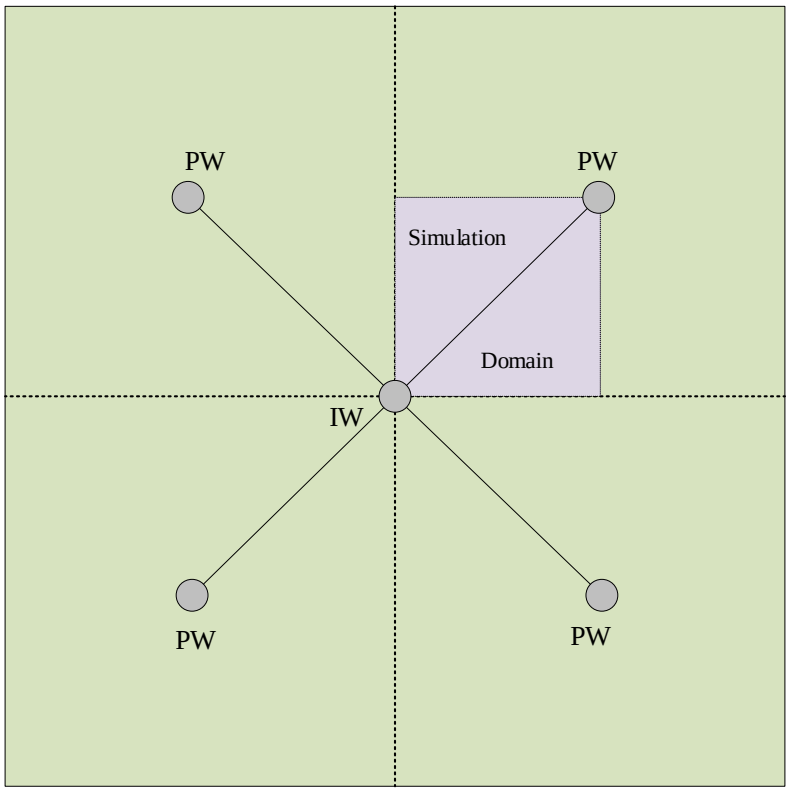

Figure 7.1 Configuration of the five-spot pattern well for CO_2-ECBM.

The simulation domain is discretised using 3-node isoparametric triangular elements with a varying mesh size, as shown in Figure 7.3. A finer grid is designed to capture the area around the stimulated fractures by means of the surface-line intersection function of the GiD pre-processing software. Most of the input parameters can be found in Table 6.4. It was assumed

that the physical and chemical parameters of the coal-gas system are the same as those used in the simulations presented in section 6.4. Additional parameters that were not used in the validation tests but are required for the present simulation scenario are provided in Table 7. 1. The thermodynamic properties of coal in the Fruitland formation of the San Juan Basin, USA, have been chosen from the literature (Qu *et al.* 2012; Ziabakhsh-Ganji and Kooi 2014; Wen *et al.* 2015; Chen *et al.* 2018; Fan *et al.* 2019b). Although the propagation of hydraulic fractures is not taken into account in current study, the closure/opening of hydraulic fractures is included, and the required mechanical properties for deformation of hydraulic fractures can be found in Table 7.1, which have been selected from Bastola and Chugh (2015) and Zhi *et al.* (2018). To show the dynamic characteristics of coupled thermo-hydro-chemo-mechanical behaviour in coal seams, four analysis points are set at the following coordinate locations (expressed in m with the IW at the origin): P1(140, 140), P2(120, 120), P3(75, 75), P4(30, 30).

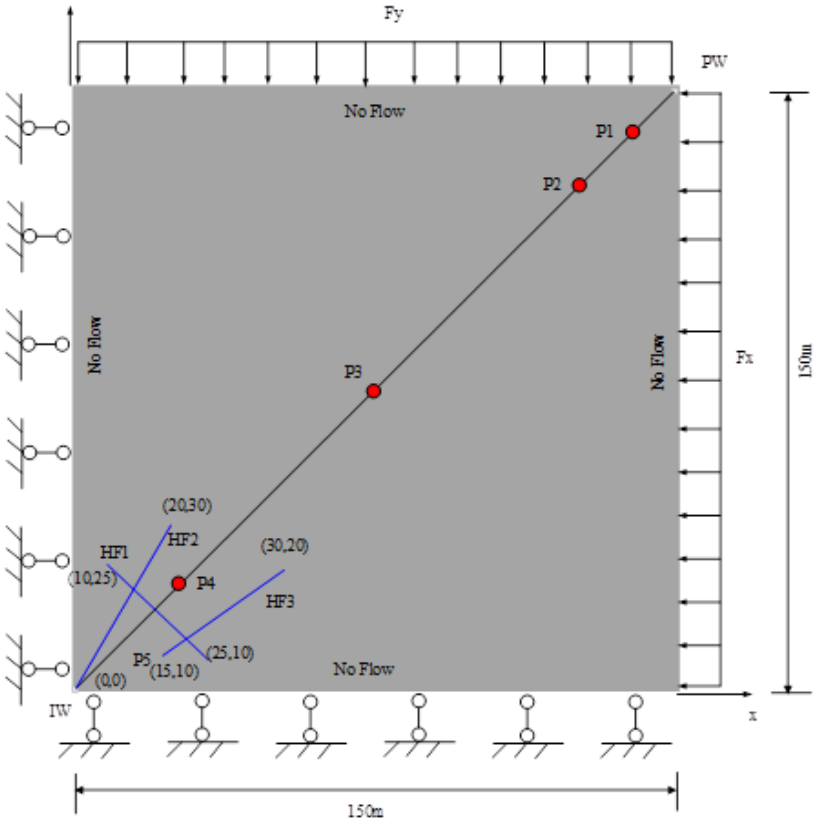

Figure 7.2 Schematic of the simulation domain used for investigating CO_2-ECBM recovery behaviour.

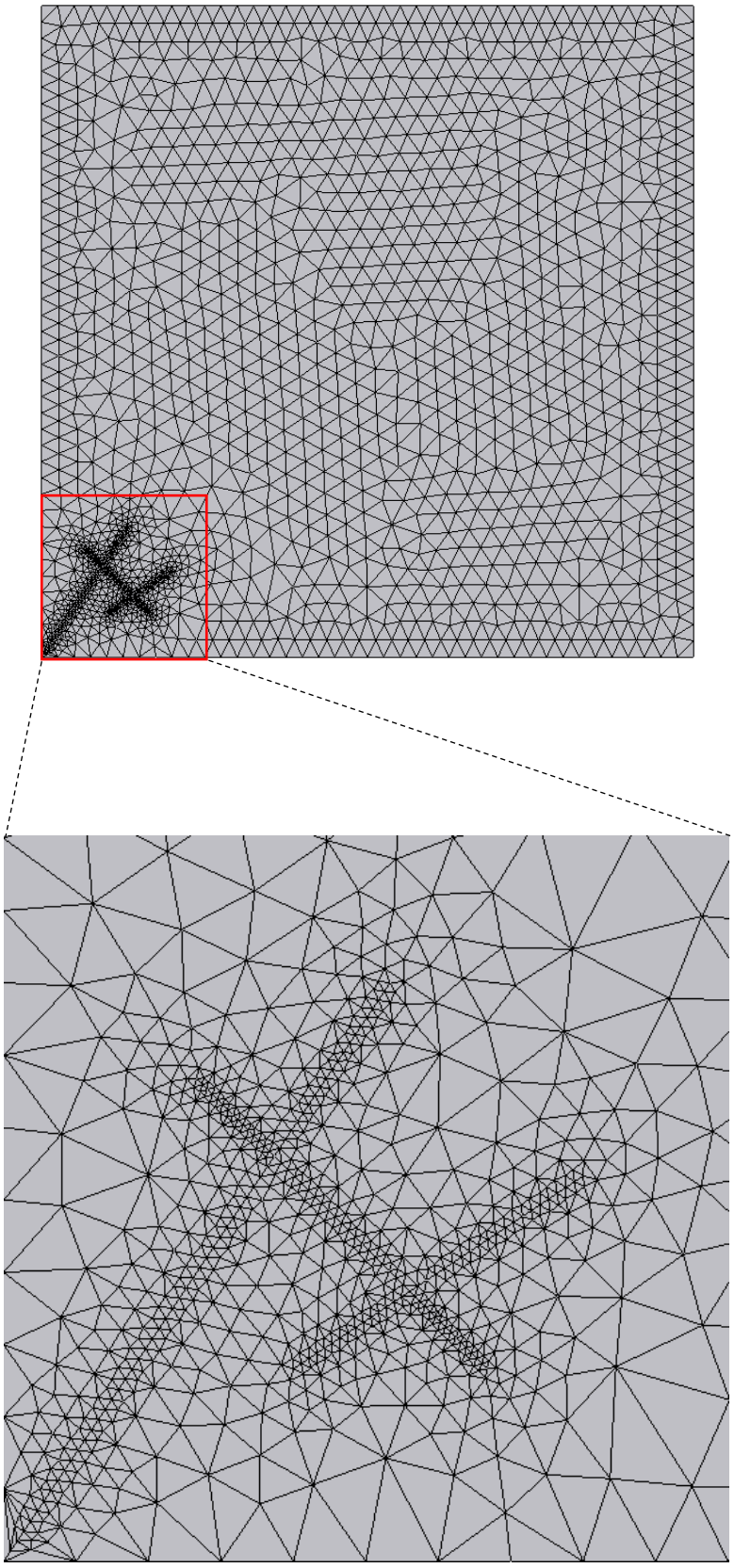

Figure 7.3 Model mesh used in the numerical simulation.

Table 7. 1 Parameters in addition to those provided in Table 6.4 required for the numerical investigation presented in this chapter.

Material parameters	**value**
Initial permeability, k_{f0} (m^2)	3.0e-15
Interaction energy of CH_4, E_{in} (J/mol)	9238
Reduction coefficient of CH_4 Φ (K^{-1})	0.0083
Langmuir volumetric strain constant, π_{CO_2} (mol/m^3)	1.6e4
Langmuir constant, B_{CO_2} (MPa^{-1})	0.73
Langmuir volumetric constant of CO_2, V_L (mol/kg)	1.5
Interaction energy of CO_2, E_{in}(J/mol)	5266
Reduction coefficient of CO_2, Φ (K^{-1})	0.023
Thermal expansion coefficient, α_T (K^{-1})	9.0e-5
Thermal conductivity of CO_2, λ_g (W/m/K)	0.0246
Thermal conductivity of CH_4, λ_g (W/m/K)	0.0371
Thermal conductivity of coal, λ_s (W/m/K)	0.33
Specific heat capacity of coal, C_{ps}(J/K/kg)	1250
Specific heat capacity of water, C_{pl}(J/K/kg)	4200
Thermal expansion coefficient of water, α_{lT} (1/K)	6.9×10^{-5}
Matrix block length, l_b (m)	0.01
Internal friction angle, Φ (°)	24
Shear dilation angle, φ (°)	6
Shear strength, τ_c (MPa)	2.5
Initial normal stiffness, K_{n0} (GPa/m)	5
Shear stiffness, K_t (GPa/m)	50
No load stimulated fracture aperture, w_0 (m)	5.0e-4
Maximum aperture closure, w_{nmax} (m)	4.9e-4

Prior to the analysis of CO_2 injection for enhanced CBM recovery, the coupled THCM behaviour of the coalbed during CBM recovery is investigated, including the variations of the water saturation, permeability evolution, and effective stress, since these are of particular importance for the design of a CBM recovery scheme. CO_2-ECBM recovery is then simulated with and without hydraulic fracturing treatment. The CO_2 is injected at a constant pressure of 12 MPa and a temperature 316 K for both injection scenarios. The fixed pressure

is defined at the production well as boundary conditions for water flow and gas transport in the simulations. The fixed injection pressure was converted to the equivalent gas concentration using the real gas law, 14215 mol/m^3. The initial CO_2 concentration in the coalbed is assumed to be, 38 mol/m^3 at atmospheric pressure, compared to the fixed gas concentration at injection well, this value can be ignored. For investigation of the coupled THCM processes for CBM recovery, the injection well is closed, which is achieved by defining a no flow boundary. While the fixed gas pressure boundary is assigned at the injection well for the numerical simulation with CO_2 injection. The simulation was performed with initial and maximum time steps of 1000 and 86400 seconds, respectively, for a simulation period of 1000 days, whilst for the simulation considering the role of hydraulic fractures, the simulation ends when the CO_2 concentration at detection point P1 exceeds the initial value.

7.2 Simulation results and discussion

In this section, the numerical results for the coupled THCM behaviour occurring during primary CBM recovery are first presented in section 7.2.1. The results are expressed in terms of the temporal evolutions of the field variables at the measurement points. Section 7.2.2 presents the numerical results for the coupled THCM processes when CO_2 is injected into the same coal seam both with and without hydraulic fracturing. An in-depth discussion of the coupled processes and behaviour involved is included in these two sections. It is worth mentioning that the main form of analysis between the different simulation scenarios is the rate of CBM production, which is also presented for all scenarios in the Section 7.2.2.

7.2.1 Coupled THCM behaviour during CBM production

Figure 7.4 and Figure 7.5 show the temporal evolution of water and gas pressure, respectively, at the selected measurement points. It can be observed that both pressures display similar trends at each of the points, decreasing with time and being overall lower closer to the production well. Because the coal seam is initially saturated with water the water relative permeability is higher at the early stage of production. With water saturation decrease, the effective permeability of gas increases leading to a decrease in gas pressure and the desorption of more CBM. Due to the coal matrix shrinkage induced by CBM

desorption, the fracture permeability experiences a large increase, especially in the area close to the production well, as shown in Figure 7.6.

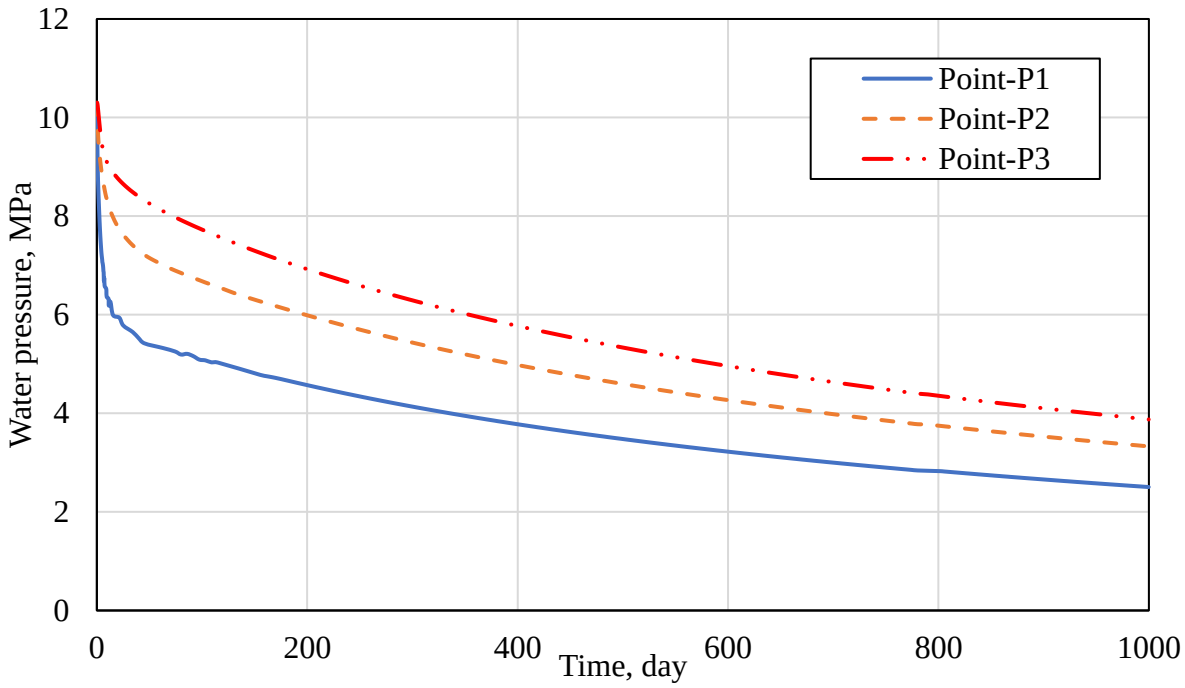

Figure 7.4 Temporal evolution of water pressure at the selected measurement points for CBM recovery without CO_2 injection.

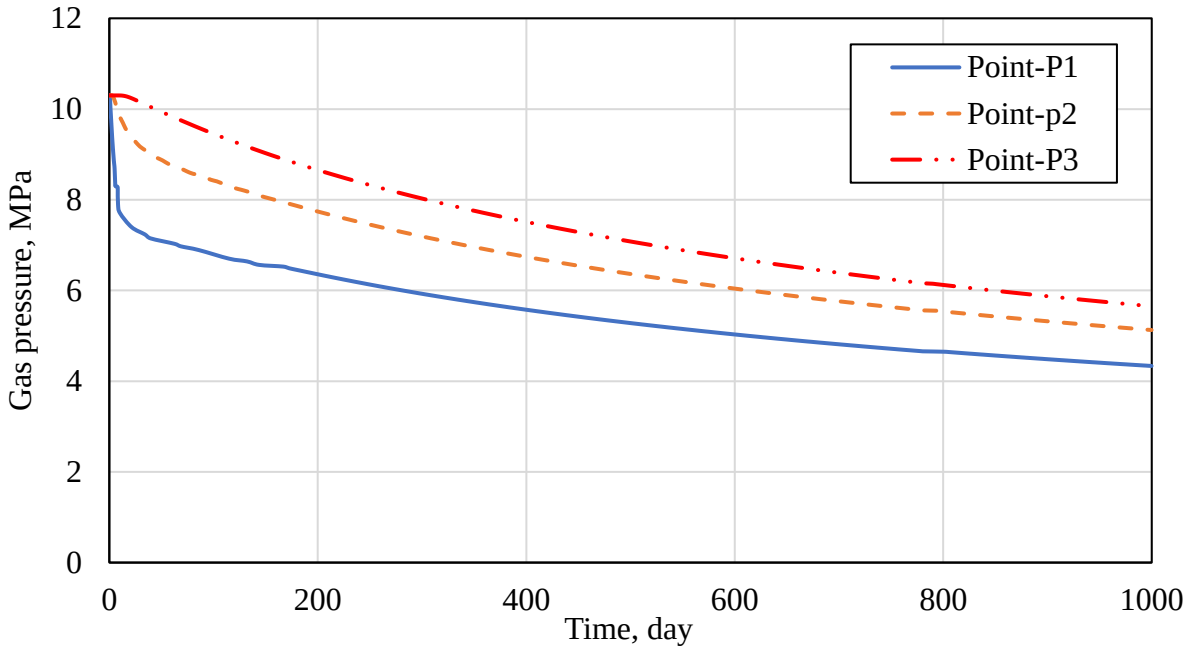

Figure 7.5 Temporal evolution of gas pressure at the selected measurement points for CBM recovery without CO_2 injection.

It is worth pointing out that the calculated water pressure in the vicinity of the production well shows a slight oscillation at the early production stage, which is attributed to the somewhat coarse mesh used in the numerical simulation and the rapid change in fracture porosity and permeability in the area close to the production well. The unstructured mesh used in the simulations presented in this chapter was adopted to avoid the high computational cost and analysis time required for finer meshes. With regards to the fracture porosity and permeability, the rapid increase in each timestep at early stage can be seen in Figure 7.6 and Figure 7.7, which affected water and gas transport and may have contributed to the numerical instability.

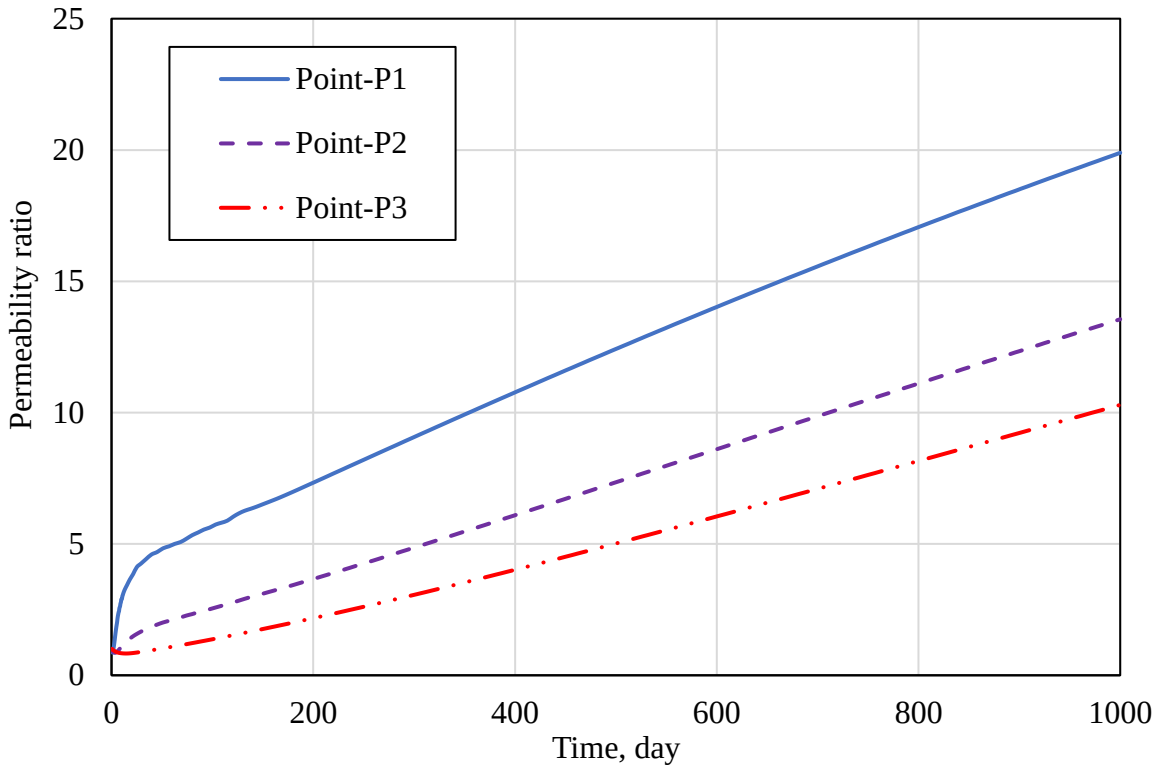

Figure 7.6 Temporal evolution of fracture permeability at the selected measurement points for CBM recovery without CO_2 injection.

An important theoretical development to enable the simulation of the coal-gas system was the description of the deformation behaviour of coal caused the by its physical and chemical interactions with the adsorptive gas. The evolutions of fracture and matrix porosity predicted in the numerical simulation for CBM production are provided in Figure 7.7 and Figure 7.8. Overall, the fracture porosity experiences an increasing trend due to gas desorption induced shrinkage, however, the difference of fracture porosity at the selected locations is worth

highlighting. In the location close to the production well, the fracture porosity shows a rapid increase as the pore pressure decreases. Hence, although the pore pressure decrease leads to an increase in effective stress that would tend to reduce porosity, this is exceeded by the competing influence of coal matrix shrinkage due to CBM desorption. This general trend can also be seen at locations further from the well.

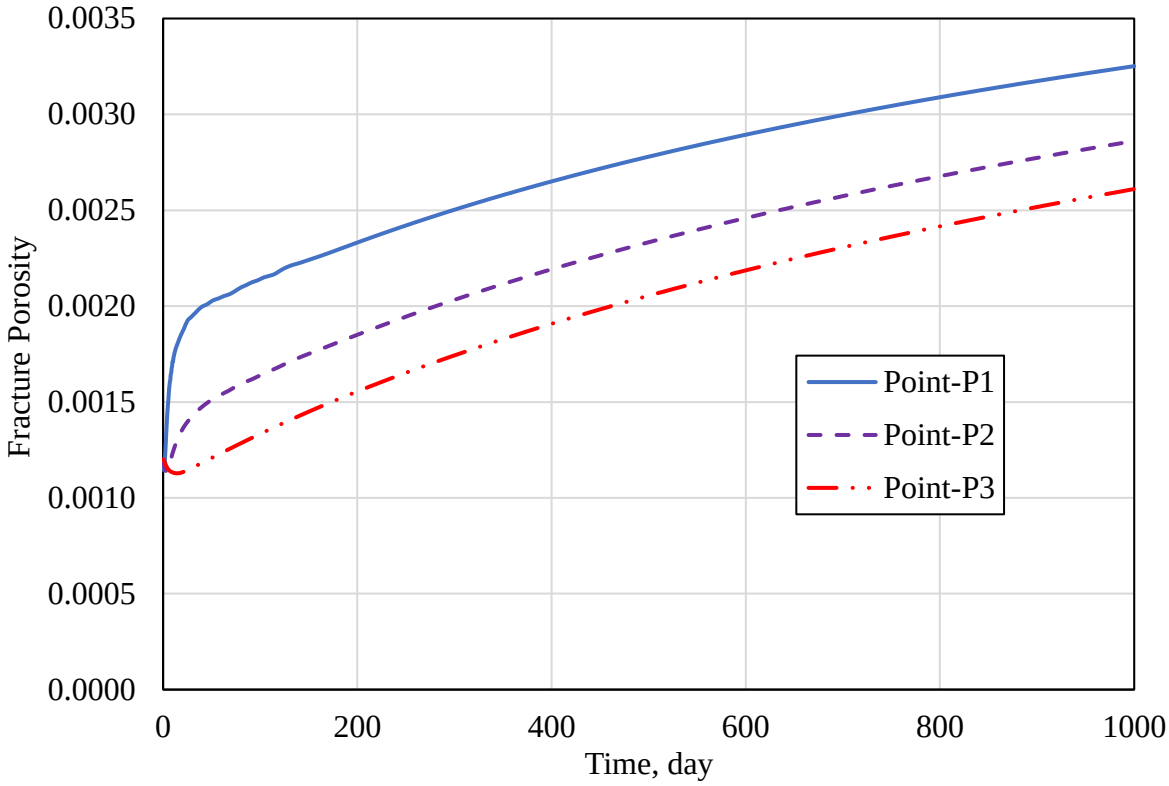

Figure 7.7 Temporal evolution of fracture porosity at the selected measurement points for CBM recovery without CO_2 injection.

In this work, it is assumed that the coal seam has a dual porosity structure and that the microporous coal matrix has a negligible contribution to the bulk coal permeability. The permeability is therefore wholly attributed to the fracture network. The cubic law is used to describe the relationship between fracture porosity and permeability and a permeability ratio can be expressed with respect to the initial permeability, as shown in Figure 7.6. Following the trend of porosity, it can be observed that the permeability increases considerably due to coal matrix shrinkage. This explains the field observations in the San Juan Basin where no permeability decline has been observed with continued production in several areas (Mitra *et al.* 2012).

In contrast to fracture porosity, the matrix porosity decreases during CBM recovery due to desorption-induced matrix shrinkage, as shown in Figure 7.8. This is because gas desorption causes variation of surface stress of the solid-gas interface, leading to shrinkage of the micropore surfaces and decrease of the micropore volume. Compared to the varying trend of gas pressure, it can be found that the matrix porosity is predominantly gas pressure dependent. In next section, the variations of both facture porosity and matrix porosity caused by CO_2 injection with enhanced CBM production will be presented and analysed. The effect of CO_2 injection and application of hydraulic fracturing on gas production will also been included below.

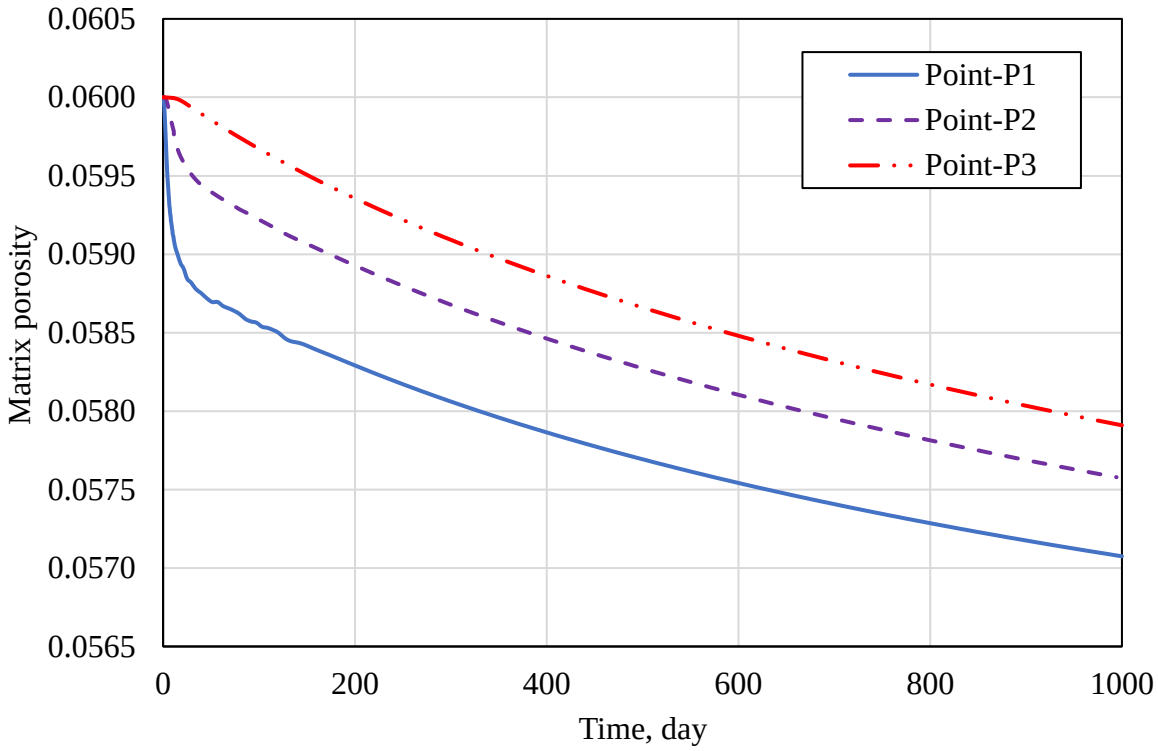

Figure 7.8 Temporal evolution of matrix porosity at the selected measurement points for CBM recovery without CO_2 injection.

The evolution of water and gas pressure in the coalbed during CBM production varied continuously, leading to a change in capillary pressure in the coalbed, which controls the evolution of the water saturation. As expected, it can be seen from Figure 7.9 that the water saturation shows a rapid decrease at the early period of CBM production, similar to the changes in water pressure. After that, the water saturation decreases more gradually due to a reduction of effective permeability to water flow in the vicinity of the wellbore. It can be

concluded that under the simulation conditions considered most of the water is retained in the low permeability coal seam during the CBM extraction.

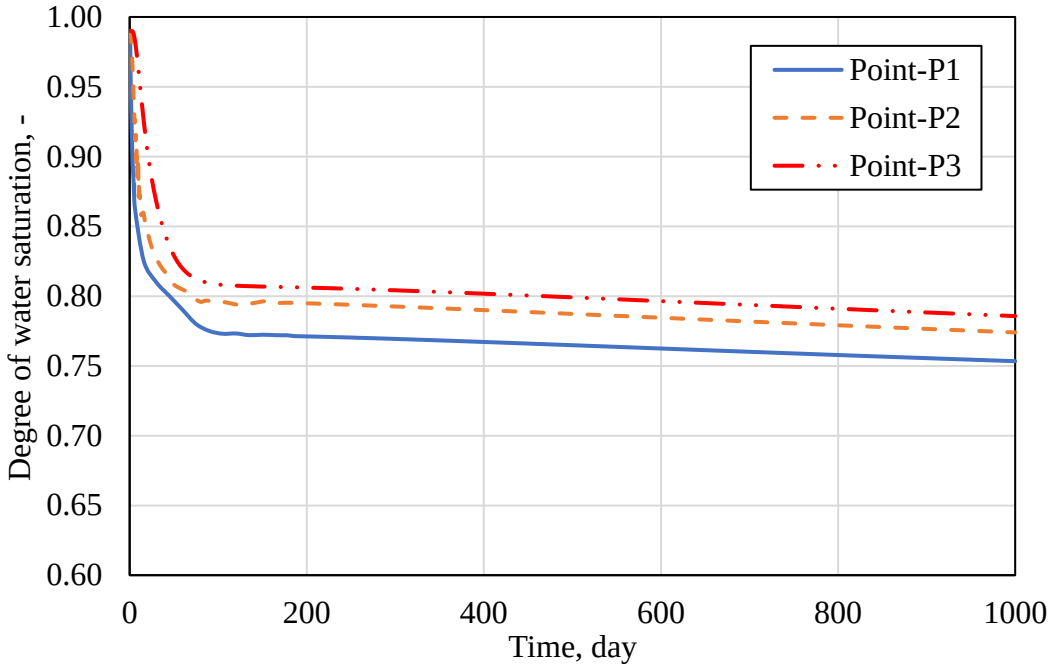

Figure 7.9 Temporal evolution of water saturation at the selected measurement points for CBM recovery without CO_2 injection.

Figure 7.10 presents the evolution of the temperature predicted in the numerical simulation for CBM production from a low permeability coal seam. It can be observed that there is a relatively large decrease of temperature at the detection point close to the production well compared to that predicted further from the well. This behaviour is attributed to the larger gas pressure gradient formed in the vicinity of the wellbore, as shown in Figure 7.5, resulting in a strong Joule-Thomson cooling effect. Heat exchange between the fracture and matrix continua is considered in the simulation, however, due to the small matrix block length (1 cm) input in this simulation analysis, the heat transfer between two systems is completed quickly and thermal equilibrium is reached.

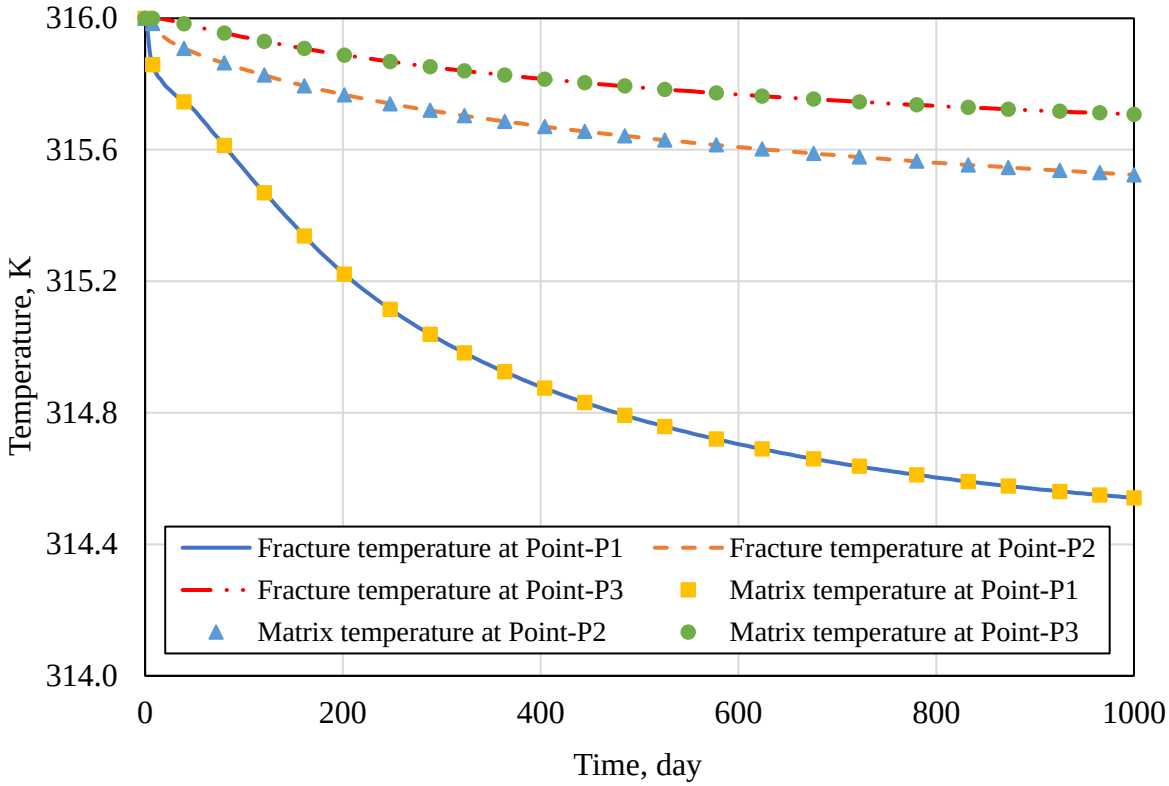

Figure 7.10 Temporal evolution of temperature at the selected measurement points for CBM recovery without CO_2 injection.

7.2.2 Coupled THCM behaviour during CO_2 injection and ECBM recovery

This section presents the results obtained from the numerical simulations performed for investigation of the coupled THCM behaviour occurring during CO_2 injection with ECBM recovery. In addition to the results shown for the primary CBM recovery, such as fluid pressure, porosity, permeability, the difference of gas production between primary CBM recovery and CO_2 enhanced CBM recovery with and without hydraulic fracturing is also included in this section. Different from exhibition of numerical results for primary CBM recovery where only one production well was used, the results of simulations for CO_2 enhanced CBM recovery where both injection well and production well are drilled are shown in terms of spatial distributions of fluid pressure, porosities, permeability, gas concentration and temperature with time in order to represent the differences of variables mentioned above in simulation domain.

Figure 7.11 shows the distribution of water pressure between the injection and production wells at selected injection times of 50 days, 250 days, and 500 days. It can be seen that water

pressure displays a similar trend across the section at the three different times, starting to decrease gradually from the injection well with a rapid drop in the vicinity of the production well. The spatial distribution of gas pressure is shown in Figure 7.12. Although high pressure CO_2 (12 MPa) is injected into the coal seam with an initial reservoir pressure of 10.3 MPa, the gas pressure does not exceed the initial reservoir pressure beyond the immediate vicinity of the injection well. This reflects that the injected CO_2 displaces the in situ CBM in the manner expected. This can also be seen in Figure 7.13; in the area where the CO_2 concentration is higher, most of the CBM has been driven toward the production well.

In addition to the drop of gas pressure in the vicinity of the production well due to extraction of CBM, there is V-type low pressure area at the displacement front of CBM by the injected CO_2. This is not necessarily the expected trend, but that closer inspection of the concentration profiles shown in Figure 7.13 indicates that the model predictions are reasonable. Hence, the observed behaviour does not appear to influence the gas transport behaviour in a significant way. The gas pressure is not used as a primary variable in numerical solution, instead, it is calculated using non-ideal gas law, which can be influenced by gas concentration, temperature and gas compressibility. It can be seen from Figure 7.13 that both CO_2 concentration and CBM concentration show reasonable trend. Besides, there is no large decrease in temperature in simulation domain. Thus, a possible cause is that CO_2 has a stronger compressibility than CBM at this pressure-temperature condition of the displacement front of CBM. When there is more CBM in the mixture, the compressibility of the mixed gas is higher, causing a higher gas pressure, on contrary, at the side of the displacement front of CBM with higher fraction of CO_2, although the concentration of CO_2 is higher, this pressure-temperature conditions is closed to the critical state of CO_2 (7.39 MPa, 304.25 K), the mixture gas is more compressed, further leading to relatively smaller gas pressure. Nonetheless, the change of gas pressure for CO_2 injection into coal seams is complex especially when the CO_2 is injected at higher pressure, this will be investigated in more detail in the future.

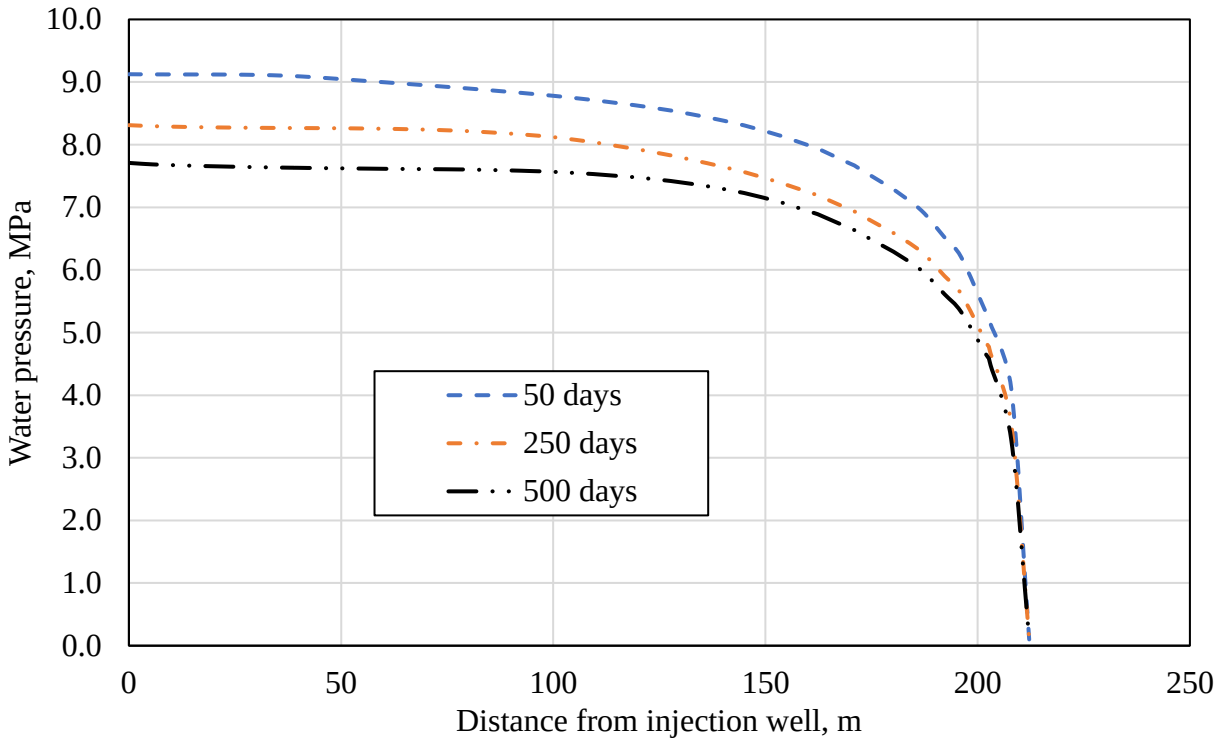

Figure 7.11 Distribution of water pressure along the diagonal between the injection and production wells at selected times for CO_2 injection with ECBM recovery.

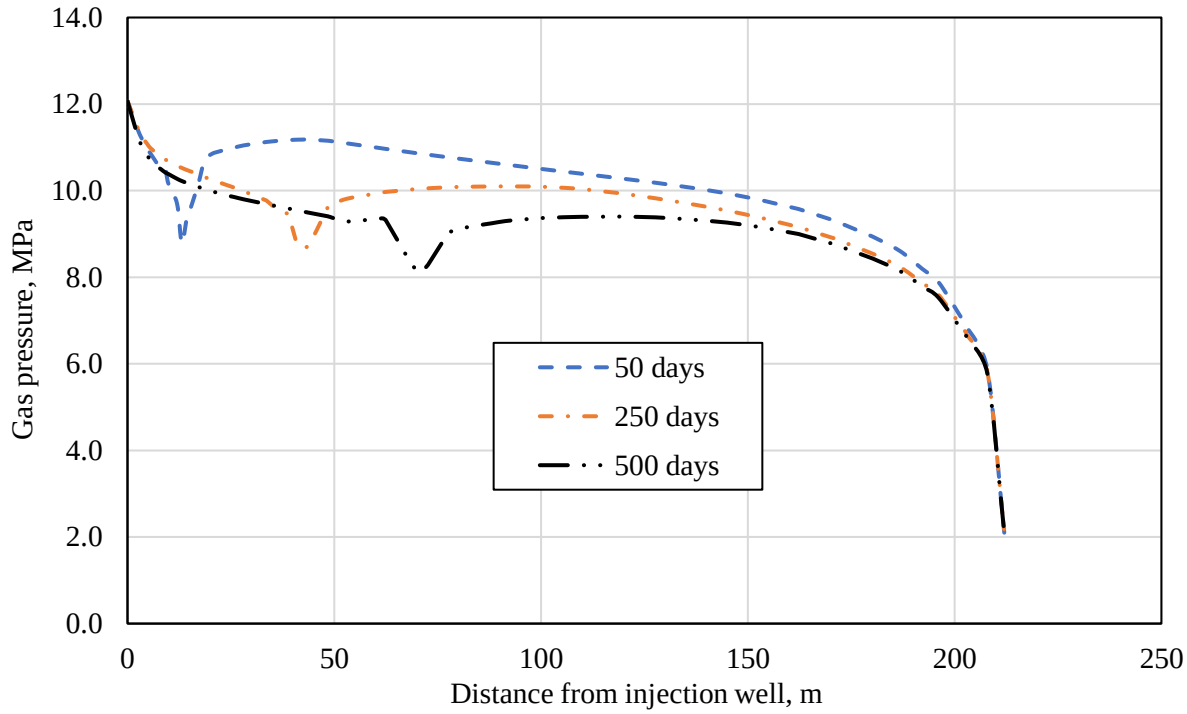

Figure 7.12 Distribution of gas pressure along the diagonal between the injection and production wells at selected times for CO_2 injection with ECBM recovery.

Similar to the simulation for CBM recovery without CO_2 injection presented in the previous section, the changes of water and gas pressure lead to a variable degree of water saturation. Figure 7.14 presents the distribution of water saturation along the along the diagonal between the injection and production wells at selected simulation times for CO_2 injection. It can be seen that the saturation in the vicinity of the injection and production wells decreases with time, as expected because of the water production and also the displacement of pore water by the injected CO_2. The variation of saturation along the diagonal depends on the change in gas pressure, hence, there the predictions are influenced by the V-type low pressure region described in relation to Figure 7.12.

Figure 7.15 and Figure 7.16 present the spatial distributions of fracture porosity and permeability during CO_2 injection, respectively. As shown in Figure 7.15 and Figure 7.16. the fracture porosity and permeability in the area close to the production well experience a large increase due to gas desorption-induced shrinkage of the coal matrix. On the other hand, CO_2 adsorption-induced swelling of the coal matrix occurred with increasing CO_2 adsorption, initiating a reduction of the fracture porosity. The deformation due to CO_2 adsorption overcomes the coal shrinkage due to CBM desorption, thereby restraining the fracture dilation due to CBM desorption. As a result, the fracture porosity and permeability in the area with a higher CO_2 concentration is lower than the initial condition.

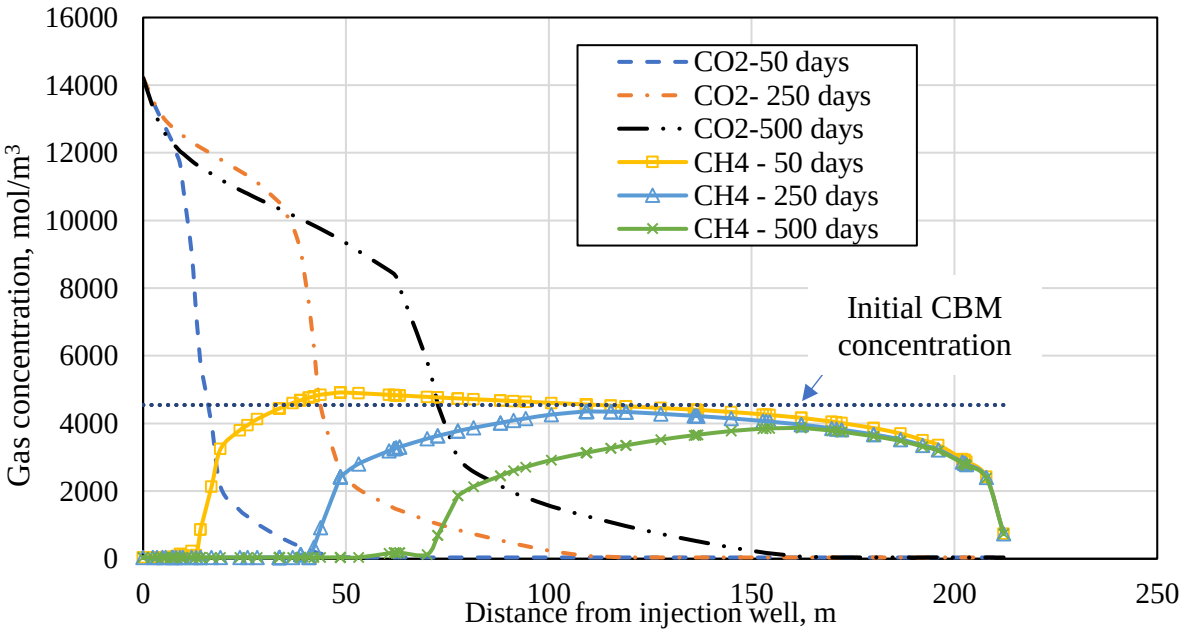

Figure 7.13 Distribution of free gas concentration along the along the diagonal between the injection and production wells at selected times for CO_2 injection with ECBM recovery.

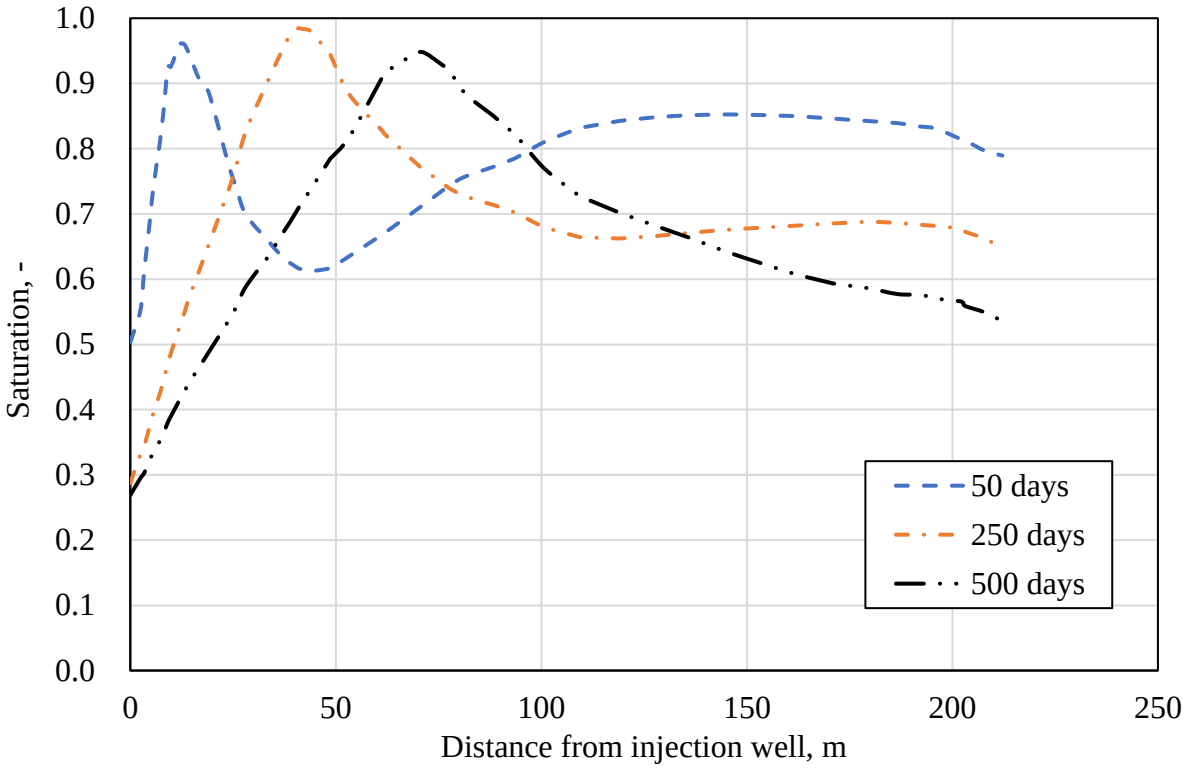

Figure 7.14 Distribution of water saturation along the along the diagonal between the injection and production wells at selected times for CO_2 injection with ECBM recovery.

The fracture porosity and permeability in the area close to injection well is larger than in areas further from the injection and production wells, this is because the fracture porosity and permeability in this area rebounds earlier. The fracture porosity and permeability experience a decrease due to CO_2 adsorption induced swelling deformation. CO_2 has a smaller Langmuir pressure, according to Langmuir isotherm, there is a quick increase in adsorbed amount of CO_2 in coal with partial gas pressure when the gas pressure is lower, thus, the swelling deformation plays a controlling role in fracture porosity and permeability at this period. With more CO_2 injected, the gas pressure increases and more CBM is displaced, the increase of CO_2 adsorption-induced swelling deformation is slow, in contrast, the shrinkage of coal caused by CBM desorption is increased, resulting in increase of fracture porosity and permeability.

Although the fracture porosity and permeability in the region closed to production displays increasing trend to that in the simulation for primary CBM recovery, this increase is smaller than that in primary CBM recovery. In addition, the fracture porosity and permeability near the production well show almost no variation with time during CO_2 injection. It can be

concluded that CO_2 injection is able to make more CBM desorbed in the area reached by CO_2, and driven toward production well, there are more CBM residing in the area closed to production compared to the scenario without CO_2 injection, as shown in Figure 7.13. This also explain why the saturation in the vicinity of production well decreases with time, namely, the gas pressure shows little change while the water pressure continues to drop, resulting capillary pressure increase and saturation decrease.

The changes of matrix porosity in different locations are different as well, Compared to the reduction of matrix porosity in the region closed to production well, the matrix porosity in vicinity of injection well shows an increase as a result of competition between coal swelling caused by CO_2 adsorption and coal shrinkage by CBM release from coal matrix, as shown in Figure 7.17.

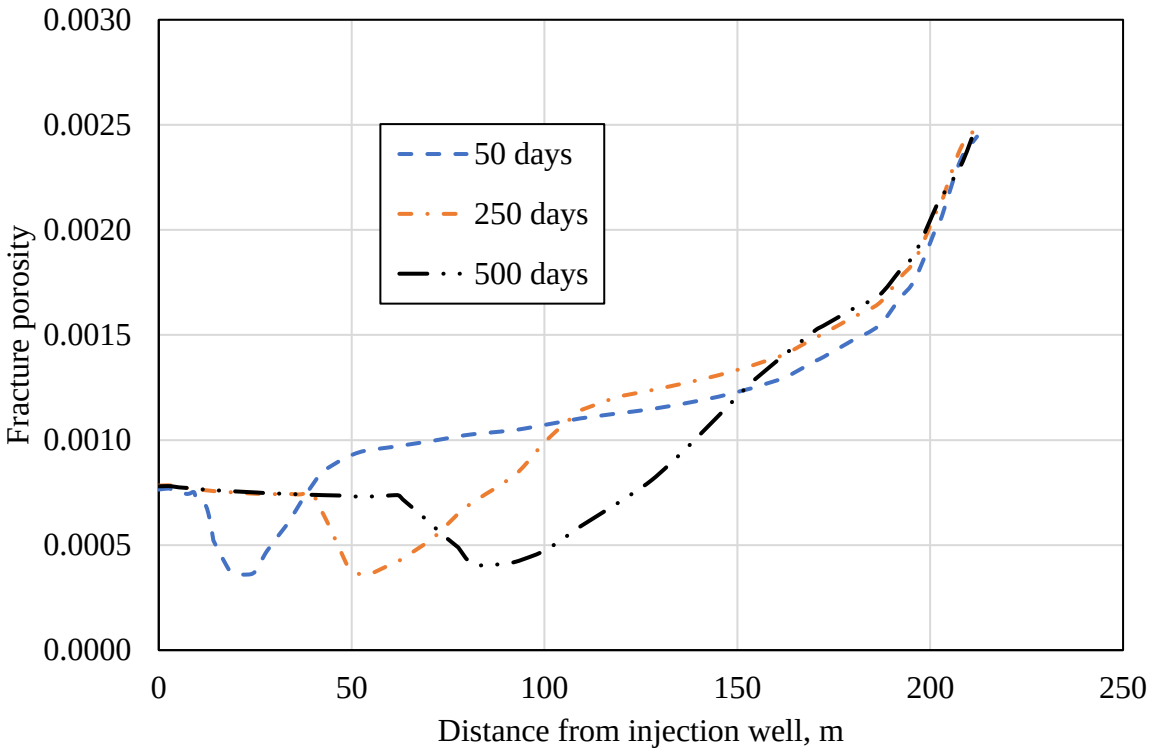

Figure 7.15 Fracture porosity along the along the diagonal between the injection and production wells at selected times for CO_2 injection with ECBM recovery.

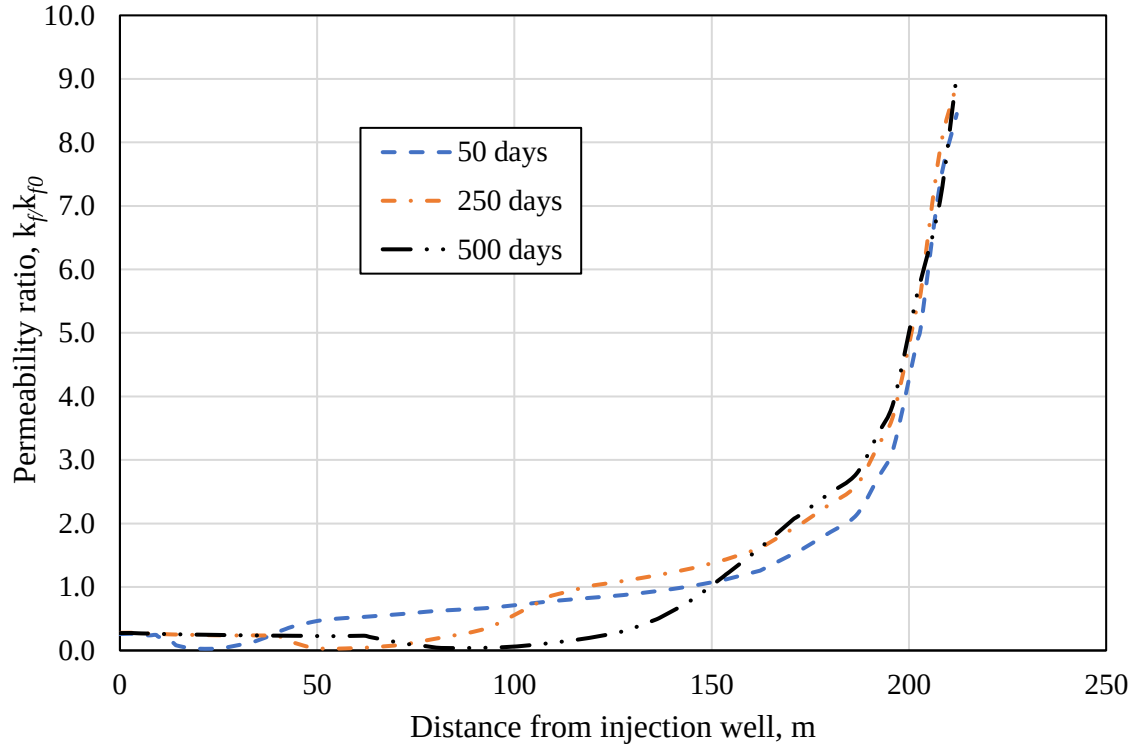

Figure 7.16 Permeability ratio along the along the diagonal between the injection and production wells at selected times for CO_2 injection with ECBM recovery.

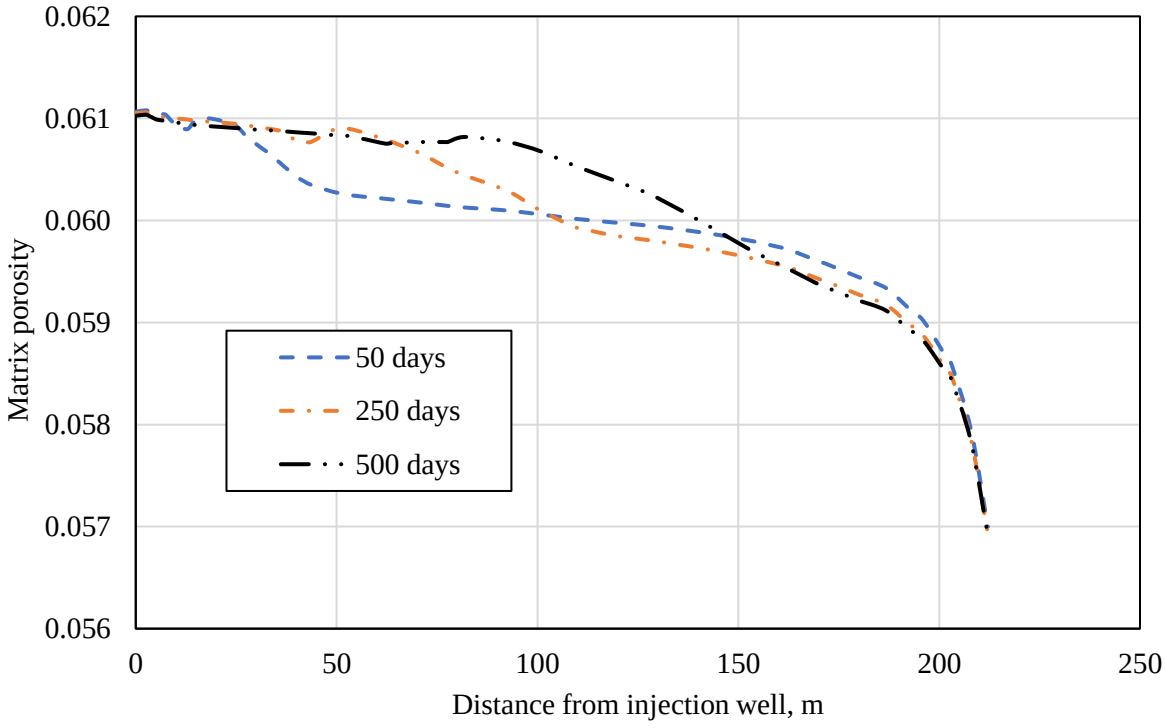

Figure 7.17 Matrix porosity along the diagonal between the injection and production wells at selected times for CO_2 injection with ECBM recovery.

Figure 7.18 presents the numerical results of temperature in the simulation during CO_2 injection. It can be seen that the temperature in regions far from the production and injection wells shows almost no change during CO_2 injection, whilst the temperature in the vicinity of both wells experiences a change, especially in the region close to the injection well. There is a cooling region in the vicinity of both well due to the Joule Thomson cooling (JTC) effect. The injection of compressed CO_2 caused a relatively greater reduction in temperature compared to CBM production, which is because CO_2 injection also causes a decrease in coal permeability, resulting in a larger pressure gradient and stronger JTC effect in the region close to injection well. Furthermore, CO_2 has a higher Joule-Thomson coefficient than CBM, hence, for the same decrease in gas pressure, there is a larger increase in the potential energy of CO_2, leading to a larger decrease in kinetic energy, and thus a greater temperature drop. The temperature near the production well shows a continuous decline because of continued CBM recovery, whilst the temperature in the region of the injection well recover as the injected CO_2 advances further into the coal seam.

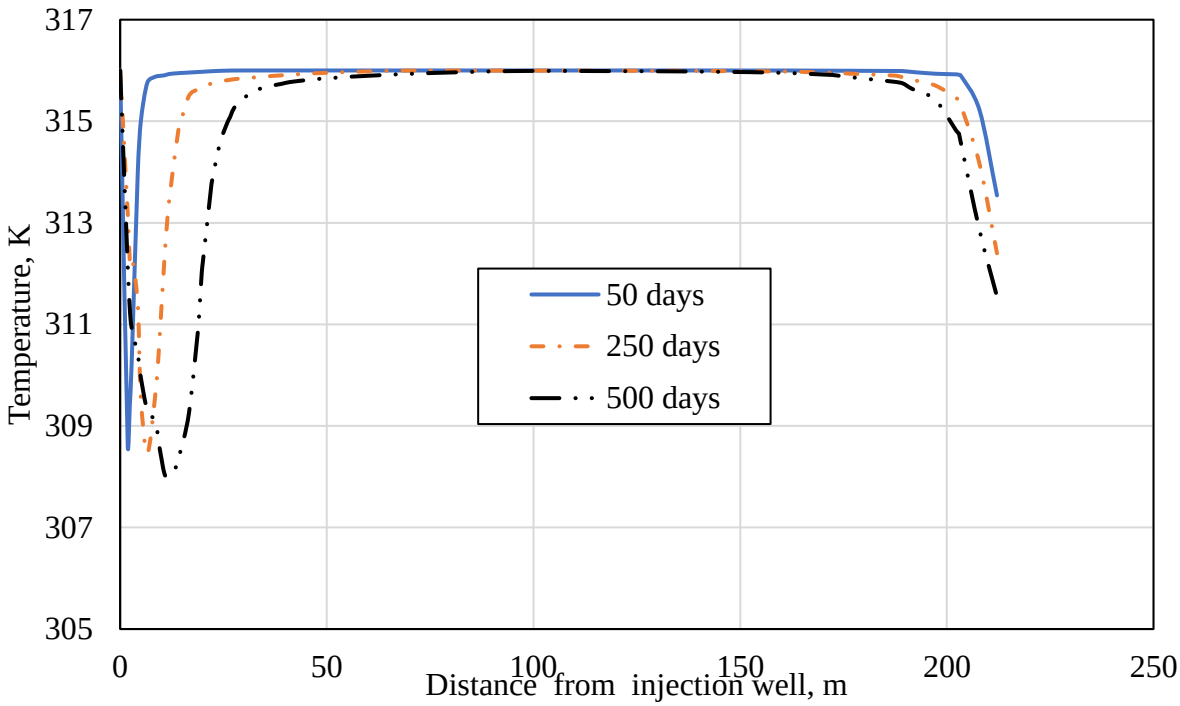

Figure 7.18 Distribution of temperature along the along the diagonal between the injection and production wells at selected times for CO_2 injection with ECBM recovery.

In order to examine the effect of CO_2 on the CBM production performance, the cumulative gas from production well is calculated for comparison, as shown in Figure 7.19. It can be

seen that the cumulative CBM production for CBM recovery without CO_2 injection displays a nonlinear increase with time. When CO_2 injection is considered, there is no improvement in CBM recovery at the early stage. This is because the injected CO_2 enhances recovery by displacing and driving the CBM from the point of injection towards the production well, leading to a gathering of CBM at the front of the advancing CO_2. As the CO_2 advances towards the production well, the displaced CBM is produced, leading to the considerable increase in cumulative CBM production as the simulation progresses.

At the time of CO_2 breakthrough at point P1, the simulations running with and without the consideration of hydraulic fracture were stopped, after 700 and 400 days, respectively. Compared to the results without hydraulic fractures, the cumulative gas production is increased significantly when the coal seam is stimulated by hydraulic fractures. The hydraulic fracture provides a preferential flow pathway for CO_2 transport and produces a large contact area with a higher fluid pressure within the coal seam, meaning that more CO_2 penetrates the coal matrix at an earlier stage. The decrease and rebound of coal permeability take places earlier in the simulation scenario with hydraulic fractures compared to the simulation scenario without hydraulic fracturing treatment, as shown as shown in Figure 7.20, which show the variation of coal permeability at measurement point P4. It can be seen that hydraulic fracturing makes the rebound of coal permeability occur earlier, which means that a higher permeability is achieved and sustained for more of the simulation period in regions of the coal seam affected by CO_2-induced coal swelling. Due to the larger area reached by CO_2, more CBM is displaced and driven toward the production well, as shown in Figure 7.21.

Figure 7.22 presents a comparison of the cumulative amount of CO_2 injected to illustrate the influence of the hydraulic fractures. It can be seen that the hydraulic fracture results in a considerable increase in the CO_2 injectivity. For the simulation without hydraulic fractures, the cumulative CO_2 injection increases slowly at the early stage, in contrast, the presence of hydraulic fractures leads to a rapid increase in the cumulative amount of injected CO_2, particularly at the start of injection.

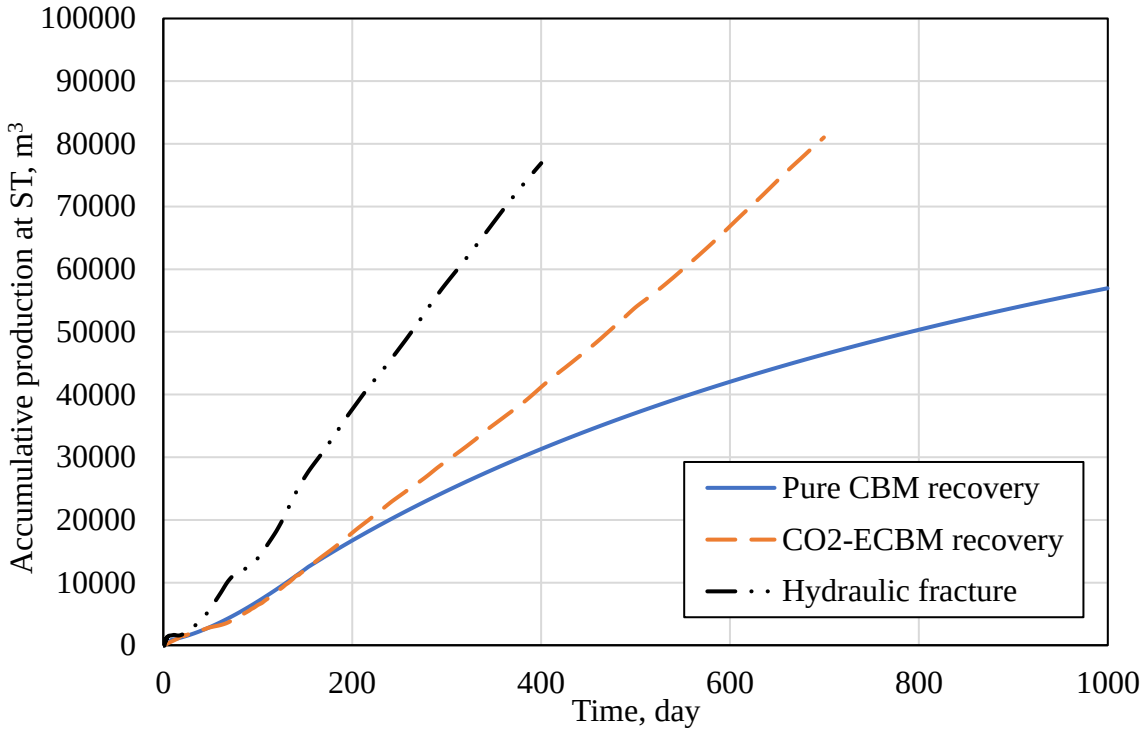

Figure 7.19 Cumulative production comparison between CBM recovery and CO_2-ECBM recovery with and without hydraulic fracturing treatment.

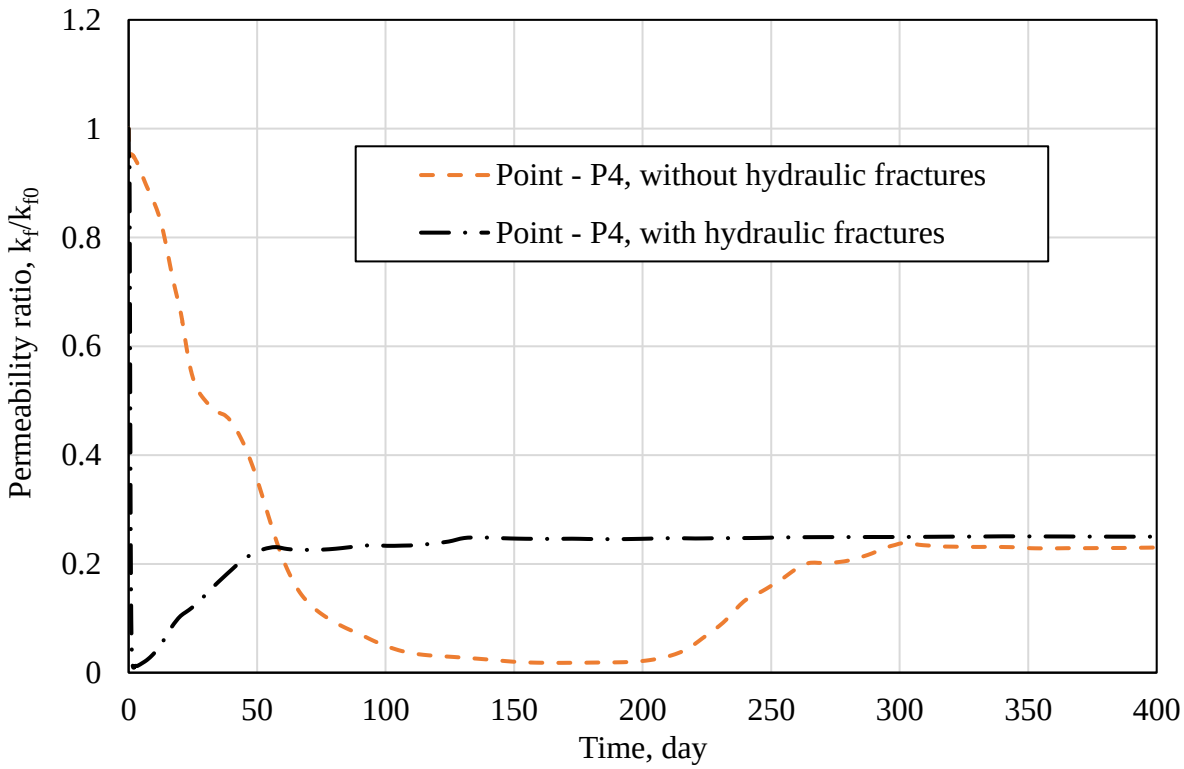

Figure 7.20 Comparison of variations in permeability ratio with time at measurement point P4 in simulation scenarios with and without hydraulic fractures.

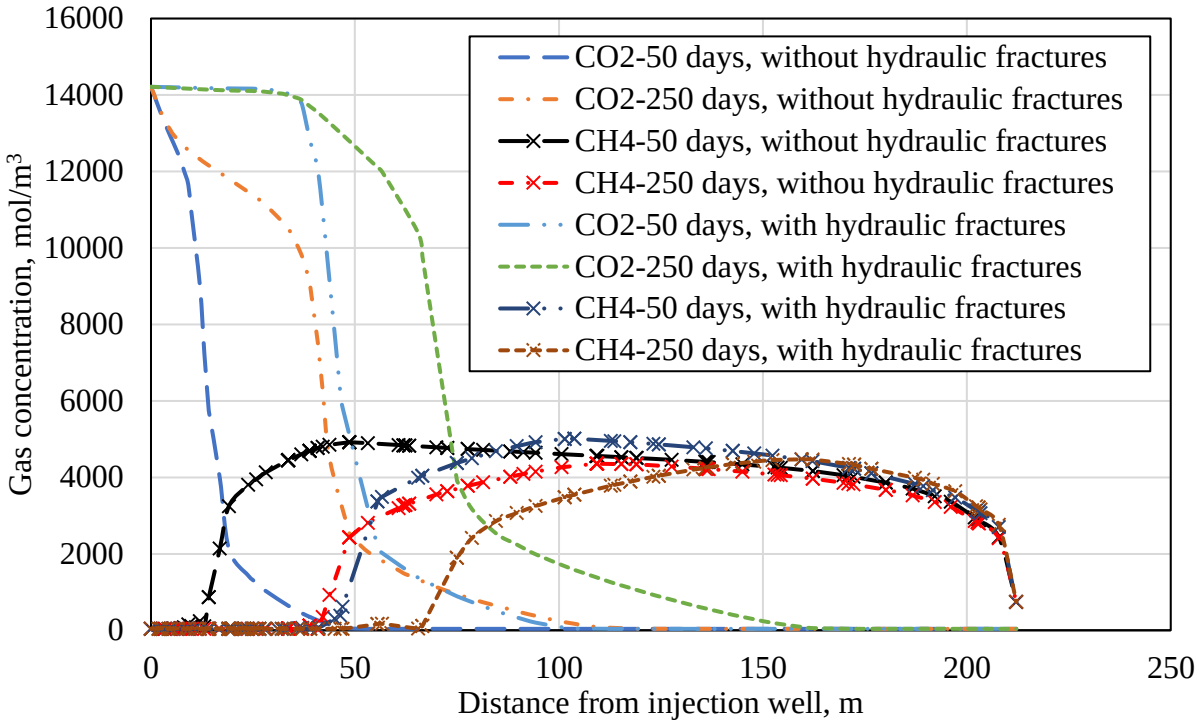

Figure 7.21 Comparison of gas concentration distributions along the diagonal at selected times in simulation scenarios with and without hydraulic fractures.

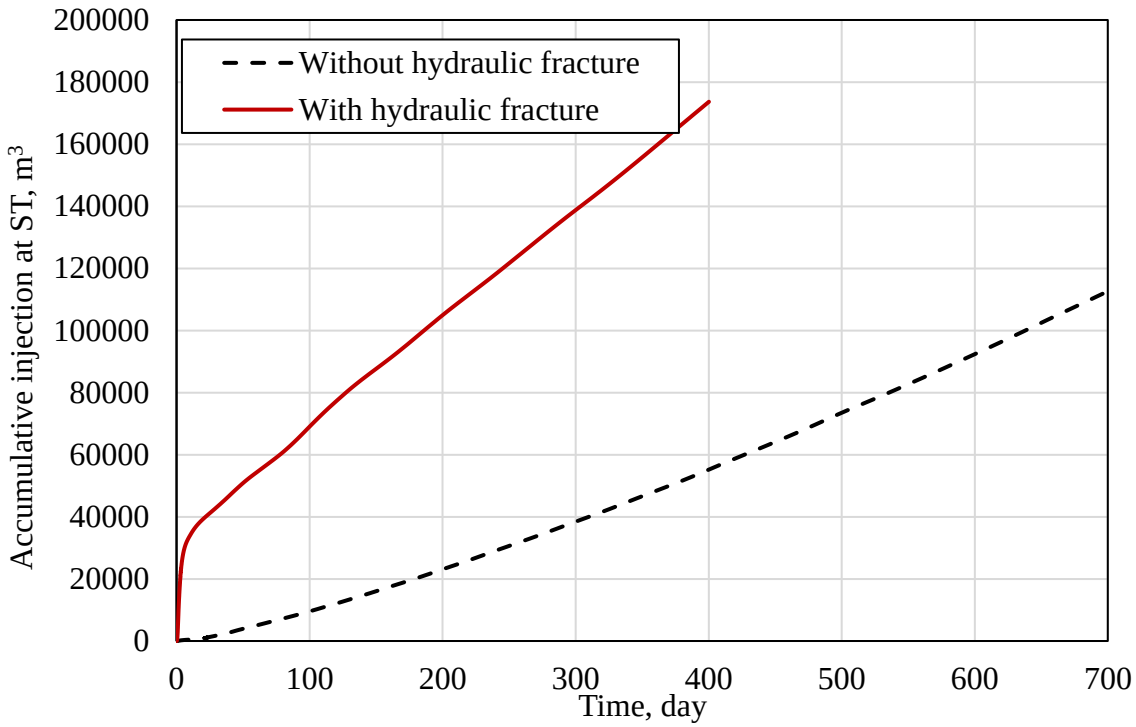

Figure 7.22 Cumulative CO_2 injection comparison between CO_2-ECBM recovery with and without hydraulic fracturing treatment.

7.3 Conclusions

The objective of this chapter was to improve the understanding of the major processes of CO_2 sequestration and CBM via the proposed model, this was achieved built upon the work of the previous chapter by presenting a set of numerical simulations that address the coupled processes involved during CBM recovery and CO_2-ECBM recovery. The influences of CO_2 injection and hydraulic fracturing on the CBM recovery process have been explored using a simulation scenario with a simple hydraulic fracture layout. The results have been presented in terms of the temporal and spatial evolutions of the field variables.

Under the adopted simulation conditions, the water and gas pressure experience rapid decrease in both simulations for primary CBM recovery and CO_2 enhanced CBM recovery. Most of the water is retained in the low permeability coal seam during the primary CBM extraction, while CO_2 injection is able to contribute to water drainage. Both CBM recovery and CO_2 injection can alter coal structure and permeability, which is the net result of two competing deformation mechanism. The increase in permeability of coal seams in the vicinity of production can be weakened by CO_2 injection. It was observed that the temperature in the vicinity of both wells experiences a change, especially in the region closed to injection well at late stage of the CO_2 injection. It can be concluded that the coupled processes involved in both primary CBM recovery and CO_2 injection can be predicted using proposed model.

The potential of CO_2 injection to enhance CBM recovery has been evaluated by comparing the results of cumulative gas production obtained from the selected simulation scenarios. At the early stage, CO_2 injection did not improve the cumulative CBM production, however, a large increase was predicted as more CO_2 was injected into the coal seam as the simulation time progressed. Compared to the results without hydraulic fractures, the cumulative gas production was increased significantly when the coal seam was stimulated by hydraulic fractures, with the cumulative amount of injected CO_2 also increasing considerably. The conclusion based on these findings can be drawn that CO_2 injection together with hydraulic fracturing treatment is an effective way to increase the CBM production and improve the injectivity of CO_2 in low permeability coal seams.

The developed model has been applied to study the coupled processes of CO_2 sequestration and CBM recovery, and the simulations and discussions provided in this chapter have focused on the practical/applied aspects of CO_2 sequestration with enhanced CBM recovery. The results of this chapter, in combination with previous chapter have provided the insight into the processes and behaviour occurred during CBM recovery and CO_2 sequestration. Although the work presented in this thesis is an initial attempt of proposed model at the study of CO_2 geo-storage and CBM recovery, it has demonstrated some of advanced features of the proposed model, these are essential capabilities in the study of application of coal seams.

7.4 References

Bastola, S. and Chugh, Y. eds. (2015). *Shear Strength and Stiffness of Bedding Planes and Discontinuities in the Immediate Roof Rocks Overlying the No 6 Coal Seam in Illinois*. 13th ISRM International Congress of Rock Mechanics. International Society for Rock Mechanics and Rock Engineering.

Chen, H., Wang, Z., Chen, X., Chen, X. and Wang, L. (2017). Increasing permeability of coal seams using the phase energy of liquid carbon dioxide. *Journal of CO_2 Utilization* **19**:112-119.

Chen, M., Hosking, L. J. and Thomas, H. R. eds. (2018). *Non-isothermal Gas Flow During Carbon Sequestration in Coalbeds*. The International Congress on Environmental Geotechnics. Springer.

Fan, C., Elsworth, D., Li, S., Zhou, L., Yang, Z. and Song, Y. (2019). Thermo-hydro-mechanical-chemical couplings controlling CH4 production and CO_2 sequestration in enhanced coalbed methane recovery. *Energy* **173**:1054-1077.

Fujioka, M., Yamaguchi, S. and Nako, M. (2010). CO_2-ECBM field tests in the Ishikari Coal Basin of Japan. *International Journal of Coal Geology* **82**(3-4):287-298.

Holditch, S., Ely, J., Semmelbeck, M., Carter, R., Hinkel, J. and Jeffrey Jr, R. eds. (1988). *Enhanced recovery of coalbed methane through hydraulic fracturing*. SPE annual technical conference and exhibition. Society of Petroleum Engineers.

Ma, T., Rutqvist, J., Oldenburg, C. M., Liu, W. and Chen, J. (2017). Fully coupled two-phase flow and poromechanics modeling of coalbed methane recovery: Impact of geomechanics on production rate. *Journal of Natural Gas Science and Engineering* **45**:474-486.

Mitra, A., Harpalani, S. and Liu, S. (2012). Laboratory measurement and modeling of coal permeability with continued methane production: Part 1–Laboratory results. *Fuel* **94**:110-116.

Qu, H., Liu, J., Chen, Z., Wang, J., Pan, Z., Connell, L. and Elsworth, D. (2012). Complex evolution of coal permeability during CO_2 injection under variable temperatures. *International Journal of Greenhouse Gas Control* **9**:281-293.

Saliya, K., Grgic, D., Giot, R. and Giraud, A. (2015). Thermo-hydro-mechanical modeling with Langmuir's adsorption isotherm of the CO_2 injection in coal. *International Journal for Numerical and Analytical Methods in Geomechanics* **39**(6):594-617.

van Bergen, F., Krzystolik, P., van Wageningen, N., Pagnier, H., Jura, B., Skiba, J., Kobiela, Z. (2009). Production of gas from coal seams in the Upper Silesian Coal Basin in Poland in the post-injection period of an ECBM pilot site. *International Journal of Coal Geology* **77**(1-2):175-187.

Wen, H., Lu, J.-h., Xiao, Y. and Deng, J. (2015). Temperature dependence of thermal conductivity, diffusion and specific heat capacity for coal and rocks from coalfield. *Thermochimica acta* **619**:41-47.

Wong, S., Law, D., Deng, X., Robinson, J., Kadatz, B., Gunter, W. D., Zhiqiang, F. (2007). Enhanced coalbed methane and CO_2 storage in anthracitic coals—micro-pilot test at South Qinshui, Shanxi, China. *International Journal of Greenhouse Gas Control* **1**(2):215-222.

Xu, J., Zhai, C. and Qin, L. (2017). Mechanism and application of pulse hydraulic fracturing in improving drainage of coalbed methane. *Journal of Natural Gas Science and Engineering* **40**:79-90.

Zhang, J. (2014). Numerical simulation of hydraulic fracturing coalbed methane reservoir. *Fuel* **136**:57-61.

Zhi, S., Elsworth, D., Wang, J., Gan, Q. and Liu, S. (2018). Hydraulic fracturing for improved nutrient delivery in microbially-enhanced coalbed-methane (MECBM) production. *Journal of Natural Gas Science and Engineering* **60**:294-311.

Ziabakhsh-Ganji, Z. and Kooi, H. (2014). Sensitivity of Joule–Thomson cooling to impure CO_2 injection in depleted gas reservoirs. *Applied Energy* **113**:434-451.

8

Conclusions and suggestions for future research

8.1 Introduction

This chapter summarises the conclusions pertinent to the developments presented in this thesis and relates them to the objectives presented at the start of the work. Key contributions and advancements are highlighted along with the opportunities for further work.

To investigate the complex non-isothermal, multiphase, multicomponent gas transport behaviour related to CO_2 sequestration in coal with enhanced coalbed methane (ECBM) recovery, a coupled numerical model of thermal, hydraulic, chemical, and mechanical (THCM) behaviour has been developed in this thesis. The modelling framework has been based on a hybrid discrete fracture-dual porosity approach with application to study the coal response and processes related to CO_2 sequestration and ECBM recovery. The main tasks of this work as stated in chapter 1 were to:

i. Develop a theoretical framework for the transport of multiphase fluid and multicomponent gases in fractured rock under coupled thermal, hydraulic, gas/chemical and deformation behaviour, based on a hybrid discrete fracture-dual porosity framework, focusing on the coals and in particular those with CO_2 sequestration.

ii. Advance a coupled thermo-hydro-chemo-mechanical (THCM) model to integrate simulation capabilities of the new hybrid discrete fracture-dual porosity model.

iii. Develop and implement appropriate relationships for describing the physical and chemical coal-gas interactions, enabling the application of the model to study the CO_2-ECBM recovery process.

iv. Build and implement appropriate numerical algorithm to couple the discrete fracture and dual porosity models for the simulation of coal reservoirs.

v. Verify and validate the newly developed model to determine its suitability for studying the coupled processes governing the performance of CO_2 sequestration and ECBM recovery.

vi. Apply the developed model to investigate the response of a coal seam during CO_2 injection to enhance CBM recovery at field scale.

These tasks provide the focus of the overall analysis of the work presented in this chapter.

A summary of the theoretical and numerical models developed for non-isothermal, multiphase, multicomponent gas transport in elastically deformable coal, including the pertinent conclusions reached, is presented in section 8.2. This is followed in section 8.3 by an overview of the verification exercises performed in this work. Sections 8.4 and section 8.5 then review how the model applications considered in this work have addressed objective vi. given above. Finally, the overall conclusions of the thesis are discussed in section 8.6 and suggestions for further work are presented in section 8.7.

8.2 Theoretical and numerical model development

Theoretical and numerical formulations for the coupled flow of water, heat, and multicomponent gas in deformable discretely fractured dual porosity geomaterials were developed within a coupled THCM framework in chapter 3 and chapter 4, respectively. In particular, the framework has been extended by implementing the newly developed dual porosity thermal transport and deformation components of the model, thereby providing advanced capabilities to simulate multiphase, multicomponent gas transport in coal under

non-isothermal conditions. A summary of the key advancements of the theoretical and numerical formulations is provided in this section.

Discretely fractured rock with a well-developed network of natural fractures was represented using a hybrid coupled dual porosity and discrete fracture approach. This new numerical model comprises three different media: the matrix continuum with relatively large porosity and low permeability, the fracture continuum with intermediate porosity and permeability, and the discrete fractures with relatively high permeability and low porosity, which interact via mass and heat exchange processes. The large-scale fractures were represented explicitly, which was achieved using a discrete fracture model. The uniformly distributed natural fracture network, composed of micro-fractures and the rock matrix itself, were modelled using a dual porosity approach. Accordingly, the governing equations were expressed in terms of three sets of primary variables and three sets of material properties in order to provide an improved physical interpretation of the pore space.

The governing equations for multiphase, multicomponent gas transport were developed by adopting the law of conservation of mass. Non-equilibrium mass exchange terms were applied considering pressure and concentration differences between the media. Considering mass exchange between the matrix continuum and the hydraulic fractures is lower than that between the fracture continuum and the hydraulic fractures, the large-scale fractures were considered to be coupled only with the surrounding fracture continuum, which in turn is coupled with the matrix continuum. It was assumed that quasi-steady state pore pressure and concentration distributions prevail in the matrix blocks, whereby the mass exchange process become a function of the averaged pressures, concentrations, and temperature of the fracture continuum and matrix continuum.

A local thermal non-equilibrium (LTNE) approach was used to represent the heat transfer in the pore space and fractures separately. The governing equations for heat transport were derived based on the law of conservation of energy. Considering the compressibility of real gas, the Joule-Thomson effect was included in the governing equations for heat transport. It was assumed that the temperature in natural fractures is identical to that in hydraulic fractures. Hence, only heat transfer between the dual continua was considered in this work. Heat exchange was separated into two processes, namely, transfer between the rock matrix

and fracture fluid by conduction through the fracture surfaces, and transfer by advection due to mass exchange between the continua.

Dual poroelastic theory was introduced to represent the deformation behaviour of fractured rock explicitly. Deformation was divided into mechanical deformation due to effective stress, thermal expansion, and adsorption-desorption-induced matrix swelling-shrinkage. Biot's poroelastic theory for a single porosity system was extended to dual porosity media to consider the fluid-solid coupling, which was achieved by evaluating the role of fluid pressure using Biot's effective stress coefficient. The deformation of discrete fractures was handled separately. The variation of fracture aperture due to the variation of normal effective stress acting on the surface of the fracture and shear stress acting along the fracture was included.

To solve the governing equations specifically for applications of CO_2 sequestration with ECBM recovery, additional relationships were required to characterise the material properties. The extended Langmuir isotherm was modified to describe the adsorbed amount of multicomponent gas by introduction of temperature dependent Langmuir constants. The surface stress of the fluid-solid interface was introduced to represent the coal deformation and porosity changes related to adsorption behaviour. High-pressure gas properties were characterised using established relationships found in the literature. The key gas properties related to the developed formulation included gas compressibility, specific heat capacity of gases, and the Joule-Thomson coefficient.

A new porosity- permeability model was derived, in which the impacts of gas flow and coal deformation were incorporated. Different from the porosity models in the literature, which only consider the change in fracture porosity, porosity change of the coal matrix was considered and also linked to the variation of fracture porosity through the matrix-fracture compartment interaction. Under this approach, interactions were considered due to the pressure difference between the fracture and matrix continua as well as local swelling deformation resulting from gas adsorption. This new porosity- permeability model provides a tool to investigate the structural change of coal. These theoretical features are essential components of the model for the accurate simulation of coupled thermal-hydraulic-chemical-mechanical behaviour in coal during CO_2 sequestration and ECBM recovery.

A numerical solution was employed to solve the series of nonlinear partial differential equations. The Galerkin finite element method was used for the spatial discretisation of the

governing equations. The discrete fractures were idealised as lower-dimensional geometric objects. Hence, lower-dimensional interface elements were used to discretise the large fracture domain. It was assumed that the flow variables (gas concentration, water pressure and temperature) are continuous over the fracture continuum and discrete fracture domain. Thus, the discrete fracture elements must be located on the edges of continuum elements with both kind of elements sharing the same nodes. The coupling between the two flow systems was achieved by using the principle of superposition. This allowed the mass exchange terms between the fracture continuum and large fracture domain to balance off so that no explicit calculation for mass exchange was required. Temporal discretisation was achieved via a finite difference scheme based on a backward difference, mid-interval time stepping algorithm. A sequential non-iterative approach (SNIA) was adopted to couple the transport model with the sink/source terms for mass/heat exchange.

The numerical model was then incorporated into an existing computer code, COMPASS.

8.3 Model verification

A series of verification exercises were presented in chapter 5 on the specific developments to the theoretical and numerical formulation presented in this work. The principle aim was to examine the accuracy of the implementation of the theoretical and numerical formulations in the model and to provide greater confidence in the numerical solutions. The key components of the model describing non-isothermal, multiphase flow in elastically deformable rock with multiscale fractures were the focus of these tests, with the benchmarks provided by analytical solutions and alternative numerical solutions found in the literature.

A test was performed to examine the implementation of isothermal unsaturated flow in fractured rock treated as a dual permeability system. In this test, the interaction between the continua was considered. Verification of this behaviour was achieved considering the benchmark provided by the results of two alternative numerical models presented in literature. The results obtained in this test verify that the numerical model is able to represent correctly the multiphase flow in a dual permeability system.

Gas adsorption behaviour at the coal surface was treated as an equilibrium reaction in this work, and the effect of adsorption on the gas transport behaviour was analysed using two

tests; one with and one without adsorption. The simulation results reflected that adsorption decreases the amount of free gas and retards flow. Comparisons with an analytical solution indicated that the adsorption reaction has been correctly included in the numerical model.

The implementation of the heat transport formulation was evaluated through two verification tests, including conductive-convective heat transport and the Joule-Thomson cooling effect. Pure convection and combined conductive-convective transport were considered separately to show the different heat transport mechanisms. The temperature change caused by the Joule-Thomson cooling effect during compressible fluid flow was shown. Comparisons were made against analytical solutions for conductive-convective transport, pure convection, and the Joule-Thomson cooling effect. The results showed that the inclusion of heat conduction produced a smoother breakthrough curve compared with purely convective heat transport, and that the injection of high pressure gas can lead to a fall of temperature as fluid pressure decreases with a high gradient. Hence, these tests provided confidence that the salient heat transfer theory has been successfully implemented in the numerical model

The deformation of isotropic elastic materials was verified against the results of an analytical solution concerned with the elastic response outside of a cylindrical hole in an infinite elastic medium subjected to a uniform in-situ stress field far from the hole. It was found that that the radial stress increased along the radial distance and reached the in-situ stress, with the maximum tangential stress occurring at the wall of the hole being double the in-situ stress and decreasing along the radial distance. Excellent correction with analytical solution indicated that the proposed numerical model was able to describe correctly the elastic deformation of rock.

A simulation test was conducted to examine the newly introduced modelling approach and finite element technique used to handle multiscale fractures. Considering the flow in a porous medium with discrete fractures, the comparison with the benchmark provided by the results of an analytical solution provided confidence in the implementation of the principle of superposition adopted for the hybrid-dimensional computational model.

A set of simulations were conducted to assess the thermo-hydro-mechanical coupling in the numerical model. The hydro-mechanical coupling was examined by the consolidation analysis for single phase fluid flow in a single porosity deformable medium, with an analytical solution used as the benchmark. The simulation results for fracture deformation

were compared with results of alternative numerical models presented in the literature. A further test was conducted to compare the numerical predictions with analytical solutions to verify the coupling between the temperature, flow, and deformation by considering the thermal contributions in the coupled thermo-hydro-mechanical model. Comparison between simulation solution and benchmark showed an excellent agreement, showing that the numerical model correctly the solve governing equations for the coupled thermo-hydro-mechanical behaviour.

The verification exercises presented in this work evaluated the numerical implementation of the theoretical framework for non-isothermal unsaturated flow in deformable fractured rock. Over the course of these tests, improved confidence was established in the accuracy of the implementation of the theoretical and numerical formulations, which encouraged the author to validate the proposed numerical model by comparison with experimental work or field trials.

8.4 Model validation and application

A series of validation tests were conducted to examine the accuracy of the proposed model with regards to the processes and material behaviour involved. Experimental data on coal-gas interaction and field data of CBM production published in the literature were used as benchmarks. An overview of the validation tests including the main conclusions reached is provided in this section.

Comparisons with the experimental results for temperature dependent adsorption behaviour of gas onto coal evaluated the validity of the modified Langmuir isotherm used in this work. An exponential relation was proposed to represent the impact of temperature on the relevant parameters, i.e. the Langmuir adsorption capacity and Langmuir pressure. It was found that temperature shows a negative impact on the amount of gas adsorption in coal, indicating that the gas adsorption is an exothermic process. From the improved fit with experimental measurements, it can be concluded that the proposed the theoretical relationship is able to represent the temperature-dependent characteristics of gas adsorption in coals.

The performance of the developed deformation model involving gas adsorption behaviour based on the surface stress approach was examined by comparing the predicted results with

two sets of experimental data, one for pure gas and another for mixed gas. The results showed that the developed swelling model is able to describe the deformation behaviour when adsorptive fluids are involved. It was observed that coal deformation involving gas adsorption is species dependent. Both coals were seen to exhibit the largest strain when adsorbing CO_2 compared to that induced by CH_4 and N_2 adsorption, because CO_2 adsorption leads to the largest adsorption stress. The adsorption-induced swelling stress showed a nonlinear relation with the normalised adsorption amount, espeically when the amount of gas adsorption exceeded half of the gas adsorption capacity, indicating although elevation of gas pressure is able to increase the adsorbed amount of gas in coals, the increases in swelling deformation is more significant.

The newly developed permeability model for dual porosity coal was applied to illustrate the physical and chemical mechanisms of deformation obeserved in experimental measurements. Validity of the model was examined by matching with experimental permeability measurements conducted on coals of different ranks. A good agreement was found between the predicted permeability trends and the exerimental data. It can be concluded that under the conditions considered, the new developed permeability model was found to have the capability of decribing the coal permeability evolution under different conditions.

A numerical simulation was performed to analyse the gas flow behaviour and structural changes of coal during CO_2 injection into a coal core at the laboratory scale. It was found that important structural changes occur during adsorptive gas transport in coal. The variation of fracture porosity was relatively complex as a result of competing effective stress and internal deformation. Compared to variations of the fracture porosity, adsorptive gas injection in coal has the potential to increase significantly the microporosity of coal, with similar findings having been reported in the literature. This seems to be an important reason for the occurrence of the swelling phenomenon during CO_2 injection into coal.

In order to demonstrate the reliability of the newly developed coupled model for predicting the coupled THCM behaviour occurring during CO_2-ECBM recovery, the coupled model was applied to simulate the pressure depletion during CBM recovery. This test examined the hydro-mechanical coupling, involving dual porosity multiphase flow, the new porosity and permeability model, adsorption behaviour, and deformation behaviour. Field data of gas and water production obtained from the boomer Fairway well located in the Fruitland

Formation, San Juan Basin, USA, was history matched. It was shown that the production performance predicted by the proposed model can achieve an acceptable match compared with the actual field data under the simulation conditions considered. The results obtained gave the confidence in the ability of numerical model to represent the coupled behaviour of coals during CO_2-CBM recovery.

Based on the validation test for the Fruitland Formation, a parameter sensitivity study was carried out to investigate the influences of various parameters on the gas production, such as initial reserovir permeability, initial water saturation, and the adsorption behaviour. it was observed that compared to the effects of water satuation and gas adsorption behaviour, the initial permeability exerts a siginificantly negagive influence on the gas production rate, to enhance the gas production, additional treatments to coal seams are required.

The encouraging results obtained from the validations of these subsets of numerical model produce the further confidence in the relability of numerical models in representating mechanisms involved, which provided a basis for further investigation of the physical mechanisms exhibited during CO_2-ECBM.

8.5 Coupled THCM behaviour during CH_4 production and CO_2 injection

The coupled THCM behaviour during primary CH_4 production and CO_2-ECBM recovery for a low permeability coal reservoir was evaluated in chapter 7 by performing a set of field scale simulations with different injection and production conditions. Furthermore, there was an emphasis on the roles of hydraulic fracturing in the CO_2-ECBM recovery process, which was achieved by comparing the results of cumulative CBM production and CO_2 injection.

The water pressure and gas pressure were observed to show a similar overall trend in the simulations for both pure CBM recovery and CO_2-ECBM recovery, which showed a decline with time. Although the water saturation showed a rapid decrease at the early period of CBM production, it then decreased slowly. Much of the water was retained in the coal seams considered during primary CBM extraction. In contrast, when high pressure CO_2 was injected, the water saturation in the vicinity of injection well was reduced, lower than that near production well, hence, more water was displaced through CO_2 injection. The

temperature of the coal seam was disturbed by CBM extraction and CO_2 injection; the temperature in the vicinity of both wells experienced a decrease, especially in the region close to injection well due to the Joule-Thomson cooling effect.

The fracture and matrix porosity were affected by the CBM desorption, effective stress, and CO_2 adsorption. The fracture and matrix porosity in the vicinity of wells were mainly the net result of two competing deformation mechanisms, namely, CO_2 adsorption-induced swelling and CBM desorption-induced shrinking. The fracture porosity and permeability showed a rapid increase due to CBM desorption-induced shrinkage in the area close to the production well, whist there was a large decrease in fracture porosity and permeability in the vicinity of the injection well when CO_2 injection was performed.

For the primary CBM recovery without CO_2 injection, the cumulative CBM production displayed a nonlinear increase with time mainly due to the nonlinear adsorption behaviour of CBM in coal and the permeability change of coal seams. However, this increase is slow compared to the results with CO_2 injection. Although CO_2 injection failed to improve the CBM production initially when no hydraulic fracturing stimulation was adopted, CBM production through CO_2 injection can exceed that during the primary CBM recovery soon and was enhanced significantly with time. When the hydraulic fracturing stimulation was applied, the CBM production can be improved soon and then increases gradually, while this increase is still rapider than that in absence of hydraulic fractures.

The cumulative amount of injected CO_2 overrides the cumulative CBM production greatly at the same time for both simulation cases with and without hydraulic fractures. Compared to the CO_2 injectivity without hydraulic fractures, the CO_2 injectivity was enhanced predominantly, especially in the beginning of CO_2 injection. It can be concluded that CO_2 injection together with hydraulic fracturing stimulation provided an effective solution for the improvement of CO_2 sequestration and CBM recovery from low permeability coal seam considered in this work.

8.6 Overall conclusions

In terms of overall conclusions that can be drawn from the research performed, the following observations are presented:

i. Several aspects relating to the theoretical and numerical modelling of non-isothermal adsorptive fluid flow in deformable fractured coals have been developed in this thesis. Based on a hybrid coupled dual porosity and discrete fracture framework, a local thermal non-equilibrium (LTNE) approach, and porothermoelastic theory, coupled thermal, hydraulic, gas, and deformation behaviour has been considered for media comprised of large scale fractures, a natural fracture network, and a porous matrix. In this work, the model developments have provided new capabilities for the investigation of CO_2 sequestration in coal with ECBM recovery, particularly with regards to the complex geomechanical behaviour involved in the presence of multiscale fractures.

ii. Appropriate relationships were included in the model to enable the analysis of CO_2 sequestration with ECBM recovery. Most notably, the surface stress approach has been introduced to describe the chemo-mechanical deformation of coal in this work, providing further insight into coal-gas interactions. A new porosity and permeability model has been derived, in which the impacts of fluid flow and coal deformation are incorporated. The change of fracture porosity was linked to the variation of matrix porosity through the matrix-fracture compartment with interactions due to the pressure difference between the fracture and matrix continua as well as local swelling resulting from gas adsorption. This development enhanced the capability of the model to predict the influence of coal swelling on coal structure with improved theoretical rigour, which is, in the author's opinion, lacking in the literature.

iii. A set of verification exercises of the developed numerical model was carried out to examine the accuracy of the implementation of the theoretical formulation and the numerical approach taken. The results indicated that the techniques employed to solve the governing equations for flow and deformation, including the sequential scheme used for solving the governing equations for non-isothermal multiphase, multicomponent transport in coal, provide an effective solution for the range of problems considered.

iv. Experimental data on coal-gas interactions and field data of CBM production published in the literature were used as benchmarks for validation of the developed theoretical and numerical models. It was demonstrated that the underlying theoretical framework of the model is valid under the test conditions considered and that the developed model is capable of simulating the salient physical and chemical phenomena related to coal-gas interactions, most notably with regards to gas transport and coal deformation.

v. Analysis of the model application results for CO_2 injection into a coal core at the laboratory scale provided further insights into the gas flow behaviour and coal structural changes. It was found that considerable structural change occurs during adsorptive gas transport in coal. Compared to the reduced fracture porosity, adsorptive gas injection in coal showed the potential to increase the microporosity of coal, a finding that is consistent with experimental results from the literature, which provides an explaination for coal swelling.

vi. The developed model has been used to investigate the influences of key parameters, such as initial coal permeability, initial and residual saturation, and adsorption behaviour on the production performance of CBM. It was found that compared to effects of saturation and adsorption behaviour, the permeability of coal plays a vital role in CBM production. Additional stimulating techniques are required for enhancing the gas production from low permeability coal seams.

vii. Analysis of model application results for CO_2 sequestration to enhance CBM production produced further insights into the coupled processes occurring during CO_2 sequestration with ECBM recovery. The results showed the manner in which the pre-existing physical and chemical equilibrium within coal seams was disturbed for both primary CBM recovery and CO_2 injection. In particular, the permeability of coal was be affected by a combination of interactions associated with CBM desorption, effective stress, and CO_2 adsorption. High pressure CO_2 injection is able to lead to coal swelling and cause loss of permeability, an eventual rebound of coal permeability can be observed during CO_2 sequestration with enhanced CBM recovery. Overall the results from the simulations demonstrated

the ability of the model to represent the coupled physical processes occurring during CO_2 sequestration with ECBM recovery.

viii. The roles of CO_2 injection and hydraulic fracturing on the CBM production and CO_2 injectivity were investigated by calculating the cumulative amount of CBM production and CO_2 injection in the presented numerical simulations. The comparison of results between different simulation scenarios showed that CO_2 injection was able to enhance the CBM production significantly. The application of hydraulic fracture stimulation can not only enhance the gas production considerably but also increase the amount of injected CO_2, especially at the earlier stage. These studies can lead to the conclusion that the proposed numerical model is able to account for the influence of multiscale fractures whilst maintaining the ability to represent the important features of behaviour highlighted in the simulation of CO_2 sequestration with ECBM recovery.

ix. Overall, it is claimed that the hybrid coupled dual porosity-discrete fracture model developed in this work has improved the capabilities of a coupled THCM model significantly. The findings presented in this thesis provide importanct insights into the geomechanical behaviour related to CO_2 sequestration in coal seams and enhanced CBM recovery and demonstrates the ability of the model to predict the multiscale flow. The newly developed model in this thesis can be further utilised in the study of a broad new range of applications involving non-isothermal, multiphase, multicomponent gas transport in unconventional gas reservoirs.

8.7 Suggestions for future research

The following suggestions are made for further research and developments especially for modelling the coupled processes related to CO_2 sequestration in coal seams.

Apart from the inclusion of discrete fractures, this study has considered the bulk coal as a homogeneous isotropic material. The naturally occurring fractures, which are an important feature of coal for CO_2 sequestration, were idealised as a fracture continuum with isotropic material properties. The nonuniform distribution of natural fractures and the anisotropy of flow have not been incorporated in this work. The role of fractures in bulk deformation of

coal is represented via the effective stress coefficient, while the difference between the matrix and fracture deformations has been ignored. Also, the material deformation due to chemo-mechanical interactions is assumed to be elastic and reversible without consideration of plastic deformation.

Continued efforts are required to study and theorise the coupled THCM behaviour of coal-gas systems at multiple scales. Whilst the surface stress concept has been introduced to describe the coal swelling/shrinkage in this study, the physical and chemical mechanisms involved need to be considered in more detail within a coupled framework to improve our current understanding and prediction of this critical behaviour under in-situ conditions. This is of particular importance to the success of CO_2 injection into coal seams.

The principal gas reaction considered in this work was the adsorption/desorption coal-gas interaction; the dissolution of high pressure gas in water has been neglected. Thus, additional theoretical advancement is required for future research of the geochemistry associated with CO_2 dissolution and transport in coal seams, which assists to advance the capabilities of numerical models for the long term study of the storage security of CO_2 sequestration.

It is well recognised that the coal swelling phenomenon is a significant constraint on the prospects for achieving CO_2 sequestration in coal at field scale. Pilot-tests have indicated that hydraulic fracturing restores permeability and may be a promising technology to increase CO_2 injectivity in low permeability coal reservoirs. In the current study, the large induced fractures have been assumed to be static and their propagation was ignored. Hence, it is suggested that further research both experimentally and numerically investigates the fracture propagation process and its effect on the permeability evolution of the coal as well as the potential role it might play in CO_2 sequestration.

In the application of the numerical model, the coal seams have been treated as an infinite two-dimensional plane strain model. The effect of overburden on coal deformation has not been investigated in this work, hence, extension of model application to three dimensional problems is suggested for future research. With the inclusion of this suggestion, the computational demands of the numerical model will increase. To allow realistic solution times for this more complex model and for large scale problems, methods to reduce the run time of a simulation should be considered. In particular, high performance computing techniques should be employed.

The suggestions mentioned above are by no means exhaustive; rather they present promising directions of further research which are most closely related to the work presented in this thesis.

Appendix A

The coefficients of the aforementioned governing equations in chapter 3 are given as following:

For equation (3.43):

$$C_{\mathrm{c_m c_m}} = \delta_{ij} n_{\mathrm{m}} S_{\mathrm{gm}} - n_{\mathrm{m}} c_{\mathrm{m}}^{i} R Z_{\mathrm{m}} T_{\mathrm{m}} \frac{\partial S_{\mathrm{lm}}}{\partial s_{\mathrm{m}}} + \rho_s \frac{\partial V^{i}}{\partial c_{\mathrm{m}}^{j}}$$

$$+ n_{\mathrm{m}} S_{\mathrm{gm}} c_{\mathrm{m}}^{i} \left[(\tilde{\mathfrak{b}}_1 - n_m) c_s + (\tilde{\mathfrak{b}}_2 - n_f)(c_m - c_s) \right] \frac{\partial u_{\mathrm{m}}^{a}}{\partial c_{\mathrm{m}}^{j}} + n_{\mathrm{m}} S_{\mathrm{gm}} c_{\mathrm{m}}^{i} \frac{\partial \varepsilon_{sl}}{\partial c_{\mathrm{m}}^{j}} \quad (3.43a)$$

$$C_{\mathrm{c_m c_f}} = -n_{\mathrm{m}} S_{\mathrm{gm}} c_{\mathrm{m}}^{i} (\tilde{\mathfrak{b}}_2 - n_f)(c_m - c_s) \frac{\partial u_{\mathrm{f}}}{\partial c_{\mathrm{f}}^{i}} \quad (3.43b)$$

$$C_{\mathrm{c_m l_m}} = n_{\mathrm{m}} c_{\mathrm{m}}^{i} \frac{\partial S_{\mathrm{lm}}}{\partial s_{\mathrm{m}}} + n_{\mathrm{m}} S_{\mathrm{gm}} c_{\mathrm{m}}^{i} \left[(\tilde{\mathfrak{b}}_1 - n_m) c_s + (\tilde{\mathfrak{b}}_2 - n_f)(c_m - c_s) \right] \frac{\partial u_{\mathrm{m}}}{\partial u_{\mathrm{lm}}} \quad (3.43c)$$

$$C_{\mathrm{c_m l_f}} = -n_{\mathrm{m}} S_{\mathrm{gm}} c_{\mathrm{m}}^{i} (\tilde{\mathfrak{b}}_2 - n_f)(c_m - c_s) \frac{\partial u_{\mathrm{f}}}{\partial u_{\mathrm{lf}}} \quad (3.43d)$$

$$C_{\mathrm{c_m T_m}} = -n_{\mathrm{m}} c_{\mathrm{m}}^{i} \frac{\partial S_{\mathrm{lm}}}{\partial s_{\mathrm{m}}} Z_{\mathrm{m}} R \sum_{j=1}^{n_g} c_{\mathrm{m}}^{j} + \rho_s \frac{\partial V^{i}}{\partial T_{\mathrm{m}}}$$

$$+ n_{\mathrm{m}} S_{\mathrm{gm}} c_{\mathrm{m}}^{i} \left[(\tilde{\mathfrak{b}}_1 - n_m) c_s + (\tilde{\mathfrak{b}}_2 - n_f)(c_m - c_s) \right] \frac{\partial u_{\mathrm{m}}^{a}}{\partial T_{\mathrm{m}}} + n_{\mathrm{m}} S_{\mathrm{gm}} c_{\mathrm{m}}^{i} \frac{\partial \varepsilon_{sl}}{\partial T_{\mathrm{m}}} \quad (3.43e)$$

$$C_{\mathrm{c_m T_f}} = -n_{\mathrm{m}} S_{\mathrm{gm}} c_{\mathrm{m}}^{i} (\tilde{\mathfrak{b}}_2 - n_f)(c_m - c_s) R Z_{\mathrm{f}} \sum_{j=1}^{n_g} c_{\mathrm{f}}^{j} - n_{\mathrm{m}} S_{\mathrm{gm}} c_{\mathrm{m}}^{i} (\tilde{\mathfrak{b}}_2 - n_f)(c_m - c_s) \frac{\partial u_{\mathrm{f}}}{\partial T_{\mathrm{f}}}$$

$$(3.43f)$$

$$C_{\mathrm{c_m u_s}} = \theta_{\mathrm{gm}} c_{\mathrm{m}}^{i} \tilde{\mathfrak{b}}_1 \mathbf{m}^{\boldsymbol{T}} \boldsymbol{B} \quad (3.43g)$$

$$Q_{\mathrm{c_m}}^{i} = \frac{1}{\tau} (c_{\mathrm{f}}^{i} - c_{\mathrm{m}}^{i}) \quad (3.43h)$$

For equation (3.44):

$$C_{\mathrm{c_f c_m}} = -n_{\mathrm{f}} S_{\mathrm{gf}} c_{\mathrm{f}}^{i} (\tilde{\mathrm{b}}_2 - n_{\mathrm{f}})(c_m - c_s) \frac{\partial u_{\mathrm{m}}^{a}}{\partial c_{\mathrm{m}}^{j}} - n_{\mathrm{f}} S_{\mathrm{gf}} c_{\mathrm{f}}^{i} \frac{\partial \varepsilon_{sl}}{\partial c_{\mathrm{m}}^{j}} \quad (3.44a)$$

$$C_{\mathrm{c_f c_f}} = \delta_{ij} n_{\mathrm{f}} S_{\mathrm{gf}} - n_{\mathrm{f}} c_{\mathrm{f}}^{i} R Z_{\mathrm{f}} T_{\mathrm{f}} \frac{\partial S_{\mathrm{lf}}}{\partial s_{\mathrm{f}}} + n_{\mathrm{f}} S_{\mathrm{gf}} c_{\mathrm{f}}^{i} \left[(\tilde{\mathrm{b}}_2 - n_m) c_s + \left(\tilde{\mathrm{b}}_2 - n_f \right) (c_m - c_s) \right] R Z_{\mathrm{f}} T_{\mathrm{f}} \quad (3.44b)$$

$$C_{\mathrm{c_f l_m}} = -n_{\mathrm{f}} S_{\mathrm{gf}} (\tilde{\mathrm{b}}_2 - n_{\mathrm{f}})(c_m - c_s) \frac{\partial u_{\mathrm{m}}}{\partial u_{\mathrm{lm}}} \quad (3.44c)$$

$$C_{\mathrm{c_f l_f}} = n_{\mathrm{f}} c_{\mathrm{f}}^{i} \frac{\partial S_{\mathrm{lf}}}{\partial s_{\mathrm{f}}} + n_{\mathrm{f}} S_{\mathrm{gf}} c_{\mathrm{f}}^{i} \left[(\tilde{\mathrm{b}}_2 - n_m) c_s + \left(\tilde{\mathrm{b}}_2 - n_f \right) (c_m - c_s) \right] \frac{\partial u_{\mathrm{f}}}{\partial u_{\mathrm{lf}}} \quad (3.44d)$$

$$C_{\mathrm{c_f T_m}} = -n_{\mathrm{f}} S_{\mathrm{gf}} c_{\mathrm{f}}^{i} (\tilde{\mathrm{b}}_2 - n_{\mathrm{f}})(c_m - c_s) \frac{\partial u_{\mathrm{m}}^{a}}{\partial T_{\mathrm{m}}} - n_{\mathrm{f}} S_{\mathrm{gf}} c_{\mathrm{f}}^{i} \frac{\partial \varepsilon_{sl}}{\partial T_{\mathrm{m}}} \quad (3.44e)$$

$$C_{\mathrm{c_f T_f}} = -n_{\mathrm{f}} c_{\mathrm{f}}^{i} \frac{\partial S_{\mathrm{lf}}}{\partial s_{\mathrm{f}}} Z_{\mathrm{f}} R \sum_{j=1}^{n_g} c_{\mathrm{f}}^{j} + n_{\mathrm{f}} S_{\mathrm{gf}} c_{\mathrm{f}}^{i} \left[(\tilde{\mathrm{b}}_2 - n_m) c_s + \left(\tilde{\mathrm{b}}_2 - n_f \right) (c_m - c_s) \right] \frac{\partial u_{\mathrm{f}}}{\partial T_{\mathrm{f}}} \quad (3.44f)$$

$$C_{\mathrm{c_f u_s}} = \theta_{\mathrm{gf}} c_{\mathrm{f}}^{i} \tilde{\mathrm{b}}_2 \mathbf{m}^{\boldsymbol{T}} \boldsymbol{B} \quad (3.44g)$$

$$K_{\mathrm{c_f c_f}} = c_{\mathrm{gf}}^{i} \frac{K_{\mathrm{f}} K_{\mathrm{rgf}}}{\mu_{\mathrm{gf}}} Z_{\mathrm{f}} R T_{\mathrm{f}} \quad (3.44h)$$

$$K_{\mathrm{c_f T_f}} = c_{\mathrm{f}}^{i} \frac{K_{\mathrm{f}} \mathrm{K}_{\mathrm{rgf}}}{\mu_{\mathrm{gf}}} Z_{\mathrm{f}} R \sum_{j=1}^{n_g} c_{\mathrm{f}}^{j} \quad (3.44i)$$

$$Q_{\mathrm{c_f}}^{i} = -\frac{1}{\tau} \left(c_{\mathrm{f}}^{i} - c_{\mathrm{m}}^{i} \right) + \Gamma_{gfF}^{i} \quad (3.44j)$$

For equation (3.45):

$$C_{\mathrm{c_F c_F}} = \delta_{ij} w S_{\mathrm{gF}} - w c_{\mathrm{F}}^{i} R Z_{\mathrm{F}} T_{\mathrm{F}} \frac{\partial S_{\mathrm{lF}}}{\partial s_{\mathrm{F}}} \quad (3.45a)$$

$$C_{\mathrm{c_F l_F}} = w c_{\mathrm{F}}^{i} \frac{\partial S_{\mathrm{lF}}}{\partial s_{\mathrm{F}}} \quad (3.45b)$$

$$C_{\mathrm{c_F T_F}} = -w c_{\mathrm{F}}^{i} \frac{\partial S_{\mathrm{lF}}}{\partial s_{\mathrm{F}}} Z_{\mathrm{f}} R \sum_{j=1}^{n_g} c_{\mathrm{F}}^{j} \quad (3.45c)$$

$$K_{\mathrm{c_F c_F}} = c_{\mathrm{F}}^{i} \frac{K_{rgF} w^3}{12 \mu_{\mathrm{gF}}} Z_{\mathrm{f}} R T_F \tag{3.45d}$$

$$K_{\mathrm{c_F T_F}} = c_{\mathrm{F}}^{i} \frac{K_{\mathrm{rgF}} w^3}{12 \mu_{\mathrm{gF}}} Z_F R \sum_{j=1}^{n_g} c_{\mathrm{F}}^{j} \tag{3.45e}$$

$$Q_{\mathrm{c_F}}^{i} = -\Gamma_{\mathrm{gfF}}^{i} \tag{3.45f}$$

For equation (3.64)

$$C_{\mathrm{l_m c_m}} = n_{\mathrm{m}} R Z_{\mathrm{m}} T_{\mathrm{m}} \frac{\partial S_{\mathrm{lm}}}{\partial s_{\mathrm{m}}} + S_{\mathrm{lm}} \left[(\tilde{\mathrm{b}}_1 - n_m) c_s + \left(\tilde{\mathrm{b}}_2 - n_f \right) (c_m - c_s) \right] \frac{\partial u_{\mathrm{m}}^{a}}{\partial c_{\mathrm{m}}^{j}} + S_{\mathrm{lm}} \frac{\partial \varepsilon_{sl}}{\partial c_{\mathrm{m}}^{j}} \tag{3.64a}$$

$$C_{\mathrm{l_m c_f}} = -S_{\mathrm{lm}} \left(\tilde{\mathrm{b}}_2 - n_f \right) (c_m - c_s) \frac{\partial u_{\mathrm{f}}}{\partial c_{\mathrm{f}}^{j}} \tag{3.64b}$$

$$C_{\mathrm{l_m l_m}} = n_{\mathrm{m}} S_{\mathrm{lm}} c_{\mathrm{l}} - n_{\mathrm{m}} \frac{\partial S_{\mathrm{lm}}}{\partial s_{\mathrm{m}}} + S_{\mathrm{lm}} \left[(\tilde{\mathrm{b}}_1 - n_m) c_s + \left(\tilde{\mathrm{b}}_2 - n_f \right) (c_m - c_s) \right] \frac{\partial u_{\mathrm{m}}}{\partial u_{\mathrm{lm}}} \tag{3.64c}$$

$$C_{\mathrm{l_m l_f}} = -S_{\mathrm{lm}} \left(\tilde{\mathrm{b}}_2 - n_f \right) (c_m - c_s) \frac{\partial u_{\mathrm{f}}}{\partial u_{\mathrm{lf}}} \tag{3.64d}$$

$$C_{\mathrm{l_m T_m}} = n_{\mathrm{m}} Z_{\mathrm{m}} R \frac{\partial S_{\mathrm{lm}}}{\partial s_{\mathrm{m}}} \sum_{i=1}^{n_g} c_{\mathrm{m}}^{i} - n_{\mathrm{m}} S_{\mathrm{lm}} \alpha_{\mathrm{lT}} + S_{\mathrm{lm}} \left[(\tilde{\mathrm{b}}_1 - n_m) c_s + \left(\tilde{\mathrm{b}}_2 - n_f \right) (c_m - c_s) \right] \frac{\partial u_{\mathrm{m}}^{a}}{\partial T_{\mathrm{m}}} + S_{\mathrm{lm}} \frac{\partial \varepsilon_{sl}}{\partial T_{\mathrm{m}}} \tag{3.64e}$$

$$C_{\mathrm{l_m T_f}} = -S_{\mathrm{lm}} \left(\tilde{\mathrm{b}}_2 - n_f \right) (c_m - c_s) \frac{\partial u_{\mathrm{f}}}{\partial T_{\mathrm{f}}} \tag{3.64f}$$

$$C_{\mathrm{l_m u_s}} = S_{\mathrm{lm}} \tilde{\mathrm{b}}_1 \mathbf{m}^{T} \boldsymbol{B} \tag{3.64g}$$

$$K_{\mathrm{l_m l_m}} = S_{\mathrm{lm}} \frac{K_{\mathrm{rlm}} K_{\mathrm{m}}}{\mu_{\mathrm{lm}}} \tag{3.64h}$$

$$Q_{\mathrm{l_m}} = \Omega_l \frac{\delta}{l^2} \frac{K_{\mathrm{rlm}} K_{\mathrm{m}}}{\mu_{\mathrm{lm}}} (u_{\mathrm{lf}} - u_{\mathrm{lm}}) \tag{3.64i}$$

For equation (3.65)

$$C_{\mathrm{l_f c_m}} = -S_{\mathrm{lf}}(\tilde{\mathrm{b}}_2 - n_{\mathrm{f}})(c_m - c_s)\frac{\partial u_{\mathrm{m}}^a}{\partial c_{\mathrm{m}}^j} - S_{\mathrm{lf}}\frac{\partial \varepsilon_{sl}}{\partial c_{\mathrm{m}}^j} \tag{3.65a}$$

$$C_{\mathrm{l_f c_f}} = n_{\mathrm{f}} R Z_{\mathrm{f}} T_{\mathrm{f}}\frac{\partial S_{\mathrm{lf}}}{\partial s_{\mathrm{f}}} + S_{\mathrm{lf}}[(\tilde{\mathrm{b}}_2 - n_{\mathrm{f}})c_s + (\tilde{\mathrm{b}}_2 - n_{\mathrm{f}})(c_m - c_s)]\frac{\partial u_{\mathrm{f}}}{\partial c_{\mathrm{f}}^j} \tag{3.65b}$$

$$C_{\mathrm{l_f l_m}} = -S_{\mathrm{lf}}(\tilde{\mathrm{b}}_2 - n_{\mathrm{f}})(c_m - c_s)\frac{\partial u_{\mathrm{m}}^a}{\partial u_{\mathrm{lm}}} \tag{3.65d}$$

$$C_{\mathrm{l_f l_f}} = n_{\mathrm{f}} S_{\mathrm{lf}} c_{\mathrm{l}} - n_{\mathrm{f}}\frac{\partial S_{\mathrm{lf}}}{\partial s_{\mathrm{f}}} + S_{\mathrm{lf}}[(\tilde{\mathrm{b}}_2 - n_{\mathrm{f}})c_s + (\tilde{\mathrm{b}}_2 - n_{\mathrm{f}})(c_m - c_s)]\frac{\partial u_{\mathrm{f}}}{\partial u_{\mathrm{lf}}} \tag{3.65c}$$

$$C_{\mathrm{l_f T_m}} = -S_{\mathrm{lf}}(\tilde{\mathrm{b}}_2 - n_{\mathrm{f}})(c_m - c_s)\frac{\partial u_{\mathrm{m}}^a}{\partial T_{\mathrm{m}}} - S_{\mathrm{lf}}\frac{\partial \varepsilon_{sl}}{\partial T_{\mathrm{m}}} \tag{3.65e}$$

$$C_{\mathrm{l_f T_f}} = n_{\mathrm{f}} Z_{\mathrm{f}} R\frac{\partial S_{\mathrm{lf}}}{\partial s_{\mathrm{f}}}\sum_{j=1}^{n_g} c_{\mathrm{f}}^j - n_{\mathrm{f}} S_{\mathrm{lf}}\alpha_{\mathrm{lT}} + S_{\mathrm{lf}}[(\tilde{\mathrm{b}}_2 - n_{\mathrm{f}})c_s + (\tilde{\mathrm{b}}_2 - n_{\mathrm{f}})(c_m - c_s)]\frac{\partial u_{\mathrm{f}}}{\partial T_{\mathrm{f}}} \tag{3.65f}$$

$$C_{\mathrm{l_f u_s}} = S_{\mathrm{lf}}\tilde{\mathrm{b}}_2 \mathbf{m}^{\boldsymbol{T}}\boldsymbol{B} \tag{3.65g}$$

$$K_{\mathrm{l_f l_f}} = \frac{K_{\mathrm{rlf}} K_{\mathrm{f}}}{\mu_{\mathrm{lf}}} \tag{3.65h}$$

$$Q_{\mathrm{l_f}} = -\Omega_l\frac{\delta}{l^2}\frac{K_{\mathrm{rlm}} K_{\mathrm{m}}}{\mu_{\mathrm{lm}}}(u_{\mathrm{lf}} - u_{\mathrm{lm}}) + \Gamma_{\mathrm{lfF}} \tag{3.65i}$$

For equation (3.66)

$$C_{\mathrm{l_F l_F}} = wS_{\mathrm{lF}} c_{\mathrm{l}} - w\frac{\partial S_{\mathrm{lF}}}{\partial s_{\mathrm{F}}} \tag{3.66a}$$

$$C_{\mathrm{l_F c_F}} = wRZ_{\mathrm{F}} T_{\mathrm{F}}\frac{\partial S_{\mathrm{lF}}}{\partial s_{\mathrm{F}}} \tag{3.66b}$$

$$C_{\mathrm{l_F T_F}} = wZ_{\mathrm{F}} R\frac{\partial S_{\mathrm{lF}}}{\partial s_{\mathrm{F}}}\sum_{i=1}^{n_g} c_{\mathrm{F}}^i - wS_{\mathrm{lF}} c_{\mathrm{lT}} \tag{3.66c}$$

$$K_{\mathrm{l_F l_F}} = \frac{K_{\mathrm{rlF}} w^3}{12\mu_{\mathrm{lF}}} \tag{3.66d}$$

$$Q_{\mathrm{l_F}} = -\Gamma_{\mathrm{lfF}} \tag{3.66e}$$

For equation (3.118)

$$C_{\mathrm{T_m T_m}} = \left(\rho_{\mathrm{m}} C_{\mathrm{pm}}\right)_{\mathrm{eff}} - n_{\mathrm{m}} \mathrm{S_{gm}}\left(\rho_{\mathrm{gm}} C_{\mathrm{pgm}} \mu_{\mathrm{JT}} + 1\right) Z_{\mathrm{m}} R \sum_{j=1}^{n_g} c_{\mathrm{m}}^{j} \tag{3.118a}$$

$$C_{\mathrm{T_m c_m}} = -n_{\mathrm{m}} S_{\mathrm{gm}}\left(\rho_{\mathrm{gm}} C_{\mathrm{pgm}} \mu_{JT} + 1\right) \mathrm{Z_m} R T_{\mathrm{m}} \tag{3.118b}$$

$$K_{\mathrm{T_m T_m}} = \lambda_{\mathrm{em}} \tag{3.118c}$$

$$K^{\mathrm{v}}_{\mathrm{T_m T_m}} = -\left(S_{\mathrm{lm}} \rho_l C_{\mathrm{pl}} \mathbf{v}_{\mathrm{lm}} + S_{\mathrm{gm}} \rho_{\mathrm{gm}} C_{\mathrm{pgm}} \mathbf{v}_{\mathrm{gm}}\right) + S_{\mathrm{gm}} \rho_{\mathrm{gm}} C_{\mathrm{pgm}} \mathbf{v}_{\mathrm{gm}} \mu_{\mathrm{JT}} Z_{\mathrm{m}} R \sum_{j=1}^{n_g} c_{\mathrm{m}}^{j} \tag{3.118d}$$

$$\mathrm{K^{v}_{T_m c_m}} = S_{\mathrm{gm}} \rho_{\mathrm{gm}} C_{\mathrm{pgm}} \mathbf{v}_{\mathrm{gm}} \mu_{\mathrm{JT}} Z_{\mathrm{m}} R T_{\mathrm{m}} \tag{3.118e}$$

$$Q_{\mathrm{T_m}} = h_T A_{fm}(T_{\mathrm{f}} - T_{\mathrm{m}}) + \left(\Gamma_{\mathrm{lfm}} c_{pl} + \Gamma_{\mathrm{gfm}} c_{\mathrm{pg}}\right)(T_{\mathrm{f}} - T_{\mathrm{m}}) + q_{\mathrm{ms}} \tag{3.118f}$$

For equation (3.119)

$$C_{\mathrm{T_f T_f}} = \left(\rho_{\mathrm{f}} C_{\mathrm{pf}}\right)_{\mathrm{eff}} - n_{\mathrm{f}} S_{\mathrm{gf}}\left(\rho_{\mathrm{gf}} C_{\mathrm{pgf}} \mu_{\mathrm{JT}} + 1\right) Z_{\mathrm{f}} R \sum_{j=1}^{n_g} c_{\mathrm{f}}^{j} \tag{3.119a}$$

$$C_{\mathrm{T_f c_f}} = -n_{\mathrm{f}} S_{\mathrm{gf}}\left(\rho_{\mathrm{gf}} C_{\mathrm{pgf}} \mu_{\mathrm{JT}} + 1\right) Z_{\mathrm{f}} R T_{\mathrm{f}} \tag{3.119b}$$

$$K_{\mathrm{T_f T_f}} = \lambda_{\mathrm{ef}} \tag{3.119c}$$

$$K^{\mathrm{v}}_{\mathrm{T_f T_f}} = -\left(S_{\mathrm{wf}} \rho_{\mathrm{l}} C_{\mathrm{pl}} \mathbf{v}_{\mathrm{lf}} + S_{\mathrm{gf}} \rho_{\mathrm{gf}} C_{\mathrm{pgf}} \mathbf{v}_{\mathrm{gf}}\right) + S_{\mathrm{gf}} \rho_{\mathrm{gf}} C_{\mathrm{pgf}} \mathbf{v}_{\mathrm{gf}} \mu_{\mathrm{JT}} Z_{\mathrm{f}} R \sum_{j=1}^{n_g} c_{\mathrm{f}}^{j} \tag{3.119d}$$

$$K^{\mathrm{v}}_{\mathrm{T_f c_f}} = S_{\mathrm{gf}} \rho_{\mathrm{gf}} C_{\mathrm{pgf}} \mathbf{v}_{\mathrm{gf}} \mu_{\mathrm{JT}} Z_{\mathrm{f}} R T_{\mathrm{f}} \tag{3.119e}$$

$$Q_{\mathrm{T_f}} = -h_{\mathrm{T}} A_{\mathrm{fm}}(T_{\mathrm{f}} - T_{\mathrm{m}}) - \left(\Gamma_{\mathrm{lfm}} c_{\mathrm{pl}} + \Gamma_{\mathrm{gfm}} c_{\mathrm{pg}}\right)(T_{\mathrm{f}} - T_{\mathrm{m}}) + q_{\mathrm{fF}} + q_{\mathrm{fs}} \tag{3.119f}$$

For equation (3.120)

$$C_{\mathrm{T_F T_F}} = w\left(\rho_{\mathrm{F}} C_{\mathrm{pF}}\right)_{\mathrm{eff}} - wS_{\mathrm{gF}}\left(\rho_{\mathrm{gF}} C_{\mathrm{pgF}} \mu_{\mathrm{JT}} + 1\right) Z_{\mathrm{F}} R \sum_{j=1}^{n_g} c_{\mathrm{F}}^{j} \tag{3.120a}$$

$$C_{\mathrm{T_F c_F}} = -wS_{\mathrm{gF}}\left(\rho_{\mathrm{gF}} C_{\mathrm{pgF}} \mu_{\mathrm{JT}} + 1\right) Z_{\mathrm{F}} R T_F \tag{3.120b}$$

$$K_{\mathrm{T_F T_F}} = w\lambda_{\mathrm{eF}} \tag{3.120c}$$

$$K^{\mathrm{v}}_{\mathrm{T_F T_F}} = -\left(wS_{\mathrm{lF}} \rho_l C_{\mathrm{pl}} \mathbf{v}_{\mathrm{lF}} + wS_{\mathrm{gF}} \rho_{\mathrm{gF}} C_{\mathrm{pgF}} \mathbf{v}_{\mathrm{gF}}\right) + wS_{\mathrm{gF}} \rho_{\mathrm{gF}} C_{\mathrm{pgF}} \mathbf{v}_{\mathrm{gF}} \mu_{\mathrm{JT}} Z_{\mathrm{F}} R \sum_{j=1}^{n_g} c_{\mathrm{F}}^{j} \tag{3.120d}$$

$$K^{\mathrm{v}}_{\mathrm{T_F c_F}} = wS_{\mathrm{gF}} \rho_{\mathrm{gF}} C_{\mathrm{pgF}} \mathbf{v}_{\mathrm{gF}} \mu_{\mathrm{JT}} Z_{\mathrm{F}} R T_{\mathrm{F}} \tag{3.120e}$$

$$Q_{\mathrm{T_F}} = -q_{\mathrm{fF}} + q_{\mathrm{Fs}} \tag{3.120f}$$

For equation (3.138)

$$C_{\mathbf{u}_{\mathrm{s}} \mathrm{c_m}} = \mathbf{B}^{\boldsymbol{T}} \mathbf{m} \tilde{\mathfrak{b}}_1 S_{\mathrm{gm}} Z_{\mathrm{m}} R T_{\mathrm{m}} - \frac{1}{3} \mathbf{B}^{\boldsymbol{T}} \boldsymbol{D}_{\mathrm{e}} \mathbf{m} A_s^j \tag{3.138a}$$

$$C_{\mathbf{u}_{\mathrm{s}} \mathrm{c_f}} = \mathbf{B}^{\boldsymbol{T}} \mathbf{m} \tilde{\mathfrak{b}}_2 S_{\mathrm{gf}} Z_{\mathrm{f}} R T_{\mathrm{f}} \tag{3.138b}$$

$$C_{\mathbf{u}_{\mathrm{s}} \mathrm{l_m}} = \mathbf{B}^{\boldsymbol{T}} \mathbf{m} \tilde{\mathfrak{b}}_1 S_{\mathrm{lm}} \tag{3.138c}$$

$$C_{\mathbf{u}_{\mathrm{s}} \mathrm{l_f}} = \mathbf{B}^{\boldsymbol{T}} \mathbf{m} \tilde{\mathfrak{b}}_2 S_{\mathrm{lf}} \tag{3.138d}$$

$$C_{\mathbf{u}_{\mathrm{s}} \mathrm{T_m}} = \mathbf{B}^{\boldsymbol{T}} \mathbf{m} \tilde{\mathfrak{b}}_1 S_{\mathrm{gm}} Z_{\mathrm{m}} R \sum_{i=1}^{n_g} c_{\mathrm{m}}^{i} - \frac{1}{3} \mathbf{B}^{\boldsymbol{T}} \boldsymbol{D}_{\mathrm{e}} \mathbf{m} A_T \tag{3.138e}$$

$$C_{\mathbf{u}_{\mathrm{s}} \mathrm{T_f}} = \mathbf{B}^{\boldsymbol{T}} \mathbf{m} \tilde{\mathfrak{b}}_2 \, S_{\mathrm{gf}} Z_{\mathrm{f}} R \sum_{i=1}^{n_g} c_{\mathrm{f}}^{i} \tag{3.138f}$$

$$C_{\mathbf{u}_{\mathrm{s}} \mathbf{u}_{\mathrm{s}}} = \mathbf{B}^{\boldsymbol{T}} \boldsymbol{D}_{\mathrm{e}} \mathbf{B} \tag{3.138g}$$